Master's thesis

NTNU
Norwegian University of Science and Technology
Faculty of Engineering
Department of Geoscience and Petroleum

Simon Fredrik Gundersen

Structural controls on selected sulphide deposits in the Mofjellet Group

Master's thesis in Geology
Supervisor: Bjørn Eske Sørensen
June 2020

NTNU
Kunnskap for en bedre verden

Simon Fredrik Gundersen

Structural controls on selected sulphide deposits in the Mofjellet Group

Master's thesis in Geology
Supervisor: Bjørn Eske Sørensen
June 2020

Norwegian University of Science and Technology
Faculty of Engineering
Department of Geoscience and Petroleum

NTNU
Norwegian University of
Science and Technology

I would like to thank Sotkamo Silver Oy, the Geological Survey of Norway (NGU), and the Norwegian University of Science and Technology (NTNU) for the challenging project they provided me, and for the doors they have opened for me into the exciting field of ore geology. I even got a trip to Finland for four weeks and experienced how a silver mine is operated! I am grateful to my supervisor prof. Bjørn Eske Sørensen, who has guided me through this thesis and provided me knowledge, good ideas and valuable discussions. Also, the highly experienced and friendly geologists at NGU, especially my co-supervisor Dr. Terje Bjerkgård and also Dr. Trond Slagstad, who has helped me with difficult questions, fieldwork, and geochronology. Despite not being my supervisor, Trond has helped me way more than I ever could have expected in the field of regional geology, proving both his friendliness and dedication to the field. I would also thank my co-supervisor prof. Rune Berg-Edland Larsen for fun and educational field trips and good discussions. Berit Berbusmel, who has been my partner-in-crime in the field and at the stay in Sotkamo, deserves a huge thanks for being a discussion partner and friend, and also for listening to my bullshit every now and then. This project would have been way more challenging without my girlfriend, Emilie, who has supported me through ups and downs during the last year, and especially during the isolated months of Corona. I would like to thank the class of ’20 and to all my friends in Trondheim for making this two forever memorable years in my life here. Lastly, I would like to thank my family for the support they have given me in my education.

Abstract

Lithological and structural controlled VMS deposit is well known from polyphase deformed terrains within the Scandinavian Caledonides. Here, the petrotectonic origin and the metamorphic and deformational evolution of selected areas within the Mofjellet Group is investigated, and compiled into a 3D-model. Geological mapping and sampling formed the basis of structural, geochronological, mineralogical, and geochemical analysis and evaluations.

The Mofjellet Group is part of the Rödingsfjället Nappe Complex (RNC) within the Uppermost Allochthon, and as found here, represents a 499 ± 12 Ma bimodal felsic volcanic arc formed adjacent to a continent. The latter is evident from the enriched geochemical pattern, calc-alkaline and peraluminous nature of the rocks, which also is reflected in the sphalerite-rich ore deposits. These are typical of felsic predominated systems, analogous to the modern island of Japan, the type locality of the Kuroko VMS deposit. The source rock was depleted peridotite overprinted by slab fluids, followed by melt fractionation, and probably crust contamination and/or magma mixing, leading to the calc-alkaline trend and dominance of felsic rocks. The high H_2O content caused the high-LIL/HFS element pattern typical for continental margin arcs, and was possibly an important contributor in the ore forming process.

Late Cambrian to Mid-Silurian deformation has metamorphosed and folded the rocks during at least four stages. F_1 produced a transposed layering evident from discontinuous quartz layers and rootless folds. F_2 produced the main S_2 foliation by tight to isoclinal folds with E-W fold axes, wherein sulphide mineralizations were remobilized and concentrated into related hinge zones. Peak metamorphic conditions at amphibolite facies were reached, and probably reached even higher grades than the estimated 600 °C and 10 kbar. The F_2 phase was followed by retrogression forming a retrogressive assemblage of chlorite, clinozoisite and zoisite. The succeeding F_3 refolded the S_2 foliation into coaxial open folds, while increasing metamorphic conditions formed new garnets, but did not reach the peak of F_2 metamorphism. The P-T estimate probably reflects the peak conditions of this phase. Titanite ages of 465 ± 21 Ma are probably related to this event and is also coeval with the Ordovician Taconian orogeny, which is familiar to other Laurentian terranes within the Uppermost Allochthon, and brings additional evidence of pre-Scandian deformation. F_4 is related to Scandian deformation and refolded the earlier structures into open NE-SW fold axes, which created the basin structure of Hesjelia-Hammertjønna due to interference with F_3 folds, and the variable plunge in the Hellerfjellet deposit due to parasitic folding. Post-F_4 extension produced boudins and open folds of late pegmatite intrusions.

The result of the polyphase deformation is built into a 3D model of the ore deposits at Hesjelia-Hammertjønna and Hellerfjellet. Based on drill cores in Hesjelia it was possible to do correlations according to the geological constraints, resulting in *four* isolated zones. The largest uncertainty concerns the deposit's structural behaviour towards Hammertjønna, wherein all observed ore lenses occur at the same level along strike. This is also the case at Hellerfjellet, and an explanation for the discontinuous pattern of the many but small lenses at these two localities is shearing during the F_2 folding phase.

Sammendrag

Litologisk og strukturelt kontrollerte VMS-avsetninger er velkjent fra polydeformerte metamorfe områder i de Skandinaviske Kaledonidene. I denne studien undersøkes den petrotektoniske opprinnelsen og den metamorfe og deformasjonsmessige utviklingen av utvalgte områder innen Mofjellgruppen, som til slutt sammenstilles til en 3D-modell. Geologisk kartlegging og prøvetaking dannet grunnlaget for strukturell, geokronologisk, mineralogisk og geokjemisk analyse og evalueringer.

Mofjellgruppen er en del av Rödingsfjället skyvedekkekompleks (RNC) innenfor den øverste Allokton, og representerer en 499 ± 12 Ma bimodal felsisk vulkansk øybue dannet nært et kontinent. Det siste utrykkes av et beriket geokjemisk mønster, kalkalkalisk og peraluminøs sammensetning av bergartene, noe som også gjenspeiles i de sinkblende-rike malmforekomstene. Dette er typisk for felsisk-dominerte systemer, analogt med dagens Japan, den typiske lokaliteten til Kuroko VMS forekomster. Kildebergarten er en utarmet peridotitt som er påvirket av væsker fra den subduserende oseaniske plate, etterfulgt av smeltefraksjonering og sannsynligvis skorpeforurensning og/eller magma-miksing, noe som førte til den kalkalkaliske trend og dominansen av felsiske bergarter. Det høye H_2O-innholdet forårsaket berikelsen av de lette jordartene og «large-ion-lithophile elements» (LILE) relativt til tunge jordarter og «high-field-strength elements» (HFSE), som er typisk for kontinentale øybuer og var muligens en viktig bidragsyter i malmformingsprosessen.

Sent-kambrisk til midt-silurisk deformasjon har metamorfosert og foldet steinene i løpet av minst fire stadier. F_1 produserte en transponert lagning beviselig fra diskontinuerlige kvartslag og rotløse folder. F_2 produserte hovedfoliasjonen S_2, ved tette til isoklinale folder med øst-vestgående foldeakser, der sulfidmineraliseringer ble remobilisert og konsentrert i relaterte hengselsoner. Maksimale metamorfe forhold nådde amfibolitt facies, og representerer sannsynligvis enda høyere forhold enn den estimerte 600 °C og 10 kbar. F_2-fasen ble fulgt av retrograd metamorfose som dannet en mineralsammensetning av kloritt, klinozoisitt og zoisitt. Den etterfølgende F_3-fasen refoldet S_2-foliasjonen til koaksiale åpne folder mens økende metamorfe forhold dannet nye granater, men nådde ikke de metamorfe forholdene til F_2. Titanitt er datert til 465 ± 21 Ma og er sannsynligvis relatert til denne foldefasen, som er sammenfallende med den ordoviciske takoniske orogenesen kjent fra andre Laurentia-deriverte skyvedekker i den Øverste Allokton, og gir ytterligere bevis på før-skandinavisk deformasjon. F_4 er relatert til skandinavisk deformasjon og refoldet de tidligere strukturene til åpne nordøst-sørvest orienterte foldeakser, noe som skapte bassengstrukturen i området Hesjelia-Hammertjønna på grunn av interferensen med F_3 folder, og samtidig forårsaket det variable stupet til malmsonen på Hellerfjellet. Post-F_4 ekstensjon produserte boudiner og åpne folder av sene pegmatittintrusjoner.

Resultatet av polydeformasjonen er utgangspunktet for en 3D-modell av malm-forekomstene ved Hesjelia-Hammertjønna og Hellerfjellet. Basert på borekjerner i Hesjelia var det mulig å gjøre korrelasjoner i henhold til de geologiske begrensningene, noe som resulterte i fire isolerte soner. Den største usikkerheten gjelder forekomstens strukturelle oppførsel mot Hammertjønna, der alle observerte malmlinser forekommer på samme nivå langs strøket. Dette er også tilfellet på Hellerfjellet, og en forklaring på det diskontinuerlige mønsteret av de mange, men små linsene på disse to lokalitetene kan være skjærbevegelser som følge av F_2 folding.

Table of contents

List of Figures

List of Tables

Abbreviations

ASI – Alumina Saturation Index

BSE – Back Scatter Electron

EDS – Energy Dispersive Spectroscopy

EPMA – Electron Probe Micro-Analyser

GQG – Graphite Quartz Gneiss

HFSE – High Field Strength Elements

HREE – Heavy Rare Earth Elements

HNC – Helgeland Nappe Complex

ICP-MS – Inductively Coupled Plasma-Mass Spectrometry

ICP-OES – Inductively Coupled Plasma-Optical Emission Spectrometry

LILE – Large Ion Lithophile Elements

LREE – Light Rare Earth Elements

QMS – Quartz Muscovite Schist

RNC – Rödingsfjället Nappe Complex

SEDEX – Sedimentary Exhalative

SEM – Scanning Electron Microscope

SPO – Shape Preferred Orientation

VMS – Volcanogenic Massive Sulphide

WDS – Wavelength Dispersive Spectroscopy

1 Introduction

1.1 Objectives and aim

The objective of this master thesis as given by the thesis statement:

The project will focus on the geology and structures in the deposit area. One important question to answer is about the nature, origin and sequence of rocks hosting the sulphides. Another task is to find out if the concentration of sulphides is controlled by structures, e.g. foliation, folding, stretching (lineations), and if so, find the main direction of the ore axis.

The "deposit area" is the Hesjelia-Hammertjønna deposit and Hellerfjellet deposit. Based on the data from the given tasks the aim is to develop a 3D geological model of both ore deposits, that fits into the regional deformational history.

1.2 Field area

The field area is located close to the city of Mo i Rana in the county of Nordland, Norway. Three ore deposits are investigated, the Hesjelia, Hammertjønna and Hellerfjellet ore deposit, where the former two is part of the Hesjelia ore zone and the latter is part of the Stangfjellet-Hellerfjellet ore zone. The Hesjelia-Hammertjønna and the Hellerfjellet field areas cover approximately 1.2 km^2 and 2.7 km^2, respectively, and is structurally a part of the Mofjellet Group within the Rödingsfjellet Nappe Complex (RNC). The Hesjelia ore zone stretches about 3km along strike from Hesjelia to Hammertjønna. In the Stangfjellet-Hellerfjellet zone the Hellerfjellet deposit was investigated in detail, however, some investigation was also done on a smaller mineralization at Hellerfjell-tjønna and a formerly unknown mineralization further west.

1.3 Geological setting

1.3.1 A tectonic overview

The ancient continent of Baltica comprises the present northern Europe, confined in the east by the Urals, and in the south by the Trans-European Suture Zone (Cocks and Torsvik, 2005). The western margin is an irregular boundary located offshore Norway in the North-Sea, determined by oceanographic and geophysical studies (Cocks and Torsvik, 2005). There is generally consensus that, around 1000 Ma, all known cratons on the earth were assembled in a supercontinent, named Rodinia (Li et al., 2008). However, there is still a debate about the relative configuration of the paleo-continents within Rodinia and the subsequent break-up history (Li et al., 2008, Corfu et al., 2015). The conventional model (Hoffman, 1991) places Laurentia and Baltica adjacent to each other similar to the position prior to the Atlantic Ocean opening (Corfu et al., 2015). On the other side, Hartz and Torsvik (2002) proposed an inverted Baltica situation, where Norway faced east towards the Ægir ocean, and not towards the Iapetus on the western side of Baltica. These two models result in a different provenance of the Neoproterozoic extension-related metasedimentary sequences found in Scandinavia, where the former suggest Iapetus origin, while the latter suggest Ægir origin (Corfu et al., 2015).

The break-up history of Rodinia is disputed, and different theories exists (Corfu et al., 2015). According to Meert and Torsvik (2003), until the early Neoproterozoic, at about 800 Ma, Protobaltica occupied the eastern part of Rodinia, before break-up and formation of the combined Laurentia-Protobaltica continent. The separation of the latter continent happened through asymmetrical northwards rifting, starting at around 580 Ma (Slagstad

et al., 2020), before complete separation of Laurentia and Baltica and formation of the Iapetus ocean at about 550 Ma (Cocks and Torsvik, 2005, Hartz and Torsvik, 2002). The consequent low latitude position of Laurentia was favourable for the formation of siliciclastic and carbonitic sequences found in the Uppermost Allochthon of the Scandinavian Caledonides, contrary to the mid- to high latitude Baltica, where tillites of similar age is more common (Roberts et al., 2007).

Convergence and subsequent subduction of the Iapetus Ocean beneath Laurentia and Baltica started in the early Ordovician (Gee et al., 2008). An early Caledonian orogenic phase called the "Finnmarkian phase" was introduced by Sturt et al. (1978) and believed to be the genesis of the Kalak Nappe Complex at around 500 Ma. Later studies, e.g. Corfu et al. (2007), have disproved this theory based on results yielding much older ages on the structures related to the Finnmarkian phase. In the Uppermost Allochthon and some parts of the Upper Allochthon there is evidence for an Ordovician orogenic phase termed the Taconian, in which north west-vergent thrusting (Yoshinobu et al., 2002) resulted in imbrication of nappe sheets onto the Laurentian margin (Prave et al., 2000, Roberts, 2003). These observations reflect the active margin along Laurentia, wherein subduction-related volcanic arcs formed as a response to the continuous convergence and subsequent Late Silurian, ca. 430 Ma (Bender et al., 2019), collision between Laurentia and Baltica, termed the Scandian phase of the Caledonian orogeny (Cocks and Torsvik, 2005, Roberts et al., 2007). The collision, partly resembling a future Australia-Asia situation (Van Staal et al., 1998), led to Baltica being subducted beneath Laurentia, resulting in an accretionary wedge consisting of rocks from the Baltican margin, Iapetus Ocean and Laurentian margin (Yoshinobu et al., 2002, Gee et al., 2008). Before the Scandian phase Baltica were softly amalgamated with Avalonia at about 443 Ma (Cocks and Torsvik, 2005).

1.3.2 The Scandinavian Caledonides

The Caledonides is an orogenic belt stretching ca. 7000 km from Svalbard, southwards through the British Isles and westwards to North America where it is known as the Appalachian (Grenne et al., 1999). The Scandinavian Caledonides, located in Norway, western Sweden and western Finland, consists of a subdivided allochthon defined by Roberts and Gee (1985) as the Lower, Middle, Upper and Uppermost Allochthon. Each part of the allochthon contains a series of juxtaposed thrust sheets or nappes of variable origin, all of which are translated eastwards for up to several hundred kilometres (Roberts and Gee, 1985). The Lower and the Middle Allochthon is originally regarded as being originated from the margin Baltica (Kumpulainen and Nystuen, 1985), although evidence of a peri-Laurentian ancestry of certain nappes dispute this (Corfu et al., 2007, Kirkland et al., 2007, Gasser et al., 2015, Slagstad and Kirkland, 2018), while there is a collective agreement on the origin of the Upper- and Uppermost Allochthon deriving from the Laurentian margin (Melezhik et al., 2002, Yoshinobu et al., 2002, Roberts, 2003, Roberts et al., 2007).

According to Corfu et al. (2015) this subdivision of the allochthon is too simplistic for the much more complex genetic relationships that have been revealed in recent years. The parautochthonous-autochthonous Baltican basement, on which the thrust-nappes were obducted, prove its presence underneath the Caledonian thrust sheet by outcropping in windows through the core of antiforms, caused by thrust-related deformation (Roberts and Gee, 1985). The basement rocks are autochthonous Precambrian crystalline rocks overlain by a thin unit of parautochthonous-autochthonous sedimentary cover of Lower Palaeozoic to Upper Proterozoic (Roberts and Gee, 1985). The former is mostly granitoids and

gneisses (Gorbatschev, 1985) while the latter is mostly Lower Cambrian sandstones and grey-black shales (Bergström and Gee, 1985). The cover sequence is laterally extensive and provided the decollement surface on which the Lower Allochthon was transported (Roberts and Gee, 1985).

1.3.3 Caledonian metallogeny

The Caledonian orogenic-metallogenic belt are known to host abundant sulphide and iron deposits of varying grades, many of which have been exploited economically. These deposits were mostly formed between the Neoproterozoic and Devonian pre-Caledonian period, when the ancient super-continent Rodinia rifted and broke up to form the Iapetus ocean, and is now conserved within the Caledonides (Grenne et al., 1999). The Uppermost Allochthon is host to two major and characteristic stratabound Zn-Pb-Cu and Zn-Cu sulphide deposits, the Bleikvassli and Mofjellet deposit (Grenne et al., 1999), along with several smaller deposits (Bjerkgård et al., 2013b). These are confined within volcanic, sedimentary to mixed sedimentary-volcanic sequences related to the Laurentian margin (Marker, 1983, Grenne et al., 1999). At the most, nine Norwegian and three Swedish base-metal mines were operating and produced over 4.0 Mt of ore per year during the late 1970s. At the same time, three iron ore mines produced 4.5 Mt of ore per year (Grenne et al., 1999). Due to decreased metal prices the number of base-metal mines in 1998 were down to two (one in Sweden and one in Norway), and one iron ore mine (Rana, Nordland). All of these mines are confined within the Caledonian orogen (Grenne et al., 1999).

1.3.4 The Uppermost Allochthon

The Uppermost Allochthon stretches, mostly discontinuously, along the coastal region of north-central Norway between the county of Trøndelag and Finnmark, a distance of more than 700 km along strike (Figure 1.1) (Roberts et al., 2007). It is widest in the central parts, extending across the border east of Mo i Rana (just east of the field area). Generally, what distinguishes the Uppermost Allochthon from the other allochthons is the abundance of platformal carbonitic sequences, granitic batholiths and stratabound iron formations (Melezhik et al., 2002, Roberts et al., 2007). In addition, there is a tectonic thrust polarity that is not observed elsewhere in the Caledonian thrust sheets, attributed to the Ordovician Taconian orogenesis documented along the Laurentian margin (Prave et al., 2000, Yoshinobu et al., 2002, Roberts et al., 2007). The Uppermost Allochthon is, based on structural and lithological boundaries, dominated by two major thrust sheets; the Helgeland Nappe Complex (HNC) and the underlying Rödingsfjellet Nappe Complex (Roberts and Gee, 1985). The transition to the Upper Allochthon, here represented by the Köli Nappe Complex, is defined by a thick thrust zone of imbricated and lensed mylonite to blastomylonite representing the time of emplacement of the Uppermost Allochthon onto the Upper Allochthon, during the Scandian phase of the Caledonian orogeny (Roberts et al., 2007). The HNC covers the west coast of Helgeland and is the structurally highest nappe complex in the Norwegian Caledonides, containing several north west-vergent nappes of psammitic, clastic, calcareous, granitoid and ophiolitic origin, reaching peak metamorphic conditions at amphibolite facies (Stephens et al., 1985, Yoshinobu et al., 2002). The RNC comprises six nappe units (Melezhik et al., 2015) of metasedimentary, metavolcanic and carbonitic rocks from medium to high metamorphic grade (Marker, 1983, Marker et al., 2012). While there is still discussions and uncertainties about the origin and

correlation of certain nappes within the different allochthons (Corfu et al., 2015), there is generally consensus about the RNC belonging to the Uppermost Allochthon.

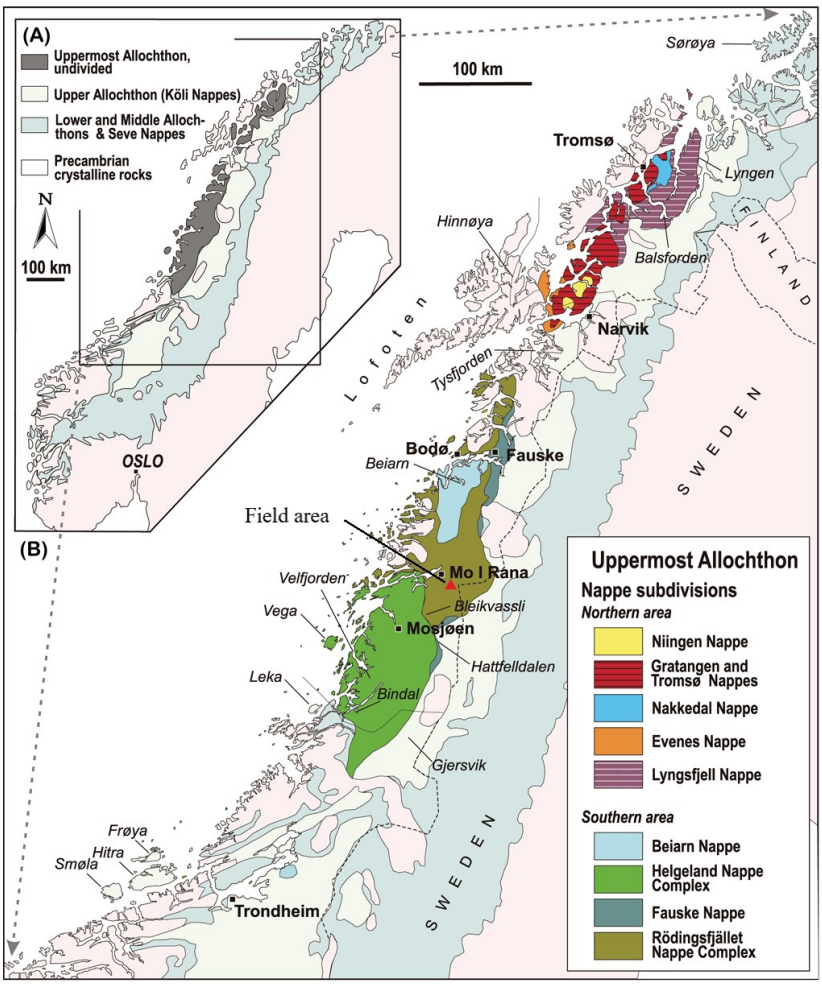

Figure 1.1: Tectonic map of the Uppermost Allochthon in the Scandinavian Caledonides, from Roberts et al. (2007).

The Mofjell Group

As a part of the Slagfjellet Nappe within the RNC the Mofjell Group stretches from Ranafjorden in the west to Rundfjell in the east, covering ca. 170 km^2 (Figure 1.2). It has tectonic contacts to the Rostafjell Group in the south, also a part of the Slagfjellet Nappe, the Plurdalen Group in the north and east, which is a part of the Plura Nappe, and the Dalselv Nappe in the west (Marker, 1983, Marker et al., 2012). It is classified as a volcanic arc close to a continental margin (Figure 1.3), and consists of complexly folded units of felsic metavolcanic rocks and metasedimentary rocks, including mixed igneous and tuffaceous amphibolites (Marker, 1983, Bjerkgård et al., 2013b). The felsic rocks are semi-massive grey gneisses, probably representing volcanic and/or greywacke metasediments, massive metarhyolite rocks dominated by quartz and feldspar with subordinate garnet, biotite, and muscovite. The metasedimentary rocks are extensive units of mica schists and the predominant host rock to the stratabound Zn-Pb-Cu deposits (Marker, 1983, Bjerkgård et al., 2013b). The mica schists form separate muscovite- and biotite horizons, whereof the former host the largest mineralizations (Bjerkgård et al., 2013b), but also grade into each other with varying proportions. The amphibolites is usually garnet-bearing and form conformable and persistent layers, possibly representing pillow lavas (Bjerkgård et al., 2013b), wherein the proportions of biotite and hornblende varies laterally within the

amphibolite horizons. The amphibolites is commonly garnet-bearing and rich in calc-silicate and carbonate minerals, the latter evident from small depressions on the rock surfaces caused by dissolution of carbonate minerals.

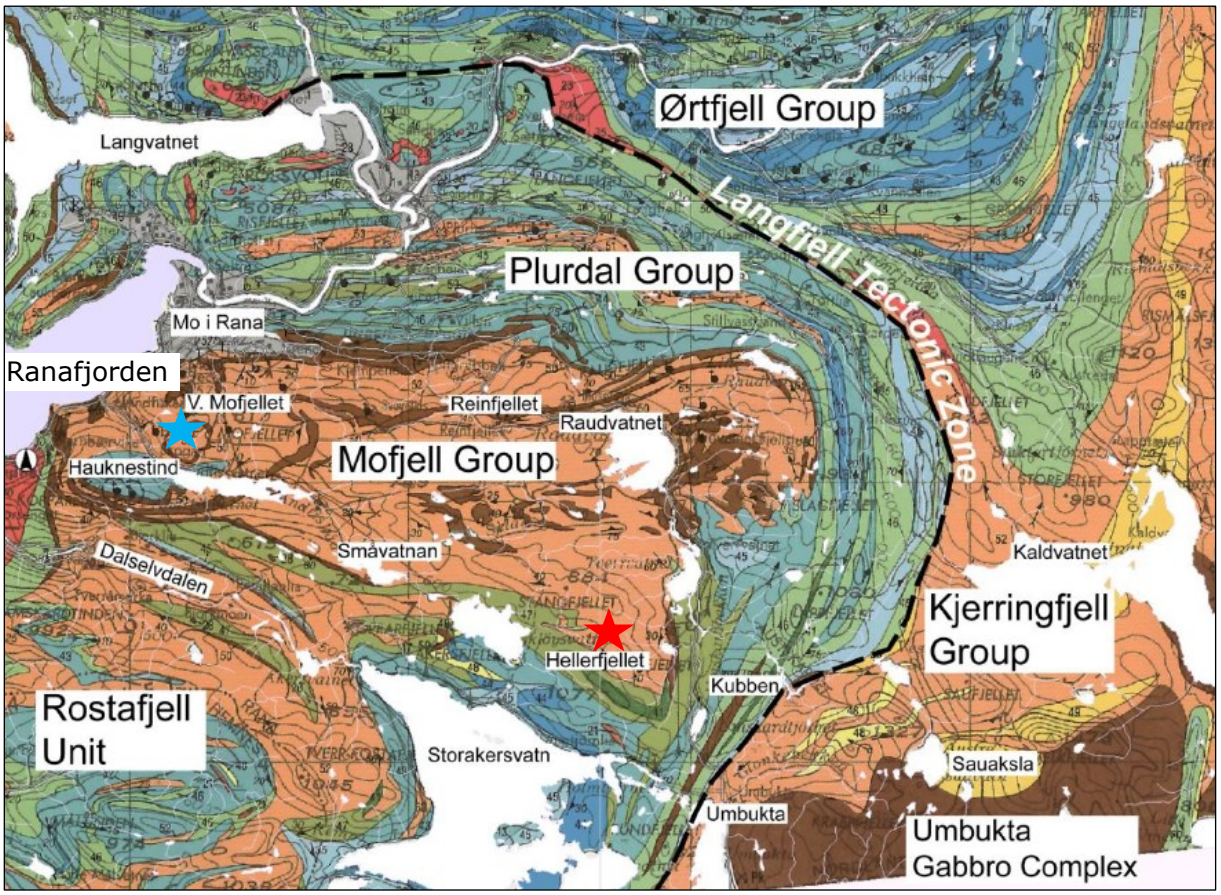

Figure 1.2: Tectonic overview of the Mofjellet Group. 1:250 000 map from Gustavson and Gjelle (1991), modified by Bjerkgård et al. (2013b). Blue start is Hesjelia-Hammertjønna field area, while red star is Hellerfjellet field area.

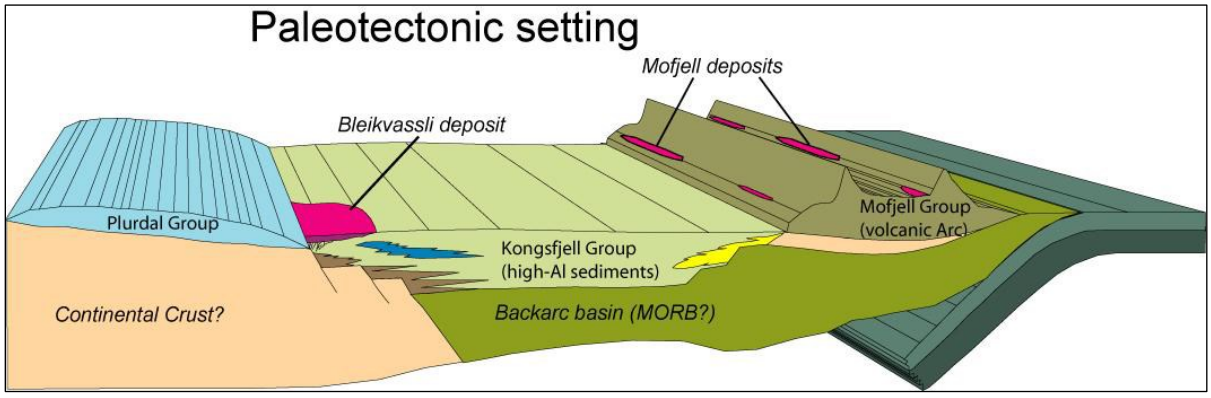

Figure 1.3: Model of the Mofjell Group and adjacent structural units from Bjerkgård et al. (2013b).The Mofjell group is interpreted as a continental marginal arc.

Previous work

The most extensive and detailed mapping of the Mofjell Group and adjacent areas was done by Søvegjarto et al. (1988), Marker (1983) and Marker et al. (2012). The former was initiated by the need to understand the structures controlling the Mofjellet ore deposit, herein revealing four folding phases. F_1 and F_2 produced tight to isoclinal folds with approximately parallel E-W trending fold axes, while the F_3 refolded these into coaxial open folds. Hence, F_1-F_3 transverses the typical Scandian south-east vergent folds, thus being related to pre-Scandian deformation events, in contrast to F_4 paralleling the Caledonian orogenic trend (Marker, 1983). F_1 has been interpreted as consequence of the Sveconorwegian-Grenville orogeny, while F_2 and F_3 has been related to the disproved Finnmarkian-phase (Corfu et al., 2007) of the Caledonian orogeny (Marker, 1983). However, recent dating of the Mofjellet Group (Slagstad et al., 2020) constrain the group to 501 ± 3 Ma and relates later deformation to the Taconian orogeny. F_4 created gentle to open folds with a NE-SW fold axis resulting in a large-scale dome and basin pattern (Marker, 1983), which has consequences for the appearance of the sulphide ores (Kruse, 1980).

Geochemical analysis on the gneisses and amphibolites suggests a continental marginal arc origin for the Mofjell Group (Bjerkgård et al., 2009), in concurrence with the geological environment of the Laurentian margin (Roberts et al., 2007), and also reveal that the grey gneisses represent higher proportions of volcanic rocks rather than sedimentary rocks (Bjerkgård et al., 2013a). The sulphide ores were, in conjunction with the earlier interpretation of larger proportions of metasedimentary rocks, regarded as a sedimentary exhalative (SEDEX), however, is now regarded as a VMS-deposit (Bjerkgård et al., 2013b).

The Mofjell Group is host to nine sulphide zones containing 20 known deposits, some of which were mined during the last century (Bjerkgård et al., 2013a). The largest mine was the Mofjellet mine (Mofjellet Gruber) extracting 4.35 Mt of ore with average grades of 3.6 % Zn, 0.7 % Pb and 0.3% Cu, in the period 1928-1987 (Bjerkgård and Hallberg, 2012). Vokes (1976) characterized the ore as a Kuroko type, based on the model of Cox and Singer (1986), wherein felsic and intermediate rocks dominate. However, due to the highly deformed and recrystallised nature of the Scandinavian sulphide ores, it is difficult to compare it directly with the Kuroko type. More recent work has classified the deposits as bimodal felsic to bimodal mafic deposits (Bjerkgård et al., 2013b), based on the lithotectonic model by Franklin et al. (2005). This is also in accordance to the VMS deposit model by Franklin (1993) based on ratios of Cu, Zn and Pb, showing that a bimodal-felsic environment correlates to higher grades of Zn and Pb, which is the case for the majority of the sulphide deposits in the Mofjell Group (Bjerkgård et al., 2013b).

The **Hesjelia ore zone**, which include the Hesjelia and the Hammertjønna ore deposit, was first drilled in 1959 and later mapped by Marker (1983) and geophysically investigated by Bergvesenet with VLF and slingram (Kruse, 1980). These investigations revealed a large-scale overturned fold-structure oriented E-W, in which the ore is concentrated in the hinge zone of an F_2 isoclinal fold. Because of the F_4-phase the outcropping mineralization in Hesjelia and Hammertjønna was interpreted to be connected. Based on this, Kruse (1980) estimated the ore zone to cover 450 000 m^2, with average grades in the drill holes of 2.9-3.4 % Zn, 0.19-0.25 % Cu and only trace amounts of Pb, in 2.95 m thickness. Later drill holes have intersected zones with thickness of 0.6-3.85 m averaging 1.4 % Zn, 0.4 % Pb, 0.2 % Cu and 7 g/t Ag, with the best intersection of 3.85 m with 3.3 % Zn, 1.1 % Pb,

0.3 % Cu and 9 g/t Ag. A transient electromagnetic (TEM) investigation done in 2007 indicated a subsurface connection, that were confirmed by a drill hole in 2008 intersecting a (weakly) mineralized zone of 0.60% Zn, 0.14 % Cu, 0.09% Pb, and 3 g/t Ag over a 6m interval. Anomalous Ba-values up to 0.3 % were intersected beneath the richest mineralization (Bjerkgård et al., 2013b).

The Hellerfjellet deposit, a part of the Stangfjellet-Hellerfjellet ore zone (Figure 1.4), is less explored but have been known since the early 1900's, when two drill holes were done (Bjerkgård et al., 2013b). 21 prospects of various size covering a length of ca. 200m have revealed massive sulphide lenses up to 3m in thickness and some meters wide (Bjerkgård et al., 2013b). TEM data suggest the ore deposit has a strike length of ca. 1.5 km and one drill hole from 2008 confirm a down dip length of minimum 250 m from the outcrops, intersecting 5 m with 1.23 % Zn, 0.35 % Cu, 0.35 % Pb, 27 g/t Ag, and 1 m with 1.82 % Zn, 0.59 % Pb, 0.16 % Cu and 24 g/t Ag (Bjerkgård et al., 2013b). Analysis from the outcrops yield high grades of sulphide metals with some exceeding 10 % of Cu+Zn+Pb and Ag > 100 g/t, with zinc and lead being the most abundant and subordinate grades of copper and silver (Bjerkgård et al., 2013b).

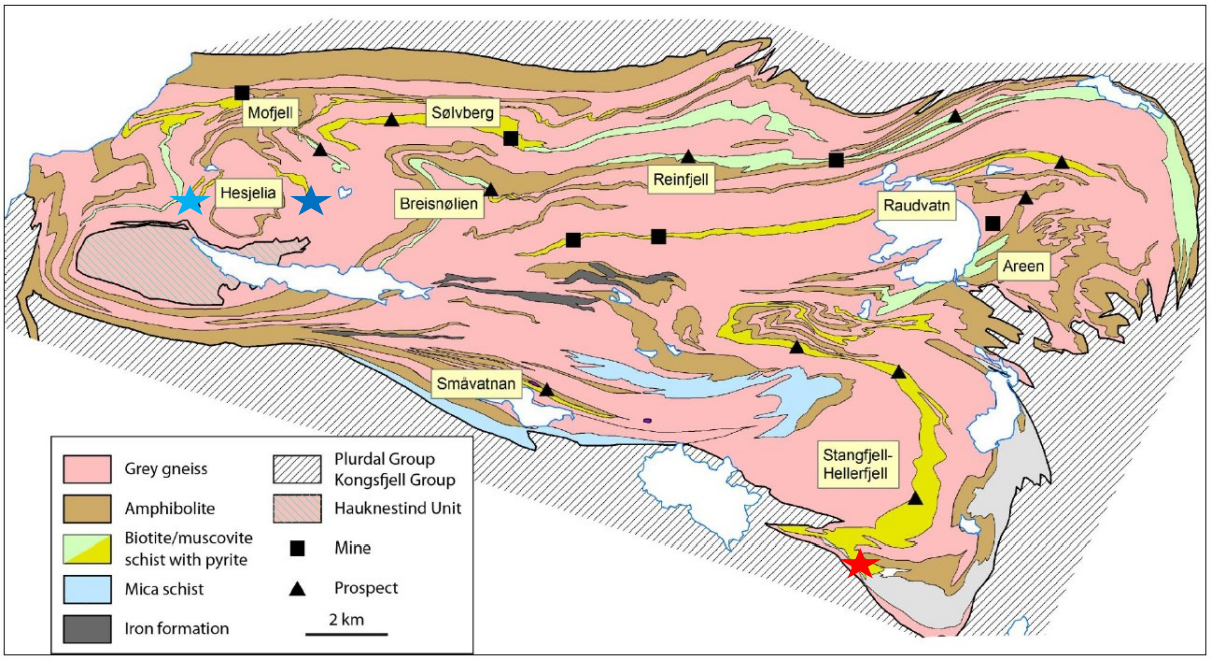

Figure 1.4: Simplified geological map of the Mofjellet Group, including the nine ore zones. Light blue star is Hesjelia, dark blue is Hammertjønna, and red start is Hellerfjellet. Map based on Marker (1983) and Marker et al. (2012), modified by Bjerkgård et al. (2013b).

2 Theory

2.1 Geochemistry

2.1.1 Major and minor elements

The major elements (>1.0 wt. % of a rock) comprises Si, Al, Fe, Mg, Ca, Na, K and is regarded as the rock forming elements constituting 99% of the continental crust (Winter, 2014), however, the minor elements (0.1-1.0 wt. %) Mn, Ti and P are often treated together with the major elements, e.g. in Harker diagrams, and both groups are usually presented as oxides (Winter, 2014). These elements are used in geochemical analysis to classify rocks and investigate the chemical evolution of crystal-melt systems by which a rock has been formed (Winter, 2014). The following sections present ways of presenting major and minor elements.

Harker and Fenner bivariate diagrams

The Harker and Fenner bivariate diagrams plot the major and minor oxides (y-axis) against SiO_2 and MgO (abscissa), respectively. The former diagram was introduced by Harker (1900, 1909) (Wilson, 1993) and is used to investigate the magmatic differentiation (evolution) of intermediate-felsic magmas occurring as a result of fractional crystallization, where Fe-Mg minerals with the highest melting point crystallizes first, making the magma continuously and relatively richer in SiO_2 (Winter, 2014). The Fenner diagram does the same for a mafic magma because it fractionates MgO by the crystallization of olivine and pyroxene in the early magmatic evolution, whereas the silica content generally varies little at this stage, hence, MgO is most suitable to track the fractional trend of mafic magmas (Wilson, 1993). A felsic magma, either produced from a continuous differentiation of a mafic magma (Bowen, 1928, Nandedkar et al., 2014, Winter, 2014) or by partial melting of the crust (Robb, 2005, Winter, 2014), becomes enriched in SiO_2 during fractional crystallization, making SiO_2 an appropriate oxide to investigate fractional trends in felsic magmas (Wilson, 1993). Both diagrams are compiled for volcanic rocks.

Tholeiitic and calc-alkaline rock suites

The division of tholeiitic and calc-alkaline rocks is a subdivision of subalkaline rocks, i.e. saturated – oversaturated in silica, and refer to rocks with respectively high Fe/Mg-ratio and little variation in silica, and rocks relatively high in K_2O + Na_2O (+ silica) and Fe-poor (Winter, 2014). Tholeiitic rocks is the prime rock type of divergent plate boundaries (MORB) (Winter, 2014), however also relates to intraoceanic subduction zones with island arcs producing iron-rich basalts, andesites and dacites (Best, 2003). Calc-alkaline rocks is primarily related to subduction-related volcanic arcs (Winter, 2014) and particularly continental arcs with thicker continental crust, producing basalts, andesites, dacites and rhyolites with higher proportions of alkalis compared to iron (Best, 2003). The tholeiitic and calc-alkaline rock suite is well correlated to the K content, which also is illustrated in the AFM diagram in figure 2.1.1 (although Na_2O also contributes here), displaying low amounts of K in the tholeiitic rocks and medium to high amounts in the calc-alkaline rocks.

The AFM diagram (Figure 2.1) distinguishes tholeiitic and calc-alkaline volcanic rocks by the relative wt. % content of A = Na_2O + K_2O, F = total Fe expressed as FeO, and M = MgO. The tholeiitic rock suites usually become strongly enriched in iron as the magma crystallizes and fractionates MgO, thus trending toward the Fe-apex of the AFM diagram. When Fe-Ti oxides start to crystallize the trendline turns towards the alkali apex as the

magma becomes subsequently enriched in alkalis (Winter, 2014). The calc-alkaline magmas evolve immediately towards the alkali apex due early crystallization of the Fe-Ti oxides (Sheth et al., 2002, Winter, 2014). The traditional differentiation trend of the tholeiitic and calc-alkaline suites is that outlined by Irvine and Baragar (1971), which is based on samples from a number of localities worldwide, while the line of Kuno (1968) is only based on samples from Japan (Sheth et al., 2002). Criticism exists in the use of AFM-diagrams. It categorizes the whole sample based on the normalization of the four components Na + K, Fe and Mg to 100 %, representing less than 50 % of the oxide weight percentages, which may lead to misrepresentation of rock suites ranging from mafic to felsic rocks, caused by an asymmetric representation of the mafic vs. felsic chemical constituents (Rollinson, 1993). The "calc-alkaline" series exclude calcium and alumina, on which basis it cannot, *sensu stricto*, define the rock series as calc-alkaline (Sheth et al., 2002).

Alumina saturation index (ASI)

Another diagram (Figure 2.1B) used for the major elements is the PI vs. ASI plot from Shand (1927), which groups igneous rocks after the total molar alkali versus alumina content (Winter, 2014).

$$\text{ASI} = \frac{Al_2O_3\ (mol)}{CaO+K_2O+Na_2O\ (mol)} \qquad [2.1]$$

Based on the molar ratios the rocks are classified either as **peraluminous** [Al_2O_3 > (CaO + K_2O + Na_2O)], **metaluminous** [Al_2O_3 < (CaO + K_2O + Na_2O) and Al_2O_3 > (K_2O + Na_2O)], or **peralkaline** [Al_2O_3 < (K_2O + Na_2O)] (Winter, 2014). This classification scheme is mostly used for felsic rocks and be used as an indication of the source rock from which the melt derived. Metaluminous rocks are often related to an igneous protolith (low-Al), whereas peraluminous rocks are thought to be sourced from a metasedimentary rock or from an igneous rock whose magma were contaminated by the crust upon ascent (Miller, 1985). A sedimentary source is based on the high alumina content in related rocks. This interpretation must be done carefully because the alkalis are more mobile than alumina and might be transported out of the magma by fluids, hence an originally metaluminous rock can turn into a peraluminous rock (Best, 2003).

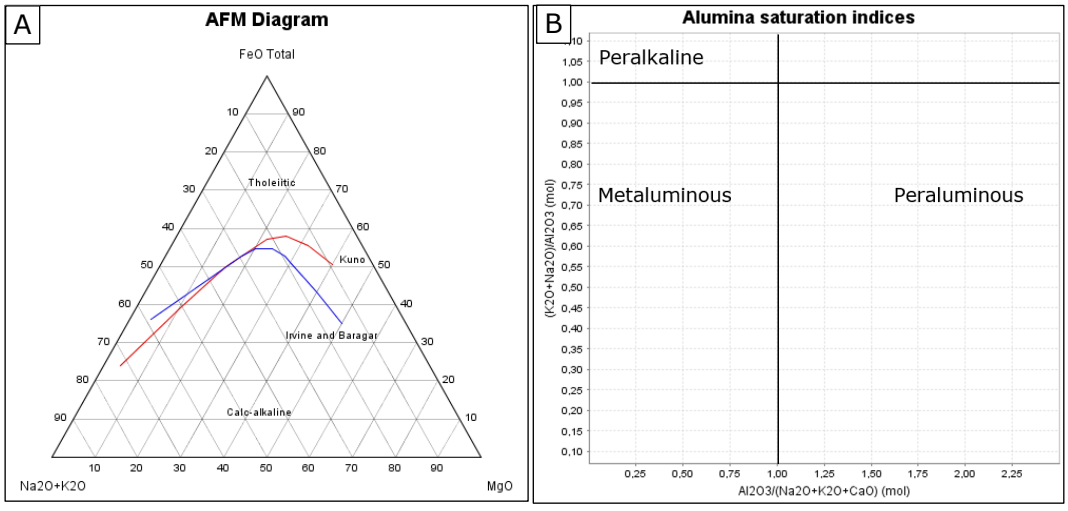

*Figure 2.1: A) AFM ternary diagram based on the relative proportions of FeO_{total} (FeO + 0.8998 * Fe_2O_3), Na_2O + K_2O and MgO in a sample. B) Alumina saturation index (ASI) of Shand (1927).*

2.1.2 Trace elements

The trace elements, presented in its elemental form, usually constitute less than 0.1 wt.% (1000 ppm) of the whole-rock composition, and therefore substitutes for the major elements under normal conditions, rather than composing their own phases (Best, 2003). If the concentration is abnormally high, like in mineral ore deposits, they form separate phases making extraction of the interesting elements economically profitable (Robb, 2005). The use of trace elements as petrogenetic indicators in for example tectonic discrimination diagrams are attributed to the variable concentration (up to a factor of 1000) they show in basalts, a rock normally used in tectonic discrimination diagrams. As a comparison, the major elements usually vary within a factor of 100 (Best, 2003).

Trace elements are subdivided into compatible and incompatible elements, which is related to the partitioning of elements into the solid or liquid phases of a crystallizing magma, respectively. The compatibility depends on the minerals involved, as different elements prefer different minerals, which is why it is commonly standardized to mantle minerals such as olivine, pyroxenes, and garnet (Winter, 2014). Compatibility is controlled not only by ionic radii and charge (Goldschmidt, 1937) but also by the electronegativity, wherein the substituting elements must be close to identical regarding these properties (Winter, 2014). Generally, the ionic radii of the substituting element must be within 15 % of the ionic radii and differ by no more than one unit charge, given that the balance can be retained by another substitution (Best, 2003, Robb, 2005). The mathematical ratio describing each elements degree of compatibility in a system is given by the partition coefficient, D, which is empirically estimated (Winter, 2014).

$$D = \frac{Concentration\ in\ mineral}{Concentration\ in\ melt} \qquad [2.2]$$

Where compatible and incompatible elements have D > 1 and D < 1, respectively (Best, 2003). Values for the concentration are in wt. % or ppm. Examples of compatible elements are Sr^{2+}, Ba^{2+} and Eu^{2+}, which readily substitutes for the major element Ca^{2+} in feldspars of a silicic magma, whereas Cr^{2+}, Ni^{2+} and Co^{2+} are compatible elements in a mafic magma, substituting for Fe^{2+} and Mg^{2+} in olivine and pyroxene (Best, 2003). Rb, Li and Nb, and rare earth elements (REE) are all incompatible (D << 1) and partitions to a low degree into minerals of basaltic magmas. To quantify the concentration of a trace element in the solid and the liquid phase during partial melting there are two models (Cox et al., 1979), presented here from Robb (2005), that must be considered. The first is "batch melting" in which the solid and the liquid phase remains in equilibrium until physical removal during emplacement as a magma, which is relevant for high viscosity granitic melts (Rollinson, 1993). The equation for this particular model is:

$$\frac{C\ (l)}{C\ (s)} = \frac{1}{[Dres + F(1 - Dres)]} \qquad [2.3]$$

Where C(l) is the concentration of a specific element in the liquid, C(s) is the concentration in the unmelted solid, D_{res} is the bulk partition coefficient of the residual solid after melt extraction and F is the weight of the melt produced. The incompatible elements have very low D_{res} and are therefore the most concentrated when F ≈ 0, i.e. in the very first melt. The second model of partial melting is "fractional melting" where the melt produced is instantaneously and constantly removed from the residual solid phase, consequently crystallizing in another system. This mode of melting relates to the less viscous mafic magmas and the equation for this model is as follows:

$$\frac{C\,(l)}{C\,(s)} = \frac{1}{D\,(s) * (1-F)^{\frac{1}{D\,(s)-1}}} \qquad [2.4]$$

Where all symbols are similar to equation 2.3, except for D(s), which is the bulk partition coefficient of the solid prior to melting. The first melt F ≈ 0 will be extremely concentrated in incompatible elements compared to the solid residual due to a low D(s) for these elements.

Concentration of trace metals in volcanic arcs starts from the dehydration of the subducting slab underneath the arcs, yielding fluids that migrates upwards and into the mantle, and consequently metasomatize the mantle peridotite (Robb, 2005).

Rare earth elements (REE)

The rare earth elements (REE) is a group of elements, from atomic number 57 (lanthanum, La) to 71 (lutetium, Lu), suitable for petrogenetic analysis of metamorphosed rocks because of being immobile during alteration (Bau, 1991), while also displaying a systematic chemical disparity causing different behaviours and partition coefficients (Best, 2003). Even though yttrium (Y) has atomic number 37 it is normally included among the REE because of its nearly identical size to the true REE-element holmium and the trivalent charge, the latter of which is the ionic charge for all REEs (Best, 2003). Eu is an element that occur also as divalent ions, while Ce^{4+} exist in very oxidized magmas. The mass of the REEs increases from La to Lu while the ionic radii decreases, making the light REEs (LREE) more incompatible than the heavy REEs (HREE) in relation to common silicate minerals (Best, 2003).

When plotting the REEs in a diagram sorted from LREE-HREE the absolute values of each element is normalized to the composition of an average chondritic meteorite, representing primitive earth (Best, 2003), and the resulting value (rock/chondrite) is plotted along the Y-axis in a logarithmic scale. This normalization smooths out the originally sawtooth like pattern (Oddo-Harkins effect) of the absolute values and gives rise to specific signature patterns depending on the petrological history of the particular sample(set). There are no standardized normalizing values for chondrites as the geochemistry for individual chondrites is inconsistent (Masuda et al., 1973), however the normalizing data of Sun and McDonough (1989) is commonly used (Figure 2.2).

One of the most distinct attributes of the rock/chondrite diagrams is the Eu anomaly/spike, that is caused by the compatibility of Eu^{2+} in the common mineral plagioclase, substituting for Ca^{2+}. The anomaly is caused by the incompatibility of the adjacent lighter and heavier trivalent elements, and a positive anomaly is the result of plagioclase accumulation, whereas a negative anomaly reflects fractionated crystallization of plagioclase and removal from the melt (Best, 2003). The slope of the chondrite-normalized pattern can be both positive, flat or negative depending on the fractionation processes that causes the HREE and LREE to be enriched *relatively* to one another (Winter, 2014). A positive slope, i.e. a *relative* depletion of LREE, can only be produced when the source itself is depleted in LREE, which is observed for low-K tholeiitic melts (Best, 2003, Winter, 2014). A negative slope, i.e. LREE enrichment, is observed for calc-alkaline melts with medium to high levels of potassium (Winter, 2014). The coherence between enrichment of the LREE and high-K content is based on the incompatibility of these elements, thus behaving similarly. A negative slope can also be produced if the HREE-compatible mineral garnet is left in the residual solid either after partial melting or fractional crystallization (Best, 2003). The

$(La/Yb)_N$ ratio is used as a ratio reflecting the slope of the REE curve, where La/Yb > 1 is positive and La/Yb < 1 is negative.

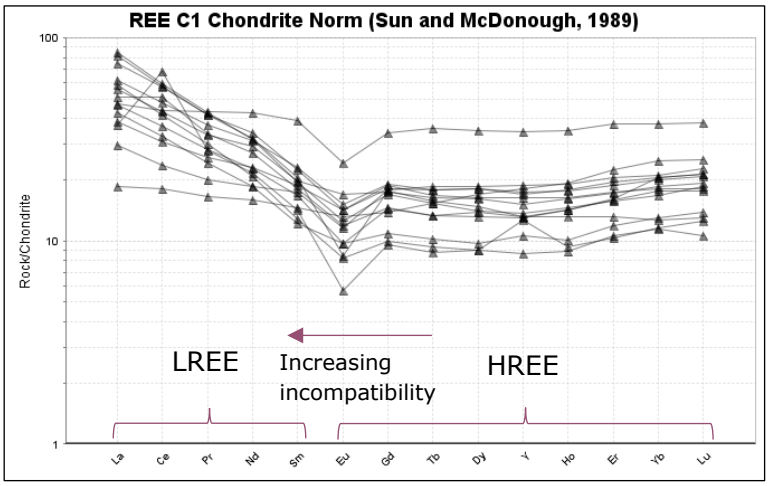

Figure 2.2: Example of a rock/chondrite normalized diagram for petrogenetic analysis of REE. Normalizing data from Sun and McDonough (1989).

Primitive mantle- and MORB-normalized spider diagrams

Other normalization diagrams, so called multi element spider diagrams, include a wider spectrum of trace elements, and two of the most used ones are the primitive mantle normalized diagram of Sun and McDonough (1989), and the mid-ocean ridge basalt (MORB) normalized diagram of Pearce (1983) (Figure 2.3). The latter use the large-ion lithophile elements (LILE) Sr, K, Rb and Ba, and the high field-strength elements (HFSE) Th, Ta, Nb, Ce, P, Zr, Hf, Sm, Ti, Y, Yb and Cr. Except for Cr the same elements in addition to Cs, Tl, W, U, La, Pb, Pr, Mo, Nd, Eu, Sn, Gd, Tb, Dy, Ho, Er, Tm, and Lu, are used in the primitive mantle normalized diagram. The latter is based on the average chondrite values multiplied by a factor of 2.9, while the former is based on the average composition of the most abundant igneous rock on the planet (Winter, 2010). In the MORB diagram the LILE and HFSE are grouped to the left and right, respectively, and by increasing incompatibility from the margins, however, some authors interpret the incompatibility of elements differently, hence, the order of the elements vary between authors (Rock, 1987). The primitive mantle normalized diagram is purely ordered by increasing incompatibility from right to left, hence, slightly mixes the LILE and HFSE. However, the degree of incompatibility changes by magma composition, whereof this specific ordering in based on mafic magmas.

The elements included in spider diagrams are almost always incompatible in relation to a mafic to intermediate mantle undergoing partial melting and (subsequent) fractional crystallization, however, exceptions do exist, like Sr being compatible with plagioclase, Ti with an Fe-Ti oxide and Y-Yb with garnet (Winter, 2010). These processes generally concentrate both LILE and HFSE equally, however, the participation of an aqueous phase decouples them enriching the aqueous phase in LILE (Winter, 2014), resulting in a negative slope from the LILE to the HFSE. Such a slope is typical of calc-alkaline rocks in island arcs, and more so in continental arcs, thereby interpreted to reflect a hydrous melt sourced from the overriding mantle wedge percolated by migrating fluids from the dehydrated subducting slab and sediments, causing fluid-fluxed melting of peridotite (Best, 2003, Kimura and Yoshida, 2006, Winter, 2014). Thus, a calc-alkaline basalt is enriched in the

incompatible elements Ba, K and Rb, however strongly depleted in the HFS-elements Nb and Ta due to low solubility in the migrating fluids, resulting in a negative anomaly (Best, 2003). In this setting, the HFSE part of the curve is usually flat and as a whole lower than that of MORB basalts (rock/MORB < 1), indicating that the source is too shallow for garnet to form and that the source is more depleted in HFSE, respectively (Pearce and Peate, 1995). A positive to flat slope indicate a source depleted in incompatible elements, like the normal-MORB (N-MORB), and is typical of island arc tholeiitic basalts (Best, 2003, Winter, 2014). The tholeiitic suite is interpreted to be derived from decompression partial melting of the mantle wedge, however with a somewhat more fertile and hydrated source than that of MORB (Winter, 2014).

The disadvantage in using multi-element normalization diagrams as petrogenetic indicators is that there is no standardized method in terms of element order, normalizing materials and normalizing values (Rock, 1987), which potentially lead to different interpretation of the same data set.

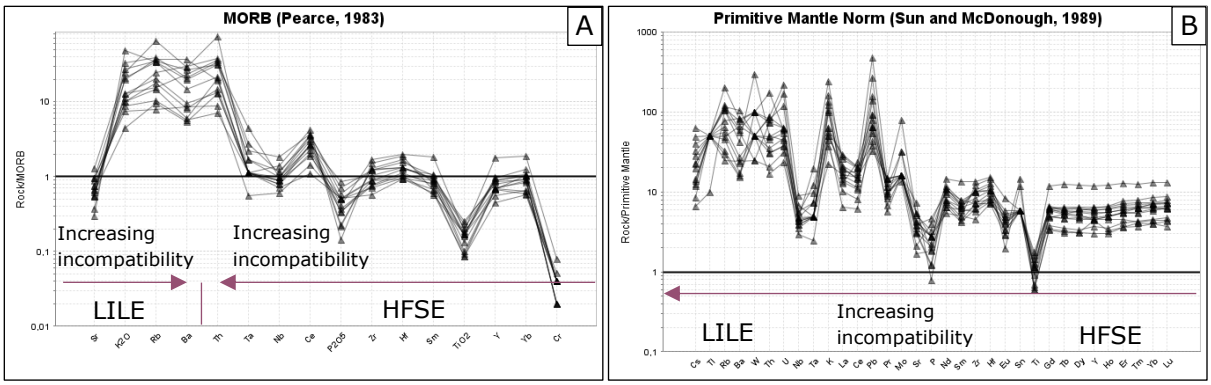

Figure 2.3: Example of a "Rock/MORB" (A) and a "Rock/Primitive Mantle" (B) spider diagram plot for petrogenetic analysis of incompatible to compatible elements. Normalizing values from (A) Pearce (1983) and (B) Sun and McDonough (1989).

2.1.3 Tectonic discrimination diagrams

Tectonic discrimination diagrams of selected trace elements are often used as proxies in metamorphosed terranes to reveal the tectonic setting from which the rocks originally derived, thereby utilize the physio-chemical characteristics controlling their behaviour in different tectonic settings (Pearce, 1996, Winter, 2014). The most suitable trace elements for this purpose is Ti, Al, Cr, Zr, Nb, Ta, Hf, Th, Ga and the REE (except La), which is typically incompatible to aqueous fluids (immobile), e.g. in subaerial weathering processes (Pearce, 1996). Thus, to achieve the best possible result it is important to choose unaltered samples. Metamafic rocks such as amphibolite or metagabbro is the most appropriate rocks to analyse to minimize the effects of fractional crystallization, assimilation, and magma mixing (Winter, 2014).

One way of investigating potential alteration geochemically is by plotting them in a major element classification diagram, such as the total alkali – silica (TAS) diagram of Le Bas and Streckeisen (1991) (Figure 2.4A), and compare to an immobile element equivalent diagram, such as the TAS proxy diagram of Floyd and Winchester (1975), modified by Pearce (1996) using > 10000 samples from a wider range of tectonic settings (Figure 2.4B). Here, the highly mobile K, Na and Si, is exchanged by the immobile equivalents Nb/Y (alkalis) and Zr/Ti (silica). Metasomatism and hydrothermal alteration are both processes that result in a change in the major element composition, however, affect the trace element geochemistry to a lesser extent, and particularly the HFSE (Best, 2003). If the rocks classify identically in both diagrams, the rocks are probably unaltered and credible to use as petrotectonic indicators.

The criticism on tectonic discrimination diagrams is based on the ambiguity regarding the mobility of elements during metamorphism and hydrothermal alteration, and the often lack of reproducibility of correlations between trace element geochemistry and tectonic environments from one diagram to another. Thus, this kind of analysis requires to be used in collaboration with geological and petrological data (Li et al., 2015).

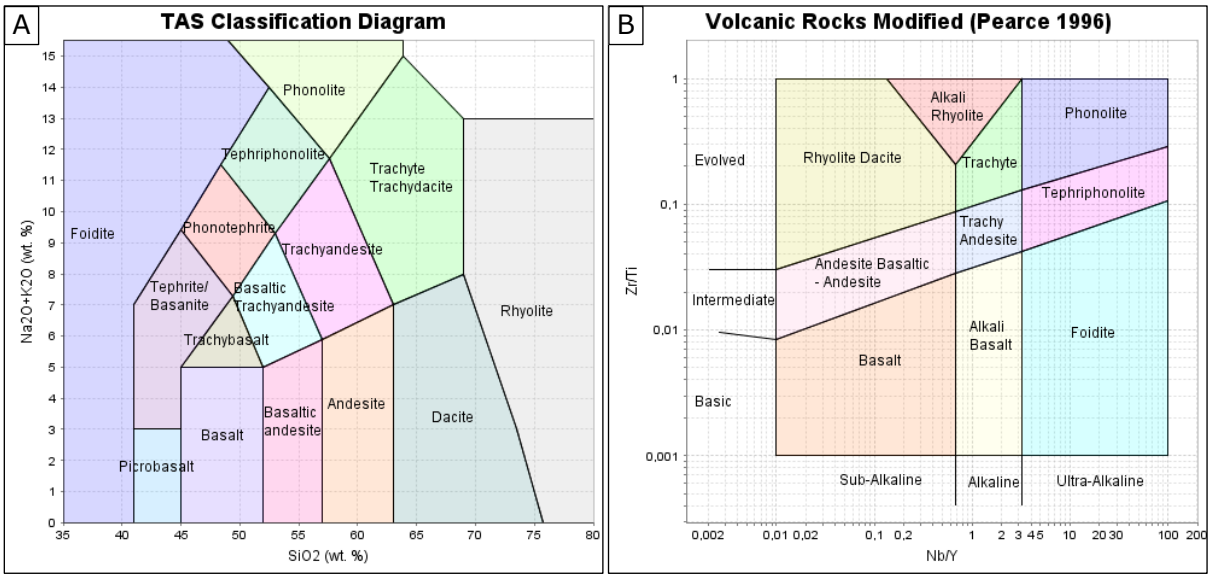

Figure 2.4: TAS volcanic rock classification. A) Original TAS diagram of Le Bas and Streckeisen (1991). B) TAS proxy diagram based on Zr/Ti vs. Nb/Y. Diagram originally from Floyd and Winchester (1975), however modified and upgraded by Pearce (1996).

The tectonic discrimination diagrams differentiate usually between three main types (Pearce, 1996): MORB, including enriched (E-MORB) and normal (N-MORB), volcanic arc basalt (VAB), including island arc tholeiites (IAT) and calc-alkaline basalt (CAB), and lastly within-plate basalt (WPB), including tholeiitic and alkalic basalts. Other intermediate types include ocean-island basalt (OIB) and back-arc basin basalt (BABB).

Ti-Zr-Y ternary diagram from Pearce and Cann (1973)

The elements Ti-Zr-Y is suitable for basalts above greenschist facies and potentially altered samples because of the high immobility of these elements (Pearce and Cann, 1973). The diagram (Figure 2.5) discriminates between the three main groups of tectonic settings for basalt production being the VAB, MORB and OIB/WPB. However, according to Vermeesch (2006) it is best at discriminating between OIB and MORB and does not manage to discriminate between VAB and MORB, which is probably caused by the diversity of volcanic arc magmas produced by complex processes underneath the arcs.

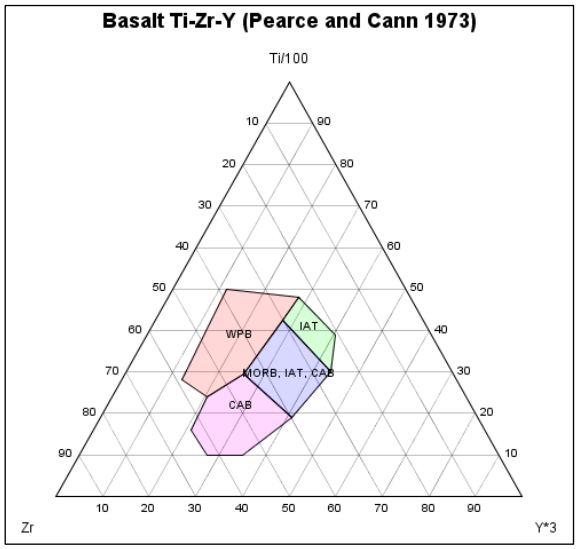

Figure 2.5: Ti-Zr-Y ternary diagram for basalts discriminating between tectonic settings. CAB = calc-alkaline basalts, MORB = mid-ocean ridge basalt, IAT = island arc tholeiites, WPB = within plate basalts. By Pearce and Cann (1973).

The Th-Hf-Ta ternary diagram by Wood (1980)

The Th-Hf-Ta ternary diagram (Figure 2.6) by Wood (1980) discriminates between VAB, MORB and WPB, and further divides VAB into calc-alkaline basalt (CAB) and island-arc tholeiite (IAT), MORB into N-MORB and E-MORB, and WPB into within-plate tholeiite basalt (or OIB) and alkalic basalt (produced mainly by continental rifting). OIB are produced from enriched melts (Winter, 2014) and separates from MORB due to higher ratios of Th/Hf and Ta/Hf, explained by the incompatibility of Th and Ta consequently partitioning in the partial melts. Volcanic arcs have a higher ratio of Th/Ta than basalts produced in MORB or OIB settings, due to Th partitioning in the aqueous fluids produced by dehydration of the slab, therefore plot towards the Th apex.

Vermeesch (2006) revisited this diagram and somewhat modified the lines separating the primary groups, in which he used IAB (island arc basalt)-MORB-OIB, and managed to achieve a better separation of the data than the Ti-Zr-Y diagram of Pearce and Cann

(1973). Contrary to the Ti-Zr-Y by Pearce and Cann (1973), this diagram manage to discriminate between MORB and IAB/VAB.

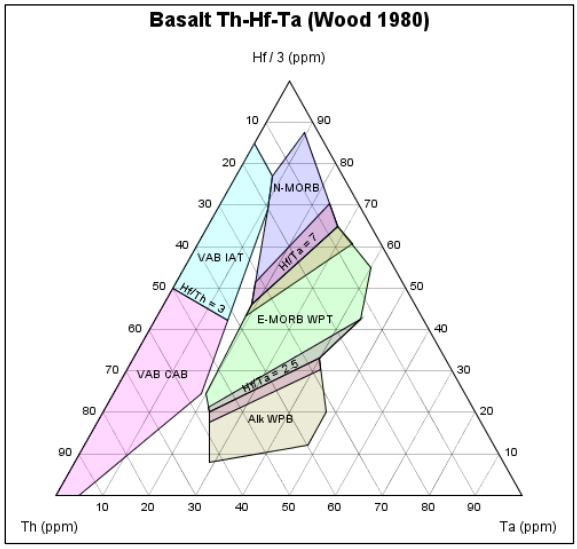

Figure 2.6: Th-Hf-Ta ternary diagram discriminating between volcanic arc basalt (VAB), including calc-alkaline basalt (CAB) and island-arc basalt (IAT), N-MORB, E-MORB within-plate tholeiite (WPT), and alkalic within plate basalt (WPB). From Wood (1980).

The Th/Yb vs. Nb/Yb bivariate diagram by Pearce and Peate (1995)

The Th/Yb vs. Nb/Yb bivariate diagram (Figure 2.7) by Pearce and Peate (1995) discriminates between continental- and oceanic arcs, N-MORB, E-MORB and OIB. Yb is used here as a denominator based on being a conservative element that is less affected by partial melting and fractional crystallization, hence, it reflects the mantle source. The Nb/Yb ratio distinguishes between a depleted or enriched source because Nb is more incompatible than Yb during partial melting, whereas Th/Yb is an indicator of fluid partitioning because Th partitions strongly into fluids (Pearce and Peate, 1995, Pearce, 2008). Therefore, basalts produced in a subduction setting plot above the N-MORB-E-MORB-OIB array.

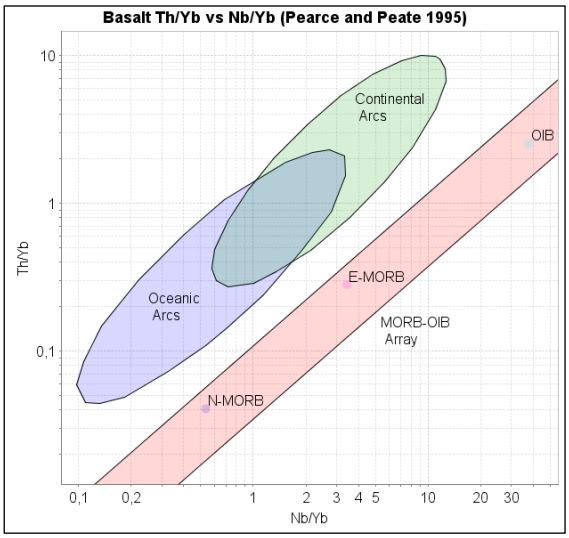

Figure 2.7: Th/Yb vs. Nb/Yb bivariate diagram by Pearce and Peate (1995) discriminating between mainly between subduction environment and MORB-OIB.

The Rb vs. (Y + Nb) diagram by Pearce et al. (1984)

The Rb vs. (Y + Nb) diagram (Figure 2.8) by Pearce et al. (1984) discriminates between volcanic-arc granite (VAG), ocean-ridge granite (ORG), within-plate granite (WPG) and syn-collisional granite (syn-COLG). WPG and ORG are separated from VAG and syn-COLG by the amount of Y + Nb, which is controlled by crystal-melt fractionation and usually low in rocks associated with hydrous magmas (Winter, 2014), like VAG and syn-COLG. The amount of Rb separates syn-COLG from VAG, and WPG from ORG, and is controlled by fractionation of the parental melt (Pearce et al., 1984). All values in the diagram are normalized to a hypothetical composition of an oceanic ridge granite (Pearce et al., 1984).

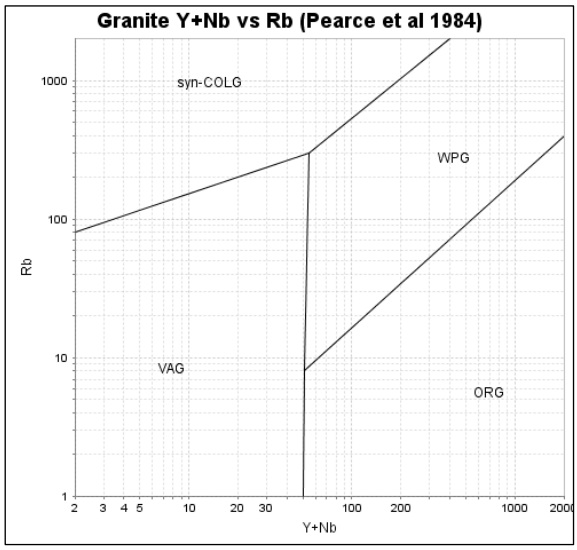

Figure 2.8: Rb vs. Y + Nb for granites discriminating between VAG = volcanic arc granite, syn-COLG = syn-collisional granite, WPG = within plate granite and ORG = ocean ridge granite. From Pearce et al. (1984).

2.2 Bimodal-felsic assemblages

A volcanogenic massive sulphide is an ore deposit related to hydrothermal activities at or near the seafloor in volcanic extensional regimes and is host to the economically important base metals Cu, Pb, Zn and precious metals Ag, and Au (Piercey, 2010). Based on their related volcanic and sedimentary units that formed synchronously with the deposits, they are divided into five categories (Franklin et al., 2005), among which is the *bimodal-felsic* assemblage. This category is associated with predominantly felsic rocks (35-75 % of the volcanic rocks), and minor mafic (20-50 % of the volcanic rocks) and sedimentary rocks (10 % in total), and is often related to a continental arc setting (Pat Shanks III and Thurston, 2012). The Zn-Pb-Cu Kuroko deposit in Japan is a classic example of this category (Robb, 2005). The general magmatism related to this environment is initiated by basaltic pillow lavas forming submarine shield volcanoes, followed by evolved silicic and pyroclastic volcanism composed of ash and pumice, crystal fragments, and lithic clasts (Pat Shanks III and Thurston, 2012). The bimodal-felsic assemblage is typical of the FII category from the classification scheme of Hart et al. (2004) (based on Lesher et al. (1986)), and categorizes VMS deposits into FI, FII, FIIIa, FIIIb, and FIV. **Feil! Fant ikke referansekilden.** summarizes the work of Hart et al. (2004) and list the geochemical parameters fundamental for this categorization. FII involves calc-alkaline dacites-rhyolites that also are widespread but often barren, however, the aforementioned Kuroko deposit and several other deposits (Hart et al., 2004) falls into this category. Categorizing of the genetically related rocks yield an indicator of potential VMS deposits within these rocks, which in practice works as a prospective tool in the exploration of new deposits (Hart et al., 2004).

Felsic rocks of evolved environments associated with post-Archean VMS deposits have rhyolites with elevated HFSE and REE contents (Piercey, 2010), and typically plot within the FIII-FII field of Figure 2.9, showing calc-alkaline chondrite-normalized trace element patterns (Hart et al., 2004).

	FI	**FII**	**FIIIa**	**FIIIb**	**FIV**
Lithology	Alkalic dacite-rhyolite	Dacite-rhyolite	Rhyodacite-high silica rhyolite	Rhyodacite-high silica rhyolite	Rhyodacite-high silica rhyolite
SiO2 (wt. %)	64-72	64-81	67-78	67-84	69-81
TiO2 (wt. %)	0.16-0.65	0.16-0.89	0.21-0.99	0.09-0.73	0.09-0.57
Y (ppm)	6.0-31.0	11.0-73.0	25.0-96.0	72.0-238.0	18.0-63.0
Zr/Y	8.8-31.0	3.2-12.12	3.9-7.7	1.7-6.2	0.67-4.8
Yb (ppm)	0.43-3.8	1.3-7.9	3.4-9.3	5.0-32.0	1.5-8.4
$[La/Yb]_{CN}$	5.8-34.0	1.7-8.8	1.5-3.5	1.1-4.9	0.22-2.1
$[Eu/Eu^*]_{CN}$	0.87-1.5	0.35-0.91	0.37-0.94	0.20-0.61	No data
Affinity	Alkaline - calc-alkaline	Calc-alkaline	Tholeiitic	Tholeiitic	Tholeiitic

Table 2.1: Overview of the geochemical characteristics of the FI, FII, FIIIa/b and FIV category from Hart et al. (2004). Chondrite normalizing values are based on Nakamura (1974) (Hart et al., 2004).

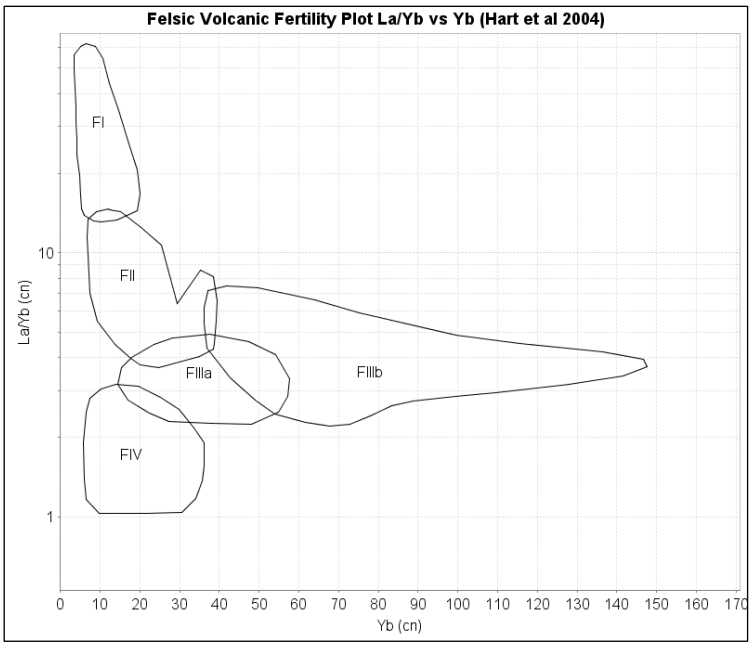

Figure 2.9: Felsic volcanic fertility plot based on chondrite-normalized La/Yb and Yb from Hart et al. (2004), which is an upgraded version based on Lesher et al. (1986).

2.3 Metamorphism

2.3.1 Geothermobarometry

To establish the peak metamorphic conditions of a rock sample the most anhydrous coexisting mineral assemblage must be established (Bucher and Grapes, 2011). A rough estimate can be achieved by using a petrogenetic grid to find a characteristic mineral assemblage, however, geothermobarometers yields a more accurate result (Bucher and Grapes, 2011). The principal foundation of geothermobarometers is that coexisting (equilibrated) minerals exchange specific components with changing P and T through *two* reactions, most commonly an *exchange reaction* and/or a *net-transfer reaction*, forming lines in a P-T diagram representing the equilibrium relationship (Bucher and Grapes, 2011).

GB – GBMP geothermobarometer

The empirically based garnet–biotite–muscovite–plagioclase (GBMP) geobarometer, by Wu (2015), builds on the same activity models as the garnet-biotite thermometer of Holdaway (2000), together yielding a garnet-biotite (GB) garnet-biotite-muscovite-plagioclase (GBMP) geothermobarometer. This geothermobarometer is constructed for both Al_2SiO_5-bearing and Al_2SiO_5-absent assemblages metapelites in the temperature (T) and pressure (P) range of 450-840 °C and 1-14 kbar, wherein the *barometer* is based on two net-transfer reactions of Fe and Mg, from Hodges and Crowley (1985) and Hoisch (1990):

$$\underset{\text{An in Pl}}{3CaAl_2Si_2O_8} + \underset{\text{Ann in Bt}}{KFe_3(AlSi_3)O_{10}(OH)_2} = \underset{\text{Alm in Grt}}{Fe_3Al_2Si_3O_{12}} + \underset{\text{Grs in Grt}}{Ca_3Al_2Si_3O_{12}} + \underset{\text{Ms in Ms}}{KAl_2(AlSi_3)O_{10}(OH)_2} \quad [2.5]$$

$$\underset{\text{An in Pl}}{3CaAl_2Si_2O_8} + \underset{\text{Phl in Bt}}{KMg_3(AlSi_3)O_{10}(OH)_2} = \underset{\text{Prp in Grt}}{Mg_3Al_2Si_3O_{12}} + \underset{\text{Grs in Grt}}{Ca_3Al_2Si_3O_{12}} + \underset{\text{Ms in Ms}}{KAl_2(AlSi_3)O_{10}(OH)_2} \quad [2.6]$$

While the garnet-biotite thermometer is based on the Fe ↔ Mg exchange-reaction:

$$\underset{\text{Alm in Grt}}{Fe_3Al_2Si_3O_{12}} + \underset{\text{Phl in Bt}}{KMg_3AlSi_3O_{10}(OH)_2} = \underset{\text{Prp in Grt}}{Mg_3Al_2Si_3O_{12}} + \underset{\text{Ann in Bt}}{KFe_3AlSi_3O_{10}(OH)_2} \quad [2.7]$$

The total pressure error of the GBMP geobarometer is ±1.2 kbar (Wu, 2015), whereas the temperature error in the GB geothermometer is ±25 °C. The Fe^{3+} contents of garnet and biotite are assumed to be 3 and 11.6 mol. %, respectively (Holdaway, 2000), whereas muscovite contain 0 mol. %, based on an assemblage containing ilmenite and/or graphite (Wu, 2015). For extremely reduced conditions the Fe^{3+} contents of biotite and garnet could be 0 mol. %, whereas for extremely oxidized conditions, wherein hematite coexists (rare), the Fe^{3+} contents of garnet and biotite are assumed to be 5 and 20 mol. % (Wu, 2015).

2.3.2 Metamorphism and deformation of VMS deposits

Metamorphism and deformation are two important factors controlling the geochemistry, mineralogy, and structural behaviour of sulphide mineralizations (Van Staal and Williams, 1984). According to Mosier et al. (2009), only 3 % out of 819 VMS deposits investigated worldwide were unmetamorphosed, whereof most of them in greenschist facies. Increasing metamorphic grades potentially lead to remobilization of pre-tectonic mineralizations, and can turn a previously uneconomic mineralization into an ore deposit by increasing the grain size and concentrate the metals in fold hinges (Marshall et al., 2000). However, folds can also be controlled by ore deposits by folding around them, thus creating the appearance

of remobilization (Van Staal and Williams, 1984). Shearing due to intense deformation result in folds being displaced along their axial trace (Marshall et al., 2000).

2.4 Geochronology

2.4.1 U/Pb dating

The use of radioactive- and radiogenic isotopes in the study of geochronology is a well-established field of geology (Schoene, 2014), where the naturally fixed decay rate, defined as the half-life (Winter, 2014), is utilized to date rocks. Uranium- and lead, which is commonly used to date the oldest rocks on earth (Schoene, 2014), is part of the U-Th-Pb system, involving the three naturally occurring radioactive isotopes of U (^{234}U, ^{235}U and ^{238}U), the radioactive isotope of Th (^{232}Th), and the three radiogenic isotopes of Pb (^{206}Pb, ^{207}Pb and ^{208}Pb), to which U and Th decay according to these lines of breakdown (Schoene, 2014, Winter, 2014):

$$^{238}U \rightarrow {}^{234}U \rightarrow {}^{206}Pb \ (\lambda = 1.5512e^{-10}\ year^{-1}) \quad [2.8]$$

$$^{235}U \rightarrow {}^{207}Pb \ (\lambda = 9.8485e^{-10}\ year^{-1}) \quad [2.9]$$

$$^{232}Th \rightarrow {}^{208}Pb \ (\lambda = 4.9475e^{-11}\ year^{-1}) \quad [2.10]$$

Where λ = the empirically defined *decay constant* (Schoene, 2014, Winter, 2014). U and Th are thus regarded as the *parent* isotope of the *daughter* isotope Pb. In reality, U and Th does not decay directly to Pb but breaks down through a chain of several short-lasting intermediate daughter isotopes. Nevertheless, if the subsequent isotopes are unaltered, U and Th can be treated as if they decayed directly to Pb (Schoene, 2014). Because U, Th and Pb are all incompatible elements they concentrate in the melt phase both during partial melting and fractional crystallization, explaining their high abundance in the continental crust (Winter, 2014, Robb, 2005). However, to produce a geochronometer (geological clock), uranium must be isolated where no net loss or gain of the parent isotope and subsequent daughter isotopes can be achieved, e.g. in a crystallizing mineral. One of the most common minerals used in dating of rocks, zircon, incorporates uranium (and negligible common lead ^{204}Pb) during crystallization, herein develops a closed *system* that, if not opened to alteration processes, represents the age of crystallization (Schoene, 2014). Its strong resistance to weathering and high closure temperature (T_C > 900°C) makes it able to avoid U-Pb loss, thus being a suitable mineral for U-Pb dating (Schoene, 2014). Titanite is another mineral used for U-Pb dating, however, due to its lower T_C than zircon the geochronometer is reset during high-grade metamorphism, hence, is more suitable at constraining maximum (cooling) ages of orogenic events or exhumations (Schoene, 2014). The exact closure temperature is not agreed upon but is commonly regarded as 650 °C depending on grain size (higher for larger grains) (Kylander-Clark et al., 2008). Evidence exists of closure temperatures of > 700 °C, in that case does not date cooling or exhumation but rather metamorphism (Frost et al., 2001). It usually incorporates significate amounts of initial common lead that, if not considered, result in an apparently older rock (Schoene, 2014).

Concordia plot

When visualizing the U-Pb age of a rock there are *three* isochron equations that can be utilized to create a concordia plot, hence, different diagrams exist, the most common being

the Tera-Wasserburg (T-W) diagram and the Wetherill diagram, whereof this study uses the former. The three isochron equations or clocks is as follows (Schoene, 2014):

$$^{206}Pb^*/^{238}U = (e^{\lambda 238t} - 1) \quad [2.11]$$

$$^{207}Pb^*/^{235}U = (e^{\lambda 235t} - 1) \quad [2.12]$$

$$^{207}Pb^*/^{206}Pb^* = (e^{\lambda 235t} - 1) \quad [2.13]$$

Where * = *radiogenic*, *t* = is the age of the rock and λ is the same as eq. 2.6-8. For the Wetherill diagram eq. 2.11 and 2.12 are placed on the y- and x-axis, respectively, yielding a downward concave concordia curve, as a consequence of the faster decay of $^{235}U \rightarrow {}^{207}Pb$ than $^{238}U \rightarrow {}^{206}Pb$, along which the closed U-Pb system develops (Schoene, 2014, Winter, 2014). The T-W diagram places eq. 2.11 and 2.13 onto the x- and y-axis, respectively, yielding an upward facing concave concordia curve because of the faster decay of ^{235}U.

If the decaying system (e.g. zircon) at one point is opened to weathering fluids (e.g. due to higher temperatures), the highly mobile Pb is depleted, of which all isotopes are depleted equally (similar D_{Rock}^{Fluid}), consequently moving the system a distance proportional to its loss of Pb *directly* towards the point of origin. Most likely, the zircon-bearing rocks have several individual crystals of zircon that are variably affected, thus have a variable loss of Pb, resulting in several points creating a line called a *discordia* (Winter, 2014). From each individual point the (new) system decays according to the equations, each creating their own concordia, however, still colinear along the discordia, that with time rotate clockwise proportional to the aging (now closed) system. The latter result in a curve crossing the original concordia at two points, in which the left point represents the *age of resetting*, whereas the right point represents the *age of crystallization*. If some zircons were unaltered, i.e. retained their Pb, these zircons plot along the original concordia, still representing the age of crystallization (Winter, 2014). The calculated discordance of the data is yielded from the following equation:

$$\text{Discordance (- \%)} = 100 - (100 * ((^{206}Pb/^{238}U) / (^{207}Pb/^{206}Pb))) \quad [2.14]$$

This principal applies to both diagrams, however, the discordia of the T-W diagram intersects the y-axis according to the amount of initial common lead, which is one of the advantageous of this diagram (Schoene, 2014), consequently enables the correction of this factor in for example titanite. In addition, all isotopes of the diagram are measured directly in the instrument, whereas for the Wetherill diagram ^{235}U is calculated based on the other isotopes creating a potential source of error.

3 Methods

3.1 Mapping and sampling

One weekend in the autumn of 2018 was used for reconnaissance of possible locations. The areas Hesjelia, Hammertjønna and Hellerfjellet were chosen to be investigated further, and were mapped during 14 days in August 2019. The area was largely above the tree line, making it possible to map on naturally occurring outcrops, however, large distances and high altitudes had to be covered to reach the interesting areas, making mapping less efficient. The mapping was done using an *Apple iPad (4th generation)* and the software *FieldMove* from Midland Valley, using a basic UTM map as basis. The iPad had an build-in GPS, which obtained horizontal and vertical data with an accuracy of ± 6 m and ± 8 m, respectively. Thus, all data collected were georeferenced, and different lithologies were given separate colours and drawn as polygons. Structural measurements were registered manually according to the measurement of the compass, although it was possible to use the build-in three axis gyroscope, however, the accuracy was uncertain. The structural measurements were initially executed using a Silva compass without the option of adjusting for declination, however, were midway in the field season changed to a geological compass of the brand Brunton Pocket Transit Geo Quad 4*90. Structural measurements reported here are given in dip/dip-direction, unless otherwise stated. The declination was not calibrated, in order to obtain similar measurements as the Silva compass. For closer investigations of the rock mineralogy a hand lens was used.

Samples were collected using a hammer and a chisel if necessary, to get as fresh samples as possible. For oriented samples it was most conveniently to measure the strike and dip and draw it on the sample as a dip-symbol. The measurements were however registered as dip/dip-direction, in accordance with all planar structural measurements, while lineaments like fold axes and lineations were measured and registered as trend and plunge. All samples were coded according to their field locality, HF (Hellerfjellet), HES (Hesjelia), and HAM (Hammertjønna), and described on mineralogy and textures on the iPad. Each sample was put in an individual bag to avoid contamination between different rock types.

Figure 3.1: Some of the field equipment. Apple iPad, field book, Silva compass, and a geological hammer.

3.2 Petrographic analysis

A total of 23 thin sections were prepared at the Department of Geology and Mineral Resources Engineering at the Norwegian University of Science and Technology (NTNU), whereof 11 were from drill core BH4508 at Hellerfjellet and 12 were made from the field samples. The latter were distributed between seven at Hellerfjellet, three at Hammertjønna, and two at Hesjelia. The thin sections from the drill core were coded according to depth and also given unique number, while field's thin sections inherit the code of the original sample. Additionally, four thin sections were kindly given by the Geological Survey of Norway (NGU) as supplement. All thin sections are 28x48 mm while the thickness depend on what thickness yield a white colour of quartz, usually ca. 30µm. Examination of the thin sections were done using a polarization microscope at NTNU's student laboratory and NGU's laboratory. Whole thin section scans were done using the Slip Scanner Olympus microscope, while detailed photographs were taken by a Nikon Eclipse E600 microscope, both at NTNU's EM laboratory. See Appendix B for thin section scans.

3.3 Major and trace elements analysis

A total of 109 samples were sent to *CRS Laboratories* in Kempele, Finland for sample preparation, while *MSALABS* in Canada performed the geochemical analysis. The results of the analysis can be found in Appendix C. The sample preparation used the following procedure:

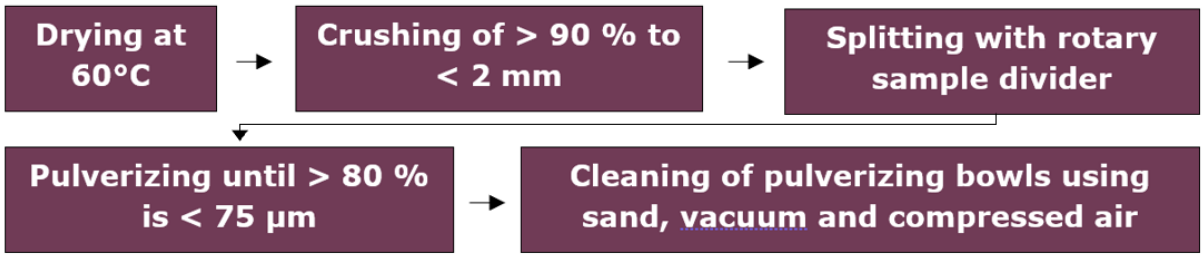

Six different methods were applied to analyse the pulverized samples. All samples are analysed using suitable reference materials, blanks, and duplicates. The following method description is the procedure outlined by MSALABS.

WRA-310 (MSALABS, 2017b)

This method was used on the major and minor elements listed below (Table 3.1), and reports in wt. %. Samples were decomposed using lithium borate fusion while heating a muffle furnace at 1000°C with lithium borate flux. The fused sampled was cooled and dissolved in mineral acids. The resulting solution was analysed by *Inductively Coupled Plasma-Optical Emission Spectrometry* (ICP-OES). *Loss on ignition* (LOI) is also reported here.

	LOD (wt. %)				
Al_2O_3	0.01	K_2O	0.01	SiO_2	0.01
BaO	0.01	MgO	0.01	SrO	0.01
CaO	0.01	MnO	0.01	TiO_2	0.01
Cr_2O_3	0.01	Na_2O	0.01	LOI	0.01
Fe_2O_3	0.01	P_2O_5	0.01		

Table 3.1: Limit of detection (LOD) for the WRA-310 method. Elements reported as oxides in wt. %.

IMS-300 (MSALABS, 2017a)

This method was used on refractories and rare earth elements (REEs) Table 3.2. All preparations in this method are identical to WRA-310. The resulting solution were analysed using *ICP - mass spectrometry* (ICP-MS), and the result was reported in parts per million (ppm). Marked by blue squares in Figure 3.2.

	LOD (ppm)				
Ba	0.5	Ho	0.01	Ta	0.1
Ce	0.1	La	0.1	Tb	0.01
Cr	10.0	Lu	0.01	Th	0.05
Cs	0.01	Nb	0.1	Tm	0.01
Dy	0.05	Nd	0.1	U	0.05
Er	0.03	Pr	0.03	V	10.0
Eu	0.03	Rb	0.2	W	1.0
Ga	0.2	Sm	0.03	Y	0.5
Gd	0.05	Sn	5.0	Yb	0.03
Hf	0.2	Sr	0.1	Zr	2.0

Table 3.2: LOD for the IMS-300 method. Elements reported in ppm.

IMS-230 (MSALABS, 2017c)

The elements analysed by this method are Ag, Cd, Co, Cu, Pb, Zn, Mo, Ni (Table 3.3). The samples were digested using hydrofluoric-, hydrochloric-, nitric-, and perchloric acid (four acid digestion). The samples were then filled up to volume with deionized water, and the solution were analysed using ICP-MS and ICP - Atomic Emission Spectrometry (ICP-AES). Result reported in ppm.

	LOD (ppm)		
Ag	0.01	Cu	0.2
Cd	0.02	Pb	0.5
Mo	0.05	Zn	2.0
Co	0.1	Ni	0.2

Table 3.3: LOD for the IMS-230 method. Elements reported as ppm.

IMS-130 (MSALABS, 2017d)

Elements analysed by this method are As, Au, Bi, Hg, Sb, Se, and Tl (Table 3.4). The samples were digested under heat with a hydrochloric- and nitric acid mixture called "aqua regia", before being filled up to volume with deionized water before the solution is analysed by ICP-MS and ICP-AES. Result reported in ppm.

	LOD (ppm)		
As	0.1	Sb	0.05
Au	0.0005	Se	0.2
Bi	0.01	Tl	0.02
Hg	0.005		

Table 3.4: LOD for the IMS-130 method. Elements reported as ppm.

SPM-512 (MSALABS, 2018b)

This method is used for analysing total carbon and sulfur. The samples were weighed into a crucible, and added iron and tungsten as accelerators, before being placed in a LECO analyser where it was heated. CO_2 and SO_2 is released as the sample heats, and this is analysed by an IR detection system. LOD is 0.01 wt.% for both elements. Result reported in ppm.

LOI-1000 (MSALABS, 2018a)

Loss on ignition (LOI) was also measured by weighing the sample material in a crucible, placed in an oven or furnace at 1000 for one hour, cooled and then weighed again. LOD = 0.01 wt. %.

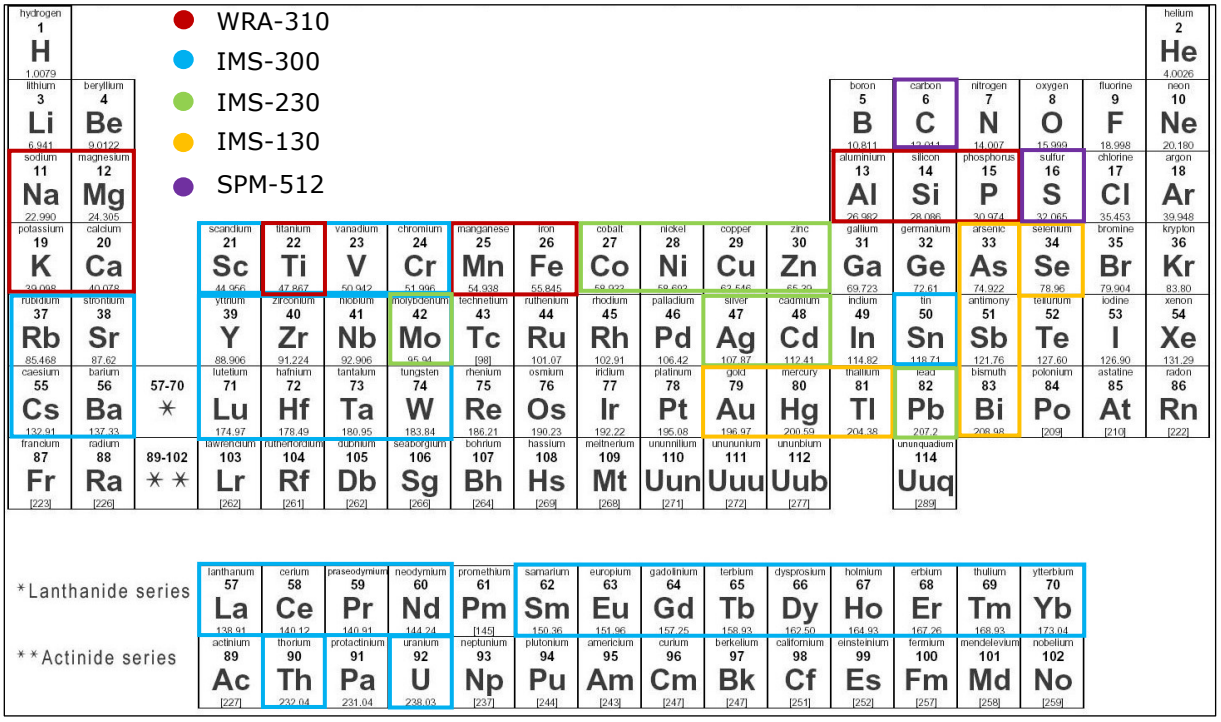

Figure 3.2: All elements analysed in the geochemical analysis. Red squares are WRA-310, blue squares are IMS-300, green squares are IMS-230, yellow squares are IMS-130, and purple squares are SPM-512.

3.4 Mineral Chemistry

To analyse the mineral chemistry a scanning electron microscope (SEM) and an electron probe micro-analyser (EPMA) were employed. SEM was performed both at the Electron Microscopy LAB at NTNU, and at NGU. Prior to analysis the samples were coated by a Cressington Carbon Coater 208 with a ca. 10 µm thick layer of graphite. This is done in order to avoid sample charging of the non-conductive samples (Reed, 2005).

3.4.1 Scanning electron microscope (SEM)

At NTNU, a Hitachi Analytical Variable Pressure SU6600 SEM accompanied by Bruker Quantax 800 Espirit software was used for analysis of one thin section. The instrument has an X-ray energy dispersive spectrometer (EDS), and the purpose of the analysis was to complement the petrographic interpretation by using semi-quantitative point analysis and mapping. The electron beam was set to an acceleration voltage of 20 kV and a working distance of 15 mm.

At NGU, the 1450 Variable Pressure (VP) SEM manufactured by LEO Electron Microscopy Ltd were used. It was equipped with an X-ray analytical system accompanied by version 4.09 of the INCA software from Oxford Instruments. The analysis was performed on zircons and titanites in relation to geochronological analysis, subsequent to mounting and polishing. The electron beam was set to an acceleration voltage of 15 kV and a working distance of 21 mm. Cathodoluminescence (CL) were obtained to reveal internal structures such as growth zoning and core-rim relationships.

3.4.2 Electron probe micro-analyser (EPMA)

Two thin sections were analysed by using the JEOL JXA-8500F Electron Probe Micro-analyser (EPMA) at the Electron Microscopy Lab, at NTNU Trondheim. The instrument is equipped with two X-ray systems, a wavelength dispersive spectrometer (WDS) and an energy dispersive spectrometer (EDS), whereof the former was used here. The accelerator voltage was set to 15 kV with a beam current of 10 nA (for all analyses) and a defocused beam width of 1-3 µm, depending on mineral and zonation. The standards for the analysis were single crystals from Astimex Scientific Ltd, and calibrations were set up by Kristian Drivenes and Bjørn Eske Sørensen. Elements, standards and detection limits for all minerals investigated are given in Table 3.5, Table 3.6, Table 3.7, and Table 3.8.

Biotite | Garnet | Chlorite

Element	Channel	Crystal	Standard	Acc. Volt. (kV)	D.L (ppm)	STD. %
Mg	1	TAPH	Diopside	15	652	4.7
Na	2	TAPL	Albite	15	211	5.4
Al	2	TAPL	Almandine	15	217	3.7
F	2	TAPL	Fluorite	15	1218	5.6
Ca	3	PETL	Diopside	15	187	0.9
Cr	3	LIFL	Chromite	15	523	0.4
K	3	PETL	Sanidine	15	164	1.1
Fe	4	LIFL	Magnetite	15	456	0.2
Ti	4	PETL	Rutile	15	318	0.6
Si	5	PETH	Diopside	15	334	3.2
Mn	5	LIFH	Rodonite	15	520	0.3
Cl	5	PETH	Tugtupite	15	145	1.6

Table 3.5: Elements, standards, and detection limits for biotite, garnet, and chlorite.

Plagioclase

Element	Channel	Crystal	Standard	Acc. Volt. (kV)	D.L (ppm)	STD. %
Mg	1	TAPH	Diopside	15	525	4.7
Na	2	TAPL	Albite	15	476	5.4
Al	2	TAPL	Sanidine	15	344	4.2
Ca	3	PETL	Diopside	15	184	0.9
Ti	3	PETL	Rutile	15	260	0.6
Sr	3	PETL	Plagioclase	15	492	2.4
Ba	4	PETL	Sanidine	15	599	0.5
Fe	4	LIFL	Magnetite	15	363	0.2
K	5	PETH	Sanidine	15	248	2.4
Si	5	PETH	Albite	15	674	1.1
Mn	5	LIFH	Rodonite	15	510	0.3

Table 3.6: Elements, standards, and detection limits for plagioclase.

Muscovite

Element	Channel	Crystal	Standard	Acc. Volt. (kV)	D.L (ppm)	STD. %
Mg	1	TAPH	Diopside	15	558	4.7
Na	2	TAPL	Albite	15	198	5.4
Al	2	TAPL	Sanidine	15	199	4.2
Fe	2	TAPL	Fluorite	15	1240	5.6
Ca	3	PETL	Diopside	15	194	0.9
Cr	3	LIFL	Chromite	15	523	0.4
K	3	PETH	Sanidine	15	164	1.1
Fe	4	LIFL	Magnetite	15	439	0.2
Ti	4	PETL	Rutile	15	290	0.6
Si	5	PETH	Diopside	15	453	3.2
Mn	5	LIFH	Rodonite	15	486	0.3
Cl	5	PETH	Tugtupite	15	147	1.6

Table 3.7: Elements, standards, and detection limits for muscovite.

Amphibole | Clinozoisite | Zoisite

Element	Channel	Crystal	Standard	Acc. Volt. (kV)	D.L (ppm)	STD. %
Mg	1	TAPH	Diopside	15	193	4.7
F	2	TAPH	Fluorite	15	135	5.6
Na	2	TAPL	Albite	15	145	5.37
Si	2	TAPL	Almandine	15	138	2.92
Al	2	TAPL	Sanidine	15	80	4.2
Ca	3	PETL	Diopside	15	69	0.86
K	3	PETL	Sanidine	15	54	1.07
Cr	3	LIFL	Chromite	15	166	0.36
Fe	4	LIFL	Magnetite	15	150	0.22
Ni	4	LIFL	Pentlandite	15	160	0.12
Mn	4	LIFL	Rodonite	15	161	0.27
Ti	5	PETH	Rutile	15	102	0.59
Zn	5	LIFH	Zn	15	300	0.67
Cl	5	PETH	Tugtupite	15	50	1.62

Table 3.8: Elements, standards, and detection limits for amphibole, clinozoisite, and zoisite.

3.5 Geothermobarometry

The GBMP geobarometric calculations were done using the Excel spreadsheet of Wu (2015), wherein the GB thermometer of Holdaway (2000) is included, together yielding a GB-GBMP geothermobarometer. The GB thermometer is applied iteratively to obtain the temperature and pressure estimate. To verify the estimates the plagioclase-amphibole geobarometer Excel spreadsheet of Molina et al. (2015) was used. Because it does not calculate the temperature, the average temperature estimate from the GB thermometer was used as input for all calculations. In both spreadsheets, only the analysis from the rims of grains shearing contacts were used in the calculations, because only these can be assumed to coexist and have transferred elements (Bucher and Grapes, 2011).

In the GB-GMBP geothermobarometer, a total of 6 calculations were done using 22 unique analysis from sample 38310 (abbreviated "10"), whereof two garnet analysis were reused. A total of 7 calculations were done in the plagioclase-amphibole geobarometer, by using 12 unique analysis from sample 38303 (abbreviated "03"), whereof two amphibole analysis were reused.

3.6 Geochronology

Two samples (HF-02 and S-6) were prepared for geochronological zircon and titanite analysis. The samples were initially crushed down from large cobbles to pebble sized fractions by putting them into a thick plastic bag and using a hammer. By using the Selfrag Lab at the Department of Geology and Mineral Resources Engineering at NTNU, the samples were crushed down to a sandy fraction that were ready to being separated.

The separation of zircons and titanite were completed at NGU by using standard techniques including water table, heavy liquids, magnetic separation, and final hand picking under a binocular microscope. The zircons were mounted in epoxy and polished to approximately half thickness.

LA–ICP–MS (Laser ablation Inductively Coupled Mass Spectrometry) analyses were conducted using the instrument set-ups at the Geological Survey of Norway (NGU): The analyses were carried out on an ELEMENT XR single collector, high-resolution ICP–MS, coupled to a UP193–FX 193 nm short-pulse excimer laser ablation system from New Wave Research. The laser was set to ablate single, up to 60 µm-long lines, using a spot size of 15 µm, a repetition rate of 10 Hz and an energy corresponding to a fluence of 3 J/cm2. Each analysis included 30 s of background measurement followed by 30 s of ablation. The masses 202, 204, 206-208, 232 and 238 were measured. For the zircon analyses, the reference material GJ–1 (Jackson et al., 2004) was used for correction of isotopic ratios, whereas 91500 (Wiedenbeck et al., 1995) and an in-house standard (OS–99–14; 1797 ± 3 Ma; Skår, 2002) were used to check precision and accuracy. For the titanite analyses, the reference material was MKED1 (Spandler et al., 2016), whereas BLR-1 (Aleinikoff et al., 2007), OLT-1 (Kennedy et al., 2010) and in-house standards OS-99-19 and OS-99-27 (both 398 Ma, Skår, unpublished data), were used to check precision and accuracy. The data were not corrected for common lead but monitoring of the signal for 204 allowed exclusion of affected data from further calculations. The data were reduced using the GLITTER® software (Van Actherbergh et al., 2001) and plots were made using Isoplot (Ludwig, 2003).

3.7 3D-modelling

The field data from the iPad were transferred to the computer software Move.2019.1.1 was used to make a 3D model of the ore deposits. The elevation data did not transfer to Move, hence all registered data was set to zero elevation. However, by projecting all measurements to a LiDAR map (downloaded from www.hoydedata.no) of the field area the altitude could be obtained with a standard deviation of only 0.026 m. By combining existing maps with field observations and sampling, the rock units could be digitized into complete maps of the field areas. This resulted in improvements of the existing maps from Søvegjarto et al. (1988) and Marker et al. (2012). Because only a limited amount of drill core data exists in both field areas, it is not possible to make an adequate 3D-model only based on this. Therefore, surface measurements including foliation- and fold axis data are the main foundation of the subsurface model. The method follows classical principle of making several 2D profiles and interpolate between them to produce 3D surfaces. A high density of sections produces an accurate model, however, the number of sections should be based on the complexity of the geology, i.e. changes in dip direction, dip, fold axis, and thickness of the rock units. Foliation- and fold axes measurements can be utilized by projecting them onto a 2D section.

The orientation of the sections is fundamental for an accurate subsurface model. The classical approach is to orient the sections along the dip direction of the bedding or foliation and extrapolate the geological contacts to depth. This approach suits only a general assessment of the orientation of rock units, and because sulphide mineralizations is known to become plastic and remobilize to concentrate in fold hinges of isoclinal folds, it often follows the fold axis' orientation (Van Staal and Williams, 1984). According to previous research in the area (e.g. Kruse (1980), Marker (1983), Søvegjarto et al. (1988)), this is the case for the Hesjelia-Hammertjønna ore zone, and most likely the Hellerfjellet ore deposit also. Thus, the sections are constructed based on the trend of the fold axis, and the subsurface dip is based on its plunge, however, also combines it with the drill core data that exist.

The result of the airborne transient electromagnetic (TEM) survey carried out by SkyTEM in 2007 is used for subsurface interpretation and correlation with the 3D-model. The TEM data is imported into the software (Move) as layers, whereof each layer represents the average conductivity of a 20-meter interval along the Z axis. An example is presented in Figure 3.3 below, along with the conductivity reference bar (siemens per meter, S/m) that the maps are colour coded according to. If the topography is below the elevation of the layer, the colour is white. In Hesjelia-Hammertjønna the lowest layer used is 240 meter above sea level (m.a.s.l.), and the highest is 420 m.a.s.l., whereas at Hellerfjellet the equivalent is 660 to 940 m (a.s.l.). The uppermost layer is almost at the topographical surface, and the lowermost layer represents the elevation at which the quality of the signal is reduced. As the data is georeferenced images it cannot be analysed automatically by the software. An alternative approach is by digitizing the anomalies as a rock unit, herein drawing a horizon around the anomaly for each individual layer, before connecting each horizon. The result is a 3D-model of the anomaly, which can be used as assistance in the geological modelling. This is only a practical method for simple anomalies and therefore only used at Hellerfjellet. The anomaly at Hesjelia-Hammertjønna is complex and thus only used to correlate the final 3D-model.

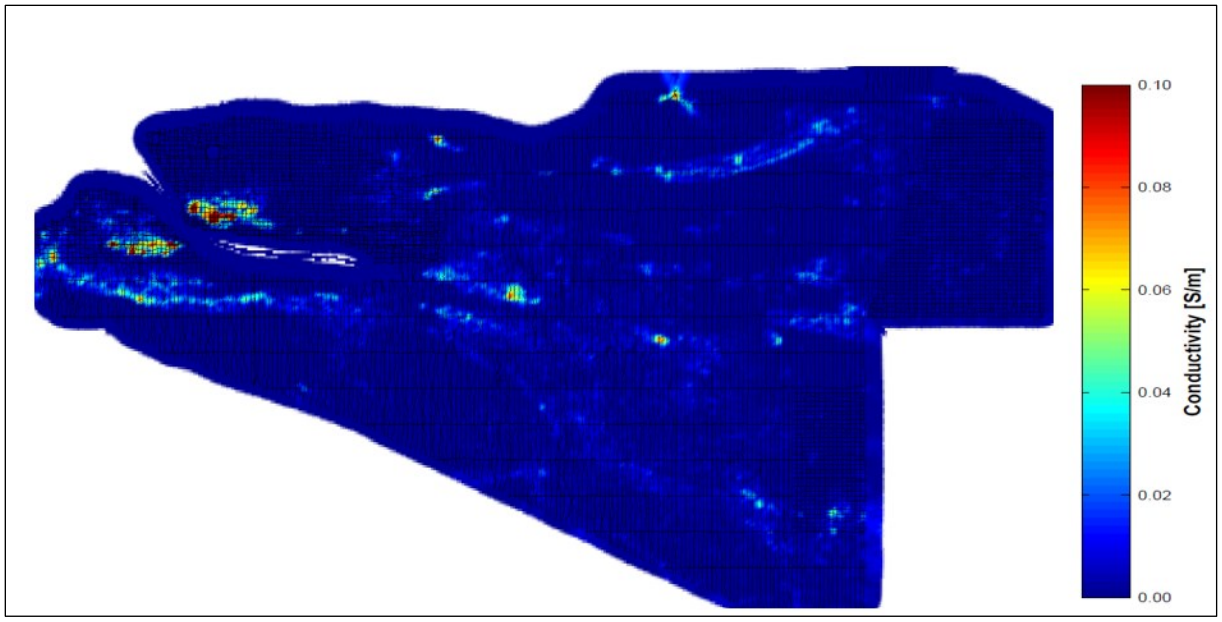

Figure 3.3: Example of a conductivity interval map (300 m.a.s.l.) from the SkyTEM survey, with reference bar.

3.8 Sources of error

Including the horizontal and vertical error (±6 and ±8 m, respectively) of the GPS on the Apple iPad, the GSP could automatically turn off sometimes during mapping. However, due to similar experiences beforehand this was quickly noticed and corrected. As stated above, the structural measurements were done with a compass without calibration of declination. Unfortunately, the 3D modelling software Move was not equipped with a function to adjust for this, hence, there are deviations of ca. +6° degrees. This will of course have consequences for the liability of the model, and increases with distance.

The drill cores in Hesjelia were plotted on a map in the NGO1948 Gauss-K reference system in Kruse (1980). Because exact coordinates were missing the map was transferred into the program Incscape v. 0.92.4 where it was possible to accurately measure the length from the longitudinal and latitudinal lines to get the coordinates. Some small scale error is associated with this method but the result was in accordance with the original map. The thickness of each unit in the drill cores were measured from constructed profiles in Kruse (1980), also this in Inscape. The total length of the drill cores was reported (ca. 580 m), and the resulting total length from the calculation only deviated by 5 m. The coordinates were then converted into UTM coordinates and plotted into the LiDAR map at www.hoydedata.no to accurately obtain the altitude.

The samples that were made thin section of were cut into two pieces to send one piece to geochemical analysis. The thin section part was only cut as large as necessary to have a large as possible sample for geochemical analysis to increase the statistical representation. Subsequent to cutting the samples were washed and dried. They were again washed and dried at CRS laboratories prior to preparations, and equipment were cleaned between crushing, milling, and pulverization of each sample.

To avoid contamination of the samples analysed for geochronology the Selfrag Lab was cleaned between different samples. The washing board and buckets used to separate and gather zircons and titanite were washed between each sample. It is important not to contaminate with lead, thus, the plucking was done using a non-lead pincette.

4 Results

4.1 Field observations and petrography

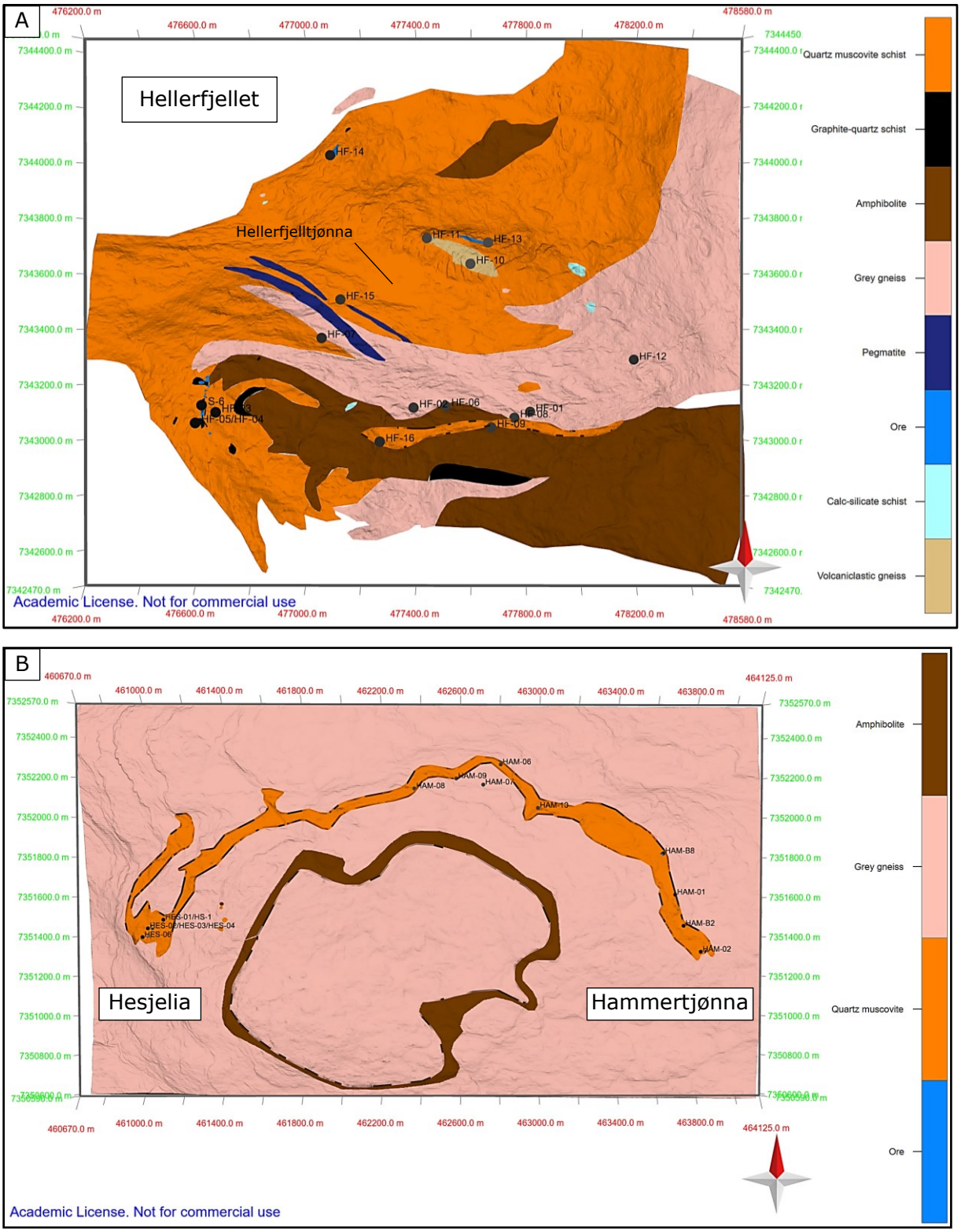

Figure 4.1: Geological maps based on field mapping in 2019 and maps from Søvegjarto et al. (1988) and Marker et al. (2012). Sample localities are also shown. A) Hellerfjellet. B) Hesjelia (west) – Hammertjønna (east).

The field area is characterized by crests of competent and well-exposed volcanic gneisses interrupted by hydrothermally altered rocks usually covered by soils and vegetation. The Hellerfjellet area has a diverse geology with sedimentary-, volcanic-, and probably mixed sedimentary-volcanic rocks, contrary to Hesjelia-Hammertjønna only containing volcanic rocks as observed from this and earlier studies, however, is less exposed due to the lower altitude. The final map (Figure 4.1) have been integrated with existing maps from Søvegjarto et al. (1988) and Marker et al. (2012), and resulted in adjustments of contacts. The raw field maps can be found in Appendix A.

4.1.1 Quartz muscovite schist (QMS)

The quartz muscovite schist (QMS) is the most common rock in the field area at Hellerfjellet and is the host rock for the massive sulphide mineralizations. It is a leucocratic, fine- to medium-grained and highly schistose rock, usually containing disseminated sulphide phases. The latter being the cause of a rusty appearance in the field (Figure 4.2A/B). At Hellerfjellet the QMS is usually graphite-bearing, grading into a graphite quartz gneiss (GQG) occurring in contact to the prospected mineralizations, in addition to one smaller occurrence just north of sample HF-14. This rock is very fine-grained, semi-massive and consist mainly of quartz, graphite, plagioclase, and only minor amounts of muscovite. Of the samples obtained from this unit the maximum total carbon (TC) content is 12.5 % (sample HF-x12b, see Appendix C, Table 8.3). Microscopy study of a sample of GQG (sample HF-05) show alternating bands of fine grained quartz + graphite and coarser grained quartz free of graphite (Figure 4.3F), possibly representing a transposed sedimentary layering. Sample HF-03 (Figure 4.3), with a TC of 4.97 %, represents a very fine grained semi-massive graphite-quartz rock with no layering observed at the scale of the thin-section, however coarser grains of quartz are also here graphite free, again indicating a sedimentary origin where the depositional environments have been too energetic to deposit the organic matter turned to graphite. The GQG is structurally subjacent and suprajacent of the massive sulphide deposit, evident both from the field and drill core logging. Tourmaline porphyries is also observed in sample HF-03.

Extensive areas within the QMS unit contain clasts that appear either like boudined veins (in that case pseudoclasts), or imbricated clasts, indicating mass flow. This occurrence can be followed somewhat abruptly along the highest level of the QMS unit, but always situated above the mineralized zones, i.e. in the hanging wall. The matrix consists of thin alternating layers of medium to coarse-grained quartz/feldspar and pervasive layers of mica resulting in a very schistose rock. The rusty surface combined with deformation made it difficult to observe relics of primary bedding, other than possible imbrication. Because of the schistose and altered nature of the clastic rock it was not possible to get a decent thin section sample, however one sample were taken for geochemistry (sample HF-11).

In Hesjelia-Hammertjønna the host rock is an altered felsic rock with a similar mineral assemblage as the QMS at Hellerfjellet, however, from previous studies (e.g. Marker (1983); Søvegjarto et al. (1988)) it is regarded as a muscovite gneiss rather than schist. This rock has a somewhat higher modal amount of muscovite than the QMS based on the thin sections, and a schistose texture that dominates throughout the unit. Thus, the muscovite gneiss is from here called quartz muscovite schist (or QMS). During the mapping, a connection of the previously separated QMS unit in Hesjelia and Hammertjønna (Søvegjarto et al., 1988) was established based on several outcrops previously mapped as grey gneiss. The rock contains disseminated sulphides throughout the unit and sample

HAM-10 from one of the newly discovered QMS-outcrops yielded 0.3 % Zn, 0.16 % Pb, 0.01 % Cu and 9.55 g/t Ag. No graphite-bearing rocks or clastic rocks were observed in this area as at Hellerfjellet. The detailed field mapping has resulted in some changes to the original map from Marker et al. (2012).

In the microscope the muscovite content is 30-50% for the altered rocks and occurs as lath-shaped crystals forming a lepidoblastic texture according to the dominant paleo-stress field. It is therefore suitable to study fold geometries and paleo-stress indicators. Minor facies are biotite, sulphides, feldspar, garnet, zircon, apatite, and monazite. The quartz content is usually 30-50% and displays anhedral grains with bulging and undulating extinction in the larger grains, whereas smaller grains are strain-free. 120° triple junctions occur in small amounts in all samples. Sulphide facies, being mainly pyrite, pyrrhotite and sphalerite, exhibit a shape-preferred orientation (SPO) parallel to the dominant foliation.

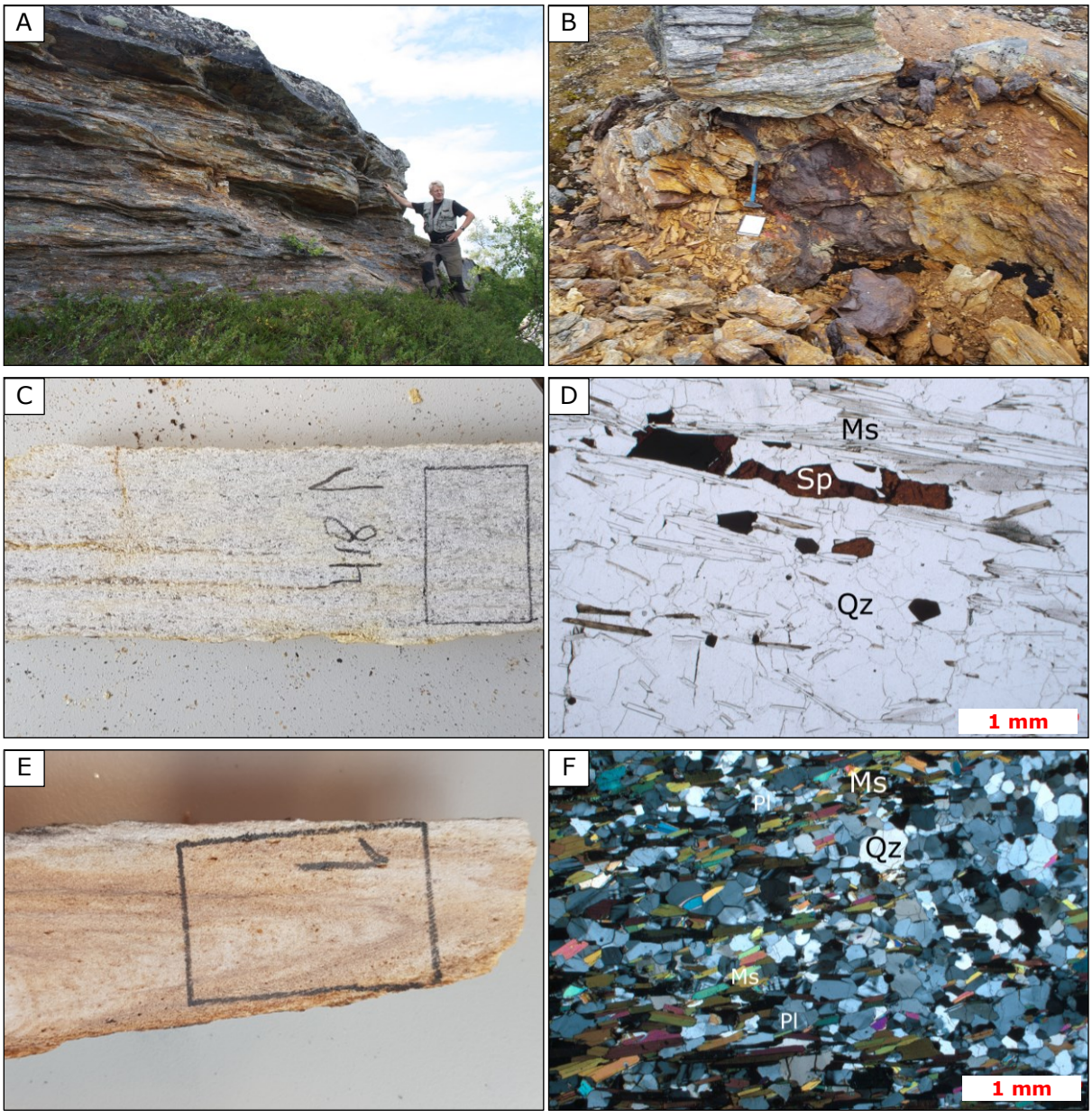

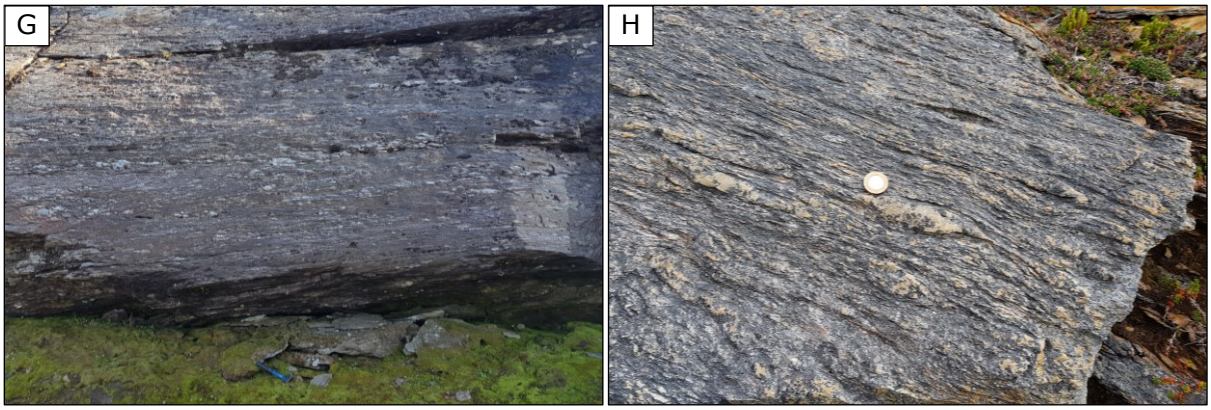

*Figure 4.2: Field-, hand sample- and thin section observations of the QMS. A) Outcrop of muscovite schist with disseminated sulphides, hence the rusty appearance. Person (ca. 170 cm) to the right for scale. B) Outcrop of the main prospect "p. M" at Hellerfjellet, surrounded by the muscovite schist host rock. C) Muscovite schist with disseminated sulphides (sample HAM-10). Marked area for 28*48 mm thin section. D) Microphotograph of HAM-10 with sphalerite (dark red/brown), muscovite and quartz, in plane polarized light. Sphalerite are elongated in the plane of foliation. E) Sample HF-16 from Hellerfjellet of an isoclinally folded muscovite schist. Marked area for 28*48 mm thin section. F) Microphotograph of HF-16 showing a mineral assemblage of quartz, mica, and plagioclase. G/H) A quartz muscovite schist with boudinaged clasts of quartz/feldspar, at Hellerfjellet. Some clasts appear imbricated (G), indicative of flow, while other appear more like boudined veins (H).*

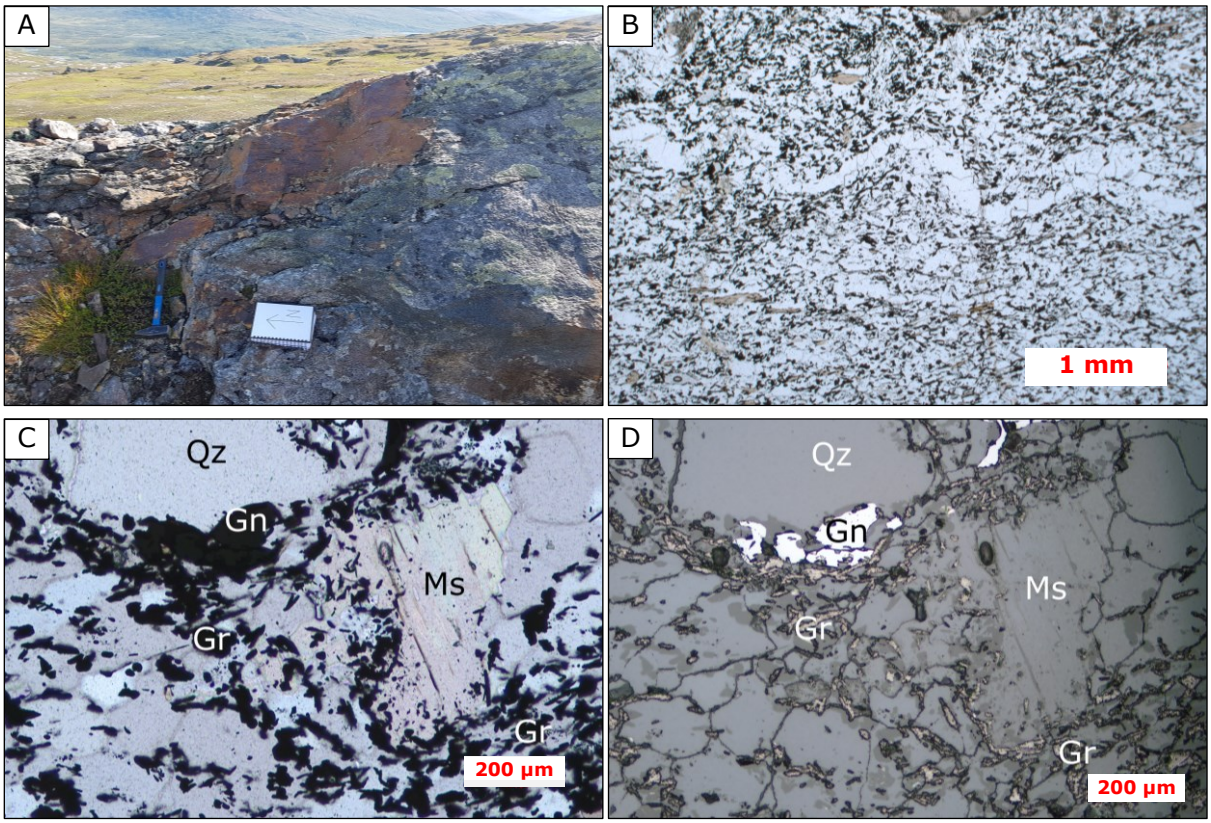

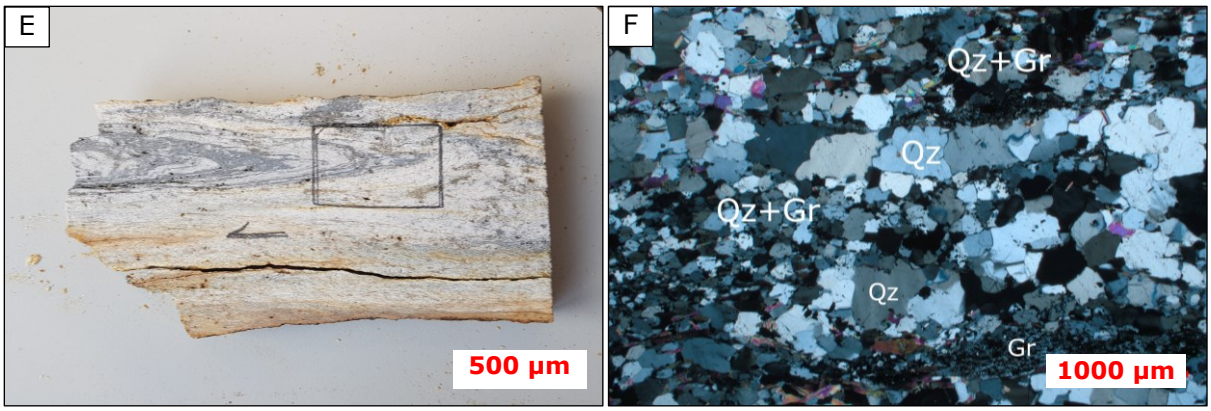

Figure 4.3: GQG samples. A) The location for sample HF-03 at Hellerfjellet. A semi-massive graphite schist encircling an ore lense. B) Microphotograph (ppl) of sample HF-03 with black coloured and very fine grained graphite with a crenulated stripe of quartz. C) Detailed microphotograph (ppl) of HF-03. D) Microphotograph (reflected light) of identical area from C, differentiating between galena and graphite. E) Sample HF-05: A graphite schist adjacent to the outcropping ore at Hellerfjellet. F) Microphotograph (xpl) of HF-05 showing the bands of fine grained quartz + graphite alternating with coarser grained bands of quartz.

4.1.2 Massive sulphide mineralizations

The sulphide-rich rock is a fine- to coarse-grained semi-massive to massive rock typically consisting of pyrite, pyrrhotite, sphalerite, galena, and chalcopyrite, while quartz, muscovite and hornblende are the major gangue minerals. At Hellerfjellet there are 21 prospects related to earlier explorations, wherein the sulphide mineralizations outcrop as lenses in the graphitic QMS host rock. These massive to semi-massive lenses appear systematically along the strike of the foliation, with a maximum thickness of ca. 1.5 m and a maximum width of ca. 3 m. The major minerals are sphalerite and pyrrhotite, while galena and chalcopyrite are minor. Overall, the surrounding QMS contain disseminated sulphides, however the sulphide grade of the area between the individual enriched lenses is difficult to establish because of overlying soil and vegetation. Two semi-massive to massive mineralized zones also exist north and north-east of Hellerfjelltjønna, respectively (Figure 4.1 and Figure 4.4C/D). The north-westerly zone can be traced 380 m along strike and consist largely of semi-massive pyrite mineralization. The north-easterly zone extends ca. 260 m along a steep cliff paralleling the trend of the mineralized zone, that consist of thin sphalerite- and galena-rich bands. The mineralizations are foliation parallel and conformable to the host rock.

In Hesjelia there are six individual outcrops of semi-massive to massive sulphide mineralizations, all having been prospected, with a thickness of up to 2 m and width of max. 10 m. Contrary to Hellerfjellet, the lenses occur seemingly random within the hinge zone of an isoclinally folded muscovite gneiss host rock. The 3D-modelling will provide answers to the outcropping pattern (see section 3.7). In Hammertjønna, there are four prospected mineralizations appearing along strike, in addition to one previously unexplored semi-massive mineralization, occurring as an extension along strike from the prospected mineralizations (sample HAM-B8 in Figure 4.1). The size of the individual outcropping mineralizations is smaller than at Hesjelia, reaching up to 1.5 m thick and 3 m wide. There are also enriched zones between the prospects, evident by sample HAM-B2. Also here are the mineralizations foliation-parallel and conformable to the host rock.

In the microscope the overall texture can be described as anhedral to subhedral, inequigranular and porphyritic. Sphalerite and galena appear as anhedral grains in a groundmass between the subhedral to euhedral pyrrhotite and pyrite. There are inclusions of sphalerite in the pyrrhotite grains and staurolite, suggesting a metamorphic transition.

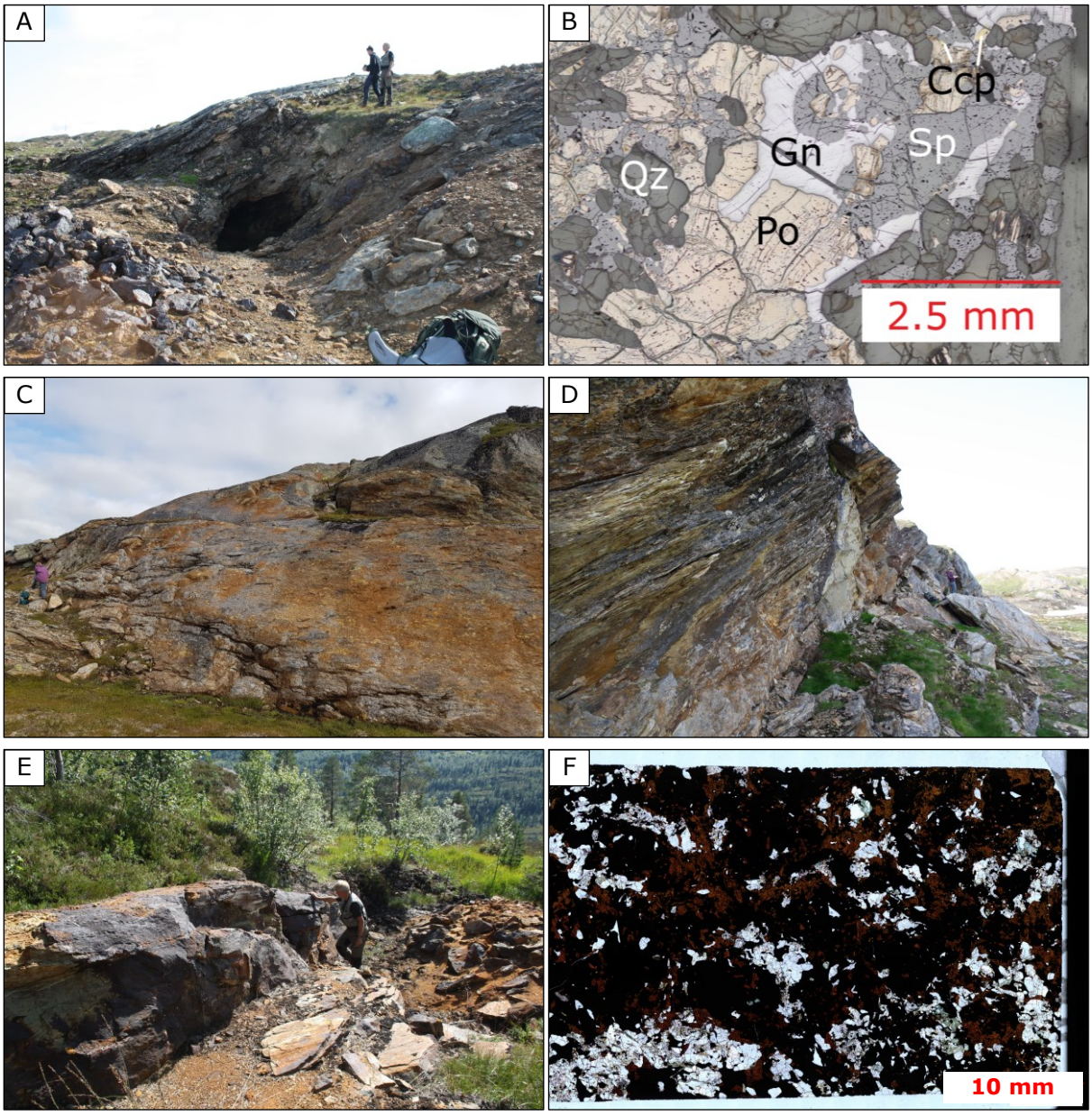

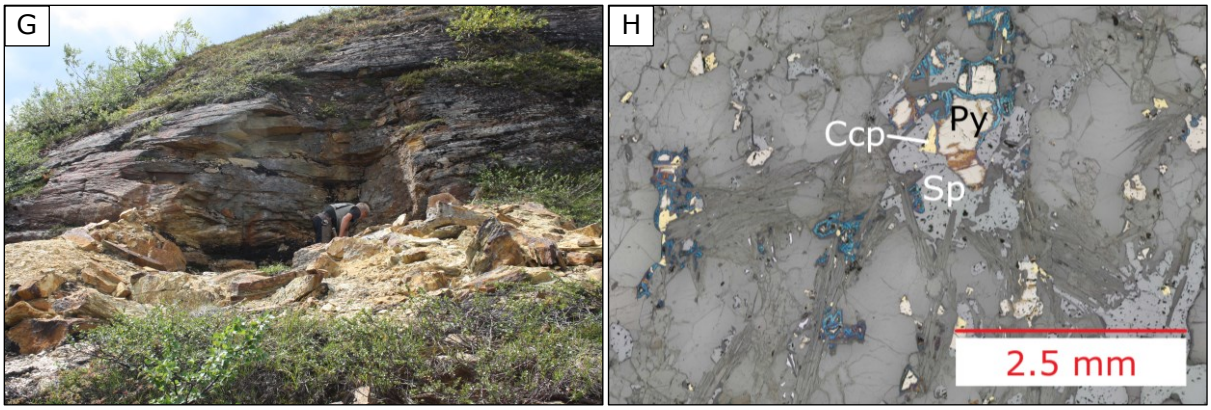

Figure 4.4: Mineralized zones and thin sections of related samples. A) Prospect nr. 4 at Hellerfjellet with graphite-bearing QMS in the hanging-wall of the ca. 3 m wide and 1.5 m thick mineralized lense. B) Microphotograph (reflected light) of a massive mineralized sample from one of the prospects on Hellerfjellet. Pyrrhotite (po) are cracked but crystal faces are still somewhat intact. Contrary, sphalerite (sp), galena (gn) and chalcopyrite (ccp) lack crystal faces and fill in cracks in the pyrrhotite and silicates, suggesting plastic deformation of these minerals. C) A new mineralized zone north of Hellerfjelltjønna with sphalerite. D) A mineralized zone, sampled as HF-13, north-east of Hellerfjelltjønna with mainly sphalerite and galena. E) Prospect nr. 4 in Hesjelia with a massive mineralization outcropping as a 1.5 – 2 m thick layer and a length of ca. 10 m. F) Microphotograph (ppl) of a sample rich in sphalerite (deep red/brown colour). G) Prospect nr. 2 in Hammertjønna. H) A sample of semi-massive mineralization from Hammertjønna. The sulphide grains have a rim of an alteration mineral, likely covellite, seen in several samples.

4.1.3 Grey gneiss and metarhyolite

The grey gneiss is typically a leucocratic, fine-grained, porphyritic rock with a massive to foliated texture and a common mineral assemblage of quartz, feldspar, muscovite, and biotite. Variations in the mica-content is evident in the field, where it largely controls the foliation in the rock. It is the most abundant rock type in the field area and especially the massive type stands out in the terrain because of its resistance to weathering. The latter type is a quartz-rich, lighter coloured, fine-grained and homogenous rock with minor plagioclase and mica, interpreted as a metarhyolite (Figure 4.5C). It was sometimes challenging to differentiate between the foliated grey gneiss and the QMS, in cases where the latter lacked a rusty appearance resulting in minor contrasts between them. There are few observed abrupt changes and contacts between the two, which can be explained both by weathering and soil cover, however, may suggest a genetic relationship.

In the microscope the feldspars are mainly plagioclase, however a microcline-rich variety were observed and sampled on Hellerfjellet (Figure 4.5F). Accessory phases include ilmenite, sulphides, zircon, and apatite. A plasticly deformed texture is evident from anhedral grains with bulging boundaries, few 120° triple junctions and quartz with undulating extinction in cross-polarised light.

Because of the extensive occurrence in the Mofjell Group this rock type has been dated by zircon U-Pb dating (see section 2.4).

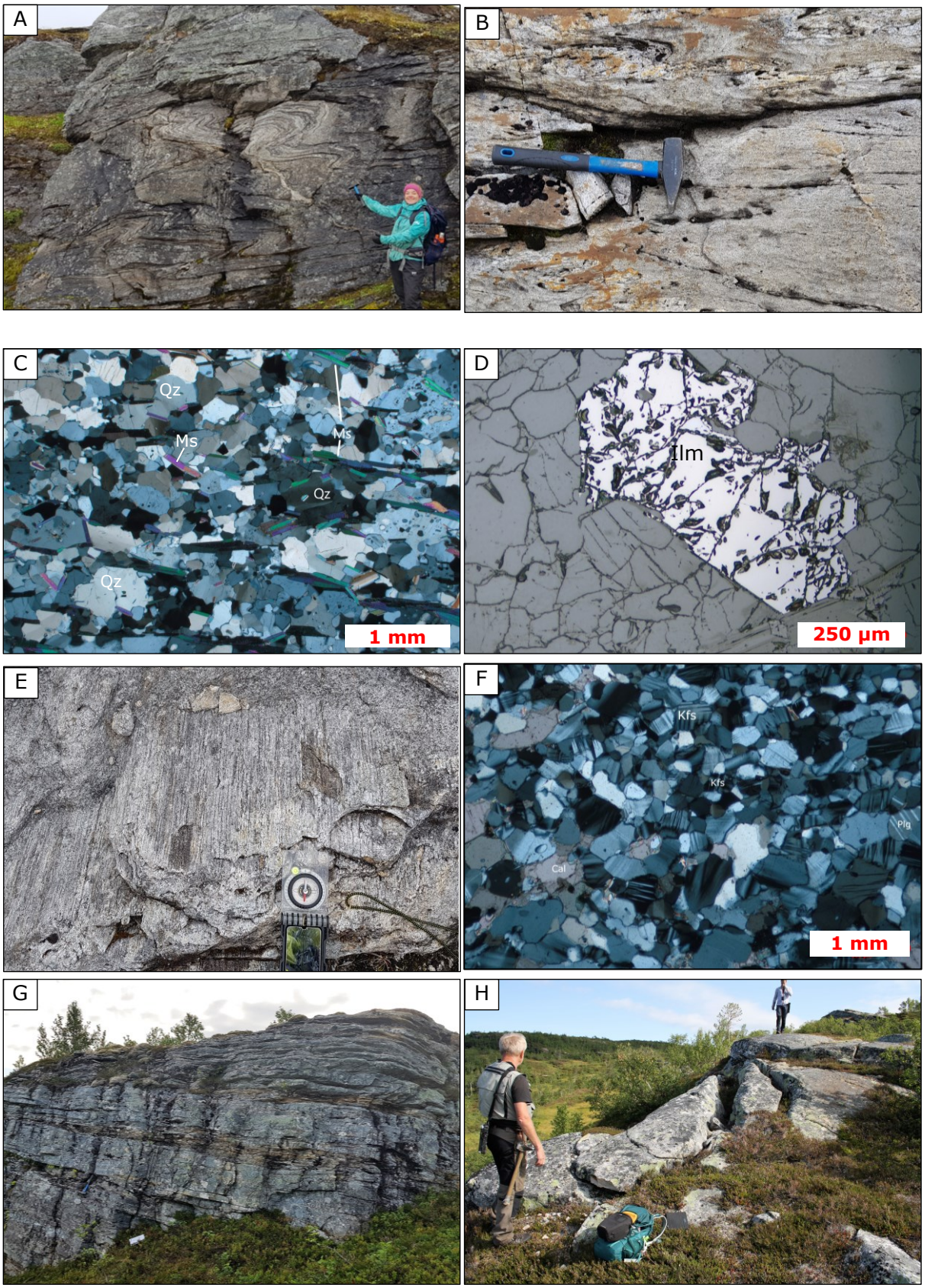

Figure 4.5: Grey gneisses and metarhyolites. A) A fine- to medium-grained, semi-massive grey gneiss outcropping at Hellerfjellet. B) Fine- to medium-grained massive grey gneiss with traces of calcite dissolution, at Hellerfjellet. Sample HF-07 represents this outcrop. C) Microphotograph (xpl) of sample TB96-030 representing a massive grey gneiss with a large amount of quartz and minor

amount of muscovite creating a weak foliation in the sample. The anhedral quartz and few occurrences of triple junctions suggest a dynamic recrystallisation. D) Microphotograph (reflected light) of sample TB96-041 showing the presence of a relatively large ilmenite grain. E) Microcline gneiss with a pervasive mineral lineation. F) Microphotograph of the microcline gneiss from E, sample HF-12. Calcite is abundant in this sample. G) Illustration of the texture variations in the grey gneiss at Hesjelia. Alternating layers of a semi-massive texture and micaceous schistose texture. F) Massive grey gneiss in Hesjelia with benching.

4.1.4 Amphibolites at Hellerfjellet

The amphibolites at Hellerfjellet is extensive and variable in both grain size and composition. It is commonly fine to medium-grained, schistose, and with a mineral assemblage of hornblende, plagioclase, biotite, and garnet, however variations without garnet also exists. The hornblende/biotite ratio and quartz content vary to the extent that it qualifies as a biotite schist in some areas. The rock face is regularly characterised by cm-sized depressions throughout the field area, indicative of calcite dissolution. Observations from drill core BH4508, intersecting amphibolite between 1-98 m, show a heterogenous rock with stripes of calcite up to 20 cm thick (Figure 4.6 C). Garnet is 1 – 10 mm large and show a systematically smaller grain size in relation to calcite compared with hornblende and biotite, i.e. the mafic minerals, which may be attributed to lower amounts of Fe-Mg-Al in calcite. Coronas of plagioclase exists around some of the larger garnets (Figure 4.6 D).

Microscopy studies of several samples from the field and drill core shows a major assemblage of hornblende, plagioclase, biotite, quartz, calcite and clinozoisite. Minor phases (<5%) include zoisite, titanite, muscovite, sulphides, iron oxides, staurolite and zircon. Hornblende displays a pale green to olive green colour in plane polarized light (Figure 4.6G) and commonly have an SPO resulting in a nematoblastic texture where biotite is not present. Plagioclase show both albite twinning and compositional zoning from core to rim (see section 3.4.2 (EPMA) for details). Garnet is poikiloblastic, skeleton-shaped and medium- to coarse-grained. The larger garnets exhibit a predominantly pre-tectonic growth evident by deflecting the foliation around the grains, whereas smaller grains partly overgrow the foliation and have an oblique internal foliation, suggesting syn- to inter-tectonic growth. The garnets are further studied in 3.4, about the P-T conditions.

Several thin sections contain coexisting zoisite/clinozoisite of variable proportions. In cross polarized light clinozoisite is primarily blue, but frequently show yellow-red-pink coloured patchy regions indicating elevated Fe content (from yellow to pink). Texturally clinozoisite and zoisite and overgrows plagioclase boundaries, suggesting a they grew on behalf of plagioclase. More about this in section 3.4.

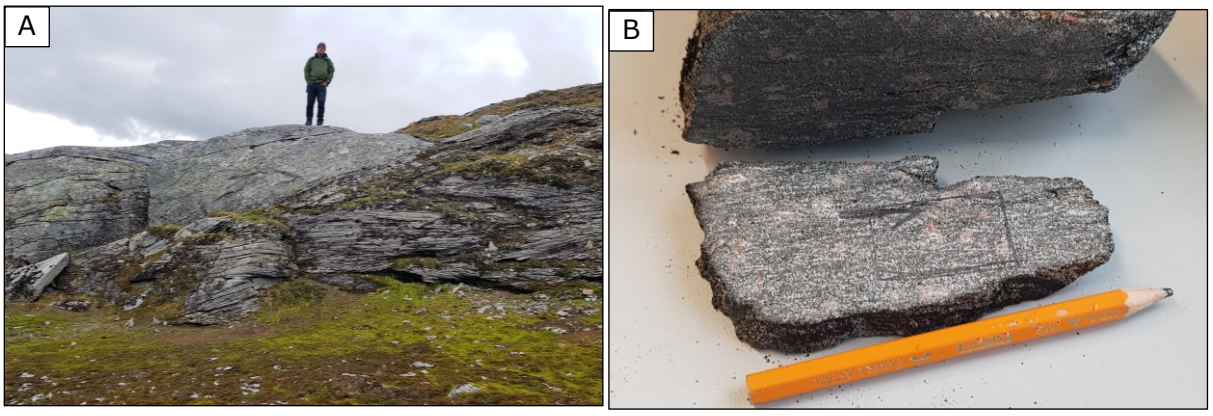

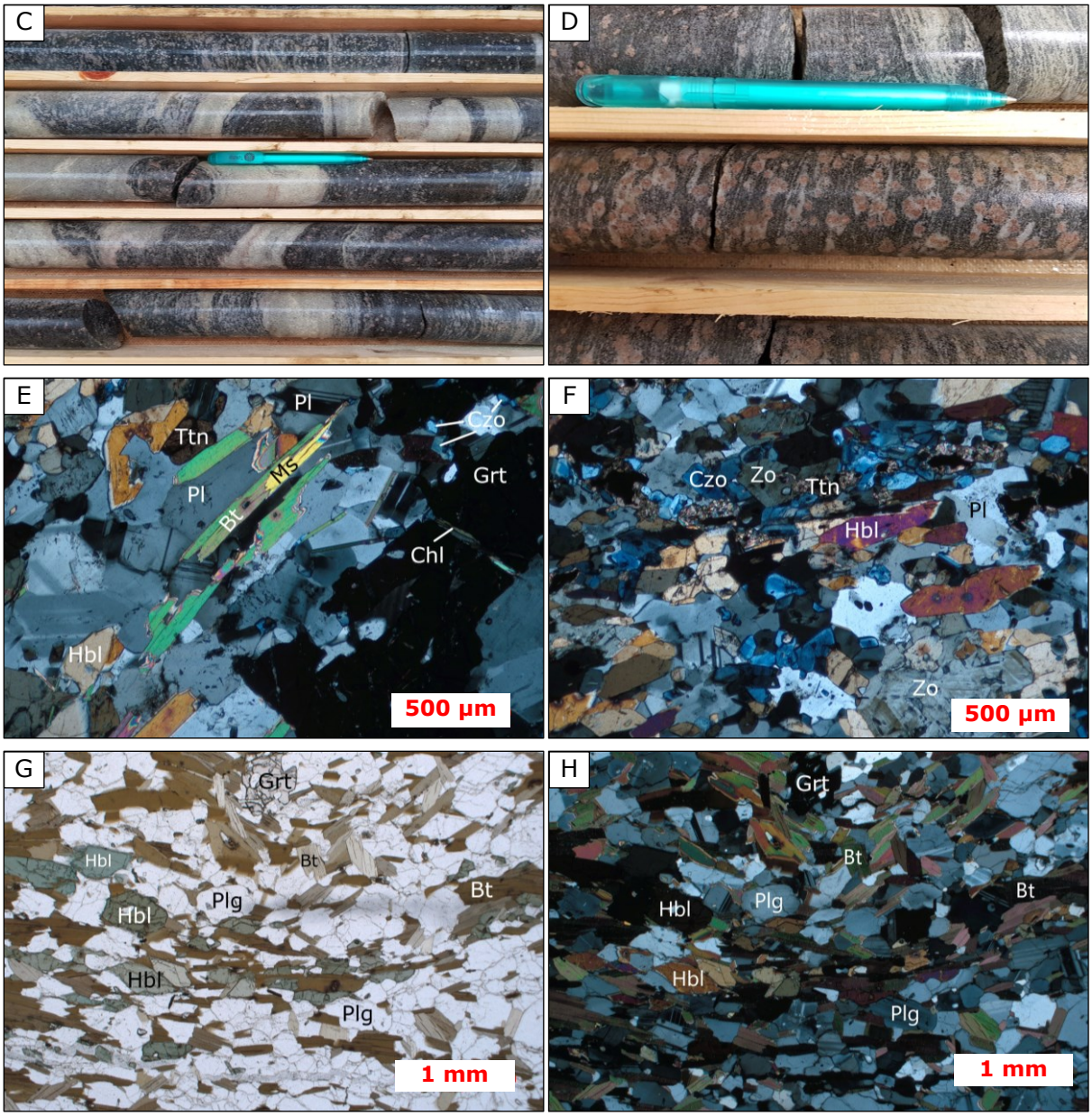

Figure 4.6: Some variations in the amphibolite unit. A) A foliation-parallel contact between a massive- and schistose amphibolite, respectively situated in the hanging- and foot-wall. The contact is oriented 050/20. B) Sample HF-08, a garnet-biotite schist. C/D) Drill core BH4508 at Hellerfjellet showing the amphibolite with stripes of calcite and garnets with depletion halos. E/F) Microphotography (xpl) of thin section 38303 sampled from drill core BH4508 at 6 m below surface, showing a mineral assemblage of plagioclase (pl), biotite (bt), muscovite (ms), hornblende (hbl), garnet (grt), clinozoisite (czo), zoisite (zo), chlorite (chl) and titanite (ttn). G/F) Microphotography (ppl and xpl) of sample HF-08 showing a mineral assemblage of plagioclase (pl), hornblende (hbl), biotite (bt) and garnet (grt).

4.2 Structural observations

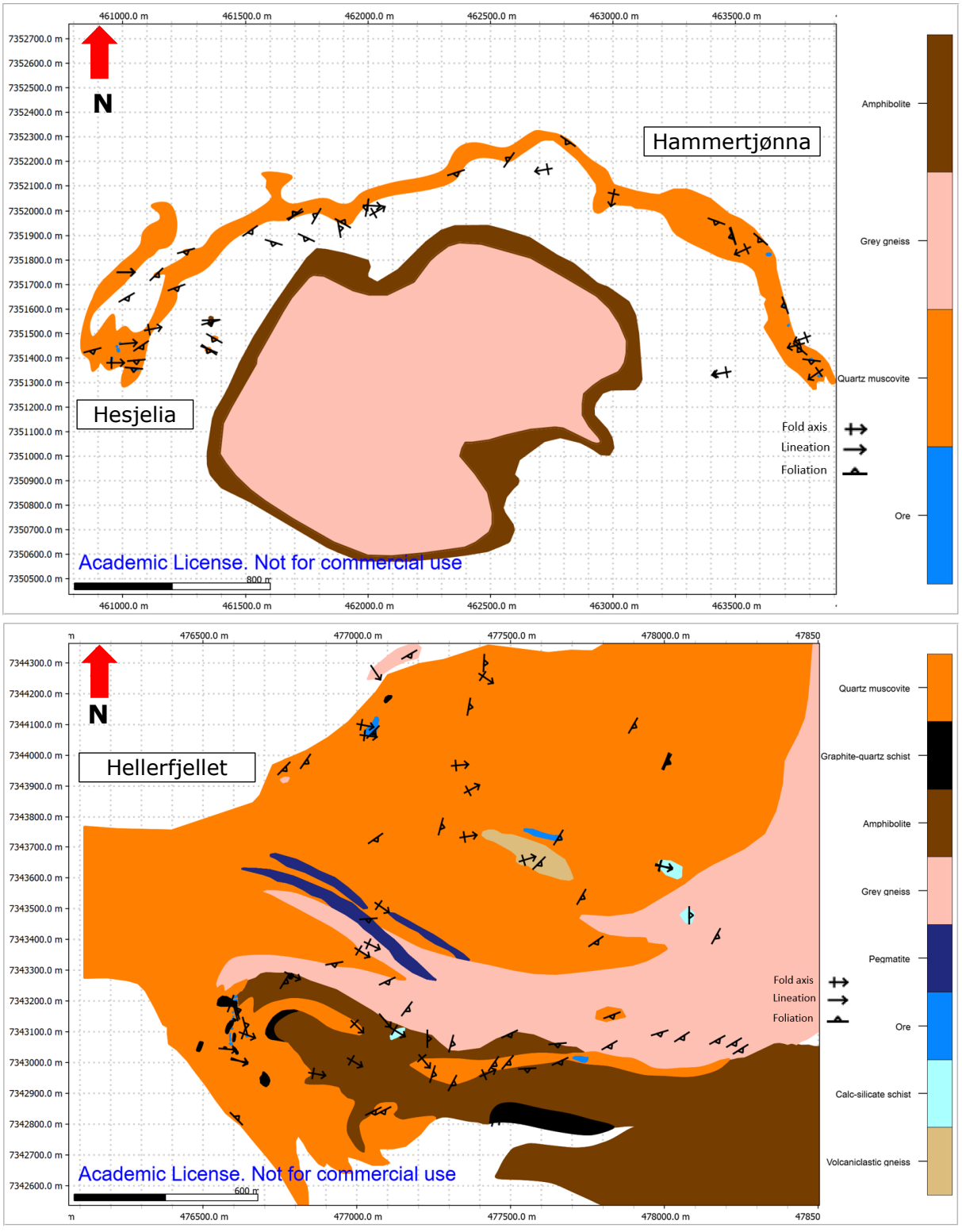

Figure 4.7: Geological maps with some of the structural measurements obtained at Hesjelia-Hammertjønna and Hellerfjellet.

The structural observations in the field focused on foliation-, fold axis- and lineation measurements (Figure 4.7) to develop a 3D geological model of the two deposits investigated. The limited amount of subsurface data from the two areas stresses the

importance of accurate and sufficient data. Observations from both field work and thin sections will be used to delineate any systematic behaviour in the structural data. This include SCAT-analysis to investigate folding phases not observed in the outcrop scale. Observations from the field indicate intense polyphase deformation all larger rock units and a general review of the structures observed in both field and thin section is presented in the following.

The earliest foliation (S_1) is represented by a transposed and discontinuous layering, evident from quartz/feldspar segregates, rootless isoclinal folds that is evident in outcrop and thin sections (Figure 4.8), and boudinaged quartz veins. The fold axis of this phase was found difficult to measure accurately because of later refolding but appear to follow an E-W trend. Relics of the S_1-foliation are observed in the hinge zone of F_2 folds (Figure 4.8 C).

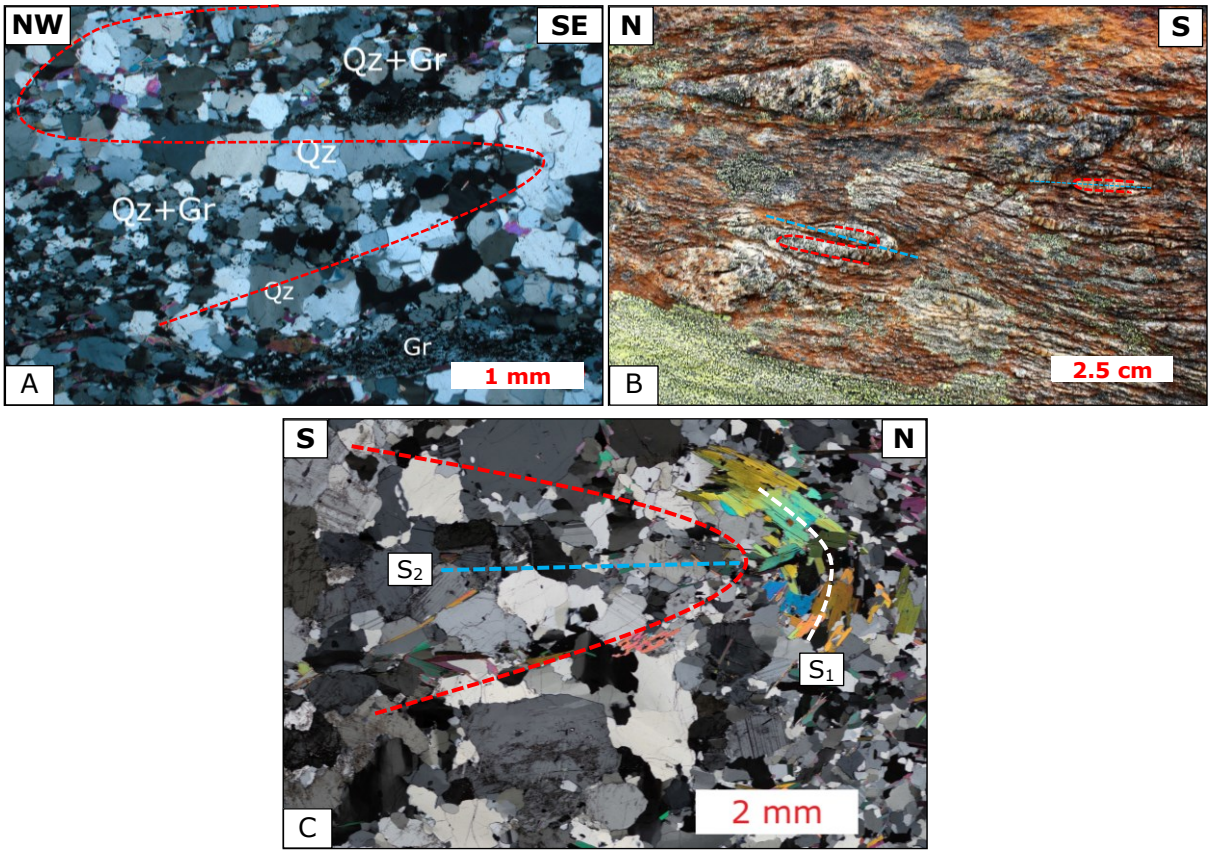

Figure 4.8: F_1 structures. Red and blue streaks follow the compositional layering and axial plane, respectively. A) Microphotograph (xpl) of a graphite-quartz schist (sample HF-05) with rootless isoclinal folds of quartz. B) Supposed volcaniclastic rock with rootless isoclinal folds and discontinuous quartz segregates of probable F_1 phase or earlier. C) Microphotograph (xpl) of a QMS-sample with a relic from the S_1 foliation in the hinge zone of a tight F_2 fold, sample HAM-07. The whole thin section can be seen in Figure 4.9H.

A subsequent deformation phase has refolded S_1 into tight to isoclinal F_2-folds with E-W fold axes and an axial plane parallel to subparallel to the foliation, creating an axial planar S_2-foliaton, being the dominant foliation in both field areas. Shearing during this phase is evident by isoclinal folds that are somewhat displaced along their axial plane, causing decoupling of their limbs, as well as sigmoidal clasts and S_2 parallel boudins. F_2 is the most prominent mesoscopic structural feature, particularly at Hellerfjellet, and fold axes are

measured from S- and Z-folds, reflecting the orientation of larger scale folds (Figure 4.9). At Hellerfjellet the F_2 fold axis plunges gently ESE, whereas at Hesjelia and Hammertjønna the fold axis plunges subhorizontal E and WSW, respectively, hence, change polarity (Figure 4.10B/D).

The foliation and fold axis varies spatially at both localities implying later refolding, however confident field observations of this are not found, suggesting a less pervasive deformation. The statistically calculated fold axes (β-axis) causing these variations is illustrated in Figure 4.10. At Hellerfjellet S_2 is predominantly rotated around a gently east-plunging β-axis, whereas the F_2 fold axis is predominantly rotated around a gently NNE-plunging fold axis. Among the foliation data there is also a noticeably NNE-SSW rotational component, evident by a scatter in the WNW-ESE direction of the stereonet. Thus, there seem to be two β-axis orientations, E-W and NNE-SSW, involved in the variation of the F_2 foliation and fold axis at Hellerfjellet, which is in agreement with the E-W trending F_3-phase and NNE-SSW trending F_4-phase as outlined by Marker (1983). The reason why the F_2 fold axis is less affected by the E-W β-axis is because they are coaxial. At Hesjelia-Hammertjønna the β-axis of the S_2 data is predominantly SW-plunging, however the N-S scatter suggest an E-W rotational component as well, which overall is in conformity with the refolding at Hellerfjellet. The F_2 fold axis is refolded around a southerly plunging β-axis, suggesting a predominantly F_4 rotation with an interference of the F_3 phase, causing the change in polarity from Hesjelia to Hammertjønna. The fold interference pattern of the approximately orthogonal F_3- and F_4- fold axes result in a dome and basin structure, which is evident by the half-circle outcrop pattern of the QMS unit at Hesjelia-Hammertjønna and the circle pattern of the amphibolite unit (Figure 4.7).

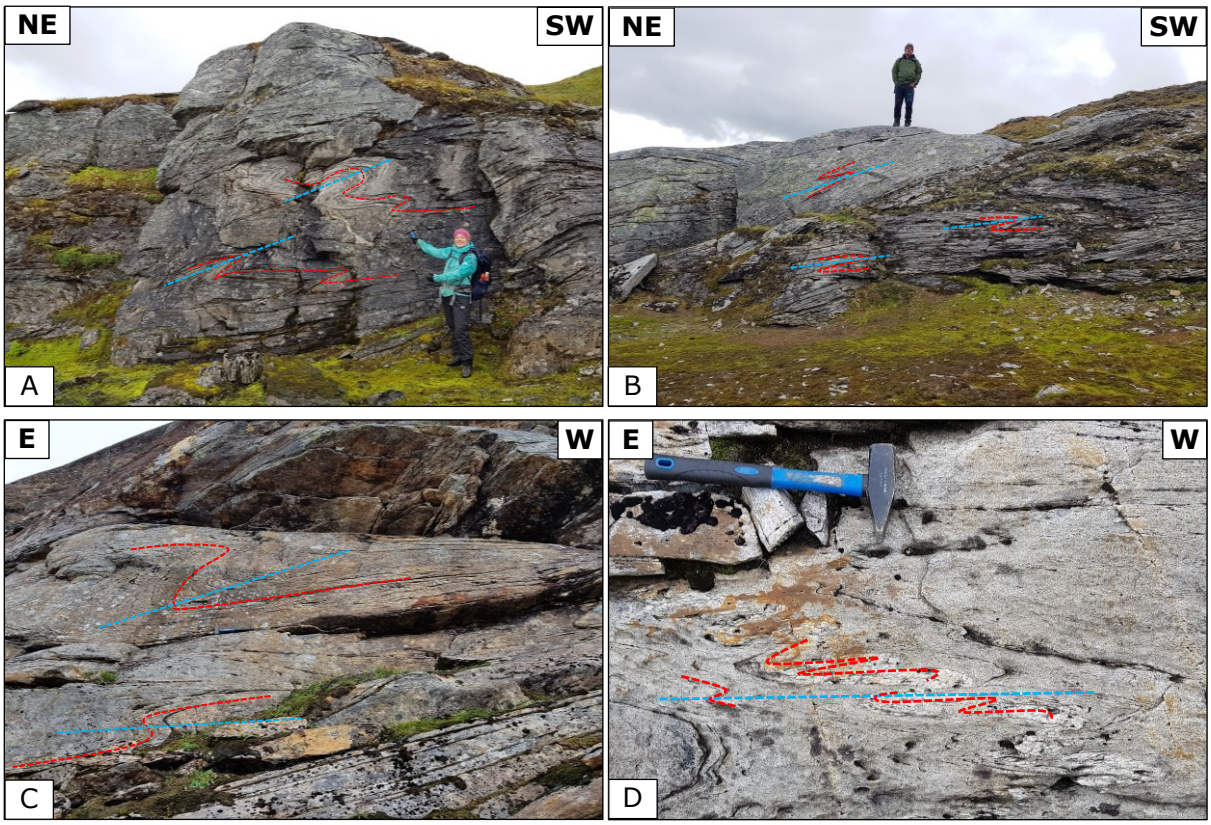

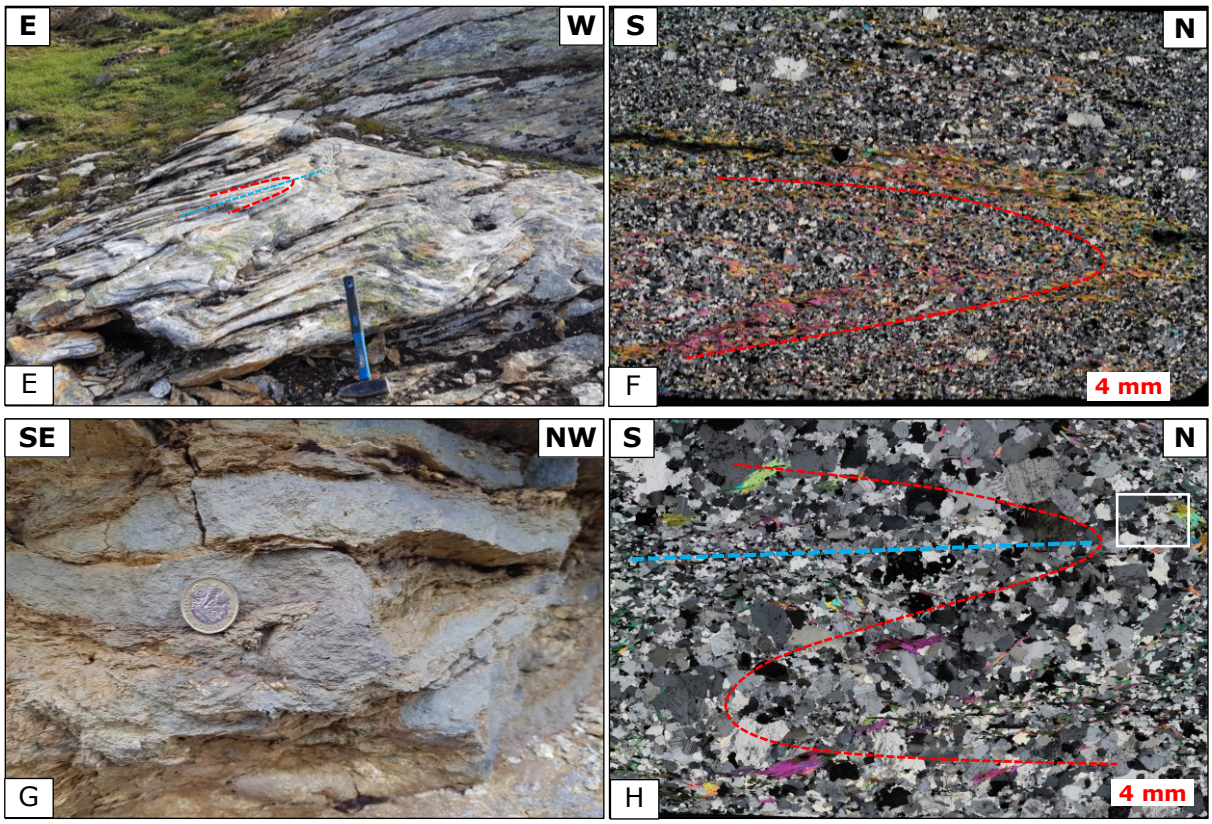

Figure 4.9: A later folding phase, probably F2, that produced the dominant foliation in the area. Red streak follow the folded foliation and blue streak illustrate the axial plane. The axial plane is subparallel to parallel to the foliation. A/B) Tight folds in an amphibolite with ESE gently plunging fold axis. C) S- and Z-folds in a grey gneiss with two fold axis measurements of 29→122 and 23→120, implying a closure towards the south-west. Beware that the orientation of the picture towards the south gives a false expression of the fold axis. D) Isoclinal folds in a grey gneiss. Stippled line follows axial plane trace from the quartz vein into the folded host rock. Two fold axis measurements give 25→122 and 29→115. E) Isoclinal F_2 folds in a muscovite schist with fold axis 24°→107. Locality for sample HF-16. F) Microphotograph (xpl) of sample HF-16 with F_2 folded muscovite layering. Thin section is cut normal to the fold axis. G) Asymmetric fold in Hammertjønna with fold axis 02→120. H) Microphotograph (xpl) of sample HAM-07 showing an F_2 folded quartz/feldspar vein with fold axis 02/260. White square marks the zoomed in area from Figure 4.8C.

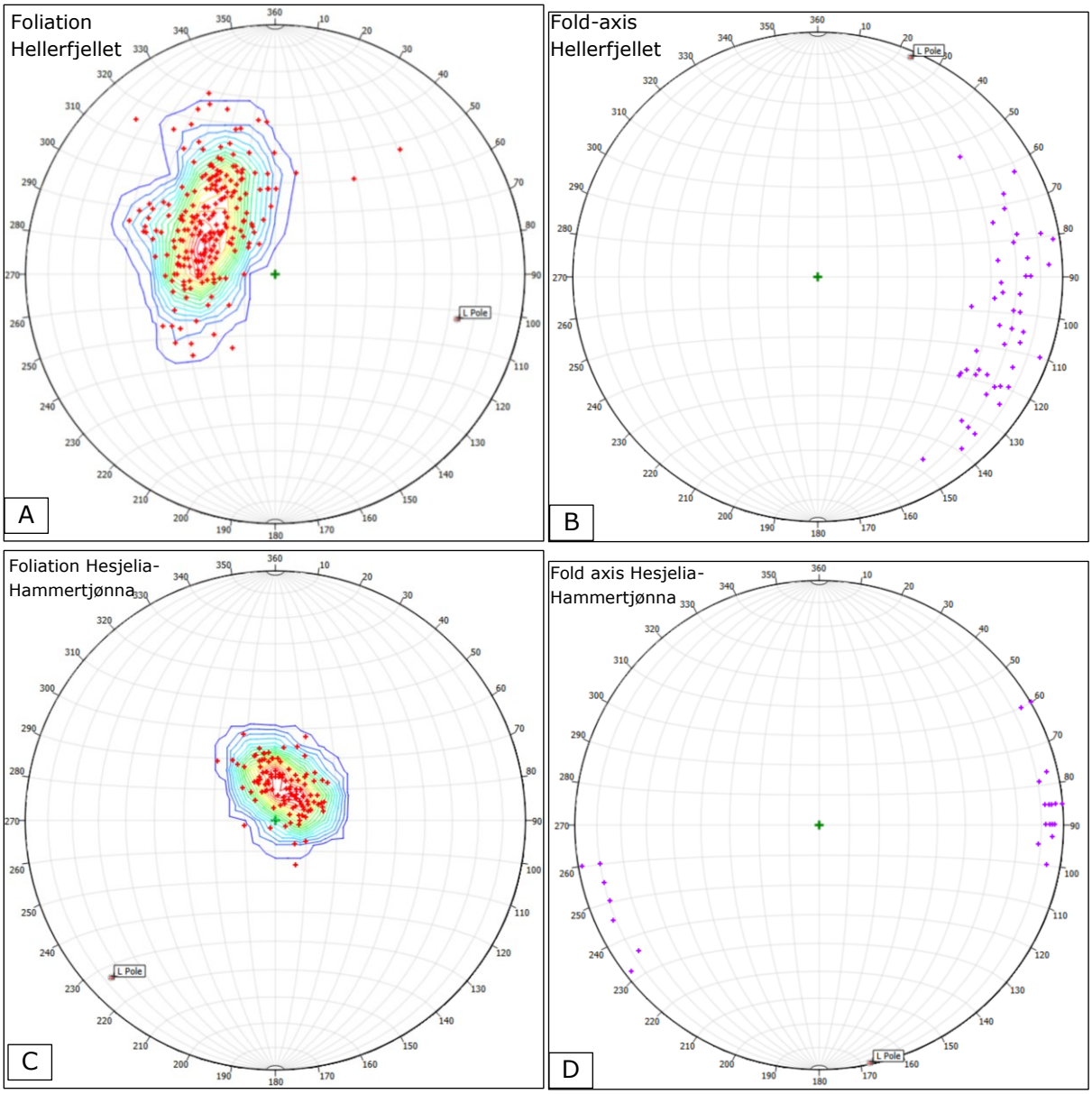

Figure 4.10: All surface measurements from both Hellerfjellet (A/B) and Hesjelia-Hammertjønna (C/D) plotted in an equal area stereonet. A) Foliation measurement showing a spatial variation of the orientation due to later refolding. The statistical fold axis or beta-axis ("L-pole" in the stereonet) is the fold axis causing the most structural change and is calculated to be plunging gently easterly (26.22→103.97), coaxial with the F_2-fold axis. There is also a noticeably change in the WNW-ESE direction which is caused by a fold axis oriented roughly NNE-SSW. B) F_2 fold axis measurements showing an easterly plunging fold axis with an average orientation of 17.34→103.36. The beta-axis is predominantly horizontally plunging NNE (2.93→22.97). C) Foliation data showing a variation due to refolding around an SW-plunging fold axis (9.83→226). There is also an E-W rotational component evident by the N-S spread of poles. D) Fold axis data showing an approximately E-W trending fold axis wherein fold axes in Hesjelia plunges east and fold axes in Hammertjønna plunges south-west. The beta-axis suggest a rotation around a southerly plunging fold axis (1→168).

F_3 and F_4 is difficult to observe in the outcrop-scale due to the gentle-open style of folding. Undulations with fold axes plunging roughly south-west were observed, however precise measurements were difficult due to the gentle folding. Crenulation- and mineral lineations plunging ESE may be caused by the F_3-phase, as well as NNE-plunging slickensides oriented orthogonal to the crenulation (Figure 4.11). Crenulation in sample HF-03 (oriented 30/100) is parallel to F_4 (Figure 4.12).

Folded and boudinaged pegmatite dikes intrudes the country rock at Hellerfjellet and cross-cut the S_2 foliation. Vertical shortening has caused subhorizontal-horizontal dikes to boudinage and subvertical-vertical dikes to fold (Figure 4.13). The fold axis of this phase, oriented south-east, parallels the strike of the dikes itself, indicating a syn-tectonic intrusion. Even though the orientation is orthogonal to the F_4 fold axis the dikes is not folded accordingly and therefore is interpreted as a post-F_4 extensional phase.

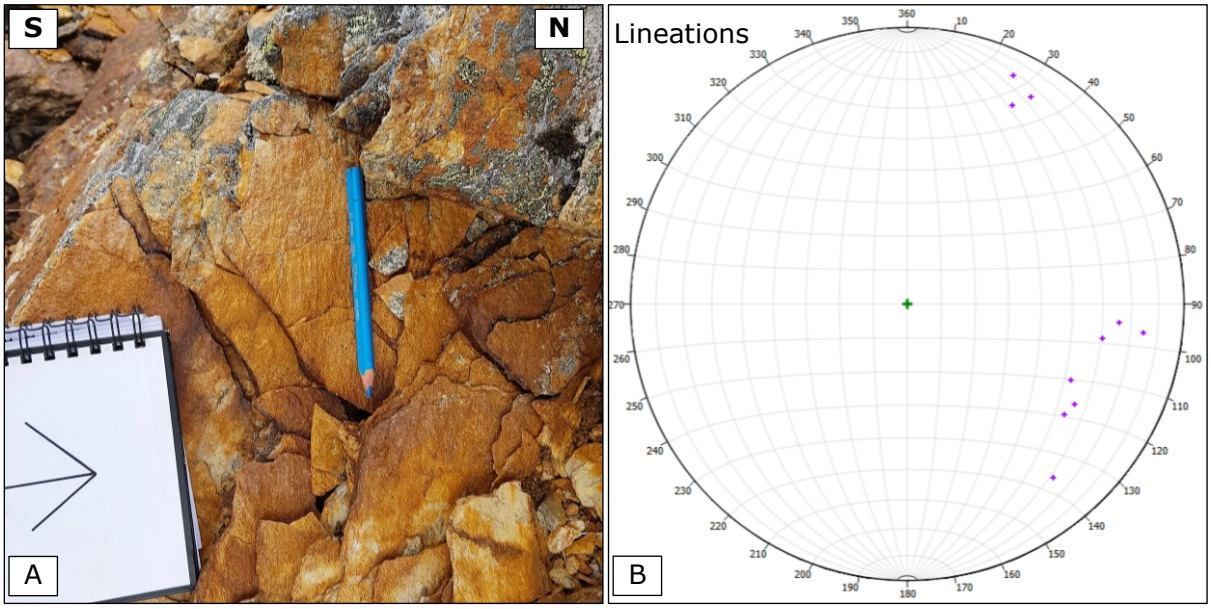

Figure 4.11: Crenulation- and mineral lineations and slickensides at Hellerfjellet. A) A weak crenulation parallel with the pencil with two orientations yielding 29→100 and 32→110. B) Stereonet (equal area) with crenulation- and mineral lineation plunging south-east, and slickensides plunging NNE, i.e. orthogonal to crenulation- and mineral lineations.

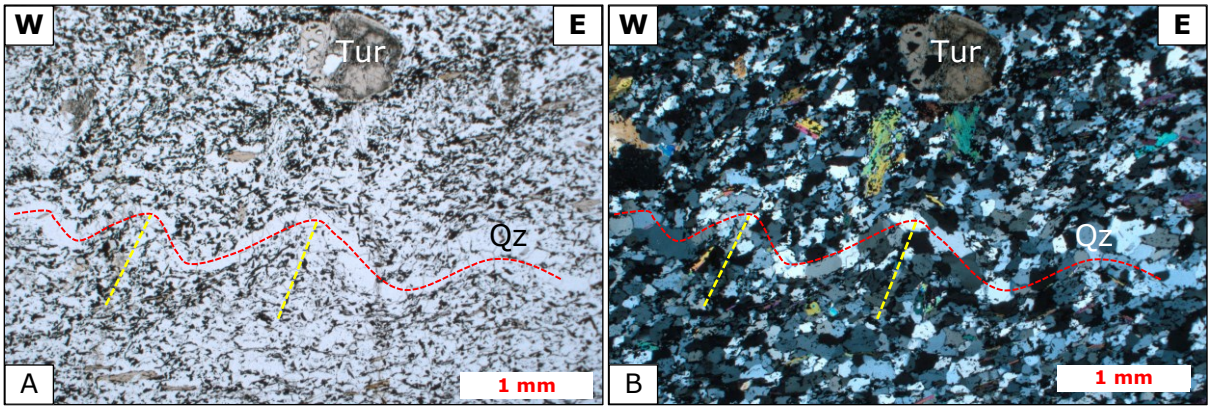

Figure 4.12: Microphotograph of F_4 crenulation in sample HF-03 cut along 30/100 (dip/dip-direction). Red streak follows crenulated S_2 foliation, while yellow streak marks the axial plane. Tur (tourmaline), qz (quartz). A) Plane-polarized light. B) Cross polarized light.

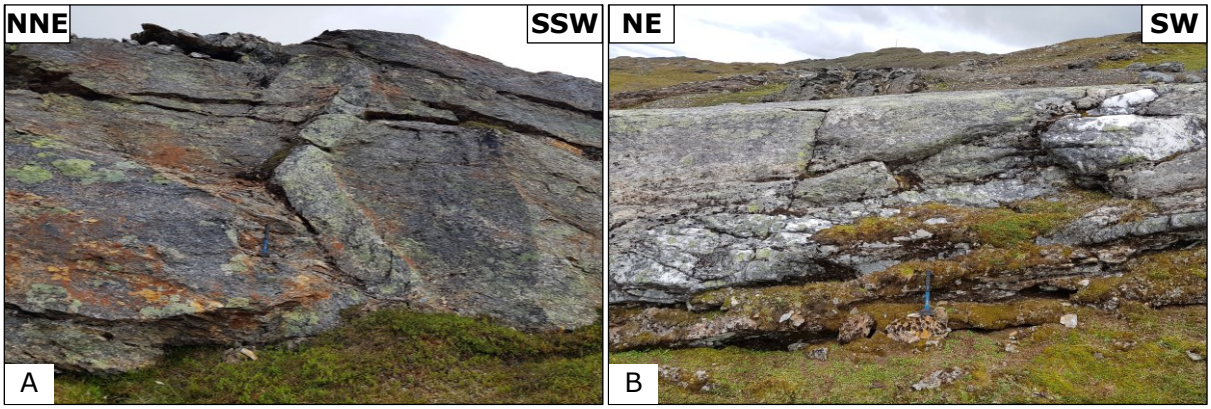

Figure 4.13: Post-F_4 cross-cutting dikes at Hellerfjellet. A) Sub-vertical dike folded along a horizontal fold axis plunging 110°ESE. B) Sub-horizontal dike boudinaged along an ESE/SE oriented fold axis. An exact measurement was not obtained.

4.3 Geochemistry plots

The following section presents the geochemical analysis of the sampled rocks from Mofjellet in the form of major- and trace element diagrams, in which the goal is to understand the nature of the rocks. The rocks have been pre-classified based on field observations and thin sections. The massive and quartz rich grey gneisses have been separated into a subdivided rock type called "metarhyolite", based on the possibly volcanic origin. 24 and 38 samples are basis for the felsic (metarhyolite and grey gneisses) and mafic (amphibolites) rocks, respectively, wherein 51 analysis were kindly given by The Geological Survey of Norway, enabling correlations on a wider basis. These are apparently unaltered rocks suitable for credible and representative results. 64 samples of muscovite- and graphite schist are altered due to the sulphide mineralization and are only used to investigate a possible genetic link to either the felsic or the mafic rocks.

4.3.1 Major and minor elements

Harker diagrams

The major and minor elements for the grey gneisses (black triangles), metarhyolites (green squares) and amphibolites (open circles) are plotted against SiO_2 in the Harker diagrams in Figure 4.14. The amphibolites have silica content of 45.5 % - 56 %, hence, some of the samples crosses the mafic-intermediate threshold (52 wt. % silica) and strictly classifies as intermediates (or basaltic andesites according to Figure 4.17, section 4.3.3). The metarhyolites and grey gneisses have a silica content of 66 – 83 wt. % and is therefore felsic (> 65 wt. % silica).

The amphibolites are scattered for all elements, only showing a negative trend for Fe_2O_3, MgO and CaO, as silica increases, possibly reflecting fractionation of the early-forming minerals olivine (Fe-Mg), pyroxene (Fe-Mg-Ca) and plagioclase (Ca). However, because alumina is scattered the decrease of CaO suggest fractionation of clinopyroxene. The weak positive trend of Na_2O in the amphibolites is most probably an artefact of the inevitability that the analyses must total to 100 %. The remaining oxides are not controlled by the silica content, as is expected for mafic magmas. The alumina content for these rocks is high, averaging 17.3 wt. % (max. 20.7 wt. %), and the average MgO-content is 6.1 %, overall reflecting a high-Al/medium-MgO basalt-basaltic andesites.

The felsic rocks show a better correlation between the oxides and silica, and all but K_2O, which is scattered, are negatively correlated, hence, decreases with increasing silica content. This indicate that fractionation has occurred, and the minerals has been removed from the melt as they crystallized, leading to a melt continuously richer in silica. The metarhyolites have a higher SiO_2-content than the grey gneisses (75 – 83 wt. % vs. 66 – 76 wt. %), suggesting the former is more fractionated and evolved. Among the alkalis only CaO and Na_2O correlates (negatively) with silica, even though the latter is scattered, whereas CaO is less so. It cannot be excluded that the scattering is due to alteration, however, the decreasing trend of CaO and Na_2O is logically explained by fractionation of plagioclase. A decreasing trend of K_2O would have been explained by fractionation of K-feldspar and/or muscovite, however, the random pattern suggests equilibrium crystallization or alteration and addition of K. Al_2O_3 show a tight and consistent negative curve (except for one outlier), indicating continuous fractionation of Al-bearing phases throughout the crystallization of the felsic rocks. The decrease of Fe_2O_3 and TiO_2 probably reflect fractionation of Fe-Ti oxides.

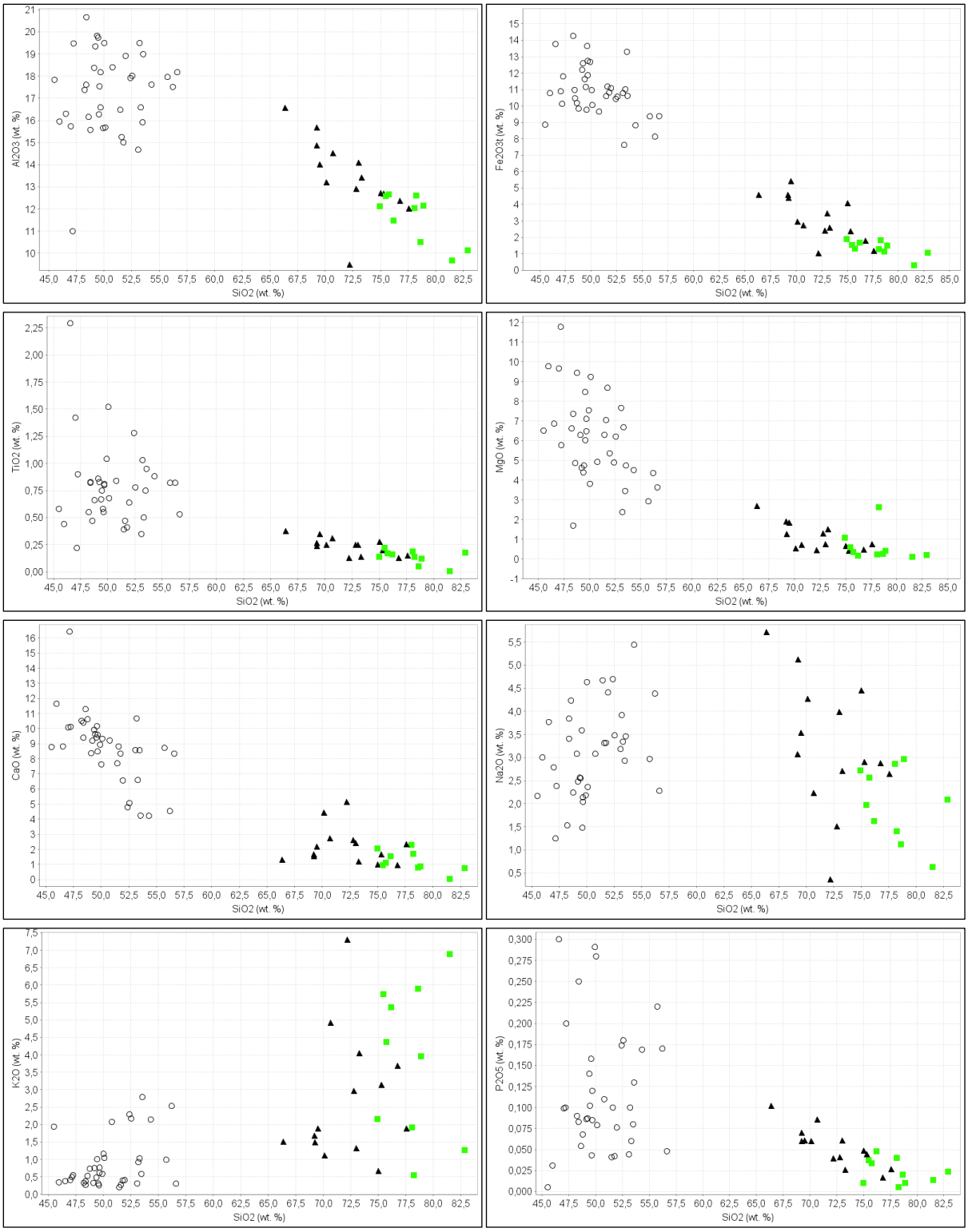

Figure 4.14: Harker diagram showing major elements vs. SiO_2 correlations for grey gneisses (triangles), metarhyolite (squares) and amphibolites (circles).

Fenner diagrams

The Fenner diagrams (Figure 4.15) for the amphibolites present oxides vs. MgO and are generally more scattered than the felsic rocks. MgO is a better indicator of fractionation for mafic magmas as it usually is incorporated in early forming minerals, such as olivine and pyroxene. Silica, alumina, TiO_2, and Na_2O is negatively correlated with MgO, whereas the opposite is true for Fe_2O_3 and CaO, consistent with early fractionation of olivine (Fe-Mg) and Ca-pyroxene, thereby enriching the melt in the former elements. The relatively steep negative curve of alumina suggests no phases are incorporating both alumina and MgO, i.e. spinel, plagioclase, and hornblende. The weak positive trend of Fe_2O_3 and MgO is a tholeiitic trend where MgO fractionates earlier than FeO, also seen in the AFM diagram in Figure 4.16A.

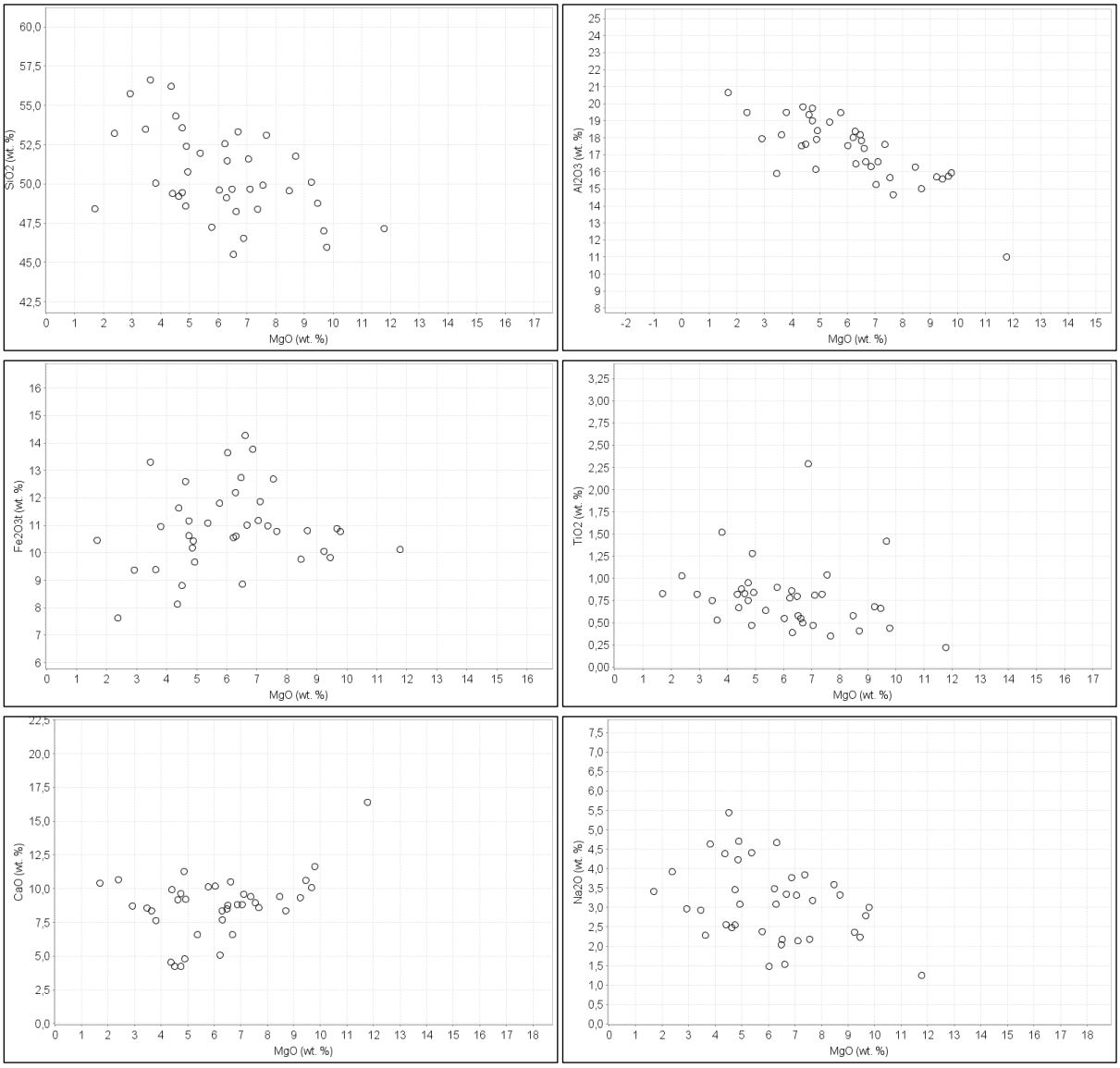

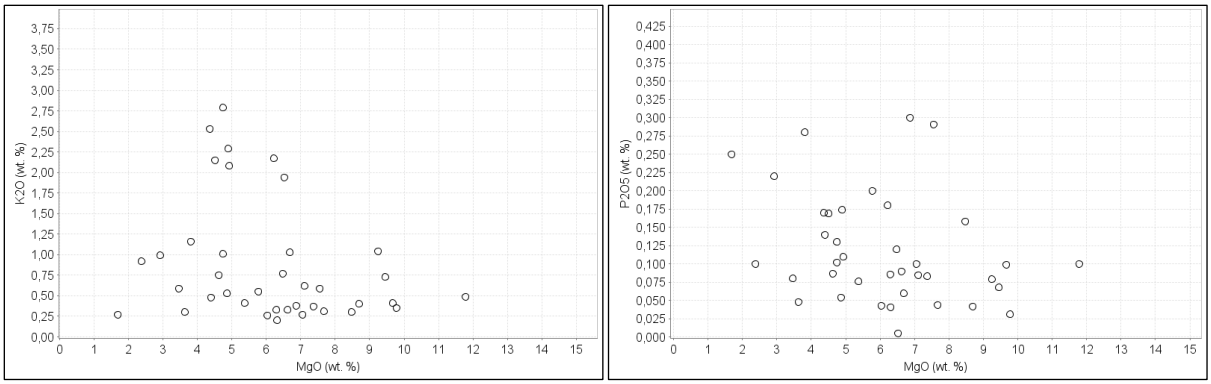

Figure 4.15: Fenner diagrams showing major element vs. MgO plots of amphibolites. Fe_2O_3 represents all Fe in the sample.

4.3.2 AFM and ASI diagrams

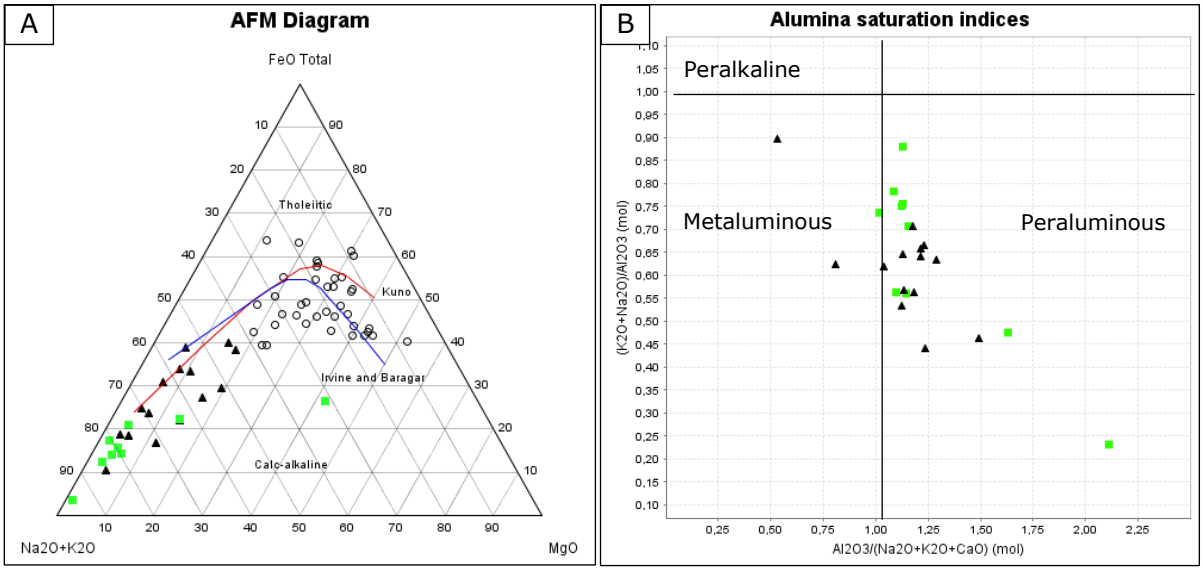

Figure 4.16: AFM- and ASI-classification diagrams. A) AFM-diagram discriminating between the mafic and felsic rocks based on alkali-, iron-, and magnesium content, subsequently placing the rocks in the tholeiitic or calc-alkaline field. Lines separate tholeiitic and calc-alkaline rocks according to Kuno (1968) and Irvine and Baragar (1971).

Overall, the AFM diagram (Figure 4.16A) show a predominantly calc-alkaline trend towards the alkali apex, however, a small tholeiitic component is evident by some of the amphibolite samples trending from MgO towards FeO. Most of the rocks plot inside the calc-alkaline field according to the line defined by Kuno (1968), however, approximately half of the amphibolite samples plot within the tholeiitic field defined by Irvine and Baragar (1971), attributed to their higher proportions of FeO_{tot}. The grey gneisses and metarhyolite rocks are generally alkali-rich and FeO- and MgO-poor, thus trending towards the A corner in the AFM diagram, wherein the metarhyolite is more alkaline, while the grey gneisses have higher ratios of FeO.

The ASI-diagram (Figure 4.16) show that the felsic rocks are predominantly peraluminous, with one metarhyolite sample being strongly peraluminous (ASI = 2.1). Only three samples (including one borderline) plot in the metaluminous field. The higher alkalinity of the metarhyolites compared to the grey gneisses is also evident here, where they plot generally

higher in the diagram. The excess of alumina in the felsic rocks suggest crustal contamination of the magma from which they crystallized.

4.3.3 Tectonic setting

TAS classification diagrams

The use of tectonic discrimination diagrams requires rocks wherein the original trace element geochemistry, from which they were formed, is unaltered. The original TAS diagram (Figure 4.17A) and the TAS proxy diagram (Figure 4.17B) are generally coherent regarding the mafic rocks, classifying largely within the basalt to basaltic andesite group. A few samples plot as trachybasalts and basaltic trachyandesite in the original diagram, whereas all samples are within the sub-alkaline field of the proxy diagram, yet are somewhat attracted towards the alkaline field. Thus, it is possible that K and Na have been provided through metasomatism, making the rocks more alkaline. The felsic rocks deviate more between the diagrams, in which the grey gneisses plot as rhyolite to dacite in the original diagram and just inside the andesite group in the proxy diagram, therefore classifying as more mafic, i.e. has a lower Zr/Ti ratio than the silica content corresponds to. This may indicate some addition of silica through metasomatism. The metarhyolites plot within the rhyolite-dacite group, except for one sample plotting within the alkali rhyolite group, the latter of which does not have a corresponding category in the original diagram. Overall, the correlation between the diagrams is high, both clustering tight, although with some outliers.

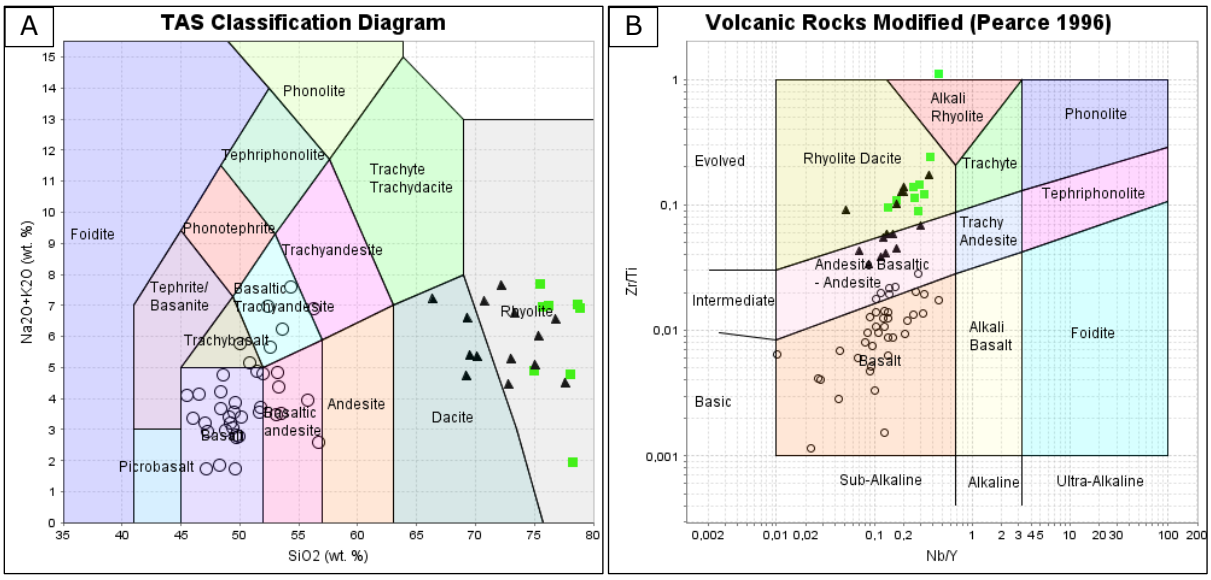

Figure 4.17: TAS classification. A) Original TAS classification diagram plotting Na2O + K2O vs. SiO2. B) TAS proxy diagram with immobile trace element equivalents Zr/Ti vs. Nb/Y.

Tectonic discrimination diagrams

In the Ti-Zr-Y diagram of Pearce and Cann (1973) (Figure 4.18A) the amphibolites plot within the MORB / IAT (island-arc tholeiite) / CAB (continental arc basalt) field(s). The amphibolites are further discriminated from MORB in the Th-Hf-Ta ternary diagram of Wood (1980) (Figure 4.18B), where they plot in the volcanic arc field and predominantly within the calc-alkaline sub-field. In the Th/Yb vs. Nb/Yb diagram of Pearce and Peate (1995) (Figure 4.18C) the amphibolites are scattered within the volcanic arc array, wherein they

are weighted more on the continental arc side, however several samples plot just outside. The group of samples plotting within the oceanic arc field are as depleted or more depleted than N-MORB because of a low Nb/Yb ratio. The Rb vs. Y + Nb diagram from Pearce et al. (1984) (Figure 4.18D) yields a volcanic arc signature for the grey gneisses and metarhyolites, in conjunction with the volcanic arc signature of the amphibolites.

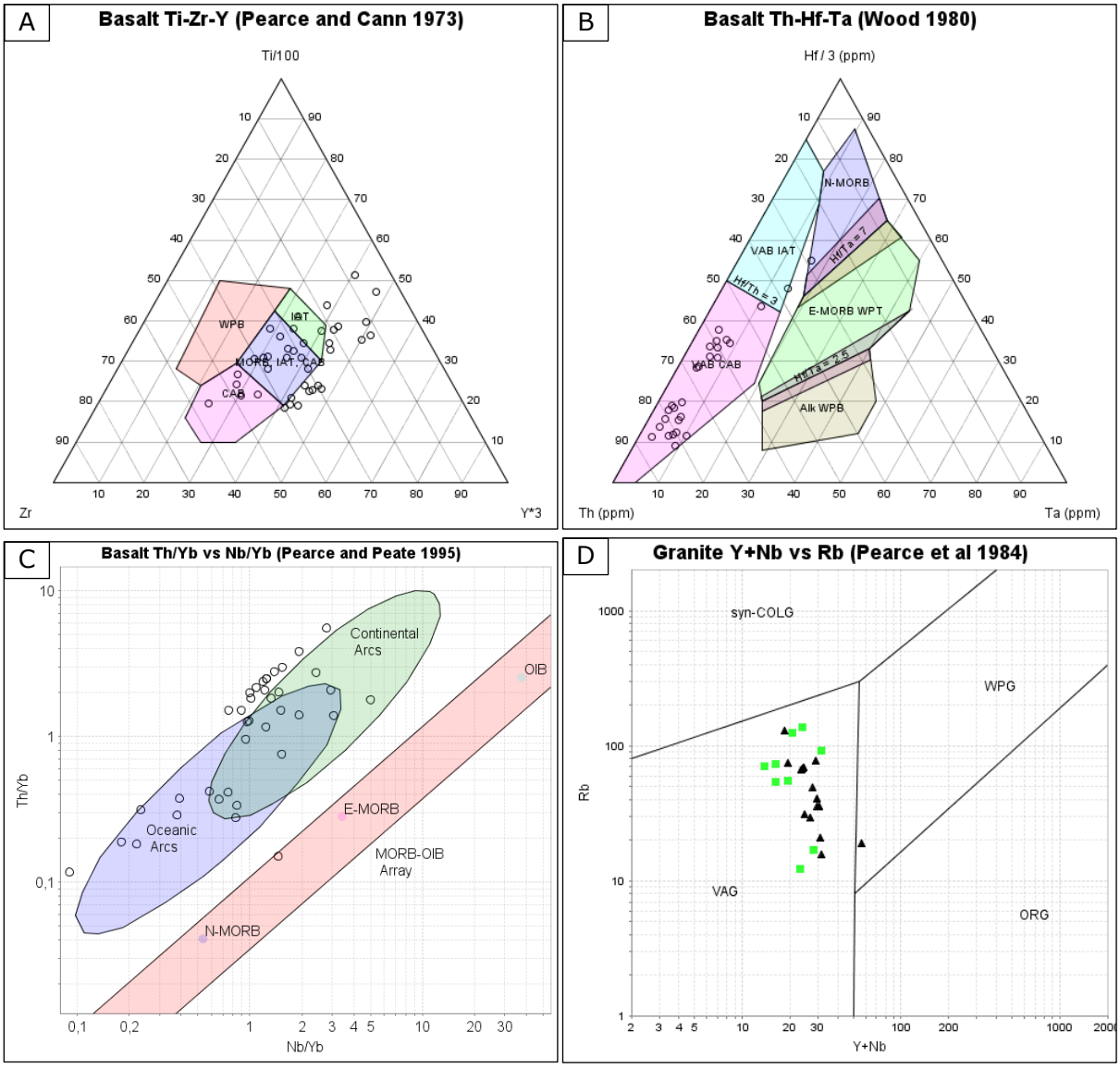

Figure 4.18: Tectonic discrimination diagrams. A) Ternary Ti-Zr-Y diagram for basalts, by Pearce and Cann (1973), discriminating between WPB (within plate basalts), IAT (island arc basalts), MORB (mid ocean ridge basalts) and CAB (continental arc basalts). B) Ternary Th-Hf-Ta diagram for basalts, by Wood (1980), discriminating between volcanic arc basalt (VAB), subdivided to calc-alkaline basalt (CAB) and island-arc basalt (IAT), N-MORB, E-MORB within-plate tholeiite (WPT), and alkalic within plate basalt (WPB). C) Bivariate Th/Yb vs. Nb/Yb diagram for basalts, by Pearce and Peate (1995), discriminating between oceanic arcs, continental arcs, N-MORB, E-MORB and OIB. D) Bivariate Rb vs. Yb + Ta diagram for granites (Pearce et al., 1984) discriminating between VAG (volcanic-arc granite), syn-COLG (syn-collisional granite), WPG (within-plate granite) and ORG (oceanic-ridge granite).

4.3.4 Geochemical VMS-classification

The geochemical parameters fundamental for the FI-FIV classification in Hart et al. (2004) are calculated for the metarhyolites and the grey gneisses, classifying as dacite-rhyolite according to the TAS diagram, and is displayed in Table 4.1. The result is given as a minimum to maximum interval with the average in parentheses, and subsequently compared to the five categories, whereby the best fitting categories (max. two) are coloured red. The chondrite normalizing values for $[La/Yb]_{CN}$ and $[Eu/Eu^{*}]_{CN}$ are from Nakamura (1974). As seen from the table, the Mofjellet rocks coincides best with the FII category (8/9 categories), followed by the FIV category (3/9 categories). This is also illustrated by the $[La/Yb]_{CN}$ vs. Yb_{CN} bivariate diagram in Figure 4.19, however, most of the samples classify here as FIV rather than FII.

	FI	**FII**	**FIIIa**	**FIIIb**	**FIV**	**Mofjellet**
Lithology	Dacite-Rhyolite	Dacite-Rhyolite	Rhyodacite-high silica rhyolite	Rhyodacite-high silica rhyolite	Rhyodacite-high silica rhyolite	Dacite-rhyolite
SiO2 (wt. %)	64.0-72.0	**64.0-81.0**	67.0-78.0	**67.0-84.0**	69.0-81.0	66.4-82.9 (74.8)
TiO2 (wt. %)	0.16-0.65	0.16-0.89	0.21-0.99	**0.09-0.73**	**0.09-0.57**	0.01-0.38 (0.20)
Y (ppm)	6.0-31.0	**11.0-73.0**	25.0-96.0	72.0-238.0	**18.0-63.0**	10.5-54.0 (21.9)
Zr/Y	8.8-31.0	**3.2-12.12**	**3.9-7.7**	1.7-6.2	0.67-4.8	1.79-10.0 (5.0)
Yb (ppm)	0.43-3.8	**1.3-7.9**	3.4-9.3	5.0-32.0	**1.5-8.4**	1.65-6.45 (2.87)
$[La/Yb]_{CN}$	5.8-34.0	**1.7-8.8**	1.5-3.5	1.1-4.9	0.22-2.1	0.7-8.03 (3.37)
$[Eu/Eu^{*}]_{CN}$	0.87-1.5	**0.35-0.91**	**0.37-0.94**	0.20-0.61		0.42-1.11 (0.7)
Affinity	Alkaline - calc-alkaline	**Calc-alkaline**	Tholeiitic	Tholeiitic	Tholeiitic	Calc-alkaline

Table 4.1: Comparing Mofjellet felsic rocks to the FI, FII, FIIIa/b and FIV category from Hart et al. (2004). Chondrite normalizing values are based on Nakamura (1974) (Hart et al., 2004).

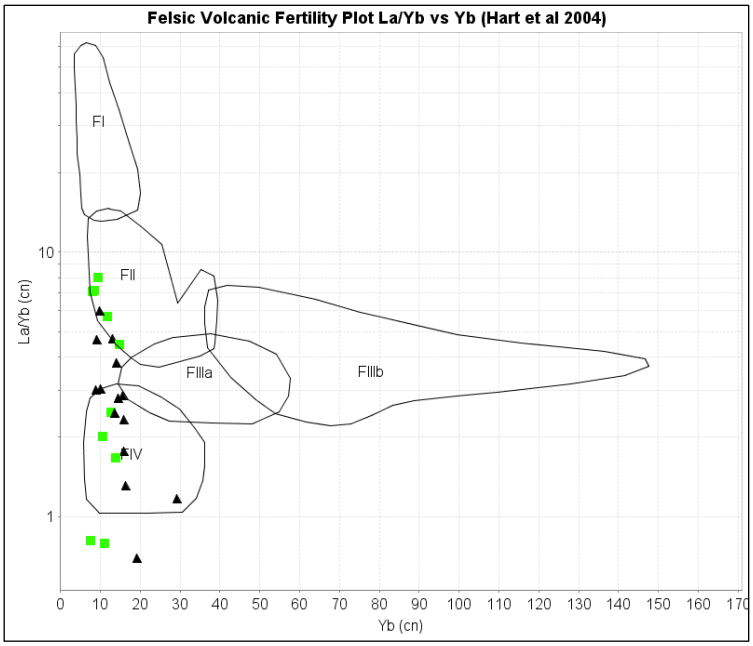

Figure 4.19: $[La/Yb]_{CN}$ vs. Yb_{CN} bivariate diagram of Hart et al. (2004), categorizing the dacitic-rhyolitic grey gneiss and metarhyolites. 12 samples (incl. two borderline) plot within FIV, seven samples plot within FII, and five samples are uncategorized. The samples show a consistent Yb_{CN}-content, contrary to the scattered $[La/Yb]_{CN}$ ratio.

4.3.5 Normalized diagrams

Rare earth elements (REE)

The Rock/Chondrite normalized REE diagrams for the amphibolites, metarhyolite and grey gneisses are presented in Figure 4.20. Overall, there is a relative enrichment of light REE (LREE) compared to heavy REE (HREE) for all rocks, evident by the negative curve where $[La/Yb]_{CN}$ for the metarhyolites is; 0.8 – 8.6 (avg. = 4.3), for the grey gneisses; 0.7 – 6.4 (avg. = 3.1) and for the amphibolites; 0.1 – 6.0 (avg. = 2.6).

Breaking it down, all rock types show a predominantly negative slope through the LREE, wherein $[La/Sm]_{CN}$ for the metarhyolites (2.1 – 6.1, avg. = 4.0) and the grey gneisses (1.2 – 4.6, avg. = 2.8) are exclusively *negative*, whereas the amphibolites have both negative *and* positive slopes ranging from (0.1 – 3.1, avg. = 1.8), including the outlier (La_{CN} = 1), still being predominantly *negative*. There is a moderate positive correlation between an increase in $[La/Sm]_{CN}$ and K_2O (R^2 = 0.34), whereas no correlation is observed between the former and SiO_2, as shown by Figure 4.20 D and E.

The HREE slope ($[Gd/Yb]_{CN}$) for the metarhyolites show on average *positive* curves (0.3 – 1.3, avg. = 0.7), while being closer to *flat* for the grey gneisses (0.6 – 1.4, avg. = 0.9) and amphibolites (0.2 – 1.8, avg. = 1.1), including the large outlier for the amphibolites (Gd_{CN} = 1). Regarding anomalies, the amphibolites have $[Eu/Eu^*]_N$ = 0.6 – 1.3 (one outlier of 2.7), altogether being largely flat, while the metarhyolites and grey gneisses have $[Eu/Eu^*]_N$ = 0.4 – 1.1 and 0.4 – 0.9, respectively, thus almost exclusively *negative*. This indicates that the amphibolite is sourced from a rock or melt with little or no plagioclase, whereas for the felsic rocks, plagioclase was either left in the residuum or fractionated during crystallization.

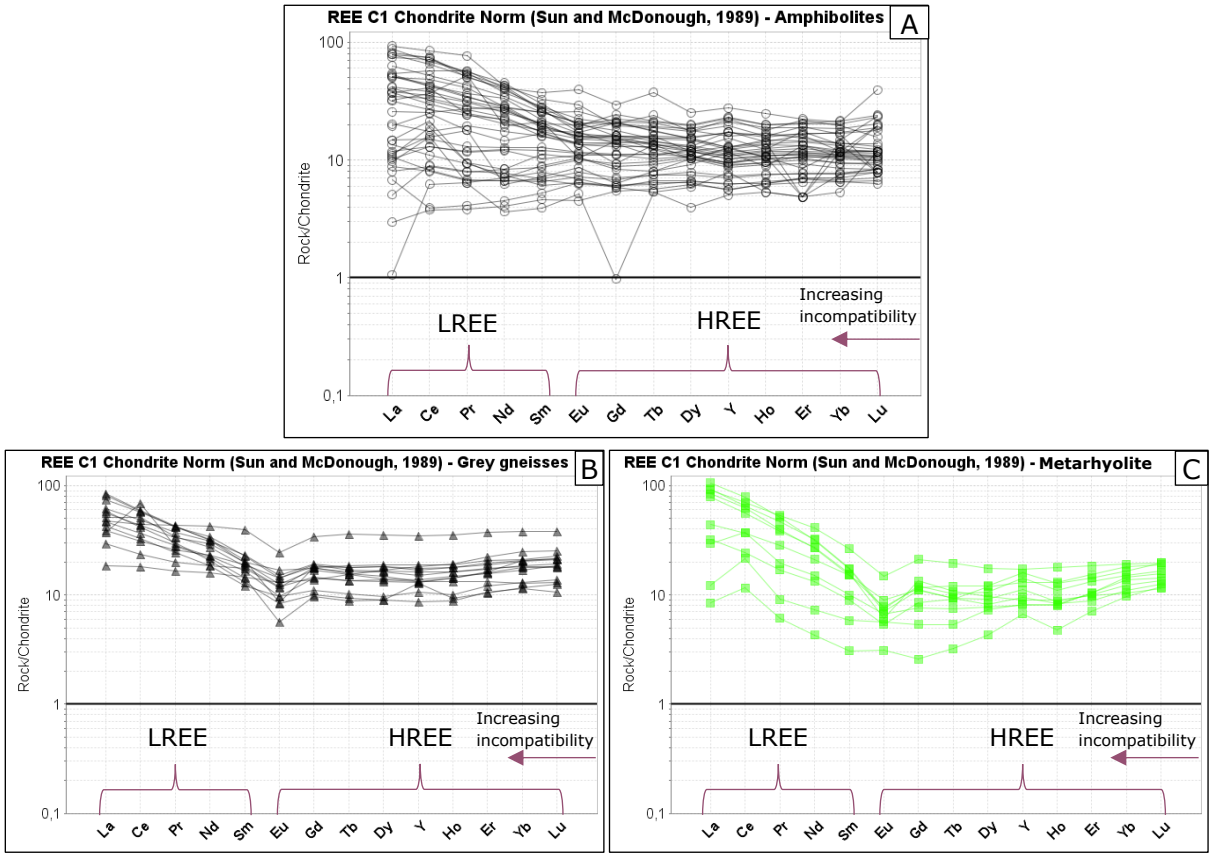

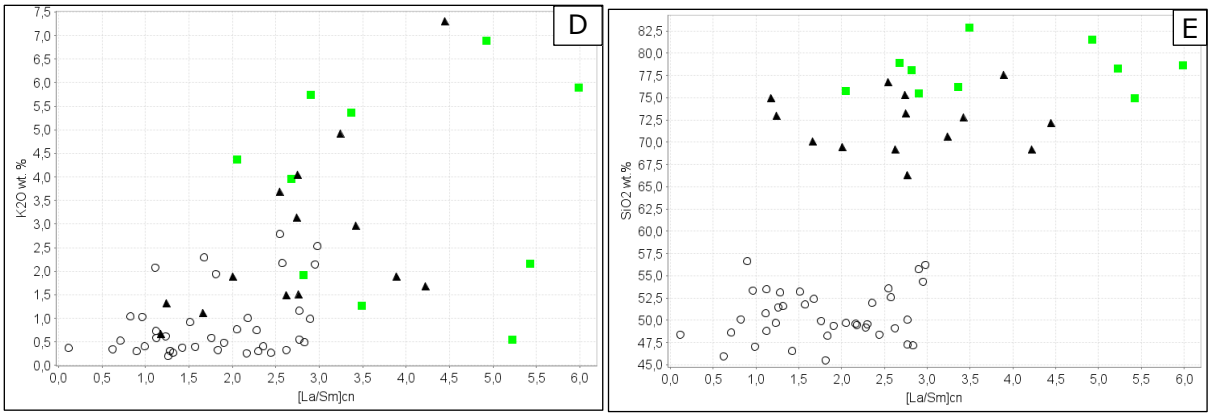

Figure 4.20: Rock/Chondrite normalized diagrams based on Sun and McDonough (1989). A) Amphibolites. B) Grey gneisses. C) Metarhyolite. D) Plot of K2O vs. [La/Sm]CN showing a slight positive correlation (R2 = 0.34). E) Plot of SiO2 vs. [La/Sm]CN showing no correlation within the felsic rocks nor within the amphibolites.

MORB normalized diagrams

The MORB normalized diagrams for the felsic rocks and amphibolites are presented in Figure 4.21. The arrows indicate increasing incompatibility through the LIL- and HFS-elements.

For all rocks, there is a relative enrichment of LIL-elements compared to HFS-elements, although more scattered in the amphibolites. The latter show a negative Sr-, Nb-, Zr-, (weak) Ti-, and Cr-anomaly. Ce appear positive because of the large negative anomalies for Ta and Nb. The *felsic* rocks have an almost identical signature to each other with negative Sr-, (weak) Ba-, Ta-, Nb-, P_2O_5-, TiO_2-, and Cr-anomaly. Here too, Ta and Nb creates an artificial Ce-anomaly. Even though the patterns of the two felsic rocks are identical, the anomalies are somewhat larger for the metarhyolites. One sample yield a large positive anomaly for Ba (being an exception). Comparing the *absolute* values to MORB (where MORB = 1) the amphibolites are enriched in LILE (although some samples = MORB), and *depleted* in HFSE (< MORB). The felsic rocks are enriched in LILE, except for Sr, and around MORB through the HFSE, except for the negative anomalies.

Overall, the pattern corresponds to the chondrite-normalized diagram showing enrichment of incompatible over compatible elements, in addition to the negative Nb (and Ta) anomaly being a typical feature of subduction generated melts (Best, 2003, Winter, 2014).

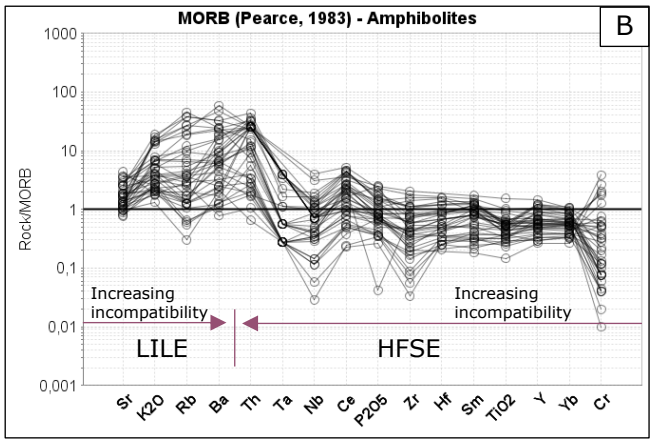

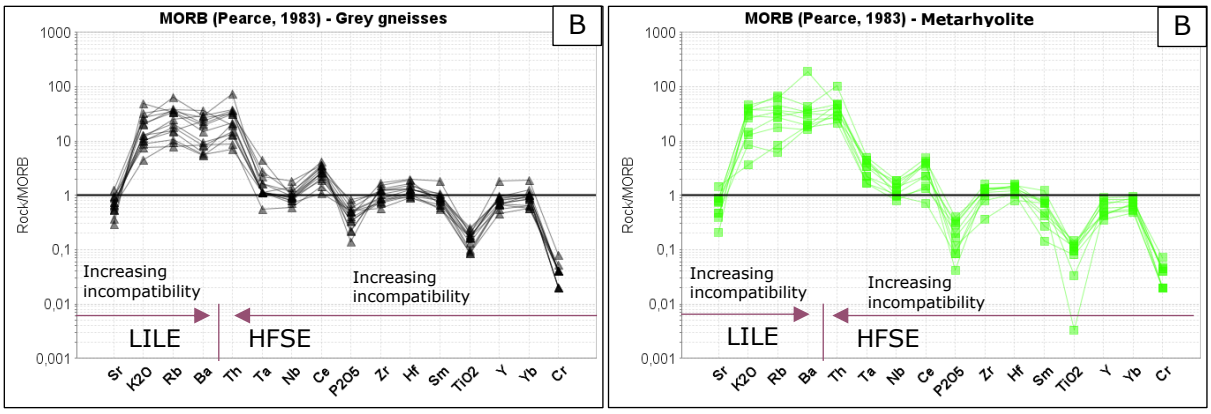

Figure 4.21: Rock/MORB normalized diagrams based on Pearce (1983). Arrows indicate increasing incompatibility from the margins to the line separating the LILE and HFSE. A) Amphibolites show an enrichment of LILE relative to HFSE, however is depleted in HFSE compared to MORB. B) Grey gneisses show an enrichment of LILE relative to HFSE, where the former is above MORB and the latter around MORB. C) Metarhyolites show an identical pattern as the grey gneisses, however, yield somewhat larger anomalies overall.

Primitive mantle normalized

The primitive mantle normalized diagrams for the amphibolites, grey gneisses and metarhyolites are presented in Figure 4.22. As for the chondrite-, and MORB-normalized diagrams the curve is "spiked" and on average negatively sloping from left to right, hence, relatively enriched in incompatible elements compared to compatible elements. The spiked pattern in the amphibolites is produced by positive anomalies for W, U, K, Pb, Mo, and Sn, and a negative anomaly for Nb, Ta, and Pr. The felsic rocks show an almost identical pattern compared to each other, with strong positive anomalies for K, Pb, and weak positive for Mo and Sn, whereas Nb, P and Ti show negative anomalies.

Overall, the pattern corresponds to that observed in both the chondrite- and MORB-normalized diagrams. Relative enrichment of incompatible elements over compatible.

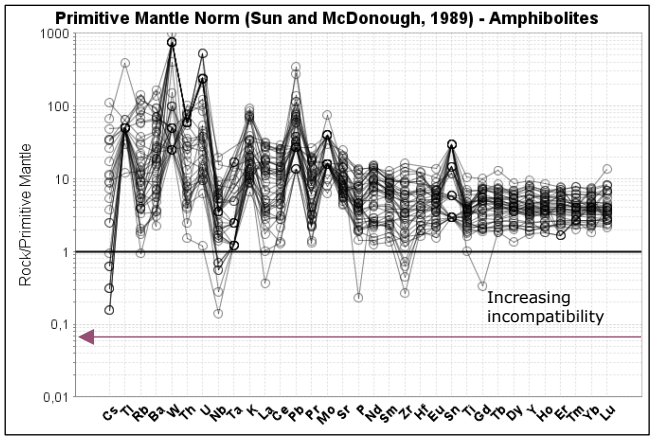

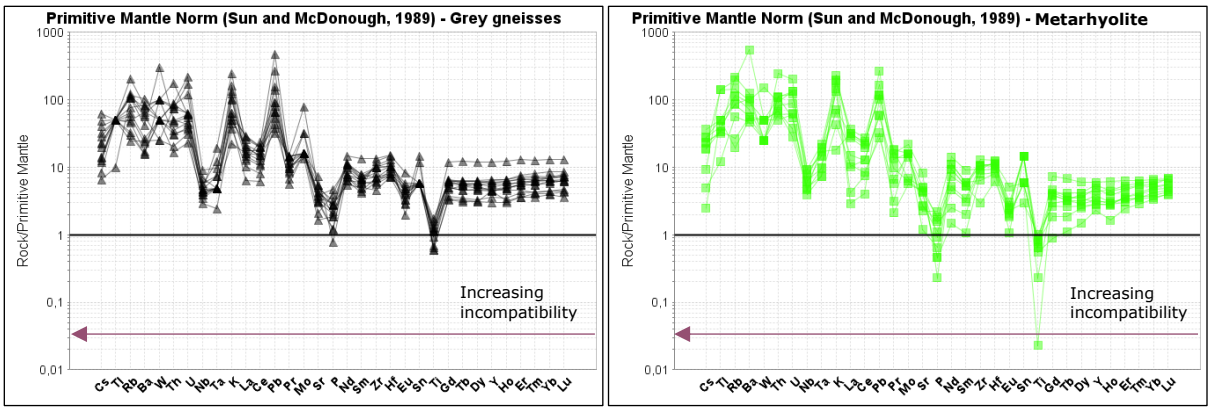

Figure 4.22: Rock/Primitive Mantle normalized diagrams based on Sun and McDonough (1989). A) Amphibolites. B) Grey gneisses. C) Metarhyolites.

4.3.6 Host rocks vs. unaltered rocks

Figure 4.23-Figure 4.25 below present REE- and spider diagrams of the QMS (blue) and the GQG (red), and compare them to the chondrite-normalized average of the felsic rocks (grey gneisses and metarhyolites) and the amphibolites, to investigate a possible genetic link. The grey gneisses and metarhyolites are merged because of the nearly identical signature they produce and represent the bright green line in Figure 4.23-Figure 4.25, while the amphibolites is represented by the black line. The samples are not differentiated between Hellerfjellet and Hesjelia-Hammertjønna, however, all of the GQG samples are from Hellerfjellet, while it is 50/50 among the QMS.

The REE diagram show that the QMS is somewhat less enriched in the incompatible LREEs compared to the GQG, and that the average value of the QMS is lower than both the felsic and mafic rocks, however, closest to the latter. The GQG is on average the most LREE-enriched compared to the other rock types, and show an almost identical graph as the felsic rocks.

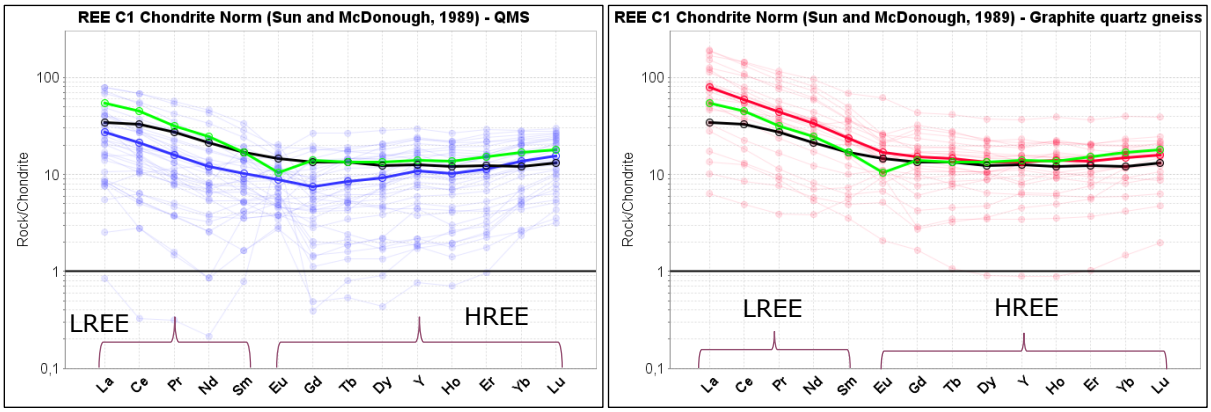

Figure 4.23: Rock/Chondrite normalized diagrams based on Sun and McDonough (1989). A) QMS (blue) compared to the chondrite-normalized average of the felsic rocks (bright green) and amphibolites (black). B) GQG (red) compared to the chondrite-normalized average of the felsic rocks and amphibolites.

The Rock/MORB pattern for both the QMS and GQG show a consistent trend from enriched LIL-elements to depleted HFS-elements, in conformity with the felsic rocks and amphibolites. The QMS has the highest absolute amount of the incompatible LIL-elements,

and the largest depletion in HFSE, wherein P, Ti and Cr have negative anomalies, similar to the felsic rocks. Overall, the QMS have a nearly identical signature to the latter, with the only exception being the larger amount of Ba in the QMS. The GQG is overall most similar to the felsic rocks, however, is somewhat drawn to the amphibolite pattern with a lack of a P-anomaly and a weaker Ti- and Cr-anomaly.

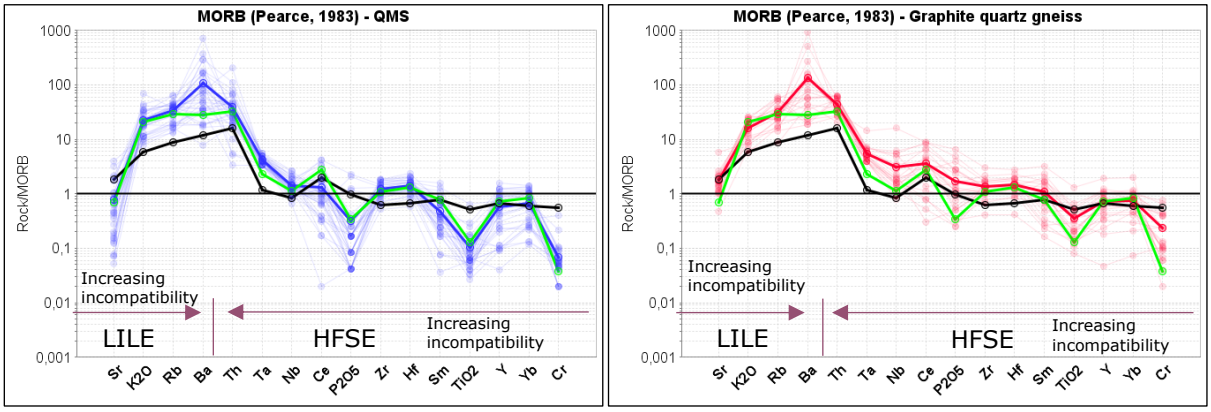

Figure 4.24: Rock/MORB normalized diagrams based on Pearce (1983). A) QMS compared to the MORB-normalized average of the felsic and mafic rocks. B) GQG compared to the MORB-normalized average of the felsic and mafic rocks.

Primitive mantle normalized

The Rock/Primitive Mantle normalized pattern for the QMS and GQG is shown in Figure 4.25 and, in accordance with the chondrite- and MORB normalized diagrams, is generally similar to the felsic rocks and amphibolites having a negatively sloping and spiked pattern. The anomalies of the QMS and GQG are amplified relative to the felsic rocks and amphibolites, reflecting the highly fractionated nature of these rocks. Because this diagram share many of the same elements as the MORB, the similarity between the QMS/GQG and the felsic rocks still count for these particular elements, however, additional elements being closer to the amphibolites are U, Sn (and W in the QMS).

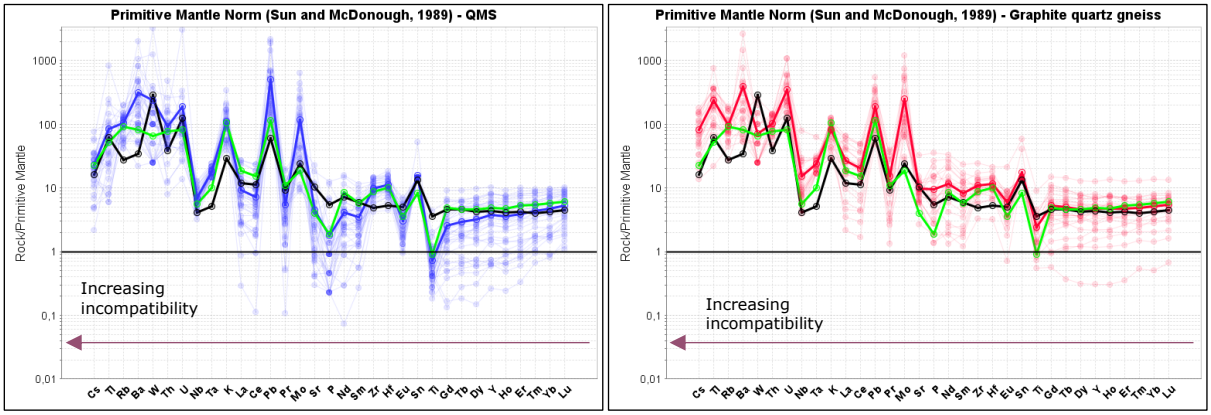

Figure 4.25: Rock/Primitive Mantle normalized diagram based on Sun and McDonough (1989). A) QMS compared to the normalized average of the felsic rocks and amphibolites. B) GQG compared to the normalized average of the felsic rocks and amphibolites.

All rock types are plotted in the ternary diagrams Zr-Al_2O_3-TiO_2 and Ti-Zr-Y in Figure 4.26. The felsic rocks are divided into the metarhyolites (green squares) and grey gneisses (black triangles). The QMS overlap most with the metarhyolites and partly the grey gneiss in both diagrams. The GQG is more scattered but coincide both with the felsic rocks and the

amphibolites in Figure 4.26A, whereas in Figure 4.26B it is more isolated in between the felsic rocks and the amphibolites, although more attracted to the felsic rocks.

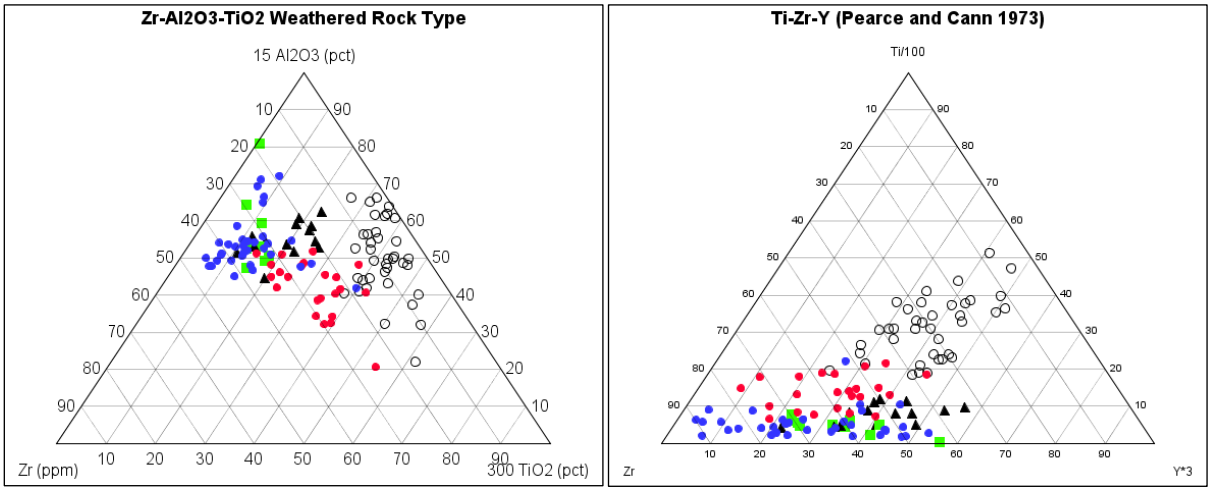

Figure 4.26: Ternary diagrams. A) Zr-Al_2O_3-TiO_2 ternary diagram comparing all rock types. B) Zr-Ti-Y ternary diagram comparing all rock types.

4.4 Metamorphism

Two samples from drill core BH4508 at Hellerfjellet named 38303 and 38308, hereafter abbreviated 03 and 08, have been analysed in the microscope, EPMA and SEM for metamorphic mineral assemblages and chemical composition of selected minerals. The goal is to establish the P-T conditions at which the minerals formed, using the GBMP-geothermobarometer from Wu (2015), and the amphibolite-plagioclase geobarometer of Molina et al. (2015). An additional sample (HF-08) of biotite-garnet amphibolite is used in the optical analysis of textures of garnets. The following section present the result of analyses of the metamorphic assemblage of said samples.

4.4.1 Mineral assemblages and textures

All three samples are shown in Figure 4.27, wherein white squares frame garnets that are investigated closer in the two following figures (Figure 4.28 and Figure 4.29). The main foliation S_2 is marked by a blue streak, while internal foliations of the garnets are marked by a red streak.

Sample 03

Sample 03 is a garnet amphibolite from the upper parts of the drill core. Thin section analysis shows a modal content of mainly hornblende, garnet, plagioclase, quartz, biotite, clinozoisite, zoisite, and minor titanite, chlorite, ilmenite and staurolite. Staurolite occur only as inclusions in two of the garnet grains, and is not observed in the matrix, suggesting it to be a relic of an earlier assemblage (Figure 4.28). The largest of the garnets with staurolite is shown in Figure 4.28A. The foliation deflects around the grain, eliminating post-tectonic growth, however, it is also overgrown, and the internal foliation of the garnet seems to be subparallel to the main foliation S_2, suggesting the grain is a syn- or inter-tectonic porphyroblast. Staurolite occur only in the outer parts of the grain, indicating that garnet formed prior to staurolite. The other garnet with staurolite, shown in Figure 4.28, have no internal foliation and clearly overgrows S_2, suggesting it to be a post-tectonic porphyroblast.

Other minerals occurring as inclusions in the garnets is mainly plagioclase and quartz, while hornblende, biotite, titanite and clinozoisite are minor. The proportion of clinozoisite seem to increase towards the rim. The rest of the garnets in the sample are smaller and show a diffuse textural relationship to the matrix, where some possesses an internal foliation transverse or subparallel to the main foliation, whereas a few have a random internal inclusion pattern (Figure 4.27A and Figure 4.28A/B). Lastly, titanite overgrow the foliation, inferring post-tectonic growth.

Sample 08

Sample 08 is part of the amphibolite unit, however, represents a segregation enriched in zoisite, together with garnet, biotite, clinozoisite, plagioclase and minor muscovite, titanite, and sulphides. The most distinguishing feature of this sample is the amount of zoisite, occurring as grey/white (in ppl) and anomalous deep blue subhedral to euhedral crystals (in xpl) (Figure 4.29). Texturally, it occurs as coarse grained poikiloblasts with inclusions of mainly biotite, clinozoisite and plagioclase, and *cross cuts* the main foliation, indicating post-tectonic growth. Staurolite is found as an inclusion in a zoisite grain (Figure 4.29), indicating that zoisite developed before staurolite unequilibrated with the matrix mineral

assemblage. Staurolite contain zinc according to EDS-maps (Figure 4.29D) and in some mineralized samples (not shown here) sphalerite occurs as inclusions in staurolite, explaining why it contain zinc.

Garnets in sample 08 is difficult to classify but generally deflect the foliation, and have inclusion trails with oblique orientation to the main foliation. Figure 4.29 A and B show two grains of garnet with an internal foliation oblique to S_2, where the former overgrows the foliation and the latter deflects it, indicating inter- and syn-tectonic growth, respectively. The garnets in this sample separates from the other samples by having a much higher proportion of clinozoisite inclusions. Calcite occur both as coarse grained twinned crystals in bands, and as fine-grained crystals, primarily without twinning, in the matrix. It has inclusions of plagioclase, quartz and clinozoisite. Garnet is often observed as fine-grained crystals along the stripes of calcite.

Sample HF-08

Sample HF-08 (Figure 4.27C) consist primarily of biotite, garnet, quartz, plagioclase, and hornblende, with minor muscovite and ilmenite. Two garnet grains (white squares in Figure 4.27) are analysed further in Figure 4.28. The garnet in Figure 4.28C (white square to the right in Figure 4.27C) have inclusions of staurolite and texturally the foliation deflects around it, and no clear internal foliation can be defined. The grain also seems to be strained, evident by the elongated shape. The other garnet (Figure 4.27C) have an internal foliation antiparallel to S_2, and also appear to be rotated into an asymmetrical sigma clast with sinistral shear sense, suggesting syn-tectonic growth.

Other inclusions in the garnets are plagioclase, quartz, and minor biotite. Hornblende is not observed as inclusions in this sample even though it occurs in the matrix, however, the fact that biotite and hornblende amount to a small proportion of the inclusions in all garnets observed, can be explained by garnet growing on behalf of these minerals.

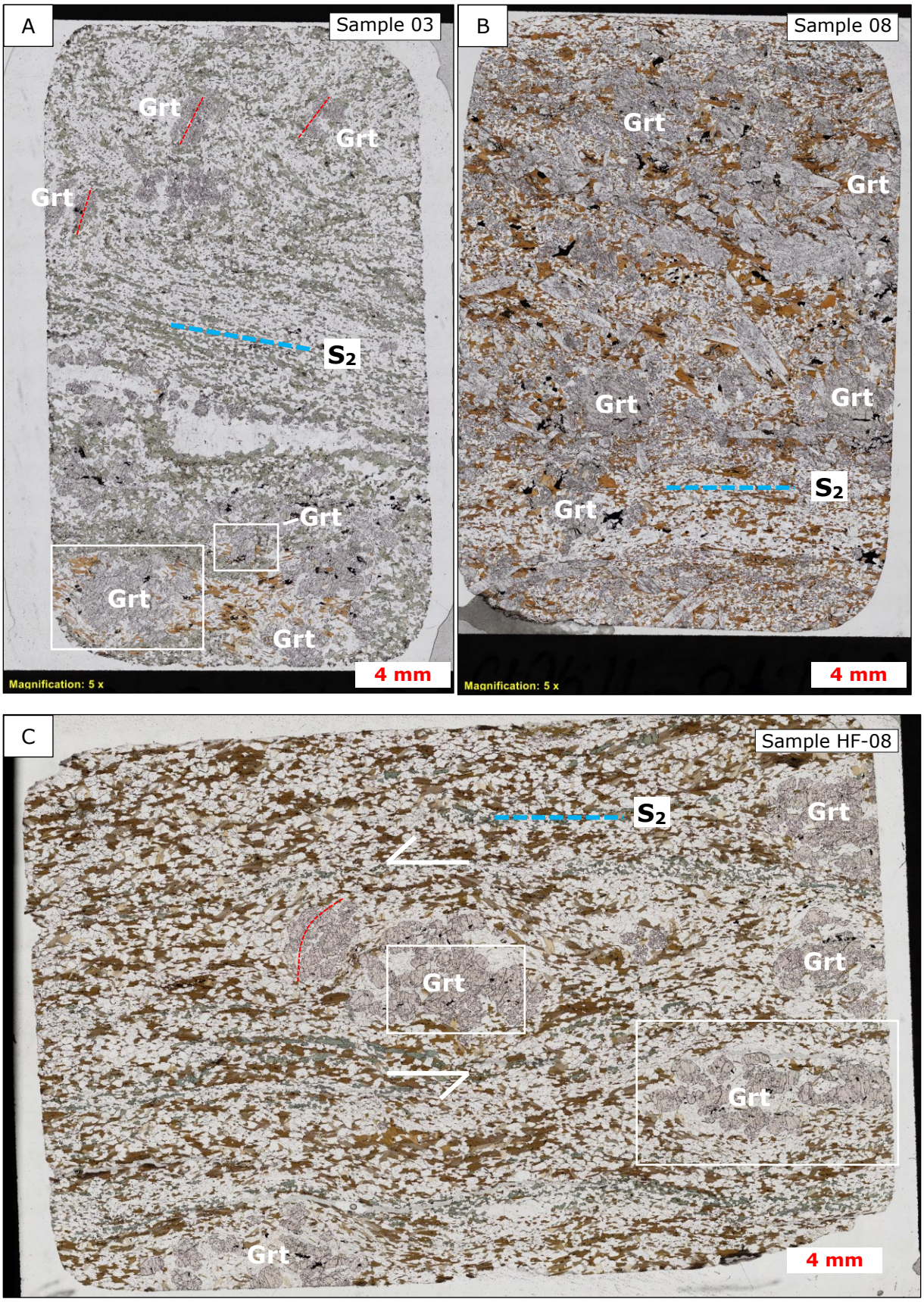

Figure 4.27: Microphotograph (ppl) of sample 03, 08 and HF-08. White squares mark the area shown in figure xx below. Red streaks reflect internal foliation where observed, while blue streaks mark S_2. A) Sample 03. The visible minerals are hornblende (olive green), garnet (high relief) and biotite (brown). Internal foliation is antiparallel to S_2. B) Sample 08. Zoisite (elongated white grains with

high relief) is subhedral to euhedral, coarse grained (~6 mm), and transverses the S_2. Other major minerals visible here are biotite (brown), garnet (grey, high relief) and sulphides (opaque).C) Sample HF-08. Visible minerals are biotite, garnet, and hornblende.

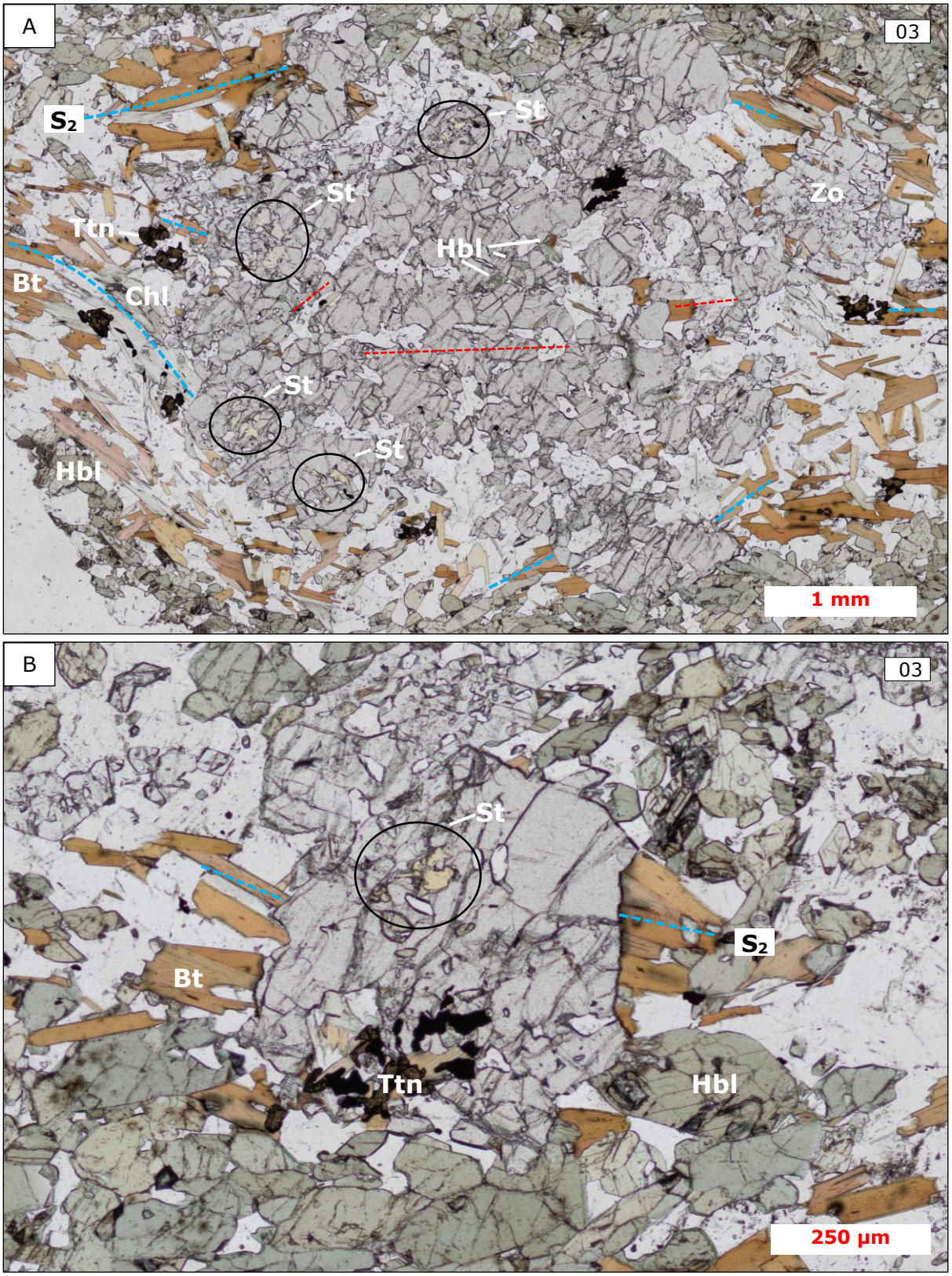

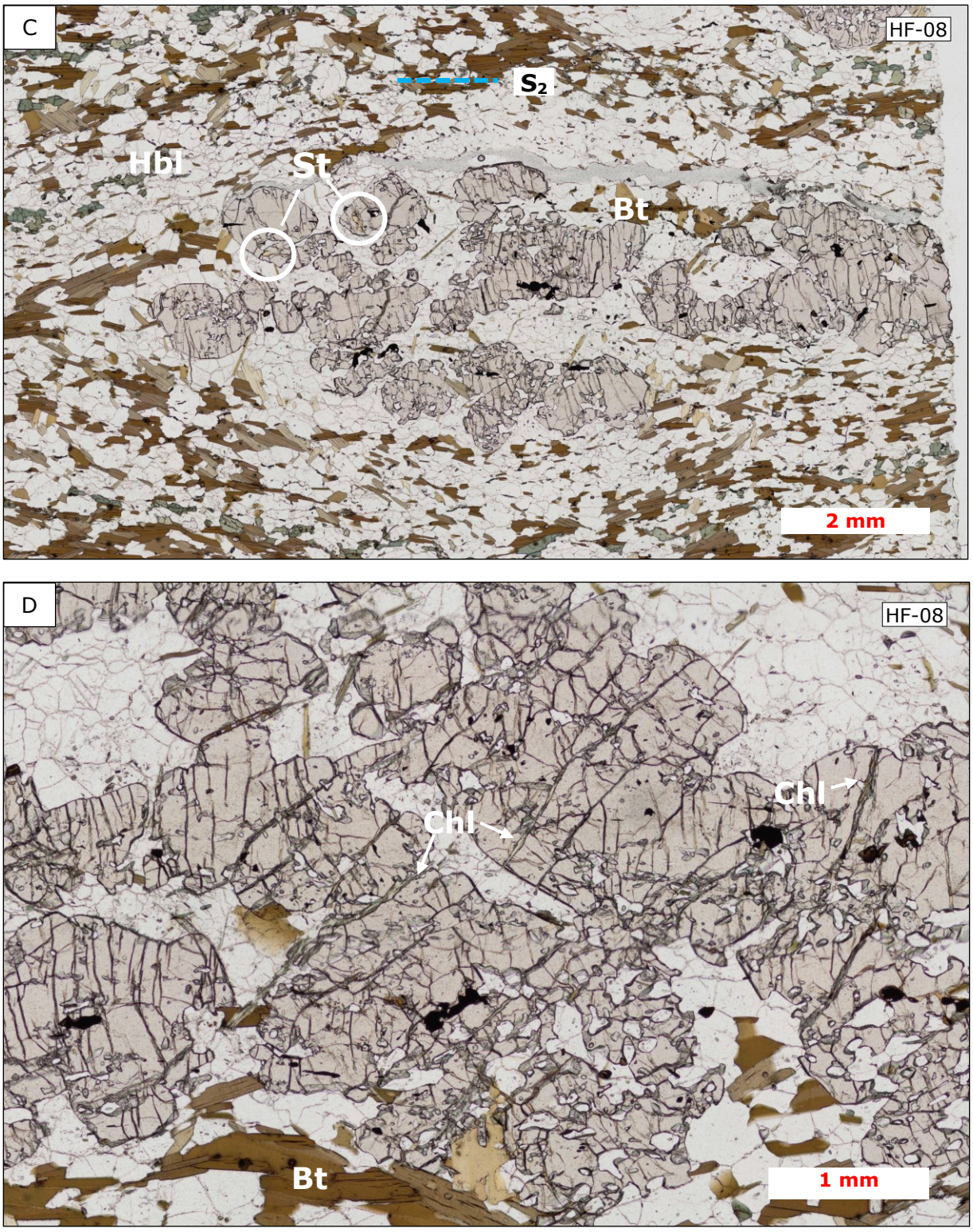

Figure 4.28: Microphotographs of staurolite inclusions in garnet in sample 03 and HF-08, and chlorite-filled cracks in the latter. A) Sample 03. Garnet grain showing inter-tectonic growth-textures with inclusions of staurolite in the outer parts of the grain. This grain was analysed in EPMA. Titanite cuts the foliation evident from overgrowth on biotite and chlorite. B) Sample 03. Inclusion of staurolite in a post-tectonic garnet grain. C) Sample HF-08. Inclusion of a staurolite grain within the outer part of a garnet grain with inter-tectonic textures, similar to A. D) Chlorite-filled cracks in garnet of sample HF-08.

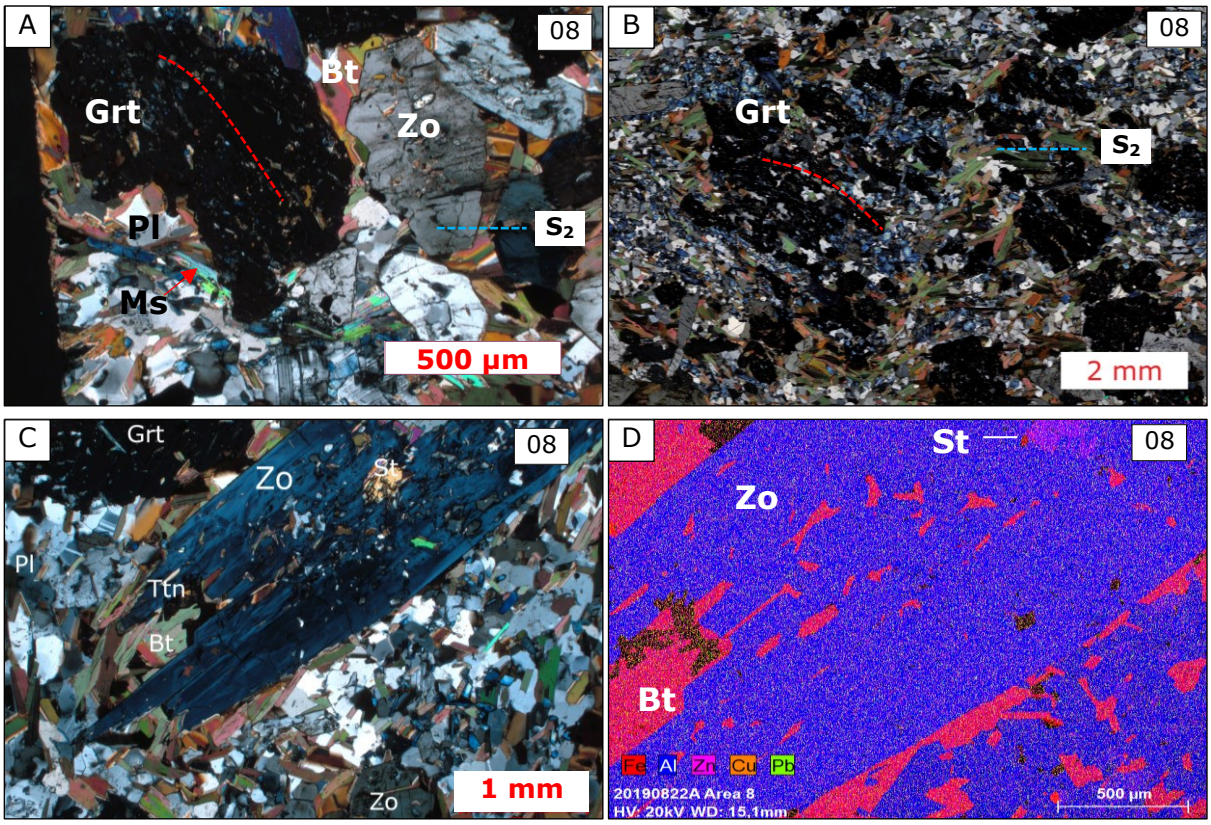

Figure 4.29: Textural relationships and chemical composition of HF-08 and 08. A) Microphotograph (xpl) of sample HF-08 showing inclusions in a garnet grain consisting of plagioclase, quartz, and minor biotite, while chlorite fills fractures. B) Microphotograph (xpl) of sample HF-08 showing an inter- or syn-tectonic garnet, evident by the inclusion trail. C) Microphotograph (xpl) of sample 08 showing a garnet grain with a weak internal foliation and inclusions of clinozoisite (blue) and biotite (brown-orange). Inter- or post-tectonic. This grain was analysed in EPMA. D) Microphotograph (xpl) of sample 08 showing another garnet grain with a clearer internal foliation and a deflection of the foliation. The inclusions are mainly clinozoisite. Possibly inter-tectonic. E) Microphotograph (xpl) of sample 08 showing a staurolite inclusion in an coarse grained euhedral zoisite cross-cutting the foliation. Titanite overgrows zoisite. F) EDS-map from SEM coloured according to Fe (red), Al (blue), Zn (pink), Cu (orange) and Pb (green). The pink colour of staurolite indicate Zn, coming from sphalerite in the sample.

4.4.2 EPMA-results – chemical characteristics of the analysed minerals

Ca. 300 point analyses were performed on garnet, biotite, plagioclase, muscovite, hornblende, clinozoisite, zoisite, and chlorite and the following section present the most important findings on each mineral. See Appendix B for full overview of the chemical analysis.

Plagioclase

Five grains of plagioclase were analysed in sample 03 with a total of 44 points, whereas three grains were analysed in sample 08 with a total of 27 points. Plagioclase in both samples is of oligoclase-andesine composition, whereof sample 03 yields An_{23-47}/Ab_{53-77}, and sample 08 yields An_{22-49}/Ab_{50-78}. The latter sample is generally more sodic, which may be explained by the higher amounts of clinozoisite. The variation in An-Ab reflect a core-rim zonation (Figure 4.30A), where the An/Ab-ratio *decreases* from the core, i.e. the core is calcic, while the rim is sodic. This composition of plagioclase is typical for amphibolite facies (Bucher and Grapes, 2011).

In sample 03 and 08 plagioclase is not observed being altered to saussurite (zoisite, clinozoisite and sericite) however in the QMS samples a large amount of the plagioclase crystals is altered (Figure 4.30B). The alteration affects only the An-component in plagioclase, and therefore decreases the An/Ab-ratio, leading to a more Na-rich plagioclase. The transition of An to saussurite follow the exsolution-twins in plagioclase and gives the grain a stripy appearance as seen in Figure 4.30B. Unrelated to this, clinozoisite-epidote overgrow plagioclase in both samples (Figure 4.36).

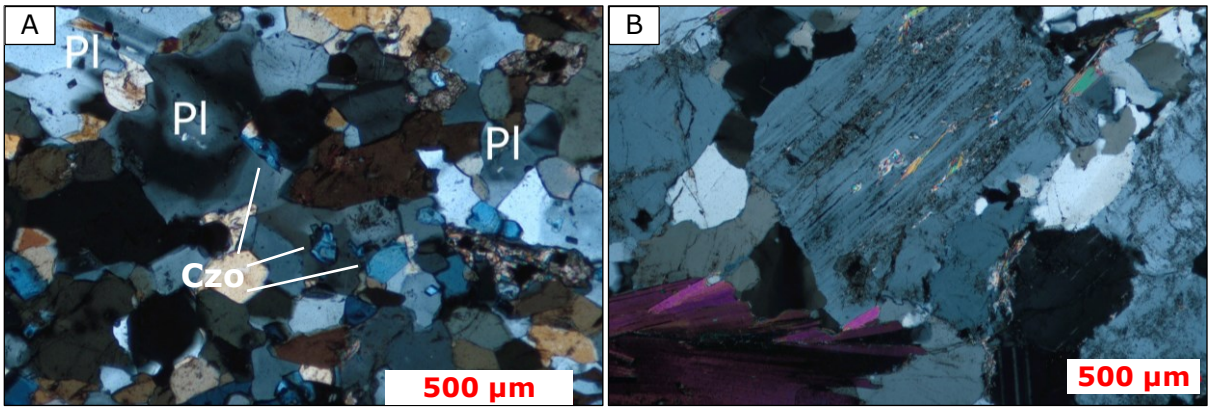

Figure 4.30: Microphotograph of plagioclases (xpl). A) Andesine to oligoclase core-rim zonation in plagioclase and twinning in the upper left of the picture. Also notice clinozoisite overgrowing plagioclase. B) Saussurization of plagioclase making the grain look "dirty" and stripy.

Garnet

Out of a few larger grains one grain of garnet was analysed in each sample with a total of 11 and 16 points in sample 03 and -08, respectively. The results yield compositions of Alm_{62-68}, Py_{14-21}, Gro_{14-18} and $Sp_{<2}$ for sample 03 and Alm_{60-67}, Py_{9-17}, Gro_{19-26} and $Sp_{<4}$ for sample 08. Hence, there is a larger Gro-component in the latter sample, which may reflect the larger abundance of Ca-bearing phases in this sample. The variation in each component is not systematic and no pattern is observed in the BSE-image. There is only minor zonation in Mn (~ 1.25 % difference) from core to rim, suggesting the investigated garnets grew at isothermal conditions.

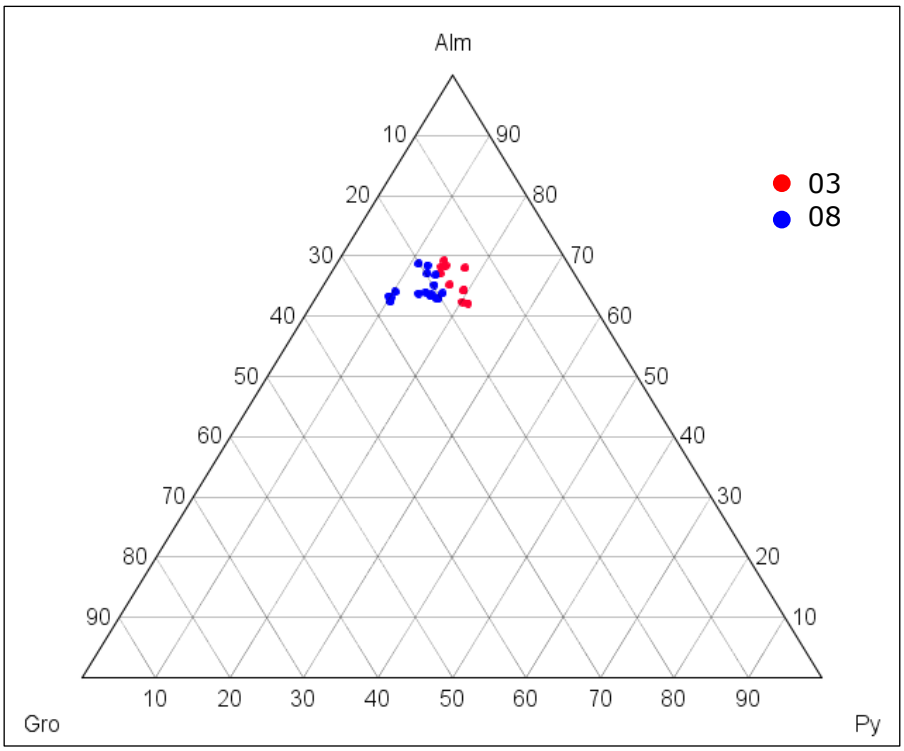

Figure 4.31: Ternary plot of the molar ratios of all analyses in sample 03 and 08. The data is clustered, reflecting the almost constant composition of the two garnets analysed. Almandine (Alm), grossular (Gro) and pyrope (Py).

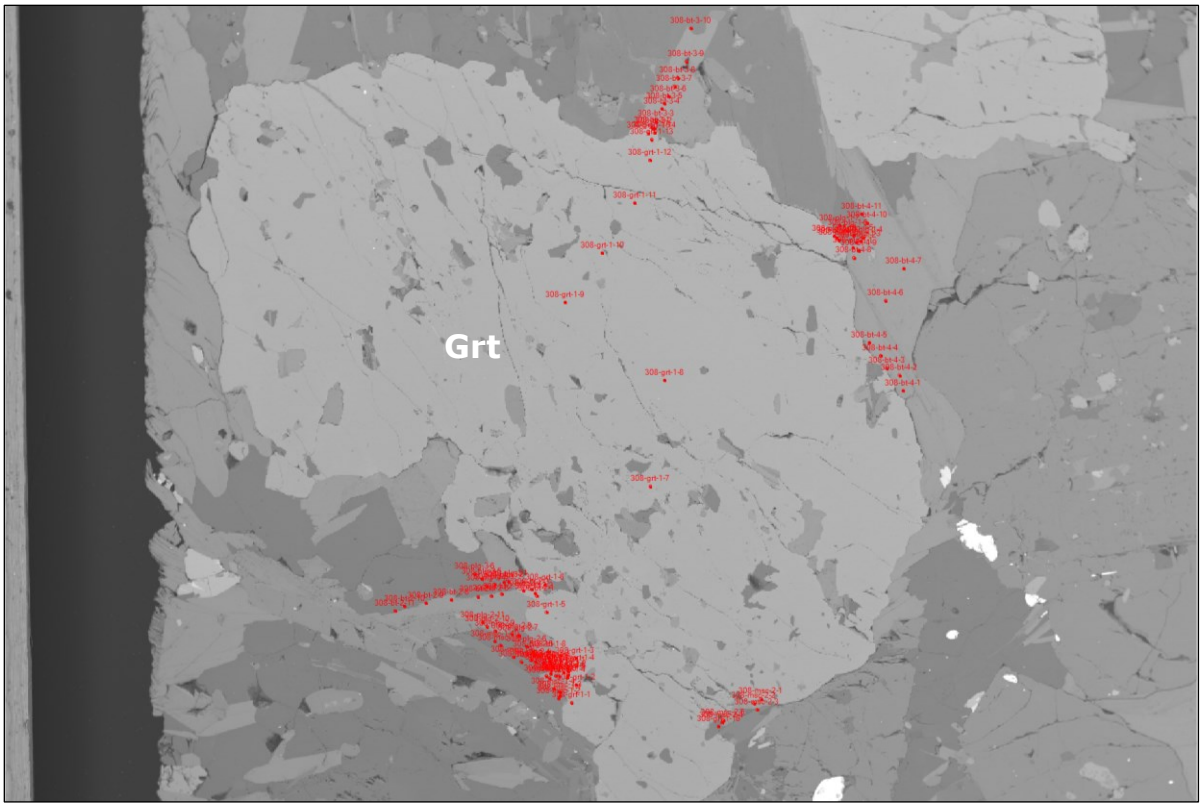

Figure 4.32 The analysed grain of garnet in sample 08 with coexisting biotite, plagioclase and muscovite analysed for P-T estimation.

Mica

The general chemical formula for mica is $X_2Y_{4-6}Z_8(OH,F)_4$ (Deer et al., 1992), and is used to calculate the average chemical formula of biotite and muscovite in both samples, represented in Table 4.2. Five grains of biotite were analysed by 29 points in sample 03, whereas four grains were analysed by 46 points in sample 08. In The chemical composition of biotite for the two samples show minor differences both internally and among the individual grains analysed, and yield a Mg-rich biotite with Al in the Y site, thus classifying as eastonite – siderophyllite.

Only one grain of muscovite was observed and analysed by six points in sample 03, whereas two grains were analysed by 15 points in sample 08. The composition of muscovite does not vary internally and have almost similar chemical composition in both samples. It classifies as a typical muscovite, however, with a small component of paragonite and celadonite due to significant amounts of Na and Fe/Mg, respectively.

The colour appearance of biotite and muscovite is presented in Figure 4.33 below, showing the reddish-brown to pale brown colour of biotite and colourless muscovite. Figure 4.33B shows the grains analysed for the GB-GBMP geothermobarometer.

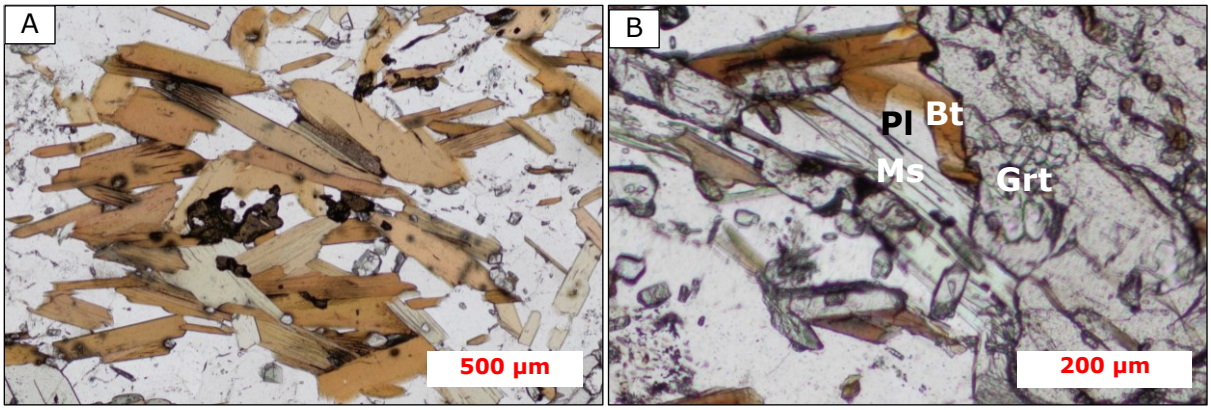

Figure 4.33: Appearance of the micas. A) Microphotograph (ppl) of biotite in sample 03 appearing both reddish-brown and pale brown. B) Microphotograph (xpl) of muscovite and biotite in sample 08.

Mineral	Sample	X	Y	Z
Biotite	**08**	$(K_{1.71}\ Na_{0.05}\ Ca_{0.02})_{1.78}$	$(Mg_{2.63}\ Fe_{2.16}\ Al_{0.79}\ Ti_{0.18}\ Mn_{0.01})_{5.76}$	$(Si_{5.54}\ Al_{2.46})_{8.00}$
	03	$(K_{1.63}\ Na_{0.26}\ Ca_{0.01})_{1.68}$	$(Mg_{2.63}\ Fe_{2.12}\ Al_{0.81}\ Ti_{0.21}\ Mn_{0.00})_{5.78}$	$(Si_{5.53}\ Al_{2.47})_{8.00}$
Muscovite	**08**	$(K_{1.52}\ Na_{0.26}\ Ca_{0.01})_{1.79}$	$(Al_{3.57}\ Mg_{0.28}\ Fe_{0.18}\ Ti_{0.07})_{4.09}$	$(Si_{6.31}\ Al_{1.69})_{8.00}$
	03	$(K_{1.45}\ Na_{0.35}\ Ca_{0.00})_{1.80}$	$(Al_{3.68}\ Mg_{0.21}\ Fe_{0.14}\ Ti_{0.07})_{4.09}$	$(Si_{6.31}\ Al_{1.69})_{8.00}$

Table 4.2: Average biotite and muscovite chemical formula for sample 03 and 08. The calculations of biotite are based on 29 and 46 analysis in sample 03 and 08, respectively, while the calculations of muscovite are based on six and 15 analysis in sample 03 and 08, respectively. The chemical formula is from Deer et al. (1992).

Amphibole

Four grains of amphibole (preclassified as hornblende from optical properties) were analysed by 11 points in sample 03. The chemical formula of the all individual point analysis are calculated from Ridolfi et al. (2018)'s mass-based model, which is based on the general formula $AB_2C_5T_8O_{22}W_2$ of Hawthorne et al. (2012), and presented in Figure 4.35. Seven of 11 analysis yield tschermakite compositions while the rest yield sadangaite compositions. The IMA 2012 nomenclature does not explicitly consider metamorphic amphiboles, as is the case here, however, Schumacher (2007) has given constraints on metamorphic amphiboles that were implemented in this analysis.

Figure xx below shows some of the colour variation in hornblende in sample 03. The colour is pale green, olive green, brownish green and bluish green.

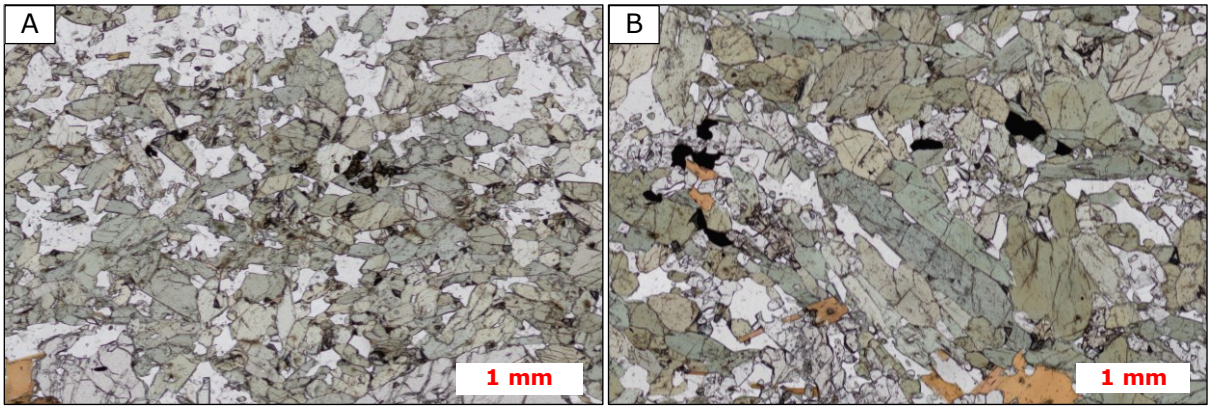

Figure 4.34: Examples of the colour appearance of hornblende in sample 03. Hornblende is pale green, olive green and bluish green.

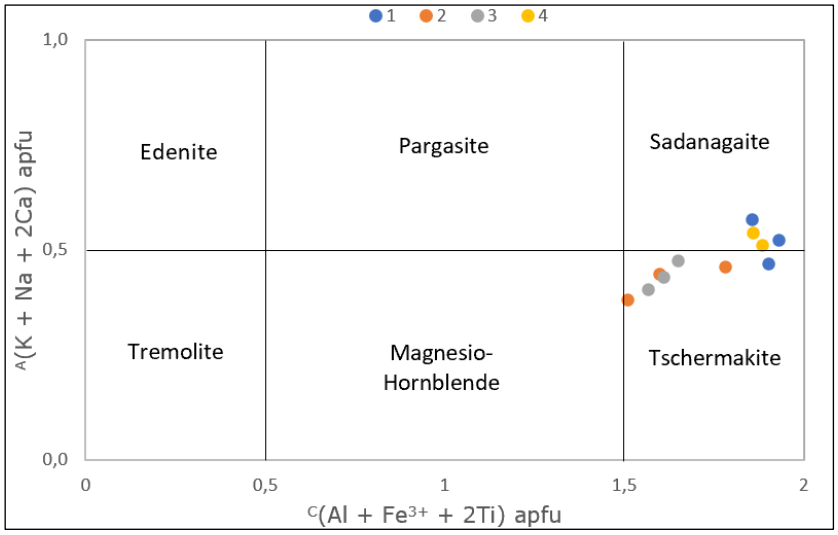

Figure 4.35: Amphibole classification (Hawthorne et al., 2012) of four grains from sample 03. The individual grains are separated by colour (see legend) to illustrate zonation patterns.

Clinozoisite-epidote and zoisite

Six grains of clinozoisite-epidote (czo-ep) and four grains of zoisite (zo) were analysed by respectively 14 and 15 points in sample 08, whereas three grains of czo-ep and two grains of zo were analysed by respectively seven and five points in sample 03. Both zo and czo-ep show internal variations in Fe-content, fluctuating between 1.46-2.31 wt. % and 3.8-5.47 wt. %, respectively.

According to Deer et al. (1992) the composition can be expressed as $X_2Y_3Z_3(O,OH,F)_{13}$. The calculated composition for the analysed czo-ep and zoisite is shown in Table 4.3 below. Fe^{3+} was calculated according to Droop (1987). The amount of Fe^{3+} in czo-ep place it compositionally in between the two endmembers in the clinozoisite-epidote series (Deer et al., 1992), and the variation of Fe is more systematic in czo-ep, showing a decrease from core to rim. Also, Al generally increases concurrently, reflecting the Al ↔ Fe^{3+} substitution (Deer et al., 1992). Czo-ep occur as inclusions in plagioclase, and the other way around. The former is more often observed to be overgrowing the boundaries of plagioclase and form euhedral crystals. Plagioclase also occur as inclusions in zoisite.

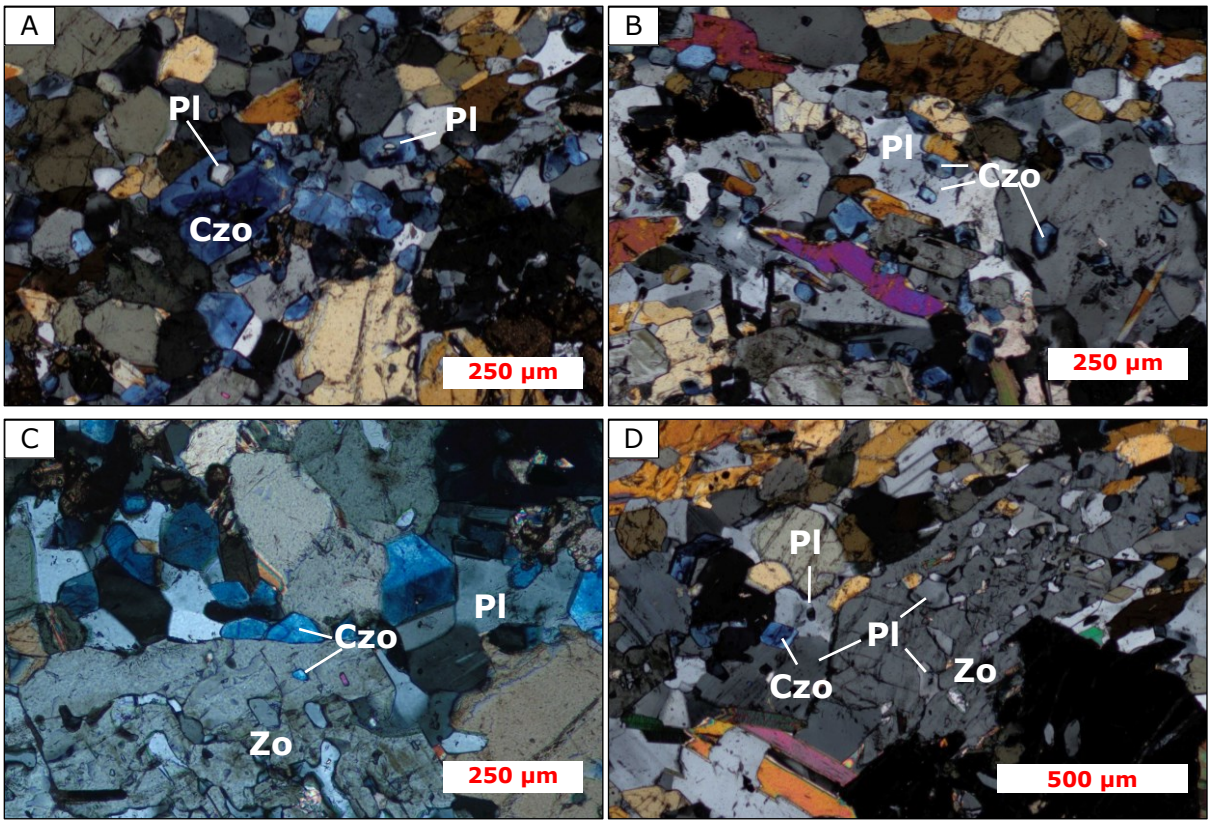

Figure 4.36: Textural relationships between czo-ep, zoisite and plagioclase, in sample 03. A) Plagioclase inclusions in czo-ep. B) Czo-ep inclusions in plagioclase. C) Coexisting clinozoisite-epidote and zoisite in sample 03. D) Czo-ep overgrows plagioclase boundaries. Plagioclase also occur as inclusions in zoisite.

Mineral	Sample	X	Y	Z
Zoisite	8	$(Ca_{1.99}\ Na_{0.01})_{2.00}$	$(Al_{2.86}\ Fe^{3+}_{0.1}\ Fe^{2+}_{0.02})_{2.98}$	$Si_{3.02}$
	3	$Ca_{1.99}$	$(Al_{2.87}\ Fe^{3+}_{0.1}\ Fe^{2+}_{0.02})_{2.99}$	$Si_{3.01}$
Czo-ep	8	$(Ca_{1.98}\ Na_{0.002}\ K_{0.001})_{1.98}$	$(Al_{2.66}\ Fe^{3+}_{0.27}\ Fe^{2+}_{0.05}\ Mg_{0.01}\ Ti_{0.01})_{2.99}$	$Si_{3.03}$
	3	$(Ca_{1.97}\ Fe^{2+}_{0.016}\ Na_{0.007}\ K_{0.001})_{1.99}$	$(Al_{2.71}\ Fe^{3+}_{0.25}\ Fe^{2+}_{0.01}\ Mg_{0.01}\ Ti_{0.01})_{2.99}$	$Si_{3.01}$

Table 4.3: Average molar amount of the elements constituting clinozoisite-epidote and zoisite in sample 03 and 08. Notice the amount of Fe^{3+} in both minerals, calculated after Droop (1987).

Chlorite

Two grains of chlorite were analysed by 16 points, only in sample 03, and yields nearly constant values overall. The FeO-, Al_2O_3- and MgO-content is highest, except for SiO_2, yielding 20.0 – 21.8 % FeO, 21.7 – 22.6 % Al_2O_3 and 17.4 – 18.33 % MgO for all analyses. The general formula for chlorite can be written as $Y_6Z_8O_{20}(OH)_4 + Y_6(OH)_{12}$, where the former represents talc-like layers and the latter represents brucite layers (Deer et al., 1992). The calculated formula, based on 28 oxygens, for the analysed chlorites yield:

$$\underbrace{(Mg_{5.448}\ Fe^{2+}_{3.652}\ Fe^{3+}_{0.033}\ Al_{2.693}\ K_{0.170}\ Ti_{0.022}\ Na_{0.012}\ Mn_{0.003}\ Ca_{0.005})_{12.04}}_{Y}\ \underbrace{(Si_{5.348}\ Al_{2.652})_{8.0}}_{Z}$$

The chlorite classifies as ripidolite, is oxidized and Fe/(Fe + Mg) = 0.4. As seen in Figure 4.37 below, chlorite overgrows biotite but also occur as foliation parallel grains. Colour is colourless to pale green in ppl.

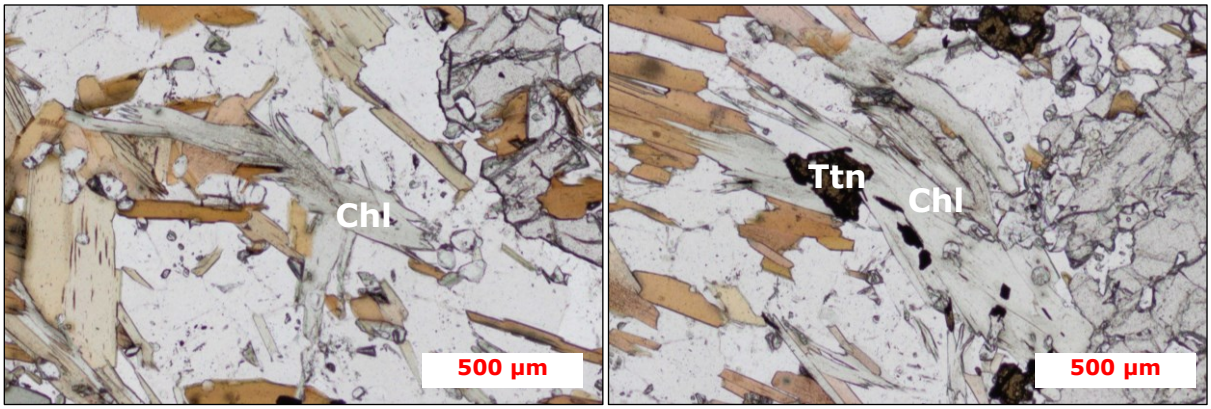

Figure 4.37: Chlorite in sample 03 is very pale green. Chlorite overgrows biotite, maybe pseudomorphically to some extent. Titanite overgrows chlorite.

4.4.3 Geothermobarometry

GB-GBMP geothermobarometer

Figure xx show the plotted P-T estimates from sample 08, based on the calculations from the GB-GBMP geothermobarometer of Wu (2015) presented in table xx. The calculations assume a ferric fraction (Fe^{3+} / (Fe^{2+} + Fe^{3+})) of 0.116 and 0.03 (Holdaway, 2000) for biotite and garnet, respectively. The GBMP-geothermobarometry is performed on the grains that confidently can be regarded as coexisting (Figure 4.39, picture from EPMA). The amount of muscovite in the samples are low (<5 %) and therefore only one grain could confidently be regarded as coexisting (grain to grain contact) with the other phases in the geothermobarometer. Four calculations (nr. 1-4 in Table 4.4) with 16 unique points, i.e. four points in each mineral, yielded an average of 595.5 °C ±19.6 and 9.6 kbar ±0.61. Two additional calculations (nr. 5 and 6) reused grt-1-1 and grt-1-2 from calculation nr. 1 and 2, respectively, and together with calculation nr.1-4 yielded an average of 602.3 °C ± 18.7 and 9.7 kbar ±0.54.

For extremely *reduced* conditions, i.e. ferric fraction of zero, the average result for calculation nr. 1-4 is 614.5 °C ±20.7 and 9.8 kbar ±0.63, and 621.3 °C ±19.5 and 9.9 kbar ±0.55 overall. For extremely *oxidized* samples with ferric fractions of 0.2 and 0.05 for biotite and garnet, respectively, the result is 580.8 °C ±18.8 and 9.4 kbar ±0.59 for calculation nr. 1-4, and 587 °C ±18 and 9.5 kbar ±0.52 overall.

Thus, the P-T estimation of sample 08, including the standard deviation for all possible ferric fractions, lies in the range of 562 – 640.8 °C and 8.81 – 10.45 kbar. However, using the standard ferric fraction, which is supported by the observation of ilmenite and graphite in genetically and spatially related rocks, the P-T conditions of this specific mineral assemblage is in the range of **575.9 – 621.0 °C and 9.0 – 10.2 kbar.**

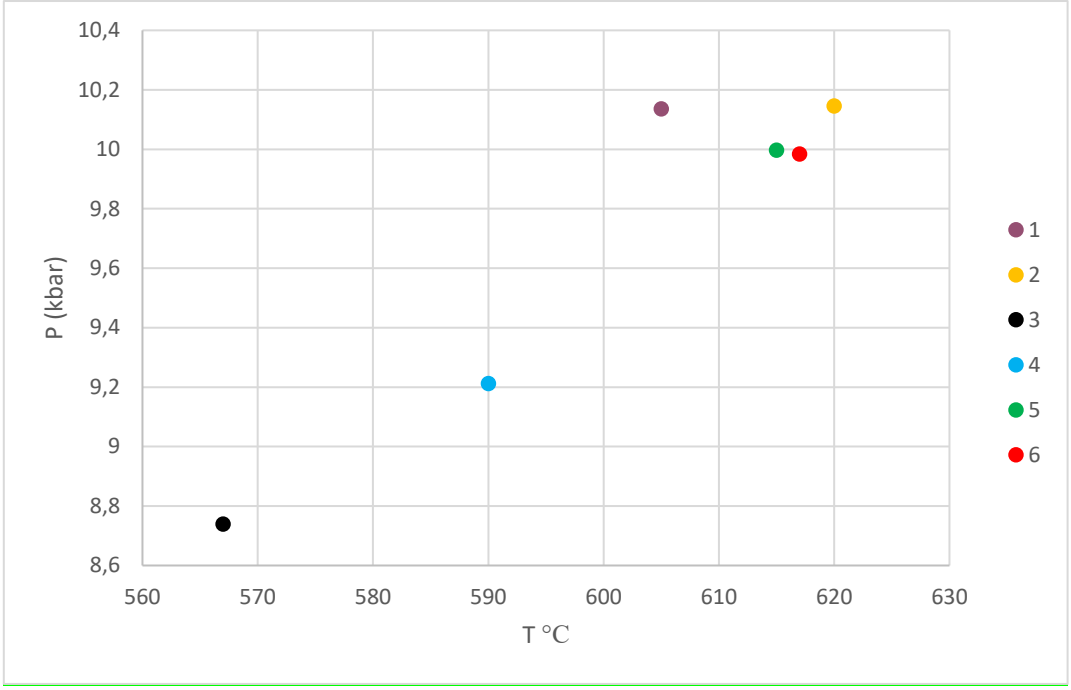

Figure 4.38: GB-GBMP (Wu, 2015) P-T plot of the six calculations from table xx using the standard ferric fraction of 0.116 and 0.03 for biotite and garnet, respectively.

Nr.	Sample 08	$Fe^{3+}/(Fe^{2+} + Fe^{3+})$ (Bt)	$Fe^{3+}/(Fe^{2+} + Fe^{3+})$ (Grt)	Input T (°C)	Input P (kbar)
1	bt-1-1, plg-2-1, grt-1-1, msc-1-1	0.116	0.03	605	10.14
2	bt-1-2, plg-2-3, grt-1-2, msc-1-2	0.116	0.03	620	10.15
3	bt-1-3, plg-2-5, grt-1-3, msc-1-3	0.116	0.03	567	8.74
4	bt-1-4, plg-2-9, grt-1-4, msc-1-4	0.116	0.03	590	9.21
5	bt-1-5, plg-2-10, grt-1-1, msc-1-5	0.116	0.03	615	10.00
6	bt-1-6, plg-2-11, grt-1-2, msc-1-6	0.116	0.03	617	9.98
	Avg. 1-4			**595.5 °C**	**9.6**
	Std. 1-4			19.6	0.6
	Avg. 1-6			**602.33°C**	**9.7**
	Std. 1-6			18.7	0.5

Table 4.4: P-T calculations from the GBMP-geothermobarometer spreadsheet of Wu (2015), using the standard ferric fraction of 0.116 and 0.03 for biotite and garnet, respectively. Four calculations wherein 16 unique points yielded 595.5 °C ±19.6 and 9.6 kbar ±0.6, whereas six calculations, of which grt-1-1 and grt-1-2 were reused, yielded 602.3 °C ± 18.7 and 9.7 kbar ±0.5. Bt = biotite, plg = plagioclase, grt = garnet, and msc = muscovite.

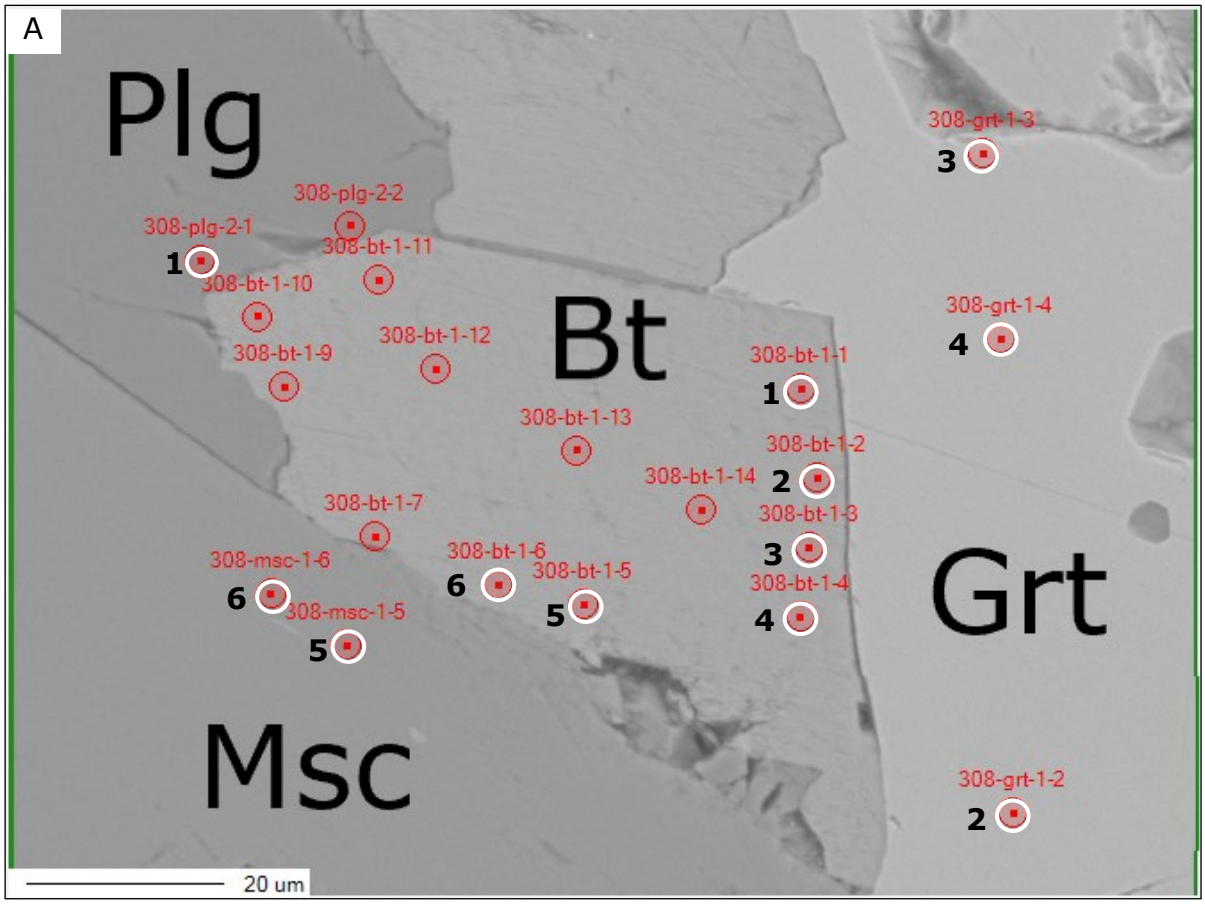

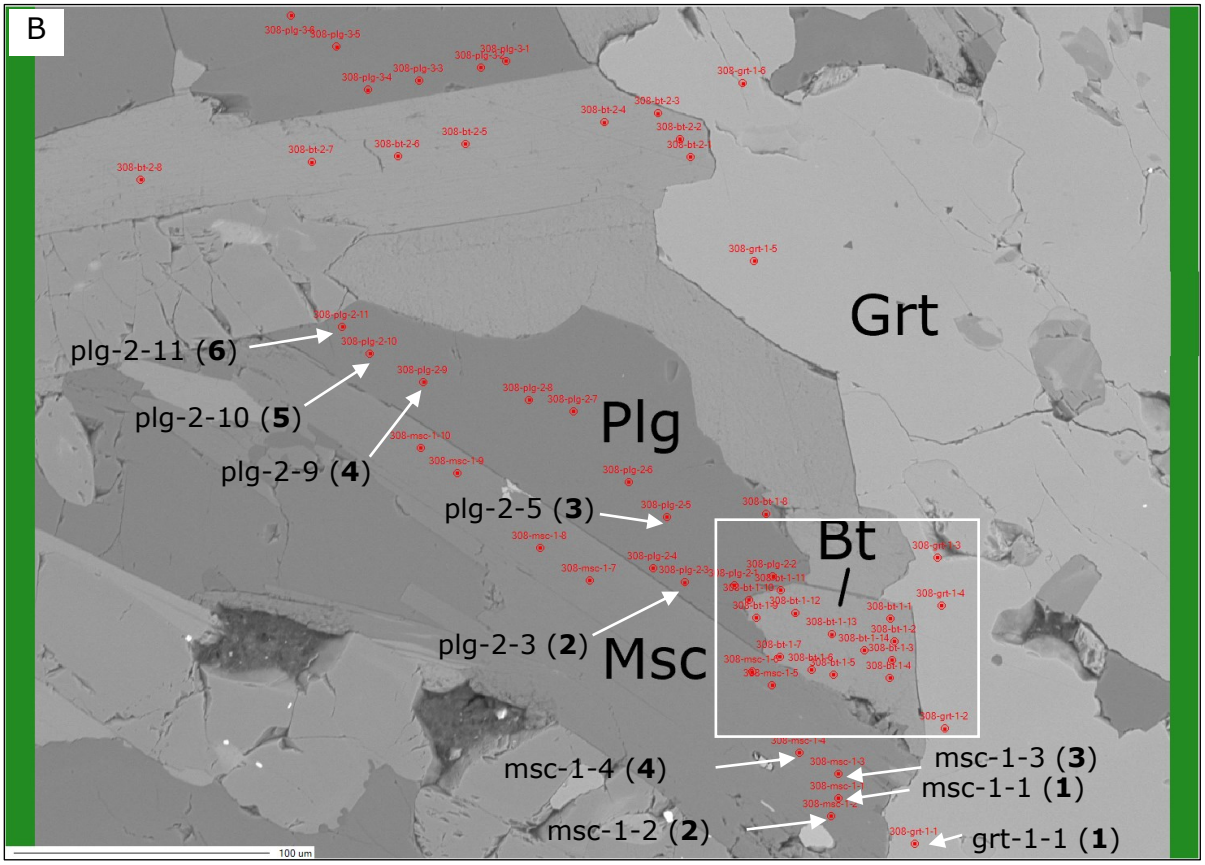

Figure 4.39: Overview of points used in P-T analysis. Other abbreviations are used here for plagioclase (plg) and muscovite (msc). A) Some of the analysed points. Points outside of this picture:

grt-1-1, msc-1-1, msc-1-2, msc-1-3, msc-1-4, plg-1-3, plg-1-5, plg-1-9, plg-1-10, and plg-1-11. B) All points of calculation nr. 1-6 are included in this photo. White square is where A is placed.

Amphibole – plagioclase geobarometer

The geobarometer of Molina et al. (2015) based on amphibole – plagioclase was used as validation for the pressure obtained from the GBMP barometer. This geobarometer is calibrated for temperatures of 650-1050 °C with uncertainties of ±1.5 to ±2.3 kbar, however, yield close to the same pressure as the GBMP barometer using 602.3°C from the GB thermometer as input for temperature.

Five amphibole – plagioclase pairs (nr. 1-5) assembled by 10 unique points in **sample 03** yielded 10.55 kbar ± 0.51 (Table 4.5). Including two additional pairs (nr. 6-7), reusing amp-3-3 and amp-2-3 from calculation nr. 3 and 4, the average was **10.36 kbar ± 0.53**. This overlaps with the standard deviation of the pressure (*P*) yielded from the GBMP barometer (9.7 kbar ±0.5). Calculation nr. 1 (11.2 kbar) increases the average pressure by 0.13 kbar, which can be explained by the geochemical data on plag-1-1, showing that Ca/Na > 1, which for plagioclase grains in general is the ratio of the core. Thus, the point may be too far from the rim to yield the actual amphibole rim – plagioclase rim equilibrium composition.

Nr.	Points	P (kbar)
1	Amp-1-3, plag-1-1	11,20
2	Amp 1-1, plag 1-3	10,89
3	Amp-2-3, plag-2-4	9,78
4	Amp-3-3, plag-3-3	10,17
5	Amp-4-2, plag-4-1	10,70
6	Amp-3-3, plag-3-1	10,14
7	Amp-2-3, plag-2-1	9,67
Avg. nr. 1-5		**10,55**
Standard dev.		0,51
Avg. nr. 1-7		**10,36**
Standard dev.		0,53

Table 4.5: Result from the geobarometric calculation using the method of Molina et al. (2015) and a temperature (T) input = 602.3 °C from the GB geothermometer.

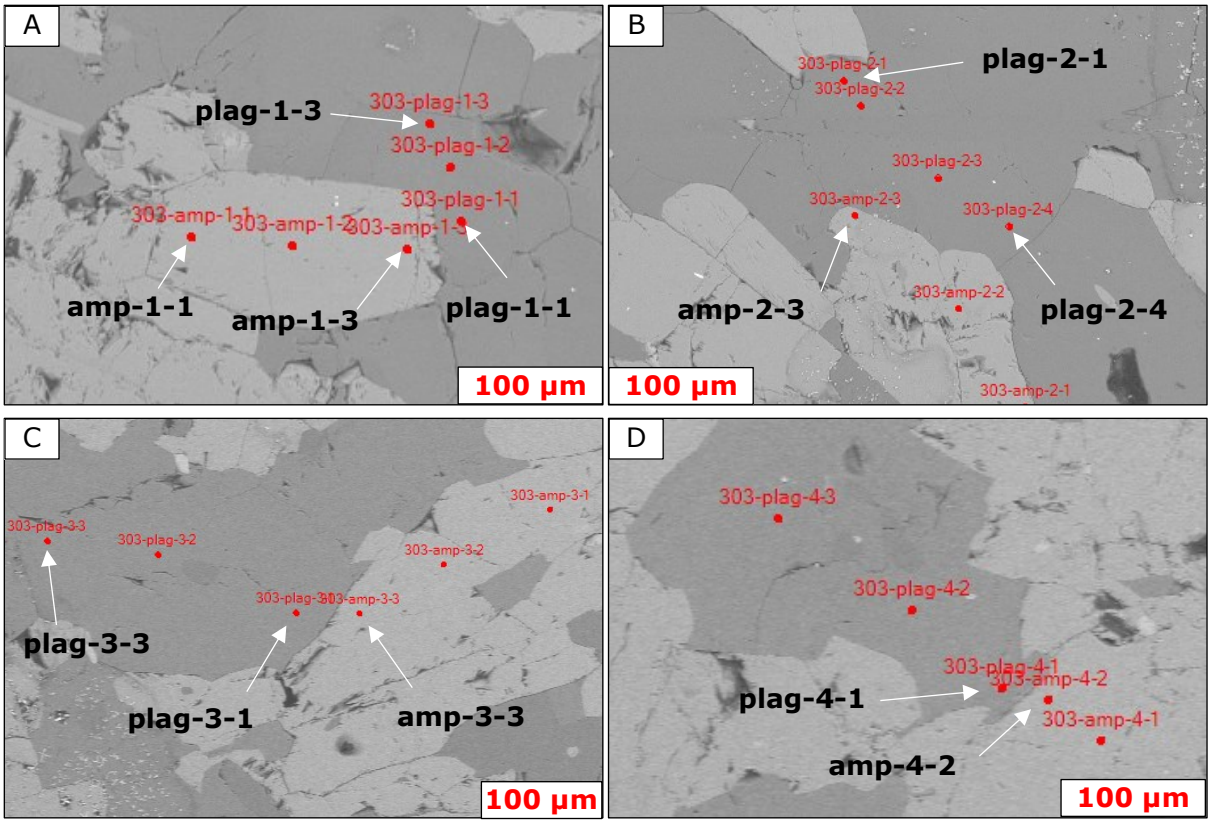

Figure 4.40: Spot-images (BSE) of amphibole – plagioclase grains. A) Amp-1-3 and plag-1-1 (pair nr. 1 in Table 4.5), and amp-1-1 and plag-1-3 (pair nr. 2). B) Amp-2-3 and 2-4, pair nr. 3. Plag-2-1 make pair nr. 7 with amp-2-3. C) Pair nr. 4 with plag-3-1 and amp-3-3, and plag-3-3 making pair nr. 6 with amp-3-3. D) Pair nr. 5 with plag-4-1 and amp-4-2.

Clinozoisite – zoisite geothermometer

Gottschalk (2004) have developed a geothermometer using the Fe^{3+} content of clinozoisite and zoisite. $X_{ep} = Fe^{3+}/(Fe^{3+} + Al - 2)$ have been calculated for all analysed grains and plotted into the phase diagram of Gottschalk (2004), below (Figure 4.41). The temperature is fixed to the average T yielded from the GB-thermometer (602.3 °C). The calculated X_{ep} is nicely situated between the 500 and 2000 MPa curves, both regarding the temperature and X_{ep}. This corresponds well to the 9.0 – 10.2 kbar (900 – 1020 MPa) yielded from the GBMP geobarometer, because the phase boundaries move to higher ratios with higher pressures. Clinozoisite plot on average similar to the X_{ep} values of 2000 MPa, and may therefore reflect an even higher temperature.

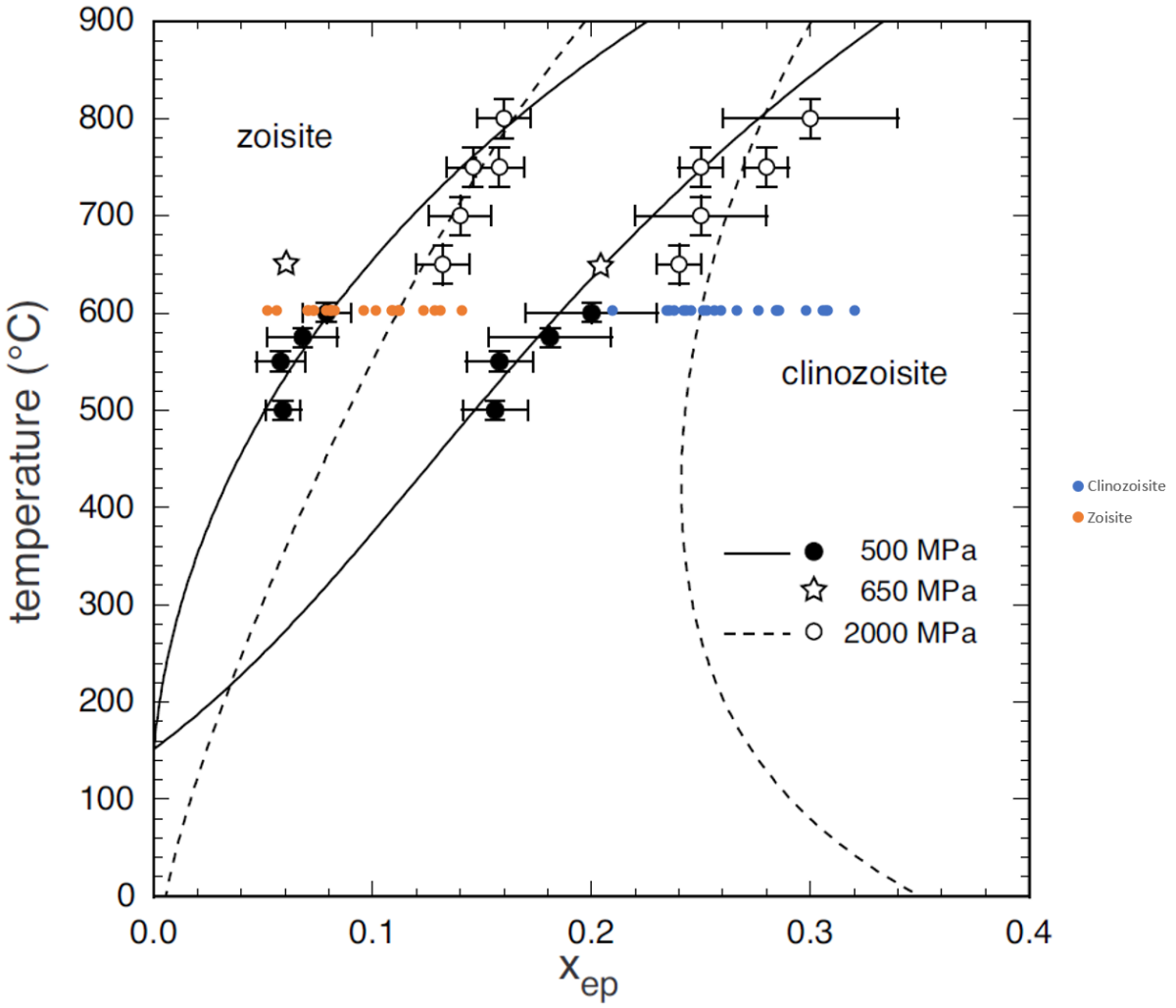

Figure 4.41: Stability diagram of clinozoisite and zoisite from Gottschalk (2004) with calculated Xep values from this study. Xep = Fe3+/(Fe3+ + Al - 2)

4.5 Geochronology

4.5.1 U-Pb data

Two samples (HF-02 and S-6) were analysed using laser-ablation inductively coupled plasma mass spectrometry (LA-ICP-MS) for zircon and titanite U-Pb ages. The zircons were obtained from an metarhyolite (HF-02), whereas titanites were obtained from a muscovite schist (S-6) of possibly sedimentary origin, both sampled at Hellerfjellet within the Mofjellet Group. This chapter presents the U-Pb ages and a geological description of the analysed zircons and titanites.

Zircon age – sample HF-02

This sample is a semi-massive metarhyolite rock mainly composed of fine- to medium grained quartz, plagioclase, and biotite. 24 analyses were done on 23 zircons, whose textures are transparent to pale-brown, subhedral to rounded, variably elongated and in the size range of 75-250 µm, averaging around 150 µm. Most of the grains show oscillatory zoning of lighter and darker areas, interpreted to be a magmatic zoning, and bright irregular rims in CL-image, interpreted to be a metamorphic overprint (Figure 4.42). Dark areas usually indicate higher uranium-content (Corfu et al., 2003). Using Isoplot, a regression line through the 24 analyses yield an upper intercept age of 499 ± 12 Ma, and a lower intercept age of 47 ± 360 Ma with MSWD = 0.47 (Figure 4.43), whereof the former age is interpreted as the age of crystallization. The two outliers at ca. 520 Ma and 560 Ma are possibly inherited zircons, or an analytical feature.

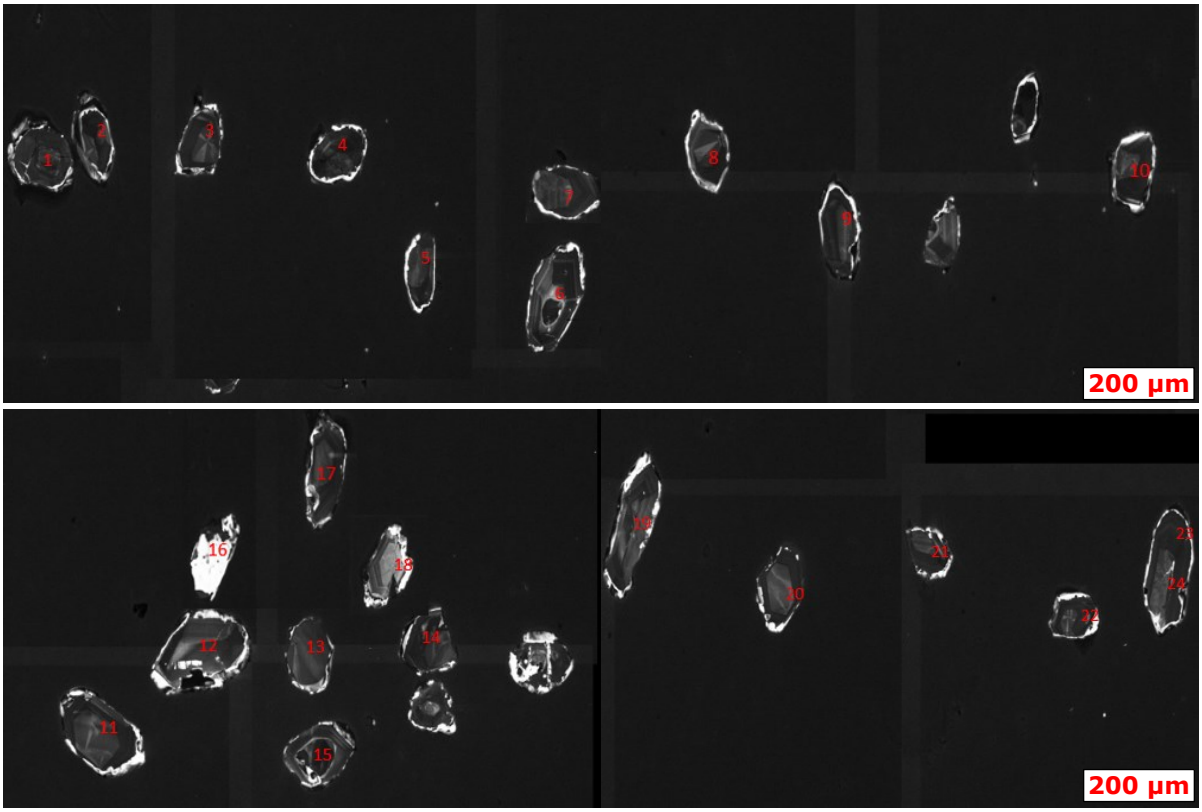

Figure 4.42: All analysed zircons in sample HF-02 numbered 1-24. Numbers are place ca. where the zircons were analysed.

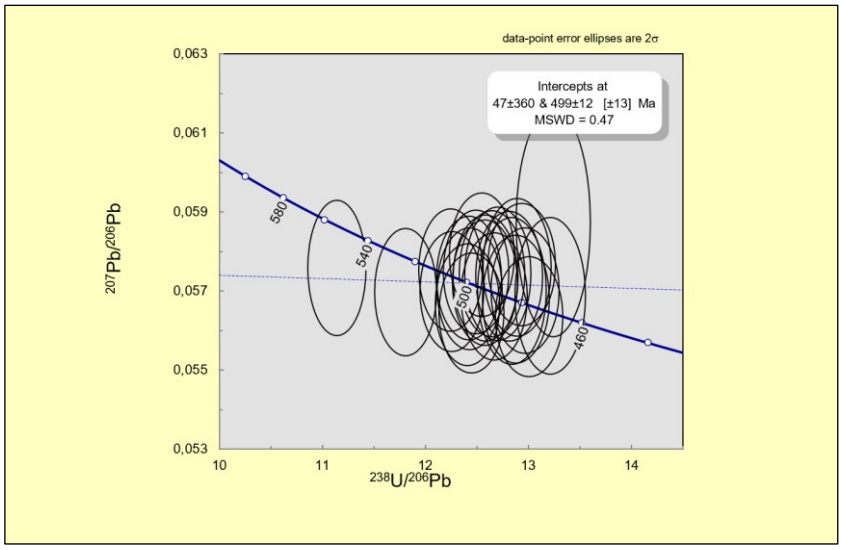

Figure 4.43: Calculated age of the zircons from sample HF-02 (using Isoplot), yielding an upper intercept of 499 ± 12 Ma and lower intercept of 47 ± 360 Ma, whereof the former is interpreted as the age of crystallization.

Titanite age – sample S-6

15 analyses were done on 15 separate titanite grains from a medium to coarse grained QMS mainly composed of muscovite, quartz, minor feldspar, and disseminated sulphides. The analysed titanites range in size from 100 to 150 µm and appear transparent to pale-brown, spherical, and rounded, as seen in Figure 4.44. A thin section from another sample (HF-05x) from the exact same locality and rock type as S-6 show somewhat larger titanites overgrowing sulphides and other silicate minerals, thus proving to be a later phase.

A regression through all 15 analysis yielded an upper intercept age of 4999 ± 98 Ma, and a lower intercept age of 465 ± 21 Ma, with MSWD = 4.8 (Figure 4.45), whereof the latter is interpreted as the age of crystallization. The line intercepts the $^{207}Pb/^{206}Pb$ axis at 0.88, being the ratio of initial radiogenic lead in the sample.

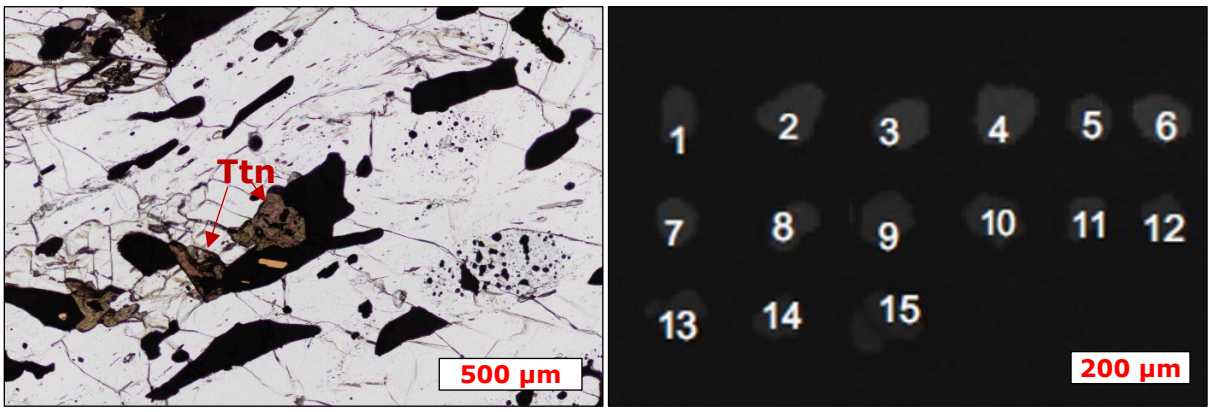

Figure 4.44: Textures of the titanites. A) Microphotography (ppl) of sample HF-05x. B) BSE (Back scatter electron) image of titanites.

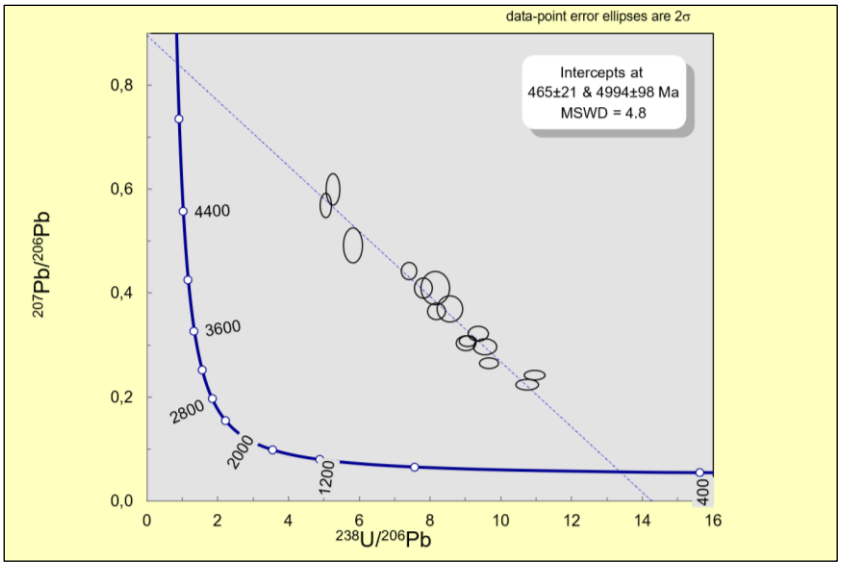

Figure 4.45: Calculated age (from Isoplot) based on 15 analyses on 15 titanites from sample S-6, yielding an upper intercept age of 4994 ± 98 Ma and a lower intercept age of 465 ± 21 Ma, whereof the latter is interpreted as the age of crystallization.

5 Discussion

The results obtained from this study yield interesting discoveries on the petrotectonic history of the Mofjellet Group from its origin through subsequent metamorphism and deformation. The following sections discuss around the results obtained.

5.1 The origin and evolution of the Mofjellet Group

The geological environment wherein the Mofjell Group originated and evolved can be inferred from the collation of (1) field observations, herein the macro- to mesoscopic petrology of the rocks and its textures, (2) the mineral assemblages along with its constituent major- and trace element geochemistry, (3) the metamorphic assemblages and tectonic history, and lastly (4), the geochronologic constrains put into the context of the regional geology.

5.1.1 Field observations

Felsic rocks and amphibolites

The Mofjell Group is dominated by the felsic grey gneisses, including the felsic metarhyolites, and is considered as having a bimodal-felsic assemblage (Bjerkgård et al., 2013b). As shown in this study, the major rock units of the field areas, being the felsic grey gneisses and metarhyolites, amphibolites, and quartz muscovite schist (QMS), have experienced high-grade metamorphism and polyphase deformation, that have obliterated primary textures and thereby complicated interpretations. The massive, and fine-grained metarhyolites and the amphibolites are the only rocks which are confidently classified as igneous and probably represent lava flows and/or tuff (Bjerkgård et al., 2013b, Slagstad et al., 2020). The grey gneiss, being somewhat diffuse in nature, is mineralogically and geochemically close to the metarhyolite and classifies as a rhyodacite-dacite (also andesite, according to the TAS proxy diagram). Bjerkgård et al. (2013b) refer to the metarhyolite rock as a "keratophyre", and also conclude that there is a higher proportion of volcanic rocks (rather than sedimentary) than previously assumed (e.g. Marker (1983)), herein referring to the grey gneisses. The foliated (semi-massive) grey gneiss probably represents greywacke-type metasediments according to Slagstad et al. (2020), but further states the grey gneiss as a whole is on average predominantly volcanic with dacitic to rhyolitic compositions.

Both the felsic rocks and especially the amphibolite at Hellerfjellet contain calcite and calcsilicate mineral associations evident from both field observations (dissolution depressions), drill core logging and thin section analysis, which is interpreted as syn-volcanic shelf sediment deposits, hence, infer that the related volcanic rocks crystallized as lava flows (pillow lavas) in a sedimentary basin close to a continent. This interpretation is compatible with earlier research in the area (Marker, 1983, Bjerkgård et al., 2013a, Slagstad et al., 2020). Because there is a lower abundance of calcsilicate assemblages in the felsic rocks, possibly infer that these rocks crystallized mostly sub-basinal or in a subaerial Ca-poor environment. Igneous textures are not observed in the hand specimen, however An-rich cores of plagioclases in the amphibolites is possibly igneous.

Quartz muscovite schist and graphite quartz gneiss

The quartz muscovite schist (QMS) is the predominant host rock of the sulphide deposits in the Mofjell Group (Bjerkgård et al., 2013b), but show clear differences from Hesjelia-

Hammertjønna to Hellerfjellet. The QMS in Hesjelia-Hammertjønna is homogenous in the way that it does not vary much compositionally and texturally (except for being foliated) throughout the unit, and is totally surrounded by a massive metarhyolitic unit with parallel foliation, suggesting they are conformable. This and the gradual transition from the QMS to the metarhyolite suggest that the QMS in Hesjelia-Hammertjønna is an altered metarhyolite, probably due to the hydrothermal fluids that transported and deposited the sulphide metals. This interpretation is also supported by the similar immobile element patterns of these rocks, which is further discussed below.

The QMS at Hellerfjellet show broadly the same mineralogy, however, is texturally different by the presence of boudinaged clasts (and/or pseudoclasts) and graphite quartz gneiss (GQG), the former of which is only observed in the hanging wall suprajacent to the GQG unit. The latter occur both subjacent and suprajacent to the ore deposit. The clastic sequence may represent boudined quartz-feldspar (barren) veins and/or crystal/lithic fragments, formed as a consequence of an explosive eruption that either deposited *in situ* or by redeposition through underwater mass flows (Pat Shanks III and Thurston, 2012). Considering the volcanic environment, the latter two options are likely, without ruling out the former. Volcaniclastic deposits often host ore deposits, reflecting the closeness to hydrothermal vents (Galley et al., 2007).

The presence of the graphite also indicates an underwater sedimentary succession, wherein the pyroclastic material from a nearby explosive eruption could be deposited. Generally, biogenic graphite is connected to sedimentary basins with low enough circulation to form anoxic (reduced) conditions or where the rate of deposition is high enough to bury the organic matter before it decomposes. If the clasts indeed are deposited by mass flows the latter process may be the best explanation for the occurrence of graphite. The volcaniclastic-sedimentary origin is further underlined by the alternating quartz + graphite and quartz layers within the GQG that possibly represent relics of sedimentary bedding. The limited extension of the graphite within the QMS unit, representing the whole extension of the basin, point towards redeposition by mass flows of restricted size. The apparently well-sorted sedimentary layering may not contradict this if the water content of the mass flow was high enough.

Nevertheless, a volcaniclastic sedimentary deposit with non-volcanic components is typical for bimodal-felsic continental arcs, wherein incipient volcanism emplaces basaltic pillow lavas before evolving towards explosive silicic volcanism with abundant pyroclastic material (Pat Shanks III and Thurston, 2012). The spatially close carbonate- and calcsilicate-bearing amphibolite supports an underwater depositional environment. Looking at the regional geology, the subjacent and syngenetic Plura nappe (510 Ma (Slagstad et al., 2020)) consist of similar rock types as the Mofjellet Group, however, have larger units of dolomite and marble, probably representing continental shelf sediments (Marker, 1983, Søvegjarto et al., 1988, Marker et al., 2012, Slagstad et al., 2020), whereas the Hellerfjellet sediments must be a deeper basin due to lower amount of sediments and less calcic sediments.

5.1.2 Geochemistry

Previous authors (e.g. Bjerkgård et al. (2013b)) have regarded the Mofjell Group as an oceanic island arc setting formed close to a continental margin. This interpretation is supported by the tectonic discrimination diagrams used here, yielding volcanic arc signatures and, in conjunction with the AFM diagram, point towards a calc-alkaline composition. This trend is also evident by the negative correlation between silica and Fe_2O_3 in the Harker diagrams, because a calc-alkaline melt becomes continuously richer in silica as it fractionates. Calc-alkaline melts are almost exclusively related to subduction zones (Winter, 2014). A tholeiitic trend, i.e. increasing FeO/MgO due to crystallization and fractionation of MgO-bearing minerals, does not change the silica content much (Winter, 2014).

The tectonic discrimination diagram of Pearce and Peate (1995) incline towards a continental arc genesis, which may be the reason why the felsic rocks are so peraluminous (A/CNK > 1), hence, suggesting a crustal component. The generally high-Al and low/medium-Mg contents of the amphibolites is typical of calc-alkaline basalts (Irvine and Baragar, 1971) and is believed to form by high H_2O contents causing fractionation of olivine and augite at the base of mature arcs (Sisson and Grove, 1993b). Experiments by Sisson and Grove (1993a) show that calc-alkaline trends in high-Al/low-Mg basalt is initiated by the early crystallization of magnetite or Cr-spinel in melts containing 4-6 wt. % H_2O, because water lowers the liquidus of the silicates only. Contrary, *tholeiitic* trends are formed in dry melts where the silicates have a *higher* liquidus than the iron oxides, thus crystallizing earlier than the iron oxides (Sisson and Grove, 1993a). However, the tholeiitic component in some of the amphibolites, even though less significant in total, is most likely related to early incipient volcanism (Pat Shanks III and Thurston, 2012). The gap from 56 – 66 wt. % SiO_2 separating the mafic amphibolites and the felsic rocks is known as the Daly gap (Winter, 2010) and illustrates the bimodal nature of volcanic arcs.

During metamorphism (and most likely allochemical metamorphism) and weathering the proportion of the major elements, in particular the alkalis (Bucher and Grapes, 2011), may change significantly, hence, the interpretation of igneous petrogenetic trends must be done with caution. Rather, trace elements are generally immobile during metamorphism and weathering, making them more credible in the investigation of igneous petrogenetic trends.

Normalized diagrams

REE diagrams and spider diagrams reflect the source and evolution of the melts in the petrotectonic environment from which they derived. A subduction-related volcanic arc environment is already inferred from the previous discussions, and this is reflected in the data presented here. The two most likely sources of magmas in these environments is the subducting oceanic lithosphere along with its overlying sediments, and the suprajacent mantle wedge peridotite (Winter, 2014).

The relative enrichment of incompatible LREE and LILE elements compared to HREE and HFSE in all normalized diagrams, together with the spiked primitive-normalized curve (including the negative Nb, Ta and Ti anomaly), indicate a process or source where the LREE and LILE were selectively enriched. The most popular and classic theory is that these elements were enriched in fluids produced from dehydration of the subducting oceanic crust (and sediments) (Tatsumi and Nakamura, 1986, Pearce and Peate, 1995), however, evidence for actual melting of the sediments, and even oceanic crust, also exist. In some cases melting of sediments and oceanic crust better explain certain signatures (like Th/Rb

and concentration of Be from sediments) (Winter, 2014). Either way, the fluid and/or melt that is produced becomes enriched in the LREE and LILE in accordance with their low partition coefficient *D*, whereas the HREE and HFSE are *relatively* depleted because of their higher *D*, explaining the high-LILE/HFSE pattern of the spider diagrams (Tatsumi and Nakamura, 1986). The fluids (and melts) migrate into the overlying mantle wedge where it interact with the ultramafic rock, being a peridotite, lowers the melting point, and thereby causes fluid-fluxed (or melt fluxed) melting of the peridotite (Winter, 2014).

Evidence for the involvement of fluids is that the increasingly negative slope is not correlated to SiO_2 (melt fractionation), because the early fractionating minerals olivine, pyroxene and plagioclase do not incorporate light versus heavy REE (Winter, 2014). Rather it is (moderately) positively correlated to the LIL-element K, which partitions strongly into fluids, hence, a fluid phase must be responsible for that trend (Winter, 2014). However, K can also be added by metasomatism, which in that case is evident by high K and low $[La/Sm]_{CN}$, or reversed, and can explain why they are only moderately correlated.

According to Pearce and Peate (1995), the HFS elements yield information about the source of the *melts* because they are less affected by fractional crystallization and fluids. The amphibolites show a low $[Gd/Yb]_{CN}$ ratio (flat HFSE slope) in the chondrite-normalized diagram, suggesting the source was not deep enough to contain garnet, hence, an eclogitic source from the subduction lithosphere is precluded (Winter, 2014). The typical model of tholeiitic basalts is decompression melting of the mantle at high levels, where H_2O contents are low (Winter, 2014), causing the silicates to crystallize before the iron oxides, as previously discussed. The amphibolites having a minor tholeiitic trend, could be explained by this model, where dry melting of a *depleted* peridotite (discussed below) caused the positive LREE curve, similar to a normal MORB. However, the majority of the samples are enriched in these elements (and LILE) which implies that the H_2O content must have been higher than a normal MORB. This is in accordance with a calc-alkaline trend, possibly produced at the base of a mature arc, wherein the primitive magma fractionated to eventually produce dacites and rhyolites (Best, 2003). Assimilation of crust rocks can contribute to initiate a calc-alkaline trend by adding fluids to the system, consequently increasing the oxygen fugacity, which promotes crystallization of iron oxides. Also, magma mixing is an important process in volcanic arc production, and form the basis of the calc-alkaline bimodal felsic-mafic suite (Winter, 2014).

The HFSE pattern is *almost* similar to MORB for both the felsic and mafic rocks, suggesting they derived from a source comparable to MORB, being mantle peridotite. However, the slightly lower amount of HFSE compared to MORB (below 1 in the MORB-normalized diagram), suggest the parental peridotite of the arc melts was depleted in these elements. This is also seen in the Th/Yb vs. Nb/Yb diagram of Pearce and Peate (1995), where ca. half of the amphibolite samples plot under Nb/Yb = 1. All of these elements behave relatively similar in a fractionation melting/crystallization process, however, small fractions of partial melting preferentially incorporate the most incompatible of them (like Nb over Yb) in the melt phase. Thus, an explanation for this already depleted peridotite must be a previous partial melting event, and a logical place for this in an island arc setting is a back-arc rift producing MORB (Pearce and Peate, 1995). According to Bjerkgård et al. (2013b), parts of the Mofjell Group host rocks and ore deposits related to a back-arc rift setting, and the Kongsfjell Group to the south of the Mofjellet Group is probably an extensional back-arc basin.

Besides from being broadly similar to the amphibolites, the felsic rocks show important differences in the normalized patterns. While the amphibolites does not have a significant

Eu-anomaly, the latter show a negative Eu-anomaly for most samples. The lack of a Eu anomaly implies that the source of the amphibolites did not contain plagioclase (or was too oxidized to contain Eu^{2+} (Best, 2003)), i.e. it was too deep for plagioclase to be a stable phase. The flat HREE slope also precludes garnet in the mantle peridotite, altogether constrain the depth of the source to 30-75 km and 10-25 kbar (Best, 2003). Here, a spinel-bearing peridotite produces the negative Cr anomaly (in the MORB diagram) by the fractionation of spinel (or left in residuum), in accordance with an Al-rich basalt.

In the felsic rocks, however, plagioclase was possibly derived from the crust and were left in the residual after partial melting or fractionated during crystallization of the felsic melts. According to Hart et al. (2004) a Eu-anomaly is typical in FII-FIII felsic magmas. Crystallization of Ca- rather than Na-plagioclase is driven by the less polymerized melt, caused by the high H_2O-content in calc-alkaline magmas (Hart et al., 2004, Winter, 2014). The water content also leads to a stronger ability to accommodate HFSE, among them yttrium (Y), and serve a possible explanation for the positive HREE curve and the positive Y-anomaly in the metarhyolites. These elements may have been incorporated in amphibole. This is also the main difference between the grey gneiss and the metarhyolites, and possibly reflect the less evolved nature of the grey gneiss (dacite), and probably the lower H_2O contents of its parental melts.

It is not likely that the amphibolites and the felsic rocks represent a line of continuous evolution fractional crystallization, due to different degrees of fluid enrichment, crustal assimilation, and magma mixing. Even within the amphibolites the source is probably different due to the variable trace element signature, whereof some are clearly dry melts (NMORB signature), whereas other are water-rich (high-LIL element). The grey gneisses and metarhyolites show the closest link and possibly represent an evolutionary path, wherein the metarhyolites are the result of further fractionation of the melt that produced the grey gneisses. Nevertheless, the depleted mantle peridotite is the most likely magma source for all rock types.

Origin of the QMS and GQG unit

Because elements like Ti, Al, and Zr are highly immobile they are rarely altered by the metasomatic processes and/or weathering that changes the major element composition and texture of the original rock (Pearce, 1996). Thus, they are suitable in the investigation of genetic relationships between the altered QMS/GQG and fresh (apparently unaltered) felsic rocks and amphibolites. The broad signature of the latter rock types in the normalized diagrams also applies to the altered rocks, confirming a close petrogenetic relationship. As expected, the most incompatible elements (LREE and LILE) shows the largest discrepancies, reflecting their high mobility in solid-fluid interactions. The comparison shows that the QMS/GQG are generally closest to the *felsic* rocks among the elements investigated, however, the GQG show an inclination towards the amphibolites also. If the interpretation of the QMS and GQG unit at Hellerfjellet indeed is volcaniclastic, a sedimentary input of the amphibolites is highly likely, particularly if the current spatial proximity reflects the original setting. Both rock types have been deposited at the seafloor where the basaltic lava and hydrothermal fluids extruded, thereby reflecting their close proximity to the magmatic conduits. Also, the graphite may have originated from a biogenic environment similar to the calcareous amphibolites. Nevertheless, the predominant source for the volcaniclastic input is felsic pyroclastic material. The QMS at Hellerfjellet does not show the same inclination towards the amphibolites, thus have a higher proportion of felsic volcanic and pyroclastic material. As already established, the QMS at Hesjelia-

Hammertjønna is originally a metarhyolite ("acid metavolcanic" in Marker (1983)), which also is reflected by the large overlap with the metarhyolites in the immobile element ternary diagram. Generally, the QMS overlaps more with the metarhyolites than the grey gneisses.

Petrogenesis from the VMS perspective

The FII classification by the scheme of Hart et al. (2004), although only considering the felsic rocks, also suggest a calc-alkaline nature, wherein a bimodal-felsic suite, like the Mofjellet Group (Bjerkgård et al., 2013b), classifies. This can also be regarded from the metalliferous perspective, where a (calc-alkaline) bimodal-felsic suite is related to sulphide deposits dominated by sphalerite (Franklin et al. (2005) cited in Bjerkgård et al. (2013b)), like almost all deposits in the Mofjellet Group, including the deposits investigated here, and most importantly the largest (mined) Mofjellet deposit (Bjerkgård et al., 2013b). Exceptions of Cu-rich deposits exits in the Mofjellet Group, and these are related to a back-arc environment (Bjerkgård et al., 2013b). A typical example of an FII deposit is the Kuroko deposit in the continental arc of Japan (Hart et al., 2004), and according to Vokes (1976) the Mofjellet deposit resembles that.

FII is associated with felsic magmas produced at a depth of 10-30 km with high H_2O-pressure and in the stability field of amphibole (T = 750 – 1100 °C), wherein low degree of partial melting result in a *peraluminous* melt moderately depleted in HFSE (Hart et al., 2004). Most FII VMS deposits are related to rhyolites that form at a depth of 10-15 km, because fracture permeability, making hydrothermal convection possible, does not reach deeper. The near saturation water content and high temperatures of the melt, result in a low viscosity melt enabling fractional crystallization (Huppert and Sparks, 1988). Fractionation in high-level magma chambers supplies both heat and/or metals to the hydrothermal system that produces VMS deposits (Campbell et al., 1981). The lack of any known large VMS deposits at Mofjellet is most likely attributed to the fact that the ore forming system cooled too quickly because of low temperature felsic magmas and too small mass of magma (Hart et al., 2004).

5.2 Metamorphism and deformation

Marker (1983) classified the peak metamorphic facies of the Mofjellet Group as amphibolite facies, herein staurolite-kyanite zone, and, based on observations of beginning anatexis, roughly estimated the *P-T* to 600 °C and 7 kbar. He further ascribed these conditions to the F_2 phase, producing the main foliation S_2, and state that no metamorphic assemblages from the F_1 phase has been observed. Also, he observed no retrograde mineral assemblages beside from post-F_4 (post-Scandian) "discordant muscovite", due to extension. On that basis, he concluded that F_1 did not reach amphibolite facies, and that the metamorphic conditions prevailing under F_2 did not change enough to allow retrograding during F_3 and F_4.

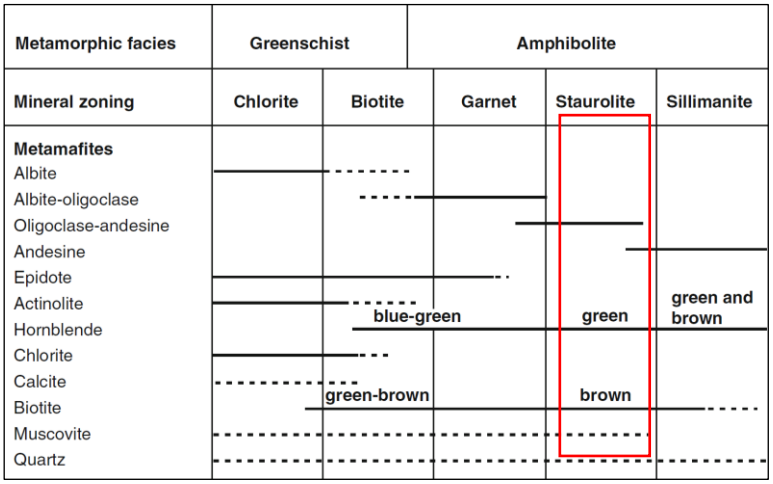

Figure 5.1: Diagram from James (1955) taken from (Bucher and Grapes, 2011). Red square is the metamorphic grade that fits best with the samples here.

The overall matrix mineral assemblage investigated here is typical of high-P amphibolite facies, with green tschermackitic hornblende, andesine-oligoclase plagioclase, brown biotite, and almandine garnet (Bucher and Grapes, 2011). Oligoclase is the dominant rim-composition of the plagioclases, thus, andesine is strictly speaking not part of the equilibrium matrix assemblage. No clinopyroxene, or K-feldspar is observed (except for the special microcline gneiss, sample HF-12), excluding upper amphibolite facies (Winter, 2014). This major assemblage is compatible with the P-T estimate of ca. 600 °C and ca. 10 kbar, plotting in the high-P section of the amphibolite facies in Figure 5.1. Muscovite is generally low in abundance in the analysed samples, which can be explained by the prograde reaction muscovite + Ca amphibole → biotite + quartz + H_2O (Deer et al., 1992).

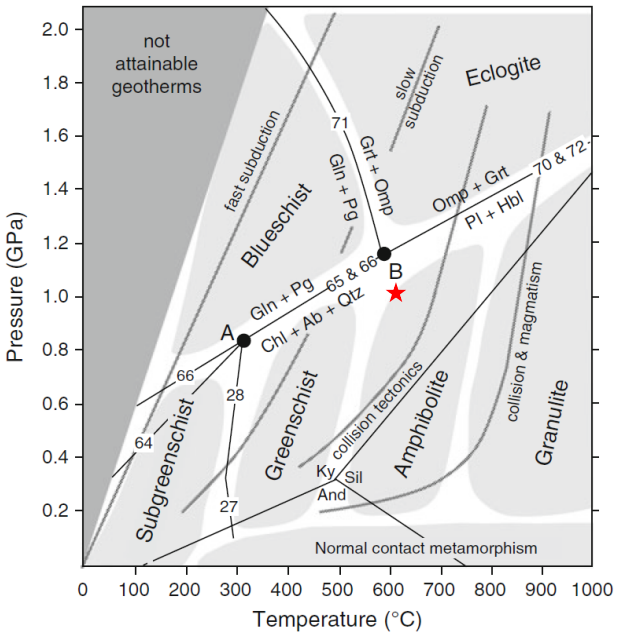

Figure 5.2: Metamorphic facies scheme from (Bucher and Grapes, 2011). Red star marks the P-T estimate in this study (ca. 600 °C and 10 kbar = 1 GPa), plotting just inside the amphibolite facies.

Additional important minerals constituting the major mineral assemblage of the amphibolites is clinozoisite-epidote, zoisite, chlorite, calcite and titanite. These minerals suggest that the protolith of the amphibolites is a calc-silicate rock, rather than a pure igneous rock. Generally, the presence of chlorite and czo-ep (+ albite + actinolite) is typical of upper *greenschist* facies, while hornblende and czo-ep (+ albite) mark the transition to *epidote-amphibolite* facies, and further hornblende and plagioclase occur at *amphibolite* facies (Deer et al., 1992). Thus, according to the typical facies assemblages there are minerals from all three aforementioned facies in the samples here, being chlorite (greenschist), czo-ep (epidote-amphibolite facies), and hornblende + oligoclase (amphibolite facies). Thus, the mineral assemblage appears transitional, with peak P-T at amphibolite facies. Usually, chlorite should be absent around 575 °C at 7kbar (Apted and Liou, 1983), while czo-ep (rarely) exists up to 600 °C, after both minerals combine to form garnet at increasingly higher P-T (Bucher and Grapes, 2011).

There are, however, some interesting and important observations complicating the metamorphic evolution of these rocks. The andesine to oligoclase core-rim zonation is problematic because plagioclase usually becomes more calcic by prograde metamorphism after 520 °C, because it consumes the calcic component from czo-ep as the metamorphic facies develops towards amphibolite facies (Bucher and Grapes, 2011). However, it cannot be excluded that the calcium-rich cores (~ An_{49}) is an igneous texture (Apted and Liou, 1983). Textural observations shows that czo-ep occur as inclusions in plagioclase, which is evidence for the prograde metamorphic reaction where czo-ep decompose to produce the An-component in oligoclase (Bucher and Grapes, 2011). However, the opposite is also observed, where czo-ep overgrows plagioclase (as seen in Figure 4.36), suggesting the reverse reaction have taken place. This could both be a prograde reaction and a retrograde reaction (Bucher and Grapes, 2011). The prograde reaction produces kyanite (Bucher and Grapes, 2011), which is not observed among the 23 thin sections analysed, however, has been reported by Marker (1983) from the QMS unit. However, this reaction usually occur within the eclogite facies, where other high P-T minerals such as clino- and orthopyroxene

should be present (Bucher and Grapes, 2011). A prograde reaction involving the decomposition of kyanite and formation of zoisite is the 2Ts (tschermak) + Ky = Grt + 2Zo + 1Qz + H_2O, which takes place at high-P amphibolite facies (Bucher and Grapes, 2011). However, zoisite is clearly cross-cutting the foliation and have grown euhedral crystals evident of unrestricted growth, a feature observed elsewhere in terranes that have undergone exhumation, consequently leading to fluids influx and *retrogression* (Brunsmann et al., 2000). Textural observations suggest that zoisite coexist with czo-ep (although the latter also occur as inclusions in zoisite), i.e. formed at roughly the same P-T, hence, inferring that czo-ep also formed by retrograde metamorphism. The stability of czo-ep and zoisite generally increases with higher oxygen fugacity (fo_2) (Deer et al., 1992), resulting in higher contents of Fe^{3+} (Brunsmann et al., 2002, Bucher and Grapes, 2011).

Staurolite is unusual in amphibolite facies of mafic rocks (Mohammad et al., 2011), however, occurrences have been reported in mafic rocks related to calcareous sediments, wherein metasomatic processes lead to the high variance of mineral assemblages (Ríos and Castellanos, 2014). In this study, staurolite occur as inclusions only (in garnet and zoisite), thus have reacted out, which can happen through a prograde reaction with muscovite and quartz, forming almandine, kyanite, biotite and H_2O (Deer et al., 1992). However, the lack of staurolite in the matrix can better be explained by retrogression, where it is replaced by chlorite (Deer et al., 1992). The latter is usually limited to the biotite zone of Figure 5.1, being a part of the upper greenschist facies, hence, it is difficult to explain the presence of chlorite as part of a prograde assemblage where staurolite has reacted out. Chlorite is observed in several samples, mostly cross-cutting but also foliation-parallel, and also fills cracks in garnet. If staurolite formed during F_1, then S_2-parallel chlorite suggest retrogression occurred before F_2. However, chlorite can grow pseudomorphically on biotite (Deer et al., 1992), hence, creating the appearance of pre-S_2 growth. Moreover, the chlorite-filled cracks probably formed as a consequence of cataclasis during the retrograde event. Staurolite is also observed in cross-cutting zoisite, indicating that the former was in equilibrium with the matrix after S_2 was produced, thus placing the retrograde event *subsequent to* F_2.

Thus, zoisite, czo-ep, and chlorite is possibly part of a retrogressive event that is placed after F_2. Similar assemblages and segregations (as sample 08) are reported elsewhere as being a part of exhumation and retrograde metamorphism, caused by the influx of fluids (Brunsmann et al., 2000). Such event could also explain the zoning in plagioclase, wherein the An component produced czo-ep and zoisite (Bucher and Grapes, 2011). Syntectonic boudinaged granitic intrusions parallel to S_2 supports extension and uplift after F_2. Generally, a zonation in epidote from an aluminium-rich core to an iron-rich rim is attributed to a retrograde event (Deer et al., 1992, Franz and Selverstone, 1992), however, this is not observed here.

Garnet have apparently grown in several stages, which is evident by external textural relationships (deflecting of foliation and/or overgrowth), mineral inclusions, and internal foliation. The earliest garnets deflect the foliation and have primarily the prograde minerals quartz, plagioclase, biotite, and hornblende as inclusions, and is more or less foliated. Among these garnets are the staurolite-bearing garnets, that, according to the interpretation above, have formed before the retrogressive event. One post-tectonic garnet grain with staurolite supports post-F_2 retrogression, in accordance with the aforementioned staurolite-bearing zoisite. The garnets show in general variable tectonic relationships, whereof some appear to have grown both prior and after F_2, whereas other show exclusively post-tectonic growth. The latter garnets have a higher proportion of czo-ep

inclusions, and some even overgrow transversal zoisite (sample 08), while also being richer in the grossular (Ca) component than garnets in sample 03. Also, they are generally free of cracks compared to earlier garnets (sample 03 and HF-08). These observations suggest that these particular garnets formed as a regrowth event after the retrogressive event, possibly during the F_3 phase. Additional evidence for this is that titanite overgrows chlorite, while also occurring as inclusions in the late garnets, e.g. sample 08. The titanite-age (discussed below) is pre-Scandian, thereby constraining the growth to prior to F_4. Thus, titanite probably formed early in the increasingly higher metamorphic conditions during F_3 deformation and metamorphism.

These lines of microtextural observations suggest that the prograde assemblage prior to the retrogressive formation is andesine + hornblende + garnet + staurolite (F_2), while the retrograde assemblage is chlorite + czo-ep + zoisite + oligoclase (post-F_2). The succeeding prograde assemblage is thus titanite + garnet (F_3). This is contrary to the observations of Marker (1983), however, the observations are local and may not apply to all parts of the Mofjellet Group.

The coronas (or haloes) around some of the garnets in drill core BH4508 from Hellerfjellet is not investigated microscopically and could have yielded more evidence into the P-T evolution of the rocks. Such features can form as a consequence of rapid exhumation, in that case may support post-F_2 retrogression (Stowell and Stein, 2005). Nevertheless, the F_3 metamorphic conditions did not reach the F_2 metamorphic conditions, because lower grade assemblages are still present.

Geothermobarometry

The garnet-biotite-muscovite-plagioclase (GBMP) assemblage analysed for P-T estimation is part of sample 08. Here, S_2 parallel muscovite and biotite were analysed together with plagioclase and garnet. Because the latter overgrows muscovite and biotite, have czo-ep inclusions, and is crack-free, it is most likely related to the regrowth of garnets during F_3. This raises uncertainty about whether it is in equilibrium with said assemblage or not. The resulting temperature and pressure (600 °C and 10 kbar) are unproportionate, because similar temperatures are most often related to lower pressures, and the other way around. As seen from Figure 5.2, the conditions plot between a slow subduction environment and continent collision. According to Bucher and Grapes (2011), retrograde exchange between Fe and Mg in garnet and biotite is normal in amphibolite facies, resulting in anomalously low temperatures when garnet-rims and adjacent biotite are analysed. The matrix of biotite is, however, negligibly affected by retrograde reactions (Tracy et al., 1976), which is in accordance with the constant composition of the biotite analysed here. Opposed to this, garnet rims are significantly affected by retrograde reactions (Tracy et al., 1976), which is *not* observed here. The garnets are fairly homogenous, which is indicative of a garnet that has grown under constant chemical conditions, probably during prograde metamorphism. This complements the interpretation of this garnet grain as being an F_3 garnet, whereas biotite represents peak metamorphic conditions during F_2, which probably apply to the foliation-parallel muscovite as well. The plagioclase classifies as oligoclase (An_{26}), and probably formed through retrograde reactions according to reasons mentioned earlier. The six calculations constituting the average P-T is not too scattered (567-620 °C, and 8.7-10.1 kbar), which would be expected from an assemblage not in equilibrium (Bucher and Grapes, 2011). Thus, the assemblage is interpreted to be in equilibrium, and represents the prograde metamorphic conditions during F_3. To complement the pressure- and temperature-estimate the plagioclase-amphibole geobarometer of Molina et al. (2015) and the clinozoisite-zoisite phase diagram of Gottschalk (2004) has been applied, respectively.

Both correspond to the P-T estimate of the GB-GBMP geothermobarometer, however, is not fully independent because the temperature from the GB-thermometer was used as input in both.

5.3 Geochronology and tectonic history

5.3.1 Cambrian to Ordovician volcanism and tectonism

The classical framework of the Scandinavian Caledonides of Roberts and Gee (1985) have, despite serving as a foundation for the research on orogenic events, been proven oversimplified in recent years due to the large number of evidence for pre-Scandian tectonometamorphic events (e.g. Kirkland et al. (2007), Corfu et al. (2015), Slagstad and Kirkland (2017), Slagstad et al. (2020)).

The zircon U/Pb-data on the metarhyolite dated here constrain the age of the volcanic Mofjellet Group to 499 ± 12 Ma, i.e. mid-late Cambrian, coinciding with the 500 ± 3 Ma age from Slagstad et al. (2020) of the same group. Coeval events include the 510 ± 6 Ma metagranite of the subjacent volcanic-sedimentary Plura Nappe, and the 497 Ma supra-subduction zone Leka ophiolite of the Helgeland Nappe Complex (HNC), interpreted to represent Iapetus contraction (Dunning and Pedersen, 1988, Furnes et al., 1988). Thus, subduction and contraction of the Iapetus had already been initiated before the emplacement of the 500 Ma volcanic metarhyolites of the Mofjellet Group. Recently, Slagstad et al. (2020) dated a syn-tectonic boudinaged pegmatite within the RNC to 515 ± 5 Ma, inferring a tectono-metamorphic event from a period previously unfamiliar to deformation, and proposed a connection to the well-documented ca. 475 Ma Taconian orogeny in the HNC, in that case pushing back the time of Iapetus contraction.

Additional evidence a for pre-Scandian tectonometamorphic event is presented here through titanite U/Pb dating of a QMS, yielding an age of 465 ± 21 Ma. T_C of titanite is not agreed upon, but evidence suggest it can reach up to 800 °C for the largest grains, however, this is through diffusion and not growth of new grains, where T_C is lower (Frost et al., 2001). The grain size of the analysed titanites here are 100-150 µm, however, larger grains of titanites (up to 300 µm) is observed in the representative sample (HF-05x) and in amphibolites (sample 03 and 08). As discussed above, these titanites have grown during F_3 prograde metamorphism, hence, it is reasonable to believe that the smaller grains also are related to this phase. No zonation patterns are observed, which could have indicated several growth stages. Because S_3 fabric is not observed in the thin sections it is not possible to confidently ascribe titanite crystallization to F_3. At least, the age obtained here most likely yields a minimum age of the F_2 deformation, producing the main foliation (S_2), in the Mofjellet Group.

Despite the large error of the calculated age it does not overlap with the around 430 Ma Scandian thrusting event, nor the 499 Ma zircon age presented here, hence, must be an isolated event. The spatially closest tectonic event is the Langfjell shear zone separating the subjacent Plura and the Ravnålia nappe, where a syntectonic pegmatite is dated to 475 Ma, and interpreted as a consequence of the Taconian orogeny (Slagstad et al., 2020). The vergence of this shear zone is not known because of later folding, however, Taconian deformation have resulted in top-to-the-west thrusting in the HNC (Yoshinobu et al., 2002). Another previous event, dated by Slagstad et al. (2020), is the 484 Ma granitic dyke at Skittreskvika south of Mofjellet (not structurally mapped but within the RNC), which cross cuts the main foliation, being a folded and previously transposed bedding (S_{N+1}), like the S_2 in the Mofjellet Group. The related NW-vergent folds plunge WSW (Slagstad et al., 2020), which is fairly similar to the E-W plunging F_2 folds producing the main foliation (S_2) of the Mofjellet Group. According to the regional study of Marker (1983) the large scale F_2 folds of the Mofjellet Group is also north-verging. In addition, a third phase is observed as

an oblique crenulation cleavage on S_{N+1}, bearing resemblance to the F_3 phase of the Mofjellet Group. Although these similarities exist Skittreskvika is too far south to be a part of the Mofjellet Group and may not record the exact same deformational events. If these areas indeed are correlated, the age of the dyke represents the minimum age of F_2 folding in the Mofjellet Group. This way, the titanite age, being 19 Ma later than the dyke, may not record the F_2 phase, but rather the later F_3 phase as indicated by the textural observations. An internal shear zone of the Mofjellet Group is the Stangfjellet shear zone which is located adjacent to the prospects at Hellerfjellet. No studies have dated this structure, however, Marker (1983) have related it to pre-F_2 deformation, thus, dating would have constrained the minimum age of F_1 and maximum age of F_2.

5.4 Structural analysis

The original shapes of VMS deposits worldwide are diverse and include, among others, sheets, lenses, mounds and stockwork (Pat Shanks III and Thurston, 2012), each with their own characteristics. However, pervasive deformation and metamorphism often destroys these shapes and textures, and lead to remobilization of the sulphide ore (Large, 1992), resulting in thickened mineralized zones in fold hinges of tight to isoclinal folds (Van Staal and Williams, 1984). Thus, considering the polyphase deformation and high-grade metamorphism, the shape of the ore-deposits in the field areas are probably not original but reflect the regional deformation and metamorphism. Therefore, the most important thing is to understand the prevailing geometry. Bjerkgård et al. (2013a) has classified the shape as a *lens-shape*, a classification agreeing with the observations here.

The 3D-modelling is based on the geological observations from field work and existing maps from the areas investigated (Kruse (1980); Søvegjarto et al. (1988); Marker et al. (2012)). Even though the focus is to model the deposits, the QMS host rock is important in aiding the interpretation of the deposit's geometry because it is stratabound, and also because most of the foliation and fold axis measurements were collected from this unit. In addition, the overlying amphibolite unit is modelled, mainly for the investigation of the TEM-anomaly. Since only limited drill core data is available the model relies mainly on foliation- and fold axis measurements. Hence, the uncertainty of the resulting subsurface model is large but follows the confidence of the geological data.

As established by Marker (1983) the rock units parallels the axial planar S_2-foliation and F_2-fold axis (peak metamorphism), however later deformational events (F_3 and F_4) have refolded the earlier structures, producing a spatial variation of the orientation of the early structures. The following sections present the interpretation of the structural data in the Hesjelia-Hammertjønna ore zone and the Hellerfjellet ore zone.

5.4.1 Hesjelia-Hammertjønna ore zone

From previous mapping and subsurface interpretations, the Hesjelia ore zone is confined within the hinge zone of an isoclinal fold in that closes to the south (e.g. Kruse (1980); Marker (1983)). This isoclinal synform is a part of a larger north-verging F_2-fold. The interference pattern between the F_3- and F_4-folds with approximately orthogonal fold axes, result in a basin pattern. Consequently, the F_2-axis, which the ore deposit is interpreted to follow, has reversed polarity on either side of the F_4 hinge zone located between Hesjelia and Hammertjønna. Thus, in Hesjelia the F_2-axis plunges to the east, whereas in Hammertjønna it plunges to the west-southwest.

In order to observe all details of the 3D-model the margins are smaller in the following sections.

The Hesjelia deposit

There are six prospects in Hesjelia, numbered p.1-6, wherein mineralized bodies outcrop (Figure 5.3). In addition, there is one outcrop, sampled as HS-1 (Figure 5.3), that have not been prospected earlier, and show an enrichment of Zn (4720 ppm) and Cu (839 ppm). The following section present the different ore zones as observed from the drill cores and correlate them to possible outcrops and prospects.

Ten closely clustered drill cores from the 1950's was logged by Kruse (1980) where seven of them intersected mineralizations of varying grades and thicknesses (Figure 5.4). Based on surface structural data and 2D profiles the author established a system of four ore zones, whereof zone 1 and 2 were spatially correlated between several drill cores, while zone 3 and 4 only intersected only one drill core. This interpretation is used as basis and further developed into a 3D model here, so that correlated intersections are directly connected to each other. However, because the drill cores only constitute a small area in Hesjelia, there are no drill cores to interpolate the data further towards Hammertjønna. Here is where the 2D sections comes in, making it possible to extrapolate the surface/drill core data subsurface, however, it is not possible to avoid simplifications by this method.

The geological data collected during the field work suggest an average fold axis- and foliation orientation of 7.64°→084.39°E and 17.45°/168.51°S, respectively. The sections used to model the ore deposit here cover an area of 136 m in the N-S direction (Figure 5.3). The drill cores in Hesjelia are projected onto the E-W sections according to the orientation of the foliation, which is the best method according to Stockwell (1950).

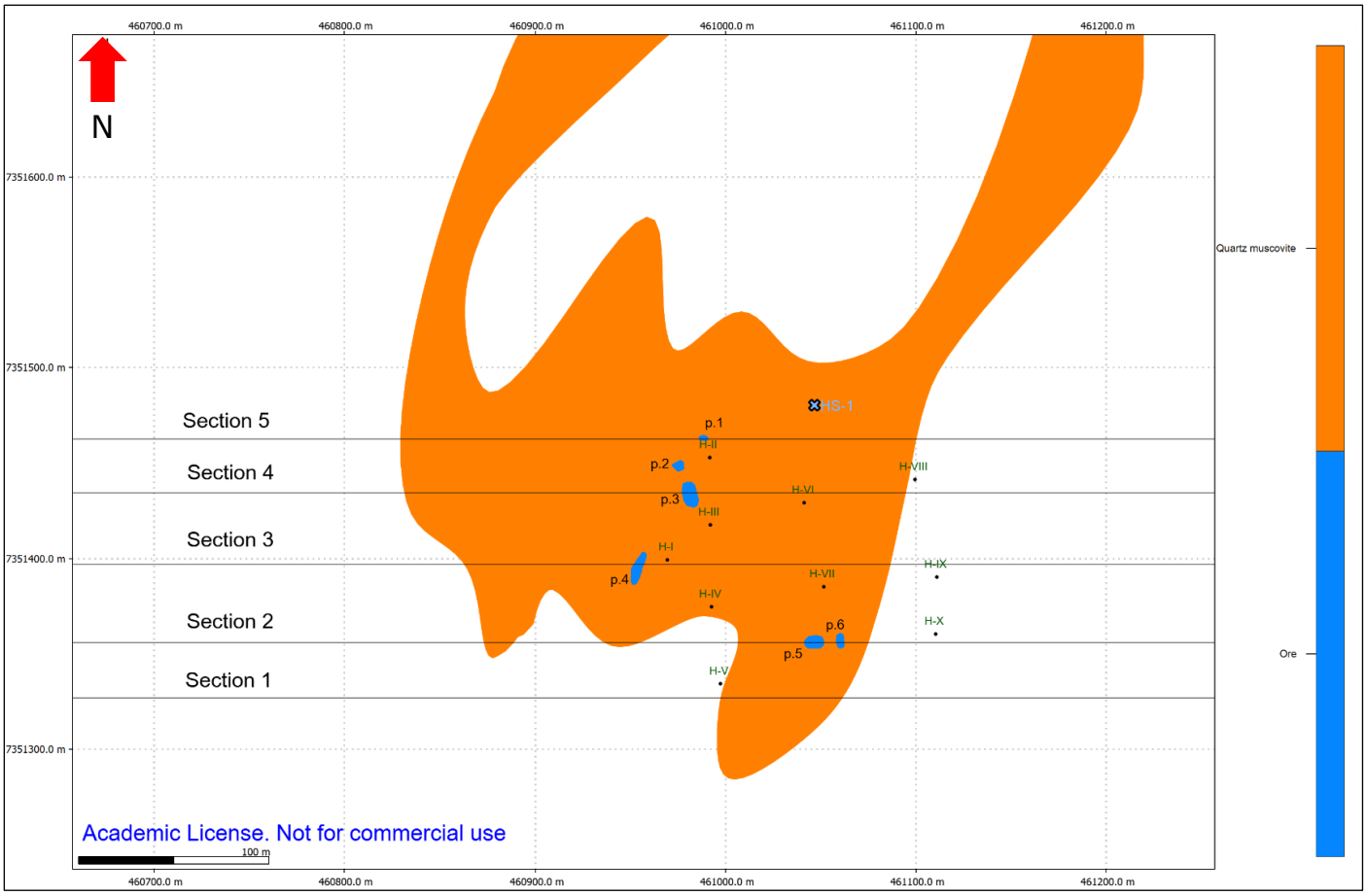

Figure 5.3: Figure 3: 2D-map of the prospects, sample HS-1 (cross) and the 2D sections in Hesjelia. Everything outside the QMS unit is grey gneiss.

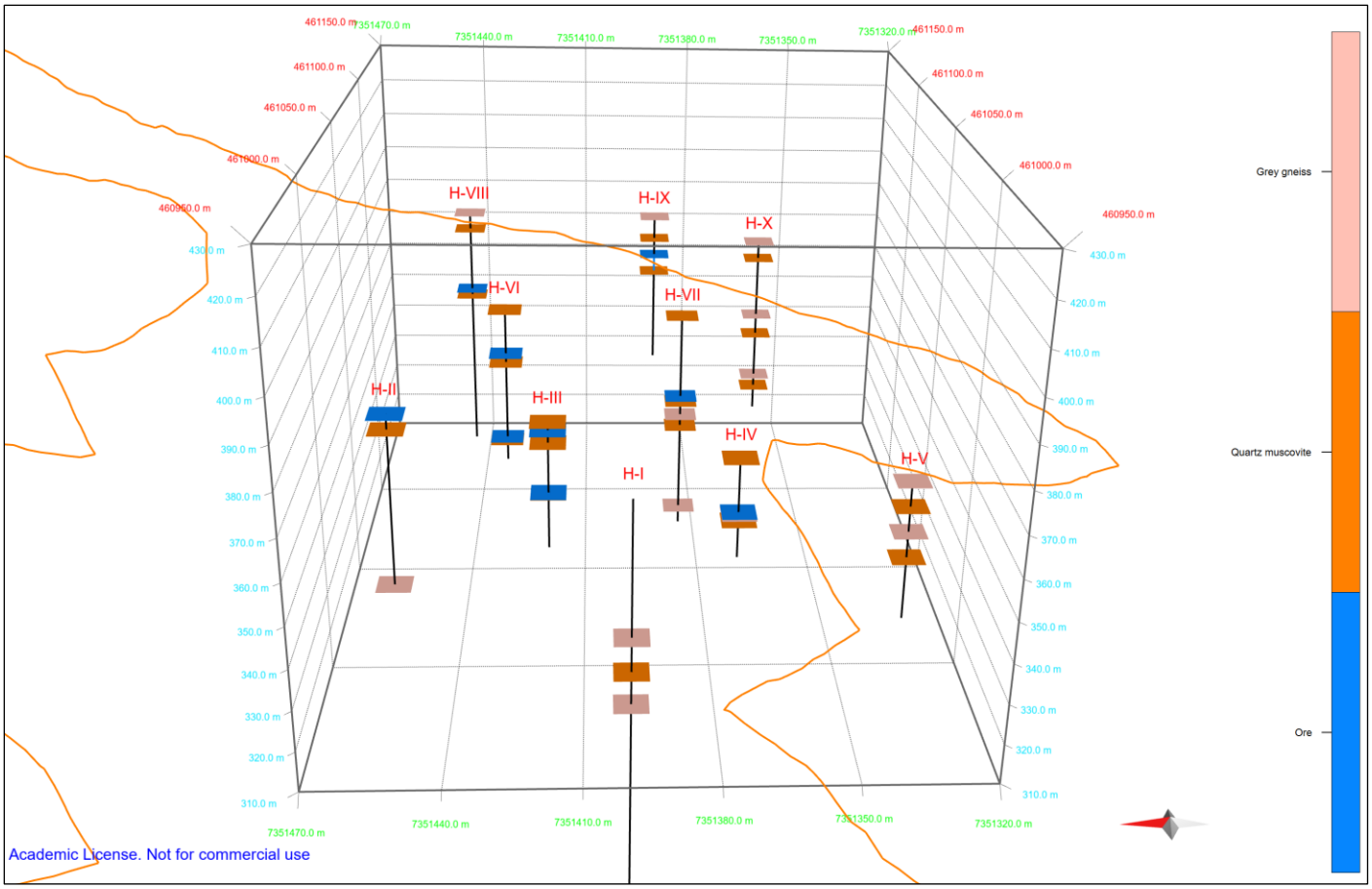

Figure 5.4: Overview of the ten drill cores in Hesjelia, as logged in Kruse (1980). Markers (squares) display contacts of the three lithologies intercepted. For visibility, only the contact between the QMS unit and the grey gneiss unit is shown. View towards east (Hammertjønna).

Ore zones

Zone 1 intersects the drill cores H-II, H-III, H-VI, and H-VIII (Figure 5.5A). The average plunge of this zone between the drill cores is ca. 5° in an easterly direction. It is constrained to the south by drill core dIX, whereas the northern limit is not constrained by any drill cores but possibly connected to the mineralized outcrop "HS-1". This is only possible within the geological constrains (foliation data) if the ore zone is folded (Figure 5.5B) in a similar style as the host rock. Nevertheless, when extrapolating the zone in a westerly direction it coincides with p.1, p.2 and p.3.

The mineralized intersection in H-VII (Figure 5.4) is attributed to **zone 3,** according to Kruse (1980). Here, it is modelled to be a part of zone 1, because an extension of zone 1 to H-VII result in a plane dipping 19° in a southerly direction (Figure 5.5A), which is within the 4.7° standard deviation of the average foliation dip of 17.45°. Drill core H-IX does *not* intersect zone 1, even though it is 085° east from H-VII, which is close to the average fold axis trend (084.39°E). However, the standard deviation of the trend is 4.5°, which makes it possible that zone 1 plunges north of H-IX. On this basis, it is likely that zone 3 actually is a part of zone 1, as illustrated in Figure 5.5.

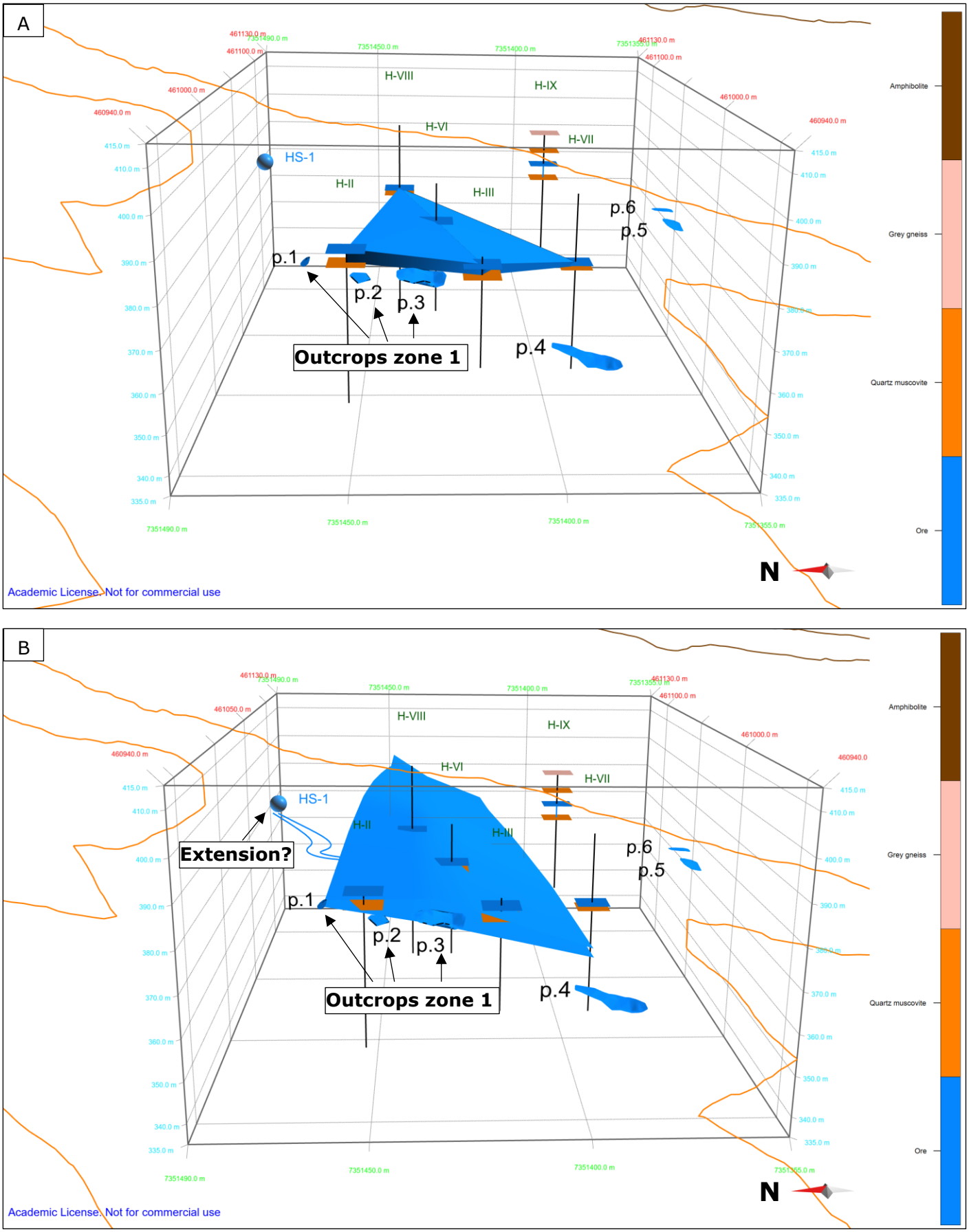

*Figure 5.5: 3D-model of ore **zone 1** in Hesjelia. Arrows indicate correlated prospects/mineralizations (p.1, p.2, and p.3). A) Construction based on drill cores only. B) The simplified large scale model stretching towards Hammertjønna and a possible folded connection to outcrop HS-1 (north of ore zone 1).*

Zone 2 intersects H-III, H-IV, and H-VI (Figure 5.6A). It is located 12 m underneath zone 1 in drill core H-III, increasing to 20 m in the easterly positioned drill core H-VI. The zone is constrained to the south by H-VII and H-IX (Figure 5.6A), despite both drill cores being positioned within the fold axis orientation, measured from drill core H-VI (southernmost intersection). The fact that the zone does not intersect H-VII suggests it has a local trend below 80°E, barely inside the standard deviation of the field measurements. The deviation can be explained by noncylindrical folds. This is also the reason why the section trace is placed on the northern side of drill core H-IX (Figure 5.6B). Prospect nr. 4 coincide with zone 2 and is interpreted as the outcropping body of this zone.

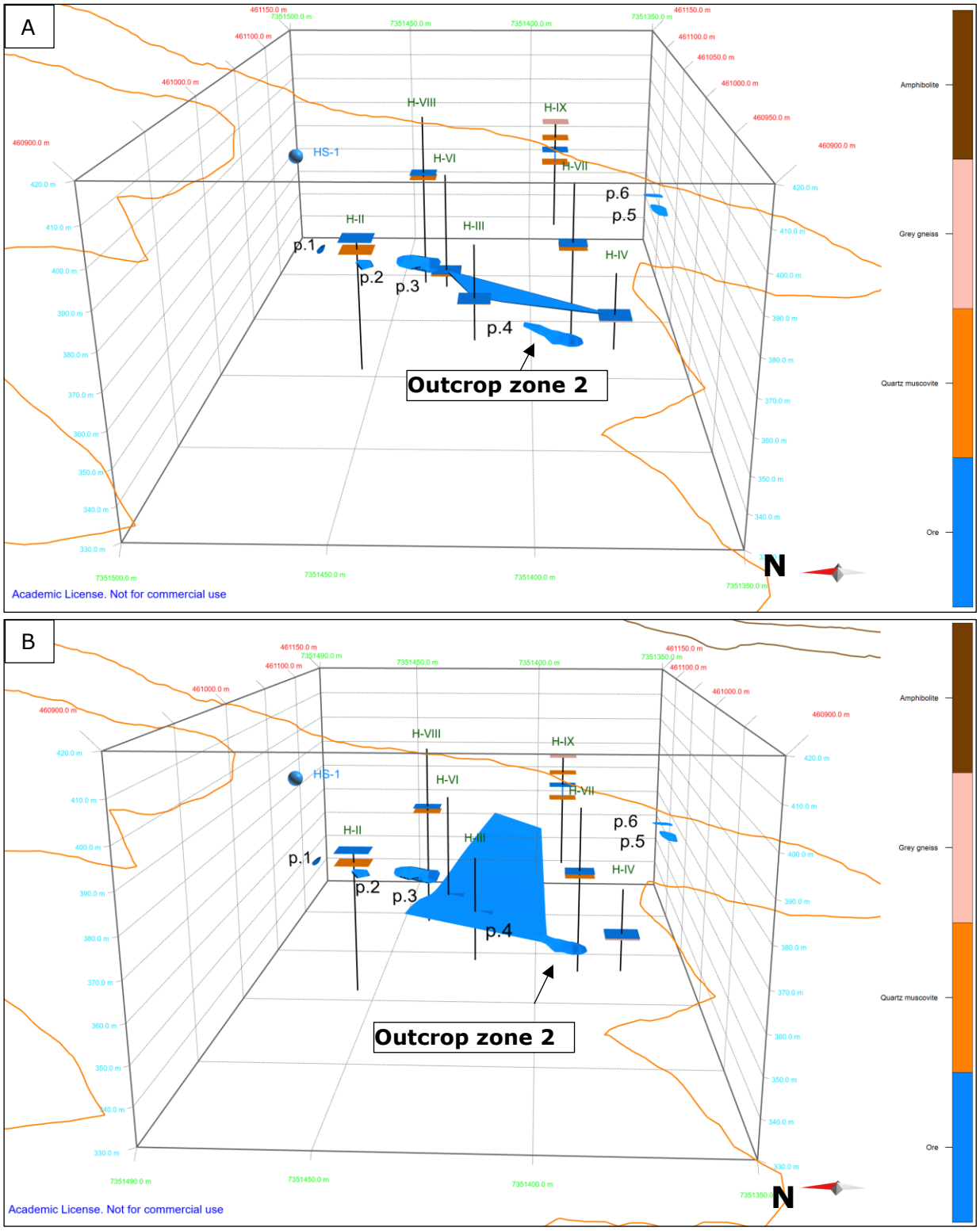

Figure 5.6: 3D-model of ore zone 2 in Hesjelia. Arrow indicate correlated prospect (p.4). A) Construction based on drill cores only. B) The simplified large scale model stretching towards Hammertjønna.

Zone 4 is only intersected in H-IX and not possible to connect to either zones within the deviation of the structural measurements and does not coincide with any outcropping ore body observed (Figure 5.7). The width of the zone is constrained to the south by H-X and to the north by H-VIII, potentially being 80 m wide. Because the width of the zone is unknown, but likely narrow, only the thickness is modelled subsurface.

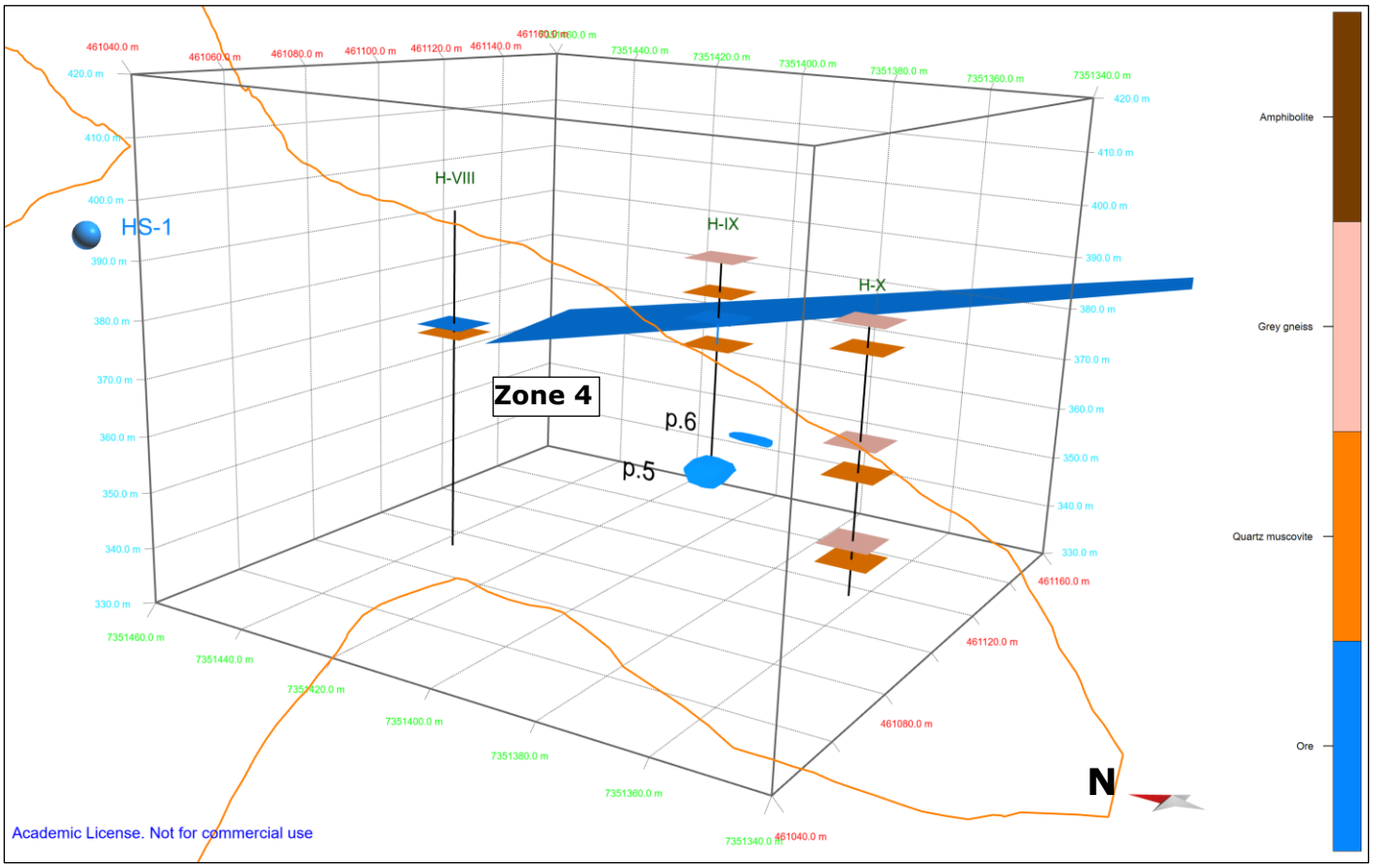

Figure 5.7: 3D-model of ore zone 4 in Hesjelia. It is constrained between H-X and H-VIII but is not connected to any known outcrop. View from southwest.

Zone 5 is a new zone presented here that has its starting point in prospect nr. 5 and 6 (Figure 5.8). It does not intersect any drill cores, the closest being H-X measuring 5 m away in a northerly direction. The only limit in the southerly direction is the extension of the quartz muscovite schist unit, making it potentially 70 m wide, however, no outcrop has confirmed this. It is correlated to prospect nr. 3 and 4 in Hammertjønna where it forms a 75 m wide zone. However, the orientation of the sections results in a 30 m wide zone in Hesjelia.

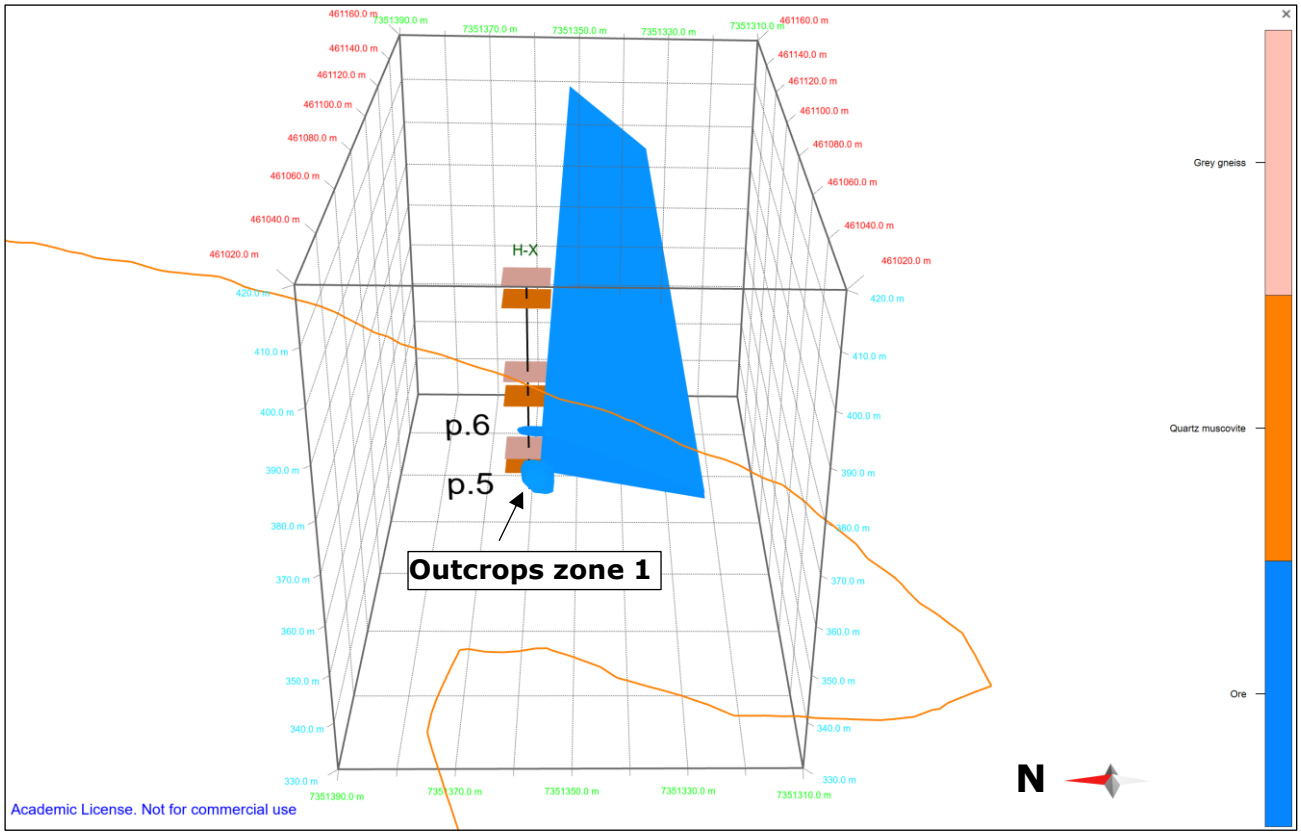

Figure 5.8: 3D-model of ore zone 5 outcropping in p.5 and p.6 in Hesjelia, seen from west.

For the sake of consistency, the four zones will be regarded as they hitherto have been named.

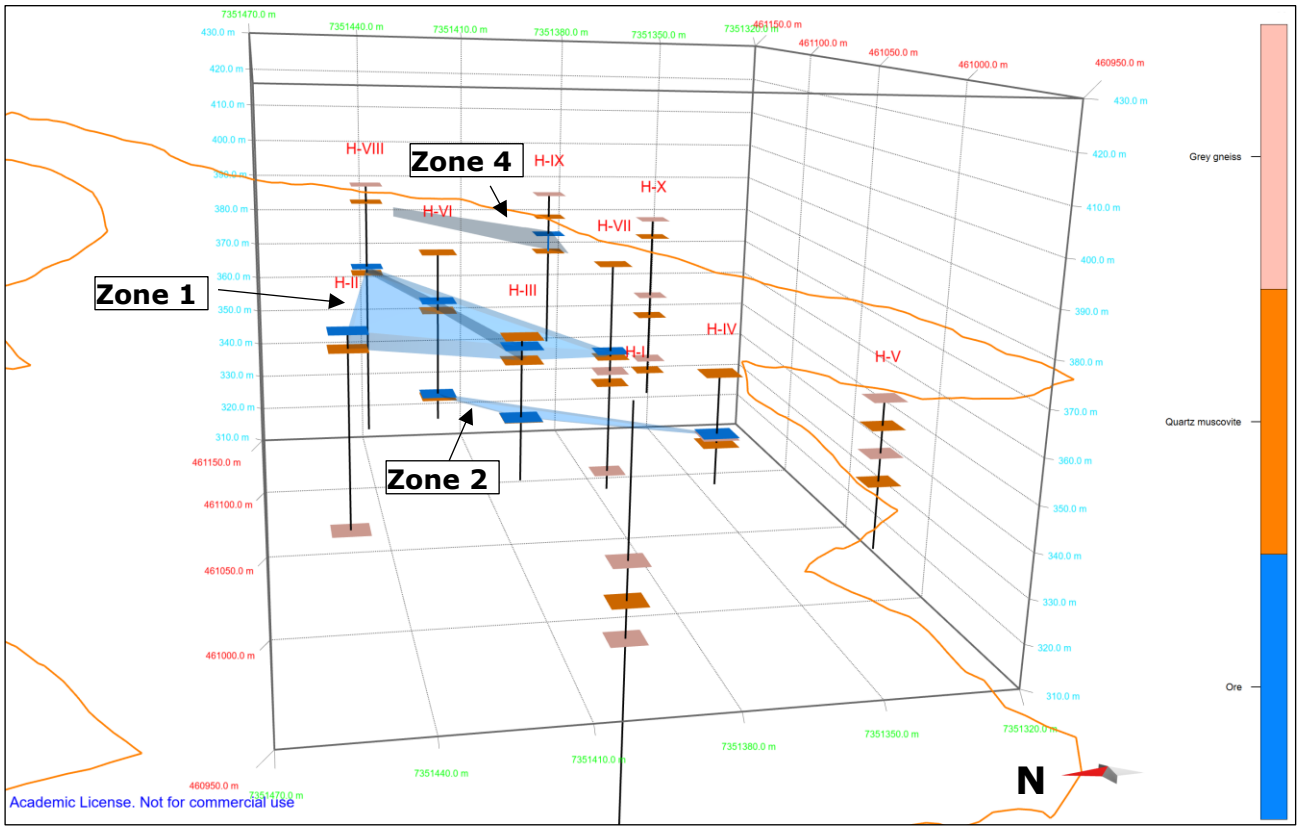

Figure 5.9: Overview of the three zones interpreted from the drill cores in Hesjelia. Zone 5 is leaved out because it does not intersect any drill core.

Hammertjønna

Four prospects numbered p.1-4 and two mineralized outcrops, sampled as "HAM-B2" and "HAM-B8", occur in a systematic way along strike over a distance of 550m (Figure 5.10). This is contrary to the ore zones in Hesjelia, occurring on different structural levels. Following the hypothesis about a connection between the two deposits, which is (weakly) indicated by TEM and a weakly mineralized drill core intersection, zone 1, 2, and 4 (situated on top of each other) in Hesjelia must either conjoin towards Hammertjønna or one of them must taper out. According to Marker (1983), the interfold angle of the isoclinally folded QMS unit tightens from Hesjelia and eastwards to Hammertjønna. This can be inferred directly from the map, on the basis that the grey gneiss unit separates the outcropping limbs in Hesjelia, but not in Hammertjønna, where the QMS unit outcrop as one layer. Because of this, the strain has possibly been higher in Hammertjønna, which possibly can explain the different outcrop pattern compared to Hesjelia. Higher strain causes isoclinal folds to shear and boudinage along the axial plane (Marshall et al., 2000).

There are no drill cores available in Hammertjønna to aid in the subsurface interpretation, except for drill core BH4808 being closer to Hammertjønna than Hesjelia. The average fold axis- and foliation measurements for Hammertjønna is 9.71°→250.8°ESE and 12.2/225.0°SE, respectively.

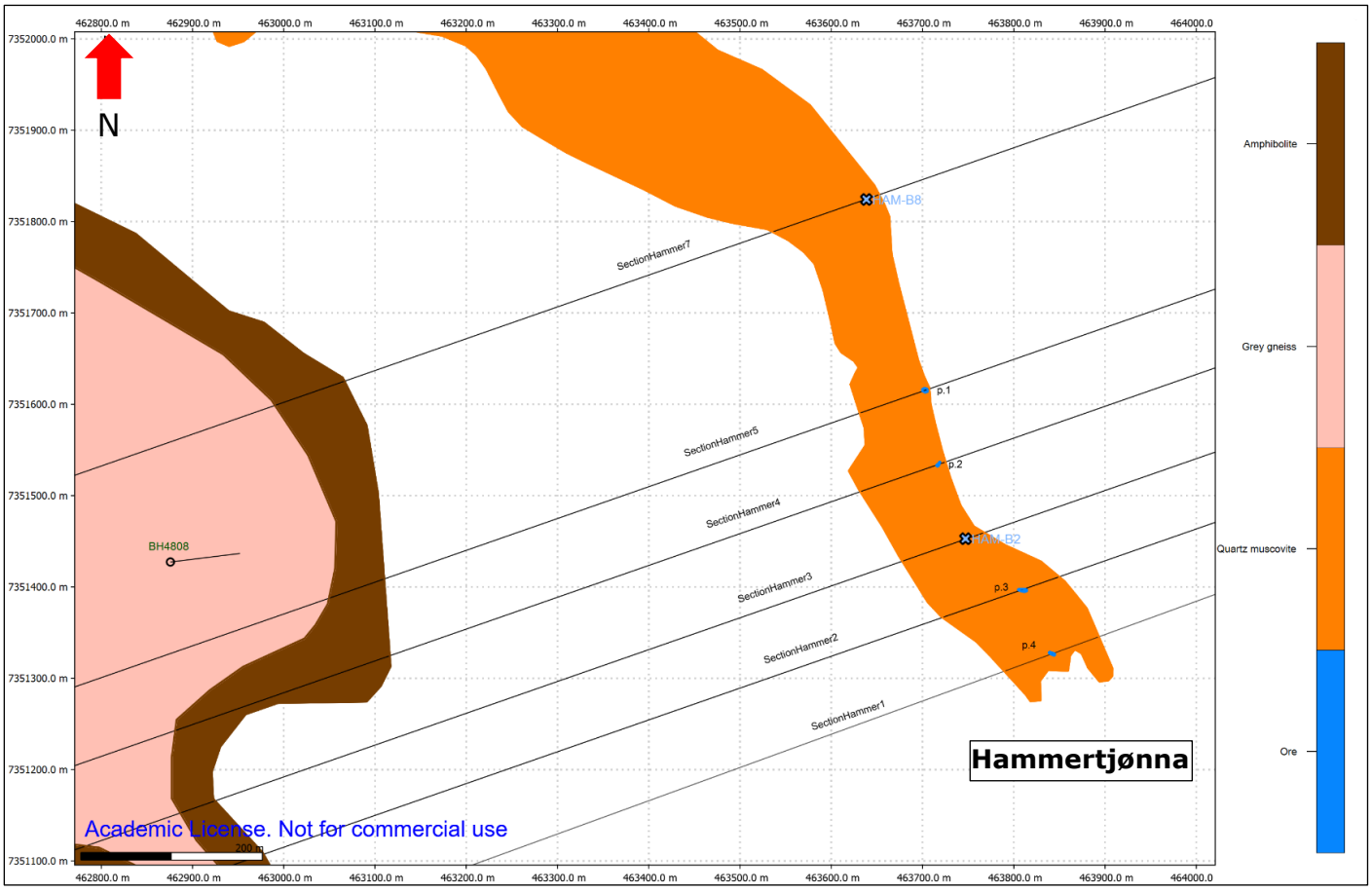

Figure 5.10: 2D-map of the prospects p.1-p.4, mineralized outcrops (HAM-B2 and HAM-B8) and the sections used to construct the 3D-model in Hammertjønna.

Because drill core BH4808 is closest to Hammertjønna it is most appropriate to address it here. Its position and path are illustrated in (Figure 5.11). The highest grades of sulphide mineralization were intersected at ca. 110-117 m yielding 0.6% Zn, 0.14 % Cu and 0.09% Pb (Bjerkgård et al., 2013b), which is well below the grades of the samples from both Hammertjønna and Hesjelia (see Appendix B, Table 8.8). According to the trend of the fold axis (250.8°), the drill core fails to intersect the richest part of the ore deposits, being the prospects, wherein the closest extrapolation is that of p.1 (as seen in both Figure 5.10 and Figure 5.11), possibly explaining why the sulphide grade is below that of the

prospects. Thus, the drill hole should have been placed further south. Nevertheless, this indicate that the area between prospect nr. 1 and HAM-B8 has an elevated sulphide content, suggesting an extension of the ore zone towards sample HAM-B8. Therefore, the ore zone is extended towards HAM-B8, as illustrated by Figure 5.11. When extrapolating between the drill core intersection and p.1 the plunge is 9.3°, which is only 0.41° off the average field measurement, thus giving credibility to the surface measurements.

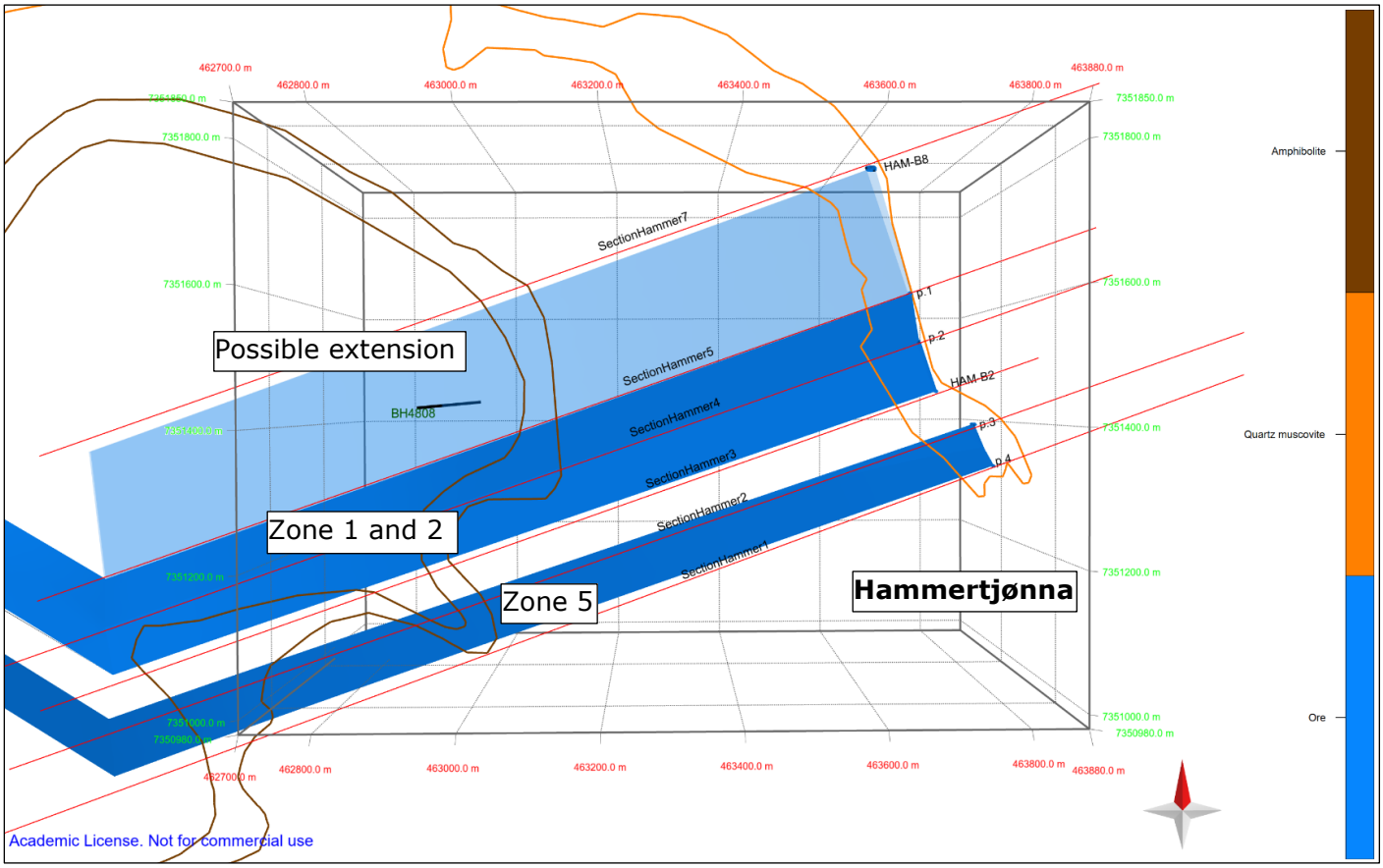

Figure 5.11: 3D-model showing the position and path of drill core BH4808 (middle left in figure). Notice that it is positioned off the fold axis of any prospect. Shaded blue colour between p.1 and HAM-B8 illustrating a possible connection. The red streaks are each section that are connected to draw out the surfaces of the 3D-model. For a clearer visualisation, only the horizons are illustrated.

5.4.2 Sections and 3D model

If Hesjelia and Hammertjønna indeed is connected, the fold axis is inferred to change orientation between the two localities. Based on this, the area is divided into *three* segments (i.e. three fold axis orientations) where each segment has a similar section orientation (Figure 5.13). These segments cover Hesjelia, Hammertjønna and the centre part in between. All 2D-sections are based on the F_2 fold axis orientation and oriented parallel to the average orientation in each segment. Some sections oriented N-S have been used for guidance in the centre part where orientation data is missing, extrapolated from where the host rock crop out in the northern part. The sections covering Hesjelia are oriented 090°E, Hammertjønna 251°ESE and the centre segment 301°ENE, which is the interpretation of the ore zone's trend subsurface. The length of the sections is determined by how far the Hammertjønna fold axis maintain its orientation before turning northwest in the centre segment and back west in Hesjelia. This is of course difficult to know because of the lack of orientation data in the central segment, however, can be inferred from the TEM-data assuming that the anomaly is produced by the ore zone. Chalcopyrite, being the main Cu-phase here, is highly conductive (Pat Shanks III and Thurston, 2012), and the amount of Cu reaches 7814 ppm in Hammertjønna (sample HAM-S1) and 7779 ppm in Hesjelia (sample HS-S3e). Silver is even higher See Appendix B Table 8.8 for ore samples. Figure 5.12 shows the TEM-anomaly for 340 m.a.s.l., which is the level that has the largest and highest anomaly (by the intensity of the colour). The

anomalous area stretches southward in accordance with the ore in Figure 5.13A, thus, there is a possibility that the anomaly is attributed to the ore. This is further discussed and correlated in section 5.4.3 below.

For the extrapolation to the subsurface ca. 7° and 9.5° is used as plunge in Hesjelia and Hammertjønna, respectively. The centre part connects these two areas where the F_2 fold axis changes polarity and direction moving towards and along the western limb of the F_4 open fold. Because of the different spatial configuration of the outcropping ores in Hammertjønna, zone 1, 2, and 4 from Hesjelia is modelled to conjoin at the start of the Hammertjønna segment. Prospect nr. 1, 2, HAM-B2 and HAM-B8 are interpreted to represent the outcrop of this compound zone in Hammertjønna. Zone 5 correspond to prospect nr. 3 and 4 in Hammertjønna and maintain its separation from the other zones because it is not placed along the same Z-axis. All individual ore zones of the whole ore deposit are displayed in Figure 5.14, and the entire 3D-model including the QMS and amphibolite unit is shown in Figure 5.15.

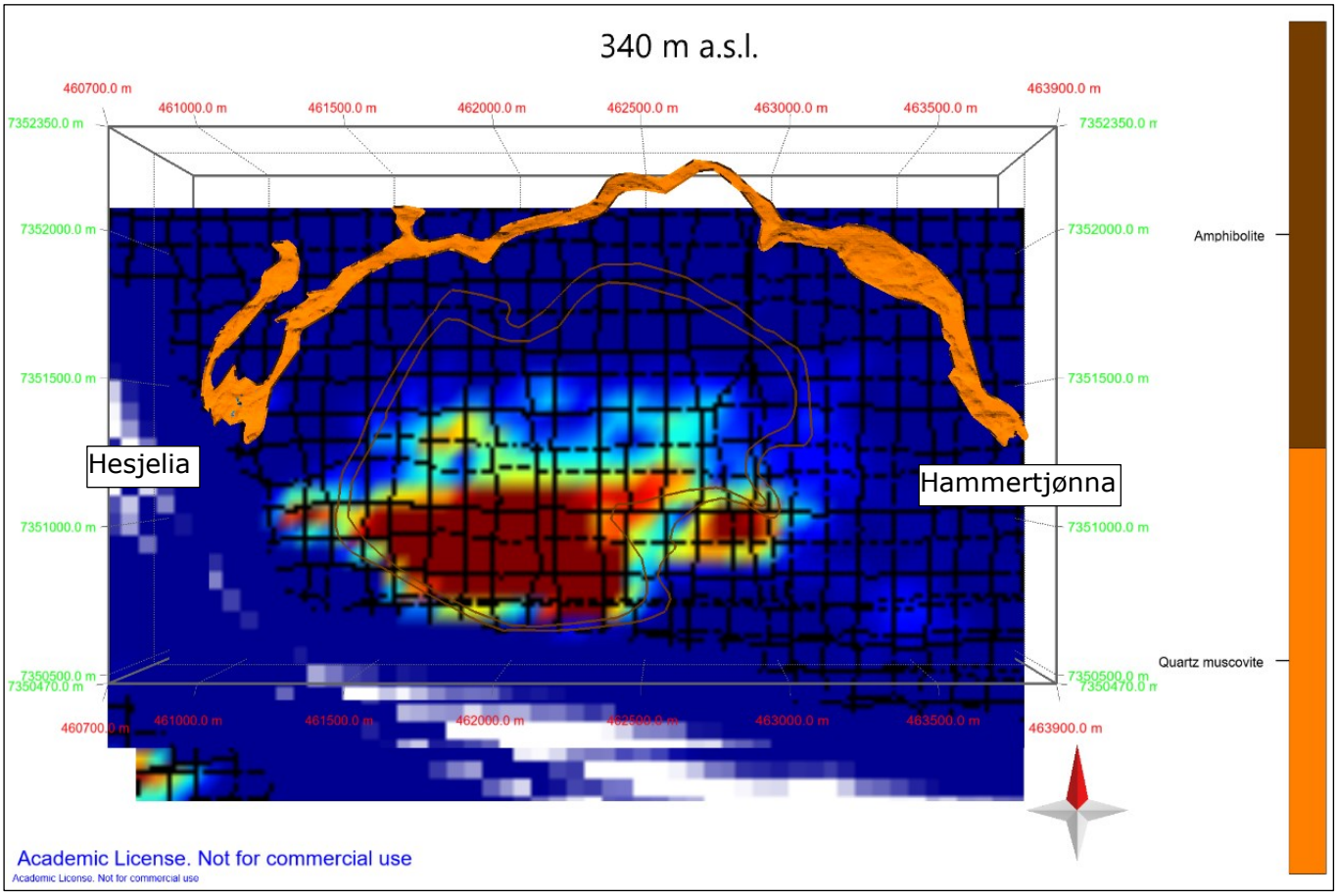

Figure 5.12: TEM anomaly at 340 m (a.s.l.). If the mineralization produces the anomaly it extends southwards.

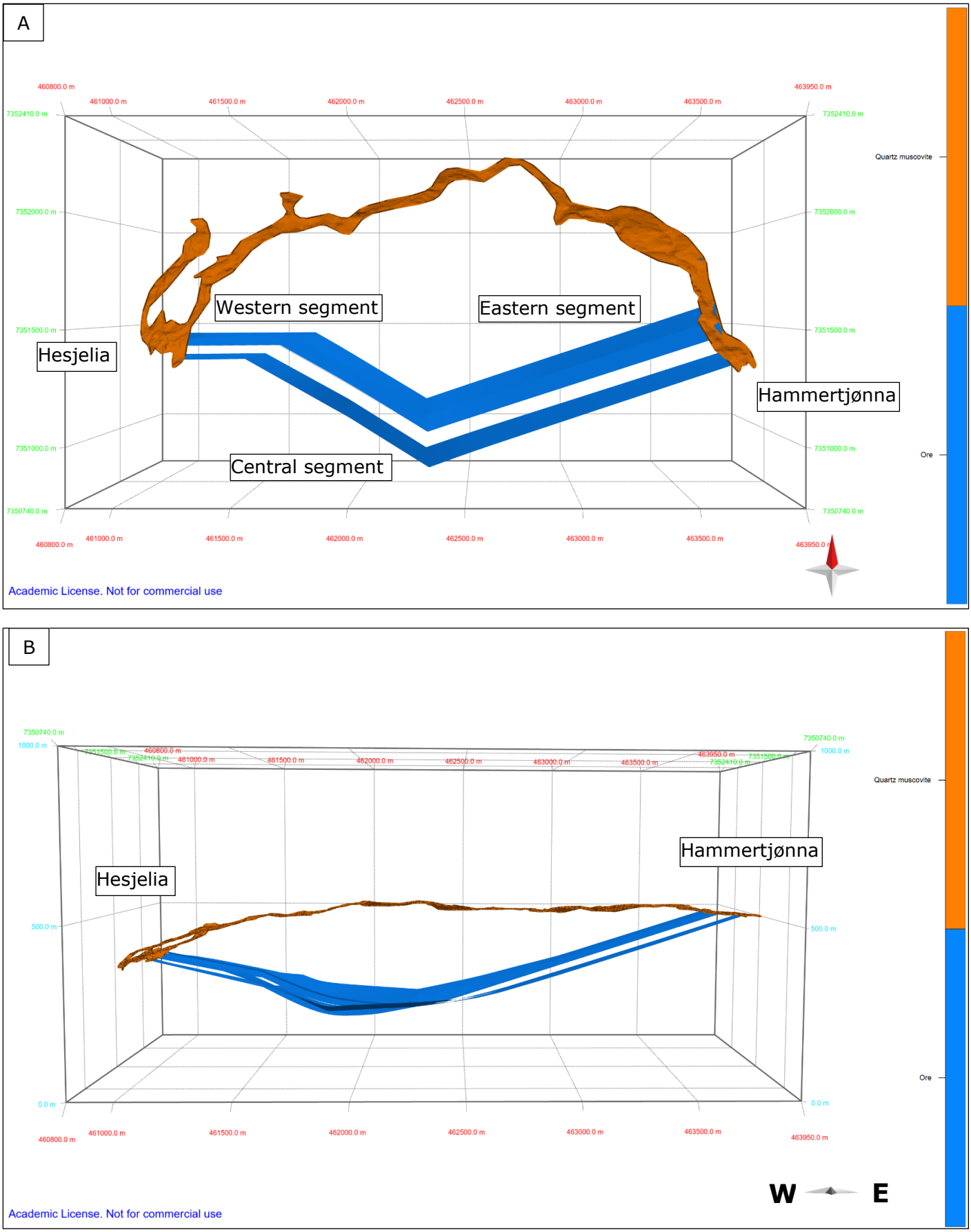

Figure 5.13: The entire model of the ore deposit in Hesjelia with zero vertical exaggeration. A) Seen from above. B) Seen from the south, horizontally.

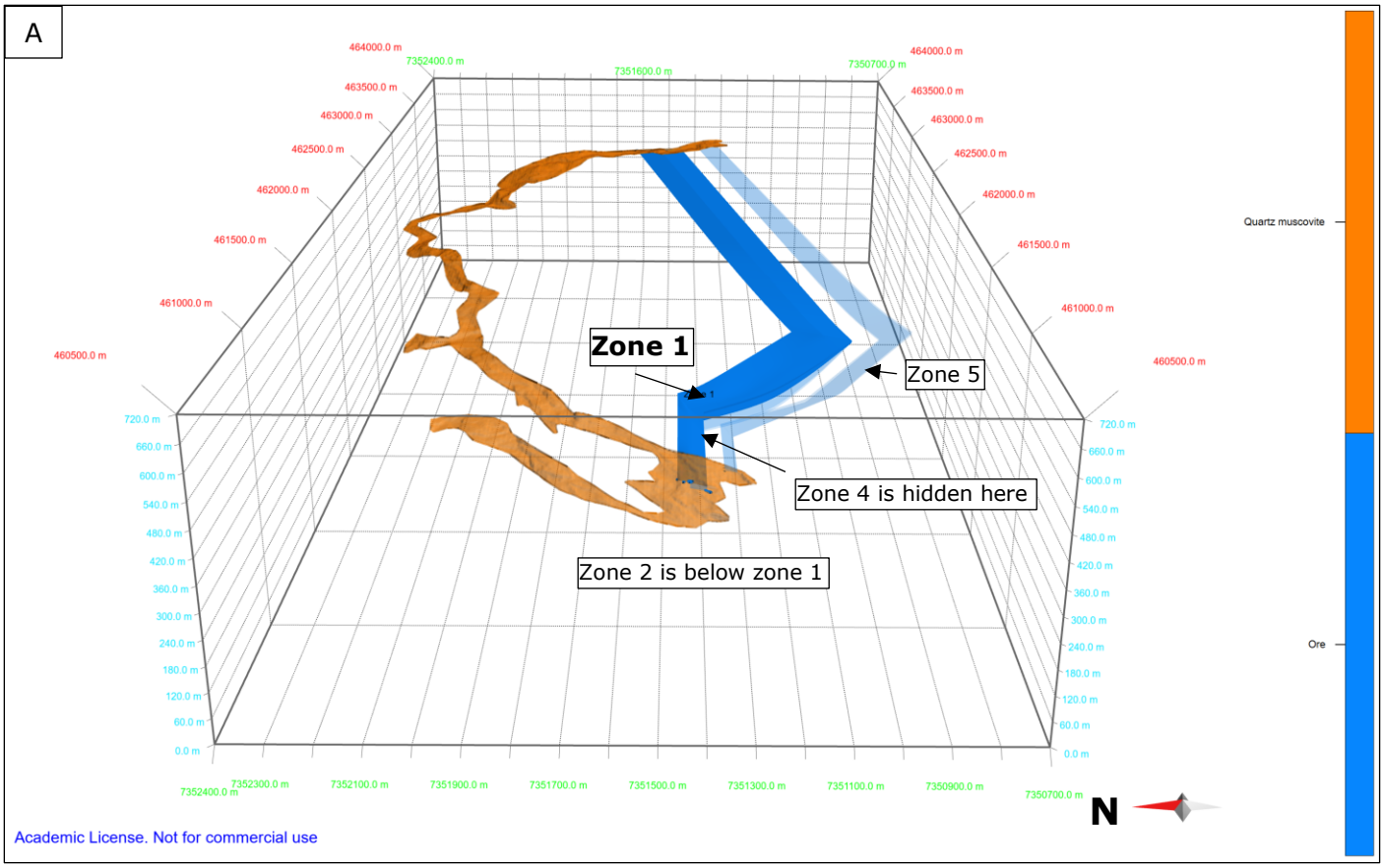
A
Zone 1
Zone 5
Zone 4 is hidden here
Zone 2 is below zone 1
Quartz muscovite
Ore
N
Academic License. Not for commercial use

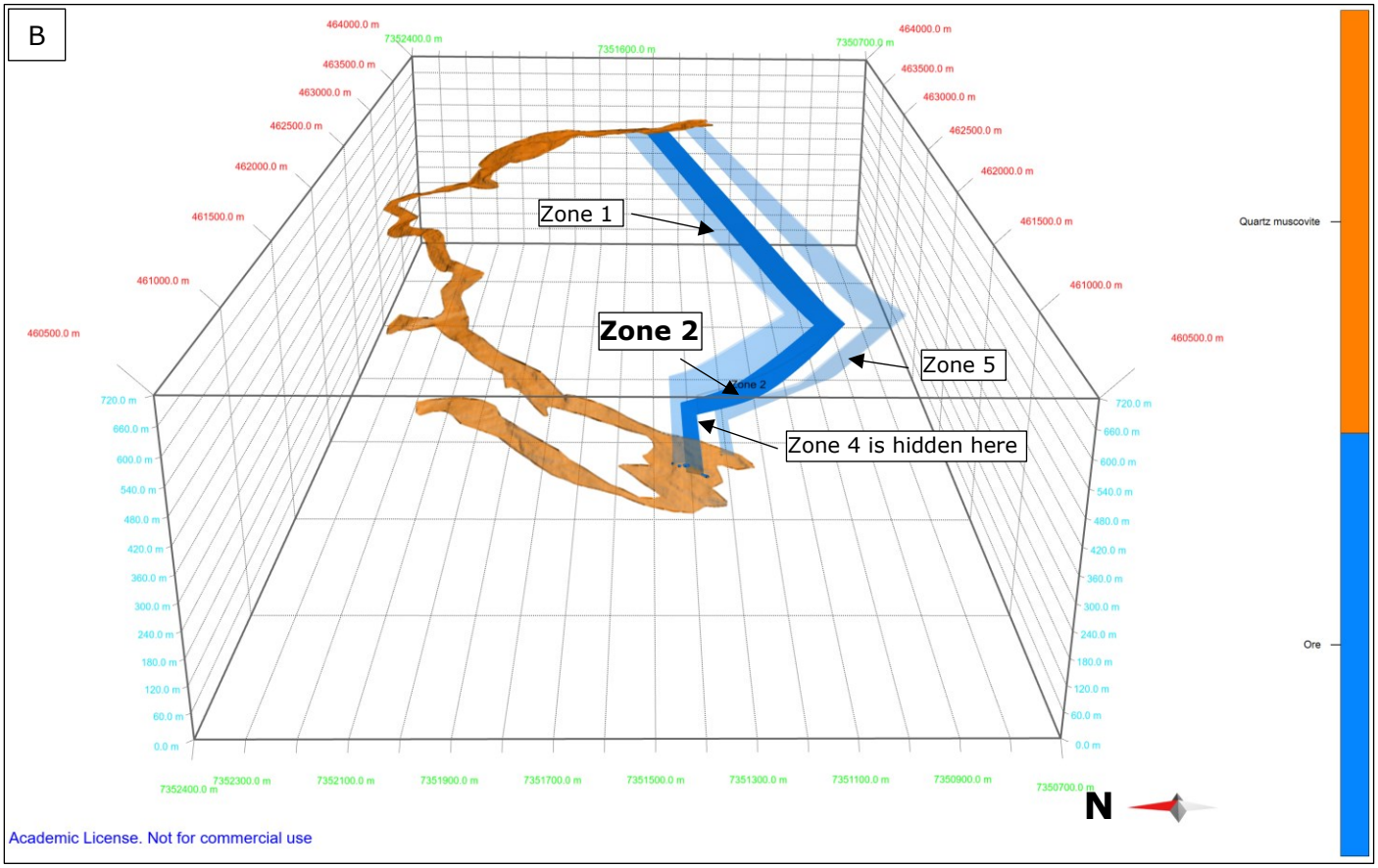
B
Zone 1
Zone 2
Zone 5
Zone 4 is hidden here
Quartz muscovite
Ore
N
Academic License. Not for commercial use

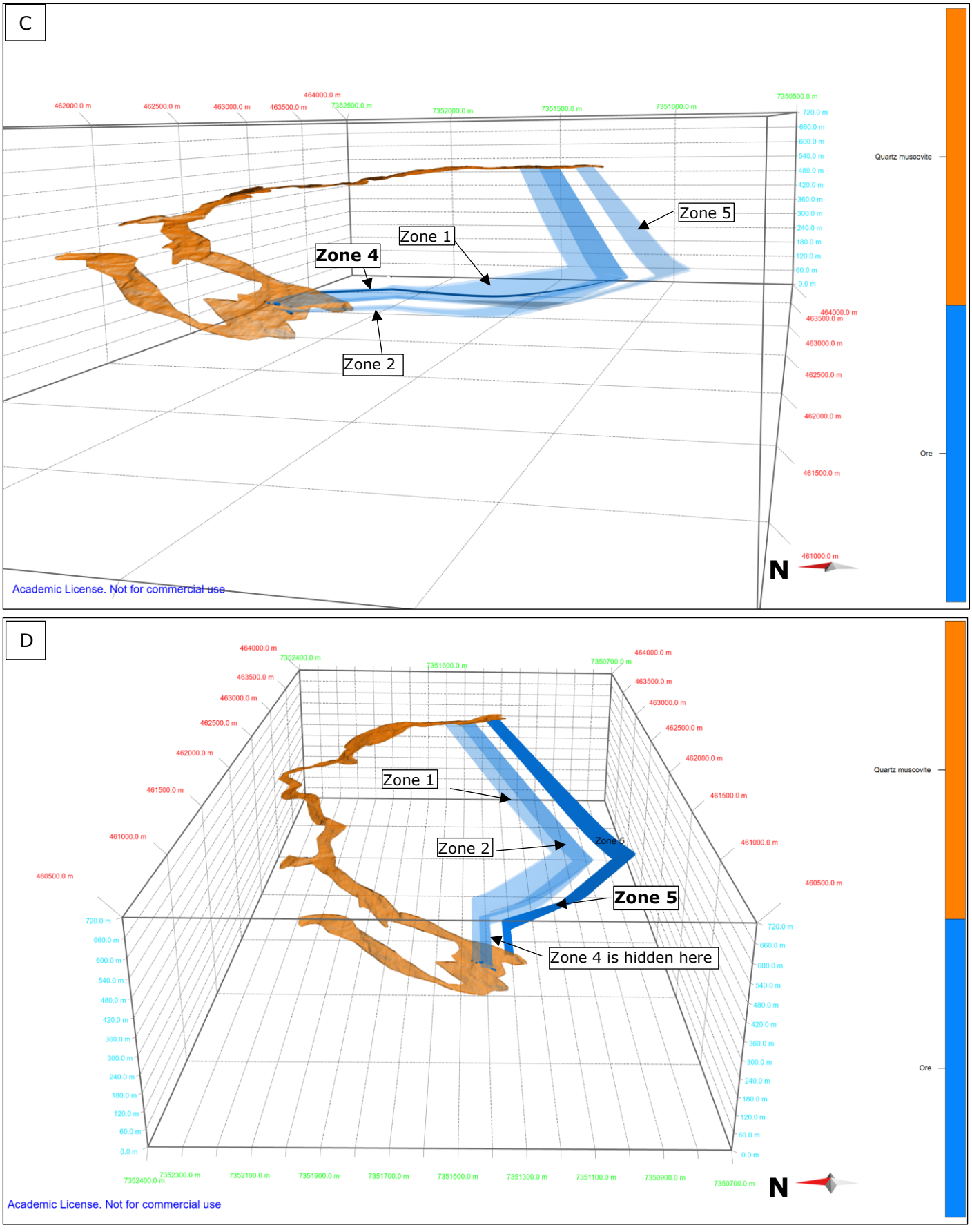

Figure 5.14: The four different ore zones seen from west. The zone in question is highlighted in each figure. A) Zone 1. Zone 2 is hidden by zone 1 because it is below. Zone 4 is hidden by the colouring. B) Zone 2. Zone 4 is hidden by colouring. C) Zone 4. Notice how it wedges out towards Hammertjønna. D) Zone 5.

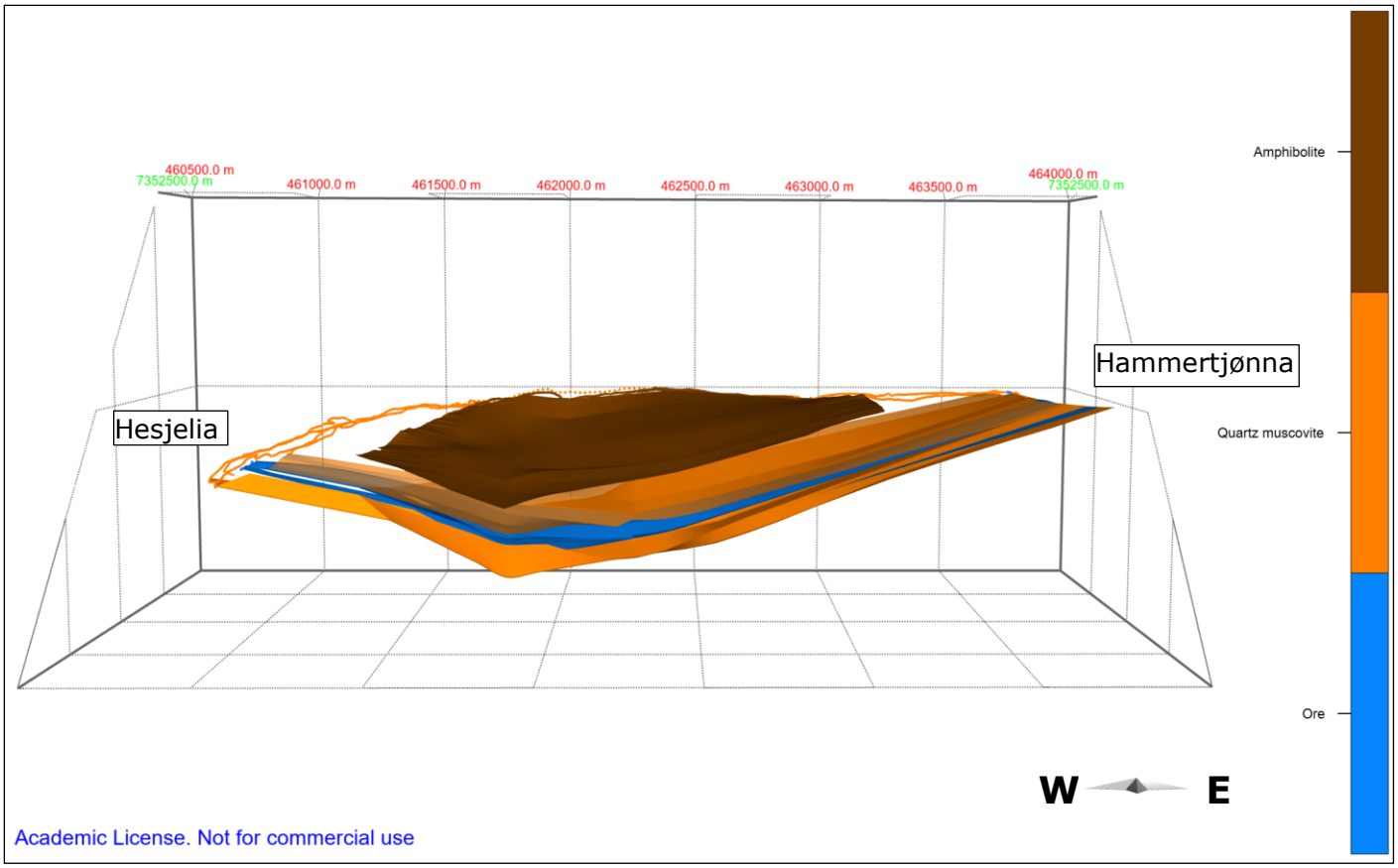

Figure 5.15: 3D-model of the Hesjelia ore zone with the muscovite schist host rock and amphibolite. Seen from the south, horizontally.

5.4.3 TEM-correlation

Electromagnetic surveys are the most used geophysical technique in VMS-exploration because of the high conductivity of sulphide minerals (Pat Shanks III and Thurston, 2012). In order to produce a large anomaly the conductive minerals need to be interconnected, hence, not disseminated (Pat Shanks III and Thurston, 2012).

The TEM-anomaly gradually increases in strength and horizontal range from 420 to 360 m.a.s.l. (Figure 5.16), before decreasing gradually in both attributes towards 300 m above sea level, while synchronously shifting towards south west. The black lines are the survey lines. Below 300 m a.s.l. the anomaly changes very little, which cannot be explained by any of the rock units investigated here, according to the geological constrains. It is not likely that there is a feeder zone below the ore zone, because metamorphism and deformation have disrupted that. The anomaly is compared to all rock units (the amphibolite unit, the QMS unit, and the ore zone) to get a better understanding of which rock units are causing the anomaly. The area between the amphibolite unit and the muscovite schist unit not covered by the model is the grey gneiss, which can be indirectly analysed.

Figure 5.18 – 5.20 visualize the intersection between the TEM-data layers and the 3D-modelled rock units. The interesting area is *between* the lines created by the intersection of the upper and lower contact of each individual rock unit. The upper contact of each rock unit is made transparent in order to make the anomaly visible through it, while the lower horizon is less transparent, attaining both a prominent intersection and a visible anomaly for a better overview. Optimally, to assign the anomaly to a specific unit with confidence, the intersection area should overlap the anomalous area at several levels, given that the conductivity is continuous along the length of the unit. Already now it is possible to see that the amphibolite unit's outcrop pattern reflects the uppermost layers of the TEM anomaly (at 420 and 400 m.a.s.l. in Figure 5.16).

Because each TEM-data layer is positioned at the bottom of the 20 m depth-interval it represents, the true spatial position of the anomaly can deviate up to +20 m. Because of the lower altitude of Hesjelia it does not appear above 360 m above sea level.

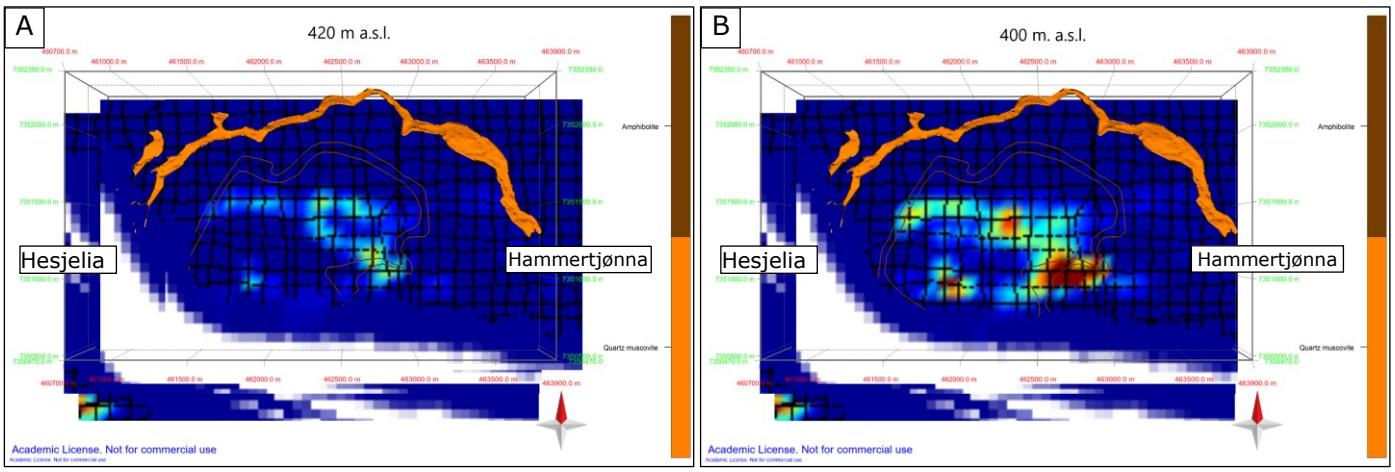

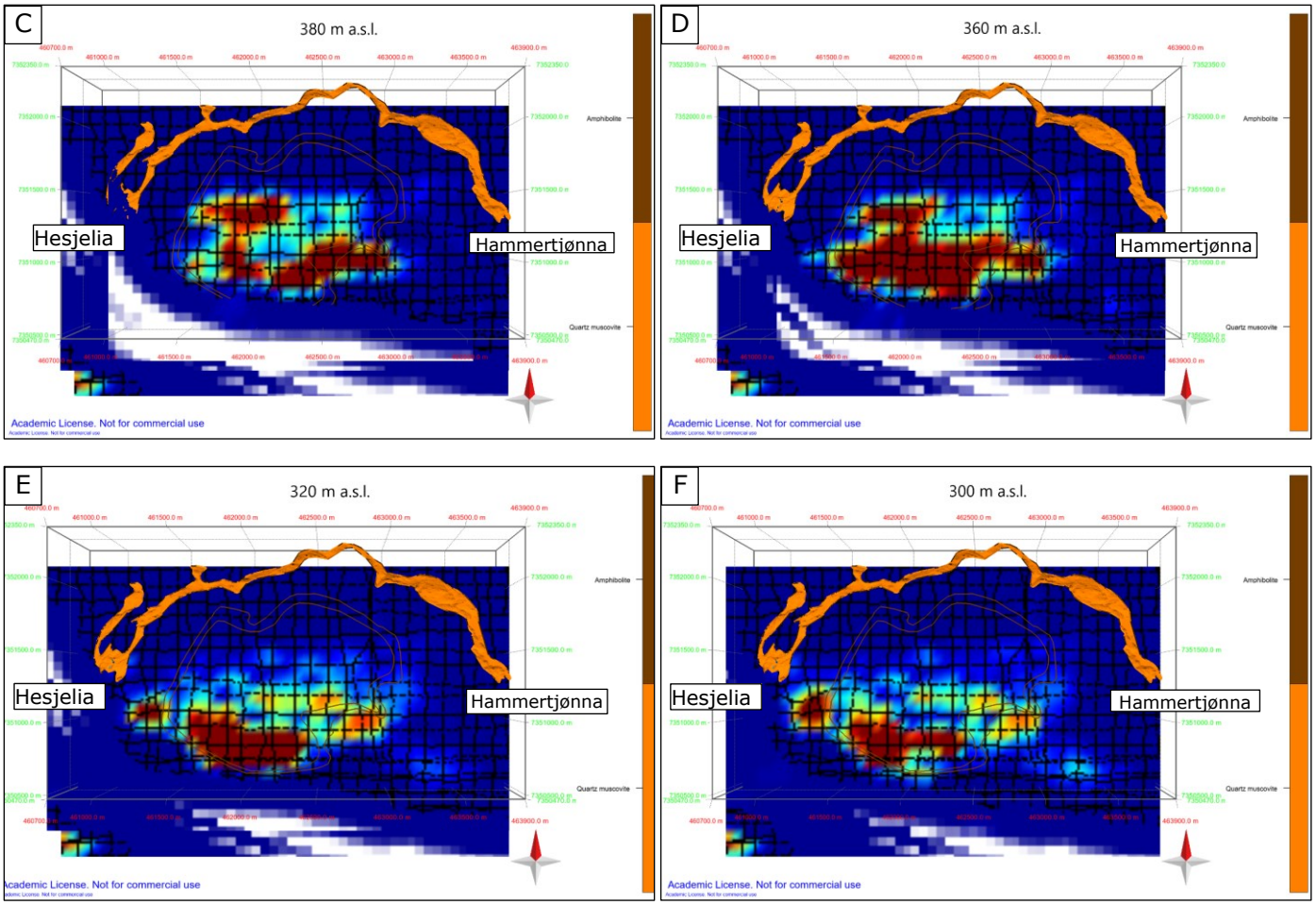

Figure 5.16: TEM-anomaly between 420 m and 300 m above sea level. A) 420 m, B) 400 m, C) 380 m, D) 360 m, E) 320 m, F) 300 m.

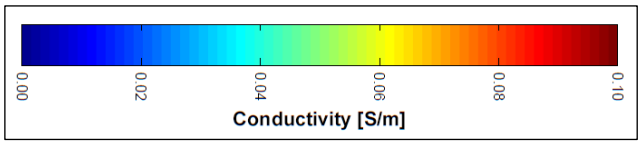

Figure 5.17: Conductivity bar in siemens per meter.

According to a visual comparison of the reference bar and the anomaly the signal is close to 0.10 S/m at the highest, e.g. in Figure 5.16B, and generally between 0.06 and 0.10 S/m. VMS deposits usually exceeds 0.5 S/m, however sphalerite can be lower than 0.1 S/m (Ford et al., 2007). Alteration zones typically range between 0.001 S/m and 0.5 S/m. More answers are to be given in the following sections.

The amphibolite unit

As seen in Figure 5.18, large parts of the TEM-anomaly, especially at 360-340 m.a.s.l., seem to be attributed to the amphibolite unit situated above the ore-hosting QMS unit (white arrows indicate the highest anomalies). According to the 3D-model the amphibolite unit is above 300 m.a.s.l., which can be seen from the 320-300 m.a.s.l. layers that are found in Appendix A, so it cannot explain the relatively high anomaly that exist deeper than this.

Any value of the conductivity of amphibolite was not possible to obtain, however, igneous and metamorphic rocks in general are < 0.001 S/m (Ford et al., 2007). The amphibolite samples (only from Hellerfjellet) is not very rich in sulphides (TS < 3.5 wt.%), whereof Cu is maximum 122 ppm (sample HF-X10), and graphite is also low (TC < 0.97 wt. %). However, if there is (ionized) water circulating in the rock the conductivity increases, yet, is less likely because there are no sediments. Because of the lower altitude of Hesjelia (370 m.a.s.l.) it does not show until level 360 m (a.s.l.).

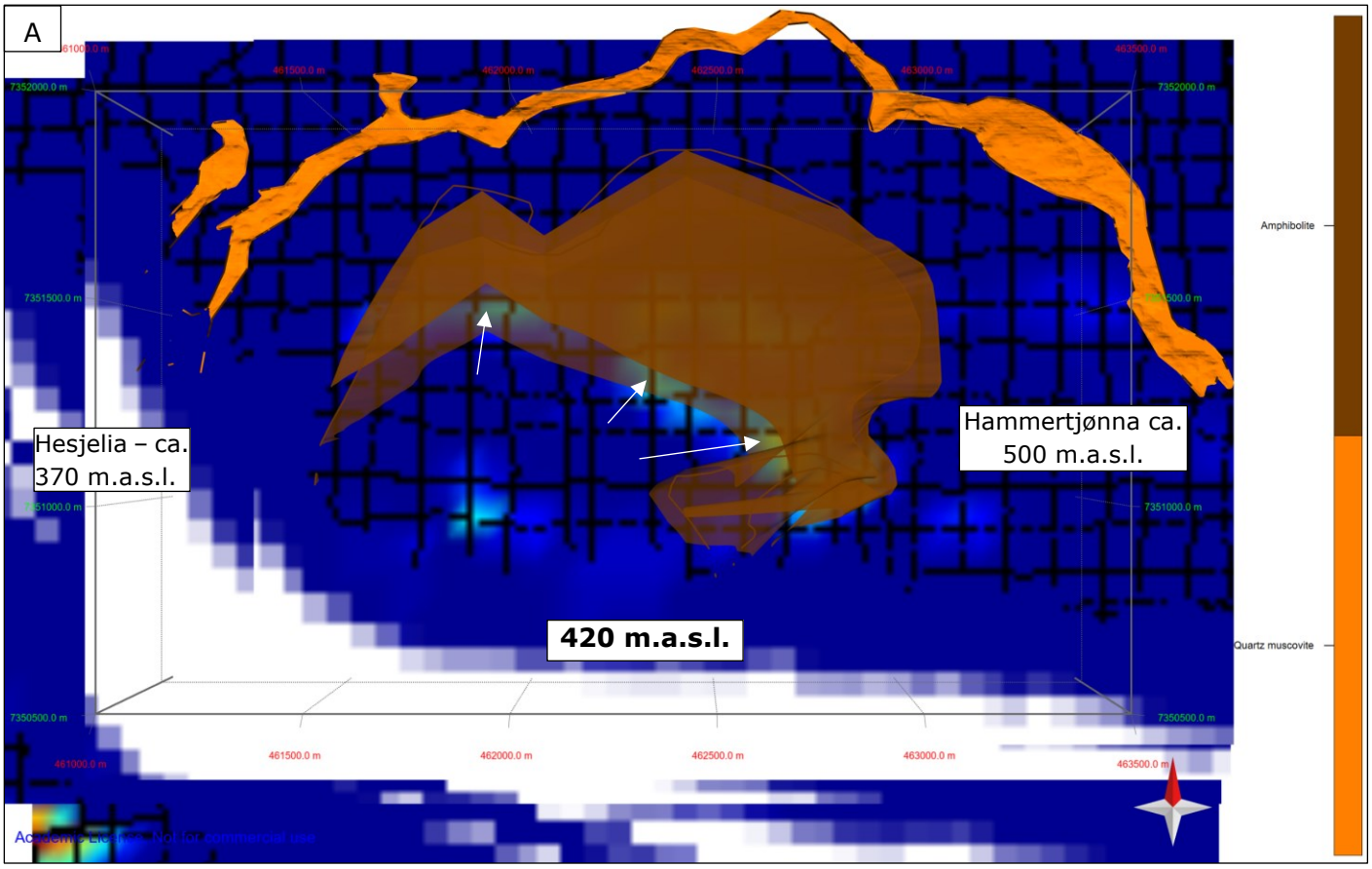

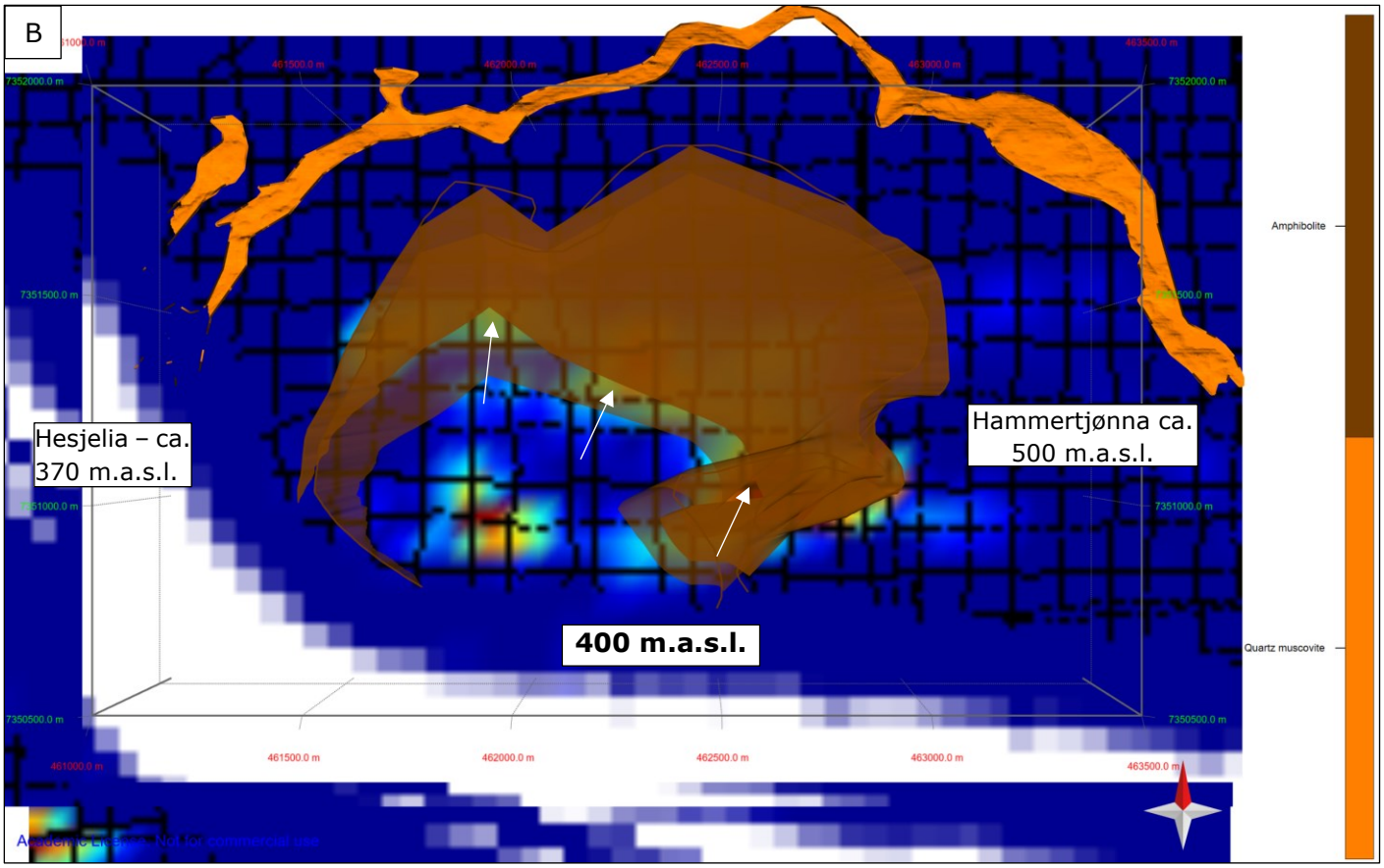
B
Hesjelia – ca. 370 m.a.s.l.
Hammertjønna ca. 500 m.a.s.l.
400 m.a.s.l.
Amphibolite
Quartz muscovite

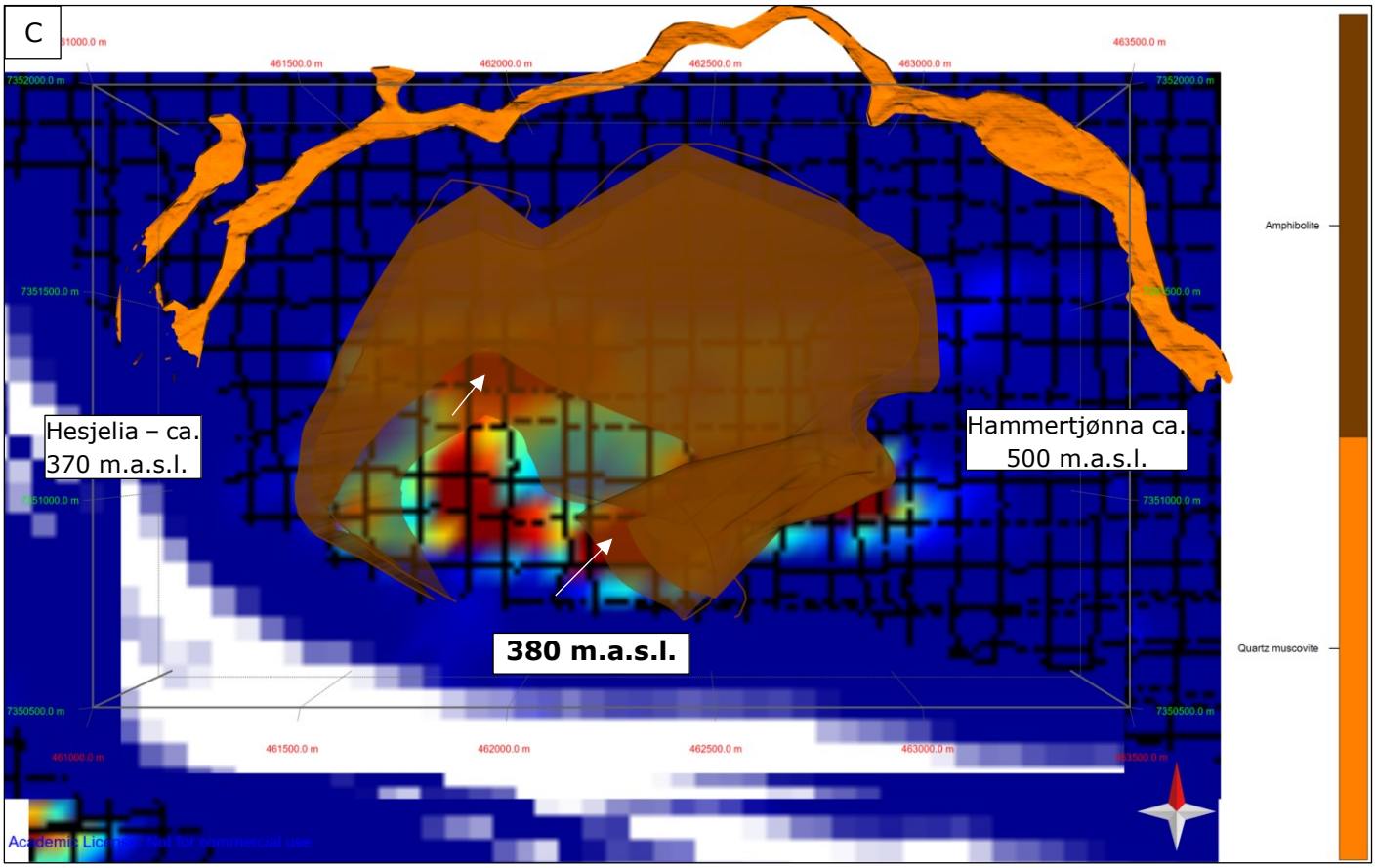
C
Hesjelia – ca. 370 m.a.s.l.
Hammertjønna ca. 500 m.a.s.l.
380 m.a.s.l.
Amphibolite
Quartz muscovite

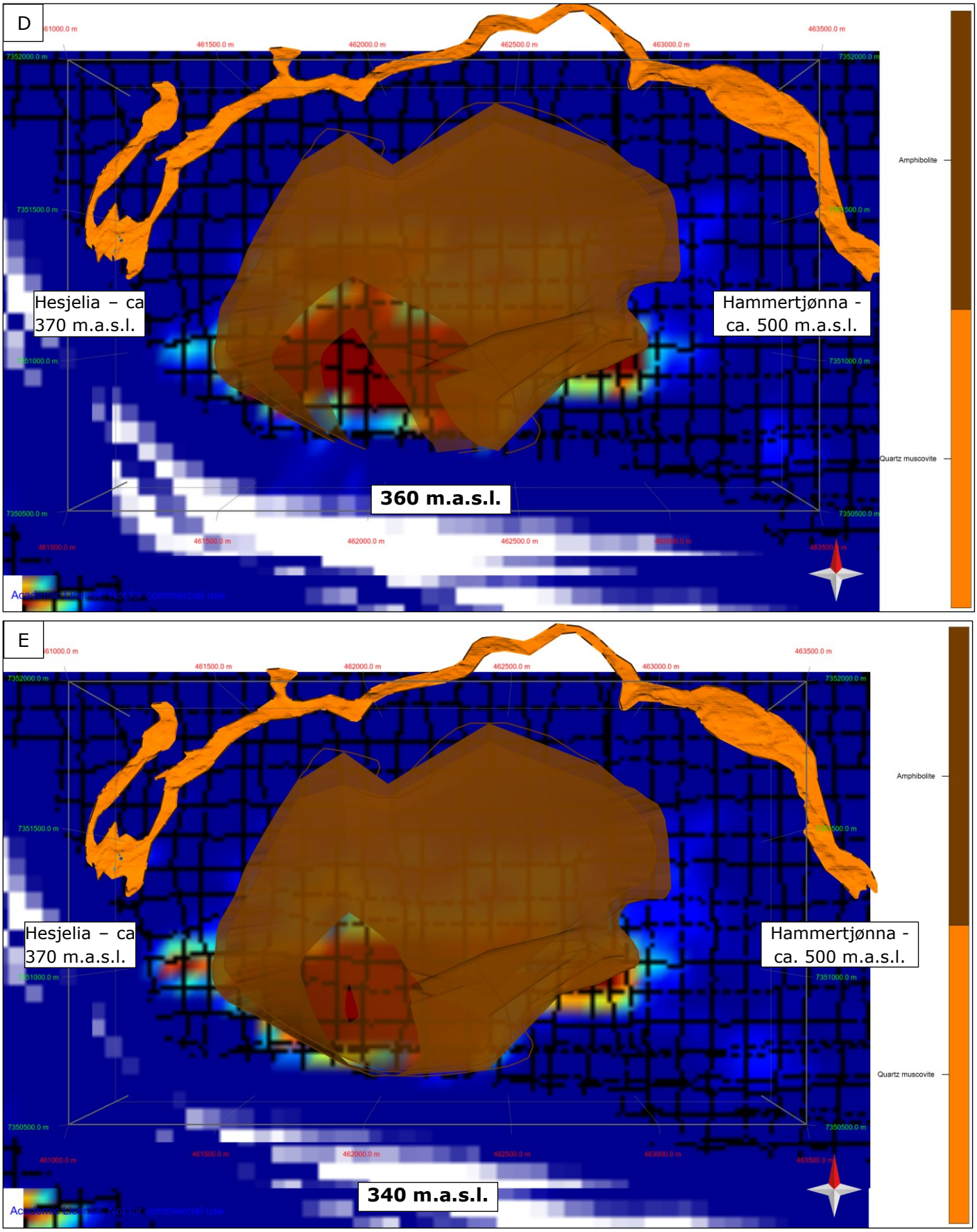

Figure 5.18: Correlation between the TEM-anomaly and the amphibolite schist unit between 420 and 340 m above sea level. Hesjelia and Hammertjønna is at ca 370 and 500 m.a.s.l. A) 420 m. B) 400 m. C) 380 m. D) 360 m. E) 340 m.

The QMS unit

The QMS unit hosting is compared to the anomaly between 340 and 260 m a.s.l., whereof it overlaps to a large degree at 320 and 300 m a.s.l. (Figure 5.19). This suggest that the QMS unit can be correlated to an anomalous signal, which most likely derive from the ore zone within the unit. However, the signal is generally no more than 0.06-0.08 S/m, which is low compared to a VMS deposit, but is normal for alteration zones (Ford et al., 2007).

If the 3D-model of the ore zone's geometry deviates from the actual geometry the muscovite schist unit could be used as a proxy for a correlation between the ore zone and the anomaly, since the ore always will be within the muscovite schist unit. The rest of the correlated layers can be found in Appendix A

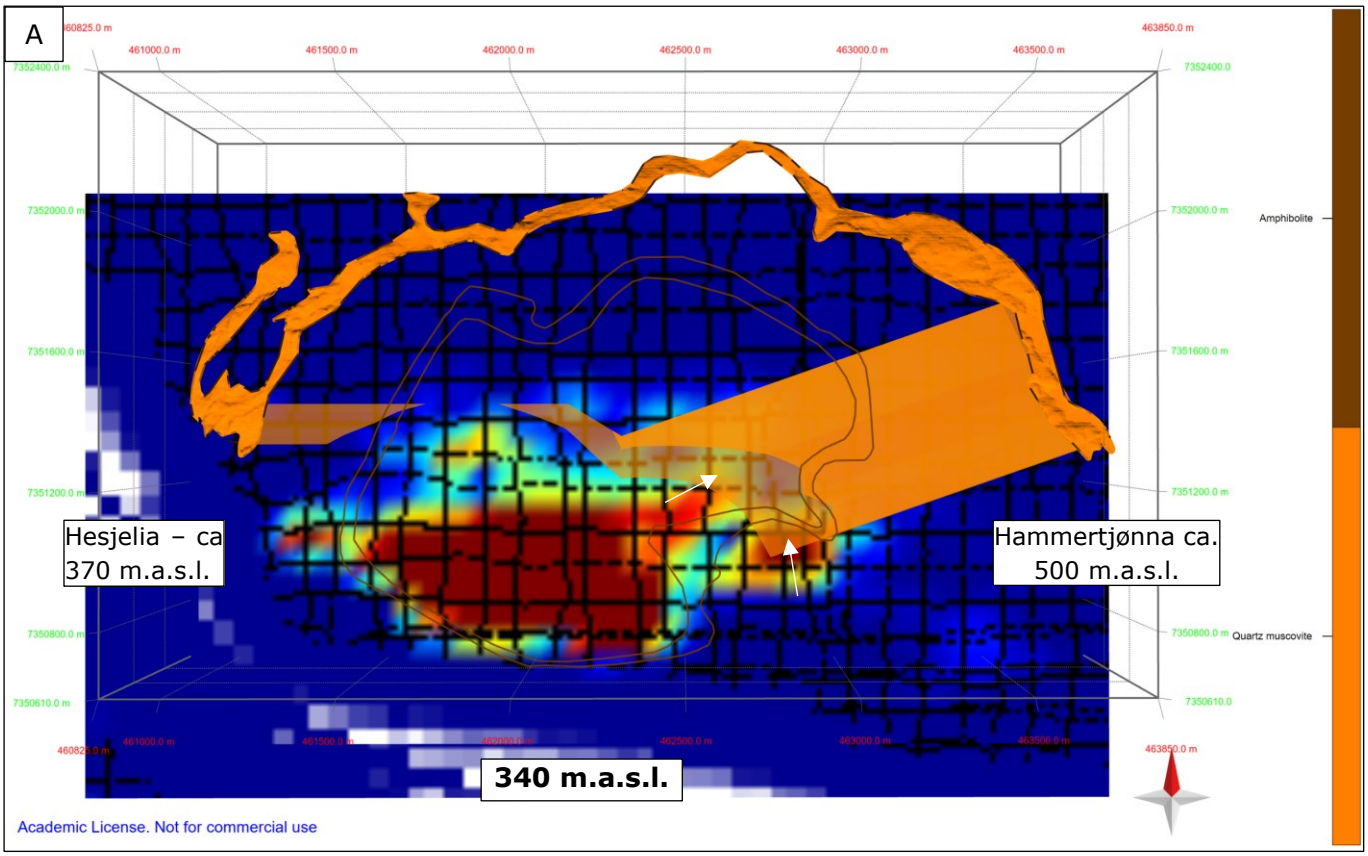

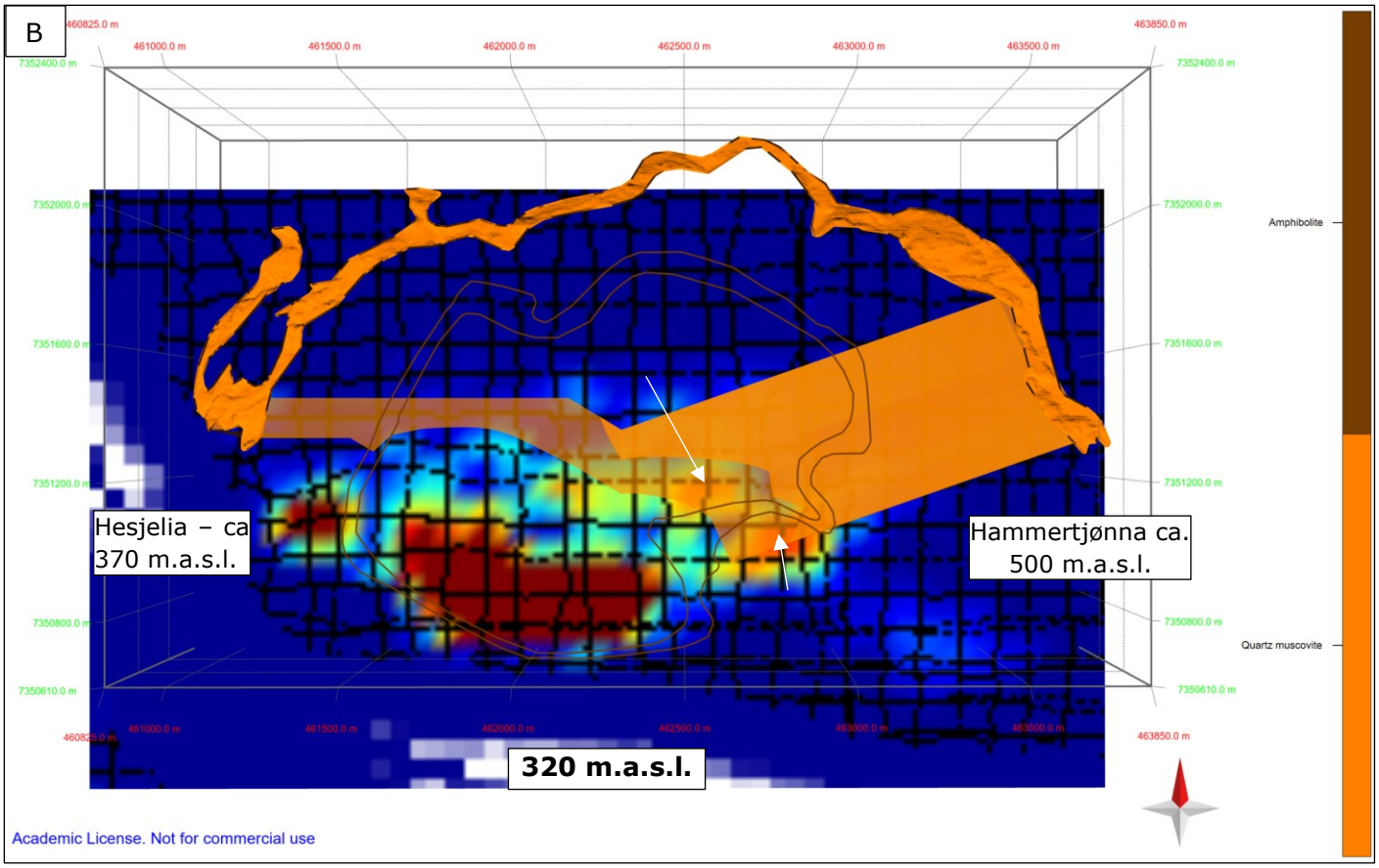
B
Hesjelia – ca 370 m.a.s.l.
Hammertjønna ca. 500 m.a.s.l.
320 m.a.s.l.
Amphibolite
Quartz muscovite
Academic License. Not for commercial use

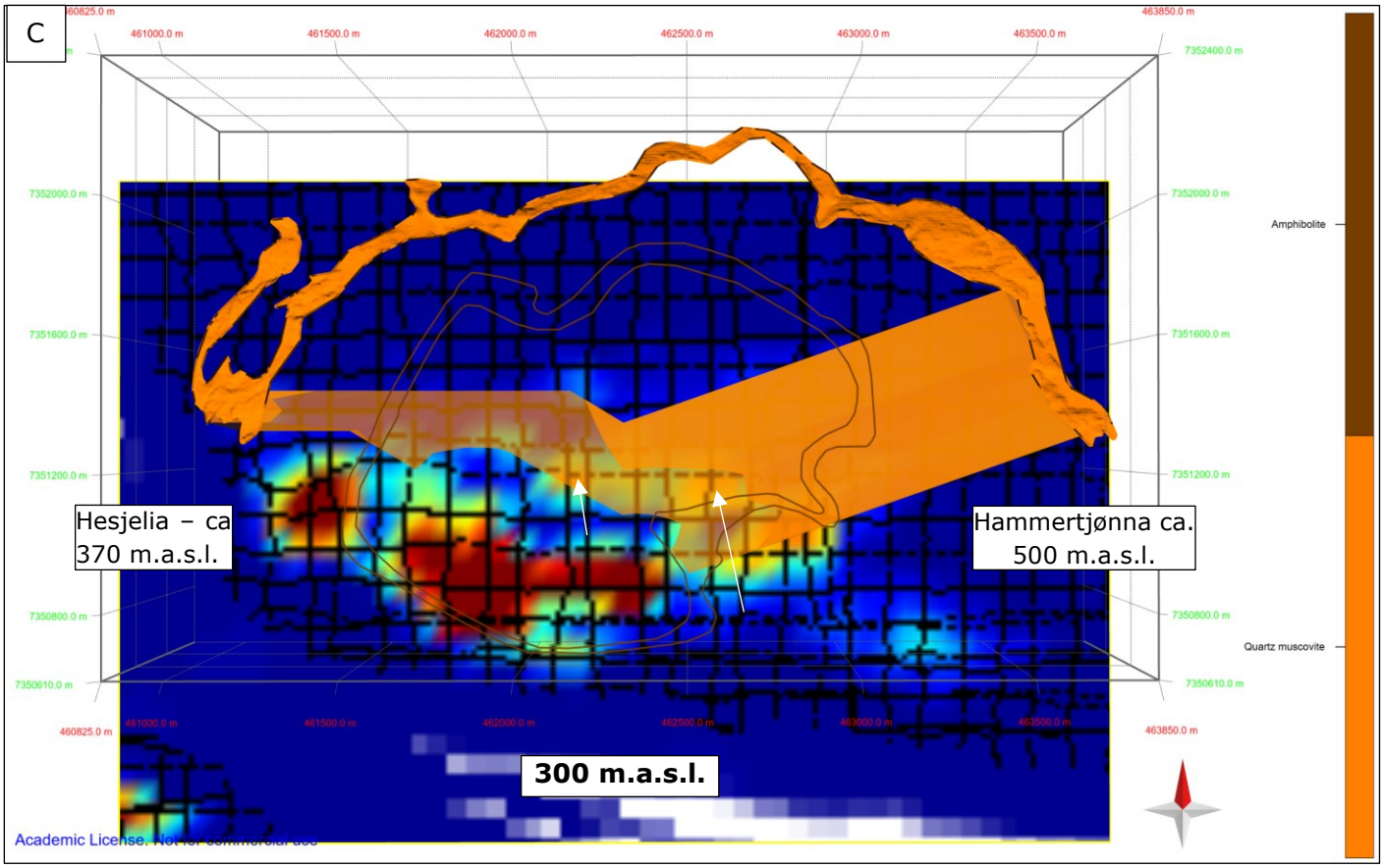
C
Hesjelia – ca 370 m.a.s.l.
Hammertjønna ca. 500 m.a.s.l.
300 m.a.s.l.
Amphibolite
Quartz muscovite
Academic License. Not for commercial use

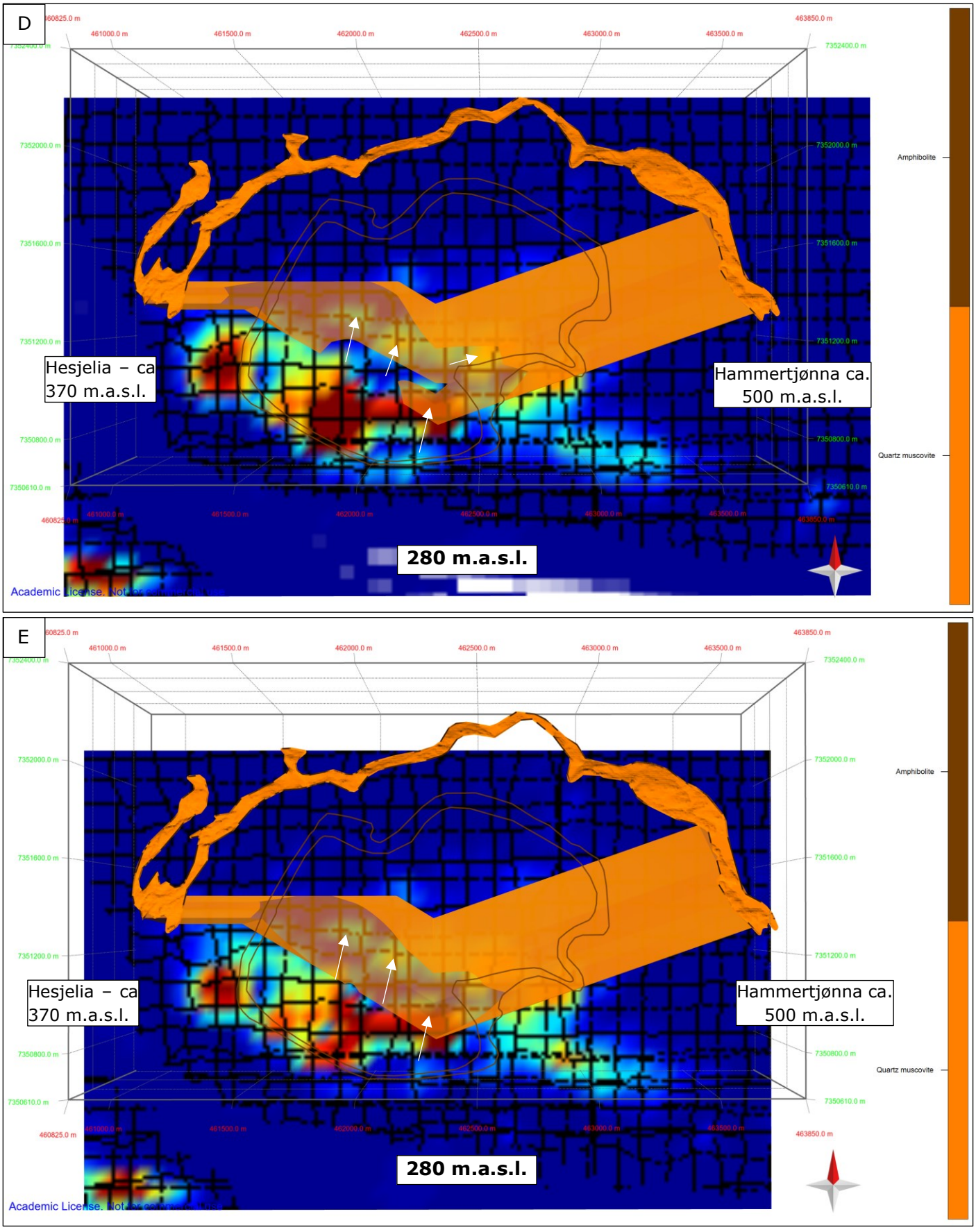

Figure 5.19: TEM-anomaly and muscovite schist correlation between 340 and 300 m above sea level. The overlap is largest in C and D. A) 340 m. B) 320 m. C) 300 m. D) 280 m. E) 260 m.

The ore zone

The ore zone and the anomaly overlap in the east-central segment between 360 and 300 m.a.s.l., with the largest overlap at 320-300 m, comparable to the QMS (Figure 5.20). Zone 5 overlap with the highest anomaly, being around 0.08 S/m. However, the anomaly does not follow this zone or any of the other zones systematically downwards. The remainder levels correlated with TEM can be found in Appendix A.

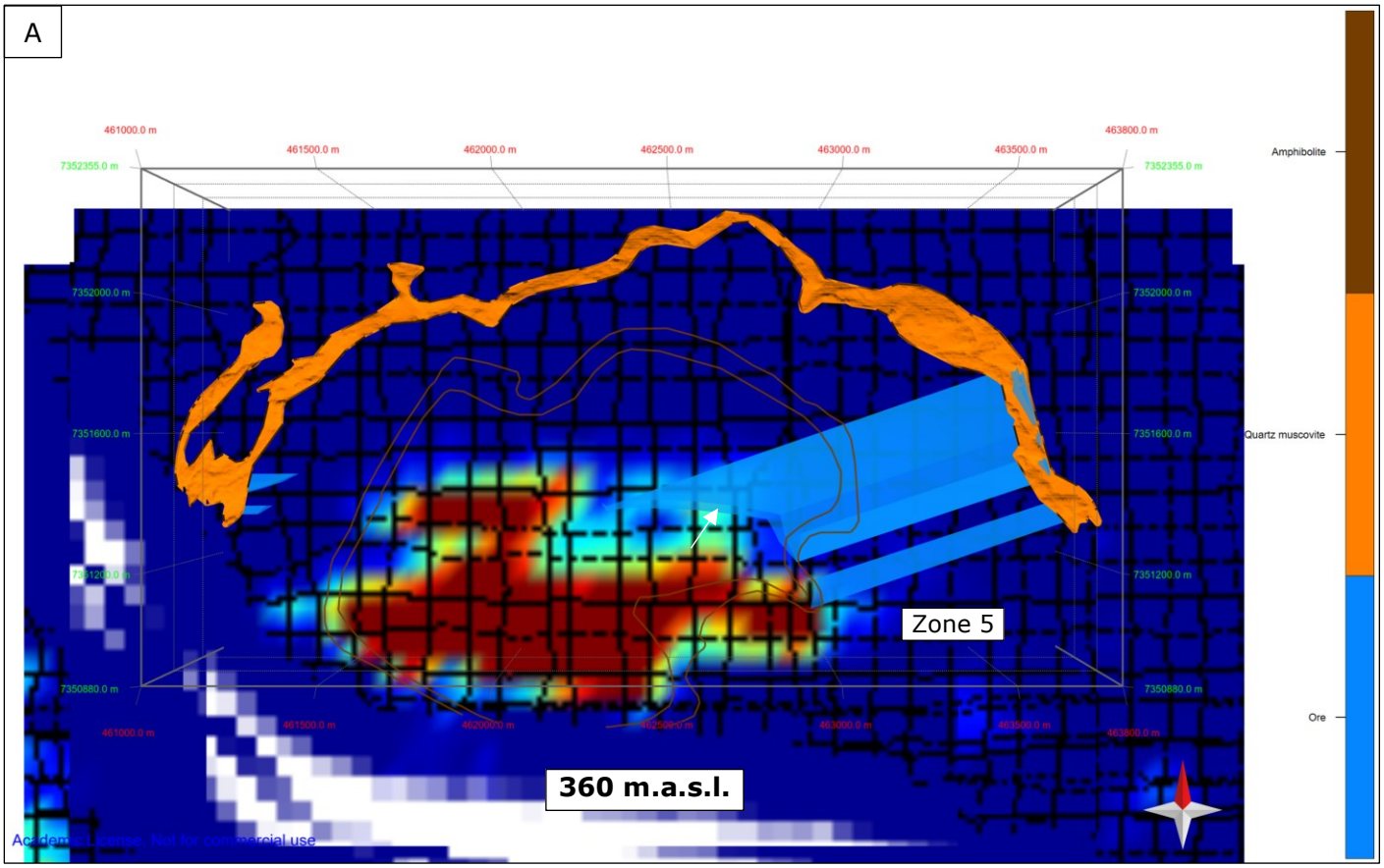

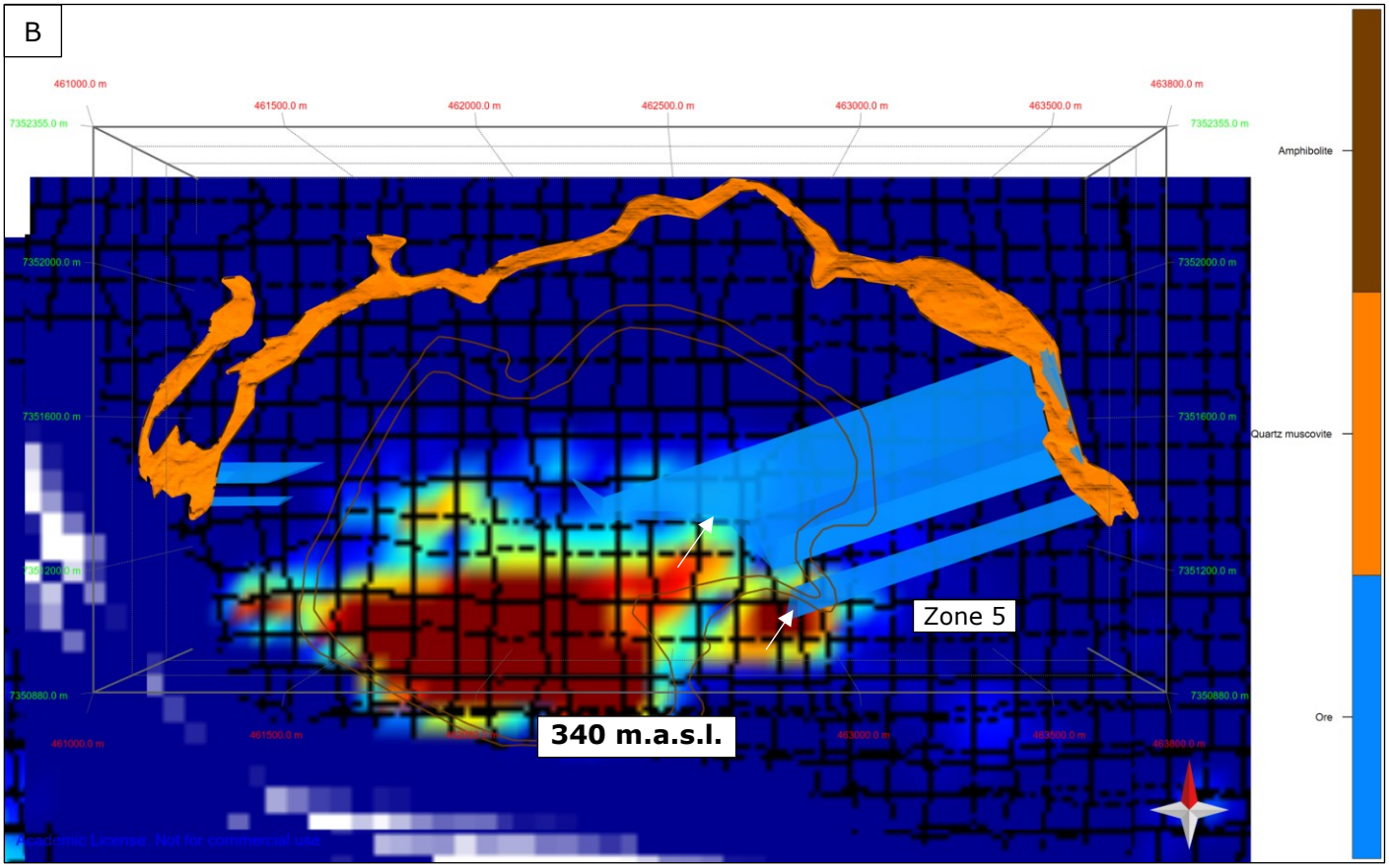

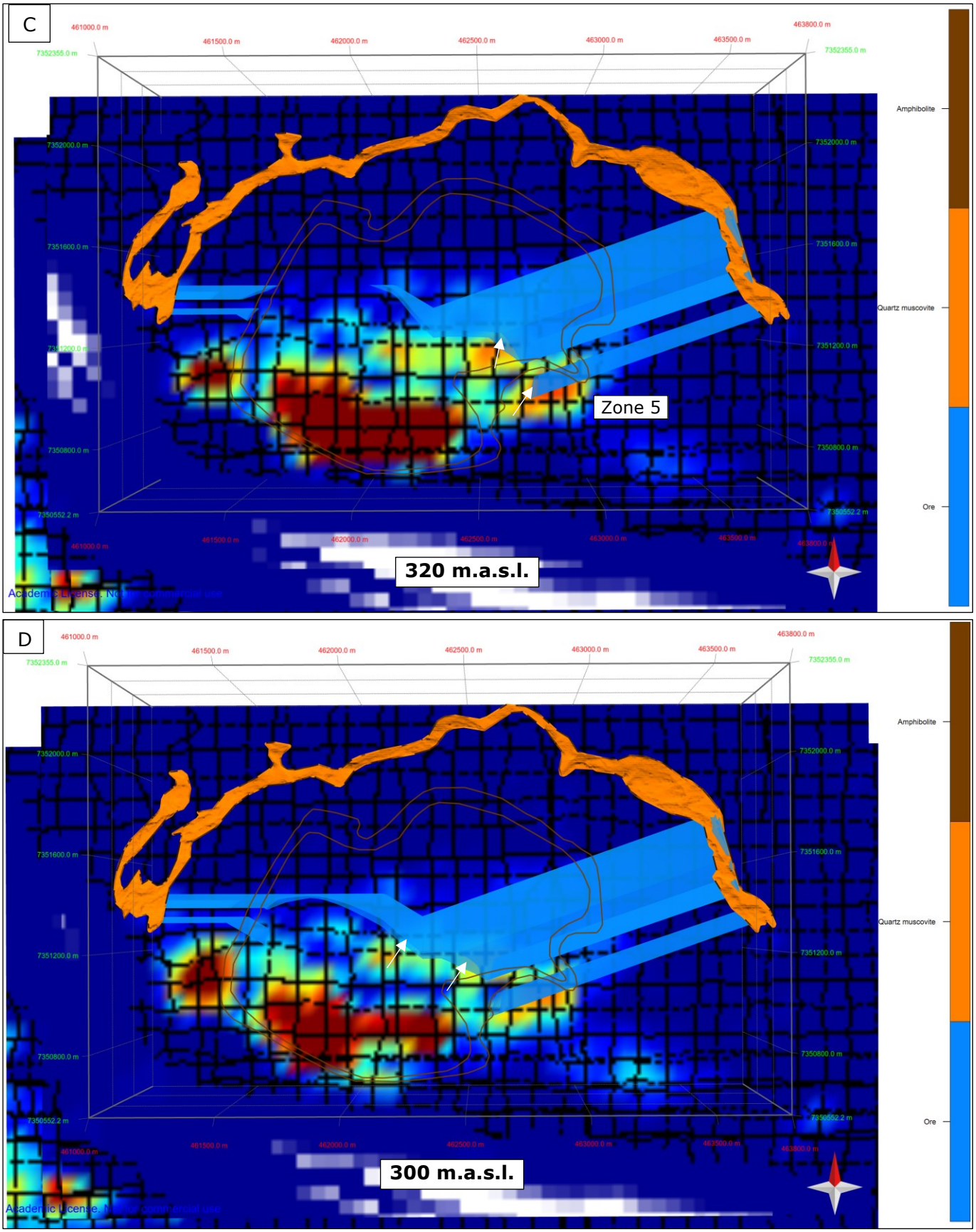

Figure 5.20: TEM-anomaly and ore correlation between 360 and 320 m above sea level. A) 360 m. B) 340 m. C) 320 m. D) 300 m.

As seen through the figures above, the amphibolite unit is the best explanation for the largest and highest anomalous area above 340 m. Below this and until 300 m, the ore hosting QMS unit correlates with the weaker centre-easterly area of the anomaly, which is probably produced by the ore zone. Nevertheless, the anomaly is interesting independent of which rock unit is causing it and should be investigated further by drilling.

5.4.4 Hellerfjellet

At Hellerfjellet there is a total of 21 smaller and larger prospects, scattered over an NNE-SSW length of ca. 210 m, with varying grades and thicknesses of sulphide mineralizations (Figure 5.21). The prospected mineralizations are located at the southern limb of an open F_3-fold with an westerly plunging fold axis, according to the map of Marker et al. (2012). Because they systematically occur along strike only 11 of them are used in the model, mainly the larger ones. As the TEM-data from Hellerfjellet is easier to correlate with the ore deposit, more focus will be devoted to this compared to Hesjelia-Hammertjønna. As in Hesjelia-Hammertjønna the 2D-sections form the basis of the 3D-model and is oriented according to the average azimuth of the F_2-fold axis, in this case 103°, in the area covered by the sections. The final 3D-model is illustrated in Figure 5.27 along with the adjacent geological units and drill core BH4508.

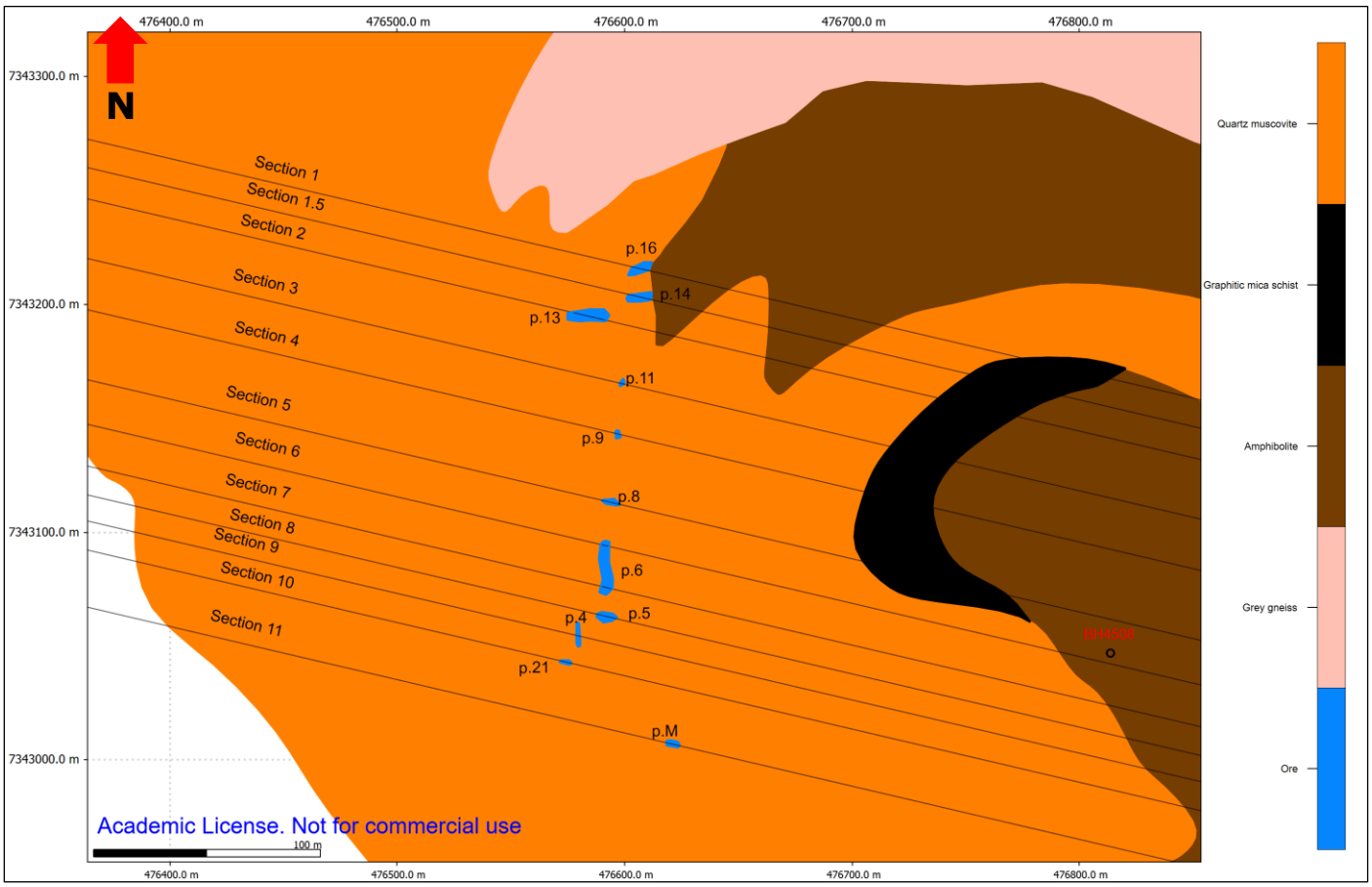

Figure 5.21: 2D-map of the 11 prospects and the 12 sections (black lines) used in the 3D-modelling. Because of the size of prospect 6 two sections are used to extrapolate it. Drill core BH4508 is also plotted.

TEM-interpretation

As seen in of the elevation maps in Figure 5.22, the TEM anomaly at Hellerfjellet does not reach the same magnitude as in Hesjelia-Hammertjønna, and range between 0.04 and 0.06 S/m. This is contrary to the expectations because of the graphite-content in the host rock, and generally high grades of sulphides in the prospects with > 10 % Cu + Zn + Pb + Ag (see Appendix C Table 8.3 and Table 8.8). The anomaly is modelled into a 3D-TEM model by drawing horizons around the areas of the highest anomalies. The modelled depth is from 940 to 660 m.a.s.l., and in Figure 5.22 layer 940 to 840 m.a.s.l. are shown as an example. The outcropping ore/prospects are coloured red for visibility against the blue background, and the contacts of the rock units are visualized for reference. The TEM anomaly has four distinct peaks at 940-920 m.a.s.l, with weakly anomalous areas in between (Fig. 19). The peaks occur over a length of ca. 980 m along strike at this level, which is longer than the length covered by the prospects and may indicate that the mineralized zone is continuing south-east. From 920 m a.s.l. and downwards the four peaks grade into two broader peaks, yet covering a smaller area that remains to the modelled level of 660 m above sea level. Beyond 720 m.a.s.l. the anomaly changes little which may indicate a loss of signal (see Appendix A). The modelled ore structure deviates from the TEM anomaly from this level. Only the northernmost peaks are modelled and correlated to the prospected mineralization.

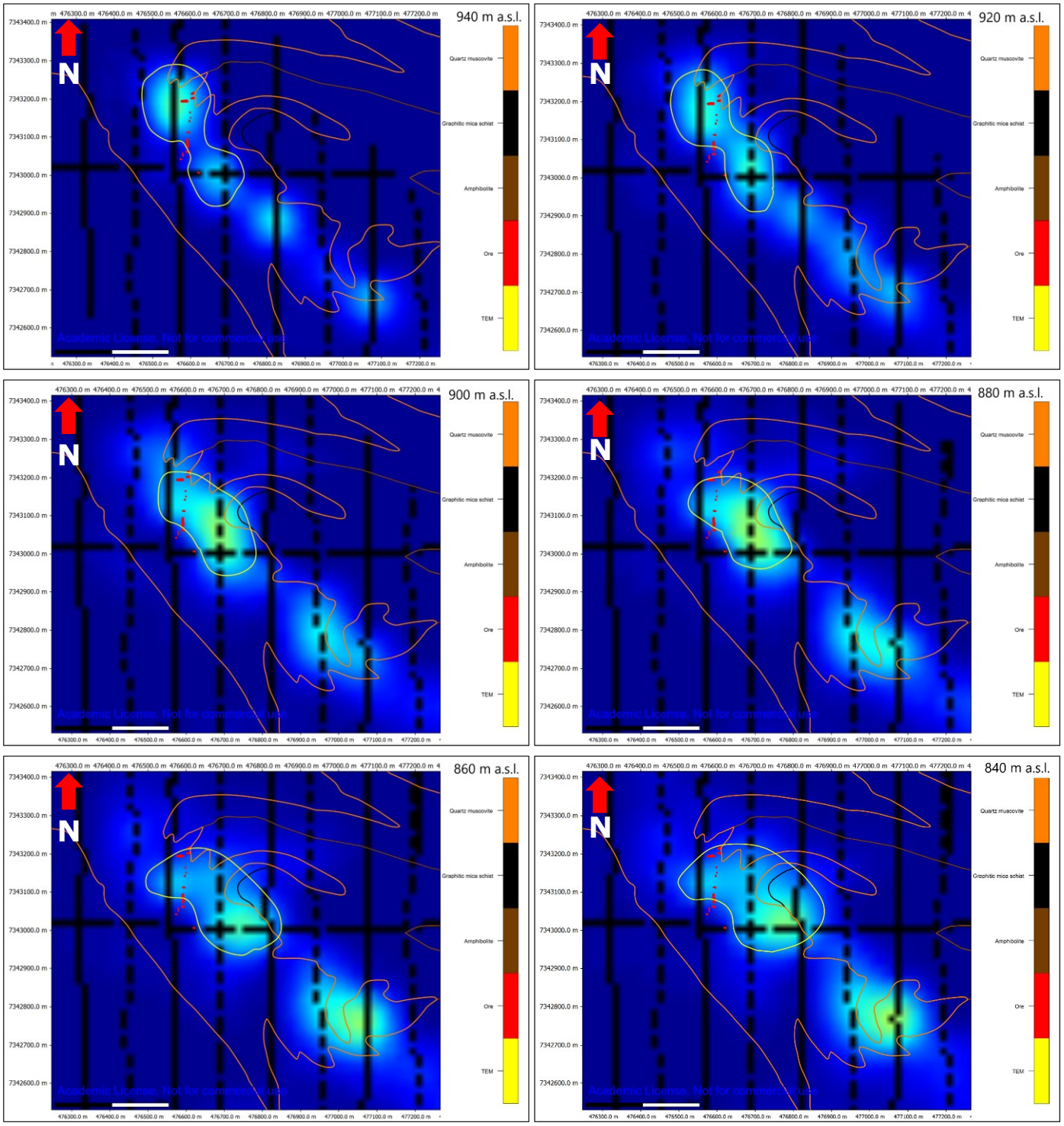

Figure 5.22: Some of the TEM maps that are used to make the 3D-TEM model. The yellow lines are drawn around the anomalous peaks for each 20 m-level between 940 and 840 m a.s.l. and form the basis of the 3D-TEM-model. For reference, the prospects/mineralizations are visualised together with the ore hosting quartz muscovite schist unit.

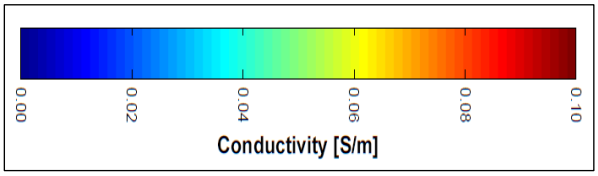

Figure 5.23: Conductivity bar for reference (siemens per meter, S/m).

3D-model

The 3D-model of the anomaly shows a steeply dipping rod-like structure (Figure 5.25). The outer border of the anomaly is interpreted as the upper contact of the conductive graphitic muscovite schist that host the ore deposit, illustrated by "section 7" in Figure 5.24. Both the TEM-anomaly and drill core BH4508 indicates that the ore plunge steeper than the average F_2 fold axis plunge of 15.95°, whereas the trend is consistent with the anomaly. The drill core intercepts an enriched zone at 110-138.5 m where stripes of sulphides alternate with graphitic muscovite schist. The richest 6 m-interval is, according to handheld XRF, 115-121 m (see Appendix G Table 8.23-Table 8.27), and the dip angle between this depth-level and prospect 6, which is interpreted as the corresponding mineralization at the surface, is 37.5°. Thus, if the ore deposit follows the F_2 fold axis it must have a variable plunge towards the depth, that is on average steeper than the measured plunge at the surface. Geologically, this can be explained by parasitic folds on the F_4 folds, caused by the low competence of the enclosing GQG unit. As seen in Figure 5.24, the eastern border of the TEM anomaly has a variable plunge, indicating a folded structure. The drill core is oriented 70°→247° and, as seen in Figure 5.26, intercepts the mineralization barely outside the extrapolated edge of the massive lens in prospect 6.

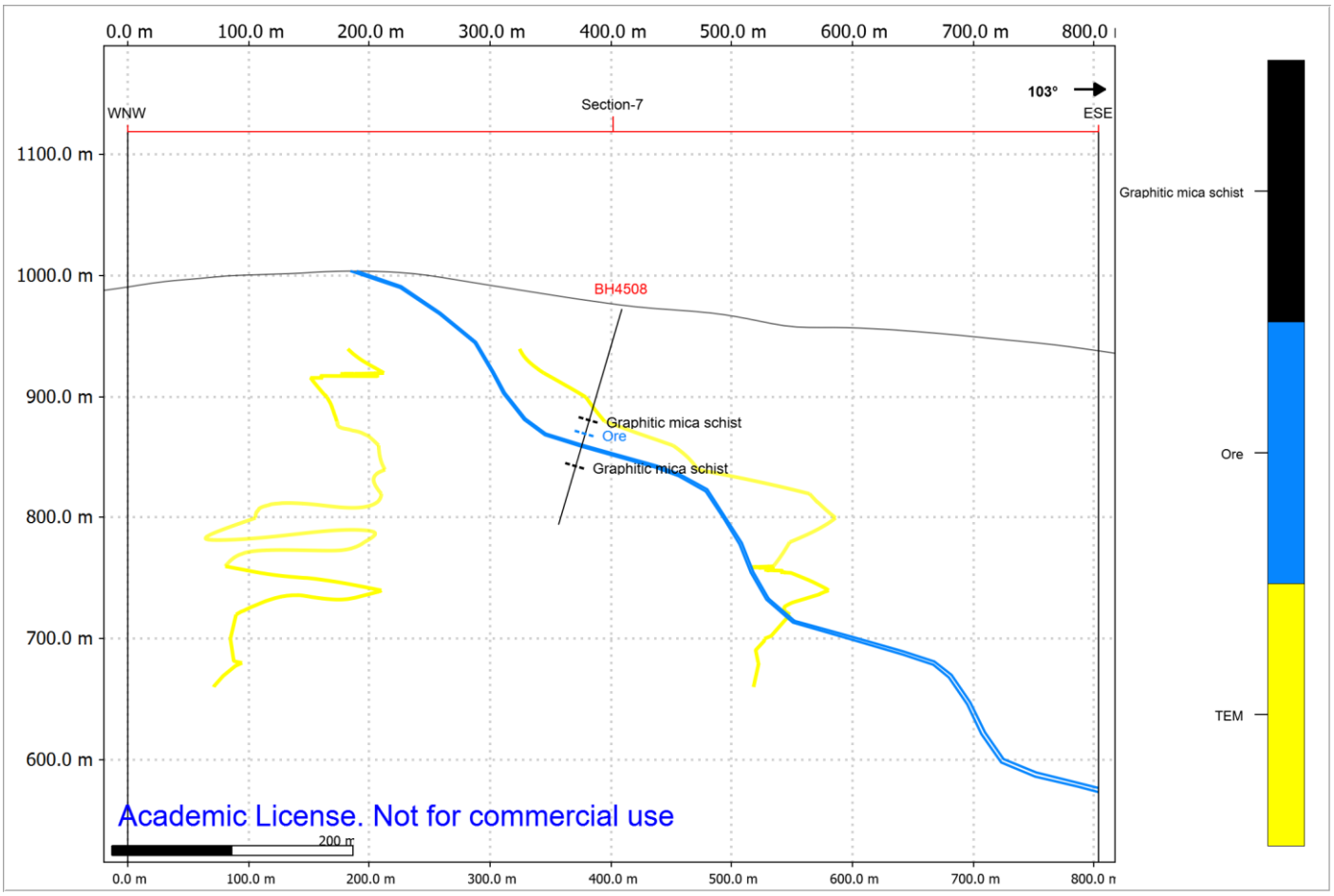

Figure 5.24: Section 7 from which prospect 6 is extrapolated intersects the richest part of the drill core. The prospect has a thickness of ca. 2 m. Markers on the drill core indicate contacts.

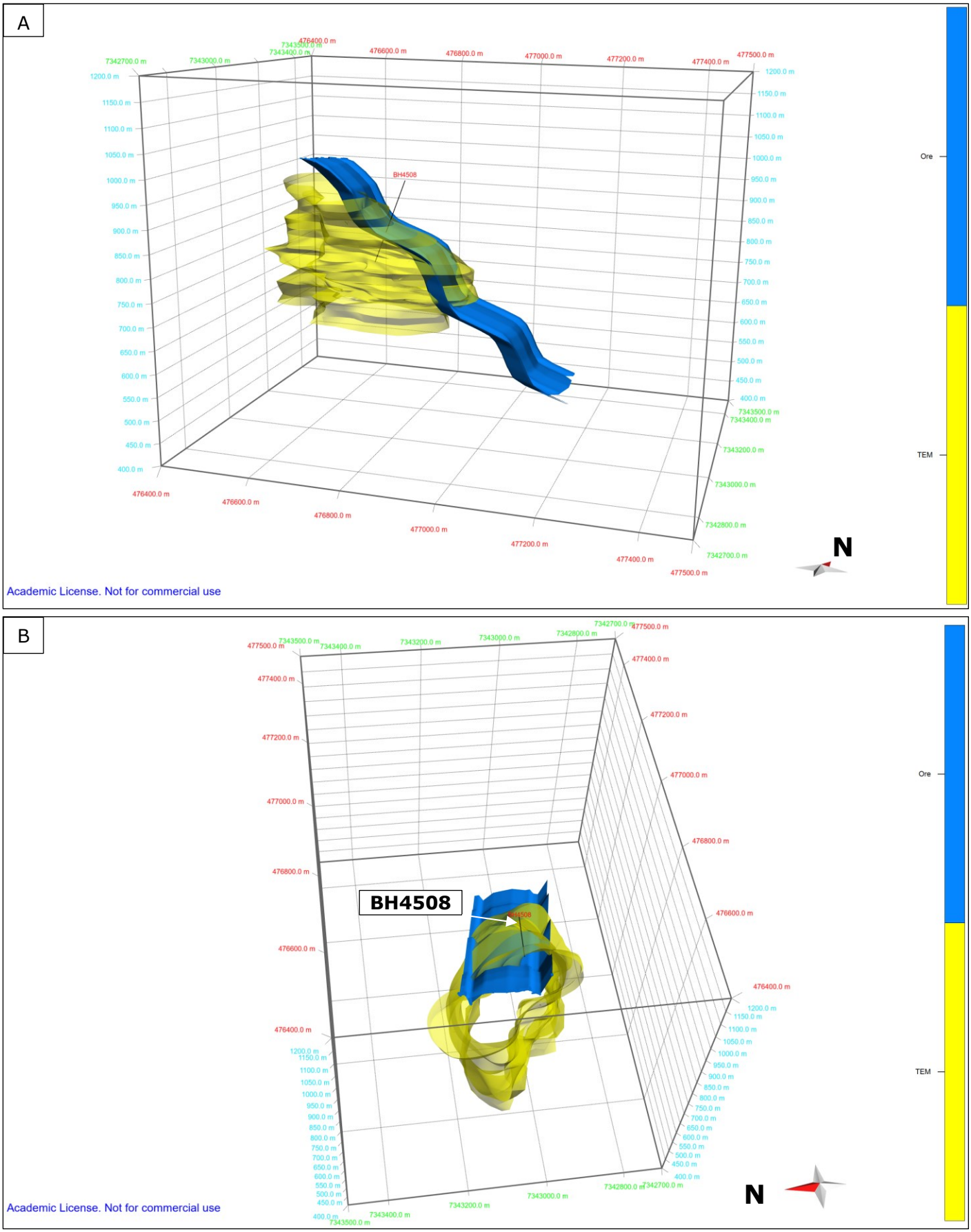

Figure 5.25: TEM/ore-correlation. A) Perspective from the south. B) Looking down plunge of the ore zone.

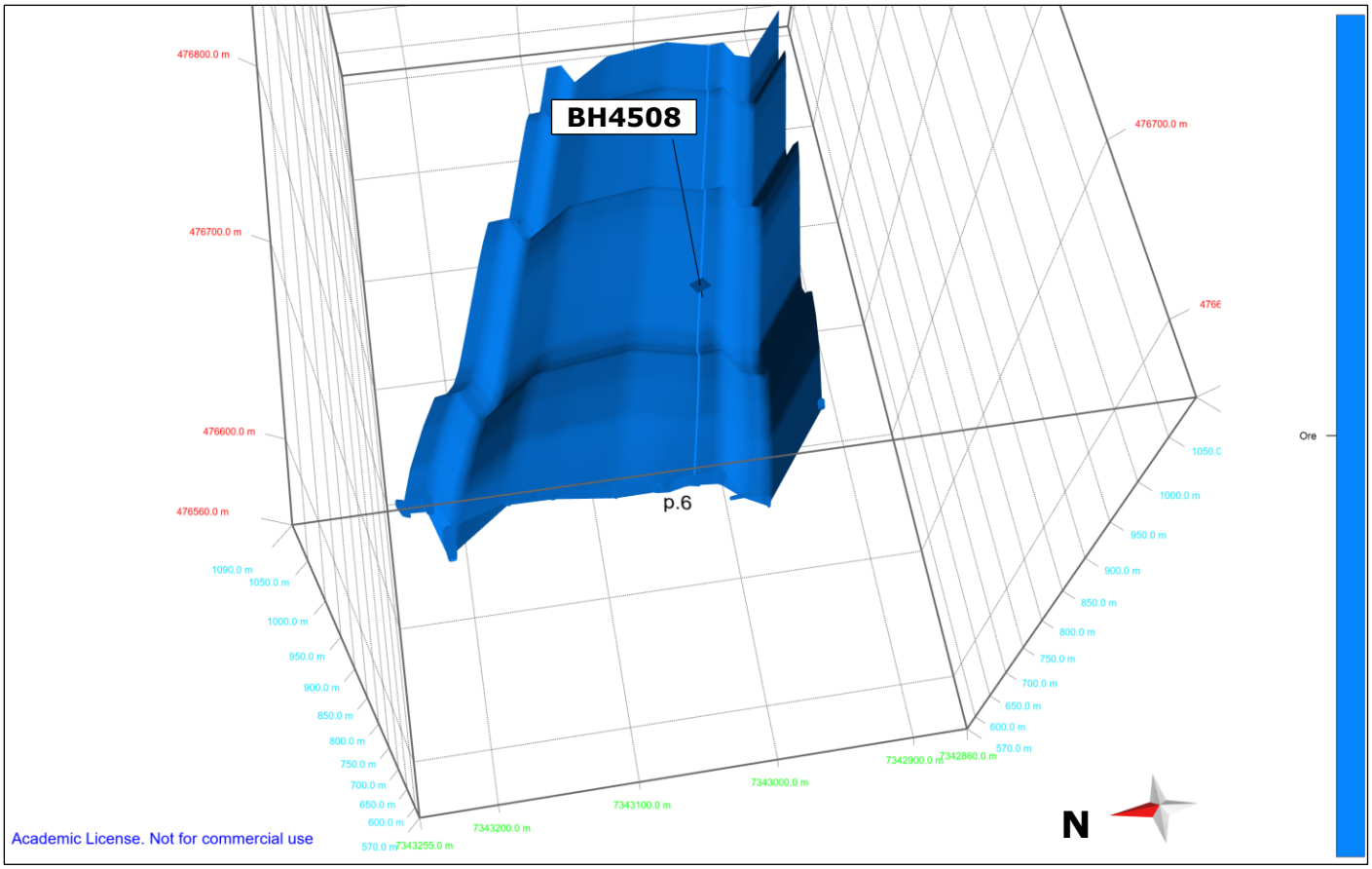

Figure 5.26: Correlation of the drill core with the model. The bold blue line is the extrapolation of the edge of prospect 6 corresponding to section 7. The blue rectangle on the drill core marks the start of the intersection at 110 m.

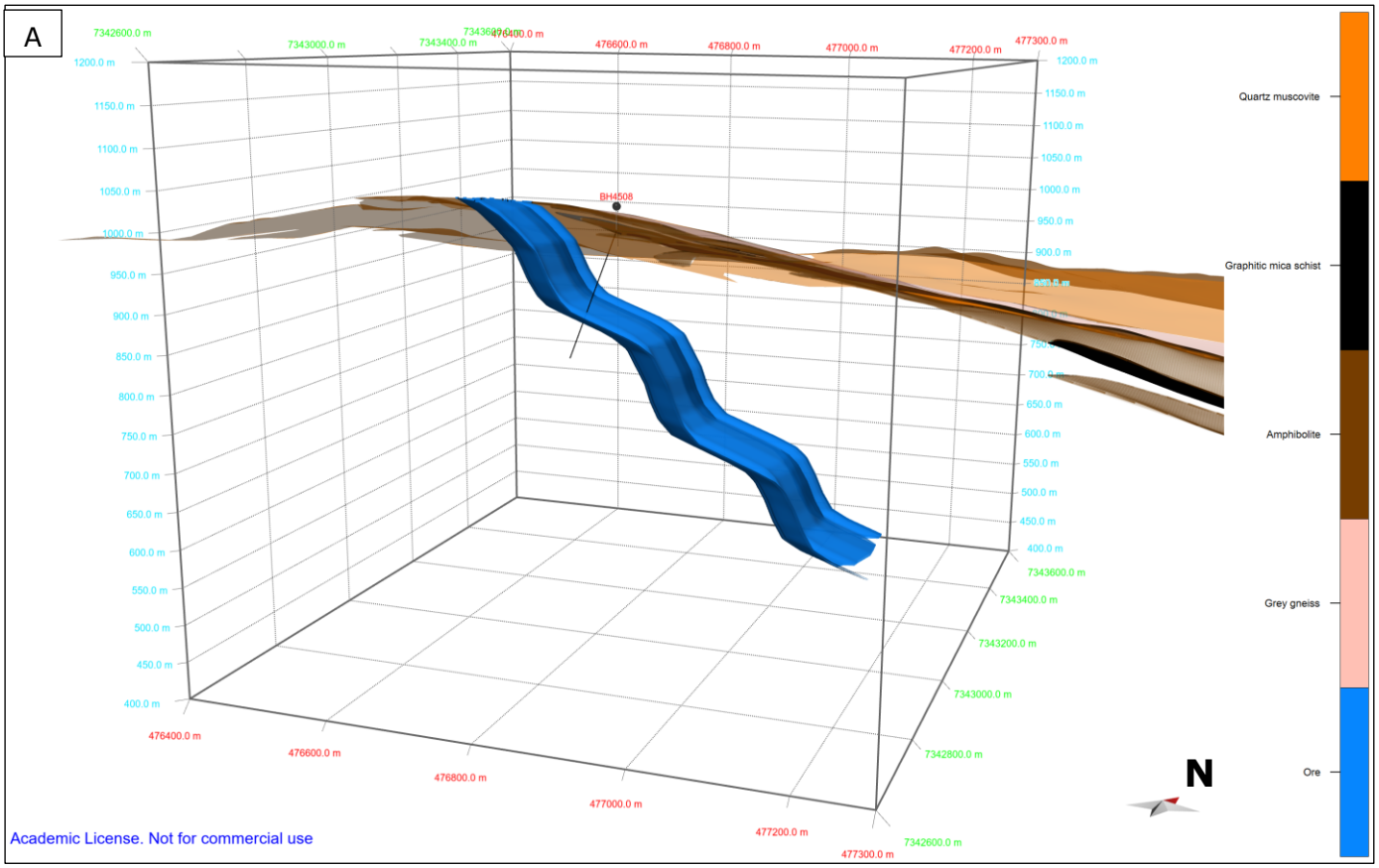

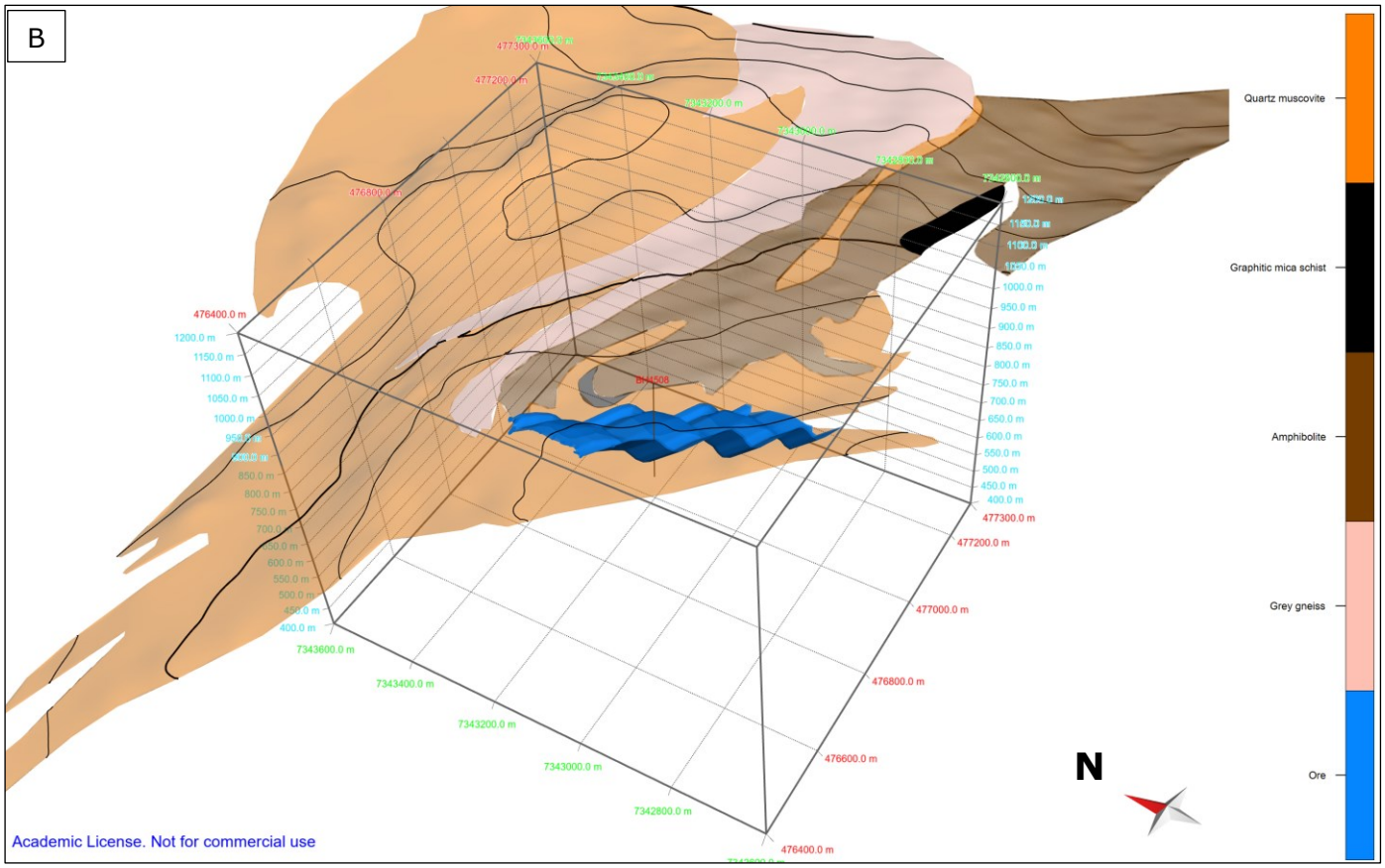

Figure 5.27: The ore deposit at Hellerfjellet modelled to a depth of ca. 570 m above sea level. The adjacent rock units and drill core BH4508 are also visualised for reference. Perspective from A) southeast and B) south west and above.

6 Conclusion

This study concludes that the Mofjellet Group were formed at 499 ± 12 Ma within an island arc setting at the margin of a continent, based on the high proportion of calc-alkaline LREE/LILE enriched felsic rocks, whose nature is peraluminous, and probably reflect crustal contamination through assimilation. The felsic predominance is also reflected by the sphalerite-rich ore deposits throughout the group, which is a typical feature of felsic dominated lithologies of the FII category, comparable to the Kuroko deposit in Japan. The small tholeiitic trend of the amphibolites probably reflect early volcanism, where the composition was similar to NMORB, reflected by the positive curve in the chondrite-normalized diagram. The major part of the amphibolites show a calc-alkaline trend towards the felsic rocks due to a magma being enriched in fluids from the subducting slab. Both rock types show a depleted peridotite signature, thus suggesting a common source of magma, despite later influence of continental crust in the felsic rocks. The QMS and GQG unit is mainly related to the felsic volcanic rocks, however, due to the volcaniclastic nature of the QMS/GQG at Hellerfjellet, a mafic component has also contributed.

The metamorphic and deformational history is closely related, the latter of which is divided into four folding phases. F_1 produced a transposed layering evident from the discontinuous quartz layers and rootless folds. Metamorphic fabrics from this phase is limited to muscovite grains in the hinge zone of the subsequent F_2 phase, the latter of which formed the main S_2 foliation by tight to isoclinal folding around an E-W oriented fold axis. Peak metamorphic conditions were reached during this phase, probably even higher than ca. 600 °C and 10 kbar, which was enough to remobilize sphalerite and galena that consequently concentrated in the hinge zone of F_2 folds. Based on textural relationships and comparison of mineral assemblages in the matrix and in porphyroblasts of garnet and zoisite, F_2 was followed by a retrogressive event, whose areal extent is unknown. The subsequent F_3 phase produced coaxial open folds and resulted in regrowth of titanite and garnet, the latter of which has been dated to 465 ± 21 Ma. This age is familiar with the Taconian orogeny on the Laurentian side of Iapetus (Prave et al., 2000), and supports the increasing evidence of pre-Scandian deformation in the Uppermost Allochthon of the Scandinavian Caledonides. The latter produced the F_4 open folds with NE-SW oriented fold axes, and were succeeded by an extensional phase, evident by boudinaged subhorizontal- and folded subvertical pegmatite intrusions.

The geometry of the ore deposits is mainly controlled by the F_2 fold axis, however, interference between F_3 and F_4 shaped the Hesjelia-Hammertjønna deposit into a basin structure, causing the F_2 fold axes to have opposite polarity on the western (Hesjelia) and eastern (Hammertjønna) side. Zone 1, 2 and 4 in Hesjelia probably converge and conjoin towards Hammertjønna, due to a smaller interlimb angle of the major south-closing fold structure (Marker, 1983), caused by higher strain. The Hellerfjellet deposit is located at the limb of an F_4 fold and are affected by parasitic folds due to the lower competence of the enclosing GQG unit, causing a variable easterly plunge of the ore deposit.

Recommendations for future work

In order to fully understand the ore deposits in both Hesjelia-Hammertjønna and Hellerfjellet more drilling is needed. This will constrain the 3D geometry further and possibly reveal more massive mineralizations than existing drill holes have intersected, especially at Hesjelia-Hammertjønna. Here, the drill hole is found to be offset of the fold

axis, and thus misses the richest ore. As inferred from this study, the south-eastern area of Hesjelia-Hammertjønna wherein the TEM anomaly overlaps with the 3D-model, is an interesting target. The anomaly caused by the amphibolite unit should also be investigated, based on the large and highly anomalous area. At Hellerfjellet, a line of drill holes going ca. N-S from the existing drill core will provide more answers to the extent of this deposit and may intersect richer ore, based on the findings here. Also, the new mineralized zones north of Hellerfjelltjønna should be investigated further, based on the high grades and extensive occurrence of sphalerite-rich bands.

When it comes to the regional geology the deformational phases must be constrained by dating of the shear zones that exist within the Mofjellet Group. More sampling from a broader area within the group is necessary to reveal more about the retrograde phase observed here, and possibly further constrain it by titanite and/or zircon dating (if syn-tectonic intrusions exist). The tectonic origin of the Mofjellet Group can be further constrained by isotope data, and should be included in a regional investigation.

7 References

ALEINIKOFF, J. N., WINTSCH, R. P., TOLLO, R. P., UNRUH, D. M., FANNING, C. M. & SCHMITZ, M. D. 2007. Ages and origins of rocks of the Killingworth dome, south-central Connecticut: Implications for the tectonic evolution of southern New England. *American Journal of Science,* 307**,** 63-118.

APTED, M. J. & LIOU, J. 1983. Phase relations among greenschist, epidote-amphibolite, and amphibolite in a basaltic system. *American Journal of Science,* 283**,** 328-354.

BAU, M. 1991. Rare-earth element mobility during hydrothermal and metamorphic fluid-rock interaction and the significance of the oxidation state of europium. *Chemical Geology,* 93**,** 219-230.

BENDER, H., GLODNY, J. & RING, U. 2019. Absolute timing of Caledonian orogenic wedge assembly, Central Sweden, constrained by Rb–Sr multi-mineral isochron data. *Lithos,* 344**,** 339-359.

BERGSTRÖM, J. & GEE, D. G. 1985. The Cambrian in Scandinavia. *In:* GEE, D. G. & STURT, B. A. (eds.) *The Caledonide orogen : Scandinavia and related areas : 1.* Chichester: Wiley.

BEST, M. G. 2003. *Igneous and metamorphic petrology,* Malden, MA, Blackwell.

BJERKGÅRD, T. & HALLBERG, A. 2012. N028 Rana-Hemnes Zn-Pb-Cu. *In:* EILU, P. (ed.) *Mineral deposits and metallogeny of Fennoscandia.* Geological Survey of Finland, Special Paper 53, pp. 100-102.

BJERKGÅRD, T., MARKER, M., SLAGSTAD, T. & SOLLI, A. 2013a. Geology and massive sulfide deposits in the Mofjell Group in the Rödingsfjället Nappe Complex, Nordland, Norway. *SGA.*

BJERKGÅRD, T., MARKER, M., SLAGSTAD, T. & SOLLI, A. 2013b. The Mofjell Project: Summary and conclusions. NGU Report 2013.048. Geological Survey of Norway.

BJERKGÅRD, T., SLAGSTAD, T., SOLLI, A. & MOGENS, M. 2009. Mofjell-prosjektet: Statusrapport pr. juni 2009. Geological Survey of Norway.

BOWEN, N. L. 1928. *The evolution of the igneous rocks,* Princeton, Princeton University press.

BRUNSMANN, FRANZ, ERZINGER & LANDWEHR 2000. Zoisite- and clinozoisite-segregations in metabasites (Tauern Window, Austria) as evidence for high-pressure fluid–rock interaction. *Journal of Metamorphic Geology,* 18**,** 1-21.

BRUNSMANN, A., FRANZ, G. & HEINRICH, W. 2002. Experimental investigation of zoisite–clinozoisite phase equilibria in the system CaO–Fe 2 O 3–Al 2 O 3–SiO 2–H 2 O. *Contributions to Mineralogy and Petrology,* 143**,** 115-130.

BUCHER, K. & GRAPES, R. 2011. *Petrogenesis of Metamorphic Rocks,* Berlin, Heidelberg, Berlin, Heidelberg: Springer Berlin Heidelberg.

CAMPBELL, I., FRANKLIN, J., GORTON, M., HART, T. & SCOTT, S. 1981. The role of subvolcanic sills in the generation of massive sulfide deposits. *Economic Geology,* 76**,** 2248-2253.

COCKS, L. R. M. & TORSVIK, T. H. 2005. Baltica from the late Precambrian to mid-Palaeozoic times: The gain and loss of a terrane's identity. *Earth Science Reviews,* 72**,** 39-66.

CORFU, F., ANDERSEN, T. & GASSER, D. 2015. The Scandinavian Caledonides: main features, conceptual advances and critical questions. *Geological Society London Special Publications,* 390**,** 9-43.

CORFU, F., HANCHAR, J. M., HOSKIN, P. W. O. & KINNY, P. 2003. Atlas of zircon textures. *Reviews in Mineralogy and Geochemistry,* 53.

CORFU, F., ROBERTS, R. J., TORSVIK, T. H., ASHWAL, L. D. & RAMSAY, D. M. 2007. Peri-Gondwanan elements in the Caledonian Nappes of Finnmark, Northern Norway: Implications for the paleogeographic framework of the Scandinavian Caledonides. *American Journal of Science,* 307**,** 434-458.

COX, D. P. & SINGER, D. A. 1986. *Mineral Deposit Models*.

COX, K. G., BELL, J. D., PANKHURST, R. J. & SPRINGERLINK 1979. *The Interpretation of Igneous Rocks,* Dordrecht, Dordrecht: Springer Netherlands.

DEER, W. A., HOWIE, R. A. & ZUSSMAN, J. 1992. *An introduction to the rock-forming minerals,* Harlow, Longman.

DROOP, G. 1987. A general equation for estimating Fe 3+ concentrations in ferromagnesian silicates and oxides from microprobe analyses, using stoichiometric criteria. *Mineralogical magazine,* 51**,** 431-435.

DUNNING, G. & PEDERSEN, R. 1988. U/Pb ages of ophiolites and arc-related plutons of the Norwegian Caledonides: implications for the development of Iapetus. *Contributions to Mineralogy and Petrology,* 98**,** 13-23.

FLOYD, P. A. & WINCHESTER, J. A. 1975. Magma type and tectonic setting discrimination using immobile elements. *Earth and Planetary Science Letters,* 27**,** 211-218.

FORD, K., KEATING, P. & THOMAS, M. 2007. Overview of geophysical signatures associated with Canadian ore deposits. *Mineral deposits of Canada–a synthesis of major deposit-types, district metallogeny, the evolution of geological provinces, and exploration methods: Geological Association of Canada, Mineral Deposits Division, Special Publication,* 5**,** 939-970.

FRANKLIN, J. M. 1993. Volcanic-associated massive sulphide deposits. *In:* KIRKHAM, R. V., SINCLAIR, W. D., THORPE, R. I. & DUKE, J. M. (eds.) *Mineral deposit modeling.* Geological Association of Canada.

FRANKLIN, J. M., GIBSON, H. L., JONASSON, I. R., GALLEY, A. G., HEDENQUIST, J. W., THOMPSON, J. F. H., GOLDFARB, R. J. & RICHARDS, J. P. 2005. Volcanogenic Massive Sulfide Deposits. *One Hundredth Anniversary Volume.* Society of Economic Geologists.

FRANZ, G. & SELVERSTONE, J. 1992. An empirical phase diagram for the clinozoisite-zoisite transformation in the system Ca (sub 2) Al (sub 3) Si (sub 3) O (sub 12) (OH)-Ca (sub 2) Al (sub 2) Fe (super 3+) Si (sub 3) O (sub 12) (OH). *American Mineralogist,* 77**,** 631-642.

FROST, B. R., CHAMBERLAIN, K. R. & SCHUMACHER, J. C. 2001. Sphene (titanite): phase relations and role as a geochronometer. *Chemical geology,* 172**,** 131-148.

FURNES, H., PEDERSEN, R. & STILLMAN, C. 1988. The Leka Opholite Complex, central Norwegian Caledonides: field characteristics and geotectonic significance. *Journal of the Geological Society,* 145**,** 401-412.

GALLEY, A. G., HANNINGTON, M. D. & JONASSON, I. 2007. Volcanogenic massive sulphide deposits. *Mineral deposits of Canada: A synthesis of major deposit-types, district metallogeny, the evolution of geological provinces, and exploration methods: Geological Association of Canada, Mineral Deposits Division, Special Publication,* 5**,** 141-161.

GASSER, D., JEŘÁBEK, P., FABER, C., STÜNITZ, H., MENEGON, L., CORFU, F., ERAMBERT, M. & WHITEHOUSE, M. J. 2015. Behaviour of geochronometers and timing of metamorphic reactions during deformation at lower crustal conditions: phase equilibrium modelling and U–Pb dating of zircon, monazite, rutile and titanite from the Kalak Nappe Complex, northern Norway. *Journal of Metamorphic Geology,* 33**,** 513-534.

GEE, D. G., FOSSEN, H., HENRIKSEN, N. & HIGGINS, A. 2008. From the early Paleozoic platforms of Baltica and Laurentia to the Caledonide orogen of Scandinavia and Greenland. *Episodes,* 31**,** 44-51.

GOLDSCHMIDT, V. M. 1937. The principles of distribution of chemical elements in minerals and rocks. The seventh Hugo Müller Lecture, delivered before the Chemical Society on March 17th, 1937. *Journal of the Chemical Society (Resumed),* 0**,** 655-673.

GORBATSCHEV, R. 1985. Precambrian basement of the Scandinavian Caledonides. *In:* GEE, D. G. & STURT, B. A. (eds.) *The Caledonide orogen : Scandinavia and related areas : 1.* Chichester: Wiley.

GOTTSCHALK, M. 2004. Thermodynamic Properties of Zoisite, Clinozoisite and Epidote. *Reviews in Mineralogy and Geochemistry,* 56**,** 83-124.

GRENNE, T., IHLEN, P. M. & VOKES, F. M. 1999. Scandinavian Caledonide Metallogeny in a plate tectonic perspective. *International Journal of Geology, Mineralogy and Geochemistry of Mineral Deposits,* 34**,** 422-471.

GUSTAVSON, M. & GJELLE, S. 1991. Geologisk kart over Norge, Berggrunnskart Mo i Rana, M 1: 250 000. *Geological Survey of Norway, Trondheim*.

HART, T. R., GIBSON, H. L. & LESHER, C. M. 2004. Trace element geochemistry and petrogenesis of felsic volcanic rocks associated with volcanogenic massive Cu-Zn-Pb sulfide deposits. *Economic Geology and the Bulletin of the Society of Economic Geologists,* 99**,** 1003-1013.

HARTZ, E. H. & TORSVIK, T. H. 2002. Baltica upside down: a new plate tectonic model for Rodinia and the lapetus Ocean.(Abstract). *Geology,* 30**,** 255.
HAWTHORNE, F. C., OBERTI, R., HARLOW, G. E., MARESCH, W. V., MARTIN, R. F., SCHUMACHER, J. C. & WELCH, M. D. 2012. Nomenclature of the amphibole supergroup.(IMA Report)(Report)(Author abstract). *American Mineralogist,* 97**,** 2031.
HODGES, K. & CROWLEY, P. T. 1985. Error estimation and empirical geothermobarometry for pelitic systems. *American mineralogist,* 70**,** 702-709.
HOFFMAN, P. 1991. Did the Breakout of Laurentia Turn Gondwanaland Inside-Out? *Science,* 252**,** 1409.
HOISCH, T. D. 1990. Empirical calibration of six geobarometers for the mineral assemblage quartz+ muscovite+ biotite+ plagioclase+ garnet. *Contributions to Mineralogy and Petrology,* 104**,** 225-234.
HOLDAWAY, M. 2000. Application of new experimental and garnet Margules data to the garnet-biotite geothermometer. *American mineralogist,* 85**,** 881-892.
HUPPERT, H. E. & SPARKS, R. S. J. 1988. The generation of granitic magmas by intrusion of basalt into continental crust. *Journal of Petrology,* 29**,** 599-624.
IRVINE, T. N. & BARAGAR, W. R. A. 1971. A Guide to the Chemical Classification of the Common Volcanic Rocks. *Canadian Journal of Earth Sciences,* 8**,** 523-548.
JACKSON, S. E., PEARSON, N. J., GRIFFIN, W. L. & BELOUSOVA, E. A. 2004. The application of laser ablation-inductively coupled plasma-mass spectrometry to in situ U–Pb zircon geochronology. *Chemical Geology,* 211**,** 47-69.
JAMES, H. L. 1955. Zones of regional metamorphism in the Precambrian of northern Michigan. *Geological Society of America Bulletin,* 66**,** 1455-1488.
KENNEDY, A. K., KAMO, S. L., NASDALA, L. & TIMMS, N. E. 2010. Grenville skarn titanite: Potential references material for SIMS U-Th-Pb analysis. *The Canadian Mineralogist,* 48**,** 1423-1443.
KIMURA, J.-I. & YOSHIDA, T. 2006. Contributions of Slab Fluid, Mantle Wedge and Crust to the Origin of Quaternary Lavas in the NE Japan Arc. *Journal of Petrology,* 47**,** 2185-2232.
KIRKLAND, C. L., STEPHEN DALY, J. & WHITEHOUSE, M. J. 2007. Provenance and terrane evolution of the Kalak Nappe Complex, Norwegian Caledonides: implications for Neoproterozoic paleogeography and tectonics. *The Journal of Geology,* 115**,** 21-41.
KRUSE, A. 1980. Undersøkelser av Hesjelia. Bergvesenet.
KUMPULAINEN, R. & NYSTUEN, J. 1985. Late Proterozoic basin evolution and sedimentation in the westernmost part of Baltoscandia. *The Caledonide Orogen—Scandinavia and Related Areas,* 1**,** 213-245.
KUNO, H. 1968. Differentiation of basalt magmas. *In:* HESS, H. H. & POLDEVAART, A. A. (eds.) *Basalts: The Poldervaart treatise on rocks of*

basaltic composition. 2 ed.: Interscience.
KYLANDER-CLARK, A., HACKER, B. & MATTINSON, J. 2008. Slow exhumation of UHP terranes: titanite and rutile ages of the Western Gneiss Region, Norway. *Earth and Planetary Science Letters,* 272**,** 531-540.
LARGE, R. R. 1992. Australian volcanic-hosted massive sulfide deposits; features, styles, and genetic models. *Economic geology,* 87**,** 471-510.
LE BAS, M. J. & STRECKEISEN, A. L. 1991. The IUGS systematics of igneous rocks. *Journal of the Geological Society,* 148**,** 825-833.
LESHER, C., GOODWIN, A., CAMPBELL, I. & GORTON, M. 1986. Trace-element geochemistry of ore-associated and barren, felsic metavolcanic rocks in the Superior Province, Canada. *Canadian Journal of Earth Sciences,* 23**,** 222-237.
LI, C., ARNDT, N. T., TANG, Q. & RIPLEY, E. M. 2015. Trace element indiscrimination diagrams. *Lithos,* 232**,** 76-83.
LI, Z. X., BOGDANOVA, S. V., COLLINS, A. S., DAVIDSON, A., DE WAELE, B., ERNST, R. E., FITZSIMONS, I. C. W., FUCK, R. A., GLADKOCHUB, D. P., JACOBS, J., KARLSTROM, K. E., LU, S., NATAPOV, L. M., PEASE, V., PISAREVSKY, S. A., THRANE, K. &

VERNIKOVSKY, V. 2008. Assembly, configuration, and break-up history of Rodinia: A synthesis. *Precambrian Research,* 160**,** 179-210.
LUDWIG, K. R. 2003. Isoplot 3.00, A Geochronological Toolkit for Microsoft Excel. *Berkley Geochronology Center, Special Publication,* 4**,** 1-74.
MARKER, M. 1983. *Caledonian and Pre-Caledonian Geology of the Mofjell Area, Nordland, Norway.* Ph.D. thesis, Københavns universitet.
MARKER, M., BJERKGÅRD, T., SLAGSTAD, T. & SOLLI, A. 2012. *Bedrock map Storakersvatnet 2027 III, M 1:50000*, 1:50000. Trondheim: Geological Survey of Norway.
MARSHALL, B., VOKES, F. & LAROCQUE, A. 2000. Regional metamorphic remobilization: upgrading and formation of ore deposits. *Reviews in Economic Geology,* 11**,** 19-38.
MASUDA, A., NAKAMURA, N. & TANAKA, T. 1973. Fine structures of mutually normalized rare-earth patterns of chondrites. *Geochimica et Cosmochimica Acta,* 37**,** 239-248.
MEERT, J. G. & TORSVIK, T. H. 2003. The making and unmaking of a supercontinent: Rodinia revisited. *Tectonophysics,* 375**,** 261-288.
MELEZHIK, V. A., IHLEN, P. M., KUZNETSOV, A. B., GJELLE, S., SOLLI, A., GOROKHOV, I. M., FALLICK, A. E., SANDSTAD, J. S. & BJERKGÅRD, T. 2015. Pre-Sturtian (800–730Ma) depositional age of carbonates in sedimentary sequences hosting stratiform iron ores in the Uppermost Allochthon of the Norwegian Caledonides: A chemostratigraphic approach. *Precambrian Research,* 261**,** 272-299.
MELEZHIK, V. A., ROBERTS, D., GOROKHOV, I. M., FALLICK, A. E., ZWAAN, K. B., KUZNETSOV, A. B. & POKROVSKY, B. G. 2002. Isotopic evidence for a complex Neoproterozoic to Silurian rock assemblage in the North-Central Norwegian Caledonides. *Precambrian Research,* 114**,** 55-86.
MILLER, C. F. 1985. Are Strongly Peraluminous Magmas Derived from Pelitic Sedimentary Sources? *The Journal of Geology,* 93**,** 673-689.
MOHAMMAD, Y. O., CORNELL, D. H., DANIELSSON, E., HEGARDT, E. A. & ANCZKIEWICZ, R. 2011. Mg-rich staurolite and kyanite inclusions in metabasic garnet amphibolite from the Swedish Eastern Segment: evidence for a Mesoproterozoic subduction event. *European Journal of Mineralogy,* 23**,** 609-631.
MOLINA, J., MORENO, J., CASTRO, A., RODRÍGUEZ, C. & FERSHTATER, G. 2015. Calcic amphibole thermobarometry in metamorphic and igneous rocks: New calibrations based on plagioclase/amphibole Al-Si partitioning and amphibole/liquid Mg partitioning. *Lithos,* 232**,** 286-305.
MOSIER, D. L. B., SINGER, V. I. & DONALD, A. 2009. Volcanogenic massive sulfide deposits of the world: Database and grade and tonnage models.
MSALABS. 2017a. *MULTI-ELEMENT DETERMINATION OF MINERALOGICAL SAMPLES USING A LITHIUM BORATE FUSION AND ICP-MS FINISH* [Online]. https://msalabs.com/services/analysis/. [Accessed 22.01.2020].
MSALABS. 2017b. *MULTI-ELEMENT DETERMINATION OF MINERALOGICAL SAMPLES USING A LITHIUM BORATE FUSION AND ICP-OES FINISH* [Online]. https://msalabs.com/services/analysis/. [Accessed 22.01.2020].
MSALABS. 2017c. *MULTI-ELEMENT DETERMINATION OF MINERALOGICAL SAMPLES USING A*

FOUR ACID DIGESTION AND ICP-AES/MS FINISH [Online]. https://msalabs.com/services/analysis/. [Accessed 22.01.2020].
MSALABS. 2017d. *MULTI-ELEMENT DETERMINATION OF MINERALOGICAL SAMPLES USING A*

TWO ACID DIGESTION AND ICP-AES/MS FINISH [Online]. https://msalabs.com/services/analysis/. [Accessed 22.01.2020].
MSALABS. 2018a. *DETERMINATION OF LOSS ON IGNITION IN MINERALOGICAL SAMPLES* [Online]. Available: https://msalabs.com/services/analysis/ [Accessed 22.01.2020].
MSALABS. 2018b. *DETERMINATION OF TOTAL CARBON AND SULFUR IN MINERALOGICAL SAMPLES* [Online]. https://msalabs.com/services/analysis/. [Accessed 22.01.2020].

NAKAMURA, N. 1974. Determination of REE, Ba, Fe, Mg, Na and K in carbonaceous and ordinary chondrites. *Geochimica et Cosmochimica Acta,* 38**,** 757-775.
NANDEDKAR, R., ULMER, P. & MÜNTENER, O. 2014. Fractional crystallization of primitive, hydrous arc magmas: an experimental study at 0.7 GPa. *Contributions to Mineralogy and Petrology,* 167**,** 1-27.
PAT SHANKS III, W. C. & THURSTON, R. 2012. Volcanogenic massive sulfide occurence model: U.S. Geological Survey Scientific Investigations Report 2010-5070-C. *In:* PAT SHANKS III, W. C. & THURSTON, R. (eds.). U.S. Geological Survey.
PEARCE, J. A. 1983. Role of the sub-continental lithosphere in magma genesis at active continental margins.
PEARCE, J. A. 1996. A user's guide to basalt discrimination diagrams. *Trace element geochemistry of volcanic rocks: applications for massive sulphide exploration. Geological Association of Canada, Short Course Notes,* 12**,** 79-113.
PEARCE, J. A. 2008. Geochemical fingerprinting of oceanic basalts with applications to ophiolite classification and the search for Archean oceanic crust. *LITHOS,* 100**,** 14-48.
PEARCE, J. A. & CANN, J. R. 1973. Tectonic setting of basic volcanic rocks determined using trace element analyses. *Earth and planetary science letters,* 19**,** 290-300.
PEARCE, J. A., HARRIS, N. B. W. & TINDLE, A. G. 1984. Trace Element Discrimination Diagrams for the Tectonic Interpretation of Granitic Rocks. *Journal of Petrology,* 25**,** 956-983.
PEARCE, J. A. & PEATE, D. W. 1995. Tectonic Implications of the Composition of Volcanic ARC Magmas. *Annual Review of Earth and Planetary Sciences,* 23**,** 251-285.
PIERCEY, S. J. 2010. An overview of petrochemistry in the regional exploration for volcanogenic massive sulphide (VMS) deposits. *Geochemistry: Exploration, Environment, Analysis,* 10**,** 119-136.
PRAVE, A., KESSLER, L., MALO, M., BLOECHL, W. & RIVA, J. 2000. Ordovician arc collision and foredeep evolution in the Gaspé Peninsula, Québec: the Taconic Orogeny in Canada and its bearing on the Grampian Orogeny in Scotland. *Journal of the Geological Society,* 157**,** 393-400.
REED, S. J. B. 2005. *Electron microprobe analysis and scanning electron microscopy in geology*, Cambridge university press.
RIDOLFI, F., ZANETTI, A., RENZULLI, A., PERUGINI, D., HOLTZ, F. & OBERTI, R. 2018. AMFORM, a new mass-based model for the calculation of the unit formula of amphiboles from electron microprobe analyses. *The American Mineralogist,* 103**,** 1112-1125.
RÍOS, C. A. & CASTELLANOS, O. M. 2014. First report and significance of the staurolite metabasites associated to a sequence of calc-silicate rocks from the Silgará Formation at the central Santander Massif, Colombia. *Revista de la Academia Colombiana de Ciencias Exactas, Físicas y Naturales,* 38**,** 418-429.
ROBB, L. 2005. *Introduction to ore-forming processes,* Malden, Mass, Blackwell.
ROBERTS, D. 2003. The Scandinavian Caledonides: event chronology, palaeogeographic settings and likely modern analogues. *Tectonophysics,* 365**,** 283-299.
ROBERTS, D. & GEE, D. G. 1985. *An introduction to the structure of the Scandinavian Caledonides,* Chichester, Wiley.
ROBERTS, D., NORDGULEN, O., MELEZHIK, V., HATCHER, R. D., JR., CARLSON, M. P., MCBRIDE, J. H. & MARTINEZ CATALAN, J. R. 2007. The uppermost allochthon in the Scandinavian Caledonides; from a Laurentian ancestry through Taconian orogeny to Scandian crustal growth on Baltica. Boulder, CO: Boulder, CO, United States: Geological Society of America (GSA).
ROCK, N. M. S. 1987. The need for standardization of normalized multi-element diagrams in geochemistry: a comment. *GEOCHEMICAL JOURNAL,* 21**,** 75-84.
ROLLINSON, H. R. 1993. *Using geochemical data : evaluation, presentation, interpretation,* Harlow, Longman.
SCHOENE, B. 2014. 4.10-U–Th–Pb Geochronology. *Treatise on geochemistry,* 4**,** 341-378.
SCHUMACHER, J. 2007. Metamorphic amphiboles: Composition and coexistence. *Amphiboles: Crystal Chemistry, Occurrence, And Health Issues,* 67**,** 359-416.
SHAND, S. J. 1927. Eruptive Rocks: Their Genesis, Composition, Classification, and Their Relation to Ore-Deposits, with a Chapter on Meteorites.

SHETH, H. C., TORRES-ALVARADO, I. S. & VERMA, S. P. 2002. What Is the "Calc-alkaline Rock Series"? *International Geology Review,* 44**,** 686-701.
SISSON, T. & GROVE, T. 1993a. Experimental investigations of the role of H 2 O in calc-alkaline differentiation and subduction zone magmatism. *Contributions to mineralogy and petrology,* 113**,** 143-166.
SISSON, T. & GROVE, T. 1993b. Temperatures and H 2 O contents of low-MgO high-alumina basalts. *Contributions to Mineralogy and Petrology,* 113**,** 167-184.
SKÅR, Ø. 2002. U–Pb geochronology and geochemistry of early Proterozoic rocks of the tectonic basement windows in central Nordland, Caledonides of north-central Norway. *Precambrian Research,* 116**,** 265-283.
SLAGSTAD, T. & KIRKLAND, C. L. 2017. The use of detrital zircon data in terrane analysis: A nonunique answer to provenance and tectonostratigraphic position in the Scandinavian Caledonides. *Lithosphere,* 9**,** 1002-1011.
SLAGSTAD, T. & KIRKLAND, C. L. 2018. Timing of collision initiation and location of the Scandian orogenic suture in the Scandinavian Caledonides. *Terra Nova,* 30**,** 179-188.
SLAGSTAD, T., SAALMANN, K., KIRKLAND, C. L., HØYEN, A. B., STORRUSTE, B. K., COINT, N., PIN, C., MARKER, M., BJERKGÅRD, T., KRILL, A., SOLLI, A., BOYD, R., LARSEN, T. & LARSEN, R. B. 2020. Late Neoproterozoic through Silurian tectonic evolution of the Rödingsfjället Nappe Complex, orogen-scale correlations and implications for the Scandian suture. *Geological Society, London, Special Publications,* 503**,** SP503-2020-10.
SPANDLER, C., HAMMERLI, J., SHA, P., HILBERT-WOLF, H., HU, Y., ROBERTS, E. & SCHMITZ, M. 2016. MKED1: A new titanite standard for in situ analysis of Sm–Nd isotopes and U–Pb geochronology. *Chemical Geology,* 425**,** 110-126.
STEPHENS, M. B., GUSTAVSON, M., RAMBERG, I. & ZACHRISSON, E. 1985. The Caledonides of central-north Scandinavia – a tectonostratigraphic overview. *In:* GEE, D. G. & STURT, B. A. (eds.) *The Caledonide orogen : Scandinavia and related areas : 1.* Chichester: Wiley.
STOCKWELL, C. The use of plunge in the construction of cross-sections of folds. Proceedings of the Geological Association of Canada, 1950. Business & Economic Service Limited, 97-121.
STOWELL, H. H. & STEIN, E. 2005. The significance of plagioclase-dominant coronas on garnet, Wenatchee block, Northern Cascades, Washington, USA. *The Canadian Mineralogist,* 43**,** 367-385.
STURT, B. A., PRINGLE, I. R. & RAMSAY, D. M. 1978. The Finnmarkian phase of the Caledonian Orogeny. *Journal of the Geological Society,* 135**,** 597-610.
SUN, S.-S. & MCDONOUGH, W. F. 1989. Chemical and isotopic systematics of oceanic basalts: implications for mantle composition and processes. *Geological Society, London, Special Publications,* 42**,** 313-345.
SØVEGJARTO, U., MARKER, M., GRAVERSEN, O. & GJELLE, S. 1988. *Berggrunnskart MO I RANA 1927 I - M.1:50 000.* Norges geologiske undersøkelse.
TATSUMI, Y. & NAKAMURA, N. 1986. Composition of aqueous fluid from serpentinite in the subducted lithosphere. *Geochemical Journal,* 20**,** 191-196.
TRACY, R. J., ROBINSON, P. & THOMPSON, A. B. 1976. Garnet composition and zoning in the determination of temperature and pressure of metamorphism, central Massachusetts. *American mineralogist,* 61**,** 762-775.
VAN ACTHERBERGH, E., RYAN, C. G., JACKSON, S. E. & GRIFFIN, W. L. 2001. Data reduction software for LA-ICP-MS. *In:* SYLVESTER, P. J. (ed.) *Laser Ablation-ICP-Mass Spectrometry in the Earth Sciences: Principles and Applications.* Mineralogical Association of Canada.
VAN STAAL, C. & WILLIAMS, P. 1984. Structure, origin, and concentration of the Brunswick 12 and 6 orebodies. *Economic Geology,* 79**,** 1669-1692.
VAN STAAL, C. R., DEWEY, J. F., NIOCAILL, C. M. & MCKERROW, W. S. 1998. The Cambrian-Silurian tectonic evolution of the northern Appalachians and British Caledonides: history of a complex, west and southwest Pacific-type segment of Iapetus. *In:* BLUNDELL, D. J. & SCOTT, A. C. (eds.) *Geological Society, London, Special Publications.*
VERMEESCH, P. 2006. Tectonic discrimination diagrams revisited. *Geochemistry, Geophysics, Geosystems,* 7**,** n/a-n/a.

VOKES, F. M. 1976. Caledonian massive sulphide deposits in scandinavia: A comparative review. *In:* WOLF, K. H. (ed.) *Handbook of strata-bound and stratiform ore deposits : 6 : Cu, Zn, Pb and Ag deposits.* Amsterdam: Elsevier.

WIEDENBECK, M., ALLE, P., CORFU, F., GRIFFIN, W. L., MEIER, M., OBERLI, F., QUADT, A. V., RODDICK, J. C. & SPIEGEL, W. 1995. Three natural zircon standards for U-Th-Pb, Lu-Hf, trace element and REE analyses. *Geostandards and Geoanalytical Research,* 19**,** 1-23.

WILSON, M. 1993. MAGMATIC DIFFERENTIATION. *J. Geol. Soc.*

WINTER, J. D. 2010. *An introduction to igneous and metamorphic petrology,* New York, Prentice Hall.

WINTER, J. D. 2014. *Principles of igneous and metamorphic petrology,* Harlow, Pearson.

WOOD, D. A. 1980. The application of a Th–Hf–Ta diagram to problems of tectonomagmatic classification and to establishing the nature of crustal contamination of basaltic lavas of the British Tertiary Volcanic Province. *Earth and Planetary Science Letters,* 50**,** 11-30.

WU, C. M. 2015. Revised empirical garnet–biotite–muscovite–plagioclase geobarometer in metapelites. *Journal of Metamorphic Geology,* 33**,** 167-176.

YOSHINOBU, A. S., BARNES, C. G., NORDGULEN, Ø., PRESTVIK, T., FANNING, M. & PEDERSEN, R. B. 2002. Ordovician magmatism, deformation, and exhumation in the Caledonides of central Norway: An orphan of the Taconic orogeny? *Geology,* 30**,** 883-886.

8 Appendix

Appendix A Field Maps and TEM Maps

Figure 8.1: Field maps on which the final maps are based on. A) Hellerfjellet. B) Hesjelia. C) Hammertjønna.

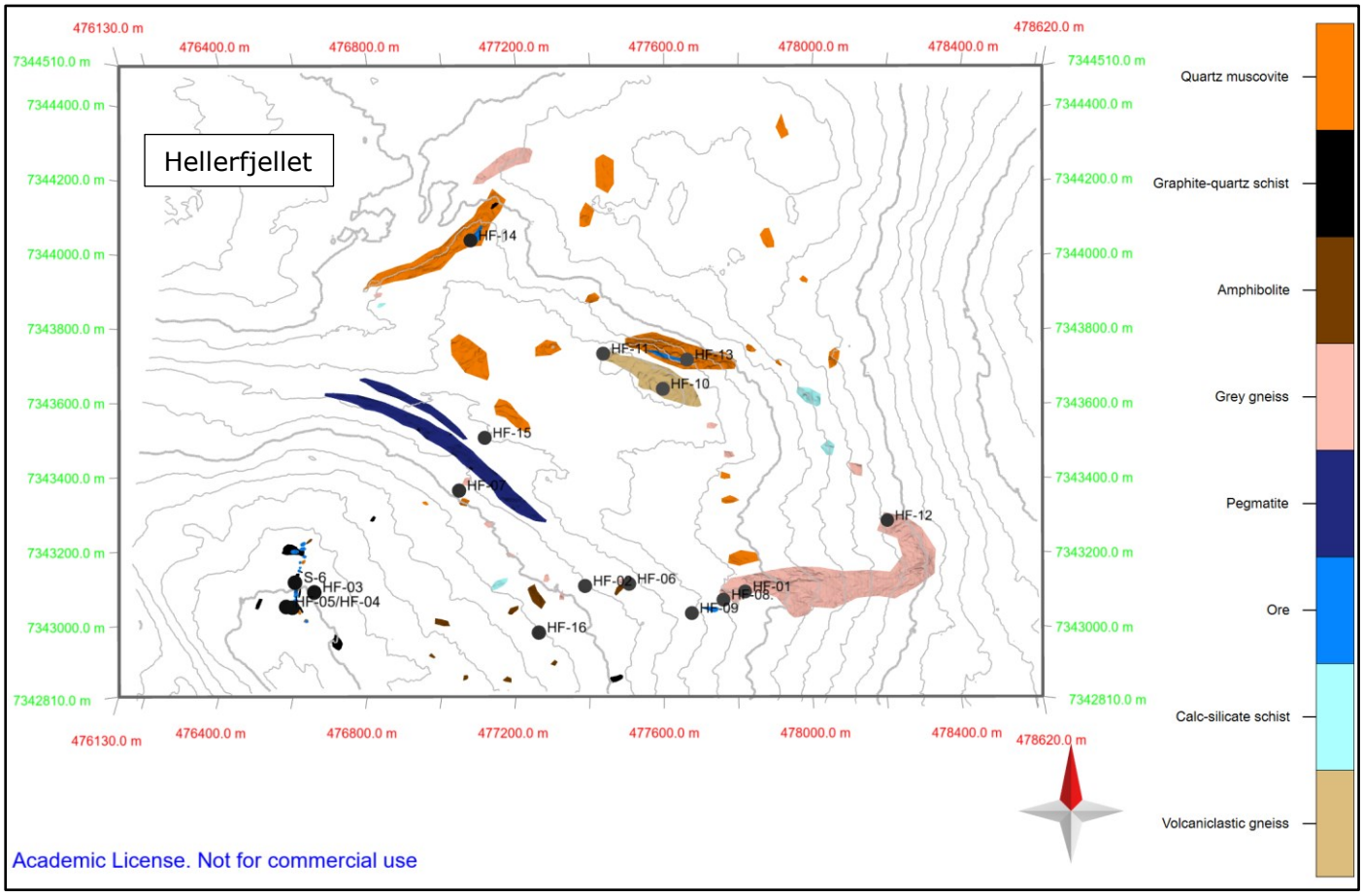

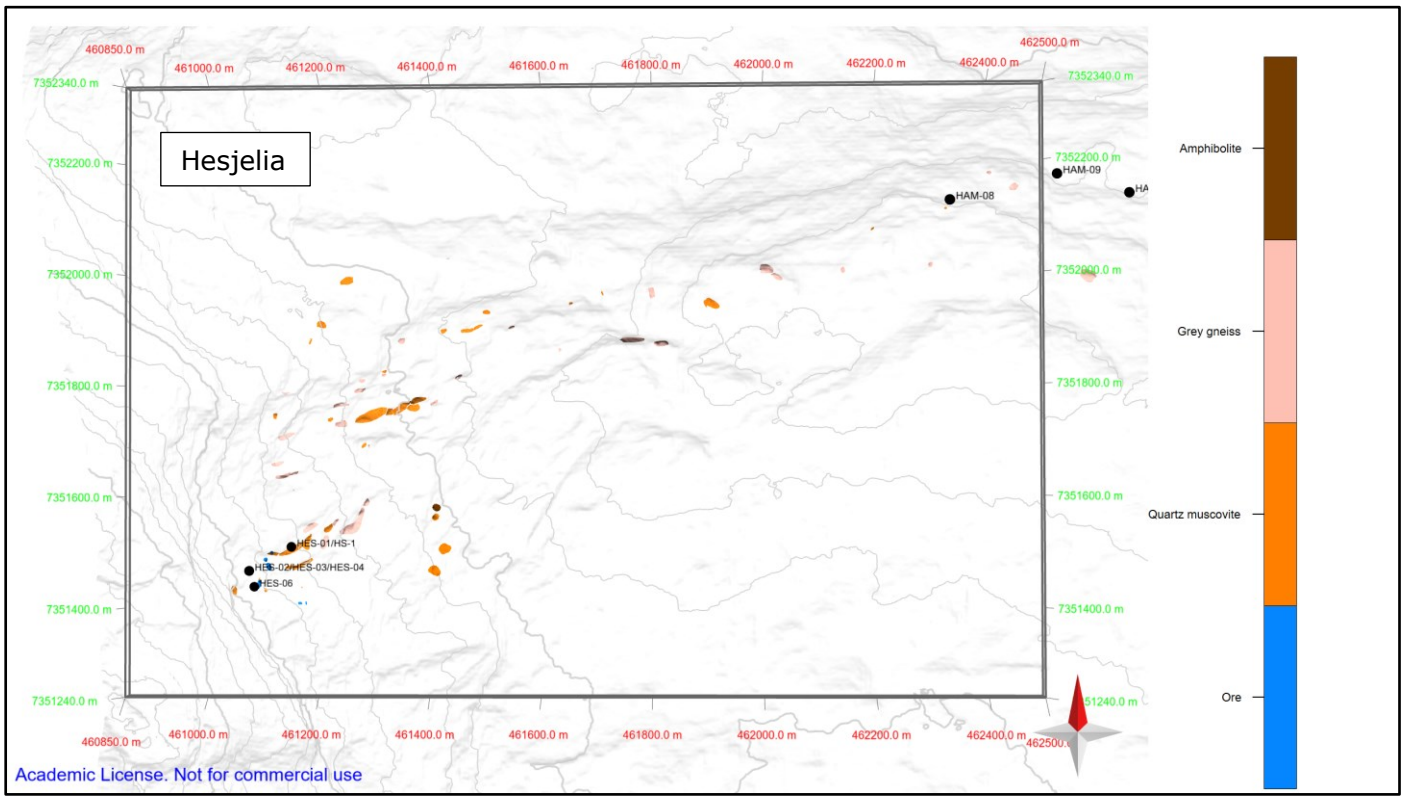

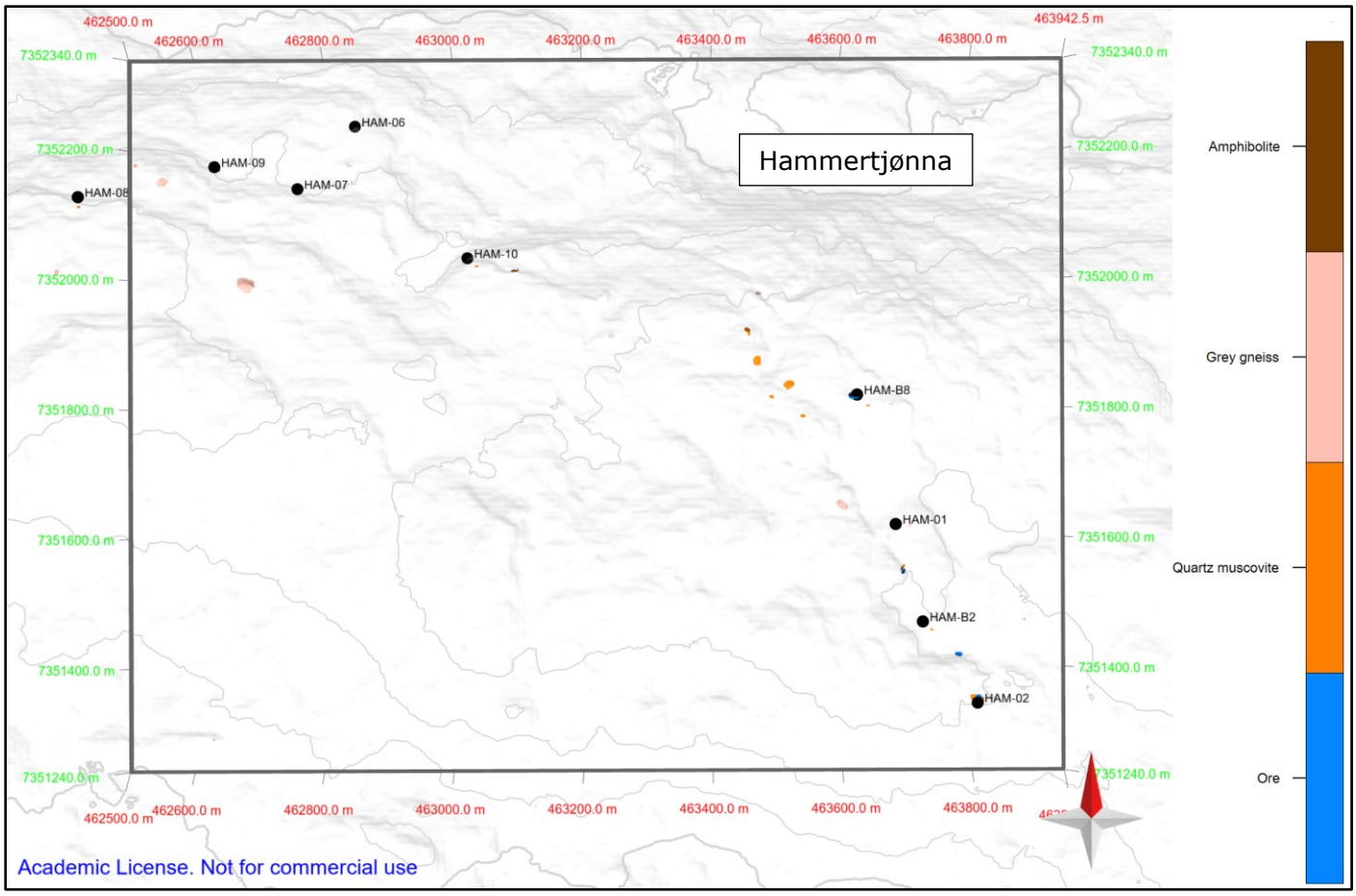
Hammertjønna
HAM-06
HAM-09
HAM-07
HAM-08
HAM-10
HAM-B8
HAM-01
HAM-B2
HAM-02
462500.0 m
462600.0 m
462800.0 m
463000.0 m
463200.0 m
463400.0 m
463600.0 m
463800.0 m
463942.5 m
7352340.0 m
7352200.0 m
7352000.0 m
7351800.0 m
7351600.0 m
7351400.0 m
7351240.0 m
Amphibolite
Grey gneiss
Quartz muscovite
Ore
Academic License. Not for commercial use

.

Figure 8.2: Amphibolite/TEM-correlation for 320 m and 300 m above sea level, in Hesjelia-Hammertjønna.

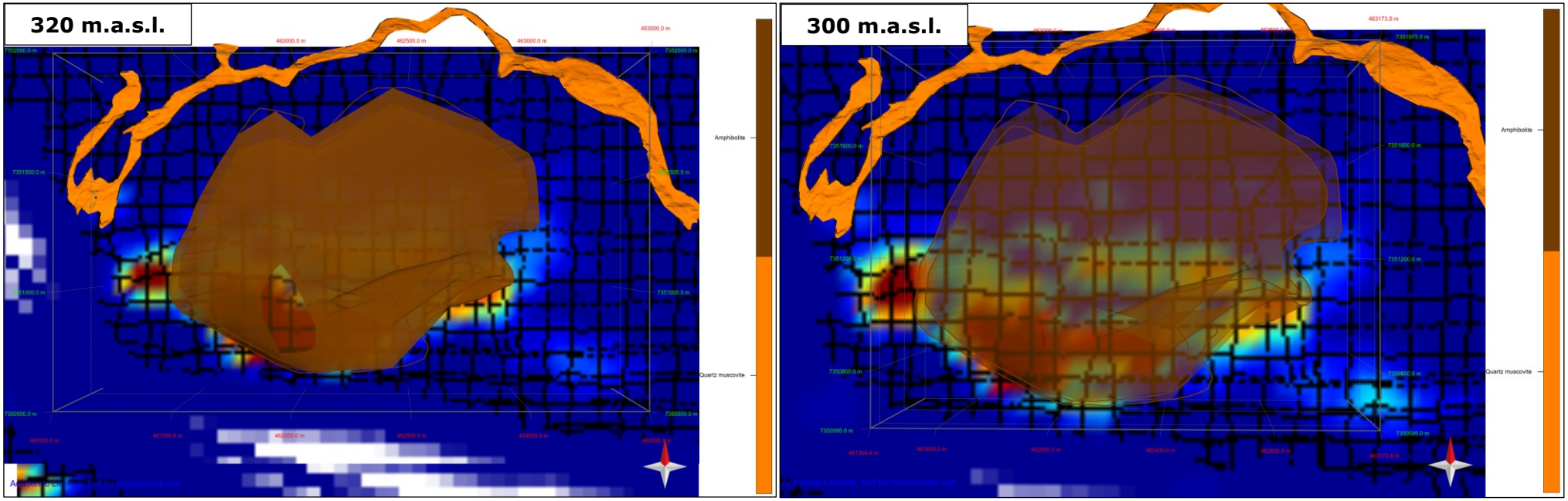

Figure 8.3: TEM/QMS-correlation for 420m, 400m, 380 m, 360 m, 300 m, 280 m, 260 m, 240 m, 220 m, 200 m, and 180 m.a.s.l., in Hesjelia-Hammertjønna.

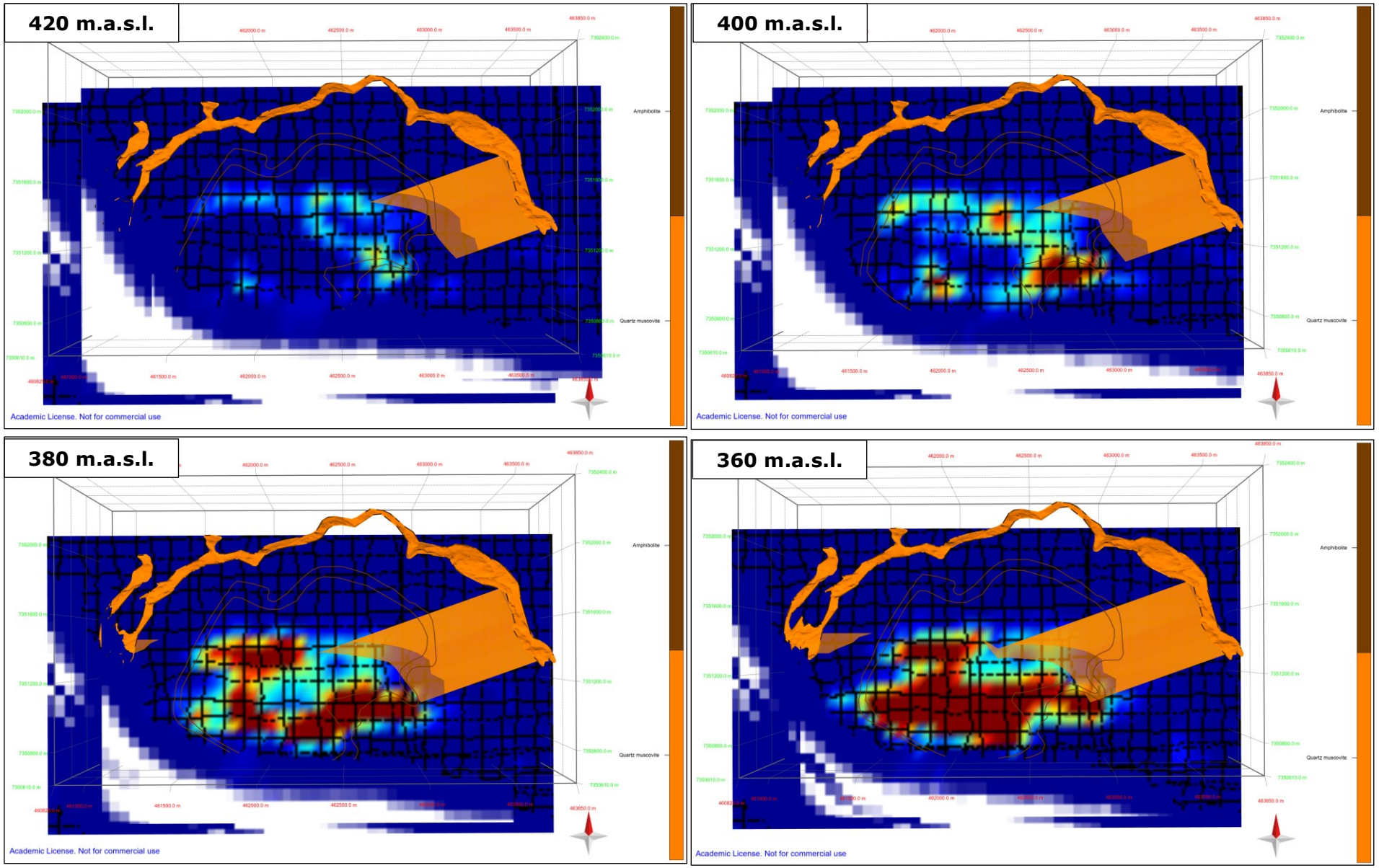

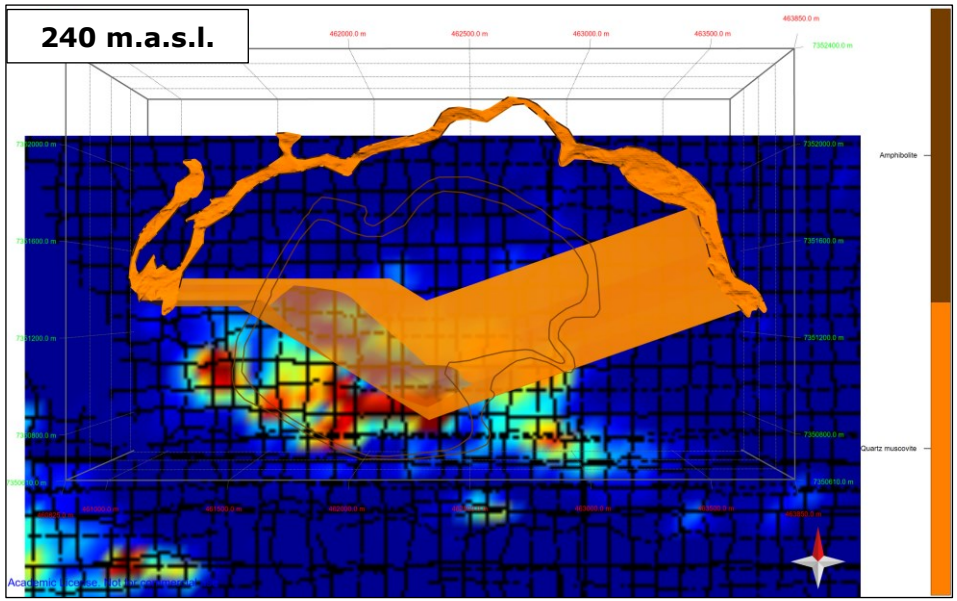
240 m.a.s.l.
Amphibolite
Quartz muscovite

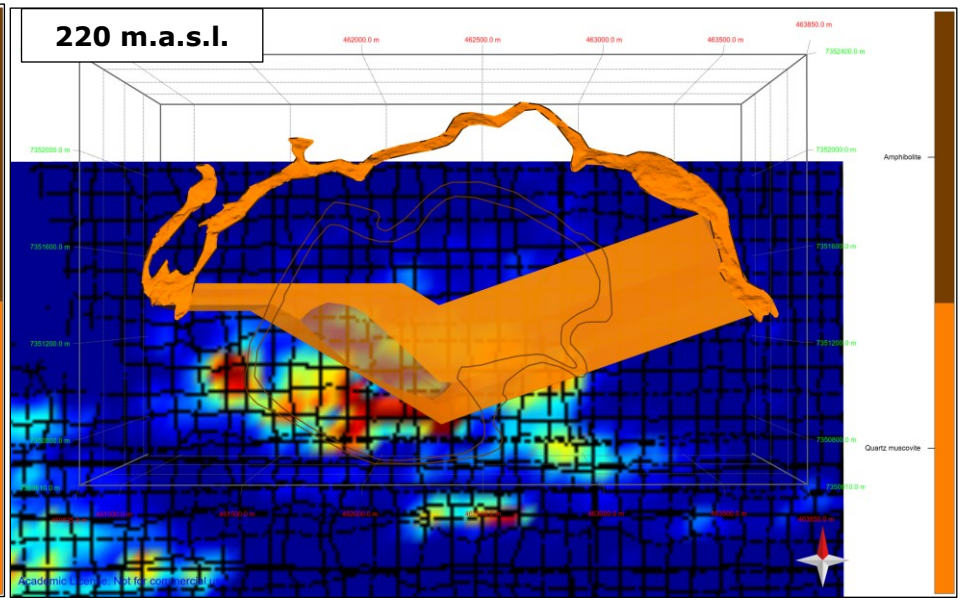
220 m.a.s.l.
Amphibolite
Quartz muscovite

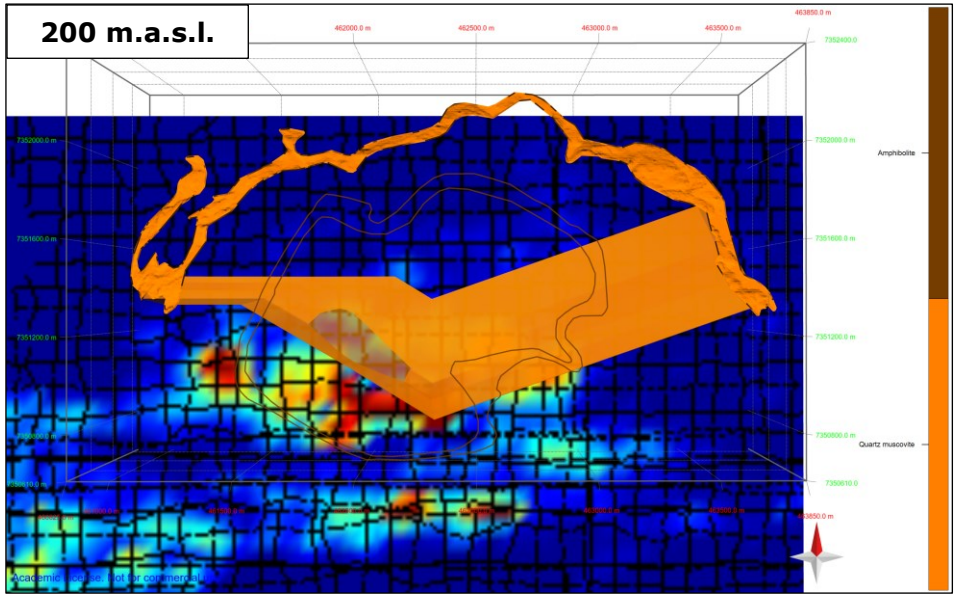
200 m.a.s.l.
Amphibolite
Quartz muscovite

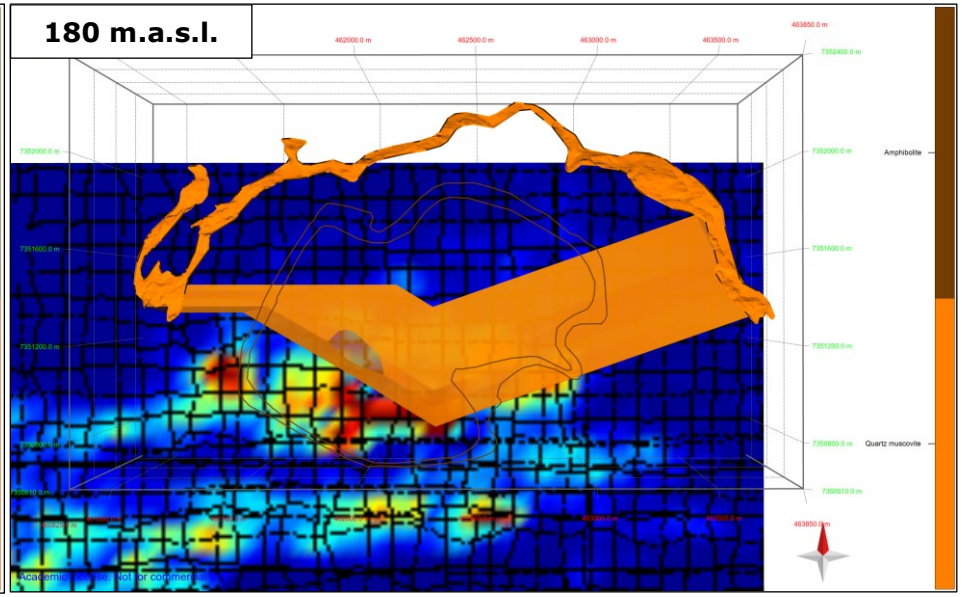
180 m.a.s.l.
Amphibolite
Quartz muscovite

Figure 8.4: TEM/Ore-correlation for 420 m, 400 m, 380 m, 280 m, 260 m, and 240 m.a.s.l., in Hesjelia-Hammertjønna.

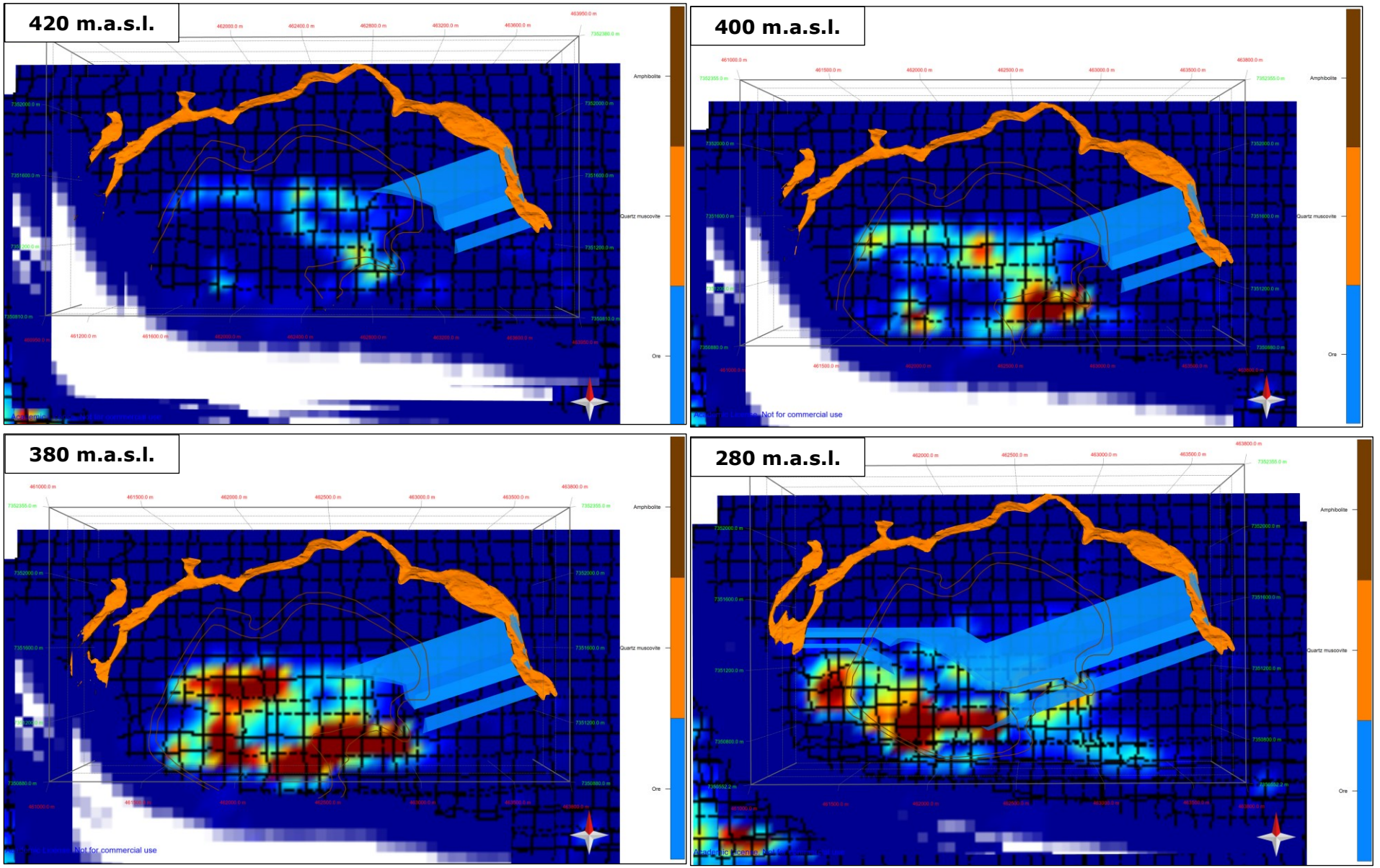

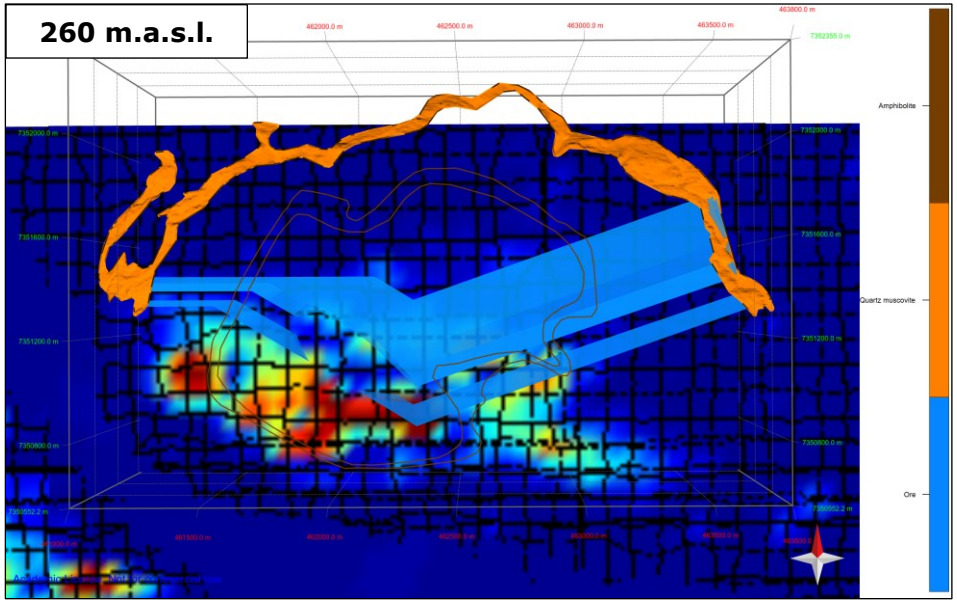
260 m.a.s.l.
Amphibolite
Quartz muscovite
Ore

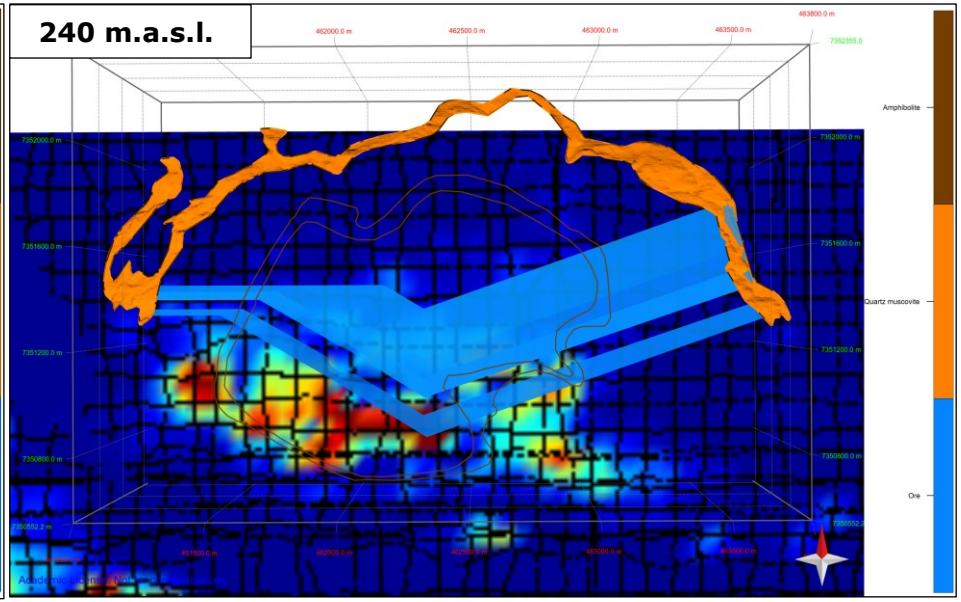
240 m.a.s.l.
Amphibolite
Quartz muscovite
Ore

Figure 8.5: TEM maps with horizon drawn around. Layer 820 to 660 m.a.s.l.

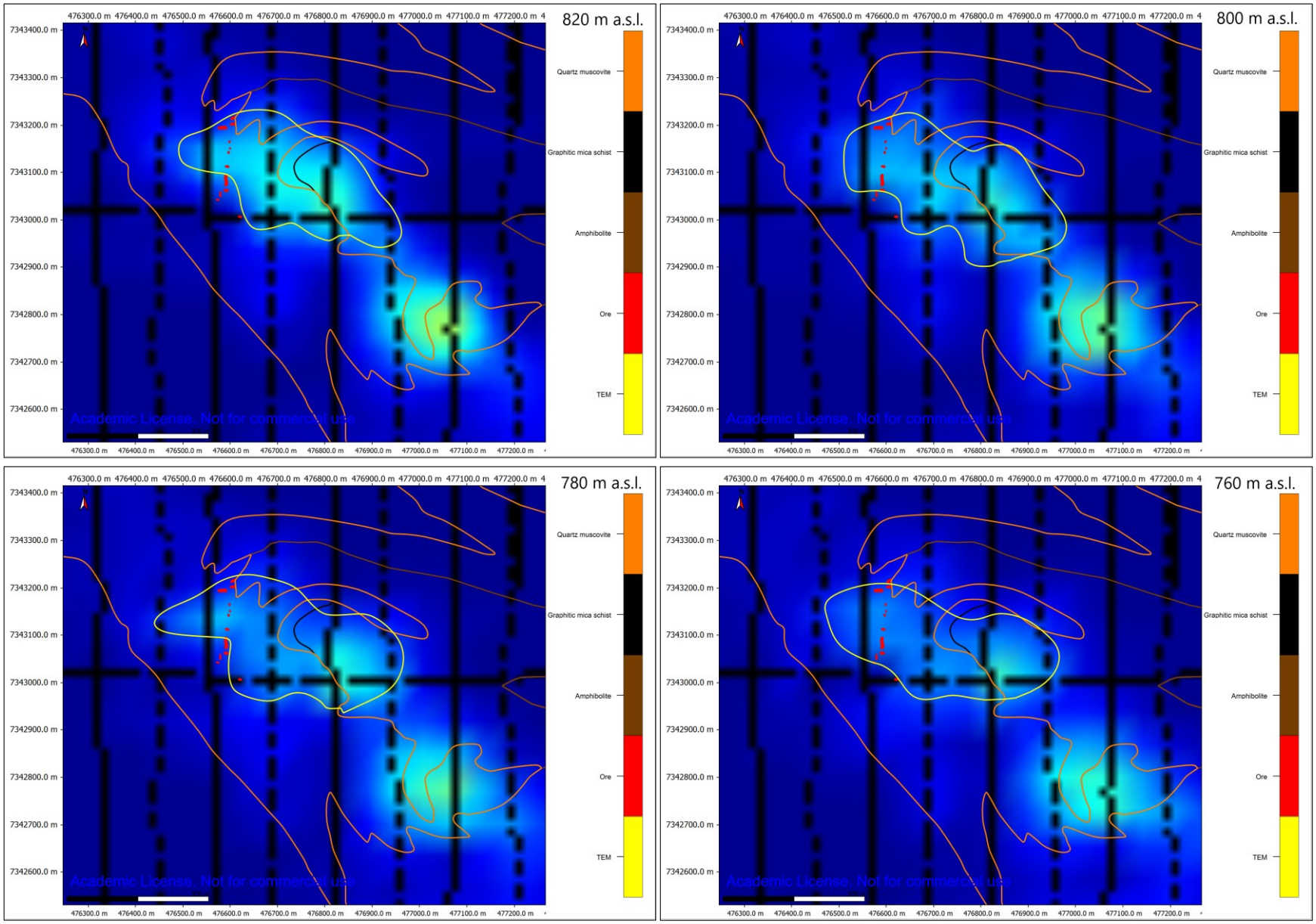

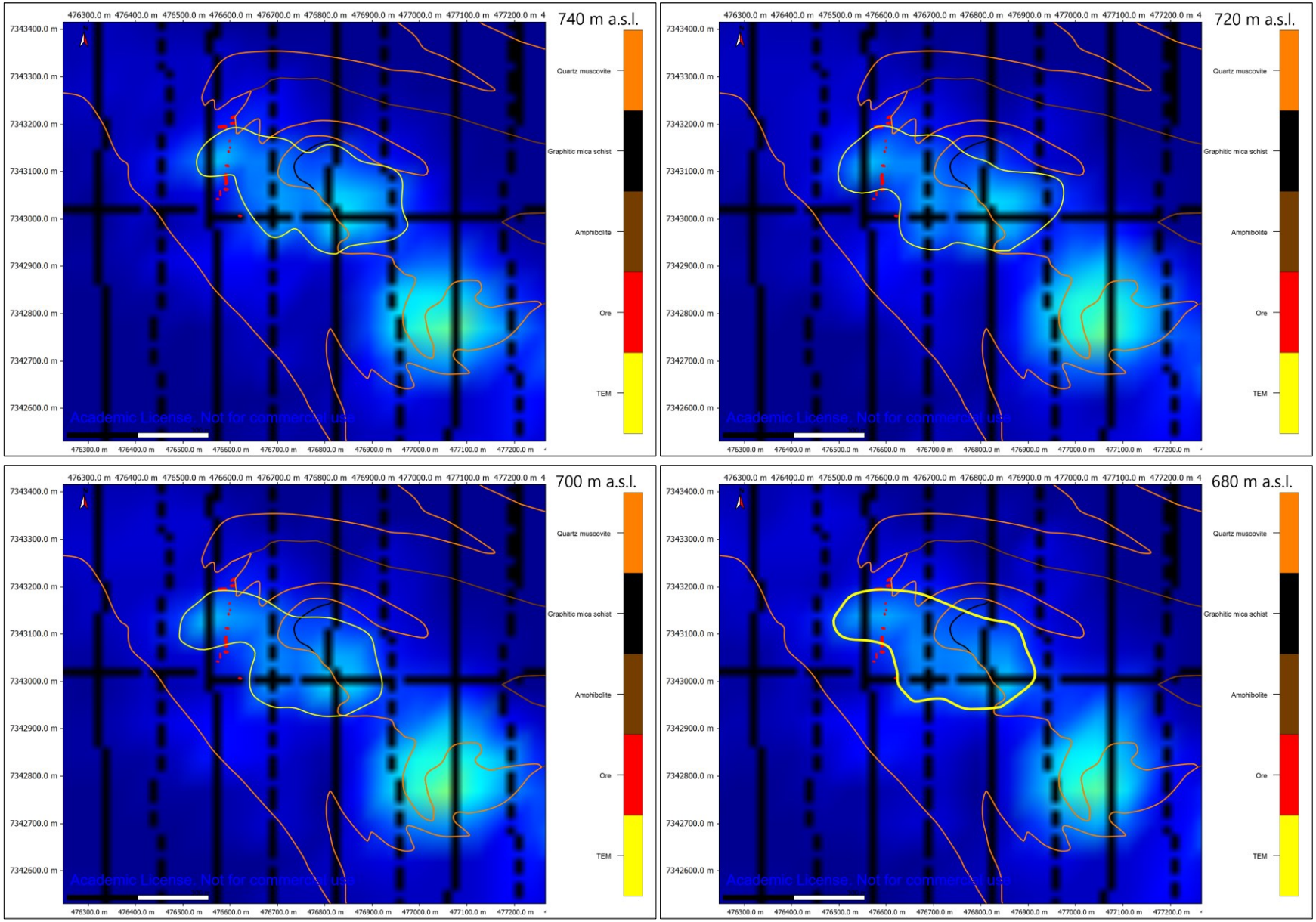
740 m a.s.l.
720 m a.s.l.
700 m a.s.l.
680 m a.s.l.
Quartz muscovite
Graphitic mica schist
Amphibolite
Ore
TEM
476300.0 m 476400.0 m 476500.0 m 476600.0 m 476700.0 m 476800.0 m 476900.0 m 477000.0 m 477100.0 m 477200.0 m
7343400.0 m 7343300.0 m 7343200.0 m 7343100.0 m 7343000.0 m 7342900.0 m 7342800.0 m 7342700.0 m 7342600.0 m
Academic License. Not for commercial use

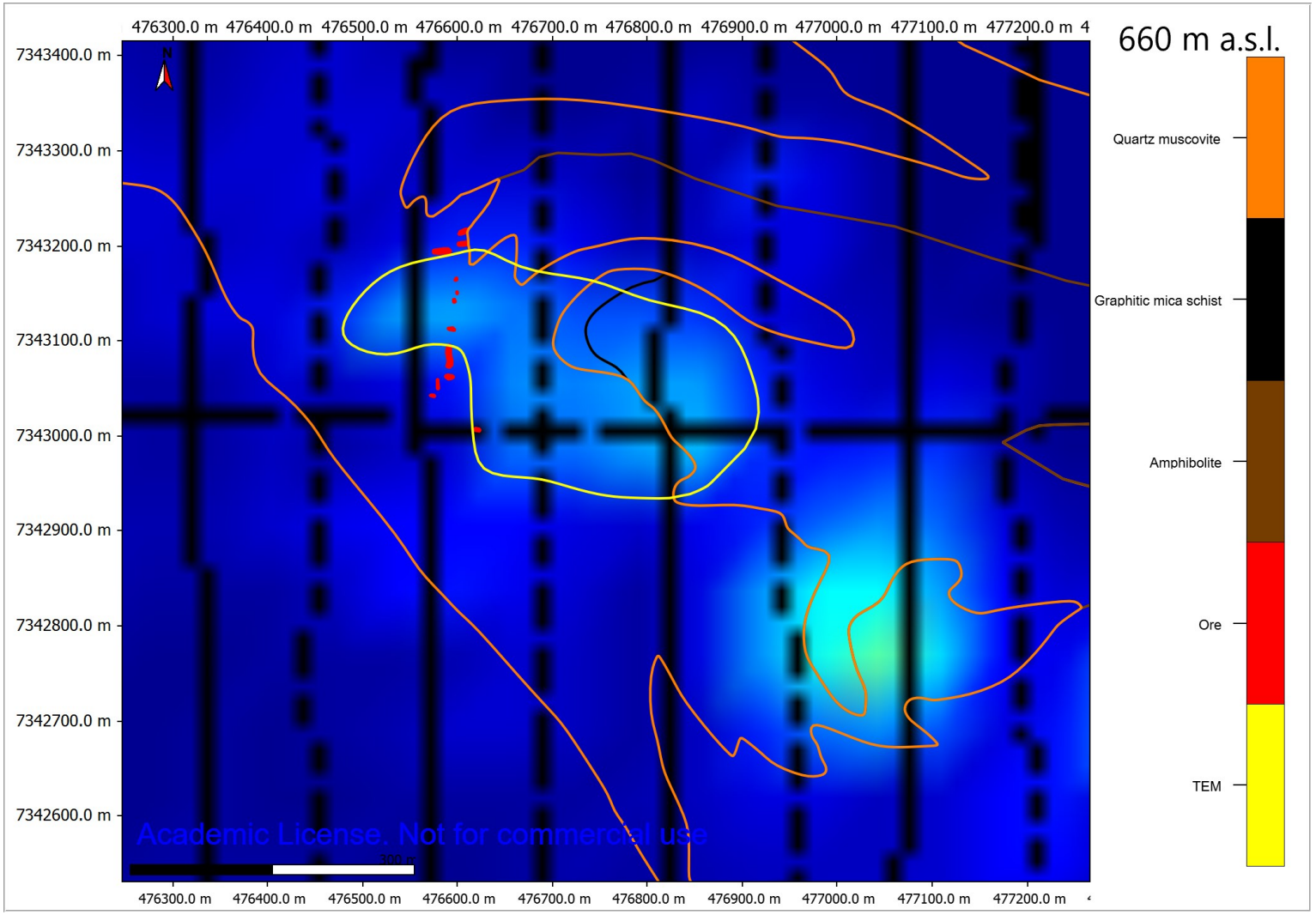
476300.0 m
476400.0 m
476500.0 m
476600.0 m
476700.0 m
476800.0 m
476900.0 m
477000.0 m
477100.0 m
477200.0 m
7343400.0 m
7343300.0 m
7343200.0 m
7343100.0 m
7343000.0 m
7342900.0 m
7342800.0 m
7342700.0 m
7342600.0 m
N
660 m a.s.l.
Quartz muscovite
Graphitic mica schist
Amphibolite
Ore
TEM
Academic License. Not for commercial use

Appendix B Thin Section Scans

Figure 8.6: HAM-02. QMS.

Figure 8.7: HAM-07. Biotite schist.

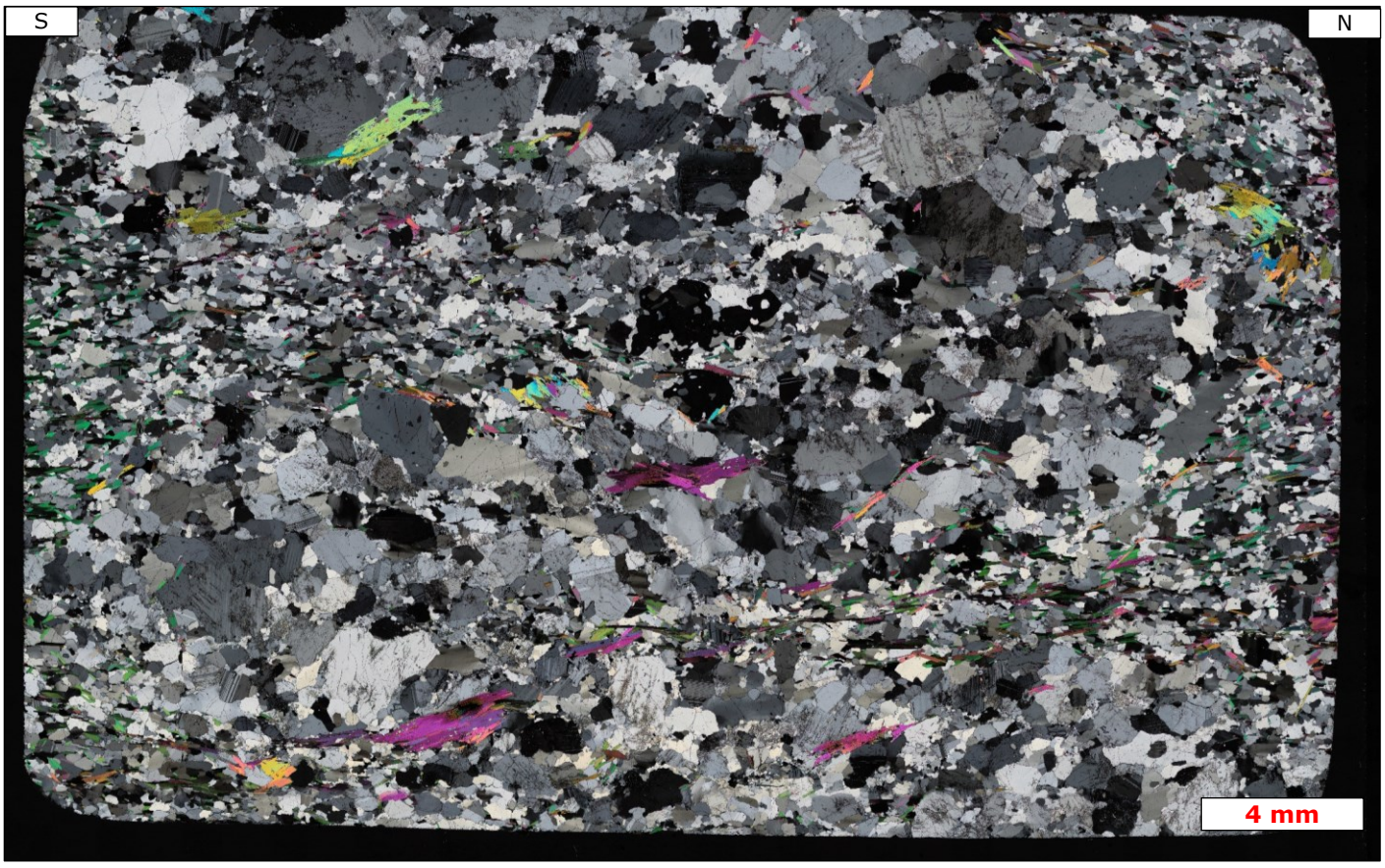

Figure 8.8: HAM-10 (left) and HES-04 (right). QMS.

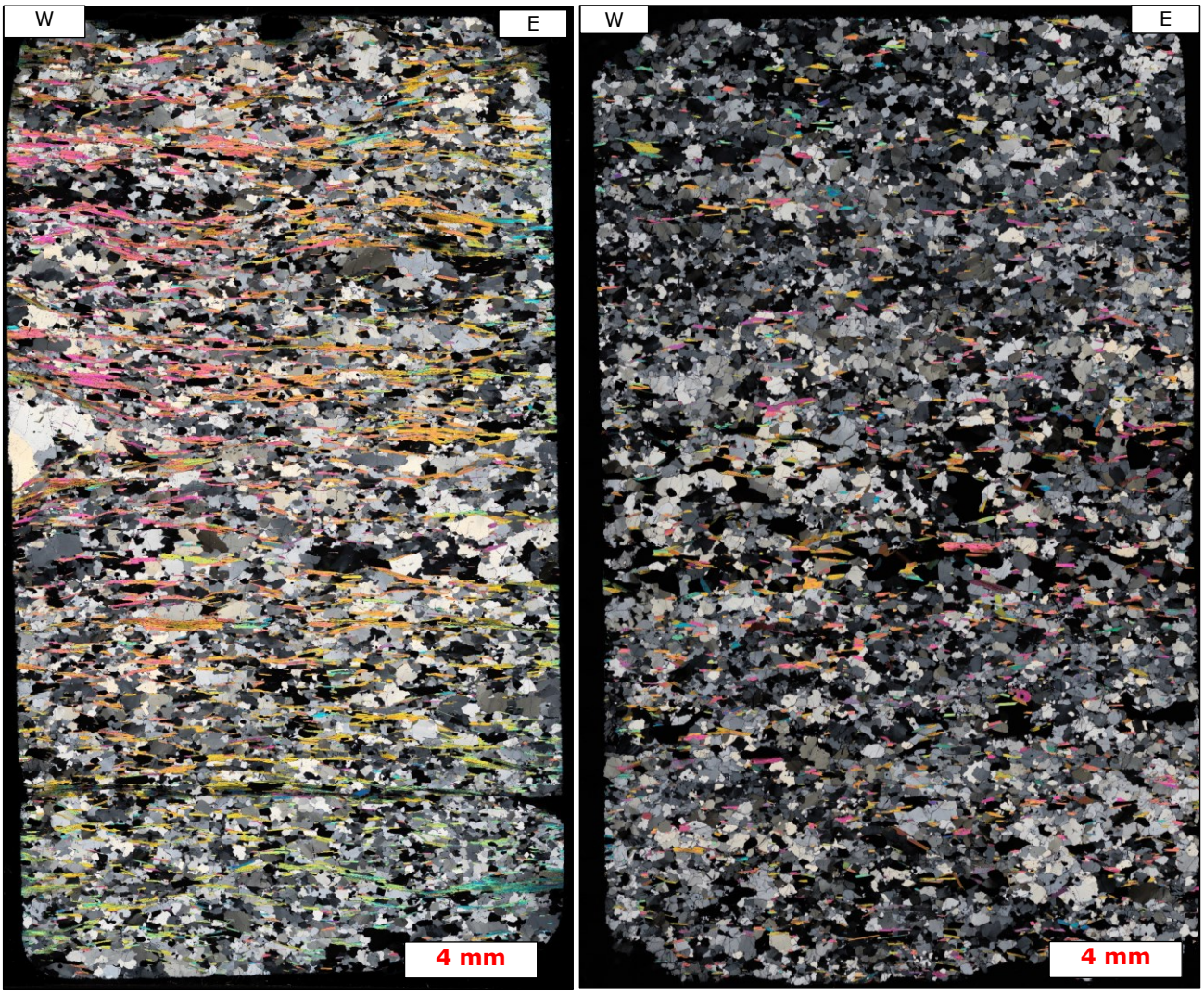

Figure 8.9: HES-06. QMS.

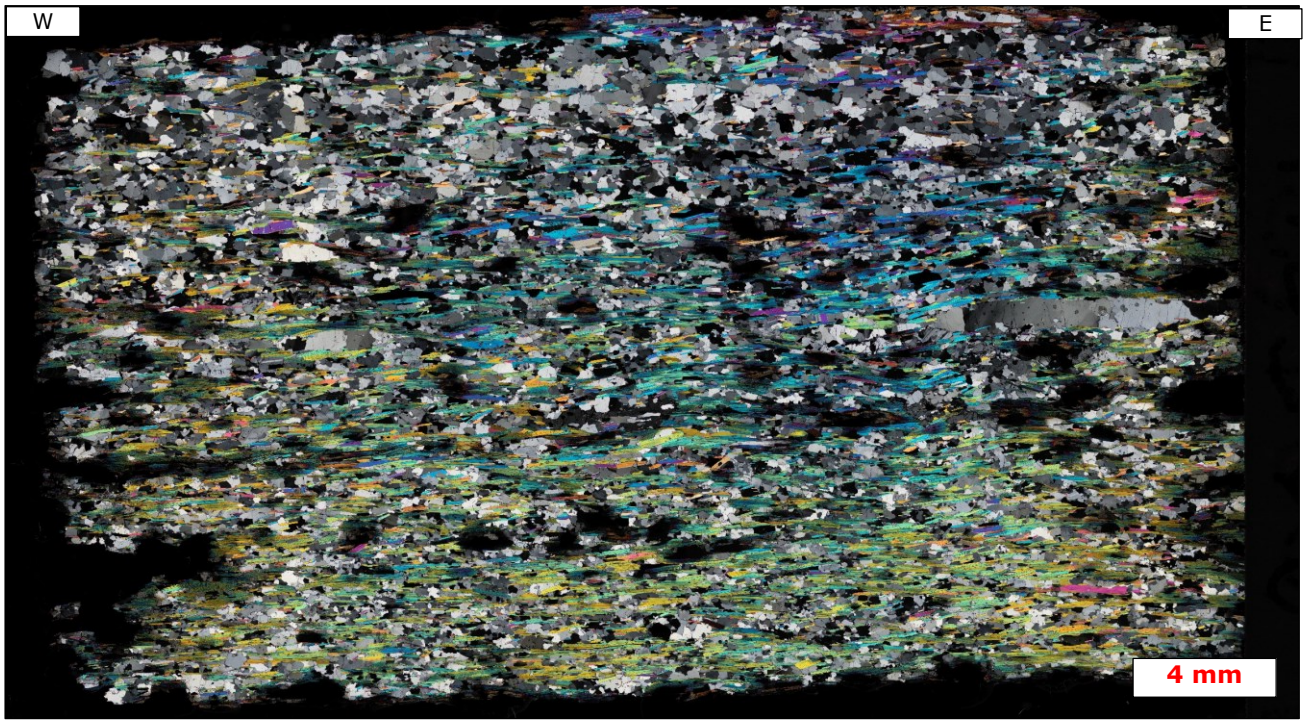

Figure 8.10: HF-05. GQG.

Figure 8.11: HF-08. Garnet biotite schist.

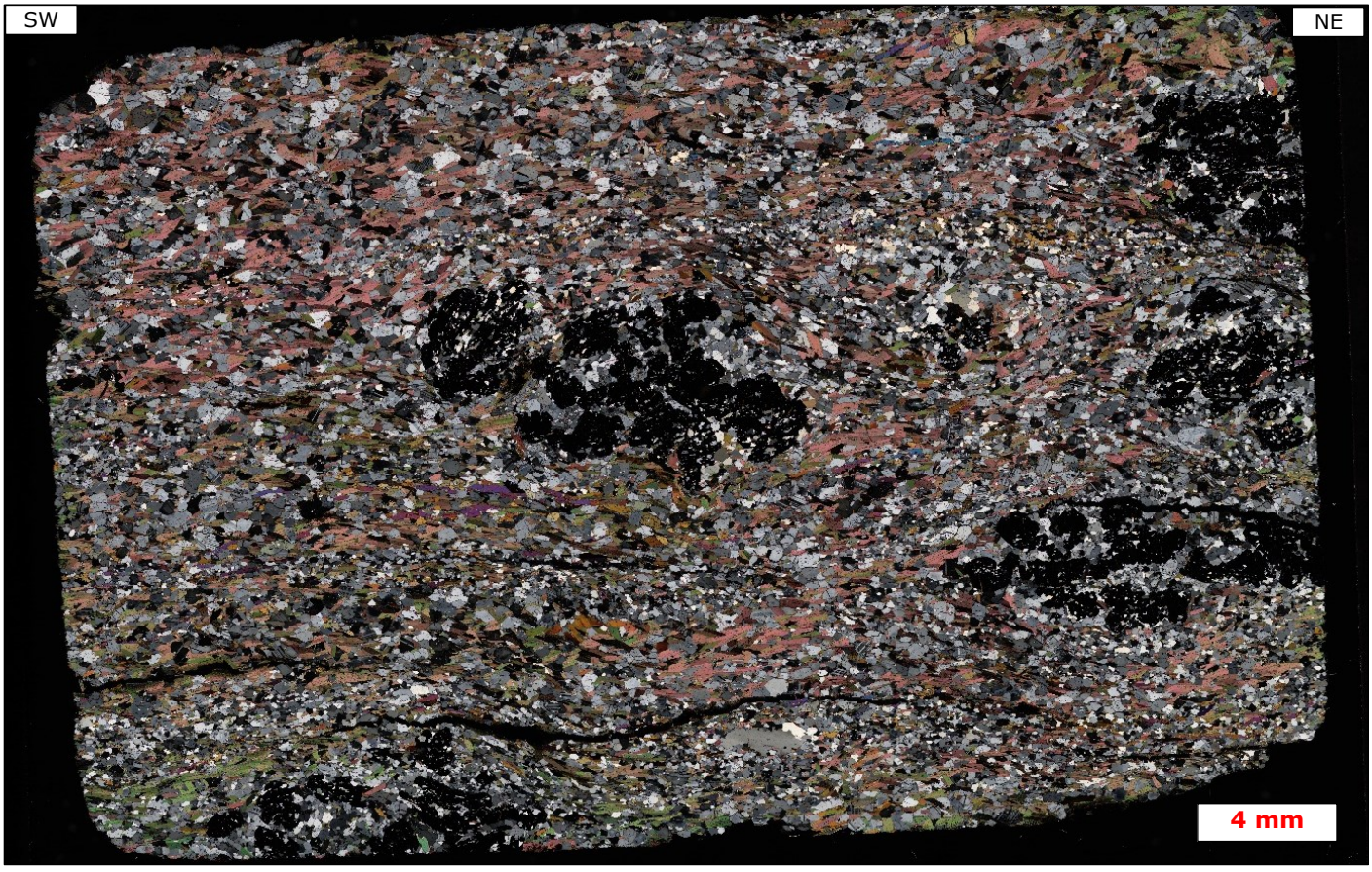

Figure 8.12: HF-09. Amphibolite.

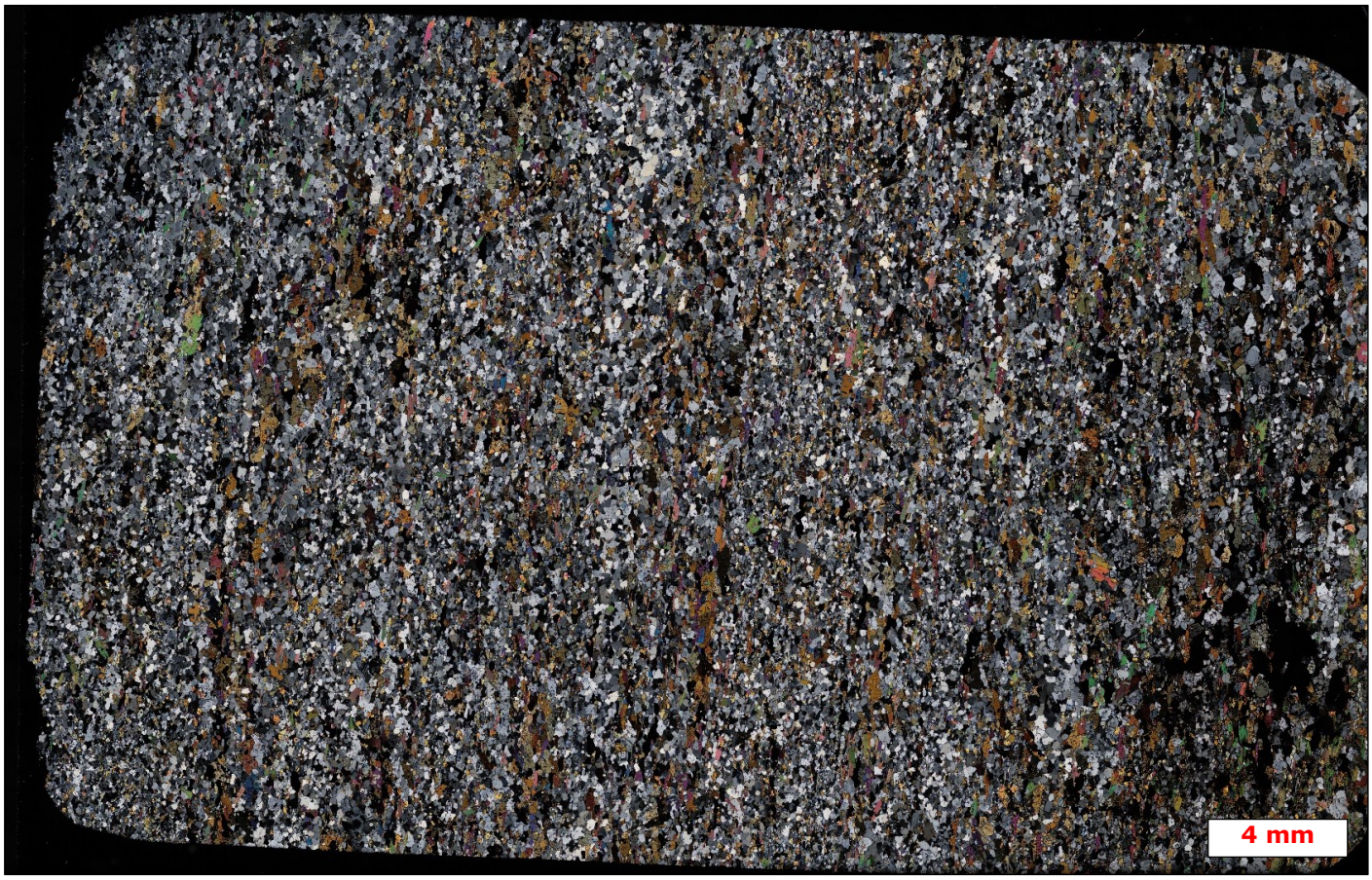

Figure 8.13: HF-12. Microcline gneiss.

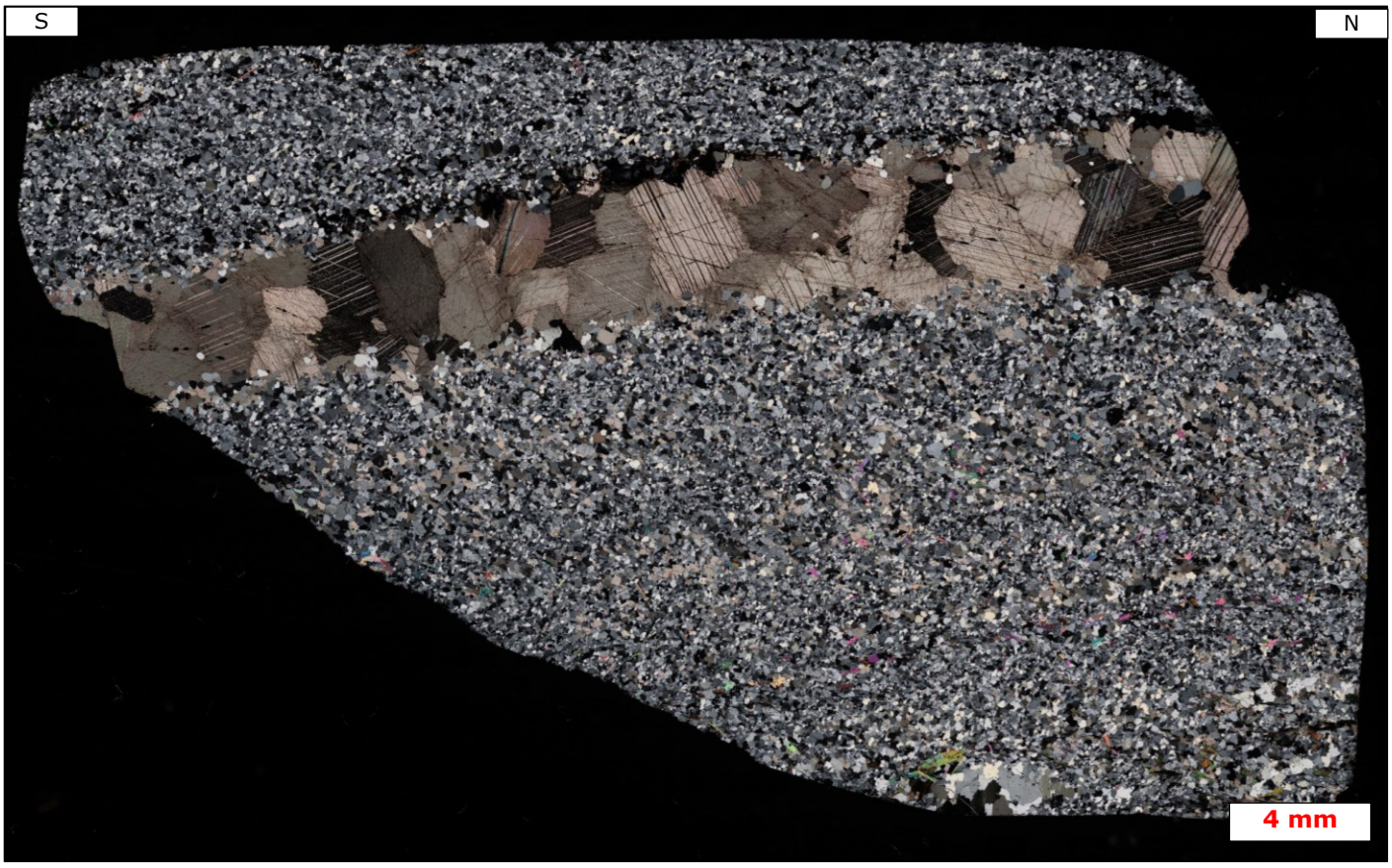

Figure 8.14: HF-13. QMS.

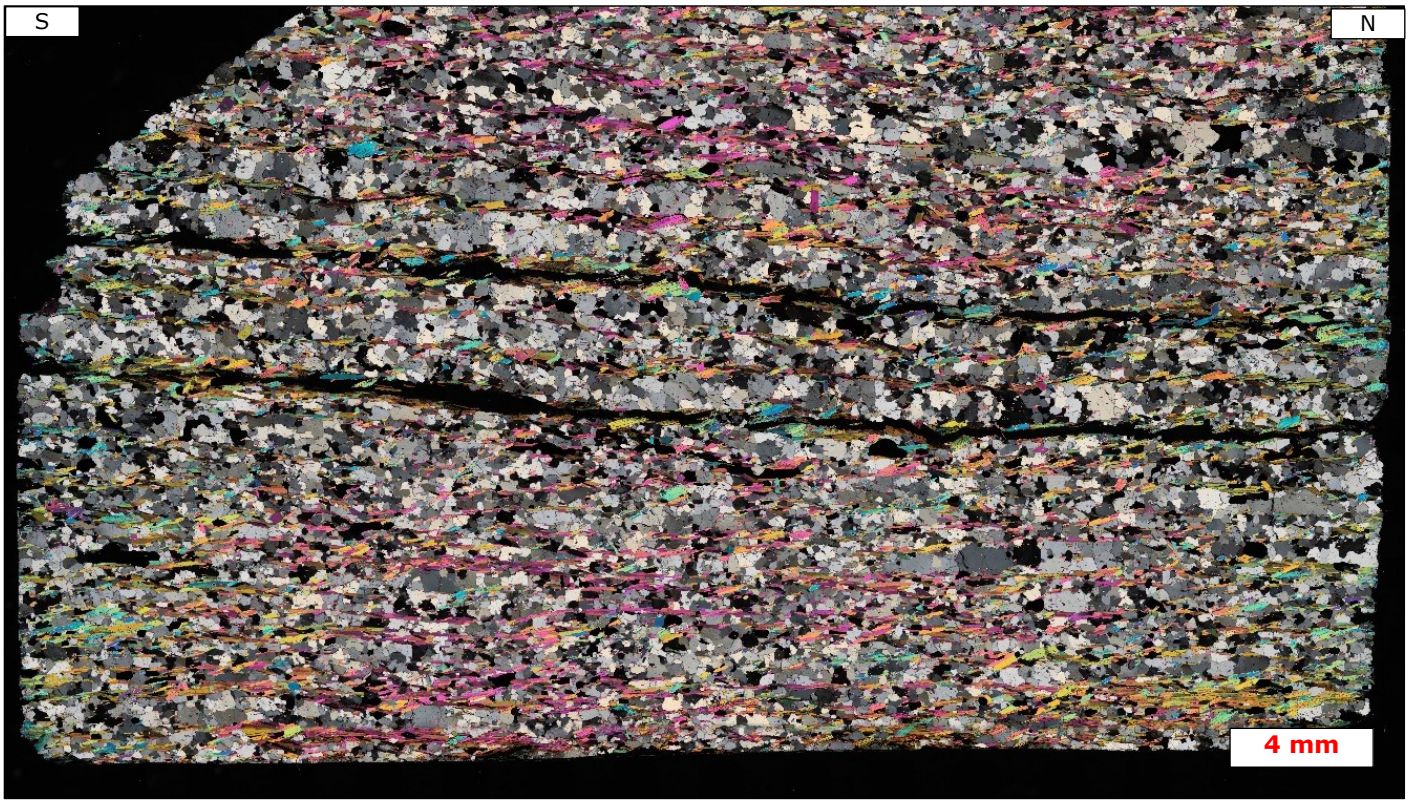

Figure 8.15: HF-16. QMS.

Figure 8.16: HF-03. Graphite quartz gneiss.

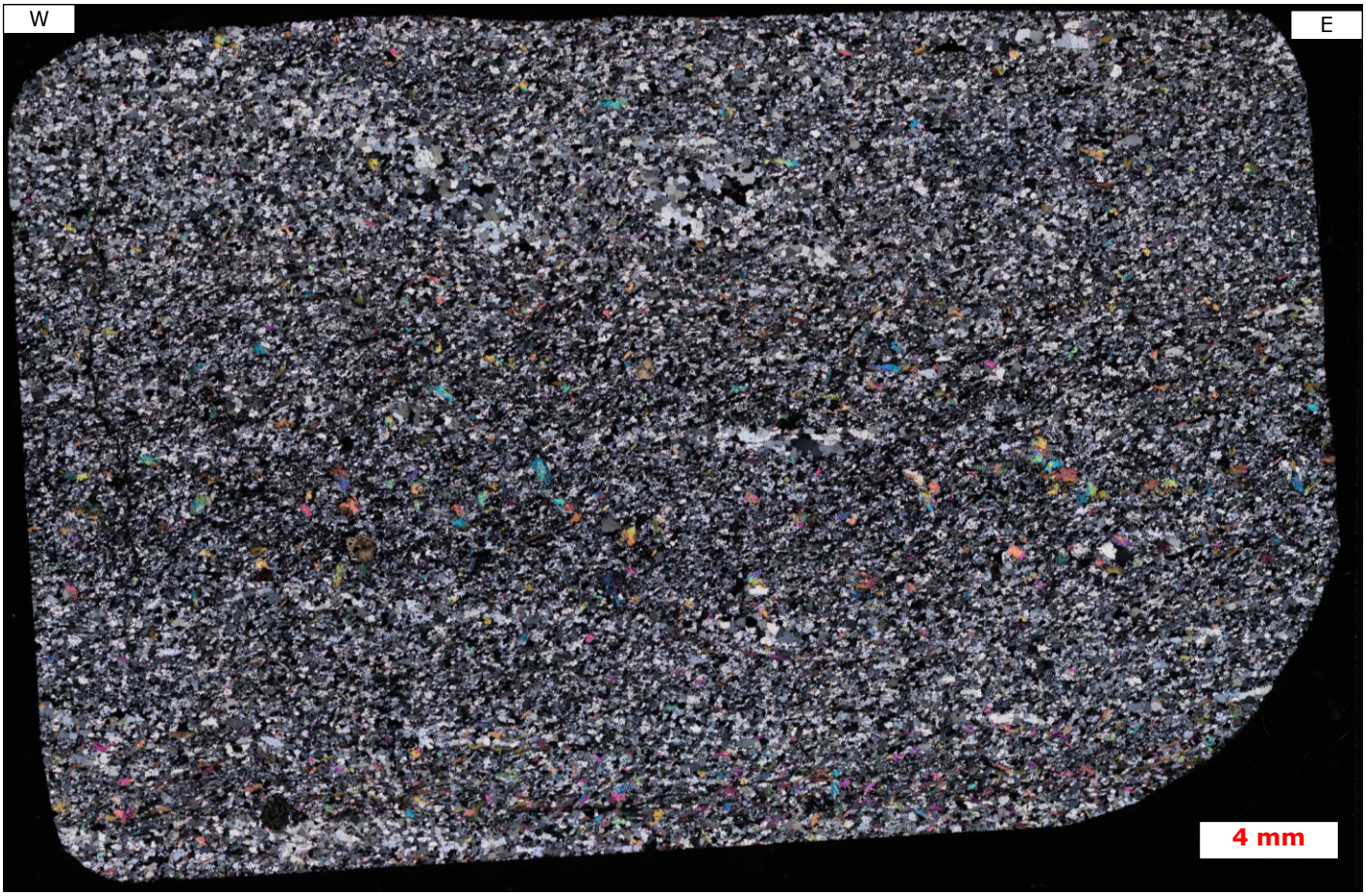

Figure 8.17: Drill core: 5.90-6.10 m. 38302 (left): Calcsilicate gneiss. 38303 (right): Garnet amphibolite.

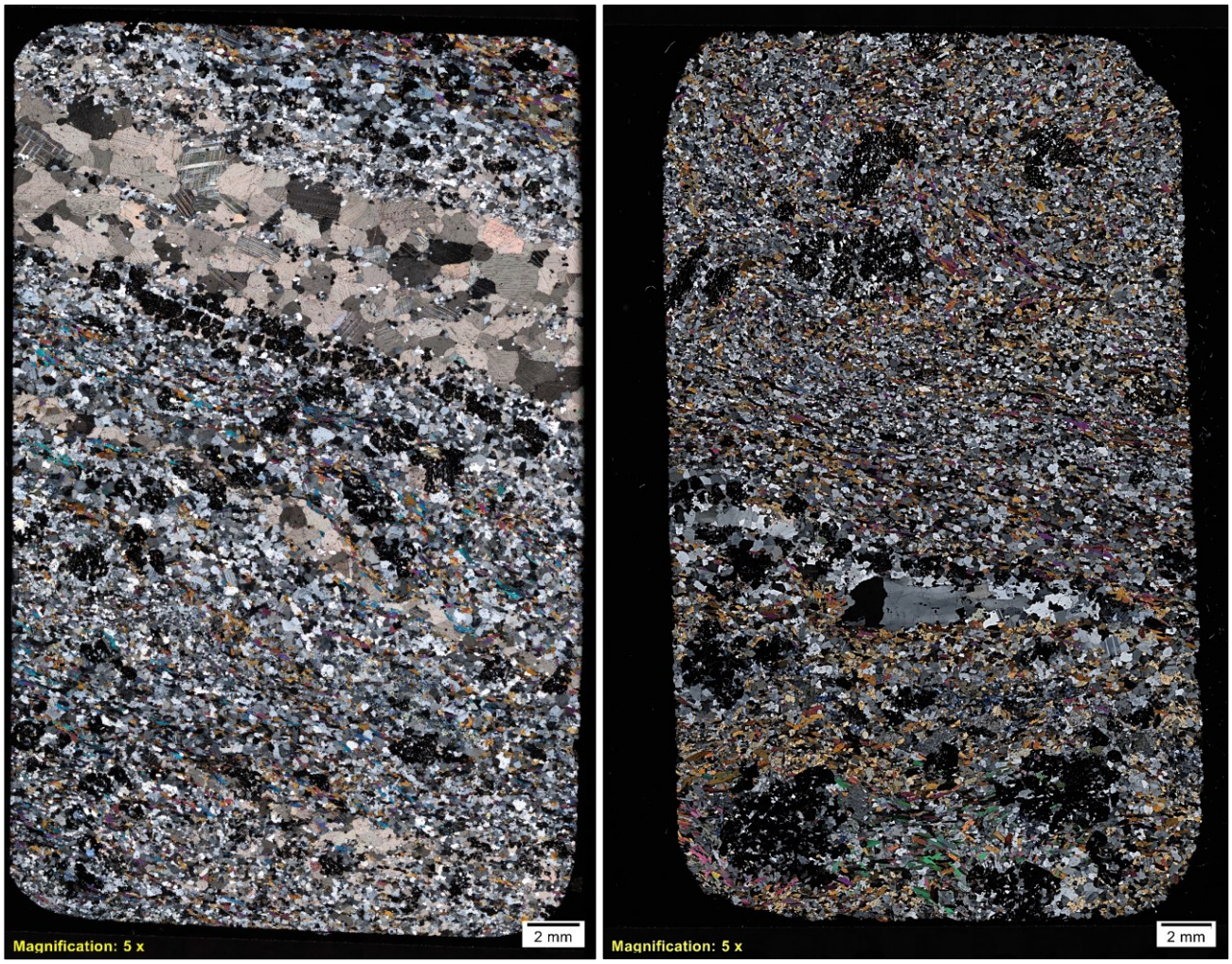

Figure 8.18: Drill core: 10.9-11.2 m. 38304. Garnet biotite gneiss.

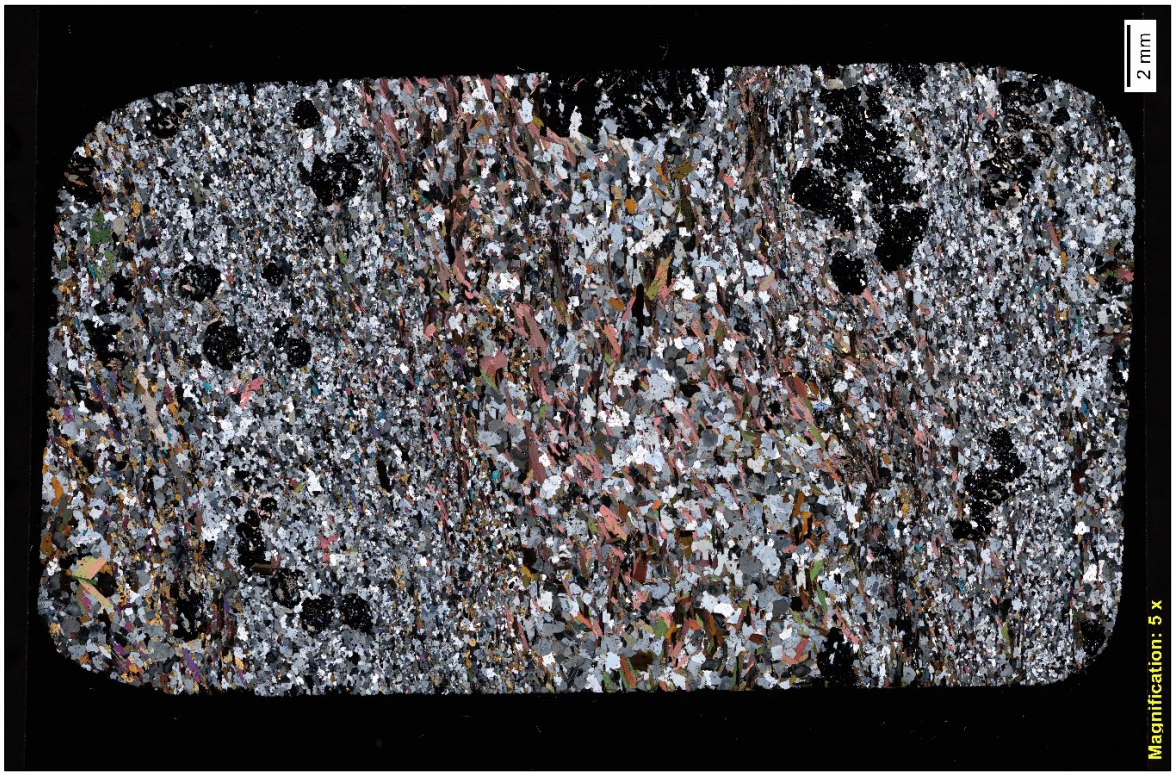

Figure 8.19: Drill core: 10.9-11.20 m. 38305. Calcsilicate gneiss.

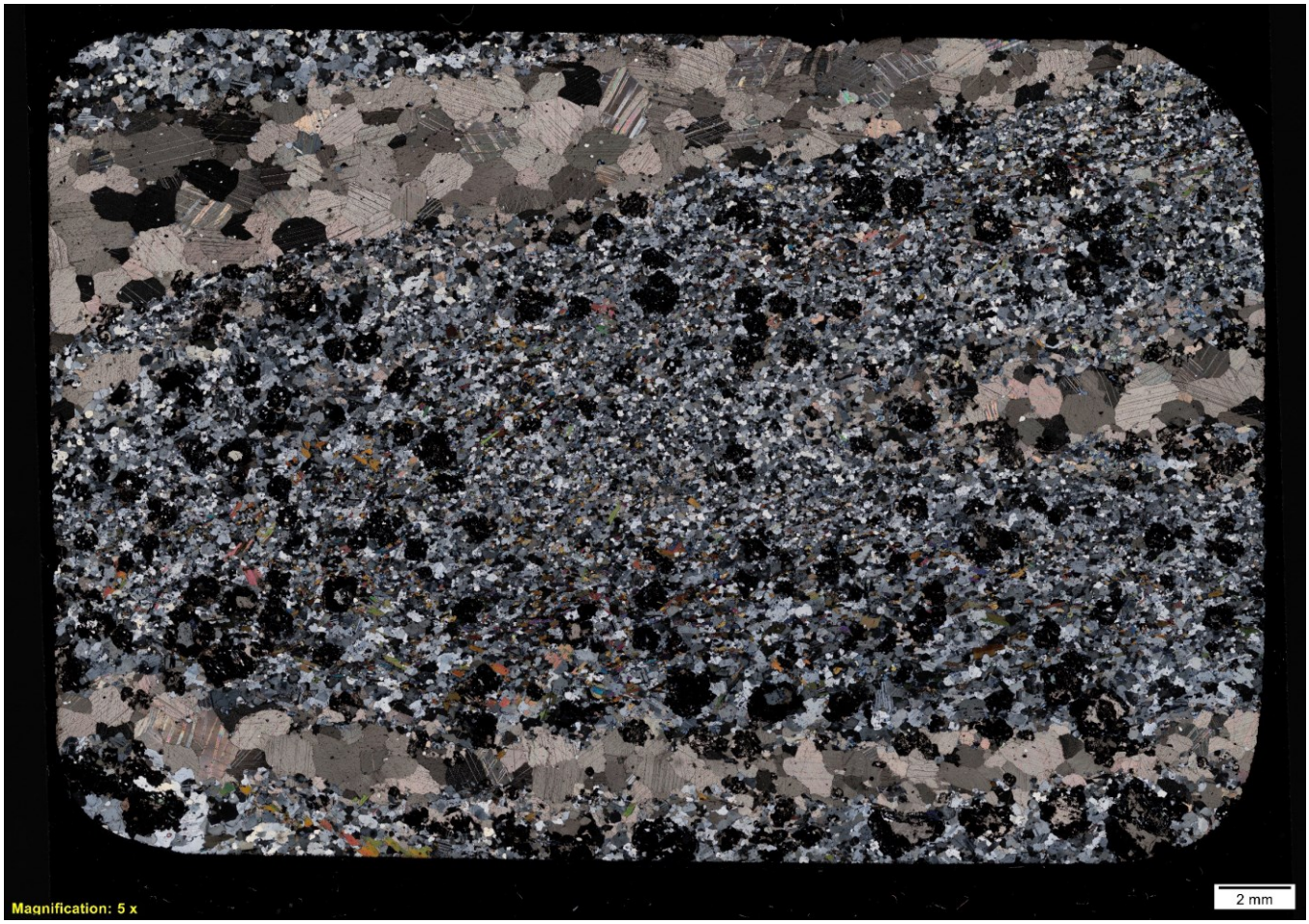

Figure 8.20: Drill core Hellerfjellet (BH4508). 38.9-39.1 m. 38306. Calcsilicate gneiss.

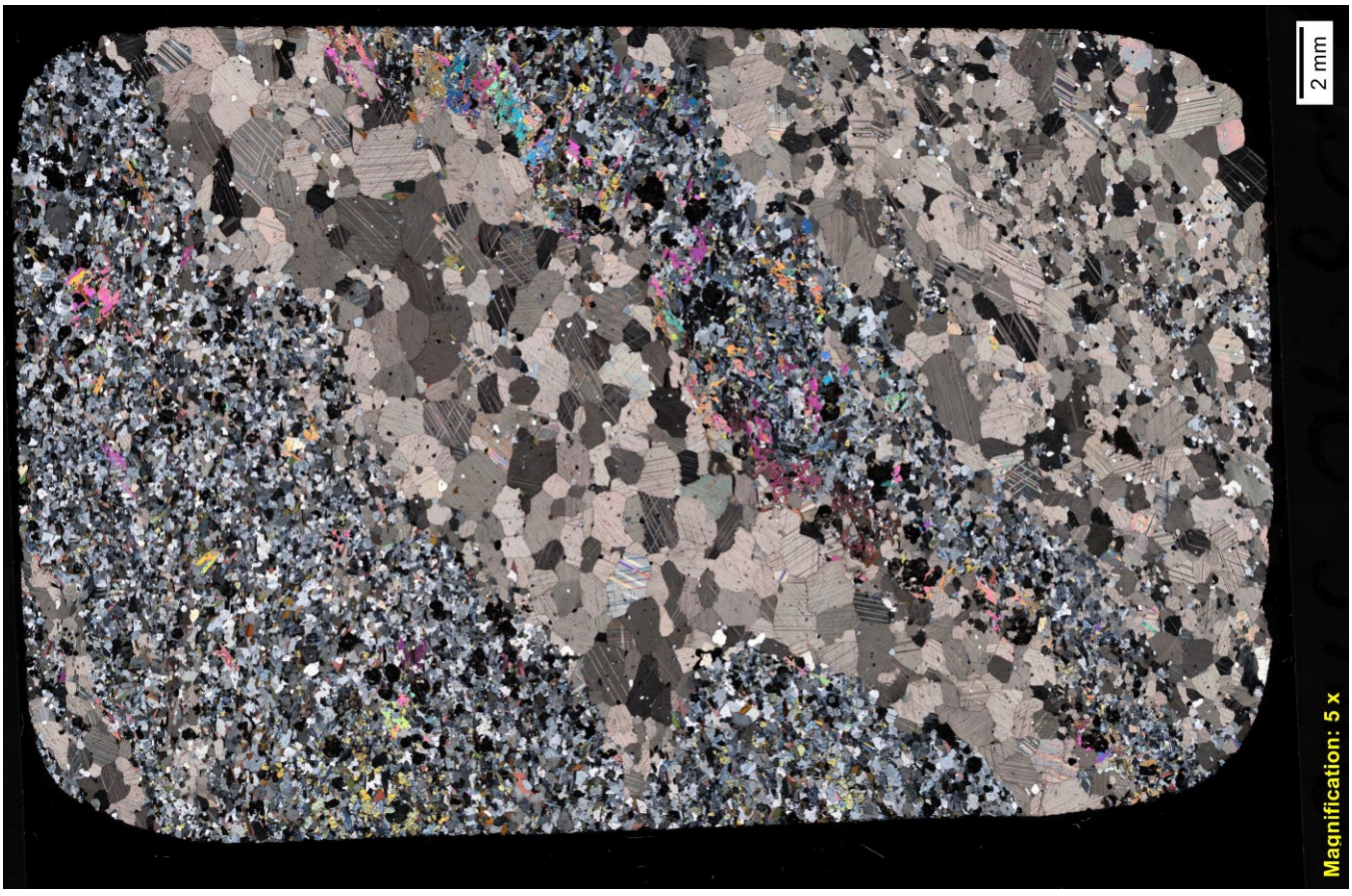

Figure 8.21: Drill core BH4508 at Hellerfjellet. 67.4-67.55 m. 38307 (left): Amphibolite. 38310 (right): Calc-silicate gneiss.

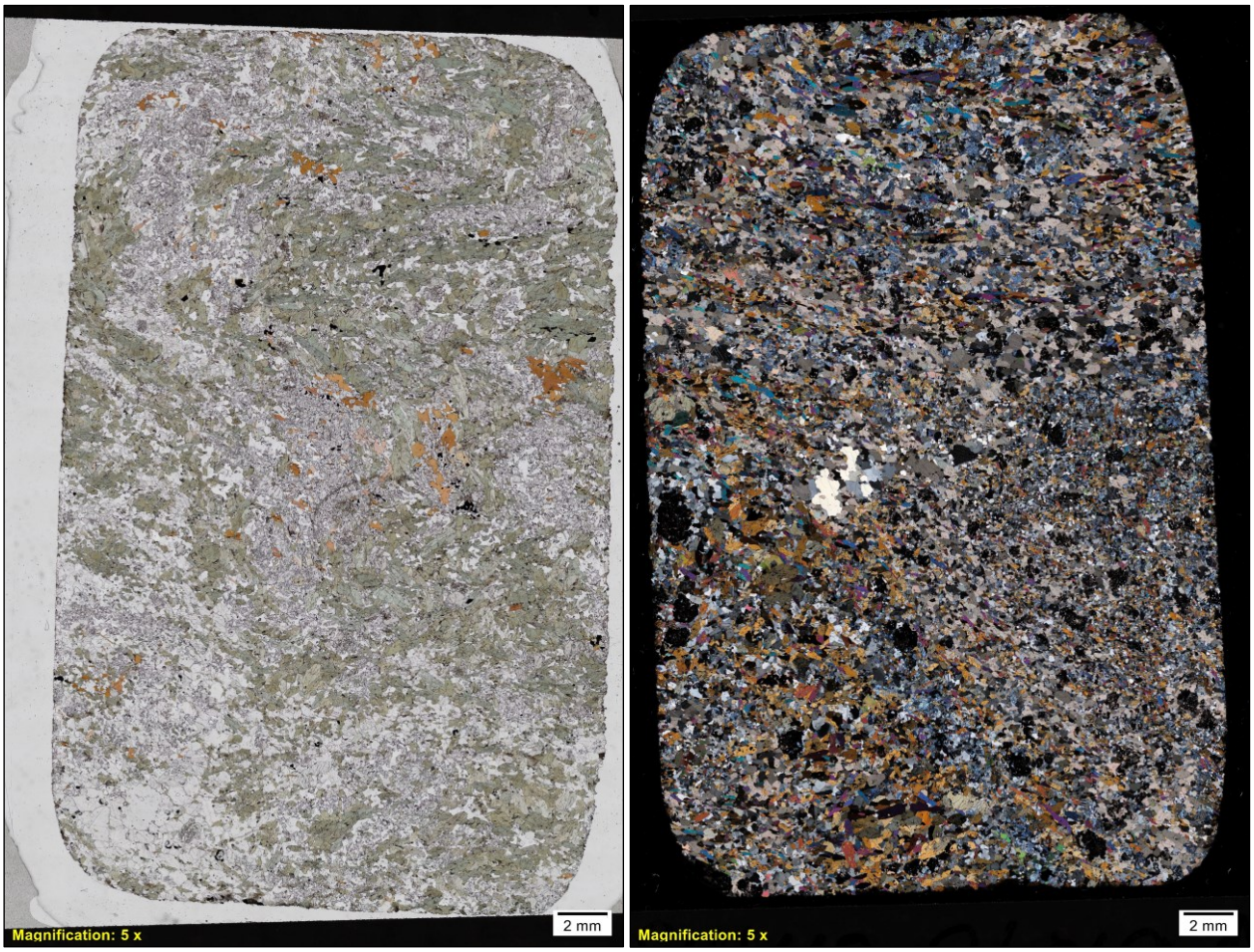

Figure 8.22: Drill core BH4508 at Hellerfjellet. 91.7-91.9 m, 38309. Amphibolite.

Figure 8.23: Drill core BH4508 at Hellerfjellet. 91.7-91.9 m, 38308 (left): Zoisite segregate within amphibolite. 105.0-105.1 m, 38311 (right): Quartz muscovite schist.

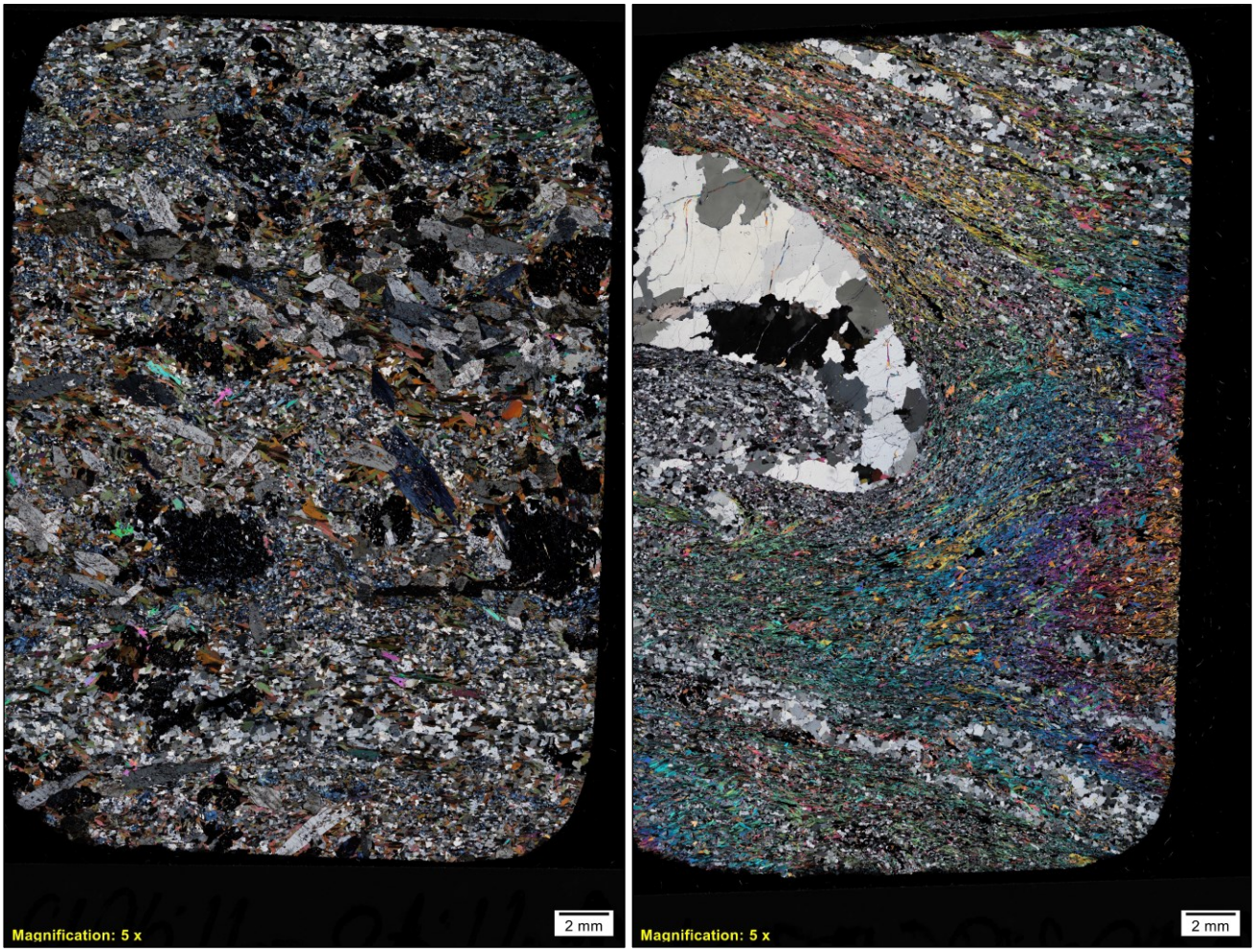

Figure 8.24: Drill core BH4508 at Hellerfjellet. 148.5-148.7 m, 38312. Quartz-muscovite schist.

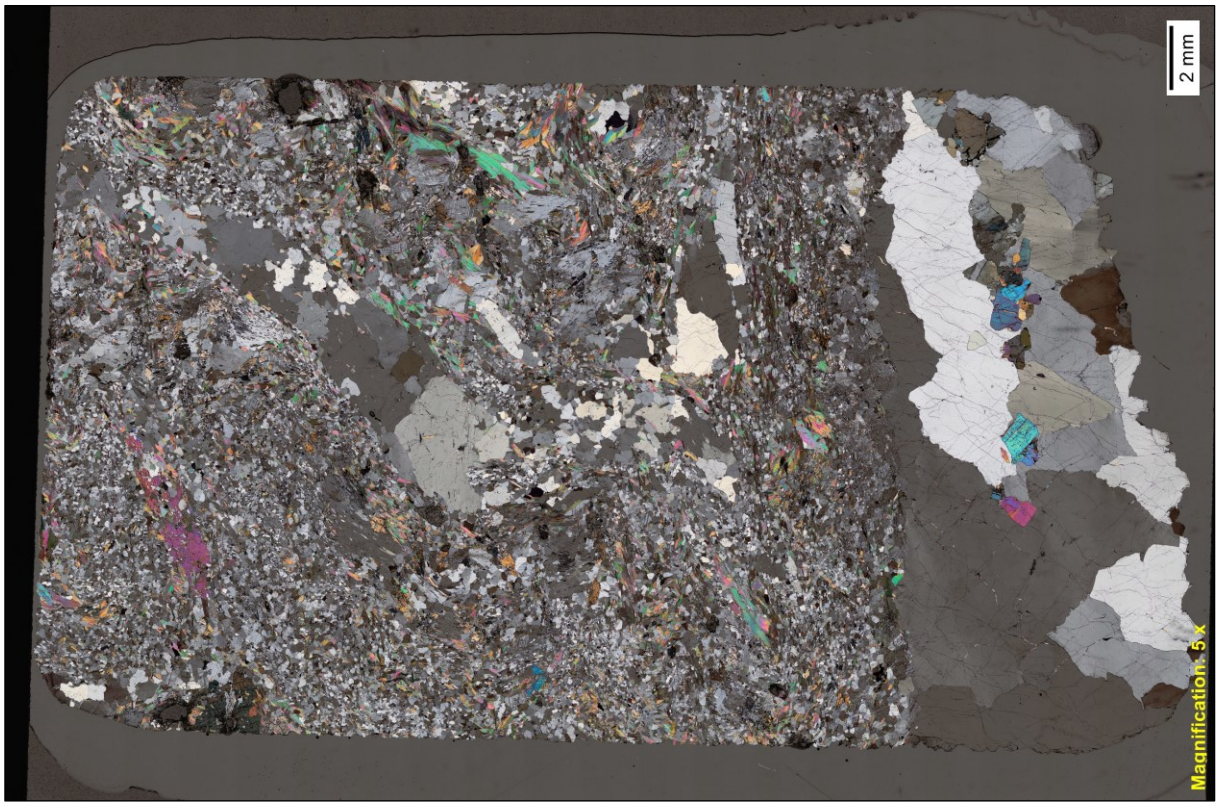

Appendix C Whole-rock Analysis

Table 8.1: Amphibolites | Major elements.

Sample	SiO2	Al2O3	Fe2O3	TiO2	MgO	CaO	Na2O	K2O	MnO	P2O5	SrO	BaO	LOI	Total	TC	TS
	Wt.%	Wt.%	Wt.%	Wt.%	Wt.%	Wt.%	Wt.%	Wt.%	Wt.%	Wt.%	Wt.%	Wt.%	Wt.%	Wt.%	Wt.%	Wt.%
HF-06	47.25	19.48	11.8	0.9	5.77	10.13	2.38	0.55	0.18	0.2	<0.01	0.03	1.05	99.78	0.09	0.01
HF-08	53.56	19	10.62	0.95	4.74	4.24	3.46	2.79	0.09	0.13	0.06	0.08	0.93	100.63	0.06	<0.01
HF-09	55.74	17.96	9.37	0.82	2.92	8.72	2.97	0.99	0.08	0.22	0.01	0.04	2.02	101.89	0.02	1.13
HF-x10	53.6	20.63	6.69	0.89	2.74	6.52	1.07	4.36	0.04	0.31	0.04	0.2	4.39	101.51	0.69	1.18
HF-x5	48.41	20.66	10.46	0.83	1.69	10.4	3.41	0.27	0.11	0.25	0.01	0.03	3.95	100.51	0.11	3.63
HF-X7	45.52	17.84	8.86	0.58	6.52	8.78	2.17	1.94	0.14	<0.01	<0.01	0.15	8.13	100.67	0.97	2.23
S-14/15	61.06	15.33	9.41	0.69	2.98	6.26	3.04	0.86	0.13	0.22	0.01	0.03	0.75	100.8	0.05	0.03
MO 019	49.22	19.35	12.60	0.83	4.62	9.19	2.48	0.75	0.18	0.09		0.02	0.39	99.70		
MO 021	49.56	16.28	9.76	0.58	8.47	9.42	3.59	0.30	0.22	0.16		0.01	0.63	98.97		
MO 022	51.47	16.48	10.60	0.39	6.31	7.70	4.67	0.20	0.20	0.04		0.01	0.99	99.05		
MO 025	51.77	15.01	10.81	0.41	8.69	8.35	3.32	0.40	0.19	0.04		0.01	0.82	99.81		
MO 036	53.10	14.67	10.78	0.35	7.67	8.58	3.18	0.31	0.27	0.04		0.01	0.85	99.80		
MO 042	49.46	19.73	11.16	0.75	4.74	9.64	2.55	1.01	0.17	0.10		0.06	0.38	99.69		
MO 043	51.96	18.92	11.08	0.64	5.37	6.58	4.41	0.41	0.15	0.08		0.02	0.26	99.86		
MO 046	49.12	18.37	12.19	0.86	6.29	8.36	3.08	0.33	0.14	0.09		0.01	0.48	99.31		
MO 052	48.60	16.15	10.18	0.47	4.86	11.29	4.23	0.53	0.17	0.05		0.01	3.26	99.79		
MO 059	49.92	15.66	12.68	1.04	7.55	8.95	2.18	0.59	0.17	0.29		0.02	0.47	99.50		
MO 060	45.98	15.95	10.77	0.44	9.78	11.65	3.00	0.35	0.15	0.03		0.01	1.53	99.63		
MO 065	49.61	17.54	13.64	0.55	6.03	10.17	1.48	0.26	0.20	0.04		0.01	0.30	99.82		
MO 067-2	47.02	15.74	10.88	1.42	9.67	10.08	2.79	0.41	0.17	0.10		0.01	0.86	99.14		
MO 083	48.40	17.61	10.98	0.82	7.37	9.40	3.84	0.37	0.17	0.08		0.01	0.71	99.75		
MO 084-2	52.40	17.92	10.43	1.28	4.89	4.79	4.70	2.29	0.15	0.17		0.06	0.81	99.83		
MO 085	49.68	16.59	11.86	0.81	7.11	9.59	2.14	0.62	0.16	0.09		0.01	0.62	99.27		
MO 088	48.78	15.57	9.83	0.66	9.45	10.62	2.24	0.73	0.15	0.07		0.02	0.86	98.96		
MO 089	50.12	15.69	10.05	0.68	9.24	9.34	2.36	1.04	0.15	0.08		0.02	0.97	99.72		
MO 093	54.32	17.62	8.81	0.88	4.51	4.23	5.44	2.15	0.26	0.17		0.08	0.73	99.12		
MO 094	56.22	17.52	8.12	0.82	4.36	4.55	4.38	2.53	0.15	0.17		0.06	0.83	99.65		
MO 099	53.49	15.91	13.30	0.75	3.46	8.57	2.93	0.59	0.25	0.08		0.01	0.17	99.50		
MO 100	56.63	18.18	9.38	0.53	3.63	8.35	2.28	0.30	0.11	0.05		0.01	0.23	99.67		
phr16	53.22	19.50	7.62	1.03	2.38	10.67	3.92	0.92	0.10	0.10		0.04	0.56	100.03		
phr20	49.39	19.83	11.63	0.67	4.40	9.93	2.56	0.48	0.11	0.14		0.01	0.85	100.00		
phr21b	51.60	15.25	11.17	0.47	7.05	8.83	3.31	0.27	0.18	0.10		0.02	0.95	99.18		
phr34	53.33	16.59	11.01	0.50	6.68	6.59	3.34	1.03	0.13	0.06		0.01	0.81	100.08		
phr36	46.54	16.30	13.77	2.29	6.87	8.83	3.77	0.38	0.20	0.30		0.04	0.32	99.56		
phr45	50.04	19.50	10.96	1.52	3.81	7.64	4.63	1.16	0.15	0.28		0.03	0.30	100.00		
phr5	49.68	18.18	12.73	0.80	6.48	8.48	2.04	0.77	0.18	0.12		0.02	0.50	99.96		
phr56	48.25	17.38	14.27	0.55	6.62	10.52	1.53	0.33	0.20	0.09		0.01	0.32	100.06		
phr65	50.78	18.41	9.66	0.84	4.93	9.21	3.08	2.08	0.11	0.11		0.11	0.46	99.69		
phr68	47.17	11.00	10.12	0.22	11.78	16.41	1.25	0.49	0.18	0.10		0.00	0.51	99.23		
phr6a	52.56	18.01	10.56	0.78	6.22	5.07	3.48	2.17	0.23	0.18		0.05	0.56	99.81		

Table 8.2: Amphibolites | Trace elements.

Sample	Cs	Cr	Sr	Rb	Y	Zr	Hf	Nb	Ta	V	W	Th	U	La	Ce	Pr	Nd	Sm	Eu	Gd	Tb	Dy	Ho	Er	Tm	Yb	Lu	Cu	Zn	Pb	Ag	Au	Bi	As	Sb	Mo	Sn	Ni	Se	Ga	Cd	Hg	Tl	Ba	Co
	ppm	ppm	ppm	ppm	ppm	ppm	ppm	ppm	ppm	ppm	ppm	ppm	ppm	ppm	ppm	ppm	ppm	ppm	ppm	ppm	ppm	ppm	ppm	ppm	ppm	ppm	ppm	ppm	ppm	ppm	ppm	ppm	ppm	ppm	ppm	ppm	ppm	ppm	ppm	ppm	ppm	ppm	ppm	ppm	ppm
HF-06	0.29	55	426.3	8.1	35.8	95	2.9	3.7	0.6	219	<1	6.67	2.18	18.6	40.2	4.84	18.5	4.23	1.15	4.53	0.78	4.98	1.13	3.4	0.57	3.65	0.61	32.6	118	20.9	0.03	<0.0005	0.05	0.6	0.06	0.62	<5	33	<0.2	18.5	0.19	<0.005	0.06	226	39.8
HF-08	3.52	25	302.3	76.3	27.1	127	3.7	4.5	0.7	189	<1	8.72	1.79	12.1	26.9	3.3	12.9	2.99	0.9	3.29	0.6	3.98	0.92	2.75	0.45	2.92	0.48	35.5	125	14.3	0.06	<0.0005	0.03	0.3	<0.05	0.4	<5	9.1	<0.2	21.4	0.19	<0.005	0.32	646	31.8
HF-09	1.09	19	357.6	23.7	36.4	98	3.3	4.2	0.7	204	<1	7.17	2.56	20.9	42.5	5.34	21.1	4.54	1.14	4.98	0.8	5.07	1.12	3.35	0.58	3.44	0.59	28.8	106	15.1	0.12	0.001	0.04	0.4	0.05	0.5	<5	12.3	<0.2	18	0.17	<0.005	0.32	316	31.5
HF-x10	4.06	316	166.9	69.8	27.9	108	3.4	7.4	0.8	263	1	11.05	5.06	21.3	43.5	5.37	20.6	4.87	1.42	4.58	0.75	4.64	1	3.15	0.53	3.33	0.56	103.4	160	27.5	0.66	<0.0005	0.1	0.3	<0.05	4.63	<5	70.4	2.6	21.1	0.87	<0.005	0.98	1723	37.4
HF-x5	0.35	19	523.8	5.7	33.2	69	2.1	4.6	0.7	326	<1	6.31	5.09	14.9	32	4.09	16.3	3.84	1.2	4.16	0.72	4.7	1.07	3.12	0.5	3.13	0.51	121.9	74	51	0.6	0.002	0.16	1.9	0.07	1.9	<5	23.9	5.2	21.4	0.73	<0.005	0.15	198	38.6
HF-X7	2.11	19	318.4	44.1	27	67	2.3	3.8	0.7	269	<1	5.21	4.42	9.1	21.6	2.95	11.8	3.16	0.88	3.28	0.57	3.88	0.88	2.8	0.46	2.85	0.45	83	139	25.6	1.03	0.001	0.17	1.3	0.07	4.7	<5	5	6.7	16.5	1.05	0.009	1.93	1161	17.5
S-14/15	0.62	29	328.5	18.2	32.9	78	2.6	3.4	0.6	17	1	6.8	2.07	14.5	33.8	4.13	16.6	3.65	0.93	3.79	0.71	4.76	1.07	3.33	0.46	3.33	0.53	12.7	138	26.6	0.27	<0.0005	0.06	0.9	0.07	0.74	<5	7.8	<0.2	17.6	0.34	0.009	0.34	287	13
MO 019	0.28	20.00	197.50	18.80	14.70	37.00	1.20	1.40	0.10	365.00	0.50	2.38	0.63	8.80	18.20	2.38	10.10	2.43	0.78	2.80	0.47	2.81	0.59	1.72	0.24	1.57	0.24	0.00	0.01	0.00	0.50					1.00	1.00	21.00	0.00	18.90			0.25	163.00	39.50
MO 021	0.08	190.00	166.50	3.90	13.60	48.00	1.30	1.40	0.10	289.00	1.00	1.83	0.80	12.20	25.90	3.51	15.70	3.34	0.98	3.20	0.46	2.61	0.52	1.55	0.23	1.45	0.21	0.00	0.01	0.00	0.50					1.00	2.00	56.00	0.00	15.50			0.25	33.90	37.40
MO 022	0.01	30.00	115.50	0.60	9.80	15.00	0.50	0.10	0.05	274.00	0.50	0.13	0.03	1.60	2.40	0.39	2.10	0.80	0.37	1.20	0.25	1.68	0.37	1.15	0.18	1.11	0.16	0.01	0.01	0.00	0.50					1.00	0.50	29.00	0.00	14.00			0.25	42.70	39.40
MO 025	0.23	320.00	91.50	7.20	11.10	17.00	0.70	0.50	0.05	271.00	0.50	0.38	0.13	2.50	5.00	0.65	3.10	1.00	0.42	1.40	0.28	1.89	0.42	1.29	0.20	1.32	0.21	0.00	0.01	0.00	0.50					1.00	0.50	78.00	0.00	13.30			0.25	49.60	36.50
MO 036	0.08	130.00	95.20	1.20	9.90	7.00	0.60	1.00	0.05	254.00	3.00	0.40	0.26	2.10	4.90	0.63	3.10	1.03	0.36	1.25	0.23	1.67	0.36	1.17	0.19	1.19	0.20	0.00	0.01	0.00	0.50					1.00	0.50	41.00	0.00	13.30			0.25	26.20	38.80
MO 042	1.11	30.00	339.00	37.80	16.80	21.00	1.20	1.50	0.10	204.00	1.00	3.02	0.80	9.90	23.30	3.03	12.70	2.86	0.93	3.07	0.51	2.99	0.67	1.96	0.30	1.99	0.27	0.00	0.01	0.00	0.50					1.00	0.50	9.00	0.00	15.20			0.25	477.00	26.80
MO 043	0.37	10.00	224.00	7.70	16.10	37.00	1.60	1.80	0.10	238.00	1.00	2.35	0.50	9.80	19.60	2.52	10.70	2.62	0.78	2.66	0.49	3.00	0.62	1.83	0.27	1.83	0.27	0.00	0.01	0.00	0.50					1.00	0.50	2.50	0.00	15.90			0.25	122.50	28.80
MO 046	0.12	50.00	220.00	3.40	17.50	62.00	2.20	3.80	0.20	289.00	2.00	2.77	0.74	12.50	25.80	3.22	13.50	3.00	0.92	3.33	0.54	3.25	0.68	2.07	0.31	1.98	0.29	0.00	0.01	0.00	0.50					1.00	1.00	16.00	0.00	17.20			0.25	110.50	39.20
MO 052	0.03	70.00	199.50	7.40	11.50	8.00	0.80	0.50	0.05	280.00	0.50	0.48	0.20	1.20	5.50	0.76	3.60	1.06	0.46	1.45	0.28	2.00	0.43	1.26	0.20	1.28	0.21	0.01	0.01	0.00	0.50					1.00	0.50	26.00	0.00	13.40			0.25	86.90	34.80
MO 059	0.17	150.00	256.00	9.10	16.80	39.00	1.60	2.30	0.10	272.00	2.00	2.17	0.95	7.50	16.50	2.28	10.40	2.68	0.87	3.00	0.50	3.11	0.65	1.93	0.25	1.86	0.27	0.00	0.01	0.00	0.50					1.00	1.00	45.00	0.00	16.60			0.25	132.00	37.90
MO 060	0.02	960.00	145.00	5.20	8.80	3.00	0.60	0.20	0.05	352.00	8.00	0.21	0.24	0.70	2.30	0.36	1.90	0.71	0.26	1.12	0.21	1.58	0.35	1.07	0.15	1.11	0.17	0.01	0.01	0.00	0.50					1.00	0.50	242.00	0.00	13.20			0.25	15.60	54.30
MO 065	0.01	10.00	141.00	2.10	8.70	5.00	0.70	1.10	0.10	388.00	1.00	1.11	0.45	3.20	6.70	0.88	3.50	0.93	0.37	1.24	0.24	1.63	0.36	1.15	0.17	1.16	0.18	0.00	0.01	0.00	0.50					1.00	0.50	16.00	0.00	16.80			0.25	24.70	42.50
MO 067-2	0.01	440.00	115.00	1.30	24.90	75.00	2.00	3.40	0.20	185.00	2.00	0.35	0.38	6.10	15.40	2.57	12.90	3.88	1.49	4.29	0.77	4.52	0.95	2.53	0.36	2.33	0.35	0.00	0.02	0.01	0.50					1.00	2.00	192.00	0.00	16.10			0.25	21.50	46.10
MO 083	0.01	90.00	119.00	1.10	14.30	20.00	0.80	0.40	0.05	327.00	0.50	0.54	1.13	0.25	3.80	0.61	3.30	1.37	0.60	1.80	0.34	2.61	0.54	1.78	0.24	1.72	0.25	0.00	0.01	0.00	0.50					1.00	0.50	51.00	0.00	16.30			0.25	25.10	46.30
MO 084-2	0.84	80.00	155.50	54.70	19.20	67.00	1.90	3.00	0.10	217.00	1.00	1.48	0.29	8.20	20.50	2.67	12.20	3.08	1.15	3.64	0.56	3.75	0.76	2.21	0.29	1.96	0.30	0.00	0.01	0.00	0.50					1.00	1.00	39.00	0.00	16.40			0.25	489.00	34.40
MO 085	0.01	120.00	185.00	2.60	18.30	25.00	1.00	1.70	0.05	317.00	1.00	0.57	0.21	4.80	10.70	1.84	8.10	2.45	0.81	2.90	0.53	3.39	0.71	2.20	0.30	2.06	0.30	0.00	0.01	0.00	0.50					1.00	0.50	47.00	0.00	16.80			0.25	50.30	34.90
MO 088	0.02	510.00	165.00	3.40	14.00	38.00	1.30	1.20	0.05	251.00	20.00	0.66	0.25	2.80	7.90	1.11	5.60	1.57	0.64	2.26	0.38	2.73	0.54	1.65	0.23	1.60	0.23	0.00	0.01	0.00	0.50					1.00	0.50	126.00	0.00	14.80			0.25	105.50	42.60
MO 089	0.55	470.00	130.50	14.20	14.90	33.00	1.10	1.20	0.05	261.00	1.00	0.67	0.20	2.40	7.90	1.13	5.70	1.83	0.66	2.28	0.42	2.76	0.61	1.86	0.28	1.81	0.26	0.00	0.01	0.00	0.50					1.00	0.50	117.00	0.00	14.90			0.25	130.00	40.90
MO 093	1.54	80.00	141.00	74.90	20.20	103.00	2.80	6.60	0.40	162.00	0.50	4.67	0.59	18.70	45.10	4.77	19.30	3.99	1.08	4.35	0.65	3.92	0.78	2.35	0.34	2.25	0.31	0.00	0.01	0.00	0.50					1.00	1.00	43.00	0.00	18.00			0.25	650.00	28.00
MO 094	1.06	160.00	133.50	90.50	20.20	140.00	3.80	5.70	0.30	145.00	1.00	6.47	0.88	19.30	45.70	5.05	20.00	4.08	0.99	4.25	0.66	3.84	0.83	2.39	0.33	2.36	0.33	0.00	0.01	0.00	0.50					1.00	1.00	72.00	0.00	17.20			0.25	489.00	26.70
MO 099	0.02	5.00	156.50	5.70	16.10	27.00	1.00	1.10	0.05	379.00	0.50	0.79	0.32	3.50	9.20	1.24	5.90	1.96	0.68	2.31	0.42	3.00	0.61	1.88	0.27	1.89	0.28	0.00	0.01	0.00	0.50					1.00	1.00	2.50	0.00	16.80			0.25	64.60	35.20
MO 100	0.01	10.00	226.00	3.00	15.00	13.00	0.60	0.40	0.05	292.00	1.00	0.33	0.30	1.90	5.40	0.75	3.90	1.33	0.58	1.91	0.36	2.70	0.58	1.75	0.41	1.81	0.25	0.00	0.01	0.00	0.50					1.00	0.50	7.00	0.00	15.30			0.25	70.20	23.90
phr16		2.50	302.00	6.00	20.50	77.00		2.50		214.00	15.00	5.00	5.00	7.70	22.50	5.00	9.10	3.20	0.60	3.00	0.60	3.00	0.80	2.70	0.30	2.00	0.30	0.00	0.01	0.00	5.00					2.50	5.00	2.50	0.00	16.00			0.00	385.00	23.00
phr20		15.00	300.00	5.00	27.40	51.00		2.50		223.00	15.00	5.00	5.00	11.80	29.80	3.90	13.30	3.90	1.20	3.30	0.50	3.30	0.80	0.80	0.20	2.50	0.60	0.00	0.01	0.00	5.00					2.50	5.00	6.00	0.00	17.00			0.00	132.00	41.00
phr21b		130.00	121.00	2.50	18.10	35.00		2.50		298.00	15.00	5.00	5.00	2.30	9.50	1.70	2.90	1.10	0.50	1.30	0.30	2.30	0.50	2.20	0.30	1.80	0.50	0.03	0.01	0.00	5.00					2.50	5.00	47.00	0.00	12.00			0.00	186.00	45.00
phr34		99.00	105.00	13.00	19.90	43.00		2.50		361.00	15.00	5.00	5.00	2.60	11.60	0.90	3.90	1.70	0.60	1.70	0.30	2.60	0.60	1.40	0.20	2.10	0.30	0.01	0.01	0.00	5.00					2.50	5.00	32.00	0.00	14.00			0.00	119.00	47.00
phr36		128.00	439.00	2.50	43.30	182.00		11.00		274.00	15.00	5.00	11.00	12.90	35.30	5.40	19.00	5.70	2.30	6.00	1.40	6.40	1.40	3.70	0.30	3.60	1.00	0.02	0.01	0.00	5.00					2.50	5.00	41.00	0.00	20.00			0.00	363.00	56.00
phr45		11.00	403.00	20.00	30.90	158.00		14.00		300.00	15.00	5.00	5.00	22.00	51.80	7.30	20.00	5.00	1.70	4.00	0.70	4.40	0.90	3.20	0.40	2.80	0.20	0.00	0.01	0.00	5.00					2.50	5.00	5.00	0.00	20.00			0.00	304.00	33.00
phr5		19.00	217.00	11.00	24.00	51.00		2.50		296.00	15.00	5.00	11.00	8.80	24.90	2.30	9.40	2.70	1.00	2.80	0.40	3.10	0.70	2.90	0.30	2.30	0.20	0.01	0.01	0.00	5.00					2.50	5.00	14.00	0.00	18.00			0.00	183.00	40.00
phr56		42.00	161.00	2.50	12.30	31.00		2.50		363.00	15.00	5.00	11.00	3.50	13.10	0.90	3.30	1.20	0.40	1.20	0.20	1.50	0.30	0.80	0.20	1.30	0.20	0.00	0.01	0.00	5.00					2.50	5.00	21.00	0.00	17.00			0.00	48.00	51.00
phr65		33.00	209.00	53.00	19.60	54.00		2.50		346.00	15.00	5.00	5.00	4.60	15.20	1.70	6.80	2.60	0.80	1.90	0.50	2.60	0.60	0.80	0.20	2.00	0.50	0.00	0.01	0.00	5.00					2.50	5.00	10.00	0.00	17.00			0.00	958.00	37.00
phr68		653.00	134.00	2.50	7.90	18.00		2.50		247.00	15.00	5.00	5.00	2.70	9.80	0.60	1.70	0.60	0.30	0.20	0.20	1.00	0.30	0.80	0.20	0.90	0.30	0.00	0.01	0.00	5.00					2.50	5.00	153.00	0.00	13.00			0.00	39.00	54.00
phr6a		29.00	200.00	37.00	35.10	101.00		5.00		162.00	15.00	5.00	5.00	17.60	44.00	5.20	17.60	4.30	1.30	4.20	0.90	4.40	1.00	3.60	0.30	3.30	0.40	0.00	0.01	0.00	5.00					2.50	5.00	9.00	0.00	16.00			0.00	447.00	28.00

Table 8.3: Graphite quartz gneiss | Major elements.

Sample	SiO2	Al2O3	Fe2O3	TiO2	MgO	CaO	Na2O	K2O	MnO	P2O5	SrO	BaO	LOI	Total	TC	TS
	Wt.%	Wt.%	Wt.%	Wt.%	Wt.%	Wt.%	Wt.%	Wt.%	Wt.%	Wt.%	Wt.%	Wt.%	Wt.%	Wt.%	Wt.%	Wt.%
HF-x16	61,38	12,57	6,37	0,76	4,46	5,93	1,03	2,58	0,14	0,58	0,03	0,05	3,39	99,29	1,18	1,31
HFx22 C	79,14	7,5	3,72	0,21	2,13	1,58	1,36	1,33	0,07	0,03	<0.01	0,05	2,23	99,38	0,82	0,34
HF-x23	58,82	14,08	7,41	0,49	4,16	5,21	0,41	3,45	0,1	0,33	0,01	0,12	5,95	100,57	3,05	1,32
HF-03	85,03	4,48	1,12	0,12	0,92	0,43	0,41	0,96	<0.01	0,04	0,02	0,11	5,86	99,47	4,97	0,07
HF-x12 b	68,85	10,15	1,1	0,44	0,64	1,02	1,46	3,11	0,03	0,06	0,02	0,28	13,78	100,92	12,5	<0.01
HF-x35	61,06	13,62	5,37	0,59	2,18	3,78	0,9	2,96	0,07	0,47	<0.01	0,13	9,36	100,52	5,82	<0.01
HF-05	71,63	15	2,05	0,3	3,06	1,64	2,13	2,88	0,02	0,03	0,01	0,29	2,3	101,35	0,38	0,09
HF-x11	74,96	9,43	4,42	0,22	1,97	2,09	1	1,74	0,03	0,06	0,03	0,28	4,27	100,5	1,7	0,15
HF-x13	72,34	11,76	2,33	0,31	1,82	2,4	1,1	2,48	0,03	0,16	0,02	0,13	5,89	100,77	3,85	<0.01
HF-X14	55,02	19,03	5,87	0,99	2,18	6,96	0,96	3,23	0,05	0,33	0,02	0,17	5,63	100,45	1,39	1,52
HF-x15	75,57	9,53	4,57	0,49	1,77	2,77	0,76	1,94	0,09	0,13	0,02	0,06	3,76	101,46	1,18	0,67
HF-x18	59,58	13,57	7,31	0,61	3,29	3,8	0,91	3,76	0,1	0,34	0,02	0,22	6,27	99,81	1,59	2,96
HF-x20	72,74	11,27	3,33	0,27	1,11	1,88	3,06	2,14	0,07	0,07	0,02	0,1	2,59	98,65	1,05	0,55
HF-x21	72,29	11,43	4,36	0,31	1,64	3,96	1,5	1,16	0,09	0,09	0,02	0,07	3,79	100,7	1,04	0,54
HF-x9	63,78	13,05	5,45	0,74	2,99	3,4	1,18	2,56	0,1	0,18	<0.01	0,09	5,23	98,8	1,74	0,58
S-1	53,28	17,53	8,54	0,77	2,73	3,17	2,04	3,7	0,04	0,28	<0.01	0,31	9,51	101,94	0,18	0,38
S-12	85,02	8,11	1,91	0,16	0,43	1,08	1,51	1,59	0,02	0,04	0,02	0,05	1,27	101,19	0,17	0,38
S-13	63,8	13,97	6,58	0,83	3,8	5,61	1,15	2,42	0,11	0,19	0,02	0,05	3,13	101,67	0,78	0,3
S-2	64,2	14,13	5,29	0,54	1,9	3,09	1,76	3,84	0,03	0,14	<0.01	0,26	4,76	99,96	0,87	1,03
S-21	62,22	13,51	7,01	0,52	2,62	3,74	1,23	3,46	0,05	0,14	0,01	2,06	3,34	99,92	0,18	3,53
S-6 a	56,76	14,89	8,12	1,96	2,48	5,73	3,76	1,29	0,09	0,78	0,02	0,48	3,94	100,34	0,23	4,1
S-6 b	71,01	12,4	3,86	0,18	2,34	3,05	3,68	0,84	0,07	0,11	0,02	0,17	2,69	100,43	1,27	0,05
S-6 c	70,82	13,54	3,65	0,34	1,79	2,88	1,66	2,48	0,03	0,12	0,07	1,14	2,5	100,96	0,55	0,34

Table 8.4: Graphite quartz gneiss | Trace elements.

Sample	Cs	Cr	Sr	Rb	Y	Zr	Hf	Nb	Ta	V	W	Th	U	La	Ce	Pr	Nd	Sm	Eu	Gd	Tb	Dy	Ho	Er	Tm	Yb	Lu	Cu	Zn	Pb	Ag	Au	Bi	As	Sb	Mo	Sn	Ni	Se	Ga	Cd	Hg	Tl	Ba	Co
	ppm	ppm	ppm	ppm	ppm	ppm	ppm	ppm	ppm	ppm	ppm	ppm	ppm	ppm	ppm	ppm	ppm	ppm	ppm	ppm	ppm	ppm	ppm	ppm	ppm	ppm	ppm	ppm	ppm	ppm	ppm	ppm	ppm	ppm	ppm	ppm	ppm	ppm	ppm	ppm	ppm	ppm	ppm	ppm	ppm
HF-x16	5,77	98	193	112,2	33,1	164	4,7	19,1	1,2	262	1	11,97	6,63	44,4	87,5	10,15	37,9	7,6	1,48	6,64	1,04	5,66	1,22	3	0,4	2,78	0,43	54,4	195	21,6	0,47	0,001	0,13	4,2	0,12	5,98	<5	62,8	1,6	18	2,93	<0.005	1,79	418	17,5
HFx22 C	2,51	33	125,8	44,2	7,1	92	2,3	4	0,7	50	3	5,48	1,69	2,4	5,2	0,73	2,7	0,75	0,3	0,56	0,12	0,92	0,28	0,92	0,18	1,58	0,27	20	80	9	0,11	<0.0005	0,12	0,5	0,06	1,96	<5	7,3	0,5	9	0,12	<0.005	1,24	460	3,5
HF-x23	4,95	190	275,6	120,2	29,8	106	3,3	21,2	1,2	590	2	12,4	22,55	45,2	81,4	8,97	33,9	6,61	1,24	6,06	1	5,88	1,27	3,27	0,49	3,34	0,49	105,4	288	45,2	0,55	<0.0005	0,25	1,9	0,06	31,13	<5	118,7	4,2	18,9	3,04	<0.005	1,79	1111	27,4
HF-03	0,8	27	56,8	17,1	1,4	37	1	5,3	0,7	445	1	4,08	3,29	3,2	7,7	0,84	2,5	0,54	0,12	0,34	0,04	0,23	0,05	0,17	0,04	0,25	0,05	3,5	25	11	0,07	<0.0005	0,1	0,5	<0.05	33,98	<5	2,2	1	5,9	0,04	<0.005	0,485	847	0,5
HF-x12 b	0,65	62	138,3	49	5,4	105	2,9	8	1,1	806	4	6,32	8,41	1,5	3	0,37	1,8	0,86	0,55	0,59	0,13	0,88	0,2	0,61	0,11	0,71	0,12	5,7	22	24,4	0,63	<0.0005	0,3	0,6	0,07	75,98	<5	1,2	3,4	14,8	0,06	<0.005	0,34	3103	0,4
HF-x35	1,55	114	167	77,3	24,6	147	4,1	9,9	1,1	1045	1	12,08	22,9	12,8	27,3	3,31	12,8	3,24	0,82	2,99	0,59	3,77	0,92	2,53	0,42	3,06	0,47	58,8	71	58,1	0,39	0,001	0,54	1,5	0,09	46,81	<5	5,1	7,1	18,5	0,68	0,011	1,29	1158	1,1
HF-05	3,72	15	130,5	51,2	20,9	151	4,5	6,6	0,7	60	<1	7,45	3,17	4,1	8	0,91	3,3	1,11	0,61	1,24	0,28	2,23	0,65	2,35	0,43	3,11	0,54	5,6	43	22,4	0,9	0,001	0,11	2,3	0,07	5,07	<5	0,7	1	15,7	0,04	<0.005	1,23	2705	0,9
HF-x11	1,63	27	137,5	32,5	12,2	107	3,4	4,4	0,7	199	1	7,67	4,96	28,5	44,9	4,66	17	3,76	0,83	2,86	0,45	2,52	0,52	1,37	0,2	1,38	0,24	18,5	60	22,5	0,97	0,001	0,07	1,6	0,07	12,97	7	2	1,4	11,1	0,12	0,005	0,97	2579	0,9
HF-x13	1,74	59	175,4	61	9,8	93	2,9	6,2	0,9	513	5	12,58	12,89	18,7	32,8	3,4	11,8	2,36	0,64	2,07	0,3	1,63	0,34	0,96	0,15	1	0,16	17,1	26	21,2	0,27	<0.0005	0,16	1,2	0,11	36,85	<5	1,9	2,2	16	0,06	0,006	0,83	1146	1,2
HF-X14	2,23	60	245,1	71,3	31,7	120	3,8	10,1	1	449	2	10,16	12,38	35,9	66,6	7,24	27,4	5,55	1,48	4,85	0,8	4,86	1,23	3,36	0,53	3,93	0,62	40,5	56	27	0,28	0,001	0,2	23,4	0,2	13,85	<5	11	2,5	24,9	0,55	0,007	0,95	1491	23,4
HF-x15	3,29	97	165,8	74,1	24,6	126	3,5	12,1	1,1	190	3	8,99	5,51	19,4	40,2	4,55	17,5	3,72	0,85	3,46	0,6	3,97	0,85	2,36	0,35	2,48	0,39	50,4	106	24,4	0,5	<0.0005	0,14	1,4	0,07	8,05	<5	42,9	1,6	14,3	1,25	<0.005	1,02	489	14,3
HF-x18	4,64	162	180,8	110,3	29,7	118	3,7	11,8	1	406	<1	8,42	12,09	14,3	33,2	4,18	17	4,37	1,15	3,83	0,72	5,02	1,2	3,42	0,55	3,75	0,56	90,55	182	30,35	1,24	0,001	0,38	1,7	0,1	20,545	<5	118	3,8	18,5	2,355	<0.005	1,82	2137	22,5
HF-x20	1,06	23	124,3	49,5	22,8	116	3,4	5,6	0,8	147	<1	7,23	4,11	20,6	39	4,43	16,7	3,62	0,8	3,44	0,6	3,74	0,87	2,42	0,38	2,74	0,47	10,2	69	14,8	0,34	<0.0005	0,1	1,3	0,07	7,52	<5	2,6	1,1	11,7	0,26	<0.005	0,45	871	2,7
HF-x21	1,08	25	222,1	35,1	20,2	117	3,2	5,7	0,8	113	<1	7,33	4,69	13,1	21,6	2,24	8	1,87	0,58	1,87	0,37	2,66	0,67	2,22	0,35	2,75	0,44	35,5	66	39,7	0,32	<0.0005	0,18	0,7	0,08	8,79	<5	17,8	2,1	12,7	0,7	<0.005	0,63	588	4,7
HF-x9	4,61	108	204,8	102,9	15,5	155	4,5	18,9	1,1	332	<1	10,73	9,58	7,8	13,7	1,58	5,7	1,54	0,64	1,56	0,32	2,25	0,52	1,7	0,32	2,07	0,38	57,7	168	31,6	0,44	<0.0005	0,24	0,3	<0.05	10,95	<5	43,6	3,4	19,3	0,96	0,01	1,41	705	12,1
S-1	1,93	23	252,9	58,3	21,2	137	4,4	6,7	0,8	207	<1	9,06	5,33	26,9	48,7	5,39	20,4	4,8	1,33	3,99	0,7	4,25	0,96	2,58	0,39	2,73	0,4	36,5	72	34,5	1,38	0,001	0,22	1,7	0,11	9,01	<5	1,2	1,3	20,2	0,15	0,01	0,91	3279	1,7
S-12	0,44	<10	118,5	28,1	17,3	69	2	3,2	0,7	<10	<1	5,23	2,54	12,7	26,7	3,22	11,7	2,32	0,47	2,4	0,4	2,69	0,55	1,75	0,28	2,07	0,34	33,9	58	65,3	0,59	<0.0005	0,2	0,8	0,2	6,64	<5	3,9	0,5	7,5	0,33	0,033	0,11	374	2,6
S-13	5,02	101	247,4	100,3	36,5	194	5,6	16,4	1,3	96	1	11,53	4,84	29,9	63,3	7,76	28,7	5,66	1,2	5,54	0,91	5,58	1,15	3,35	0,48	3,37	0,52	35,6	206	71,4	0,63	<0.0005	0,14	1,2	0,16	4,34	<5	24,3	1,6	18,5	1,31	0,023	1,8	374	7,6
S-2	1,42	31	211,3	49	13,1	99	2,9	4,9	0,8	271	<1	8,06	3,17	16,8	32,9	3,66	14	3,22	0,93	2,56	0,43	2,66	0,6	1,55	0,23	1,58	0,22	12,7	61	40,1	0,77	0,001	0,32	4	0,15	4,79	<5	3	1	16,8	0,23	0,008	0,52	2523	8,9
S-21	2,16	15	154,9	46,1	24,9	62	2,1	2,8	0,7	41	2	5,5	1,69	11	27	3,73	15,2	5,36	1,52	3,57	0,65	4,2	0,84	2,57	0,39	2,61	0,42	23,2	127	15	0,35	<0.0005	0,21	3,7	0,11	1,76	<5	7,1	0,3	15,1	0,18	0,009	0,48	>10000	22
S-6 a	2,86	10	693	45,9	57,8	272	6,6	56,6	2,6	175	<1	6,21	8,83	39,9	88,1	10,99	44,9	10,46	3,58	8,89	1,55	9,41	2,22	6,1	0,96	6,75	0,99	738,6	177	62,2	6,37	0,001	0,04	4,2	0,15	3,98	10	59,3	5,6	13,8	2,18	0,01	3,8	5348	20,3
S-6 b	3,56	17	256	33,7	10,2	123	3,5	5,4	0,9	223	<1	12,26	4,04	6,6	11,2	1,08	3,8	0,95	0,39	0,87	0,17	1,2	0,36	1,25	0,24	1,96	0,33	9,8	56	12,4	0,32	<0.0005	0,03	0,6	0,08	4,06	<5	2,2	0,4	14,8	0,34	<0.005	1,42	1634	1
S-6 c	2,37	25	317,3	59,5	18,5	87	2,8	7,3	0,9	118	2	11,32	4,57	11,5	23,2	2,75	9,6	3,14	1,08	2,19	0,4	2,69	0,59	1,93	0,31	1,98	0,31	762,6	47	101,1	3,32	0,001	0,18	2	0,27	6,92	<5	3	3	17,4	0,21	0,008	1,9	>10000	2,8

Table 8.5: Grey gneiss and metarhyolite | Major elements.

Sample	SiO2	Al2O3	Fe2O3	TiO2	MgO	CaO	Na2O	K2O	MnO	P2O5	SrO	BaO	LOI	Total	TC	TS
	Wt.%	Wt.%	Wt.%	Wt.%	Wt.%	Wt.%	Wt.%	Wt.%	Wt.%	Wt.%	Wt.%	Wt.%	Wt.%	Wt.%	Wt.%	Wt.%
HF-12	72,19	9,49	1,05	0,13	0,45	5,16	0,37	7,31	0,11	0,04	0,05	0,05	4,11	100,47	1,25	<0.01
MO 020	69,51	14,02	5,42	0,35	1,86	2,19	3,54	1,90	0,15	0,06		0,02	0,76	99,76		
MO 023	69,22	14,88	4,60	0,27	1,91	1,70	3,08	1,69	0,20	0,07		0,07	1,79	99,41		
MO 024	70,13	13,21	2,95	0,25	0,55	4,47	4,27	1,12	0,07	0,06		0,02	2,60	99,68		
MO 041	69,24	15,68	4,40	0,24	1,29	1,57	5,13	1,50	0,08	0,06		0,02	0,64	99,83		
MO 047	72,79	12,93	2,42	0,25	1,30	2,62	1,51	2,97	0,05	0,04		0,09	1,81	98,69		
MO 048	73,29	13,44	2,61	0,14	1,53	1,21	2,71	4,06	0,06	0,03		0,07	0,64	99,72		
MO 053	73,02	14,11	3,46	0,25	0,77	2,45	3,99	1,33	0,11	0,06		0,02	0,39	99,94		
MO 054	75,31	12,69	2,38	0,20	0,43	1,67	2,91	3,15	0,04	0,05		0,04	0,61	99,44		
MO 055	70,69	14,54	2,73	0,31	0,74	2,74	2,24	4,92	0,10	0,09		0,05	0,69	99,79		
MO 061	66,36	16,59	4,60	0,38	2,70	1,35	5,72	1,51	0,10	0,10		0,02	0,51	99,92		
MO 067-1	75,02	12,72	4,09	0,28	0,68	1,00	4,46	0,67	0,10	0,05		0,02	0,37	99,44		
MO 092	77,58	12,04	1,20	0,15	0,77	2,36	2,65	1,90	0,04	0,03		0,05	0,34	99,06		
MO 104	76,78	12,37	1,79	0,13	0,48	0,99	2,88	3,69	0,02	0,02		0,07	0,41	99,56		
HF-01	78,25	12,61	1,83	0,14	2,62	1,69	1,41	0,54	0,02	<0.01	<0.01	0,05	1,06	100,24	0,04	<0.01
HF-02	74,96	12,13	1,89	0,14	1,08	2,08	2,72	2,16	0,02	0,01	<0.01	0,09	0,84	98,14	0,05	<0.01
HF-07	78,08	12,05	1,29	0,19	0,22	2,32	2,86	1,92	0,04	0,04	0,02	0,04	0,73	99,78	0,14	<0.01
HS-2	78,64	10,51	1,15	0,05	0,26	0,79	1,12	5,9	0,03	0,02	0,02	0,09	0,54	99,11	0,02	<0.01
HS-3	78,9	12,15	1,51	0,12	0,4	0,87	2,97	3,96	0,02	0,01	<0.01	0,07	0,41	101,41	0,02	<0.01
MO 063	76,20	11,49	1,68	0,16	0,17	1,55	1,62	5,36	0,03	0,05		0,08	1,39	99,70		
MO 064	81,50	9,66	0,30	0,01	0,11	0,04	0,63	6,89	0,01	0,01		0,45	0,21	99,33		
MO 087	75,48	12,58	1,54	0,22	0,59	0,97	1,97	5,74	0,02	0,04		0,08	0,38	99,53		
MO 090	75,74	12,67	1,33	0,17	0,36	1,10	2,57	4,37	0,01	0,03		0,05	0,38	98,73		
MO 091	82,89	10,12	1,05	0,18	0,19	0,77	2,09	1,27	0,02	0,02		0,04	0,72	99,32		

Table 8.6: Grey gneiss and metarhyolite | Trace elements.

Sample	Cs	Cr	Sr	Rb	Y	Zr	Hf	Nb	Ta	V	W	Th	U	La	Ce	Pr	Nd	Sm	Eu	Gd	Tb	Dy	Ho	Er	Tm	Yb	Lu	Cu	Zn	Pb	Ag	Au	Bi	As	Sb	Mo	Sn	Ni	Se	Ga	Cd	Hg	Tl	Ba
	ppm	ppm	ppm	ppm	ppm	ppm	ppm	ppm	ppm	ppm	ppm	ppm	ppm	ppm	ppm	ppm	ppm	ppm	ppm	ppm	ppm	ppm	ppm	ppm	ppm	ppm	ppm	ppm	ppm	ppm	ppm	ppm	ppm	ppm	ppm	ppm	ppm	ppm	ppm	ppm	ppm	ppm	ppm	ppm
HF-12	0,21	13	35,3	67,1	20	79	2,2	3,4	0,8	12	<1	6,33	3,56	13,9	25,6	2,84	9,7	1,97	0,48	2,05	0,35	2,29	0,53	1,71	0,3	1,98	0,32	2,8	14	14,8	0,02	<0.0005	0,04	0,5	<0.05	0,85	<5	0,8	<0.2	7,1	0,08	<0.005	0,05	391
MO 020	1,29	10,00	79,00	40,90	26,50	81,00	2,50	3,10	0,20	45,00	1,00	2,62	0,77	9,20	18,90	2,45	10,70	2,89	0,82	3,73	0,67	4,57	1,01	3,25	0,51	3,48	0,54	0,00	0,01	0,01	0,50					1,00	1,00	5,00	0,00	15,30			0,25	189,00
MO 023	0,46	10,00	107,00	49,10	21,50	110,00	3,20	6,40	0,40	25,00	1,00	7,49	4,64	20,10	36,50	4,06	14,80	3,00	0,73	3,48	0,57	3,58	0,83	2,59	0,40	2,85	0,47	0,00	0,03	0,01	0,50					5,00	1,00	7,00	0,00	15,50			0,25	588,00
MO 024	0,27	10,00	115,00	15,60	29,60	64,00	2,30	2,10	0,10	36,00	0,50	1,76	0,65	7,00	14,40	1,89	8,70	2,65	0,67	3,66	0,69	4,74	1,07	3,40	0,54	3,57	0,58	0,00	0,01	0,00	0,50					1,00	1,00	5,00	0,00	11,90			0,25	170,50
MO 041	0,72	5,00	90,80	35,80	27,30	79,00	3,00	3,40	0,20	6,00	1,00	2,97	0,97	14,70	29,50	3,54	14,60	3,53	0,88	3,91	0,67	4,60	1,00	3,11	0,48	3,42	0,53	0,00	0,01	0,00	0,50					1,00	1,00	2,50	0,00	15,40			0,25	161,50
MO 047	1,56	10,00	114,00	74,60	16,60	68,00	2,50	2,80	0,20	17,00	1,00	3,87	1,14	10,10	20,20	2,30	8,70	1,86	0,56	2,24	0,38	2,46	0,57	1,98	0,32	2,22	0,35	0,00	0,01	0,00	0,50					2,00	1,00	2,50	0,00	11,20			0,25	729,00
MO 048	0,73	10,00	64,10	69,70	20,40	117,00	4,00	4,10	0,30	10,00	2,00	6,22	1,33	12,10	31,50	3,21	12,70	2,77	0,69	3,01	0,50	3,34	0,80	2,68	0,46	3,48	0,54	0,00	0,01	0,00	0,50					2,00	1,00	2,50	0,00	13,20			0,25	539,00
MO 053	0,44	10,00	89,20	20,80	28,50	51,00	2,20	2,50	0,20	2,50	1,00	1,42	0,49	4,40	11,00	1,57	7,40	2,24	0,76	2,83	0,57	4,30	1,09	3,70	0,59	4,21	0,64	0,00	0,01	0,00	0,50					1,00	1,00	2,50	0,00	13,60			0,25	112,50
MO 054	0,91	5,00	65,10	67,40	20,80	70,00	2,70	3,20	0,20	9,00	6,00	4,28	0,92	11,10	22,50	2,69	10,60	2,55	0,56	2,94	0,50	3,50	0,80	2,63	0,41	3,00	0,45	0,00	0,01	0,00	0,50					1,00	1,00	2,50	0,00	11,80			0,25	294,00
MO 055	2,01	5,00	44,70	77,80	25,50	110,00	3,70	3,40	0,30	21,00	2,00	6,85	2,48	17,70	35,10	3,99	15,90	3,44	0,82	3,88	0,63	4,16	0,92	2,88	0,46	3,09	0,46	0,00	0,01	0,00	0,50					1,00	1,00	2,50	0,00	13,60			0,25	415,00
MO 061	0,38	5,00	81,00	29,20	23,80	93,00	3,20	3,10	0,20	24,00	1,00	4,12	1,28	13,30	26,70	3,16	13,60	3,03	0,98	3,60	0,61	4,11	0,91	2,84	0,47	3,16	0,49	0,00	0,01	0,00	0,50					1,00	1,00	2,50	0,00	15,80			0,25	121,00
MO 067-1	0,40	20,00	73,50	18,90	54,00	152,00	4,70	2,80	0,20	7,00	2,00	2,58	0,80	11,20	26,80	4,11	19,90	5,99	1,41	7,02	1,34	8,90	1,99	6,21	0,93	6,41	0,97	0,00	0,00	0,00	0,50					1,00	1,00	2,50	0,00	14,90			0,25	108,00
MO 092	0,63	10,00	67,40	31,00	20,70	113,00	3,20	3,90	0,50	7,00	1,00	7,24	1,32	19,40	35,50	3,99	15,00	3,14	0,49	3,64	0,59	3,77	0,75	2,17	0,31	2,16	0,33	0,00	0,00	0,00	0,50					1,00	1,00	2,50	0,00	10,90			0,25	463,00
MO 104	1,04	10,00	154,00	129,00	13,60	136,00	4,50	4,90	0,20	2,50	2,00	14,85	1,25	8,80	42,00	2,63	10,10	2,18	0,33	1,97	0,33	2,29	0,50	1,75	0,27	1,95	0,27	0,00	0,00	0,00	0,50					1,00	2,00	2,50	0,00	14,00			0,25	573,00
HF-01	0,72	18	175,3	16,8	22,4	117	3,2	5,6	0,7	<10	<1	9,55	2,54	22	39,9	4,41	15,1	2,65	0,43	2,48	0,38	2,68	0,62	2,2	0,39	2,57	0,42	1,6	39	22,1	0,06	0,001	0,04	0,4	<0.05	1,37	<5	0,6	<0.2	11,7	0,11	<0.005	0,17	385
HF-02	0,89	12	89	55,4	15	122	3,4	4,3	0,6	<10	<1	9,27	1,12	20	38,2	3,78	12,6	2,32	0,52	2,29	0,35	2,08	0,47	1,45	0,27	1,87	0,32	1,8	40	22	0,07	<0.0005	0,12	0,2	0,09	0,88	<5	0,6	<0.2	11,3	0,1	<0.005	0,2	729
HF-07	0,16	11	91,5	35,5	24,8	145	3,9	4,9	0,8	12	<1	6,92	1,86	10,4	22,6	2,69	9,9	2,32	0,45	2,39	0,45	3,08	0,72	2,36	0,41	2,8	0,5	4,6	28	10,6	0,03	0,001	0,05	<0.1	0,05	0,39	<5	3,3	<0.2	11,8	0,06	<0.005	0,06	324
HS-2	0,76	11	104,3	136,7	17,5	72	2,5	6,6	0,9	<10	<1	20,58	4,24	25,1	48,4	4,88	14,9	2,64	0,41	2,26	0,35	2,3	0,49	1,65	0,26	2,09	0,34	4,9	31	30,5	0,13	0,001	0,08	1,2	0,07	0,43	<5	0,5	<0.2	10,9	0,04	0,014	0,16	866
HS-3	0,59	<10	94,5	70,4	10,5	88	2,6	3,4	0,8	<10	<1	5,14	1,31	2	7,1	0,58	2	0,47	0,18	0,53	0,12	1,09	0,27	1,17	0,21	1,65	0,3	1,5	52	18,8	0,03	<0.0005	0,03	0,4	<0.05	0,36	<5	0,6	<0.2	10,4	<0.02	0,01	0,17	496
MO 063	0,61	5,00	47,50	92,30	27,10	104,00	3,70	4,60	0,40	9,00	3,00	7,85	2,83	21,60	42,70	5,06	19,30	4,04	0,86	4,34	0,73	4,43	1,01	3,05	0,47	3,24	0,50	0,00	0,00	0,00	0,50					1,00	1,00	2,50	0,00	11,20			0,70	681,00
MO 064	0,30	5,00	25,10	124,00	14,20	33,00	1,90	6,50	0,60	2,50	1,00	9,22	2,78	18,70	34,20	3,63	12,70	2,39	0,35	2,75	0,40	2,47	0,51	1,62	0,25	1,76	0,29	0,00	0,01	0,00	0,50					1,00	1,00	2,50	0,00	8,00			0,70	3800,00
MO 087	0,88	10,00	108,00	73,50	12,70	118,00	3,40	3,60	0,30	11,00	1,00	5,70	0,79	7,00	22,80	1,84	7,00	1,52	0,39	1,57	0,28	1,96	0,46	1,71	0,29	2,34	0,36	0,00	0,00	0,00	0,50					1,00	0,50	2,50	0,00	12,10			0,25	647,00
MO 090	1,17	5,00	55,60	53,60	12,90	117,00	3,50	3,30	0,40	7,00	1,00	5,82	0,59	2,90	13,20	0,86	3,40	0,89	0,33	1,10	0,20	1,85	0,45	1,73	0,31	2,45	0,40	0,00	0,00	0,00	0,50					1,00	1,00	2,50	0,00	12,40			0,25	391,00
MO 091	0,08	10,00	57,20	12,30	20,30	102,00	2,90	2,80	0,30	2,50	1,00	4,23	1,28	7,60	14,80	1,60	6,20	1,37	0,31	1,75	0,34	3,01	0,74	2,53	0,43	3,06	0,48	0,00	0,00	0,00	0,50					1,00	1,00	2,50	0,00	8,60			0,25	358,00

Table 8.7: Ore samples (TS > 30.75 wt. % and/or Cu + Zn + Pb + Ag > 1931 ppm) | Major elements

Sample	SiO2	Al2O3	Fe2O3	TiO2	MgO	CaO	Na2O	K2O	MnO	P2O5	SrO	BaO	LOI	Total	TC	TS
	Wt. %	Wt. %	Wt. %	Wt. %	Wt. %	Wt. %	Wt. %	Wt. %	Wt. %	Wt. %	Wt. %	Wt. %	Wt. %	Wt. %	Wt. %	Wt. %
HAM-02	74,9	8,43	6,35	0,07	1,1	0,91	1,2	2,49	0,02	0,02	0,02	0,51	2,11	98,13	0,04	**3,05**
HAM-10	78,69	8,41	4,08	0,25	0,87	0,55	1,21	1,68	0,03	0,03	0,01	0,67	2,92	99,37	<0.01	**2,63**
HAM-B2	78,34	7,21	5,73	0,05	0,57	0,35	0,9	3,1	0,02	0,03	0,03	1,72	2,9	100,95	0,03	**3,61**
HAM-S1	46,05	8,02	12,1	0,04	4,74	1,77	0,17	2,2	0,11	0,68	<0.01	4,59	8,9	89,4	0,06	**10,77**
HAM-S2	64,27	6,39	13,97	0,03	3	0,63	0,48	1,88	0,06	0,18	<0.01	0,96	7,82	99,67	0,01	**10,48**
HAM-S3 a	48,51	6,61	13,07	0,03	8,89	1,34	0,13	3,51	0,13	0,25	0,03	2,43	7,5	92,42	0,1	**7,81**
HAM-S3 b	84,93	6,9	2,18	0,04	0,4	0,42	1,19	2,05	0,01	0,01	0,01	0,17	1,17	99,47	0,02	**0,59**
HAM-S4	61,34	4,48	15,66	<0.01	0,42	0,26	0,16	1,85	0,07	0,01	0,01	3,33	12,35	99,95	<0.01	**12,51**
HES-04	74,92	6,35	7,43	0,06	0,58	0,23	0,59	2,93	0,03	<0.01	<0.01	1,59	4,37	99,09	0,03	**5,59**
HF-13	76,35	11,74	4,62	0,18	0,68	0,06	0,17	3,63	0,02	0,03	<0.01	0,05	3,53	101,08	0,03	**2,72**
HF-x12	66,44	11,53	2,92	0,16	1,21	0,68	0,61	2,01	0,02	0,11	0,02	9,79	3,08	98,59	0,02	**1,89**
HF-x33	73,62	11,26	5,22	0,16	0,94	0,12	0,2	3,87	0,07	0,03	<0.01	0,07	3,69	99,24	0,04	**3,09**
HF-X4	77,43	10,88	3,51	0,2	0,63	0,04	0,36	3,21	0,03	<0.01	0,03	0,08	2,96	99,33	0,02	**2,5**
HF-x6a	73,03	9,49	5,88	0,16	0,57	0,03	0,28	2,78	0,03	0,03	<0.01	0,05	4,3	96,63	0,06	**4,63**
HF-x6c	77,5	8,12	3,87	0,14	0,52	0,03	0,2	2,48	0,02	0,01	<0.01	0,05	2,92	95,85	0,02	**3,07**
HS-1	77,21	8,92	5,73	0,09	0,74	0,05	0,18	3,13	0,03	0,01	<0.01	0,35	3,83	100,25	0,02	**3,93**
HS-S3 a	21,06	2,79	38,37	0,03	0,34	0,34	0,13	1,33	0,13	0,05	<0.01	1,59	17,53	83,72	0,02	**25,8**
HS-S3 b	59,46	10,15	5,54	0,13	0,6	1,15	0,72	4,09	0,06	0,05	<0.01	4,86	4,01	90,89	0,01	**7,13**
HS-S3 d	73,3	13,53	3,61	0,08	0,18	2,03	3,88	2,57	0,02	0,02	0,07	1,34	1,23	101,83	0,03	**1,83**
HS-S3 e	36,33	4,23	32,66	0,04	0,32	0,17	0,27	2,04	0,1	0,01	0,06	2,35	12,22	90,76	<0.01	**20,95**
HS-S4	26,13	2,71	35,91	0,04	0,29	0,75	0,08	1,19	0,12	0,02	0,07	3,49	18,62	89,38	<0.01	**26,29**
HS-S5	15,22	1,77	41,33	0,03	0,06	0,39	0,4	0,34	0,12	0,04	0,02	0,01	21,98	81,69	<0.01	**30,75**
HS-S6	35,01	<0.01	27,7	<0.01	<0.01	<0.01	<0.01	0,05	0,04	<0.01	0,03	<0.01	23,47	86,27	0,02	**33,56**
S-10	58,87	9,2	3,8	0,28	2,46	2,64	0,37	2,48	0,09	0,25	0,04	1,95	6,84	89,23	2,81	**3,91**
S-16	66,73	6,65	9,26	0,05	0,17	0,77	0,8	1,93	0,04	0,04	0,03	0,13	5,89	92,48	0,11	**7,36**
S-17	47,18	9,48	6,82	0,06	17,84	6,37	0,49	3,15	0,22	0,52	0,04	1,06	5,18	98,39	0,1	**4,7**
S-19	80,28	8,43	2,66	0,09	0,79	0,5	0,14	2,13	0,01	0,12	0,01	1,85	2,42	99,42	0,85	**0,21**
S-3	62,77	10,75	5,39	0,27	5,42	4,17	0,71	2,64	0,1	0,19	0,03	1,06	4,91	98,4	0,77	**3,05**
S-9	49,11	8,56	5,73	0,2	6,63	5,1	0,54	2,08	0,15	0,47	0,03	1,23	3,32	83,17	0,08	**6,48**
S-H	45,175	5,82	25,55	0,06	2,045	0,32	0,12	1,8	0,06	0,03	0,02	1,58	12,23	94,785	0,03	**14,9**
S-HB	80,48	9,35	3,55	0,07	0,66	0,14	0,25	2,36	0,01	0,03	0,04	1,46	2,68	101,05	0,03	**1,61**

Table 8.8: Ore samples (TS > 30.75 wt.% and/or Cu + Zn + Pb + Ag > 1931 ppm) | Trace elements

Sample	Cs	Cr	Sr	Rb	Y	Zr	Hf	Nb	Ta	V	W	Th	U	La	Ce	Pr	Nd	Sm	Eu	Gd	Tb	Dy	Ho	Er	Tm	Yb	Lu	Cu	Zn	Pb	Ag	Au	Bi	As	Sb	Mo	Sn	Ni	Se	Ga	Cd	Hg	Tl	Ba	Co
	ppm	ppm	ppm	ppm	ppm	ppm	ppm	ppm	ppm	ppm	ppm	ppm	ppm	ppm	ppm	ppm	ppm	ppm	ppm	ppm	ppm	ppm	ppm	ppm	ppm	ppm	ppm	ppm	ppm	ppm	ppm	ppm	ppm	ppm	ppm	ppm	ppm	ppm	ppm	ppm	ppm	ppm	ppm	ppm	ppm
HAM-02	0,64	16	146,6	47,1	5,1	90	2,6	3,9	0,6	15	<1	2,74	2,76	2	4,4	0,52	2	1,12	0,59	0,49	0,09	0,67	0,17	0,64	0,15	1,05	0,2	**2003,6**	**4942,5**	**160,3**	**1,42**	**0,006**	1,26	0,8	0,3	14,84	<5	2,65	1,6	12,7	21,83	0,134	1,21	5164	1,3
HAM-10	0,42	17	34,1	33,4	21,2	78	2,2	2,4	0,7	41	2	3,11	2,4	6,2	10,3	1,1	3,9	1,85	0,7	1,41	0,33	2,62	0,71	2,38	0,4	2,55	0,41	**102,5**	**2978**	**1595,1**	**9,55**	**0,073**	0,26	4,1	41,66	79,17	<5	3,5	1,2	13,2	12,51	0,543	0,43	7076	2
HAM-B2	0,57	25	188,9	47,7	5,8	109	3,2	3,4	0,7	<10	1	4,28	3,7	2,8	7,2	0,88	3,1	2,41	0,91	0,91	0,16	0,94	0,21	0,7	0,12	1,08	0,19	**2592,7**	**5873**	**546,8**	**1,85**	**0,006**	2,47	1	0,32	8,01	<5	3,2	2,2	11,9	26,39	0,142	0,56	>10000	2,4
HAM-S1	1,52	11	287,2	57	26,7	37	1,3	5,7	0,7	<10	<1	2,53	11,91	7	18,2	2,51	10,2	7,61	2,45	4,06	0,8	4,67	0,89	2,62	0,36	2,27	0,33	**7813,6**	**83800**	**2915,5**	**2,99**	**0,011**	8,58	6,8	0,64	122,67	<5	8,4	7,1	36,9	299,8	0,288	2,24	>10000	4,9
HAM-S2	1,94	12	93,5	50,1	4,9	25	1	2,5	0,6	<10	4	1,8	2,72	0,9	3,1	0,29	1	1,17	0,53	0,38	0,08	0,66	0,19	0,71	0,12	0,87	0,15	**2565,3**	**22200**	**444,9**	**1,38**	**0,022**	2,21	7,5	0,68	93,57	<5	4,6	8	16,6	78,64	1,274	4,68	9937	2,6
HAM-S3 a	5,23	<10	91,4	123,8	30,6	46	1,8	3,3	0,7	<10	1	2,2	7,05	3,9	9,6	1,25	5,8	4,52	1,55	3,39	0,7	5,06	1,03	3,23	0,45	2,95	0,46	**4781,7**	**48700**	**627,7**	**4,53**	**0,016**	7,58	1,8	0,78	243,55	<5	4,9	6,9	35,8	190,59	0,868	13,39	>10000	3,2
HAM-S3 b	0,27	17	47,5	27,9	7,4	28	1,1	2,6	1	<10	6	4,12	3,44	3,5	7,5	0,77	2,6	0,63	0,23	0,66	0,13	1	0,25	0,83	0,17	1,29	0,23	**2041,3**	**98**	**19900**	**158**	**0,397**	295,63	7,1	45,55	0,82	<5	0,8	10	6,9	16,73	0,269	0,76	1567	0,9
HAM-S4	0,44	15	238,2	29,7	17,2	59	1,8	2,4	0,7	<10	1	3,22	3,34	1,2	4,2	0,63	2,9	4,35	1,75	1,52	0,38	2,61	0,59	1,91	0,3	1,93	0,28	**2789**	**75300**	**1213,4**	**6,33**	**0,018**	6,75	0,5	1,32	25,7	<5	8,5	3,1	17,6	334,49	2,485	0,7	>10000	1,2
HES-04	0,63	37	144,2	48,7	13,9	94	2,8	2,7	0,6	46	<1	3,45	3,04	1,9	3,3	0,43	1,9	2,51	1,06	0,99	0,24	1,76	0,44	1,55	0,29	1,84	0,32	**2965,2**	**19000**	**1527,2**	**8,78**	**0,018**	7,23	6	4,11	14,3	<5	8,8	1,8	14	78,74	0,813	2,73	>10000	3,2
HF-13	0,65	13	16,9	86,3	20,3	128	3,7	4,8	0,7	12	2	8,7	2,66	17,5	40	4,54	15,3	3,26	0,45	2,98	0,48	2,8	0,63	2,01	0,37	2,56	0,43	**120,4**	**3120**	**3628,5**	**3,51**	**0,015**	0,12	24,7	2,4	1,36	<5	0,6	<0.2	11,5	7,58	0,194	0,19	413	1,9
HF-x12	1,66	22	209,9	49,4	14,4	119	4,1	4,5	0,9	132	10	8,55	11,39	23,2	40,5	4,03	12,6	14,38	4,93	2,62	0,53	2,58	0,6	1,72	0,29	1,96	0,31	**2835,3**	**1829**	**1051,2**	**41**	**0,030**	0,31	64,3	12,81	75,46	7	19,8	2,3	28,3	12,23	0,407	4,83	>10000	3,4
HF-x33	1,08	11	13	99,4	6,8	135	3,9	5,6	0,8	27	2	10,09	2,8	0,8	1,9	0,21	0,8	0,24	0,09	0,23	0,06	0,61	0,23	0,96	0,22	2,03	0,38	**158,8**	**2916**	**1406,9**	**4,13**	**0,007**	0,35	19,1	1,98	5,13	<5	2,4	0,3	12,3	7,95	0,239	0,27	591	1,9
HF-X4	0,37	17	15,9	80	22,1	129	3,9	4,8	0,7	15	3	5,49	2,19	5,8	11,3	1,34	5,1	1,28	0,72	1,72	0,38	2,83	0,7	2,19	0,39	2,55	0,44	**1554,9**	**15500**	**6715,4**	**9,45**	**0,037**	3,78	6,1	3,74	6,07	<5	5,7	0,4	12,6	56,12	1,124	0,14	620	1,5
HF-x6a	0,35	16	12	72,3	20,4	103	3	3,8	0,7	18	2	6,42	2,23	5,2	9,7	1,12	4	0,98	0,31	1,5	0,34	2,54	0,59	1,97	0,37	2,27	0,38	**2027,9**	**24000**	**2190,9**	**9,34**	**0,049**	15,67	19,9	2,58	3,68	<5	2	0,4	11,6	91,49	1,154	0,12	389	2,1
HF-x6c	0,37	15	10,4	64,5	14,4	95	2,7	3,5	0,6	10	<1	4,03	1,77	3,9	6,7	0,8	2,9	0,66	0,24	1,01	0,21	1,52	0,42	1,36	0,27	1,74	0,32	**1210,3**	**16800**	**632,8**	**3,11**	**0,065**	1,82	9,8	0,55	2,43	<5	1	<0.2	9,6	63,61	1,113	0,16	351	1,6
HS-1	1,11	<10	25,1	71,7	27,5	102	3,4	3,9	0,7	<10	2	6,59	1,23	2,2	4,8	0,53	2	0,86	0,36	1,45	0,42	3,65	0,96	3,25	0,48	3,41	0,54	**839,2**	**4720**	**218,3**	**3,91**	**0,069**	4,17	7,5	2,04	1,5	<5	0,6	1	12,8	17,16	0,236	0,24	3295	0,6
HS-S3 a	0,76	<10	114	27,4	19,8	19	0,6	1,3	0,6	<10	1	2,39	1,53	9	22,1	2,88	11,1	4,32	1,82	2,89	0,55	3,43	0,71	2,08	0,3	1,86	0,29	**4277,8**	**12730**	**88,6**	**5,02**	**0,010**	0,23	6,7	2,91	7,91	<5	27,5	11,5	13,4	588,55	5,556	3,27	>10000	1,6
HS-S3 b	1,19	23	609,8	76,9	26,3	93	2,9	5	0,7	41	2	6,78	7,43	12,7	28,3	3,51	13,1	7,79	3,11	3,49	0,67	4,33	0,9	2,79	0,44	3,02	0,44	**276,4**	**81200**	**3307,3**	**13,88**	**0,019**	10,07	16,8	11,37	28,53	<5	10,8	2,9	34,7	366,65	4,659	5,42	>10000	2,6
HS-S3 d	0,49	<10	597,6	44	9	48	1,6	7,4	1	<10	1	5,75	3,46	2	5	0,61	2,4	1,93	1,32	0,79	0,19	1,23	0,3	1,01	0,14	1,2	0,17	**1366,9**	**7193**	**870,7**	**3,77**	**0,006**	2,71	2,9	1,66	1,7	<5	2,6	0,4	17,8	28,32	0,228	1,4	>10000	0,4
HS-S3 e	0,71	<10	138,7	39,6	14,8	48	1,5	1,4	0,5	<10	1	2,15	2,62	4,6	11,6	1,53	6,4	3,6	1,44	1,89	0,36	2,3	0,51	1,64	0,23	1,56	0,24	**7778,8**	**67100**	**268,9**	**8,27**	**0,045**	0,89	10,2	2,23	20,76	<5	22,3	3,2	14,6	283,45	2,783	5,04	>10000	4,1
HS-S4	0,14	47	208,8	16,9	19	43	1,4	1,5	0,8	<10	3	2,93	2,5	8,3	19,5	2,41	9,3	5,79	2,16	2,67	0,51	3,21	0,68	2,03	0,3	1,98	0,27	**4360,9**	**85200**	**102,7**	**5,29**	**0,012**	0,7	40,9	1,37	29,01	<5	32,5	6,9	14,9	392,1	3,648	0,76	>10000	34,5
HS-S5	0,06	<10	18,8	6,2	8,8	6	0,2	0,3	0,1	<10	<1	0,87	0,44	1,9	6	0,76	3	0,72	0,33	0,98	0,2	1,33	0,27	0,81	0,11	0,79	0,11	**514,2**	**55**	**9,7**	**4,02**	**0,001**	0,26	1,7	0,21	43,71	<5	29,7	4,3	2,3	0,15	0,008	0,05	96	3,4
HS-S6	0,02	13	2,5	1	<0.5	<2	<0.2	<0.1	0,5	<10	<1	<0.05	0,1	<0.1	<0.1	<0.03	<0.1	<0.03	0,04	<0.05	<0.01	<0.05	<0.01	<0.03	0,02	0,05	<0.01	**8,2**	**63**	**1,3**	**0,59**	**<0.0005**	0,03	18,5	0,06	23,76	<5	7,7	0,9	0,7	0,24	0,008	<0.02	245	15,8
S-10	2,16	64	144,1	65,1	10,7	73	2,1	4,9	0,7	452	3	7,73	19,28	19,7	38,1	4,45	14,9	4,24	1,37	2,26	0,35	1,77	0,34	0,94	0,13	0,89	0,13	**1162,9**	**46300**	**44400**	**141**	**0,010**	7,15	9,6	124,78	142,09	10	1,9	46,4	34,7	388,73	3,69	2,27	>10000	4,9
S-16	0,33	<10	102,8	16,7	3,1	36	1,5	2,3	0,8	20	2	9,84	3,62	5,7	11,6	1,3	4,4	0,89	0,35	0,63	0,1	0,61	0,12	0,41	0,07	0,48	0,08	**476,5**	**60800**	**10800**	**9,13**	**0,004**	2,14	0,8	6,71	12,37	<5	25,3	2	8,5	294,01	0,422	0,11	1203	7,9
S-17	16,85	13	81	123,4	32,4	73	2,5	1,7	0,7	<10	1	4,37	10,92	11,8	29,3	4,05	16,1	5,79	1,25	5,17	0,87	5,64	1,16	3,49	0,5	3,52	0,57	**8158,6**	**11900**	**491,7**	**17,34**	**0,011**	0,7	18,8	3,45	34,34	10	25,4	11,8	19,1	94,27	0,809	8,37	>10000	8,7
S-19	1,02	17	50,5	45,8	11	89	2,6	3,3	0,7	<10	1	4,44	1,91	6	12,7	1,57	5,5	2,61	0,9	0,99	0,21	1,32	0,32	1,25	0,2	1,67	0,33	**1078,9**	**256**	**574,7**	**21,75**	**0,014**	0,24	5,1	10,89	6,84	18	1,2	2,9	14,3	2,06	0,125	0,57	>10000	0,5
S-3	3,44	42	184,3	71	30,6	125	3,6	6,6	0,9	322	<1	8,07	10,7	20,7	41,9	5	18,9	5,44	1,47	4,05	0,78	5,05	1,18	3,28	0,51	3,68	0,54	**1483,4**	**13800**	**4206,1**	**16,53**	**0,002**	3,81	1,6	6,88	39,67	16	56,2	9,3	19,7	106,73	0,352	2,65	>10000	8,3
S-9	3,18	35	152,1	61,1	27,7	87	2,7	4	0,8	165	4	7,11	8,75	14,8	32,4	4,09	15,7	4,98	1,28	4,2	0,74	4,47	0,89	2,62	0,37	2,39	0,37	**866,1**	**72300**	**41000**	**91,4**	**0,032**	148,72	3,25	33,27	180,75	13	18,6	52,55	21,1	631,06	1,088	3,08	>10000	9,5
S-H	3,33	14	79,4	52,5	15,9	76	2,3	2,8	0,7	65	1	3,77	4,45	5,9	12,7	1,55	6,3	3,21	1,12	1,52	0,33	2,37	0,66	1,9	0,33	2,31	0,35	**1694,9**	**36200**	**13100**	**59,96**	**0,011**	1,33	64,7	36,31	40,65	82	52,9	48,4	16,8	283,87	2,57	4,4	>10000	34,5
S-HB	1,17	10	45,9	52,8	16	114	3,2	3,3	0,7	<10	2	4,87	3,21	9,7	20,1	2,4	9,1	3,56	1,01	1,7	0,31	2,22	0,64	2,08	0,36	2,97	0,51	**1504,5**	**2554**	**1174,5**	**11,74**	**0,025**	0,12	17,3	6,56	12,77	22	2	4,7	17,3	17,1	0,231	0,42	>10000	1

Table 8.9: Quartz muscovite schist | Major elements

Sample	SiO2	Al2O3	Fe2O3	TiO2	MgO	CaO	Na2O	K2O	MnO	P2O5	SrO	BaO	LOI	Total	TC	TS
	Wt.%	Wt.%	Wt.%	Wt.%	Wt.%	Wt.%	Wt.%	Wt.%	Wt.%	Wt.%	Wt.%	Wt.%	Wt.%	Wt.%	Wt.%	Wt.%
HAM-01	80,86	8,82	1,63	0,07	3,13	0,72	1,29	1,74	0,03	0,02	0,03	0,12	1,46	99,89	0,05	0,06
HAM-07	74,74	11,3	2,8	0,14	2,15	0,94	3,78	1,34	0,03	0,02	<0.01	0,02	0,96	98,22	0,04	0,13
HAM-08	70,68	13,18	3,88	0,16	2,39	1,18	2,52	2,71	0,04	0,03	0,02	0,05	1,92	98,74	0,1	<0.01
HAM-B1	71,16	7,68	10,02	0,04	0,66	0,15	0,18	2,56	0,03	<0.01	<0.01	0,54	5,66	98,68	0,05	6,77
HAM-B3	84,29	3,82	5,38	0,29	2,45	0,3	0,24	1,6	0,05	<0.01	<0.01	0,03	2,16	100,61	0,11	1,7
HAM-B4	71,51	12,64	3,71	0,22	1,89	1,25	1,73	3,08	0,14	0,04	0,02	0,06	2,23	98,5	0,05	1,37
HAM-B5	69,06	10,97	3,82	0,13	3,32	6,06	1,54	2,73	0,2	0,02	<0.01	0,04	0,73	98,63	0,02	<0.01
HAM-B6	81,81	9,73	1,7	0,09	0,34	0,45	2,14	2,08	0,01	<0.01	<0.01	0,04	1,32	99,7	0,08	0,03
HAM-B7	76,615	12,05	1,905	0,36	2,095	0,19	1,335	3,25	0,08	0,02	0,01	0,16	2,09	100,33	<0.01	0,42
HAM-B8	74,91	13,18	3,45	0,12	1,31	0,53	1,15	3,57	0,03	0,01	<0.01	0,29	3,23	101,78	0,08	2,08
HES-01	80,16	8,33	5,35	0,09	0,64	0,17	0,35	2,98	0,02	<0.01	0,01	0,22	2,98	101,3	0,08	1,44
HES-03	67,73	12,93	7	0,1	0,73	0,21	0,78	5,12	0,01	<0.01	<0.01	1,58	3,23	99,46	0,02	3,245
HES-05	73,81	14,33	1,84	0,09	0,16	1,3	2,6	5,06	<0.01	0,03	0,03	0,15	1,14	100,55	0,02	0,55
HES-06	70,51	14,61	2,09	0,08	2,46	0,54	0,62	4,2	0,02	<0.01	0,02	0,7	2,6	98,45	0,06	0,44
HF-11	80,38	10,09	3,7	0,15	0,47	0,03	0,25	2,85	0,06	0,01	0,04	0,06	2,22	100,29	0,07	0,1
HF-14	87,92	5,13	3,27	0,09	0,17	0,02	0,12	1,55	<0.01	<0.01	<0.01	0,09	2,03	100,38	0,09	0,4
HF-16	75,63	14,79	1,2	0,06	0,42	0,23	1,16	6,01	<0.01	0,02	<0.01	0,35	1,71	101,62	0,12	0,01
HF-X1	74,07	15,25	3,6	0,1	0,38	0,01	0,05	4,77	0,02	0,01	<0.01	0,17	3,05	101,48	0,02	0,75
HF-X2	79,19	11,64	1,96	0,05	0,06	1,44	2,5	3,37	<0.01	0,02	0,03	0,08	0,9	101,25	0,02	0,59
HF-x22 A	81,42	11,8	1,46	0,14	0,15	1,06	2,52	1,93	0,02	0,02	0,01	0,09	1,32	101,95	0,05	0,15
HF-x22 B	73,84	12,09	2,19	0,18	0,63	0,37	0,33	5,18	0,03	0,02	0,02	0,31	2,17	97,34	0,07	0,04
HF-x24	70,21	13,82	2,61	0,37	0,13	0,3	1,12	10,3	0,01	0,25	0,01	0,08	1,48	100,68	0,01	1,22
HF-x25	77,74	6,42	8,46	0,05	0,22	0,14	0,6	1,45	0,02	<0.01	0,03	0,21	4,99	100,31	0,03	6,04
HF-x26	77,79	9,95	4,89	0,12	0,5	0,08	0,47	2,6	0,02	0,02	<0.01	0,23	3,45	100,11	0,04	2,85
HF-x27	76,48	8,58	5,8	0,09	0,36	0,03	0,19	2,56	0,02	0,14	<0.01	0,17	3,83	98,25	0,08	2,92
HF-x29	81,49	9,85	2,74	0,09	0,91	0,55	1,14	2,25	0,1	0,03	<0.01	0,08	1,94	101,17	0,04	0,94
HF-X3	66,09	18,28	3,32	0,27	2,25	1,55	1,58	4,53	0,04	0,02	<0.01	0,39	2,85	101,19	0,08	0,09
HF-x30	76,4	12,08	3,22	0,11	1,2	0,42	1,57	1,78	0,08	<0.01	<0.01	0,14	1,56	98,55	0,02	0,37
HF-x31	75,03	11,34	5,85	0,18	0,75	0,1	0,27	3,32	0,49	0,02	<0.01	0,11	3,72	101,19	0,08	2,94
HF-x32	76,52	13,77	2,71	0,24	0,54	0,53	1,18	3,6	0,02	0,03	<0.01	0,09	2,6	101,83	0,05	1,16
HF-x34	75,88	10,73	5,34	0,1	0,51	0,03	0,45	3,03	0,03	0,01	<0.01	0,13	3,53	99,77	0,02	2,9
HF-x36A	58,86	20,03	6,52	0,95	2,09	4,95	3,55	1,16	0,03	0,27	<0.01	0,08	3,11	101,64	0,03	3,34
HF-x6b	77,42	11,12	4,16	0,08	0,06	<0.01	0,14	3,15	0,01	<0.01	0,06	0,05	3,68	99,87	<0.01	3,09
HS-4	73,79	14,09	3,62	0,26	0,93	2,13	3,73	1,68	0,11	0,04	<0.01	0,05	1,07	101,5	0,05	0,04
HS-5	77,49	11,84	3,04	0,09	2,79	0,55	1,96	1,68	0,06	0,01	0,01	0,09	1,94	101,53	0,05	1,23
HS-6	78,42	8,11	6,57	0,06	0,97	0,06	0,18	2,88	0,03	0,01	0,01	0,13	3,81	101,22	0,05	3,03
HS-7	78,01	8,26	3,28	0,06	1,32	0,16	0,35	3,23	0,03	<0.01	<0.01	0,34	2,55	97,59	0,08	1,57
HS-7 b	66,89	15,65	3,67	0,44	0,86	1,15	1,08	6,45	0,25	0,15	<0.01	0,2	2,58	99,38	0,07	0,74
HS-8	80,44	9,59	3,22	0,1	1,07	0,03	0,24	3,33	0,04	0,01	<0.01	0,18	2,525	100,79	0,05	1,34
HS-S3 c	74,67	14,67	1,57	0,09	0,3	2,17	3,6	1,68	0,01	0,05	0,01	0,55	1,07	100,48	0,02	0,43

Table 8.10: Quartz muscovite schist | Trace elements

Sample	Cs	Cr	Sr	Rb	Y	Zr	Hf	Nb	Ta	V	W	Th	U	La	Ce	Pr	Nd	Sm	Eu	Gd	Tb	Dy	Ho	Er	Tm	Yb	Lu	Cu	Zn	Pb	Ag	Au	Bi	As	Sb	Mo	Sn	Ni	Se	Ga	Cd	Hg	Tl	Ba	Co
	ppm	ppm	ppm	ppm	ppm	ppm	ppm	ppm	ppm	ppm	ppm	ppm	ppm	ppm	ppm	ppm	ppm	ppm	ppm	ppm	ppm	ppm	ppm	ppm	ppm	ppm	ppm	ppm	ppm	ppm	ppm	ppm	ppm	ppm	ppm	ppm	ppm	ppm	ppm	ppm	ppm	ppm	ppm	ppm	ppm
HAM-01	0,88	24	73,3	32,6	36,4	115	3,4	3,6	0,7	<10	<1	3,48	1,75	9,7	20,4	2,68	10,9	2,94	0,76	3,64	0,71	5,18	1,2	3,62	0,63	4,09	0,67	61,4	92	268,6	1,45	0,004	2,05	1,3	1,04	6,87	<5	0,9	0,4	12,8	0,13	0,011	1,23	948	0,3
HAM-07	0,86	16	87,2	31,6	29,4	92	2,6	3,8	0,6	12	<1	3,58	2,23	11,5	22,7	2,7	10,4	2,47	0,42	2,87	0,54	3,67	0,83	2,6	0,41	2,78	0,45	28,2	96	50,8	0,28	0,002	0,17	0,7	<0.05	6,82	<5	2	<0.2	12	0,32	<0.005	0,36	155	1,3
HAM-08	1,14	26	76,4	70,8	25,6	145	4,2	4,7	0,6	<10	<1	4,73	1,53	5,3	11,4	1,49	5,9	1,38	0,57	1,72	0,35	2,65	0,69	2,47	0,44	3,4	0,6	8,8	160	23,7	0,1	0,001	0,07	0,5	<0.05	2,81	<5	0,9	0,3	17,8	0,12	<0.005	0,44	389	0,6
HAM-B1	0,58	14	33,2	55,6	2,7	103	3,5	3,9	0,6	<10	4	1,03	0,59	0,6	1,7	0,15	0,4	0,59	0,3	0,23	0,05	0,34	0,11	0,4	0,08	0,84	0,2	30,2	417,5	125,05	1,41	0,006	2,73	5,7	0,24	8,13	<5	0,6	3,9	12,3	1,53	0,135	0,25	5707	1,1
HAM-B3	0,75	13	23	46,6	1	149	4,4	8,2	0,7	<10	4	0,48	1,58	<0.1	0,1	<0.03	<0.1	<0.03	0,06	<0.05	<0.01	0,1	0,03	0,16	0,03	0,45	0,11	496,5	355	20,6	0,78	0,005	0,87	0,6	0,15	57,41	<5	5	2	8,2	0,24	0,007	1,1	247	2,4
HAM-B4	0,52	<10	50,8	60,7	25	109	3,1	4,3	0,6	10	2	5,44	1,61	7,7	17,3	2,25	9	2,38	0,64	2,51	0,44	3,29	0,86	3,07	0,51	3,7	0,59	14,7	298	168	0,65	0,001	0,33	1,6	0,07	1,66	<5	1,8	<0.2	14,1	0,76	<0.005	0,26	461	2,5
HAM-B5	0,68	10	100,7	35,3	32,4	117	3,3	4,3	0,7	<10	3	6,1	1,48	16,1	33,6	4,01	15,6	3,69	0,89	4,03	0,65	4,59	1,1	3,62	0,56	3,81	0,58	3,3	79	29	0,06	<0.0005	0,1	0,9	<0.05	0,64	<5	1,1	<0.2	13,9	0,38	<0.005	0,19	368	0,7
HAM-B6	0,27	11	44,8	37,3	37,8	117	3,1	5	0,8	<10	2	6	1,77	8,7	17,8	2,33	9,7	2,72	0,42	3,73	0,71	5,21	1,21	3,83	0,62	4,22	0,65	3,6	37	14,8	0,05	<0.0005	0,06	0,6	<0.05	0,75	<5	0,7	<0.2	11,2	0,06	<0.005	0,03	310	0,4
HAM-B7	0,885	<10	57,45	65,9	26,05	109,5	3,2	3,8	0,7	16,5	3,5	2,92	1,54	10,65	20,4	2,56	10,3	2,55	0,76	3,065	0,54	3,81	0,95	3,06	0,49	3,255	0,51	15,9	91	64	0,35	0,004	0,1	1,3	0,09	2,13	<5	0,7	<0.2	13,7	0,09	0,053	1,04	1382	0,9
HAM-B8	0,64	13	42,6	79,1	18,7	139	4,8	5,3	0,8	<10	2	5,77	1,73	3,3	6,9	0,9	3,6	1,29	0,5	1,41	0,3	2,48	0,73	2,61	0,46	3,52	0,63	1,2	664	43,2	0,24	<0.0005	0,15	1,2	0,15	1,84	<5	0,5	0,3	16,9	2,8	0,079	0,41	2647	0,2
HES-01	0,9	100	47,5	69,3	7,9	101	3,3	4,4	0,7	<10	5	1,09	0,55	1,9	3,1	0,36	1,5	0,64	0,22	0,58	0,13	0,98	0,26	0,87	0,18	1,15	0,25	7,5	44	38,7	0,58	0,003	0,8	10,1	0,09	6,95	<5	1,7	3,4	11,8	<0.02	0,022	0,11	2027	1,3
HES-03	0,88	54	208,9	87,6	15,3	158	4,3	4,6	0,6	37	3	5,06	7,06	4	8,1	0,99	3,8	2,96	1,18	1,33	0,29	2,01	0,49	1,78	0,34	2,35	0,46	1549,9	992	372,7	2,34	0,010	0,25	3,3	1,47	40,33	<5	6,2	1,7	17,3	5,9	0,027	1,05	>10000	1,3
HES-05	0,49	26	211	73,4	7	56	1,9	4,1	0,6	<10	<1	4,41	0,74	5,9	10,9	1,25	4,8	1,28	0,72	1,14	0,19	1,12	0,24	0,69	0,13	0,74	0,13	11,9	29	97	0,36	0,001	0,07	1,7	0,16	1,55	<5	0,9	<0.2	16,3	0,08	0,006	0,12	1319	0,7
HES-06	1,9	19	124,8	96,5	14,9	162	5,7	8,1	0,8	15	25	7,26	1,96	4,9	10,7	1,38	5,2	2,3	0,68	1,55	0,33	2,19	0,53	1,77	0,37	2,57	0,54	113,5	207	33,7	0,46	0,001	0,02	0,7	0,12	0,56	<5	1,2	0,6	20,9	0,57	<0.005	4,16	7415	0,7
HF-11	0,15	15	9,3	74,8	17,2	91	2,9	4,3	0,7	18	1	3,87	0,86	3,8	7,5	0,89	3,3	0,79	0,2	1,13	0,26	1,96	0,5	1,6	0,3	1,87	0,29	73,1	31	100,9	1,64	0,022	3,69	23,7	0,12	11,38	<5	0,5	2,1	11,4	<0.02	0,021	0,07	528	0,4
HF-14	0,07	14,5	6,3	33,1	2,85	47	1,4	2,3	0,6	<10	1	0,675	0,29	0,2	0,2	0,03	0,1	0,12	0,95	0,08	0,03	0,23	0,08	0,29	0,07	0,455	0,09	3	13	67,9	0,97	0,004	1,5	12,7	0,13	15,34	<5	0,6	7	7,05	<0.02	<0.005	0,13	677	1,4
HF-16	0,52	<10	242,2	81,7	12,3	72	2,9	9,3	1	<10	<1	13,23	3,05	3,7	9,7	0,83	3	1,09	0,43	0,88	0,19	1,43	0,39	1,49	0,3	2,02	0,35	1,8	25	35,8	0,13	0,001	0,19	1,9	0,06	1,5	<5	0,5	<0.2	14,4	0,03	<0.005	0,03	3251	0,3
HF-X1	0,33	11	20,3	95,1	1,2	85	3,1	9	0,9	<10	2	13,92	1,06	1,8	1,7	0,14	0,4	0,25	0,17	0,1	0,02	0,11	0,04	0,16	0,05	0,4	0,11	7,6	49	122	5,14	0,134	0,05	20,9	1,63	17,38	<5	0,9	<0.2	13,7	<0.02	0,092	0,25	1420	0,5
HF-X2	0,66	14	257,8	76,5	3,4	62	2,2	3,3	0,7	<10	<1	8,13	2,1	6,6	11,6	1,25	3,8	0,78	0,28	0,64	0,09	0,49	0,1	0,37	0,08	0,44	0,08	6,1	13	26,2	0,32	0,001	0,14	0,8	0,06	1,09	<5	0,9	<0.2	10,7	0,09	<0.005	0,03	589	1,3
HF-x22 A	0,16	11	51,4	38,2	11,5	107	3	7,3	1	20	65	9,37	2,83	8,2	16,5	1,84	6,4	1,39	0,32	1,21	0,23	1,58	0,4	1,31	0,26	1,93	0,32	1,8	25	13,5	0,06	<0.0005	0,14	0,5	<0.05	0,71	<5	0,7	<0.2	11,1	0,03	<0.005	0,04	734	0,9
HF-x22 B	1,03	15	125,95	85,3	3,4	166,5	5,05	5,2	0,9	19	3,5	4,05	1,94	2	3,3	0,36	1,2	0,64	0,375	0,3	0,06	0,445	0,14	0,54	0,14	1,23	0,26	4,3	13	27,9	0,09	<0.0005	0,17	0,7	0,05	3,54	<5	0,7	0,9	13,2	<0.02	<0.005	0,09	3326	0,6
HF-x24	0,41	12	16,5	76,4	24,9	116	3,4	4,8	0,8	18	2	6,86	4	1,8	6,2	1,09	5,7	2,09	0,92	2,46	0,54	3,65	0,9	2,51	0,39	3,01	0,51	1,3	5	84,8	0,15	0,001	0,3	16,8	0,18	2,13	<5	1,4	0,5	9,3	0,02	<0.005	0,04	716	4,8
HF-x25	0,16	13	14,7	26,4	18,8	90	3	2,8	0,8	<10	4	4,02	1,77	6,4	13,3	1,56	6,6	1,84	0,6	1,93	0,43	3,02	0,79	2,24	0,35	2,27	0,34	2,5	16	56,1	1,21	0,002	3,61	14,8	0,2	22,17	<5	1,2	4,6	8,9	0,06	<0.005	0,36	1973	12,8
HF-x26	0,36	22	18,4	53,1	27,7	101	3,1	5,4	0,8	17	3	7,09	3,03	9,6	18,7	2,17	8,3	2,13	0,59	2,32	0,51	3,93	1,08	3,23	0,53	3,92	0,64	98,5	66	130,8	1,03	0,002	2,9	4,6	0,07	15,95	<5	2,7	1,9	11,7	0,18	<0.005	0,31	2065	4,4
HF-x27	0,43	17	23,9	60,5	2,9	80	2,4	3,5	0,8	<10	<1	40,97	2,15	7,6	8,9	0,73	2,5	0,81	0,37	0,42	0,07	0,55	0,15	0,48	0,11	0,89	0,18	19,3	112	99,8	1,03	0,004	4	5,6	<0.05	5,52	9	1,1	2,4	10,8	0,44	0,014	0,05	1553	2,2
HF-x29	0,26	12	32,2	45,4	21,3	99	3	4	0,8	<10	<1	9,67	2,1	16,7	29,2	3,28	11,8	2,53	0,34	2,11	0,39	2,91	0,75	2,28	0,4	2,91	0,47	2,8	548	588	0,84	0,005	1,19	4,2	0,32	1,66	<5	0,4	<0.2	10,1	1,44	0,1	0,26	665	0,7
HF-X3	2,46	12	102,1	125,3	3	154	4,9	6,7	0,8	12	2	16,26	1,76	2,1	3,9	0,48	1,8	0,8	0,34	0,38	0,08	0,43	0,11	0,42	0,1	0,91	0,23	7,5	67	37,8	0,43	0,002	0,19	0,3	0,08	4,99	<5	0,7	<0.2	18,5	0,04	<0.005	0,53	3561	0,6
HF-x30	0,44	12	63,6	43	36,1	142	4,3	5,6	0,9	<10	<1	8,37	2,62	15,4	31,2	3,59	15	4,01	0,9	3,89	0,79	5,56	1,41	3,91	0,63	4,61	0,74	32,3	83	22,7	0,19	0,002	0,18	1,7	<0.05	0,89	<5	0,4	<0.2	13,8	0,48	<0.005	0,47	1221	0,4
HF-x31	0,25	14	8,7	88,8	26,4	130	4	5,6	0,6	26	2	8,76	2,98	4,8	9	0,99	3,6	1,15	0,28	2,05	0,54	3,98	1,01	2,85	0,46	3,52	0,57	236,8	118	66,9	0,8	0,007	4,48	11,5	0,06	9,47	<5	2,6	1,1	12,4	0,5	0,01	0,18	937	3,6
HF-x32	1,13	11	59,9	80,1	16,1	163	4,7	7,4	0,9	40	2	12,71	63,96	5,4	9,8	0,9	2,6	0,54	0,22	0,72	0,19	1,85	0,56	1,78	0,31	2,25	0,36	133,4	110	71,9	1,17	0,004	0,09	9	0,2	27,79	<5	7,1	0,3	13,8	0,54	0,006	0,12	733	2,6
HF-x34	0,61	12	22,3	81,2	9,3	102	3	4,7	0,7	<10	1	8,88	2,92	9,4	17,4	1,74	5,9	1,21	0,26	0,9	0,17	1,23	0,35	1,12	0,22	1,62	0,28	191,7	2820	345,7	3,61	0,027	7,56	17,2	0,11	8,95	<5	0,6	0,3	11,9	16,54	0,352	0,17	1150	1,3
HF-x36A	1,77	23	382,4	27,3	22,4	132	4	5,7	0,9	212	<1	9,75	2,69	18,6	41,6	5,09	20,1	4,36	1,11	3,73	0,64	4,07	0,96	2,66	0,44	3,37	0,53	29,1	134	15,3	0,04	<0.0005	0,07	3,6	<0.05	1,82	<5	8,1	<0.2	21,2	0,19	<0.005	0,35	660	24,3
HF-x6b	0,22	10	8,6	75,2	6,9	66	2,2	6,2	0,8	10	<1	3,51	0,93	2	3,3	0,35	1,2	0,25	0,16	0,29	0,07	0,56	0,17	0,62	0,13	0,82	0,14	2,2	108	20,7	0,91	0,022	0,04	42,2	0,34	2,64	<5	0,5	<0.2	14	0,11	0,189	0,48	338	0,9
HS-4	0,51	12	100,7	39,7	21,3	97	2,7	2,8	0,6	28	2	5,82	1,67	10,4	16,5	1,6	5	0,99	0,27	0,86	0,16	1,88	0,57	2,16	0,37	2,78	0,46	9,3	83	42,3	0,07	0,001	0,09	0,6	<0.05	0,6	<5	0,8	<0.2	13,6	0,11	0,005	0,24	363	1,1
HS-5	0,91	16	54,8	37,5	46,5	142	4,3	4,9	0,7	<10	<1	5,41	2,38	18,7	41,7	5,42	21,5	5,11	0,97	5,44	0,99	7,18	1,51	4,84	0,71	4,79	0,76	22	134	48,7	0,06	0,001	0,1	4	0,05	2,67	<5	0,6	<0.2	15,5	<0.02	0,012	0,44	687	0,3
HS-6	0,54	<10	15,4	56,9	23	87	2,8	3,3	0,6	<10	8	2,02	1,07	1,3	3,9	0,44	1,7	0,54	0,22	1,02	0,28	2,62	0,69	2,49	0,38	2,76	0,45	6,5	202	126,6	1,39	0,006	2,85	5,5	0,18	8,47	<5	0,6	2,7	9,5	0,62	0,047	0,27	1014	1
HS-7	1,09	<10	54,8	78,4	13	117	3,8	4,3	0,7	<10	2	4,93	1,35	2,5	6,6	0,75	3	1	0,32	0,94	0,21	1,7	0,44	1,58	0,25	2,04	0,35	13,1	1627	52,5	0,28	0,001	0,1	1,4	0,14	6,45	<5	0,6	<0.2	11,5	6,62	0,26	0,73	3262	0,3
HS-7 b	1,14	<10	84,1	127,6	36,3	117	3,9	4,5	0,7	17	3	5,38	1,46	3,6	6,4	0,77	3,3	1,37	0,68	1,81	0,52	4,86	1,25	4,35	0,66	4,69	0,71	1,9	61	30,9	0,6	0,008	0,08	1,9	0,05	1,64	<5	0,6	<0.2	18,2	<0.02	0,007	0,33	1841	1,3
HS-8	0,68	<10	18,1	65,2	38,1	96	3,2	3,9	0,7	<10	2	6,66	1,66	7,5	17,1	2,09	8,1	2,15	0,42	2,97	0,67	5,25	1,23	3,99	0,62	4,39	0,68	44,2	1224	76,5	0,2	0,001	0,15	1,5	0,06	1,17	<5	0,6	<0.2	11,6	4,68	0,138	0,16	1552	0,4
HS-S3 c	0,71	12	480	45,9	5,9	128	3,9	6,6	0,9	<10	7	22,15	5,66	17,2	32,7	3,31	10,3	2,14	0,66	1,39	0,2	1,17	0,23	0,74	0,12	0,99	0,16	575,1	1007	402,6	2,36	0,007	0,2	20,2	4,11	2,92	<5	1,7	0,2	18,4	4,67	0,072	0,56	5799	0,8

Appendix D EPMA-Analysis

Table 8.11: Amphibole EPMA analysis. Blue colour indicates analyses used in the GBMP geobarometer.

Analysis	Na2O	MgO	F	SiO2	Al2O3	CaO	K2O	Cr2O3	FeO	NiO	MnO	TiO2	ZnO	Cl	Tot.
	Wt.%	Wt.%	Wt.%	Wt.%	Wt.%	Wt.%	Wt.%	Wt.%	Wt.%	Wt.%	Wt.%	Wt.%	Wt.%	Wt.%	Wt.%
303-amp-1-1	1.94	7.73	<d.l.	40.16	18.28	10.98	0.78	<d.l.	15.65	<d.l.	0.05	0.75	0.04	0.01	96.38
303-amp-1-2	1.95	8.33	0.07	40.35	18.08	11.07	0.76	0.03	15.53	<d.l.	0.05	0.79	0.14	0.01	97.14
303-amp-1-3	1.90	7.87	0.20	40.85	17.94	11.17	0.68	<d.l.	15.32	<d.l.	0.03	0.62	0.03	0.01	96.61
303-amp-2-1	1.62	9.11	0.03	43.43	14.45	11.28	0.57	<d.l.	15.66	0.03	0.11	0.58	0.16	<d.l.	97.03
303-amp-2-2	1.74	9.23	0.10	42.12	13.87	11.11	0.68	<d.l.	15.60	<d.l.	0.09	0.89	0.11	0.04	95.58
303-amp-2-3	1.81	8.30	0.09	40.66	16.11	10.92	0.59	<d.l.	16.25	<d.l.	0.07	0.49	0.07	0.05	95.42
303-amp-3-1	1.61	8.91	0.05	42.18	15.29	11.18	0.58	0.02	15.95	<d.l.	0.09	0.65	0.13	<d.l.	96.64
303-amp-3-2	1.58	9.12	0.05	42.59	14.41	11.25	0.57	<d.l.	15.80	<d.l.	0.09	0.73	0.08	0.01	96.28
303-amp-3-3	1.72	8.56	0.07	41.97	15.68	11.28	0.69	<d.l.	16.38	<d.l.	0.07	0.73	0.04	<d.l.	97.18
303-amp-4-1	1.87	8.22	0.02	40.52	18.22	11.19	0.74	<d.l.	15.02	<d.l.	0.03	0.64	0.08	<d.l.	96.54
303-amp-4-2	1.96	8.35	0.07	40.49	17.70	11.20	0.80	<d.l.	14.97	<d.l.	0.02	0.74	0.11	<d.l.	96.40

Table 8.12: Clinozoisite and zoisite EPMA analysis. Black line separates sample 03 and 08.

Analysis	Na2O	MgO	F	SiO2	Al2O3	CaO	K2O	Cr2O3	FeO	NiO	MnO	TiO2	ZnO	Cl	Tot.
	Wt.%	Wt.%	Wt.%	Wt.%	Wt.%	Wt.%	Wt.%	Wt.%	Wt.%	Wt.%	Wt.%	Wt.%	Wt.%	Wt.%	Wt.%
303-czo-1-1	<d.l.	0.08	<d.l.	38.61	29.51	23.55	0.01	<d.l.	4.42	<d.l.	0.05	0.20	<d.l.	<d.l.	96.43
303-czo-1-2	<d.l.	0.15	<d.l.	38.53	30.02	23.47	<d.l.	<d.l.	4.27	<d.l.	0.07	0.16	0.05	0.00	96.73
303-czo-1-3	<d.l.	0.05	<d.l.	38.86	29.40	23.66	0.01	<d.l.	4.56	<d.l.	<d.l.	0.24	0.09	<d.l.	96.87
303-czo-2-1	<d.l.	0.04	<d.l.	38.65	30.05	23.88	0.01	<d.l.	4.06	<d.l.	<d.l.	0.15	0.07	0.01	96.92
303-czo-2-2	0.05	0.03	<d.l.	38.91	29.64	23.77	<d.l.	<d.l.	4.07	<d.l.	<d.l.	0.15	<d.l.	<d.l.	96.62
303-czo-3-1	0.09	0.11	<d.l.	39.10	29.55	23.82	<d.l.	<d.l.	4.29	<d.l.	0.05	0.17	0.05	0.01	97.23
303-czo-3-2	<d.l.	0.06	<d.l.	39.15	29.56	23.78	<d.l.	0.06	4.37	0.02	0.03	0.26	<d.l.	0.01	97.29
303-zo-1-1	<d.l.	<d.l.	<d.l.	39.34	31.93	24.28	<d.l.	<d.l.	1.61	<d.l.	<d.l.	0.06	<d.l.	0.01	97.23
303-zo-1-2	<d.l.	<d.l.	<d.l.	39.36	32.06	24.36	<d.l.	0.02	1.99	<d.l.	<d.l.	0.08	<d.l.	<d.l.	97.87
303-zo-2-1	<d.l.	<d.l.	<d.l.	39.37	32.05	24.29	0.01	0.05	1.60	<d.l.	<d.l.	0.05	<d.l.	<d.l.	97.42
303-zo-2-2	<d.l.	<d.l.	<d.l.	39.21	31.50	24.37	0.01	<d.l.	2.13	<d.l.	<d.l.	0.07	0.06	<d.l.	97.35
303-zo-2-3	<d.l.	<d.l.	<d.l.	39.19	31.59	24.24	<d.l.	<d.l.	1.99	<d.l.	0.03	0.08	<d.l.	<d.l.	97.11
308-czo-1-1	<d.l.	0.03	<d.l.	39.13	29.02	23.97	<d.l.	<d.l.	5.28	<d.l.	0.05	0.11	<d.l.	0.01	97.59
308-czo-1-2	<d.l.	0.06	<d.l.	39.29	29.63	24.28	<d.l.	<d.l.	4.65	<d.l.	<d.l.	0.08	<d.l.	0.01	97.99
308-czo-2-1	<d.l.	0.04	<d.l.	39.08	29.10	23.70	<d.l.	<d.l.	5.15	<d.l.	<d.l.	0.12	<d.l.	<d.l.	97.19
308-czo-2-2	0.06	0.07	<d.l.	39.00	28.99	23.87	0.01	<d.l.	5.22	<d.l.	<d.l.	0.17	0.08	<d.l.	97.46
308-czo-3-1	<d.l.	0.06	<d.l.	39.42	29.29	23.79	0.02	<d.l.	4.62	<d.l.	0.03	0.21	<d.l.	<d.l.	97.44
308-czo-3-2	0.07	0.06	0.04	39.22	28.51	23.51	<d.l.	0.02	5.47	<d.l.	0.02	0.19	0.04	<d.l.	97.15
308-czo-3-3	<d.l.	<d.l.	<d.l.	39.20	29.08	23.80	0.02	0.02	4.90	<d.l.	0.12	0.07	<d.l.	<d.l.	97.21
308-czo-4-1	<d.l.	0.03	<d.l.	39.36	29.51	23.84	0.01	<d.l.	4.54	<d.l.	<d.l.	0.14	0.10	<d.l.	97.54
308-czo-4-2	<d.l.	0.07	<d.l.	39.02	28.75	23.81	0.01	<d.l.	5.30	<d.l.	<d.l.	0.26	0.06	0.01	97.28
308-czo-5-1	<d.l.	<d.l.	<d.l.	39.08	29.45	23.86	0.01	<d.l.	4.56	<d.l.	0.03	0.15	<d.l.	<d.l.	97.15
308-czo-5-2	<d.l.	0.03	<d.l.	39.15	29.53	23.88	<d.l.	0.02	4.73	<d.l.	<d.l.	0.16	<d.l.	<d.l.	97.51
308-czo-5-3	<d.l.	0.06	0.05	39.32	30.07	24.03	<d.l.	<d.l.	3.80	<d.l.	0.03	0.20	<d.l.	<d.l.	97.56
308-czo-6-1	<d.l.	0.03	<d.l.	38.99	28.70	23.69	<d.l.	<d.l.	5.39	<d.l.	0.02	0.22	0.03	<d.l.	97.07
308-czo-6-2	<d.l.	0.02	<d.l.	39.07	29.12	23.91	<d.l.	<d.l.	5.00	<d.l.	0.02	0.14	<d.l.	<d.l.	97.28
308-zo-1-1	<d.l.	<d.l.	<d.l.	39.72	32.11	24.51	<d.l.	<d.l.	1.54	<d.l.	<d.l.	0.08	0.05	<d.l.	98.01
308-zo-1-2	<d.l.	<d.l.	<d.l.	39.45	32.23	24.41	<d.l.	<d.l.	1.46	<d.l.	0.06	0.07	<d.l.	<d.l.	97.68
308-zo-1-3	<d.l.	<d.l.	<d.l.	39.75	32.01	24.41	<d.l.	<d.l.	1.66	<d.l.	<d.l.	0.08	0.09	0.00	98.00
308-zo-2-1	<d.l.	<d.l.	<d.l.	39.68	31.73	24.32	<d.l.	<d.l.	2.07	0.03	0.03	0.08	0.06	<d.l.	97.99
308-zo-2-2	<d.l.	<d.l.	<d.l.	39.61	31.74	24.36	0.01	0.02	1.73	<d.l.	<d.l.	0.06	<d.l.	<d.l.	97.53
308-zo-2-3	0.06	<d.l.	0.02	39.80	31.87	24.46	<d.l.	<d.l.	1.83	<d.l.	<d.l.	0.05	<d.l.	<d.l.	98.09
308-zo-3-1	0.24	0.06	0.07	39.82	31.53	24.30	0.01	<d.l.	2.14	0.03	<d.l.	0.09	<d.l.	<d.l.	98.29
308-zo-3-2	0.04	<d.l.	<d.l.	39.67	31.56	24.54	<d.l.	0.03	2.07	<d.l.	0.03	0.04	<d.l.	<d.l.	97.99
308-zo-3-3	<d.l.	<d.l.	0.02	39.91	32.09	24.51	<d.l.	<d.l.	1.67	<d.l.	0.02	0.07	<d.l.	<d.l.	98.29
308-zo-3-4	0.17	<d.l.	<d.l.	39.68	31.87	24.55	<d.l.	<d.l.	1.65	<d.l.	0.02	0.08	<d.l.	<d.l.	98.02
308-zo-3-5	0.06	<d.l.	<d.l.	39.68	31.70	24.40	<d.l.	<d.l.	2.17	0.02	<d.l.	0.09	<d.l.	<d.l.	98.11
308-zo-3-6	<d.l.	<d.l.	0.05	39.67	31.49	24.31	<d.l.	0.02	2.31	0.03	0.02	0.09	<d.l.	<d.l.	97.99
308-zo-4-1	<d.l.	<d.l.	<d.l.	39.93	32.18	24.40	<d.l.	<d.l.	1.53	<d.l.	0.03	0.07	0.05	<d.l.	98.18
308-zo-4-2	<d.l.	<d.l.	<d.l.	39.82	32.03	24.39	<d.l.	<d.l.	1.54	<d.l.	<d.l.	0.06	<d.l.	<d.l.	97.84
308-zo-4-3	<d.l.	<d.l.	<d.l.	39.76	32.02	24.39	<d.l.	<d.l.	1.73	<d.l.	<d.l.	0.08	<d.l.	<d.l.	97.98

Table 8.13: Biotite EPMA analysis. Blue colour indicates analyses used in the GB-GBMP geothermobarometer. Black line separates sample 03 and 08.

Analysis	Na2O	MgO	Al2O3	F	CaO	Cr2O3	K2O	FeO	TiO2	SiO2	MnO	Cl	H	Tot.
	Wt.%	Wt.%	Wt.%	Wt.%	Wt.%	Wt.%	Wt.%	Wt.%	Wt.%	Wt.%	Wt.%	Wt.%	Wt.%	Wt.%
303-bt-1-1	0.10	11.95	17.91	0.34	<d.l.	<d.l.	8.11	17.75	1.42	37.12	<d.l.	<d.l.	4.00	98.77
303-bt-1-2	0.11	11.93	17.96	0.32	0.02	<d.l.	8.66	17.62	1.71	36.17	<d.l.	<d.l.	4.00	98.56
303-bt-1-3	0.10	11.69	17.89	0.39	<d.l.	<d.l.	8.40	17.49	1.83	37.04	<d.l.	<d.l.	4.00	98.86
303-bt-1-4	0.11	11.78	18.06	0.40	0.03	<d.l.	8.28	17.39	1.85	35.05	<d.l.	<d.l.	4.00	96.97
303-bt-2-1	0.13	11.82	18.65	0.34	0.03	<d.l.	7.31	17.12	1.30	36.64	<d.l.	<d.l.	4.00	97.35
303-bt-2-2	0.10	11.83	18.69	0.43	0.03	<d.l.	7.28	17.07	1.41	37.21	<d.l.	<d.l.	4.00	98.12
303-bt-3-1	0.10	11.96	18.97	0.18	0.06	<d.l.	7.97	16.46	1.17	36.67	<d.l.	<d.l.	4.00	97.59
303-bt-3-2	0.12	12.28	18.77	0.37	0.15	<d.l.	8.69	16.41	1.39	36.29	<d.l.	<d.l.	4.00	98.50
303-bt-3-3	0.12	11.76	18.78	0.28	0.07	<d.l.	7.45	16.39	1.47	36.80	<d.l.	<d.l.	4.00	97.19
303-bt-3-4	0.12	11.78	18.91	0.34	0.09	<d.l.	7.48	16.19	1.58	36.74	<d.l.	0.02	4.00	97.28
303-bt-3-5	0.12	11.91	18.96	0.30	0.06	<d.l.	7.52	16.50	1.50	37.41	<d.l.	<d.l.	4.00	98.28
303-bt-3-6	0.16	11.24	19.16	0.35	0.08	<d.l.	8.03	16.69	1.63	36.36	<d.l.	<d.l.	4.00	97.75
303-bt-3-7	0.12	11.68	18.98	0.38	0.19	<d.l.	8.67	15.15	1.49	36.71	0.08	<d.l.	4.00	97.50
303-bt-4-1	0.16	11.90	18.38	0.41	0.08	<d.l.	7.70	16.93	1.27	36.31	<d.l.	<d.l.	4.00	97.18
303-bt-4-2	0.25	11.96	18.41	0.36	0.06	<d.l.	7.75	16.87	1.23	36.87	<d.l.	0.05	4.00	97.84
303-bt-4-3	0.17	11.94	18.27	0.43	0.07	<d.l.	7.63	16.81	1.32	36.57	<d.l.	<d.l.	4.00	97.28
303-bt-4-4	0.12	11.87	18.52	0.51	0.06	<d.l.	7.88	17.08	1.38	36.73	<d.l.	<d.l.	4.00	98.18
303-bt-5-1	0.10	11.76	17.93	0.35	<d.l.	<d.l.	9.27	16.95	2.55	36.40	<d.l.	<d.l.	4.00	99.34
303-bt-5-10	0.13	11.34	18.69	0.35	0.11	<d.l.	9.13	15.97	2.26	35.39	<d.l.	0.02	4.00	97.40
303-bt-5-11	0.13	11.80	18.35	0.35	0.09	<d.l.	9.07	16.42	2.05	37.15	<d.l.	0.02	4.00	99.44
303-bt-5-12	0.19	11.08	18.76	0.33	0.17	<d.l.	8.78	16.12	2.27	37.13	<d.l.	<d.l.	4.00	98.83
303-bt-5-2	0.14	11.67	17.98	0.30	0.15	<d.l.	9.02	17.11	2.47	36.24	<d.l.	<d.l.	4.00	99.08
303-bt-5-3	0.14	11.58	18.17	0.35	0.04	<d.l.	9.24	16.32	2.50	36.42	<d.l.	<d.l.	4.00	98.82
303-bt-5-4	0.11	11.60	18.23	0.28	0.04	<d.l.	9.28	16.73	2.46	36.54	<d.l.	<d.l.	4.00	99.34
303-bt-5-5	0.15	11.45	18.25	0.22	<d.l.	<d.l.	9.27	16.78	2.40	36.47	<d.l.	<d.l.	4.00	99.02
303-bt-5-6	0.13	11.37	18.14	0.39	0.08	<d.l.	9.23	16.98	2.40	36.66	<d.l.	<d.l.	4.00	99.42
303-bt-5-7	0.15	11.34	18.26	0.25	0.03	<d.l.	9.23	17.28	2.52	36.31	<d.l.	<d.l.	4.00	99.40
303-bt-5-8	0.10	11.12	17.78	0.21	0.03	<d.l.	9.09	17.48	2.52	36.05	0.06	<d.l.	4.00	98.45
303-bt-5-9	0.13	11.50	18.58	0.35	0.12	<d.l.	9.13	16.15	2.22	36.20	<d.l.	<d.l.	4.00	98.41
308-bt-1-1	0.15	11.67	18.51	0.31	0.13	<d.l.	9.08	16.97	1.74	36.93	0.07	0.02	4.00	99.59
308-bt-1-10	0.15	11.68	18.41	0.28	0.10	<d.l.	8.99	16.62	1.90	35.69	<d.l.	0.03	4.00	97.89
308-bt-1-11	0.15	11.63	18.25	0.40	0.11	<d.l.	8.96	16.63	1.82	36.99	<d.l.	0.02	4.00	99.01
308-bt-1-12	0.16	11.70	18.14	0.23	0.08	<d.l.	8.91	16.51	1.96	36.90	<d.l.	0.02	4.00	98.64
308-bt-1-13	0.12	11.65	18.15	0.37	0.07	<d.l.	9.02	16.42	2.05	36.72	0.05	0.05	4.00	98.70
308-bt-1-14	0.12	11.60	18.10	0.46	0.09	<d.l.	9.15	16.58	1.85	37.29	<d.l.	0.03	4.00	99.32
308-bt-1-2	0.16	11.62	18.63	0.27	0.11	<d.l.	8.99	16.81	2.07	36.88	0.08	0.03	4.00	99.66
308-bt-1-3	0.13	11.78	18.39	0.28	0.12	<d.l.	9.02	17.21	1.88	36.78	0.09	0.03	4.00	99.72
308-bt-1-4	0.15	11.63	18.26	0.33	0.12	<d.l.	8.86	17.15	1.81	36.51	0.08	0.03	4.00	98.93
308-bt-1-5	0.17	10.96	18.65	0.47	0.10	<d.l.	8.92	16.83	1.97	34.78	<d.l.	0.03	4.00	96.94
308-bt-1-6	0.20	11.03	18.57	0.24	0.16	<d.l.	8.92	15.78	2.04	36.46	<d.l.	0.06	4.00	97.51
308-bt-1-7	0.53	3.86	28.38	<d.l.	0.11	<d.l.	8.44	5.09	0.81	41.61	<d.l.	0.17	4.00	93.08
308-bt-1-8	8.97	0.05	25.01	<d.l.	4.86	<d.l.	0.11	0.33	<d.l.	64.54	<d.l.	0.02	4.00	107.92
308-bt-1-9	0.32	11.36	17.99	0.30	0.18	<d.l.	8.81	16.69	2.02	37.61	<d.l.	0.03	4.00	99.37
308-bt-2-1	0.16	12.00	18.46	0.39	0.11	<d.l.	9.00	16.99	1.26	36.80	<d.l.	0.02	4.00	99.25
308-bt-2-10	0.14	11.99	17.99	0.33	0.08	<d.l.	9.12	16.97	1.82	36.71	<d.l.	0.02	4.00	99.22
308-bt-2-11	0.16	11.87	18.48	0.35	0.18	<d.l.	8.43	16.62	1.82	35.03	0.08	0.02	4.00	97.06
308-bt-2-2	0.15	12.47	18.71	0.30	0.07	<d.l.	8.82	17.57	1.19	36.83	<d.l.	0.02	4.00	100.20
308-bt-2-3	0.14	12.16	18.33	0.39	0.07	<d.l.	9.03	17.13	1.24	37.27	0.08	0.02	4.00	99.86
308-bt-2-4	0.18	12.12	18.13	0.30	0.09	<d.l.	9.11	16.85	1.43	37.09	<d.l.	0.02	4.00	99.39
308-bt-2-5	0.15	11.85	18.43	0.43	0.04	<d.l.	9.04	16.95	1.55	36.89	<d.l.	0.02	4.00	99.41
308-bt-2-6	0.17	11.63	18.41	0.27	0.12	<d.l.	8.66	16.91	1.61	36.28	<d.l.	0.02	4.00	98.10
308-bt-2-7	0.14	11.86	18.17	0.40	0.11	<d.l.	9.01	17.00	1.69	36.86	<d.l.	0.02	4.00	99.27
308-bt-2-8	0.14	12.19	18.36	0.41	0.15	<d.l.	8.26	17.02	1.57	36.05	0.06	<d.l.	4.00	98.24
308-bt-2-9	0.15	11.87	17.74	0.34	0.09	<d.l.	8.93	16.90	1.73	36.94	0.07	0.02	4.00	98.78
308-bt-3-1	0.10	8.70	17.38	0.14	1.10	<d.l.	6.65	15.47	0.97	34.03	0.26	0.19	4.00	88.98
308-bt-3-10	0.81	1.40	34.28	<d.l.	0.03	<d.l.	8.35	1.79	0.94	46.71	<d.l.	<d.l.	4.00	98.45
308-bt-3-2	0.09	10.65	17.88	0.20	0.40	<d.l.	8.23	17.00	1.31	35.58	0.12	0.07	4.00	95.53
308-bt-3-3	0.12	11.00	18.04	0.38	0.04	<d.l.	9.20	17.26	1.37	36.61	<d.l.	0.02	4.00	98.09
308-bt-3-4	0.15	11.19	18.15	0.32	0.04	<d.l.	9.11	17.89	1.44	36.86	0.10	0.02	4.00	99.26
308-bt-3-5	0.14	11.21	18.05	0.34	<d.l.	<d.l.	9.07	17.78	1.44	36.02	<d.l.	<d.l.	4.00	98.13
308-bt-3-6	0.13	11.53	18.17	0.24	0.02	<d.l.	9.17	17.68	1.44	36.01	0.09	<d.l.	4.00	98.50
308-bt-3-7	0.18	11.47	18.06	0.33	0.06	<d.l.	8.90	17.44	1.41	35.47	<d.l.	<d.l.	4.00	97.37
308-bt-3-8	0.14	11.31	18.16	0.33	<d.l.	<d.l.	9.22	17.82	1.43	36.19	0.07	<d.l.	4.00	98.70
308-bt-3-9	0.15	11.55	17.97	0.35	0.05	<d.l.	8.93	18.13	1.44	36.92	<d.l.	<d.l.	4.00	99.53
308-bt-4-1	0.19	12.15	18.11	0.38	0.03	<d.l.	8.98	16.20	1.28	37.62	<d.l.	0.02	4.00	99.03
308-bt-4-10	0.15	12.07	18.07	0.42	0.12	<d.l.	8.57	16.97	1.17	36.10	0.06	0.02	4.00	97.71
308-bt-4-11	0.17	12.24	17.73	0.37	0.09	<d.l.	8.86	17.05	1.12	37.34	0.07	0.03	4.00	99.06
308-bt-4-2	0.17	11.97	18.16	0.39	0.04	<d.l.	8.77	17.08	1.32	36.97	0.09	0.02	4.00	98.99
308-bt-4-3	0.15	12.17	17.89	0.35	0.09	<d.l.	8.97	17.30	1.23	36.70	0.06	0.02	4.00	98.93
308-bt-4-4	0.14	11.60	18.02	0.28	0.09	<d.l.	8.75	17.64	1.41	37.09	0.07	0.03	4.00	99.12
308-bt-4-5	0.16	11.69	17.74	0.24	0.05	<d.l.	8.73	18.08	1.38	36.94	0.06	0.04	4.00	99.11
308-bt-4-6	0.17	11.72	18.40	0.26	0.03	<d.l.	8.85	17.53	1.38	36.49	<d.l.	0.03	4.00	98.90
308-bt-4-7	0.17	11.84	18.20	0.31	0.03	<d.l.	8.95	17.26	1.52	37.05	0.07	<d.l.	4.00	99.42
308-bt-4-8	0.15	11.90	17.93	0.34	0.10	<d.l.	8.84	17.00	1.26	37.74	0.06	0.02	4.00	99.33
308-bt-4-9	0.16	11.84	18.39	0.41	0.05	<d.l.	9.06	17.26	1.41	35.45	0.08	0.02	4.00	98.13

Table 8.14: Chlorite EPMA analysis.

Analysis	Na2O	MgO	Al2O3	F	CaO	Cr2O3	K2O	FeO	TiO2	SiO2	MnO	Cl	H	Total
	Wt.%	Wt.%	Wt.%	Wt.%	Wt.%	Wt.%	Wt.%	Wt.%	Wt.%	Wt.%	Wt.%	Wt.%	Wt.%	Wt.%
303-chl-1-1	<d.l.	18.01	22.36	<d.l.	<d.l.	<d.l.	<d.l.	21.35	0.08	25.71	<d.l.	<d.l.	12.46	99.97
303-chl-1-2	<d.l.	18.12	22.35	<d.l.	<d.l.	<d.l.	<d.l.	21.27	0.04	25.57	0.06	<d.l.	12.57	99.98
303-chl-1-3	<d.l.	18.16	21.98	<d.l.	0.03	<d.l.	<d.l.	20.78	<d.l.	25.88	0.06	<d.l.	12.97	99.86
303-chl-1-4	0.03	17.76	21.93	<d.l.	0.04	<d.l.	<d.l.	19.96	0.07	25.54	<d.l.	<d.l.	14.63	99.97
303-chl-1-5	<d.l.	18.33	22.38	<d.l.	<d.l.	<d.l.	<d.l.	21.40	0.09	25.73	<d.l.	<d.l.	11.95	99.88
303-chl-1-6	<d.l.	17.53	22.34	<d.l.	0.02	<d.l.	<d.l.	21.78	0.07	25.54	<d.l.	<d.l.	12.68	99.96
303-chl-1-7	<d.l.	17.91	22.55	<d.l.	<d.l.	<d.l.	0.02	21.25	0.04	25.67	<d.l.	<d.l.	12.42	99.86
303-chl-2-1	0.03	17.74	21.72	<d.l.	0.02	<d.l.	0.06	21.35	0.09	24.93	<d.l.	0.03	13.94	99.92
303-chl-2-2	<d.l.	17.75	21.81	<d.l.	<d.l.	<d.l.	0.32	21.75	0.14	25.40	<d.l.	<d.l.	12.77	99.93
303-chl-2-3	0.07	14.24	19.35	0.22	0.07	<d.l.	4.64	19.16	1.12	30.31	<d.l.	0.03	10.77	99.98
303-chl-2-4	0.06	17.66	21.86	<d.l.	<d.l.	<d.l.	<d.l.	21.10	0.08	25.63	<d.l.	0.02	13.49	99.90
303-chl-2-5	<d.l.	17.75	21.94	<d.l.	<d.l.	<d.l.	0.09	21.74	0.09	24.60	<d.l.	<d.l.	13.74	99.94
303-chl-2-6	0.03	17.78	21.17	<d.l.	0.09	<d.l.	<d.l.	21.82	0.09	25.87	0.06	0.02	13.00	99.92
303-chl-2-7	<d.l.	18.03	21.78	<d.l.	0.05	<d.l.	0.08	21.33	0.06	25.60	<d.l.	0.02	12.96	99.91
303-chl-2-8	<d.l.	17.77	21.79	0.13	0.02	<d.l.	<d.l.	21.23	0.10	25.73	<d.l.	<d.l.	13.17	99.94
303-chl-2-9	0.02	17.44	21.70	<d.l.	<d.l.	<d.l.	0.13	21.69	0.10	25.36	0.06	<d.l.	13.44	99.94

Table 8.15: Muscovite EPMA analysis. Blue colour indicates analyses used in the GBMP geobarometer. Black line separates sample 03 and 08.

Analysis	Na2O	MgO	Al2O3	F	CaO	Cr2O3	K2O	FeO	TiO2	SiO2	MnO	Cl	H	Total
	Wt.%	Wt.%	Wt.%	Wt.%	Wt.%	Wt.%	Wt.%	Wt.%	Wt.%	Wt.%	Wt.%	Wt.%	Wt.%	Wt.%
303-msc-1-1	1.28	1.15	33.80	0.22	<d.l.	<d.l.	8.36	1.30	0.94	46.44	<d.l.	<d.l.	6.50	99.98
303-msc-1-2	1.31	0.89	34.32	<d.l.	<d.l.	<d.l.	8.51	1.23	0.70	45.59	<d.l.	<d.l.	7.43	99.98
303-msc-1-3	1.24	1.17	33.99	<d.l.	<d.l.	<d.l.	8.47	1.27	0.64	46.47	<d.l.	<d.l.	6.64	99.88
303-msc-1-4	1.35	0.95	34.33	<d.l.	<d.l.	<d.l.	8.36	1.23	0.46	44.84	<d.l.	<d.l.	8.43	99.95
303-msc-1-5	1.40	0.91	34.60	<d.l.	<d.l.	<d.l.	8.28	1.21	0.51	45.82	<d.l.	<d.l.	7.13	99.87
303-msc-1-6	1.34	1.03	34.18	<d.l.	<d.l.	<d.l.	8.31	1.16	0.61	45.52	<d.l.	<d.l.	7.78	99.93
308-msc-1-1	0.89	1.45	32.84	<d.l.	<d.l.	<d.l.	9.12	1.55	0.81	46.78	<d.l.	<d.l.	6.49	99.92
308-msc-1-10	1.00	1.30	33.69	<d.l.	<d.l.	<d.l.	9.01	1.42	0.41	46.96	<d.l.	<d.l.	6.09	99.88
308-msc-1-2	0.99	1.26	33.46	<d.l.	0.02	<d.l.	8.85	1.48	0.54	46.23	<d.l.	<d.l.	7.16	100.00
308-msc-1-3	0.86	1.42	32.98	<d.l.	<d.l.	<d.l.	9.15	1.56	0.64	45.86	<d.l.	<d.l.	7.45	99.92
308-msc-1-4	0.91	1.37	32.97	<d.l.	<d.l.	<d.l.	8.95	1.55	0.82	47.03	<d.l.	<d.l.	6.31	99.90
308-msc-1-5	0.75	1.36	33.73	<d.l.	<d.l.	<d.l.	8.95	1.61	0.52	45.67	<d.l.	<d.l.	7.34	99.93
308-msc-1-6	0.89	1.99	33.09	<d.l.	<d.l.	<d.l.	9.04	2.62	0.44	46.04	<d.l.	<d.l.	5.79	99.90
308-msc-1-7	1.06	1.35	33.33	<d.l.	<d.l.	<d.l.	8.96	1.41	0.49	47.14	<d.l.	<d.l.	6.16	99.90
308-msc-1-8	1.03	1.32	33.80	<d.l.	<d.l.	<d.l.	8.72	1.40	0.47	46.81	<d.l.	<d.l.	6.38	99.93
308-msc-1-9	1.00	1.27	33.91	<d.l.	<d.l.	<d.l.	8.93	1.45	0.45	47.17	<d.l.	<d.l.	5.75	99.94
308-msc-2-1	0.69	1.23	27.42	<d.l.	0.06	<d.l.	7.49	1.62	0.77	54.52	<d.l.	<d.l.	6.15	99.95
308-msc-2-2	0.68	1.43	32.83	<d.l.	<d.l.	<d.l.	8.80	1.43	0.99	46.55	<d.l.	<d.l.	7.23	99.95
308-msc-2-3	0.74	1.33	33.04	<d.l.	<d.l.	<d.l.	9.01	1.51	0.82	46.75	<d.l.	<d.l.	6.76	99.96
308-msc-2-4	2.23	0.95	31.29	<d.l.	0.89	<d.l.	7.50	1.42	0.80	48.91	<d.l.	0.02	5.92	99.94
308-msc-2-5	0.75	1.46	32.66	<d.l.	0.04	<d.l.	8.83	1.60	1.04	46.27	<d.l.	<d.l.	7.30	99.96

Table 8.16: Plagioclase EPMA analysis 1. Red colour indicates an erroneous results. Blue colour indicates analyses used in the GBMP geobarometer. Black line separates sample 03 and 08.

Comment	Na2O	MgO	Al2O3	CaO	TiO2	SrO	BaO	FeO	K2O	SiO2	MnO	Total
	Wt.%	Wt.%	Wt.%	Wt.%	Wt.%	Wt.%	Wt.%	Wt.%	Wt.%	Wt.%	Wt.%	Wt.%
303-plg-1-1	8.64	<d.l.	23.74	5.17	0.03	0.12	<d.l.	0.41	<d.l.	62.85	0.00	100.95
303-plg-1-2	8.06	1.00	22.36	4.19	0.16	0.13	<d.l.	1.29	1.06	60.33	0.00	98.58
303-plg-1-3	7.66	<d.l.	25.10	6.42	<d.l.	0.17	<d.l.	0.33	<d.l.	58.43	0.00	98.10
303-plg-1-4	7.24	0.58	24.24	6.59	0.06	0.17	<d.l.	0.70	0.48	57.84	0.01	97.91
303-plg-1-5	7.57	<d.l.	24.89	6.53	<d.l.	0.20	<d.l.	0.20	<d.l.	59.09	0.00	98.49
303-plg-1-6	7.68	<d.l.	24.89	6.46	<d.l.	0.21	<d.l.	0.18	<d.l.	61.01	0.00	100.43
303-plg-1-7	8.15	<d.l.	24.42	6.00	<d.l.	0.14	<d.l.	0.29	<d.l.	62.02	0.01	101.03
303-plg-1-8	6.93	<d.l.	26.05	7.79	<d.l.	0.22	<d.l.	0.11	<d.l.	57.84	0.01	98.95
303-plg-2-1	7.21	<d.l.	25.99	7.94	<d.l.	0.18	<d.l.	0.10	<d.l.	58.35	0.00	99.77
303-plg-2-2	6.40	<d.l.	26.95	8.92	<d.l.	0.26	<d.l.	0.10	<d.l.	56.98	0.02	99.62
303-plg-2-3	6.04	<d.l.	27.33	9.29	<d.l.	0.21	<d.l.	0.09	<d.l.	56.98	0.01	99.95
303-plg-2-4	6.32	<d.l.	27.18	8.99	<d.l.	0.18	<d.l.	0.05	<d.l.	57.24	0.02	99.98
303-plg-2-5	6.51	<d.l.	27.18	8.86	<d.l.	0.21	<d.l.	<d.l.	<d.l.	57.09	0.00	99.85
303-plg-2-6	6.59	<d.l.	26.51	8.39	<d.l.	0.16	<d.l.	0.05	<d.l.	57.82	0.05	99.57
303-plg-2-7	6.72	<d.l.	26.54	8.48	<d.l.	0.18	<d.l.	0.09	<d.l.	58.56	0.00	100.57
303-plg-2-8	8.21	<d.l.	24.38	5.81	<d.l.	0.22	<d.l.	0.12	<d.l.	61.45	0.02	100.21
303-plg-3-1	8.81	<d.l.	23.31	4.67	<d.l.	0.16	<d.l.	0.22	<d.l.	63.39	0.02	100.57
303-plg-3-2	8.67	<d.l.	23.48	4.70	<d.l.	0.15	<d.l.	0.19	<d.l.	63.30	0.00	100.50
303-plg-3-3	8.37	<d.l.	24.30	5.32	<d.l.	0.20	<d.l.	0.19	<d.l.	62.33	0.00	100.71
303-plg-3-4	8.22	<d.l.	24.07	5.70	<d.l.	0.15	<d.l.	0.17	<d.l.	61.10	0.00	99.42
303-plg-3-5	8.45	<d.l.	23.93	5.21	<d.l.	0.15	<d.l.	0.17	<d.l.	62.13	0.02	100.05
303-plg-3-6	8.04	<d.l.	24.16	5.70	<d.l.	0.13	<d.l.	0.15	<d.l.	61.94	0.00	100.13
303-plg-3-7	8.06	<d.l.	24.17	5.48	<d.l.	0.15	<d.l.	0.16	<d.l.	62.85	0.00	100.87
303-plg-3-8	8.49	<d.l.	23.94	5.38	<d.l.	0.14	<d.l.	0.19	<d.l.	62.26	0.01	100.41
303-plg-3-9	8.01	0.63	22.82	4.69	0.07	0.21	<d.l.	0.73	0.54	59.58	0.00	97.28
303-plg-4-1	8.45	<d.l.	24.26	5.72	<d.l.	0.16	<d.l.	0.09	<d.l.	61.21	0.00	99.89
303-plg-4-10	7.98	0.30	23.69	5.64	0.09	0.11	<d.l.	0.57	0.33	59.55	0.01	98.26
303-plg-4-2	7.95	<d.l.	24.71	6.39	<d.l.	0.17	<d.l.	0.10	<d.l.	59.77	0.04	99.12
303-plg-4-3	7.77	<d.l.	25.00	6.58	<d.l.	0.15	<d.l.	0.10	0.16	60.45	0.00	100.21
303-plg-4-4	7.88	<d.l.	24.78	6.68	<d.l.	0.18	<d.l.	0.08	<d.l.	60.63	0.00	100.24
303-plg-4-5	7.06	<d.l.	26.15	8.04	<d.l.	0.21	<d.l.	0.24	<d.l.	58.33	0.01	100.04
303-plg-4-6	7.22	<d.l.	25.81	7.54	<d.l.	0.17	<d.l.	0.22	<d.l.	59.77	0.00	100.72
303-plg-4-7	7.06	<d.l.	26.24	8.13	<d.l.	0.21	<d.l.	0.25	<d.l.	57.16	0.00	99.04
303-plg-4-8	7.88	0.13	24.65	6.27	0.04	0.19	<d.l.	0.33	0.14	60.34	0.00	99.97
303-plg-4-9	6.89	0.39	23.99	6.48	0.21	0.18	<d.l.	0.76	0.50	56.74	0.03	96.16
303-plg-5-1	7.69	<d.l.	25.01	6.71	<d.l.	0.21	<d.l.	0.19	<d.l.	59.35	0.02	99.18
303-plg-5-2	7.33	<d.l.	25.36	7.20	<d.l.	0.17	<d.l.	0.13	<d.l.	59.72	0.00	99.91
303-plg-5-3	7.63	<d.l.	25.30	6.78	<d.l.	0.19	<d.l.	0.18	<d.l.	58.61	0.02	98.71
303-plg-5-4	6.82	<d.l.	26.21	8.07	<d.l.	0.14	<d.l.	0.09	<d.l.	57.96	0.00	99.29
303-plg-5-5	7.20	<d.l.	25.72	7.53	<d.l.	0.18	<d.l.	0.13	<d.l.	58.49	0.00	99.24
303-plg-5-6	6.17	<d.l.	27.36	9.54	<d.l.	0.15	<d.l.	<d.l.	<d.l.	55.69	0.01	98.92
303-plg-5-7	6.01	<d.l.	27.61	9.48	<d.l.	0.18	<d.l.	<d.l.	<d.l.	56.71	0.02	100.01
303-plg-5-8	6.71	<d.l.	26.70	8.72	<d.l.	0.17	<d.l.	<d.l.	<d.l.	57.92	0.00	100.22
303-plg-5-9	7.72	<d.l.	25.05	6.78	<d.l.	0.13	<d.l.	0.08	<d.l.	60.29	0.00	100.05
308-plg-1-1	6.43	2.56	20.30	2.93	0.36	0.07	<d.l.	4.79	2.10	51.69	0.04	91.26
308-plg-1-10	3.34	1.38	20.85	6.65	<d.l.	0.06	<d.l.	17.72	<d.l.	44.66	0.94	95.60
308-plg-1-2	7.67	<d.l.	25.40	6.89	<d.l.	0.18	<d.l.	0.29	<d.l.	59.50	0.00	99.93
308-plg-1-3	9.05	<d.l.	23.62	4.67	<d.l.	0.16	<d.l.	0.36	<d.l.	62.06	0.03	99.95
308-plg-1-4	7.59	<d.l.	25.22	6.79	<d.l.	0.22	<d.l.	0.33	<d.l.	59.97	0.00	100.12
308-plg-1-5	7.53	<d.l.	25.36	7.01	<d.l.	0.20	<d.l.	0.17	<d.l.	59.27	0.00	99.55
308-plg-1-6	7.51	<d.l.	25.16	7.00	<d.l.	0.21	<d.l.	0.14	<d.l.	60.12	0.02	100.16
308-plg-1-7	7.90	<d.l.	24.92	6.76	<d.l.	0.18	<d.l.	0.16	<d.l.	60.27	0.00	100.19
308-plg-1-8	7.61	0.10	22.08	5.20	<d.l.	0.19	<d.l.	1.07	0.22	57.34	0.07	93.88
308-plg-1-9	5.57	0.37	20.17	5.12	<d.l.	0.13	<d.l.	5.40	0.14	49.85	0.30	87.04
308-plg-2-1	7.78	1.01	23.00	4.39	0.17	0.14	<d.l.	1.63	0.89	60.09	0.00	99.09
308-plg-2-10	8.54	<d.l.	24.02	5.45	<d.l.	0.09	<d.l.	0.11	<d.l.	61.99	0.00	100.20
308-plg-2-11	8.50	<d.l.	24.17	5.38	<d.l.	0.16	<d.l.	0.19	<d.l.	62.48	0.05	100.93
308-plg-2-2	1.79	9.17	18.52	0.95	1.62	0.08	0.26	13.83	7.54	41.45	0.03	95.24
308-plg-2-3	8.50	<d.l.	24.17	5.44	<d.l.	0.21	<d.l.	0.10	<d.l.	61.14	0.02	99.58
308-plg-2-4	6.07	0.25	25.02	3.50	0.13	0.15	0.42	0.43	2.56	54.16	0.02	92.70
308-plg-2-5	8.32	<d.l.	24.27	5.50	<d.l.	0.15	<d.l.	0.12	<d.l.	61.51	0.00	99.87
308-plg-2-6	8.55	<d.l.	24.19	5.55	<d.l.	0.16	<d.l.	0.12	<d.l.	62.32	0.00	100.89
308-plg-2-7	8.52	<d.l.	24.12	5.52	<d.l.	0.14	<d.l.	0.13	<d.l.	60.79	0.01	99.23
308-plg-2-8	8.32	<d.l.	24.09	5.55	<d.l.	0.20	<d.l.	0.10	<d.l.	61.42	0.00	99.68
308-plg-2-9	8.30	<d.l.	24.08	5.54	<d.l.	0.12	<d.l.	0.16	<d.l.	61.66	0.00	99.86
308-plg-3-1	8.72	<d.l.	23.86	5.29	<d.l.	0.14	<d.l.	0.29	<d.l.	62.34	0.00	100.64
308-plg-3-2	8.25	0.07	23.90	5.44	<d.l.	0.15	<d.l.	0.35	0.13	61.58	0.00	99.87
308-plg-3-3	6.83	1.71	23.74	5.44	0.25	0.17	<d.l.	2.66	1.40	57.77	0.00	99.97
308-plg-3-4	6.29	2.28	23.14	5.06	0.37	0.13	0.08	3.22	1.91	55.52	0.00	98.01
308-plg-3-5	7.68	<d.l.	25.14	6.76	<d.l.	0.20	<d.l.	0.12	<d.l.	60.23	0.00	100.13
308-plg-3-6	8.25	<d.l.	24.59	6.14	<d.l.	0.18	<d.l.	0.11	<d.l.	61.99	0.00	101.26

Table 8.17: Plagioclase EPMA analysis 2. Blue colour indicates analyses used in the plagioclase-amphibole geobarometer. Black line separates sample 03 and 08.

Analysis	Na2O	MgO	Al2O3	CaO	TiO2	SrO	BaO	FeO	K2O	SiO2	MnO	Total
	Wt.%	Wt.%	Wt.%	Wt.%	Wt.%	Wt.%	Wt.%	Wt.%	Wt.%	Wt.%	Wt.%	Wt.%
303-plag-1-1	6.98	<d.l.	25.77	7.81	<d.l.	0.14	<d.l.	0.07	0.05	57.95	0.00	98.76
303-plag-1-2	6.98	<d.l.	25.73	7.98	<d.l.	0.13	<d.l.	0.04	0.05	58.22	0.00	99.13
303-plag-1-3	7.51	0.02	24.97	6.90	<d.l.	<d.l.	<d.l.	0.02	0.04	60.66	0.00	100.13
303-plag-2-1	8.28	<d.l.	24.15	5.88	<d.l.	0.05	<d.l.	0.08	0.08	60.96	0.00	99.48
303-plag-2-2	8.09	<d.l.	24.27	6.03	0.01	<d.l.	<d.l.	0.04	0.09	61.25	0.00	99.78
303-plag-2-3	7.53	<d.l.	25.09	6.99	0.02	0.10	<d.l.	0.04	0.08	59.72	0.03	99.60
303-plag-2-4	8.06	<d.l.	24.17	5.87	<d.l.	0.07	0.05	0.07	0.08	60.92	0.00	99.28
303-plag-3-1	8.21	<d.l.	24.16	5.93	<d.l.	0.04	<d.l.	0.09	0.06	61.01	0.00	99.50
303-plag-3-2	7.55	<d.l.	25.09	6.90	<d.l.	<d.l.	<d.l.	0.02	0.07	60.03	0.00	99.66
303-plag-3-3	8.00	<d.l.	24.48	6.22	<d.l.	<d.l.	<d.l.	0.04	0.17	60.61	0.01	99.53
303-plag-4-1	8.30	<d.l.	24.15	5.74	0.02	0.07	<d.l.	0.08	0.06	61.87	0.03	100.32
303-plag-4-2	7.36	<d.l.	25.41	7.33	<d.l.	0.11	<d.l.	0.04	0.07	59.93	0.00	100.24
303-plag-4-3	7.88	<d.l.	24.70	6.53	<d.l.	0.07	<d.l.	0.02	0.08	60.17	0.00	99.45
308-plag-1-1	6.20	<d.l.	27.22	9.43	<d.l.	0.04	<d.l.	0.04	0.05	56.73	0.00	99.71
308-plag-1-2	7.52	<d.l.	25.03	7.02	<d.l.	0.11	<d.l.	0.03	0.07	59.58	0.00	99.36
308-plag-2-1	8.52	<d.l.	23.96	5.61	<d.l.	0.06	0.04	0.02	0.05	61.97	0.01	100.25
308-plag-2-2	6.02	<d.l.	27.44	9.75	0.01	0.08	<d.l.	<d.l.	0.04	55.75	0.01	99.10
308-plag-2-3	8.58	<d.l.	23.72	5.37	<d.l.	0.12	<d.l.	0.10	0.05	61.66	0.02	99.63
308-plag-3-1	8.03	<d.l.	24.65	6.40	<d.l.	0.09	<d.l.	0.09	0.04	61.46	0.00	100.75
308-plag-3-2	8.18	<d.l.	23.95	5.75	0.01	<d.l.	<d.l.	0.09	0.05	62.09	0.00	100.12
308-plag-3-3	8.24	<d.l.	23.95	5.48	0.02	0.06	<d.l.	0.14	0.07	62.39	0.01	100.36
308-plag-3-4	7.82	<d.l.	25.03	6.90	0.02	0.10	<d.l.	0.19	0.06	59.68	0.02	99.81
308-plag-3-5	7.63	<d.l.	25.14	7.00	<d.l.	<d.l.	<d.l.	0.25	0.06	59.81	0.00	99.89
308-plag-4-1	8.30	<d.l.	23.93	5.41	0.02	0.07	<d.l.	0.03	0.07	61.86	0.00	99.69
308-plag-4-2	6.14	<d.l.	27.32	9.37	0.01	0.06	<d.l.	0.02	0.06	56.90	0.01	99.90
308-plag-5-1	5.70	<d.l.	27.76	10.16	<d.l.	0.10	<d.l.	<d.l.	0.05	55.25	0.01	99.04
308-plag-5-2	7.56	<d.l.	25.00	6.97	0.01	0.07	<d.l.	0.02	0.06	59.75	0.01	99.46
308-plag-6-1	7.17	<d.l.	25.86	7.76	<d.l.	0.08	<d.l.	0.05	0.05	58.85	0.00	99.82
308-plag-6-2	6.48	<d.l.	26.81	8.91	<d.l.	0.14	<d.l.	<d.l.	0.04	57.71	0.01	100.10
308-plag-6-3	6.82	<d.l.	26.09	8.26	<d.l.	0.30	<d.l.	0.18	0.04	58.04	0.00	99.72

Table 8.18: Garnet EPMA analysis. Red colour indicates an erroneous result. Blue colour indicates analyses used in the GB-GBMP geothermobarometer. Black line separates sample 03 and 08.

Analysis	SiO2	TiO2	Al2O3	FeO	MnO	MgO	CaO	Na2O	K2O	F	Cr2O3	Total
	Wt.%	Wt.%	Wt.%	Wt.%	Wt.%	Wt.%	Wt.%	Wt.%	Wt.%	Wt.%	Wt.%	Wt.%
303-grt-1-1	33.87	<d.l.	19.95	20.39	0.13	4.88	4.79	<d.l.	<d.l.	<d.l.	<d.l.	84.01
303-grt-1-2	38.25	<d.l.	21.61	29.25	0.26	4.94	5.77	<d.l.	<d.l.	<d.l.	<d.l.	100.08
303-grt-1-3	38.36	<d.l.	21.43	30.65	0.37	4.48	5.02	0.07	<d.l.	<d.l.	<d.l.	100.39
303-grt-1-4	37.68	0.11	21.27	30.28	0.68	3.76	6.35	<d.l.	<d.l.	<d.l.	<d.l.	100.12
303-grt-1-5	37.81	0.06	21.19	30.70	0.71	3.56	5.69	<d.l.	<d.l.	<d.l.	<d.l.	99.72
303-grt-1-6	37.48	0.05	21.20	30.64	0.75	3.77	5.82	<d.l.	<d.l.	<d.l.	<d.l.	99.71
303-grt-1-7	38.39	0.05	21.48	28.47	0.22	5.17	6.21	<d.l.	<d.l.	<d.l.	<d.l.	99.99
303-grt-1-8	38.16	<d.l.	21.71	28.90	0.19	4.89	5.69	<d.l.	<d.l.	<d.l.	<d.l.	99.54
303-grt-1-9	37.99	<d.l.	21.50	29.13	0.30	4.27	6.18	0.05	<d.l.	<d.l.	<d.l.	99.41
303-grt-1-10	37.48	<d.l.	21.26	30.34	0.79	3.61	6.03	0.03	<d.l.	<d.l.	<d.l.	99.53
303-grt-1-11	37.68	<d.l.	21.63	28.47	0.26	5.42	6.03	0.04	<d.l.	<d.l.	<d.l.	99.54
308-grt-1-1	38.00	0.05	21.10	29.65	1.06	3.25	6.82	0.04	<d.l.	<d.l.	<d.l.	99.97
308-grt-1-2	37.42	0.05	21.22	30.02	0.80	3.62	6.59	<d.l.	<d.l.	<d.l.	<d.l.	99.72
308-grt-1-3	37.83	<d.l.	21.09	30.01	1.13	2.72	6.87	<d.l.	<d.l.	<d.l.	<d.l.	99.65
308-grt-1-4	37.75	0.05	21.18	30.09	0.80	3.08	6.56	<d.l.	<d.l.	<d.l.	<d.l.	99.50
308-grt-1-5	36.79	<d.l.	21.32	27.96	1.46	2.43	9.27	<d.l.	<d.l.	<d.l.	<d.l.	99.23
308-grt-1-6	38.07	0.04	21.41	28.94	0.40	3.95	7.44	<d.l.	<d.l.	<d.l.	<d.l.	100.25
308-grt-1-7	38.03	<d.l.	21.42	28.59	0.76	3.42	7.95	<d.l.	<d.l.	<d.l.	<d.l.	100.17
308-grt-1-8	38.31	0.08	21.42	28.29	0.27	4.20	7.16	0.08	<d.l.	<d.l.	<d.l.	99.81
308-grt-1-9	37.96	<d.l.	21.41	29.03	0.28	4.28	6.90	<d.l.	<d.l.	<d.l.	<d.l.	99.86
308-grt-1-10	37.94	0.05	21.27	28.75	0.33	3.65	7.56	0.03	<d.l.	<d.l.	<d.l.	99.58
308-grt-1-11	37.83	<d.l.	21.51	28.76	0.26	4.24	7.33	<d.l.	<d.l.	<d.l.	<d.l.	99.93
308-grt-1-12	38.49	0.07	21.43	28.87	0.42	3.94	7.55	<d.l.	<d.l.	<d.l.	<d.l.	100.77
308-grt-1-13	36.49	<d.l.	21.36	27.56	1.56	2.58	9.35	<d.l.	<d.l.	<d.l.	<d.l.	98.90
308-grt-1-14	37.73	0.04	21.34	27.73	1.22	2.52	9.18	<d.l.	<d.l.	<d.l.	<d.l.	99.76
308-grt-1-15	37.51	<d.l.	21.34	28.17	1.28	2.54	8.77	0.03	<d.l.	<d.l.	<d.l.	99.64
308-grt-1-16	36.51	<d.l.	21.47	29.19	0.77	3.77	6.93	0.04	<d.l.	<d.l.	<d.l.	98.68

Appendix E Geobarometry

Table 8.19: GB-GBMP geothermobarometric calculation

Sample	308: Bt-1-1, plg-2-1, grt-1-1, msc-1-1	308: bt-1-2, plg-2-3, grt-1-2, msc-1-2	308: bt-1-3, plg-2-5, grt-1-3, msc-1-3	308: bt-1-4, plg-2-9, grt-1-4, msc-1-4	308: bt-1-5, plg-2-10, grt-1-1, msc-1-5	308: bt-1-6, plg-2-11, grt-1-2, msc-1-6
Fe3+/(Fe2++Fe3+) (Bt)	0,116	0,116	0,116	0,116	0,116	0,116
Fe3+/(Fe2++Fe3+) (Grt)	0,03	0,03	0,03	0,03	0,03	0,03
Input T (ºC)	605	620	567	590	615	617
Input P (bars)	10136,5	10146,2	8740,0	9212,8	9997,4	9984,3
T(GB, ºC)	605,4	620,0	566,9	590,4	614,8	616,7
P(GBMP-ave,bar)	10136,5	10146,2	8740,0	9212,8	9997,4	9984,3
P(GBMP-Fe,bar)	10137,1	10143,7	8759,5	9219,5	9998,5	9985,4
P(GBMP-Mg,bar)	10136,0	10148,7	8720,4	9206,1	9996,3	9983,2
SiO2 (Bt)	36,9	36,9	36,8	36,5	34,8	36,5
TiO2 (Bt)	1,7	2,1	1,9	1,8	2,0	2,0
Al2O3 (Bt)	18,5	18,6	18,4	18,3	18,7	18,6
FeO tot (Bt)	17,0	16,8	17,2	17,2	16,8	15,8
MnO (Bt)	0,1	0,1	0,1	0,1	0,0	0,0
MgO (Bt)	11,7	11,6	11,8	11,6	11,0	11,0
CaO (Bt)	0,1	0,1	0,1	0,1	0,1	0,2
Na2O (Bt)	0,2	0,2	0,1	0,1	0,2	0,2
K2O (Bt)	9,1	9,0	9,0	8,9	8,9	8,9
SiO2 (Pl)	60,1	61,1	61,5	61,7	62,0	62,5
TiO2 (Pl)	0,2	0,0	0,0	0,0	0,0	0,0
Al2O3 (Pl)	23,0	24,2	24,3	24,1	24,0	24,2
FeO tot (Pl)	1,6	0,1	0,1	0,2	0,1	0,2
MnO (Pl)	0,0	0,0	0,0	0,0	0,0	0,0
MgO (Pl)	1,0	0,0	0,0	0,0	0,0	0,0
CaO (Pl)	4,4	5,4	5,5	5,5	5,5	5,4
Na2O (Pl)	7,8	8,5	8,3	8,3	8,5	8,5
K2O (Pl)	0,9	0,0	0,0	0,0	0,0	0,0
SiO2 (Grt)	38,0	37,4	37,8	37,8	38,0	37,4
TiO2 (Grt)	0,1	0,0	0,0	0,0	0,1	0,0
Al2O3 (Grt)	21,1	21,2	21,1	21,2	21,1	21,2
FeO tot (Grt)	29,7	30,0	30,0	30,1	29,7	30,0
MnO (Grt)	1,1	0,8	1,1	0,8	1,1	0,8
MgO (Grt)	3,3	3,6	2,7	3,1	3,3	3,6
CaO (Grt)	6,8	6,6	6,9	6,6	6,8	6,6
Na2O (Grt)	0,0	0,0	0,0	0,0	0,0	0,0
K2O (Grt)	0,0	0,0	0,0	0,0	0,0	0,0
SiO2 (Ms)	46,8	46,2	45,9	47,0	45,7	46,0
TiO2 (Ms)	0,8	0,5	0,6	0,8	0,5	0,4
Al2O3 (Ms)	32,8	33,5	33,0	33,0	33,7	33,1
FeO tot (Ms)	1,6	1,5	1,6	1,6	1,6	2,6
MnO (Ms)	0,0	0,0	0,0	0,0	0,0	0,0
MgO (Ms)	1,4	1,3	1,4	1,4	1,4	2,0
CaO (Ms)	0,0	0,0	0,0	0,0	0,0	0,0
Na2O (Ms)	0,9	1,0	0,9	0,9	0,7	0,9
K2O (Ms)	9,1	8,9	9,2	9,0	9,0	9,0
Ratio (Bt)	4,5	4,5	4,5	4,5	4,7	4,6
Ratio (Pl)	2,7	2,7	2,7	2,7	2,7	2,6
Ratio (Grt)	4,8	4,8	4,8	4,8	4,8	4,8
Ratio (Ms)	4,1	4,1	4,1	4,0	4,1	4,1
Fe(tot) (Bt)	1,1	1,1	1,1	1,1	1,1	1,0
Mg (Bt)	1,3	1,3	1,3	1,3	1,3	1,3
Al(VI) (Bt)	0,4	0,4	0,4	0,4	0,4	0,4
Ti (Bt)	0,1	0,1	0,1	0,1	0,1	0,1
Ca (Pl)	0,2	0,3	0,3	0,3	0,3	0,3
Na (Pl)	0,7	0,7	0,7	0,7	0,7	0,7
K (Pl)	0,1	0,0	0,0	0,0	0,0	0,0
Fe(tot) (Grt)	2,0	2,0	2,0	2,0	2,0	2,0
Mg (Grt)	0,4	0,4	0,3	0,4	0,4	0,4
Ca (Grt)	0,6	0,6	0,6	0,6	0,6	0,6
Mn (Grt)	0,1	0,1	0,1	0,1	0,1	0,1
Fe(tot) (Ms)	0,1	0,1	0,1	0,1	0,1	0,1
Mg (Ms)	0,1	0,1	0,1	0,1	0,1	0,2
AlVI (Ms)	1,8	1,8	1,8	1,8	1,8	1,7
X(Fe)Grt	0,6	0,6	0,7	0,7	0,6	0,6
X(Mg)Grt	0,1	0,1	0,1	0,1	0,1	0,1
X(Ca)Grt	0,2	0,2	0,2	0,2	0,2	0,2
X(Mn)Grt	0,0	0,0	0,0	0,0	0,0	0,0
Fea	0,2	0,2	0,2	0,2	0,2	0,2
Feb	0,0	0,0	0,0	0,0	0,0	0,0
Fec	-766,0	-718,6	-743,8	-699,3	-766,0	-718,6
Mga	-3,0	-2,7	-3,4	-3,0	-3,0	-2,7
Mgb	0,0	0,0	0,0	0,0	0,0	0,0
Mgc	9611,3	9030,1	10148,8	9493,0	9611,3	9030,1
Caa	-2,6	-2,7	-2,6	-2,6	-2,6	-2,7
Cab	0,0	0,0	0,0	0,0	0,0	0,0
Cac	5996,0	6198,0	5672,5	5857,5	5996,0	6198,0
X(An)	0,2	0,3	0,3	0,3	0,3	0,3
X(Ab)	0,7	0,7	0,7	0,7	0,7	0,7
X(Or)	0,1	0,0	0,0	0,0	0,0	0,0
Fa	0,4	0,0	0,0	0,0	0,0	0,0
Fb	0,0	0,0	0,0	0,0	0,0	0,0
Fc	11026,8	10256,2	10215,5	10202,7	10259,6	10269,2
X(Fe) Bt	0,3	0,3	0,3	0,3	0,4	0,3
X(Mg) Bt	0,5	0,5	0,5	0,5	0,5	0,5
X(Al) Bt	0,1	0,1	0,1	0,1	0,1	0,2
X(Ti) Bt	0,0	0,0	0,0	0,0	0,0	0,0
X(Fe)Ms	0,0	0,0	0,0	0,0	0,0	0,1
X(Mg)Ms	0,1	0,1	0,1	0,1	0,1	0,1
X(Al)Ms	0,9	0,9	0,9	0,9	0,9	0,8
T(GB00,ºC)	605,4	620,0	566,9	590,4	614,8	616,7
ln[Kd(1)ideal]	4,2	3,5	3,6	3,4	3,5	3,5
GBMP-Fe-a	24077,4	24081,7	22422,7	22840,6	23905,6	24489,9
GBMP-Fe-b	-14189,6	-14001,0	-13719,6	-13679,3	-13970,4	-14566,6
GBMP-Fe-c	1,0	1,0	1,0	1,0	1,0	1,0
P(GBMP-Fe)	10137,1	10143,7	8759,5	9219,5	9998,5	9985,4
ln[Kd(2)ideal]	-1,6	-2,0	-2,8	-2,5	-2,1	-2,1
GBMP-Mg-a	10991,3	10801,2	9356,7	9906,0	10519,3	10555,4
GBMP-Mg-b	-1109,8	-711,5	-691,8	-756,3	-583,1	-630,2
GBMP-Mg-c	1,0	1,0	1,0	1,0	1,0	1,0
P(GBMP-Mg)	10136,0	10148,7	8720,4	9206,1	9996,3	9983,2

Table 8.20: Amphibole - plagioclase geobarometric calculations.

id (paste below)	Amp-1-3 + plag-1-1	Amp-2-3 + plag-2-4	Amp-2-3 + plag-2-1	Amp-3-3 + plag-3-1	Amp-3-3 + plag-3-3	Amp-4-2 + plag-4-1	Amp-1-1 + plag-1-3
T(ºC)1	602,3	602,3	602,3	602,3	602,3	602,3	602,3
T(ºC)2	0	0	0	0	0	0	0
P(kbar) Plg-amp-bar (at TC=1)	11,20	9,78	9,67	10,14	10,17	10,70	10,89
P(kbar) Plg-amp-bar (at TC=2)	-7,70	-9,32	-9,45	-7,92	-7,53	-10,50	-10
Si_23O	6,102	6,143	6,143	6,235	6,235	6,058	6,006
Ti_23O	0,069	0,056	0,056	0,081	0,081	0,083	0,084
Al_23O	3,158	2,869	2,869	2,745	2,745	3,121	3,222
Cr_23O	0,000	0,000	0,000	0,000	0,000	0,000	0,000
Ni_23O	0,000	0,000	0,000	0,000	0,000	0,000	0,000
FeT_23O	1,914	2,053	2,053	2,035	2,035	1,873	1,957
Mn_23O	0,003	0,010	0,010	0,009	0,009	0,002	0,007
Mg_23O	1,753	1,870	1,870	1,896	1,896	1,863	1,724
Ca_23O	1,788	1,768	1,768	1,795	1,795	1,795	1,759
Na_23O	0,550	0,530	0,530	0,495	0,495	0,569	0,563
K_23O	0,129	0,114	0,114	0,130	0,130	0,152	0,149
F_23O	0,093	0,045	0,045	0,031	0,031	0,034	0,000
Cl_23O	0,003	0,014	0,014	0,000	0,000	0,000	0,002
Fe3_23O	0,243	0,554	0,554	0,407	0,407	0,285	0,367
Fe2_23O	1,670	1,499	1,499	1,628	1,628	1,588	1,590
AlIV_23O	1,898	1,857	1,857	1,765	1,765	1,942	1,994
AlVI_23O	1,261	1,012	1,012	0,980	0,980	1,179	1,228
NaM4_23O	0,212	0,232	0,232	0,205	0,205	0,205	0,241
NaA_23O	0,338	0,298	0,298	0,291	0,291	0,364	0,322
A_23O	0,467	0,412	0,412	0,421	0,421	0,516	0,471

Appendix F Geochronology

Table 8.21: Zircon U/Pb calculation.

	Isotope ratios									Age estimates (ma)							Concentrations				
	Concordia output					Tera-Wasserburg output															Pb com.
Analysis_#	Pb207 U235	1s%	Pb206 U238	1s%	roh	238/206	1s%	207/206	1s%	Pb207 Pb206	1s	Pb207 U235	1s	Pb206 U238	1s	conc	Th/U	U*	Th*	Pbtot*	>LLD (%)
HF02_01	0,64744	1,12	0,08166	1,03	0,48	12,245898	1,03	0,05753	1,10	511,5	23,81	506,9	4,46	506	5,02	98,9	0,52	477	249	47	2
HF02_02	0,64075	1,11	0,08159	1,03	0,48	12,256404	1,03	0,05698	1,09	490,2	24,12	502,8	4,39	505,6	5,01	103,1	0,46	617	283	60	1
HF02_03	0,61189	1,33	0,07789	1,05	0,39	12,838619	1,05	0,057	1,33	491	29,39	484,8	5,14	483,5	4,88	98,5	0,45	450	203	42	-
HF02_04	0,61856	1,18	0,07894	1,04	0,46	12,667849	1,04	0,05686	1,16	485,5	25,7	488,9	4,56	489,8	4,88	100,9	0,73	934	678	94	-
HF02_05	0,66487	1,18	0,08469	1,04	0,46	11,80777	1,04	0,05697	1,16	489,6	25,81	517,6	4,78	524,1	5,21	107,0	0,42	576	240	58	1
HF02_06	0,60774	1,17	0,07765	1,03	0,45	12,8783	1,03	0,05679	1,16	482,7	25,59	482,1	4,49	482,1	4,81	99,9	0,37	331	122	30	1
HF02_07	0,62692	1,15	0,07951	1,03	0,46	12,577034	1,03	0,05721	1,14	499,2	25	494,2	4,49	493,2	4,91	98,8	0,35	529	185	49	1
HF02_08	0,626	1,15	0,07908	1,04	0,47	12,645422	1,04	0,05744	1,13	508,1	24,67	493,6	4,49	490,6	4,88	96,6	0,41	480	196	45	-
HF02_09	0,62786	1,15	0,07947	1,03	0,46	12,583365	1,03	0,05733	1,13	503,6	24,76	494,8	4,49	493	4,91	97,9	0,41	405	168	38	-
HF02_10	0,63605	1,13	0,0805	1,03	0,47	12,42236	1,03	0,05733	1,12	504	24,34	499,9	4,45	499,1	4,96	99,0	0,55	469	259	46	-
HF02_11	0,61467	1,11	0,07733	1,03	0,48	12,931592	1,03	0,05767	1,09	517,2	23,42	486,5	4,30	480,2	4,77	92,8	0,40	589	236	54	-
HF02_12	0,62326	1,21	0,07873	1,04	0,44	12,701639	1,04	0,05744	1,20	508,1	25,97	491,9	4,71	488,5	4,89	96,1	0,47	297	141	28	2
HF02_13	0,60586	1,16	0,07712	1,04	0,46	12,966805	1,04	0,05701	1,14	491,2	25,29	480,9	4,43	478,9	4,78	97,5	0,34	370	127	33	-
HF02_14	0,63414	1,13	0,08006	1,04	0,47	12,490632	1,04	0,05748	1,11	509,4	24,19	498,7	4,46	496,5	4,94	97,5	0,39	454	176	43	2
HF02_15	0,62489	1,12	0,08034	1,03	0,48	12,4471	1,03	0,05644	1,10	469	24,32	492,9	4,37	498,1	4,95	106,2	0,75	692	519	71	-
HF02_16	0,61144	1,99	0,07554	1,11	0,26	13,23802	1,11	0,05873	2,01	557,3	43,21	484,5	7,65	469,4	5,05	84,2	0,32	287	91	25	7
HF02_17	0,62935	1,12	0,0806	1,03	0,47	12,406948	1,03	0,05666	1,11	477,5	24,44	495,7	4,40	499,7	4,97	104,6	0,40	510	201	48	1
HF02_18	0,71248	1,22	0,08978	1,04	0,43	11,138338	1,04	0,05758	1,22	513,6	26,09	546,2	5,17	554,3	5,53	107,9	0,39	313	122	33	-
HF02_19	0,59703	1,12	0,07688	1,03	0,48	13,007284	1,03	0,05635	1,10	465,4	24,45	475,3	4,27	477,5	4,75	102,6	0,41	534	217	49	1
HF02_20	0,61577	1,24	0,07757	1,04	0,43	12,891582	1,04	0,0576	1,23	514,2	26,33	487,2	4,78	481,6	4,83	93,7	0,30	252	77	22	-
HF02_21	0,61717	1,18	0,07805	1,04	0,45	12,8123	1,04	0,05738	1,17	505,7	25,37	488,1	4,56	484,5	4,84	95,8	0,50	555	280	52	-
HF02_22	0,63623	1,12	0,07971	1,03	0,47	12,545477	1,03	0,05792	1,10	526,5	24,3	500	4,43	494,4	4,92	93,9	0,42	521	219	50	-
HF02_23	0,63272	1,12	0,08046	1,03	0,48	12,428536	1,03	0,05706	1,10	493,2	24,43	497,8	4,41	498,9	4,96	101,2	0,32	528	169	49	1
HF02_24	0,59329	1,43	0,07569	1,06	0,37	13,211785	1,06	0,05688	1,42	486,2	31,6	473	5,41	470,3	4,79	96,7	0,34	256	86	22	-

Table 8.22: Titanite U/Pb calculations.

	Isotope ratios											Age estimates (ma)						
	Concordia output						Tera-Wasserburg output											
Analysis_#	Pb207 / U235	1s%	Pb206 / U238	1s%	roh		238/206	1s%	207/206	1s%		Pb207 Pb206	1s	Pb207 / U235	1s	Pb206 / U238	1s	conc
S6_01	3,78377	1,47	0,10341	1,14	0,32		9,6702447	1,14	0,26543	1,55		3279,2	24,18	1589,3	11,84	634,4	6,88	19,3
S6_02	4,73685	1,70	0,10682	1,27	0,27		9,3615428	1,27	0,32168	1,82		3577,9	27,77	1773,8	14,26	654,3	7,92	18,3
S6_03	4,27367	2,02	0,10455	1,41	0,23		9,5648015	1,41	0,29653	2,18		3452,2	33,41	1688,3	16,63	641	8,57	18,6
S6_04	15,50505	1,57	0,19781	1,35	0,34		5,0553561	1,35	0,5686	1,69		4429,7	24,46	2846,8	15,00	1163,6	14,35	26,3
S6_05	4,67602	1,32	0,11028	1,09	0,36		9,0678273	1,09	0,30758	1,38		3508,8	21,14	1763	11,06	674,4	6,98	19,2
S6_06	6,15224	1,67	0,12226	1,26	0,29		8,17929	1,26	0,36504	1,77		3771	26,59	1997,7	14,57	743,6	8,83	19,7
S6_07	8,22677	1,49	0,13497	1,18	0,33		7,4090539	1,18	0,44219	1,56		4059,1	23,11	2256,3	13,49	816,1	9,06	20,1
S6_08	3,04743	1,52	0,09127	1,13	0,32		10,956503	1,13	0,24223	1,58		3134,7	24,83	1419,6	11,62	563	6,07	18,0
S6_09	4,63891	1,80	0,1109	1,28	0,27		9,0171326	1,28	0,30346	1,91		3488	29,24	1756,3	15,05	678	8,25	19,4
S6_10	2,87166	1,84	0,09309	1,24	0,26		10,742292	1,24	0,22379	1,93		3008,2	30,66	1374,5	13,84	573,8	6,77	19,1
S6_11	6,93318	2,95	0,12277	2,04	0,19		8,1453124	2,04	0,40969	3,25		3945	47,87	2102,9	26,14	746,5	14,43	18,9
S6_12	5,95426	2,57	0,11682	1,74	0,21		8,5601781	1,74	0,36978	2,79		3790,5	41,63	1969,2	22,34	712,2	11,70	18,8
S6_13	15,70711	1,93	0,19005	1,49	0,30		5,2617732	1,49	0,59958	2,06		4507	29,57	2859,2	18,43	1121,6	15,31	24,9
S6_14	11,6432	2,58	0,17167	1,91	0,24		5,8251296	1,91	0,49203	2,81		4217,5	40,87	2576,1	24,13	1021,3	18,02	24,2
S6_15	7,2278	1,84	0,12806	1,30	0,28		7,8088396	1,30	0,40946	1,93		3944,2	28,73	2139,9	16,45	776,8	9,56	19,7

Appendix G Handheld XRF data

Table 8.23: Handheld XRF measurements from box 20 of drill core BH4508 at Hellerfjellet.

Point	Meters	Cu	Zn	Pb	Ba	Fe	Ag	Mo	Sb	Sn	Cd	As	Ni	Co	Se	Bi	Mn	S	Ca	K	Al	P	Si	Mg
K20	ppm	ppm	ppm	ppm	ppm	ppm	ppm	ppm	ppm	ppm	ppm	ppm	ppm	ppm	ppm	ppm	ppm	ppm	ppm	ppm	ppm	ppm	ppm	ppm
2	110	25,7	91,2	13,7	440,6	25293,9	< LOD	10,1	< LOD	< LOD	< LOD	< LOD	< LOD	< LOD	< LOD	< LOD	< LOD	10897,3	18527,7	17950,6	39044,2	< LOD	364303,5	7634,0
3	110,1	55,3	163,8	24,2	1018,0	38382,3	< LOD	13,0	< LOD	< LOD	< LOD	5,4	< LOD	< LOD	< LOD	< LOD	< LOD	13443,4	11052,5	50437,0	69268,2	416,8	281258,3	14610,8
4	110,2	69,0	258,0	48,1	625,5	46713,8	< LOD	4,7	< LOD	< LOD	< LOD	< LOD	44,5	< LOD	< LOD	< LOD	< LOD	14914,2	42876,5	29609,7	72804,5	830,1	286889,6	30181,1
5	110,3	34,2	117,2	13,1	586,5	20089,1	< LOD	6,3	< LOD	< LOD	< LOD	5,3	< LOD	< LOD	< LOD	< LOD	< LOD	9467,1	13750,1	31415,5	44874,6	507,6	354706,3	< LOD
6	110,4	32,4	237,7	8,0	487,2	29915,3	< LOD	7,0	< LOD	< LOD	< LOD	7,2	< LOD	< LOD	< LOD	< LOD	< LOD	8769,2	13414,8	36253,5	34394,1	< LOD	291541,9	< LOD
7	110,5	28,8	201,3	13,8	696,8	29796,4	< LOD	11,8	< LOD	< LOD	< LOD	< LOD	< LOD	< LOD	< LOD	< LOD	< LOD	19723,9	13288,2	36102,6	52191,8	791,6	318555,7	< LOD
8	110,6	23,1	175,2	15,3	561,2	26944,3	< LOD	8,9	< LOD	< LOD	< LOD	< LOD	< LOD	202,5	< LOD	< LOD	< LOD	27634,0	23179,9	< LOD	41469,4	< LOD	349132,4	13837,3
9	110,7	33,0	253,2	24,6	523,9	38817,8	< LOD	< LOD	< LOD	< LOD	< LOD	< LOD	< LOD	< LOD	< LOD	< LOD	< LOD	18090,1	25507,8	24616,6	48882,6	< LOD	312041,0	9989,1
10	110,8	60,2	585,9	33,4	811,0	51407,0	< LOD	3,6	< LOD	< LOD	< LOD	< LOD	< LOD	183,6	< LOD	< LOD	< LOD	19412,2	23393,3	38205,8	79137,7	2498,4	260261,4	14058,0
11	110,9	24,3	149,1	28,5	347,7	25735,5	< LOD	< LOD	< LOD	< LOD	< LOD	< LOD	< LOD	< LOD	< LOD	< LOD	2118,2	9800,8	95784,7	< LOD	35873,4	686,2	327184,2	22093,3
12	111	0,0	310,0	30,4	876,2	58637,0	< LOD	4,8	17,0	< LOD	< LOD	< LOD	67,0	< LOD	< LOD	< LOD	< LOD	20045,7	27108,6	44329,7	69378,3	< LOD	228975,6	40974,1
13	111,1	31,9	143,0	25,7	380,2	23444,2	< LOD	< LOD	< LOD	< LOD	< LOD	< LOD	< LOD	< LOD	3,2	< LOD	< LOD	8906,7	21189,1	18262,3	41439,3	729,1	367034,8	< LOD
14	111,2	35,0	266,3	24,8	469,8	38276,5	< LOD	3,0	< LOD	< LOD	< LOD	< LOD	< LOD	< LOD	< LOD	< LOD	< LOD	13482,8	24767,5	24948,0	51479,0	< LOD	285572,0	17646,5
15	111,6	17,1	103,4	16,5	549,1	22961,4	< LOD	2,9	< LOD	< LOD	< LOD	< LOD	< LOD	< LOD	< LOD	< LOD	< LOD	11320,9	8912,0	25476,9	27240,3	< LOD	393315,5	< LOD
16	111,7	53,3	354,5	38,5	728,4	43721,9	< LOD	< LOD	< LOD	< LOD	< LOD	< LOD	< LOD	< LOD	< LOD	< LOD	< LOD	10078,9	29873,0	35087,4	61420,9	489,1	282431,8	< LOD
17	111,8	41,5	272,3	20,0	492,7	35376,5	< LOD	< LOD	< LOD	< LOD	< LOD	< LOD	< LOD	< LOD	< LOD	< LOD	< LOD	13711,1	31082,3	21647,4	48308,9	831,7	325099,2	11425,9
18	111,9	49,9	116,3	14,6	634,3	30956,8	< LOD	8,1	< LOD	< LOD	< LOD	< LOD	< LOD	< LOD	< LOD	< LOD	< LOD	22642,5	8515,7	25428,3	42153,4	< LOD	372428,8	< LOD
19	112	42,2	223,4	29,5	681,3	29424,7	< LOD	10,2	< LOD	< LOD	< LOD	< LOD	< LOD	< LOD	< LOD	< LOD	< LOD	13978,7	15741,8	34897,5	53311,1	796,2	312247,9	21911,0
20	112,1	0,0	99,8	23,3	291,5	18547,8	< LOD	7,5	< LOD	< LOD	< LOD	< LOD	< LOD	< LOD	< LOD	< LOD	< LOD	9434,4	28257,1	19223,9	42218,2	< LOD	364883,3	< LOD
21	112,2	26,1	154,5	21,1	531,2	33643,3	< LOD	7,5	< LOD	< LOD	< LOD	< LOD	< LOD	< LOD	< LOD	< LOD	< LOD	16317,3	27071,9	< LOD	44481,0	606,5	378018,8	9681,9
22	112,3	28,2	104,6	17,2	1218,5	26281,5	< LOD	6,9	< LOD	< LOD	< LOD	< LOD	< LOD	< LOD	< LOD	< LOD	< LOD	16310,5	16319,1	26055,2	53110,6	1188,0	367365,7	15657,9
23	112,4	82,0	279,1	23,9	783,8	45179,5	< LOD	8,7	< LOD	< LOD	< LOD	5,6	48,5	< LOD	3,8	< LOD	< LOD	20370,9	19877,5	39184,8	62873,6	925,3	306135,1	< LOD
24	112,5	33,3	226,3	32,5	514,2	37159,1	< LOD	< LOD	< LOD	< LOD	< LOD	< LOD	< LOD	< LOD	< LOD	< LOD	< LOD	9297,2	98129,8	28145,3	48455,7	540,9	279917,5	21897,6
25	112,6	22,4	128,8	18,4	339,9	26182,7	< LOD	< LOD	< LOD	< LOD	< LOD	< LOD	< LOD	< LOD	< LOD	< LOD	< LOD	9656,2	42263,2	< LOD	33225,1	< LOD	358882,4	< LOD
26	112,7	0,0	105,6	37,6	289,7	23267,3	< LOD	< LOD	< LOD	< LOD	< LOD	< LOD	41,0	< LOD	< LOD	< LOD	< LOD	7522,0	159427,3	< LOD	28711,0	< LOD	258111,6	< LOD
27	112,8	22,2	202,7	18,5	899,6	37540,0	< LOD	12,3	18,2	< LOD	< LOD	< LOD	< LOD	< LOD	< LOD	< LOD	< LOD	16745,5	15657,6	25929,3	57555,4	870,8	344413,2	< LOD
28	112,9	28,7	195,3	22,6	631,2	41949,4	< LOD	< LOD	< LOD	< LOD	< LOD	< LOD	< LOD	< LOD	< LOD	< LOD	< LOD	12841,5	28664,2	29907,2	65057,4	< LOD	289825,9	13776,1
29	113	49,1	163,9	14,8	836,4	33396,4	< LOD	8,5	< LOD	< LOD	< LOD	< LOD	< LOD	< LOD	< LOD	< LOD	< LOD	19123,7	11560,2	35196,1	53661,9	921,1	337719,4	22245,4
30	113,1	0,0	71,4	10,0	250,5	8390,0	< LOD	< LOD	18,3	< LOD	< LOD	< LOD	< LOD	105,5	< LOD	< LOD	< LOD	8028,3	9092,7	15412,0	28294,3	< LOD	444612,6	9005,9
31	113,2	30,8	126,4	12,0	492,5	13765,4	< LOD	2,8	< LOD	< LOD	< LOD	4,5	< LOD	< LOD	< LOD	< LOD	< LOD	11001,1	9992,3	23564,6	35870,7	< LOD	380603,2	15218,1
32	113,3	49,8	169,2	20,6	687,8	30016,8	< LOD	10,8	< LOD	< LOD	< LOD	< LOD	< LOD	< LOD	< LOD	< LOD	< LOD	11094,6	16918,3	34128,8	52629,7	1093,1	375816,2	13721,7
33	113,4	31,0	238,4	39,7	768,8	37524,1	< LOD	< LOD	< LOD	< LOD	< LOD	< LOD	< LOD	< LOD	< LOD	< LOD	< LOD	18828,3	26187,9	44038,6	77664,9	740,0	263892,8	32647,7
34	113,5	44,6	156,3	20,0	471,8	22866,8	< LOD	< LOD	< LOD	< LOD	< LOD	< LOD	< LOD	< LOD	< LOD	< LOD	< LOD	8667,6	25030,1	24860,8	57174,8	< LOD	305484,9	< LOD
35	113,6	23,6	125,7	25,8	308,8	16427,4	< LOD	< LOD	< LOD	< LOD	< LOD	< LOD	< LOD	< LOD	< LOD	< LOD	< LOD	9619,6	22098,0	21039,7	34532,2	588,7	381550,7	< LOD
36	113,7	32,3	136,9	17,4	586,4	24901,8	< LOD	6,2	< LOD	< LOD	< LOD	5,6	< LOD	143,1	< LOD	< LOD	< LOD	15681,4	14839,3	25640,0	49923,2	1182,4	388557,5	< LOD
37	113,8	49,6	194,3	16,2	966,2	28811,6	< LOD	10,9	< LOD	< LOD	< LOD	6,2	< LOD	< LOD	< LOD	< LOD	< LOD	18088,1	17952,0	33396,0	71185,1	< LOD	341477,6	22898,5
38	113,9	105,4	103,1	10,4	1637,4	33625,7	< LOD	36,9	< LOD	< LOD	< LOD	< LOD	< LOD	179,2	< LOD	< LOD	< LOD	10503,5	12951,4	41426,6	43836,7	943,3	171610,5	< LOD
39	114	31,2	196,3	37,0	571,0	27183,5	< LOD	26,3	14,7	< LOD	< LOD	6,4	< LOD	< LOD	< LOD	< LOD	< LOD	18161,4	37563,9	34300,9	73746,8	2566,6	310370,8	18701,6
40	114,1	47,1	219,5	26,6	528,5	24971,1	< LOD	7,8	< LOD	< LOD	< LOD	< LOD	< LOD	< LOD	< LOD	< LOD	< LOD	10963,3	24368,5	21220,9	52102,4	1331,0	356990,0	< LOD
41	114,2	33,4	122,0	27,5	659,9	33587,5	< LOD	10,8	< LOD	< LOD	< LOD	< LOD	< LOD	< LOD	< LOD	< LOD	< LOD	19983,7	18361,0	32013,0	51655,2	1008,9	285171,1	< LOD
42	114,3	0,0	253,2	6,2	384,9	18173,1	< LOD	2,8	< LOD	< LOD	< LOD	7,2	< LOD	< LOD	< LOD	< LOD	2755,8	3048,2	94793,8	23143,6	27634,7	< LOD	265074,0	24107,7
43	114,4	0,0	84,2	19,3	547,0	14415,1	< LOD	5,8	< LOD	< LOD	< LOD	5,3	< LOD	< LOD	4,2	< LOD	< LOD	9747,2	14709,5	19274,5	48669,0	903,0	378548,5	9497,3
44	114,5	35,6	155,6	26,2	802,4	30009,6	< LOD	13,5	< LOD	< LOD	< LOD	< LOD	< LOD	< LOD	2,9	< LOD	< LOD	12366,4	20393,5	32189,8	51781,5	1167,4	323187,3	< LOD
45	114,6	66,1	493,4	31,1	763,0	64461,0	< LOD	< LOD	< LOD	26,8	< LOD	< LOD	< LOD	< LOD	< LOD	< LOD	< LOD	22091,9	38123,0	55463,9	83948,1	963,3	239240,8	28197,8
46	114,7	19,3	97,5	13,9	760,0	14402,2	< LOD	7,6	< LOD	< LOD	< LOD	< LOD	< LOD	< LOD	< LOD	< LOD	< LOD	8585,2	12670,5	16973,3	29224,0	834,0	393018,9	< LOD
47	114,8	28,8	163,0	16,9	661,8	21324,6	< LOD	5,7	< LOD	< LOD	< LOD	< LOD	< LOD	< LOD	< LOD	< LOD	< LOD	27155,2	14012,3	25729,0	42759,6	706,0	366971,7	10269,0
48	114,9	0,0	105,0	< LOD	178,3	11217,3	< LOD	7,8	< LOD	< LOD	< LOD	5,2	< LOD	< LOD	< LOD	< LOD	< LOD	3658,3	141645,1	< LOD	7289,6	684,1	314749,0	41604,7
49	115	46,4	148,9	27,0	383,2	24206,8	< LOD	5,2	< LOD	< LOD	< LOD	< LOD	< LOD	< LOD	< LOD	< LOD	< LOD	17264,0	32986,4	18196,6	42186,1	1466,4	382314,3	15721,9
50	115,1	0,0	105,3	16,1	852,1	14985,2	< LOD	7,7	< LOD	20,9	< LOD	< LOD	< LOD	< LOD	< LOD	< LOD	< LOD	10478,4	13082,0	23814,5	43298,3	614,7	359378,8	8913,1
51	115,2	27,1	169,2	15,6	783,1	13693,4	< LOD	< LOD	< LOD	< LOD	< LOD	< LOD	< LOD	< LOD	< LOD	< LOD	< LOD	14793,2	14609,3	30656,2	54560,0	< LOD	346796,0	< LOD
52	115,3	26,3	269,3	13,2	217,6	17881,1	< LOD	3,3	< LOD	< LOD	< LOD	< LOD	< LOD	< LOD	< LOD	< LOD	2506,4	2038,1	197935,1	< LOD	8390,1	< LOD	186437,7	< LOD
53	115,4	71,5	182,5	49,6	644,8	45028,0	< LOD	48,6	< LOD	< LOD	< LOD	< LOD	57,8	< LOD	3,3	< LOD	< LOD	50241,3	50134,6	< LOD	69461,3	1049,6	250963,8	19135,7

Table 8.24: Handheld XRF measurements from box 21 of drill core BH4508 at Hellerfjellet.

Point	Meters	Cu	Zn	Pb	Ba	Fe	Ag	Mo	Sb	Sn	Cd	As	Ni	Co	Se	Bi	Mn	S	Ca	K	Al	P	Si	Mg
K21	ppm	ppm	ppm	ppm	ppm	ppm	ppm	ppm	ppm	ppm	ppm	ppm	ppm	ppm	ppm	ppm	ppm	ppm	ppm	ppm	ppm	ppm	ppm	ppm
54	115,5	69,21	1343,13	35,8	477,45	58517,65	0	< LOD	< LOD	16,53	< LOD	< LOD	< LOD	< LOD	4,97	< LOD	< LOD	19271,99	32994,93	47383,96	57368,03	< LOD	223409,08	18761,82
55	115,6	0	23,31	0	126,2	1264,9	0	< LOD	< LOD	< LOD	< LOD	4,77	< LOD	< LOD	< LOD	< LOD	< LOD	769,04	104693	< LOD	4962,14	< LOD	399778,78	9884,96
56	115,7	62,69	218,45	21	477,16	36809,15	0	7,98	< LOD	< LOD	< LOD	< LOD	< LOD	< LOD	< LOD	< LOD	< LOD	16496,4	17972,21	26549,89	52054,56	< LOD	327020,19	16842,9
57	115,8	38,73	141,23	22,55	656,99	18573,99	0	4,6	< LOD	< LOD	< LOD	< LOD	< LOD	< LOD	< LOD	< LOD	< LOD	11042,45	18161,64	32241,87	55469,3	1005,96	367048,72	10984,33
58	115,9	19,71	177,43	22,05	615,37	17971,74	0	3,71	< LOD	< LOD	< LOD	< LOD	< LOD	< LOD	< LOD	< LOD	< LOD	22560,48	17834,81	22193,52	55249,14	631,4	343296,69	13614,92
59	116	43,39	158,41	48,94	623,35	26639,9	0	19,33	< LOD	< LOD	< LOD	< LOD	< LOD	< LOD	2,91	< LOD	< LOD	16590,43	48171,26	25058,96	65662,02	1531,09	319972,94	< LOD
60	116,1	143,98	257,6	24,67	737,98	24589,83	0	8,94	< LOD	< LOD	< LOD	< LOD	< LOD	< LOD	< LOD	< LOD	< LOD	21538,65	23851,83	22120,91	51734,59	495,26	379174,09	14139,22
61	116,2	82,28	142,42	22,43	656,76	23072,38	0	3,91	< LOD	< LOD	< LOD	< LOD	< LOD	< LOD	4,47	< LOD	< LOD	25121,5	22016,34	< LOD	46880,91	1211,58	388501,59	< LOD
62	116,3	28,62	109,37	16,83	742,63	22201,26	0	5,86	< LOD	< LOD	< LOD	< LOD	< LOD	130,65	< LOD	< LOD	< LOD	16911,45	18376,52	21150,98	36213,01	< LOD	429121,38	10713,14
63		20,2	45,15	13,43	516,36	11507,59	0	27,47	< LOD	< LOD	< LOD	< LOD	< LOD	< LOD	2,97	< LOD	< LOD	11821,26	12271,71	17567,88	35802,08	504,44	430916,81	< LOD
64		0	49,18	0	456,06	11963,12	0	18,79	< LOD	< LOD	< LOD	4,51	< LOD	117,63	< LOD	< LOD	< LOD	11874,72	5727,64	15334,28	28672,37	< LOD	458916,63	< LOD
65	116,4	36,52	65,37	7,57	528,35	12400,63	0	5,46	< LOD	< LOD	< LOD	5,8	< LOD	< LOD	< LOD	< LOD	2243,04	10165,07	15430,78	16937,44	42276,29	1061,18	437880,59	9410,34
66	116,5	45,61	140,05	13,47	968,76	7031,9	0	< LOD	< LOD	< LOD	< LOD	< LOD	< LOD	< LOD	< LOD	< LOD	< LOD	8750,47	12745,83	20182,88	57816,79	< LOD	408074,13	17051,59
67	116,6	65,76	333,46	61,55	1038,49	20223,62	0	6,79	< LOD	< LOD	< LOD	8,9	< LOD	< LOD	< LOD	< LOD	< LOD	20420,59	12946,73	37196,68	54695,38	751,36	389997,13	< LOD
68	116,7	79,74	451,29	30,87	1906,59	29577,9	0	13,79	< LOD	< LOD	< LOD	< LOD	< LOD	< LOD	< LOD	< LOD	< LOD	24804,22	5323,81	59264,06	90538,63	< LOD	314307,94	18178,62
69	116,8	120,3	478,02	49,91	2072,3	25377,07	0	8,53	< LOD	< LOD	< LOD	11,18	< LOD	< LOD	< LOD	< LOD	< LOD	28706,1	10501,73	35815,65	71154	590,06	350824	15802,45
70	116,9	202,86	177,64	22,92	3189,73	19299	0	8,23	< LOD	< LOD	< LOD	< LOD	< LOD	< LOD	3,09	< LOD	< LOD	21316,02	11023,38	< LOD	63330,38	925,05	436934,28	10884,03
71	117	1202,93	175,25	65,84	8079,96	29332,51	0	20,05	< LOD	19,49	< LOD	< LOD	50,78	195,84	7,87	< LOD	< LOD	26956,92	22152,43	< LOD	74836,59	< LOD	433584,41	18231,08
72	117,2	389,64	10833,47	943,83	10122,19	54793,86	0	82,27	< LOD	59,48	70,11	< LOD	< LOD	< LOD	9,9	< LOD	< LOD	44204,84	380988,6	< LOD	< LOD	2892,69	18493,94	< LOD
73	117,2	4682,65	10947,55	541,43	13727,85	65563,18	13,69	13,45	< LOD	137,23	90,01	16,86	84,95	< LOD	4,34	< LOD	< LOD	16705,72	21088,67	101625	6946,2	< LOD	78174,46	14403,79
74	117,3	563,75	6047,29	2421,38	29523,81	22786,69	0	18,28	< LOD	< LOD	40,93	< LOD	106,02	< LOD	7,08	< LOD	< LOD	21073,04	< LOD	< LOD	9567,05	328,49	298846,22	< LOD
75	117,4	67,82	6200,56	11537,23	10124,54	39980,29	25,09	5,12	26,33	27,16	38,22	< LOD	< LOD	< LOD	19,12	< LOD	< LOD	19747,52	< LOD	< LOD	9672,45	143,12	37738,8	< LOD
76	117,5	1165,13	646,88	7348,49	22537,83	17868,06	47,69	5,17	21,4	45,04	< LOD	< LOD	98,36	< LOD	12,27	< LOD	< LOD	10004,48	61125,22	< LOD	36175,53	< LOD	101317,25	< LOD
77	117,6	1406,76	673,49	6060,25	7537,74	12966	94,22	< LOD	26,42	< LOD	< LOD	336,27	< LOD	< LOD	10,96	< LOD	< LOD	16772,37	62826,65	< LOD	63187,61	800,98	338013,5	23654,23
78	117,7	26,51	145,74	36,73	11595,98	3404,88	0	< LOD	< LOD	< LOD	< LOD	6,15	77,99	< LOD	< LOD	< LOD	< LOD	5146,09	< LOD	< LOD	59056,38	368,45	268131,09	< LOD
79	117,8	43,67	236,76	54	9034,47	4970,79	0	< LOD	< LOD	< LOD	< LOD	< LOD	< LOD	< LOD	3,08	< LOD	< LOD	13624,84	< LOD	< LOD	79922,76	< LOD	446866,41	< LOD
80	117,9	95,74	402,52	44,31	9531,52	8735,03	0	< LOD	< LOD	< LOD	< LOD	19,03	< LOD	< LOD	< LOD	< LOD	< LOD	20415,51	< LOD	< LOD	57656,11	< LOD	391009,22	22097,27
81	118	314,34	1266,77	477,82	3303,39	12407,28	0	4,2	< LOD	< LOD	< LOD	< LOD	< LOD	< LOD	< LOD	< LOD	< LOD	19469,4	4250,54	< LOD	33942,28	< LOD	361493,75	14636,88
82	118,1	533,58	1463,38	81,31	4327,86	21504,49	7,32	6,87	< LOD	< LOD	< LOD	32,42	< LOD	< LOD	3,52	< LOD	< LOD	44351,57	< LOD	< LOD	21472,47	< LOD	446662	< LOD
83	118,2	691,93	1147,87	22,85	6292,45	18063,07	0	10,53	< LOD	< LOD	< LOD	8,01	< LOD	< LOD	< LOD	< LOD	< LOD	18956,17	< LOD	< LOD	29398,39	< LOD	467757,22	26352,95
84	118,3	47,35	155,45	16,21	6004,47	4528,26	0	< LOD	< LOD	< LOD	< LOD	< LOD	36,78	< LOD	< LOD	< LOD	< LOD	2121,05	< LOD	35886,18	45850,63	< LOD	314292,81	58356,28
85	118,4	163,97	1825,84	80,88	5903,42	15995,75	0	9,63	< LOD	< LOD	< LOD	< LOD	< LOD	< LOD	< LOD	< LOD	< LOD	17084,5	< LOD	< LOD	50509,37	< LOD	390235,06	41887,38
86	118,5	337,48	380,35	17,64	7465,1	12277,94	0	< LOD	< LOD	< LOD	< LOD	8,56	< LOD	< LOD	< LOD	< LOD	< LOD	17389,71	< LOD	< LOD	33022,05	< LOD	317183,16	13155,31
87	118,6	93,37	495,77	39,74	9809,57	6603,27	0	< LOD	< LOD	< LOD	< LOD	10,93	53,89	< LOD	< LOD	< LOD	< LOD	12257,72	< LOD	< LOD	35515,18	< LOD	334890,97	< LOD
88	118,7	60,47	131,85	17,64	9107,79	4877,07	0	< LOD	< LOD	< LOD	< LOD	< LOD	43,8	< LOD	< LOD	< LOD	< LOD	22812,69	< LOD	< LOD	26079,26	< LOD	315199,22	10468
89	118,8	445,09	763,42	34,24	8495,88	13660,06	0	6,35	< LOD	< LOD	< LOD	12,98	61,05	< LOD	< LOD	< LOD	< LOD	24653,09	< LOD	< LOD	36124,59	< LOD	457011,16	< LOD
90	118,9	626,86	1158,95	46,82	7875,36	19465,33	0	7,26	< LOD	< LOD	12,68	10,09	< LOD	< LOD	3,5	< LOD	< LOD	17395,4	< LOD	< LOD	32760,83	< LOD	291967,41	22690,2
91	119	353,93	746,67	36,53	5914,69	14248,69	0	7,99	< LOD	< LOD	< LOD	6,21	< LOD	< LOD	< LOD	< LOD	< LOD	18741,43	< LOD	< LOD	30289,97	544,71	353675,09	14264
92	119,1	100,1	102,18	7,62	5262,12	3626,17	0	< LOD	< LOD	< LOD	< LOD	< LOD	< LOD	< LOD	< LOD	< LOD	< LOD	7798,25	< LOD	< LOD	24549,64	< LOD	452855,06	15783,65
93	119,2	276,52	3538,51	17,36	5205,84	8704,14	0	3,39	< LOD	< LOD	47,39	< LOD	< LOD	< LOD	< LOD	< LOD	< LOD	20287,68	< LOD	< LOD	23168,61	< LOD	391329,09	19774,44
94	119,3	165,19	827,54	33,21	4349,23	12823,9	0	< LOD	< LOD	< LOD	< LOD	28,63	38,6	< LOD	< LOD	< LOD	< LOD	45406,23	15551,07	< LOD	49689,25	553,28	385011,06	16462
95	119,4	345,55	87,44	151,88	3810,94	7696,04	0	< LOD	< LOD	< LOD	< LOD	26,66	< LOD	< LOD	2,85	< LOD	< LOD	9774,67	6171,24	< LOD	29245,39	449,63	391509,03	9915,22
96	119,5	489,89	376,06	31,42	5229,15	10532,83	0	7,65	< LOD	< LOD	< LOD	< LOD	< LOD	< LOD	3,06	< LOD	< LOD	36634,61	9575,34	< LOD	35262,48	649,52	378554,72	< LOD
97	119,6	906,8	1179,95	193,06	3987,87	27281,35	0	< LOD	< LOD	< LOD	< LOD	27,95	< LOD	< LOD	< LOD	< LOD	< LOD	61976,17	11055,92	< LOD	32264,78	< LOD	348003,03	< LOD
98	119,7	209,3	136,49	43,13	3603,07	7087,85	0	< LOD	< LOD	< LOD	< LOD	13,38	< LOD	< LOD	< LOD	< LOD	< LOD	25941,65	5814,9	< LOD	26368,23	< LOD	417935,22	17660,56
99	119,8	62,54	81,95	77,85	424,6	1567,1	14,11	< LOD	< LOD	< LOD	< LOD	29,18	< LOD	< LOD	< LOD	< LOD	< LOD	23215,05	4956,5	< LOD	3887,21	< LOD	485778,66	< LOD
100	119,9	809,26	128,75	44,36	9453,22	29900,22	0	< LOD	< LOD	< LOD	< LOD	7,91	< LOD	< LOD	4,87	< LOD	< LOD	43938,8	< LOD	< LOD	33131,89	< LOD	448237,91	13821,34
101	120	475,91	2344,56	93,71	8937,6	19923,1	0	4,07	< LOD	< LOD	32,81	8,89	< LOD	< LOD	< LOD	< LOD	< LOD	41820,53	< LOD	< LOD	37777,88	< LOD	385317,03	33066,13
102	120,1	799,35	252,55	108,09	19761,72	9567,74	0	< LOD	< LOD	< LOD	< LOD	< LOD	174,64	< LOD	3,98	< LOD	< LOD	11898,98	< LOD	< LOD	40819,07	< LOD	180657,3	< LOD
103	120,2	275,58	1378,04	377,38	5691,51	9259,88	0	4,36	< LOD	< LOD	< LOD	< LOD	< LOD	< LOD	< LOD	< LOD	< LOD	51822,56	8446,6	< LOD	25114,4	721,12	410341,75	< LOD
104	120,3	195,75	225899,4	721,27	13890,54	155487,5	19,56	< LOD	< LOD	< LOD	1397,75	< LOD	98,03	< LOD	39,33	< LOD	< LOD	314878,1	< LOD	< LOD	25973,88	1244,86	78079,62	< LOD
105	120,4	371,38	5732,31	1566,17	4335,92	4102,24	11,43	4,94	16,81	< LOD	53,85	< LOD	< LOD	< LOD	3,25	< LOD	< LOD	11274,57	< LOD	< LOD	22145,18	< LOD	345562,72	< LOD
106	120,5	60,53	22,44	37,53	5511,98	1215,72	0	< LOD	< LOD	< LOD	< LOD	< LOD	< LOD	< LOD	< LOD	< LOD	< LOD	3700,87	< LOD	< LOD	18756,89	< LOD	507653,47	< LOD
107	120,6	611,07	94,6	45,56	17618,1	10720,53	0	< LOD	< LOD	< LOD	< LOD	11,46	< LOD	< LOD	4,19	< LOD	< LOD	11247,59	< LOD	< LOD	34177,59	< LOD	360673,88	< LOD
108	120,7	593,37	12754,98	2360,49	11871,16	113037,3	14,84	9,56	32,75	< LOD	72,49	< LOD	< LOD	< LOD	9,55	< LOD	< LOD	101481,3	24853,88	< LOD	64713,43	< LOD	257514,72	40746,55
109	120,8	749,42	385,98	140,32	28189,31	20278,07	0	52,96	< LOD	< LOD	< LOD	18,49	134,33	< LOD	5,66	< LOD	< LOD	6792,33	< LOD	< LOD	49286,24	< LOD	165749,89	< LOD
110	120,9	214,18	177,88	122,2	7690,98	5014,2	0	< LOD	< LOD	< LOD	< LOD	14,17	< LOD	< LOD	4,19	< LOD	< LOD	25127,99	13587,39	< LOD	31198,53	< LOD	438871,56	< LOD
111	121	215	655,94	111,44	13503,85	6621,74	0	38,68	< LOD	< LOD	< LOD	< LOD	107,4	< LOD	< LOD	< LOD	< LOD	21243,28	< LOD	< LOD	30255,05	< LOD	318027,81	9998,18
112	121,1	1051,93	124,12	658,73	16379,16	29134,79	31,12	< LOD	< LOD	< LOD	< LOD	< LOD	111,04	< LOD	7,38	< LOD	< LOD	44233,45	< LOD	< LOD	58380,61	< LOD	451742,78	12599,04
113		454,6	204118,7	10646,26	7271,42	315199,5	48,66	< LOD	< LOD	53,44	1162,66	421,46	< LOD	< LOD	41,22	< LOD	< LOD	324250,3	13405,9	< LOD	42020,48	< LOD	67690,18	< LOD
114	121,2	3654,69	118956,9	34916,19	9647,73	129397,6	293,11	19,89	140,17	< LOD	818,96	765,47	< LOD	< LOD	86,89	< LOD	< LOD	187869	157442,2	< LOD	27145,13	1264,51	98795,4	< LOD

Table 8.25: Handheld XRF measurements from box 22 of drill core BH4508 at Hellerfjellet.

Point	Meters	Cu	Zn	Pb	Ba	Fe	Ag	Mo	Sb	Sn	Cd	As	Ni	Co	Se	Bi	Mn	S	Ca	K	Al	P	Si	Mg
K22	ppm	ppm	ppm	ppm	ppm	ppm	ppm	ppm	ppm	ppm	ppm	ppm	ppm	ppm	ppm	ppm	ppm	ppm	ppm	ppm	ppm	ppm	ppm	ppm
115	121,3	859,67	116,35	220,66	28142,5	22657,13	< LOD	< LOD	< LOD	< LOD	< LOD	< LOD	177,73	< LOD	6,08	< LOD	< LOD	11590,6	< LOD	< LOD	81224,8	< LOD	173877,44	< LOD
116	121,4	458,01	54,51	52,22	8537,13	7001,19	< LOD	< LOD	< LOD	< LOD	< LOD	6,45	< LOD	< LOD	4,64	< LOD	< LOD	8811,12	< LOD	< LOD	33676,33	329,06	358172,19	10786,16
117	121,5	994,48	126,38	38,54	22434,77	20112,24	< LOD	< LOD	< LOD	< LOD	< LOD	8,74	90,19	< LOD	4,73	< LOD	< LOD	10365,07	< LOD	< LOD	91272,2	< LOD	216082,48	20687,77
118	121,6	1633,85	204,95	22,45	15532,68	25605,75	< LOD	6,37	< LOD	< LOD	< LOD	< LOD	118,77	< LOD	4,29	< LOD	< LOD	13351,8	< LOD	< LOD	61637,06	< LOD	262414,59	< LOD
119	121,7	728,3	123,32	44,63	19696,88	15627,82	< LOD	18,1	< LOD	< LOD	< LOD	< LOD	106,9	< LOD	5,47	< LOD	< LOD	7514,03	< LOD	< LOD	60908,89	< LOD	226277,2	< LOD
120	121,8	616,33	257,98	37,47	20756,15	26500,38	< LOD	< LOD	< LOD	< LOD	< LOD	< LOD	131,33	< LOD	3,92	< LOD	< LOD	14092,62	< LOD	< LOD	52682,43	< LOD	269264,75	< LOD
121	121,9	470,23	38,84	24,6	19325,97	11161,89	< LOD	5,63	< LOD	< LOD	< LOD	< LOD	79,05	< LOD	3,9	< LOD	< LOD	6190,24	< LOD	< LOD	57442,97	< LOD	214514,73	< LOD
122	122	824,48	20029,35	226,49	6168,74	71700,63	7	21,18	< LOD	25,83	78,38	< LOD	< LOD	< LOD	10,54	< LOD	< LOD	70912,05	100626,9	< LOD	39922,84	< LOD	274489,47	< LOD
123	122,1	1179,87	782,1	70,11	18151,25	32144,12	< LOD	< LOD	< LOD	< LOD	< LOD	< LOD	88,53	< LOD	8,2	< LOD	< LOD	21943,53	< LOD	< LOD	67809,62	< LOD	284590,78	13373,45
124	122,2	1427,28	115,14	31,11	23909,18	15638,89	< LOD	5,52	< LOD	< LOD	< LOD	12,21	128,36	< LOD	4,43	< LOD	< LOD	9049,66	< LOD	< LOD	83810,4	< LOD	179098,25	< LOD
125	122,3	39,01	19,37	< LOD	136,95	< LOD	< LOD	< LOD	< LOD	< LOD	< LOD	< LOD	< LOD	< LOD	1	12,6	< LOD	2194,31	4979,08	< LOD	3365,77	1947,64	529107,94	< LOD
126	122,4	44,75	28,66	17,12	6460,47	1758,72	< LOD	17,98	< LOD	< LOD	< LOD	< LOD	< LOD	< LOD	< LOD	< LOD	< LOD	2584,98	< LOD	< LOD	31182,31	< LOD	522546,34	11752,28
127	122,5	328,41	565,98	214,08	6734,74	17242,53	< LOD	16,33	< LOD	< LOD	< LOD	< LOD	< LOD	< LOD	4,81	< LOD	< LOD	12858,49	< LOD	< LOD	39109,48	< LOD	399020,38	16470,23
128	122,6	79,08	117,91	64,67	588,21	3345,73	< LOD	< LOD	< LOD	< LOD	< LOD	8,71	< LOD	< LOD	< LOD	< LOD	< LOD	8261,43	26522,1	< LOD	59401,52	< LOD	357903,88	< LOD
129	122,7	1264,4	166,2	3576,67	455,95	4406,67	258,7	< LOD	34,64	< LOD	< LOD	< LOD	< LOD	< LOD	< LOD	< LOD	< LOD	9935,22	14134,75	25833,47	53208,85	< LOD	387444,56	< LOD
130	122,8	85,65	76,33	154,29	404,24	2047,37	< LOD	< LOD	< LOD	< LOD	< LOD	< LOD	< LOD	< LOD	3,3	13,26	< LOD	4264,99	10163,05	48457,59	52829,31	< LOD	411404,41	< LOD
131	122,9	124,26	205,47	331,11	1070,09	2825,41	< LOD	< LOD	< LOD	< LOD	< LOD	< LOD	< LOD	< LOD	< LOD	< LOD	< LOD	10899,38	8559,43	54019,91	47696,71	< LOD	377963,25	< LOD
132	123	1286,45	44,27	3723,32	249,81	17400,4	45,15	< LOD	< LOD	33,1	< LOD	< LOD	< LOD	< LOD	8,26	< LOD	< LOD	12468,04	25154,37	13789,98	72040,53	< LOD	330729,88	< LOD
133	123,1	50,41	22,5	207,09	257,51	< LOD	< LOD	< LOD	< LOD	< LOD	< LOD	< LOD	< LOD	< LOD	< LOD	< LOD	< LOD	2570,09	2865,02	105452,1	75072,84	< LOD	388395,28	< LOD
134	123,2	24,66	32,26	65,97	586,43	3049,04	< LOD	< LOD	< LOD	< LOD	< LOD	< LOD	< LOD	< LOD	< LOD	< LOD	< LOD	1205,64	16524,88	23154,06	55740,97	< LOD	397476	< LOD
135	123,3	2886,1	288,19	19020,3	< LOD	5822,95	1397,98	< LOD	211,17	< LOD	16,11	< LOD	< LOD	< LOD	12,3	< LOD	< LOD	18899,29	20096,09	39128	93991,02	688,7	390055,59	13062,96
136	123,4	1629,99	81,89	2364,1	216,26	4717,64	174,57	< LOD	43,78	41,31	< LOD	< LOD	< LOD	< LOD	< LOD	< LOD	< LOD	6980,25	11285,91	33765,58	67674,7	499,57	391674,81	9355,52
137	123,5	39,43	86,18	48,53	745,23	5649,52	< LOD	< LOD	< LOD	< LOD	< LOD	< LOD	< LOD	< LOD	< LOD	< LOD	< LOD	3684,4	11576,82	30662,85	63391,84	< LOD	381421,44	< LOD
138	123,6	33,32	57,01	75,46	217,2	1432,98	< LOD	< LOD	16,8	< LOD	< LOD	< LOD	< LOD	< LOD	< LOD	< LOD	< LOD	5288,77	19810,17	14628,94	47211,27	767,36	387627,53	< LOD
139	123,7	81,08	199,67	79,98	334,03	5414,28	< LOD	< LOD	< LOD	< LOD	< LOD	11,64	< LOD	< LOD	< LOD	< LOD	< LOD	8924,8	16580,21	21327,34	51201,05	555,84	354928,94	< LOD
140		65,15	275,83	65,27	202,11	9227,08	< LOD	< LOD	< LOD	< LOD	< LOD	11,42	< LOD	< LOD	< LOD	< LOD	< LOD	13356,75	31501,97	25856,75	40770,69	901,15	302920,03	< LOD
141		92,62	110,35	184,34	3318,26	3308,57	< LOD	< LOD	< LOD	< LOD	< LOD	13,06	< LOD	< LOD	< LOD	< LOD	< LOD	9395,66	11397	30500,93	59827,39	< LOD	355169,41	11074,05
142		502,89	3065,17	625,02	7762,69	14889,59	< LOD	3,73	< LOD	< LOD	< LOD	< LOD	< LOD	< LOD	< LOD	< LOD	< LOD	13915,19	< LOD	< LOD	39168,09	593,07	469115,06	< LOD
143		327,55	818,48	36	5130,96	9832,01	< LOD	3,24	< LOD	< LOD	< LOD	< LOD	< LOD	< LOD	< LOD	< LOD	< LOD	8687,82	< LOD	< LOD	33681,79	< LOD	471920,69	13340,17
144	123,8	461,41	98,19	53,37	6249,52	13906,68	< LOD	9,59	< LOD	< LOD	< LOD	< LOD	36,08	< LOD	< LOD	< LOD	< LOD	13492,68	< LOD	< LOD	28308,34	< LOD	391516,66	10956,14
145	123,9	92,55	131,11	10,7	4138,63	4201,75	< LOD	< LOD	< LOD	< LOD	< LOD	< LOD	< LOD	< LOD	< LOD	< LOD	< LOD	2946,6	< LOD	< LOD	24531,87	< LOD	433742,34	14653,86
146	124	798,95	528,89	532,18	1452,51	20217,23	< LOD	4,35	< LOD	< LOD	< LOD	< LOD	< LOD	< LOD	3,22	< LOD	< LOD	16851,59	< LOD	< LOD	5826,71	< LOD	507371,06	< LOD
147	124,1	1302,5	941,12	326,49	11661,41	12426,57	< LOD	31,51	< LOD	< LOD	< LOD	< LOD	75,65	< LOD	< LOD	< LOD	< LOD	9700,04	< LOD	< LOD	48513,12	< LOD	274939,38	24269,87
148	124,2	20,51	< LOD	< LOD	137,96	< LOD	< LOD	< LOD	< LOD	< LOD	< LOD	< LOD	< LOD	< LOD	< LOD	< LOD	< LOD	3220,84	1450,19	< LOD	1687,2	< LOD	511853,97	< LOD
149	124,3	653,02	1958,39	585,79	8194,85	13814,76	< LOD	4,65	< LOD	< LOD	< LOD	< LOD	< LOD	< LOD	3,87	< LOD	< LOD	12812,98	9684,19	< LOD	32060,01	< LOD	461283,41	< LOD
150	124,5	3084,23	2603,52	508,28	26327,91	11792,1	< LOD	28,21	< LOD	< LOD	< LOD	< LOD	100,3	< LOD	5,82	< LOD	< LOD	8717,99	< LOD	< LOD	96776,01	< LOD	136012,16	< LOD
151	124,6	1115,46	1214,78	193,4	13646,51	23911,67	< LOD	24,09	< LOD	< LOD	< LOD	< LOD	49,28	194,35	< LOD	< LOD	< LOD	10079,48	< LOD	< LOD	55114,12	< LOD	259984,05	< LOD
152	124,7	665,74	3503,94	1148,21	11321,5	19095,54	7,58	7,12	< LOD	< LOD	< LOD	< LOD	< LOD	< LOD	4,4	< LOD	< LOD	20524,14	< LOD	< LOD	46691,74	< LOD	432902,41	< LOD
153	124,8	307,12	204,77	77,97	16963,6	8541,53	< LOD	< LOD	< LOD	< LOD	< LOD	< LOD	93,18	< LOD	< LOD	< LOD	< LOD	5341,36	6550,79	< LOD	65456,6	< LOD	257545,38	< LOD
154	124,9	252,09	667,27	299,7	10883,31	8623,45	< LOD	< LOD	< LOD	< LOD	< LOD	< LOD	53,93	< LOD	< LOD	< LOD	< LOD	7818,94	7261,82	< LOD	44055,32	< LOD	466559,91	< LOD
155	125	270,68	61,01	23,11	10852,75	6020,57	< LOD	3,22	< LOD	< LOD	< LOD	< LOD	38,8	< LOD	< LOD	< LOD	< LOD	20327,45	< LOD	< LOD	34635,38	< LOD	354741,38	< LOD
156	125,1	223,45	95,06	44,47	1914,84	5020,09	< LOD	< LOD	< LOD	< LOD	< LOD	< LOD	< LOD	< LOD	< LOD	< LOD	< LOD	4314,88	< LOD	< LOD	11331,72	< LOD	421627,5	< LOD
157	125,2	460,68	658,69	118,01	9790,8	11815,94	< LOD	8,69	< LOD	< LOD	< LOD	< LOD	49,99	< LOD	< LOD	< LOD	< LOD	7973,76	< LOD	< LOD	44079,84	< LOD	431688,22	8345,29
158	125,3	122,41	81,36	24,86	17697,21	26866,11	< LOD	< LOD	< LOD	< LOD	< LOD	8,16	62,58	< LOD	3,81	< LOD	< LOD	14601,76	36963,29	< LOD	109887,7	741,97	307768,88	< LOD
159	125,4	39,79	68,81	37,96	7944,41	23204,48	< LOD	3,72	< LOD	< LOD	< LOD	< LOD	195,38	< LOD	< LOD	< LOD	< LOD	27080,67	40522,31	< LOD	105565,4	953,36	323195,22	23292,73
160	125,5	1928,62	92,68	2069,17	400,16	8434,27	196,44	< LOD	37,77	30,08	< LOD	< LOD	< LOD	< LOD	< LOD	< LOD	3149,1	13103,02	14358,44	15286,88	53357,63	< LOD	407632,63	< LOD
161	125,6	27,64	61,08	12,88	2282,72	5522,12	< LOD	3,63	< LOD	< LOD	< LOD	< LOD	< LOD	< LOD	< LOD	< LOD	< LOD	8217,92	20024,31	< LOD	31486,28	463,78	384588,06	12080,42
162	125,7	57,61	95,15	22,56	1770,31	18435,38	< LOD	< LOD	< LOD	< LOD	< LOD	< LOD	< LOD	135,17	3,08	< LOD	< LOD	11694,93	54515,82	23894,41	46646,59	1161,39	381978,34	< LOD
163	125,8	103,93	497,06	61,69	1786,6	26753,21	< LOD	< LOD	< LOD	< LOD	< LOD	18,4	< LOD	< LOD	< LOD	< LOD	< LOD	26064,74	100884	< LOD	62784,2	< LOD	267284,41	16038,53
164	125,9	< LOD	54,01	28,81	458,97	7389,82	< LOD	2,76	< LOD	< LOD	< LOD	< LOD	< LOD	< LOD	< LOD	< LOD	3902,92	5030,23	341107,3	< LOD	29241,89	< LOD	108583,2	< LOD
165	126	44,82	65,98	18,12	1415,78	17635,91	< LOD	< LOD	< LOD	< LOD	< LOD	< LOD	< LOD	< LOD	< LOD	< LOD	2537,76	12039,53	203982,1	< LOD	46354,34	< LOD	223672,47	< LOD
166	126,1	19,26	241,22	16,97	2872,94	33769,21	< LOD	< LOD	< LOD	< LOD	< LOD	5,94	< LOD	< LOD	5,14	< LOD	< LOD	13480,02	30988,84	36871,43	97645,84	< LOD	268836,66	20479,43
167	126,2	46,19	157,34	< LOD	1009,41	32147,98	< LOD	< LOD	< LOD	< LOD	< LOD	< LOD	< LOD	< LOD	< LOD	< LOD	< LOD	33944,71	43477,53	< LOD	42035,26	< LOD	381259,31	< LOD
168	126,3	18,4	70,9	< LOD	2575,19	10469,22	< LOD	< LOD	12,49	< LOD	< LOD	< LOD	< LOD	< LOD	< LOD	< LOD	< LOD	4956,4	14943,9	< LOD	39145,61	< LOD	385767,56	< LOD
169	126,4	25,29	143	15,43	2383,82	27373,02	< LOD	23,4	< LOD	< LOD	< LOD	< LOD	39,94	< LOD	4,35	< LOD	< LOD	18177,51	29581,24	< LOD	73515,46	1418,26	369463,56	< LOD
170	126,5	30,42	168,54	24,99	824,69	20330,41	< LOD	< LOD	< LOD	< LOD	< LOD	< LOD	< LOD	< LOD	< LOD	< LOD	< LOD	2397,66	79090,77	< LOD	43296,23	< LOD	241328,02	< LOD
171	126,6	< LOD	20,9	13,79	307,43	5688,86	< LOD	< LOD	< LOD	< LOD	< LOD	5,22	< LOD	< LOD	< LOD	< LOD	2256,42	2340,08	267282,5	< LOD	18822,29	1713,54	196463,64	< LOD
172	126,7	22,26	24,23	17,16	244,9	11608,37	< LOD	< LOD	< LOD	< LOD	< LOD	< LOD	< LOD	< LOD	< LOD	< LOD	< LOD	3241,34	253320,8	< LOD	22597,7	1830,45	204379,31	< LOD
173		< LOD	167,1	21,76	1273,5	30781,32	< LOD	< LOD	< LOD	< LOD	< LOD	< LOD	< LOD	< LOD	3,57	< LOD	< LOD	11923,53	99017,96	< LOD	68099,2	< LOD	322513,53	< LOD
174	126,8	106,81	437,38	48,21	2112,99	28225,62	< LOD	< LOD	< LOD	< LOD	< LOD	9,72	< LOD	< LOD	< LOD	< LOD	< LOD	12196,79	54015,19	< LOD	69522,1	1046,23	359669,94	< LOD

Table 8.26: Handheld XRF measurements from box 23 of drill core BH4508 at Hellerfjellet.

Point	Meters	Cu	Zn	Pb	Ba	Fe	Ag	Mo	Sb	Sn	Cd	As	Ni	Co	Se	Bi	Mn	S	Ca	K	Al	P	Si	Mg
K23	ppm	ppm	ppm	ppm	ppm	ppm	ppm	ppm	ppm	ppm	ppm	ppm	ppm	ppm	ppm	ppm	ppm	ppm	ppm	ppm	ppm	ppm	ppm	ppm
175	126,9	57,63	190,69	7,41	4400,05	21570,38	< LOD	< LOD	< LOD	< LOD	< LOD	< LOD	< LOD	< LOD	< LOD	< LOD	< LOD	17453,53	12766,92	44171,82	99940,72	< LOD	293018,94	< LOD
176	127	26,83	208,05	12,65	2762	20871,69	< LOD	< LOD	< LOD	< LOD	< LOD	< LOD	< LOD	< LOD	< LOD	< LOD	< LOD	9740,42	12828,43	38084,57	65445,2	< LOD	297413,69	< LOD
177	127,1	30,02	229,97	25,43	3118,4	46311,59	< LOD	< LOD	< LOD	< LOD	< LOD	< LOD	< LOD	< LOD	< LOD	< LOD	< LOD	22724,95	59564,6	< LOD	108984,2	879,22	251969,22	25004,6
178	127,2	55,07	91,02	10,31	1511,97	14402,58	< LOD	< LOD	< LOD	< LOD	< LOD	< LOD	< LOD	< LOD	< LOD	< LOD	< LOD	7125,35	104997,6	22221,09	53226,19	1561,99	304286,53	< LOD
179	127,3	63,74	311,92	7,2	1036,55	23571,25	< LOD	< LOD	< LOD	< LOD	< LOD	5,86	< LOD	< LOD	< LOD	< LOD	< LOD	20193,55	21233,71	< LOD	37770,09	829,97	413180,53	< LOD
180	127,4	25,24	118,23	8,66	1365,9	20176,06	< LOD	< LOD	< LOD	< LOD	< LOD	85,75	< LOD	< LOD	< LOD	< LOD	< LOD	12462,63	144430,5	23231,74	56039,05	< LOD	292740,25	< LOD
181	127,5	63,32	122,17	26,54	980,63	25939,72	< LOD	< LOD	< LOD	< LOD	< LOD	< LOD	< LOD	< LOD	< LOD	< LOD	< LOD	17878,02	152917,8	< LOD	54880,6	< LOD	263842,31	21955,18
182	127,6	133,04	244,29	24,29	532,64	45885,24	< LOD	7,45	< LOD	< LOD	< LOD	11,08	< LOD	< LOD	5,03	< LOD	2791,58	24679,76	224902,6	< LOD	37551,19	< LOD	269835,13	< LOD
183	127,7	65,27	77,28	25,21	989,53	18214,66	< LOD	< LOD	< LOD	< LOD	< LOD	< LOD	< LOD	< LOD	< LOD	< LOD	5044,27	17383,4	356332,6	< LOD	21061,45	1694,73	88233,55	< LOD
184	127,8	643,74	20298,14	2369,9	4483,76	22901,6	34,38	36,88	28,83	22,61	149,03	< LOD	< LOD	< LOD	< LOD	< LOD	< LOD	48178,42	30148,59	< LOD	41508,57	< LOD	405659,19	< LOD
185	127,9	24,9	65,43	14,25	5570,06	2065,18	< LOD	< LOD	< LOD	< LOD	< LOD	8,22	< LOD	< LOD	< LOD	< LOD	< LOD	7226,96	< LOD	< LOD	33947,92	< LOD	402685,09	< LOD
186	128	46,13	46,17	28,35	7508,09	5004,91	< LOD	3,22	< LOD	< LOD	< LOD	21,5	41	< LOD	< LOD	< LOD	< LOD	21757,78	< LOD	< LOD	44849,38	697,84	477005,78	< LOD
187	128,1	68,85	90,57	54,99	5598,3	5356,72	< LOD	< LOD	< LOD	< LOD	< LOD	21,88	65,67	< LOD	< LOD	< LOD	< LOD	12048,27	< LOD	< LOD	39647,17	889,84	444626,16	< LOD
188	128,2	75	191,47	52,46	1935,13	4270,27	< LOD	< LOD	< LOD	< LOD	< LOD	< LOD	< LOD	< LOD	< LOD	< LOD	< LOD	8592,28	8840,51	< LOD	28668,44	< LOD	448443,66	< LOD
189	128,3	95,79	1292,33	464,25	5503,26	7675,43	< LOD	30,74	< LOD	< LOD	< LOD	< LOD	< LOD	< LOD	< LOD	< LOD	< LOD	17121,13	< LOD	< LOD	46788,73	< LOD	426188,63	< LOD
190	128,4	46,05	121,63	17,6	4871,24	5014,14	< LOD	3,19	< LOD	< LOD	< LOD	9,1	< LOD	< LOD	< LOD	< LOD	< LOD	12993,82	< LOD	< LOD	41498,46	< LOD	467907,16	13197,61
191	128,5	126,12	961,86	120,53	10807,07	10826,89	< LOD	4,65	< LOD	< LOD	< LOD	14,11	67,83	< LOD	5,65	< LOD	< LOD	17298,38	< LOD	< LOD	50571,65	713,49	285129,72	< LOD
192	128,6	232,33	128,35	< LOD	3755,89	12447,32	< LOD	21,53	< LOD	< LOD	< LOD	4,6	< LOD	< LOD	3,61	< LOD	< LOD	19226,35	3185,95	< LOD	32365,77	596,62	392639,63	14135,45
193	128,7	161,47	131,97	12,87	4930,55	6429,32	< LOD	7,82	< LOD	< LOD	< LOD	6,92	< LOD	< LOD	< LOD	< LOD	< LOD	16175,55	< LOD	< LOD	49036,9	751,85	421164,41	13628,44
194	128,8	607,23	533,11	37,33	4217,59	8970,94	< LOD	4,77	< LOD	< LOD	< LOD	< LOD	< LOD	< LOD	< LOD	< LOD	< LOD	19505,36	< LOD	< LOD	24868,41	< LOD	459308	< LOD
195	128,9	91,82	131,37	19,69	3371,65	14604,39	< LOD	10,04	< LOD	< LOD	< LOD	< LOD	< LOD	< LOD	< LOD	< LOD	< LOD	12877,32	< LOD	24708,07	45710,98	< LOD	422934,56	25426,37
196	129	112,43	168,76	83,66	2845,76	4898,64	< LOD	2,66	< LOD	< LOD	< LOD	< LOD	< LOD	< LOD	< LOD	< LOD	< LOD	11802,67	< LOD	< LOD	32992,62	546,1	470775,16	< LOD
197	129,1	338,73	14776,95	292,03	6554,85	40672,22	< LOD	6,93	< LOD	< LOD	121,12	< LOD	< LOD	< LOD	< LOD	< LOD	< LOD	37372,96	11715,81	< LOD	69230,45	1131,76	388244,72	< LOD
198	129,2	399,6	833,84	63,1	6154,29	44512,92	< LOD	30,09	< LOD	< LOD	< LOD	12,42	126,91	< LOD	7,35	< LOD	< LOD	40585,82	19112,3	< LOD	77749,44	1617,04	394671,38	16305,94
199	129,3	209,09	224,26	78,58	3048,75	17041,86	< LOD	13,62	< LOD	< LOD	< LOD	< LOD	< LOD	< LOD	3,07	< LOD	< LOD	25688,35	30002,78	< LOD	60787,31	1449,69	374064,06	< LOD
200	129,4	113,03	136,41	24,36	2060,55	13354,81	< LOD	21,03	< LOD	< LOD	< LOD	< LOD	< LOD	< LOD	< LOD	< LOD	< LOD	19343,14	10480,42	< LOD	32268,57	1462,67	478097,63	< LOD
201	129,5	197,24	277,23	35,38	3240,05	20381,69	< LOD	25,95	< LOD	< LOD	< LOD	< LOD	65,22	< LOD	4,87	< LOD	< LOD	25713,3	15156,09	< LOD	58463,91	2196,44	411156,56	18421,3
202	129,6	189,44	128,7	94,59	4122,71	64967,12	< LOD	43,21	< LOD	< LOD	< LOD	8,73	125,24	< LOD	11,42	< LOD	< LOD	45488,35	22002,08	< LOD	80454,95	1963,68	355656,78	< LOD
203	129,7	284,55	174	40,79	3796,04	18702,3	< LOD	27,89	< LOD	< LOD	< LOD	< LOD	< LOD	< LOD	< LOD	< LOD	< LOD	20609,6	11792,8	< LOD	56379,68	1333,01	407054,63	< LOD
204	129,8	224,21	99,31	28,71	2587,88	10732,85	< LOD	11,2	< LOD	< LOD	< LOD	< LOD	< LOD	< LOD	< LOD	< LOD	< LOD	24155,54	19838,36	< LOD	60587,21	864,51	410005,16	13037,25
205	129,9	380,06	503,66	36,22	4680,52	48713,23	< LOD	33,72	< LOD	< LOD	< LOD	< LOD	75,33	< LOD	6,02	< LOD	< LOD	48479,22	21800,58	< LOD	76496,44	2041,93	369744,88	< LOD
206	130	449,07	173,27	26	2515,1	28543,08	< LOD	20,19	< LOD	< LOD	< LOD	< LOD	< LOD	< LOD	< LOD	< LOD	< LOD	27121,98	15585,31	< LOD	59897,57	3531	429068,22	< LOD
207	130,1	189,86	161,2	25,01	3585,84	16731,93	< LOD	14,39	< LOD	< LOD	< LOD	6,09	37,5	< LOD	< LOD	< LOD	< LOD	19945,91	16217,56	< LOD	68060,86	2179,97	435301,97	29209,18
208	130,2	263,55	14081,55	291,93	3903,9	30586,77	< LOD	33,2	< LOD	< LOD	71,72	< LOD	< LOD	< LOD	< LOD	< LOD	< LOD	39565,3	39022,57	< LOD	71974,87	1864,12	361380,38	< LOD
209	130,3	390,84	216,28	132,35	5545,53	23108,78	< LOD	10,24	< LOD	< LOD	< LOD	< LOD	49,51	< LOD	4,51	< LOD	< LOD	21432,66	12858,93	< LOD	67456,26	803,97	446120,34	22035,86
210	130,4	501,41	313,37	46,67	6499,12	15967,46	< LOD	2,98	< LOD	< LOD	< LOD	< LOD	< LOD	< LOD	< LOD	< LOD	< LOD	17365,42	4388,77	< LOD	44120,39	< LOD	486277,63	< LOD
211	130,5	116,81	413,39	175,22	7410,88	4757,94	< LOD	< LOD	< LOD	< LOD	< LOD	< LOD	< LOD	< LOD	6,14	< LOD	< LOD	9621,35	< LOD	< LOD	48182,23	< LOD	490383,47	< LOD
212	130,6	91,11	112,83	13,35	6492,94	4572,74	< LOD	10,42	< LOD	< LOD	< LOD	< LOD	< LOD	< LOD	3,53	< LOD	< LOD	9293,25	< LOD	< LOD	44878,78	< LOD	465999,31	< LOD
213	130,7	113,66	254,15	47,74	4381,71	10111,18	< LOD	3,9	< LOD	< LOD	< LOD	< LOD	< LOD	< LOD	< LOD	< LOD	< LOD	17754,28	< LOD	< LOD	27059,85	642,44	503567,81	9802,35
214	130,8	2710,2	265,15	77,22	14628,98	34781,48	< LOD	5,4	< LOD	< LOD	< LOD	< LOD	59,34	< LOD	3,8	< LOD	< LOD	43071,25	23935,21	< LOD	116606,2	1565,56	315562,94	< LOD
215	130,9	35,13	396,31	13,1	4279,18	4846,02	< LOD	4,92	< LOD	< LOD	< LOD	< LOD	< LOD	< LOD	< LOD	< LOD	< LOD	6992,97	< LOD	< LOD	22148,84	592,22	513014,03	< LOD
216	131	< LOD	15,64	< LOD	127,97	< LOD	< LOD	< LOD	< LOD	< LOD	< LOD	< LOD	< LOD	< LOD	< LOD	< LOD	< LOD	1827,39	1058,69	< LOD	5294,94	< LOD	520585,13	< LOD
217	131,1	75,93	48,12	< LOD	6329,25	2898,94	< LOD	< LOD	< LOD	< LOD	< LOD	< LOD	< LOD	< LOD	< LOD	< LOD	< LOD	4322,47	< LOD	< LOD	39590,45	< LOD	385685,53	11519,95
218	131,2	< LOD	20,09	< LOD	706,13	< LOD	< LOD	< LOD	< LOD	< LOD	< LOD	< LOD	< LOD	< LOD	< LOD	< LOD	< LOD	3431,71	1853,59	< LOD	11365,4	< LOD	512560,97	< LOD
219	131,3	406,12	414,8	15,18	7053,75	16923,11	< LOD	11,27	< LOD	< LOD	< LOD	< LOD	< LOD	< LOD	< LOD	< LOD	< LOD	15880,44	< LOD	< LOD	50516,16	< LOD	452310,28	< LOD
220	131,4	24,6	30,37	6,94	5659,57	1102,34	< LOD	8,06	< LOD	< LOD	< LOD	< LOD	< LOD	< LOD	5,28	< LOD	< LOD	2719,81	< LOD	< LOD	26816,41	846,06	521717,94	11743,61
221	131,5	103,38	78,86	11,4	2345,83	2040,44	< LOD	< LOD	< LOD	< LOD	< LOD	< LOD	< LOD	< LOD	< LOD	< LOD	< LOD	4286,24	2230,49	< LOD	8197,62	< LOD	391137,31	< LOD
222	131,6	216,01	968,07	15,6	8861,79	18757,75	< LOD	< LOD	< LOD	< LOD	< LOD	< LOD	55,37	< LOD	< LOD	< LOD	< LOD	8567,05	< LOD	< LOD	46476,31	< LOD	302534,19	12694,36
223	131,7	83,83	702,59	83,72	7225,41	7116,34	< LOD	5,06	< LOD	< LOD	< LOD	< LOD	< LOD	< LOD	< LOD	< LOD	< LOD	31631,66	5050,71	< LOD	42808,74	699,71	434972,69	9023,7
224	131,8	126,79	89,78	34,36	17563,67	8985,51	< LOD	6,97	< LOD	< LOD	< LOD	< LOD	71,32	< LOD	< LOD	< LOD	< LOD	17904,45	< LOD	< LOD	49478,54	< LOD	212964,23	< LOD
225	131,9	391,9	502,58	216,53	6862,65	18825,33	< LOD	35,38	< LOD	< LOD	< LOD	14,26	< LOD	< LOD	3,58	< LOD	< LOD	17879,02	< LOD	< LOD	37792,54	936,22	454674,03	< LOD
226	132	128,46	97,83	155,8	3240,83	6509,29	< LOD	4,21	< LOD	< LOD	< LOD	< LOD	< LOD	< LOD	< LOD	< LOD	< LOD	27569,7	10878,27	< LOD	26335,19	< LOD	443624,53	< LOD
227	132,1	238,52	121,29	29,62	7159,68	10762,15	< LOD	5,82	< LOD	< LOD	< LOD	< LOD	< LOD	< LOD	3,13	< LOD	< LOD	17594,65	< LOD	< LOD	53303,07	< LOD	258750,08	35421,72
228	132,2	366,73	192,46	116,32	8471,07	17028,81	< LOD	39,01	< LOD	< LOD	< LOD	< LOD	< LOD	< LOD	< LOD	< LOD	< LOD	10736,4	< LOD	24432,14	52392,43	818,32	224889,19	19275,43
229	132,3	305,84	35,83	41,88	3909,23	7873,63	< LOD	< LOD	< LOD	< LOD	< LOD	< LOD	< LOD	< LOD	< LOD	< LOD	< LOD	18068,27	< LOD	< LOD	25253,87	600,77	477857,13	< LOD
230	132,4	107,21	119,52	28,76	3648,11	16213,37	< LOD	9,77	< LOD	< LOD	< LOD	8,2	< LOD	< LOD	< LOD	< LOD	< LOD	19528,89	< LOD	24960,16	35220,32	< LOD	386214,56	15869,23
231	132,5	286,62	254,45	199,38	4978,17	10738	5,67	3,75	< LOD	< LOD	< LOD	< LOD	< LOD	< LOD	< LOD	< LOD	< LOD	22210,7	3938,27	23640,04	43048,45	< LOD	397495,78	28194,34
232	132,6	558,49	45,46	21,55	7942,87	20785,4	< LOD	< LOD	< LOD	< LOD	< LOD	9,19	< LOD	< LOD	3,08	< LOD	< LOD	27373,04	< LOD	< LOD	48786,39	931,61	438892,22	< LOD
233		1293,86	121,24	57,82	11847,64	9393,78	23,13	< LOD	< LOD	< LOD	< LOD	< LOD	75,97	< LOD	4,49	< LOD	< LOD	8885,85	< LOD	< LOD	35197,39	< LOD	310128,41	< LOD
234	132,7	33,89	133,07	28,74	1666,28	4039,56	< LOD	< LOD	< LOD	< LOD	< LOD	10,54	< LOD	< LOD	< LOD	< LOD	< LOD	13028,49	99315,55	< LOD	19257,33	2423,1	367217,13	< LOD

Table 8.27: Handheld XRF measurements from box 24 of drill core BH4508 at Hellerfjellet.

Point	Meters	Cu	Zn	Pb	Ba	Fe	Ag	Mo	Sb	Sn	Cd	As	Ni	Co	Se	Bi	Mn	S	Ca	K	Al	P	Si	Mg
K24	ppm	ppm	ppm	ppm	ppm	ppm	ppm	ppm	ppm	ppm	ppm	ppm	ppm	ppm	ppm	ppm	ppm	ppm	ppm	ppm	ppm	ppm	ppm	ppm
235	132,8	3142,46	669,38	50,18	8340,44	11432,44	86,23	< LOD	< LOD	< LOD	< LOD	< LOD	< LOD	< LOD	< LOD	< LOD	< LOD	15861,22	< LOD	< LOD	30694,12	760,86	406972,28	< LOD
236	132,9	292,27	583,4	290,06	3205,1	10378,98	8,79	4,92	< LOD	< LOD	9,05	< LOD	< LOD	< LOD	< LOD	< LOD	< LOD	12135,9	25336,86	< LOD	20228,76	859,01	529568,75	< LOD
237	133	449,47	253,27	26,22	8872,86	15019,3	< LOD	22,28	< LOD	< LOD	< LOD	< LOD	< LOD	< LOD	< LOD	< LOD	< LOD	10175,13	15479,83	< LOD	51425,46	1564,28	339628,34	< LOD
238	133,1	387,62	140,95	61,84	7426,74	33700,5	< LOD	21,84	< LOD	< LOD	< LOD	< LOD	74,8	< LOD	4,91	< LOD	< LOD	29928,67	22631,21	< LOD	89786,89	1509,85	381201,5	< LOD
239	133,2	481,9	129,7	35,1	4269,75	22051,52	< LOD	9,6	< LOD	< LOD	< LOD	< LOD	< LOD	< LOD	4,89	< LOD	< LOD	18686,58	25052,23	< LOD	61680,46	766,19	374375,91	< LOD
240	133,3	417,62	173,1	31,62	3049,25	29045,66	< LOD	22,39	< LOD	< LOD	< LOD	< LOD	< LOD	160,07	3,62	< LOD	< LOD	27735,11	24975,98	< LOD	62117,96	1835,02	382866,56	< LOD
241	133,4	627,36	208,74	40,41	4496,77	33985,93	< LOD	24,26	< LOD	< LOD	< LOD	6,75	44,56	< LOD	3,01	< LOD	< LOD	28840,27	16748,71	< LOD	62555,88	890,81	389147,91	< LOD
242	133,5	182,93	85,72	60,25	1076,99	22196,92	< LOD	26,97	< LOD	< LOD	< LOD	< LOD	< LOD	< LOD	< LOD	< LOD	< LOD	27119,27	39693,82	< LOD	55550,34	2271,86	389051,72	17386,67
243	133,6	439,93	279,55	28,09	2830,05	39232,61	< LOD	22,13	< LOD	< LOD	< LOD	< LOD	< LOD	< LOD	< LOD	< LOD	< LOD	41242,05	18801	< LOD	42166,66	2157,53	408426,47	23887,88
244	133,7	879,83	65,11	108,81	4770,15	24535,61	< LOD	45,08	< LOD	< LOD	< LOD	< LOD	< LOD	< LOD	3,49	< LOD	< LOD	35002,08	19302,72	< LOD	58740,37	623,39	386484,31	< LOD
245	133,8	1097,12	120,17	26,07	7478,85	32616,28	< LOD	40,43	< LOD	< LOD	< LOD	< LOD	< LOD	< LOD	8,04	< LOD	< LOD	30820,98	31503,92	< LOD	72015,04	1551,17	347773,97	< LOD
246	133,9	628,34	229,2	17,33	11218,46	32745,55	< LOD	34,18	< LOD	< LOD	< LOD	9,18	77,81	< LOD	6,38	< LOD	< LOD	31137,54	8842,88	< LOD	81737,05	< LOD	369746,03	< LOD
247	134	503,38	13694,91	2534,08	14325,54	50804,69	14,2	33,49	< LOD	38,24	105,51	< LOD	< LOD	< LOD	9,88	< LOD	< LOD	64448,09	19252,28	< LOD	67670,4	< LOD	432287,72	< LOD
248	134,1	873,05	85227,42	16804,18	15063,93	38620,02	83,82	35,04	78,05	111,46	437,78	< LOD	< LOD	< LOD	33,57	< LOD	< LOD	99330,05	26237,75	< LOD	78375,45	< LOD	290342,13	< LOD
249	134,2	674,79	209,88	21,98	7648,97	24961,77	< LOD	26,8	< LOD	< LOD	< LOD	12,34	67,67	190,44	3,18	< LOD	< LOD	19066,43	28464,34	< LOD	77820,98	806,64	329619,91	< LOD
250	134,3	375,44	524,23	27,56	1165,43	30633,67	< LOD	11,6	< LOD	< LOD	< LOD	< LOD	< LOD	< LOD	4,86	< LOD	< LOD	32503,92	33772,54	< LOD	61524,74	1773,85	326437,69	36648,23
251	134,4	182,68	144,27	31,28	1059,18	23120,42	< LOD	10,49	< LOD	< LOD	< LOD	< LOD	< LOD	< LOD	< LOD	< LOD	< LOD	18336,74	27577,51	25916,41	61508,38	1080,45	357103,72	< LOD
252		60,28	93,3	20,36	623,23	12862,14	< LOD	7,03	< LOD	< LOD	< LOD	< LOD	< LOD	125,84	< LOD	< LOD	< LOD	21339,75	19558,21	26033,45	42304,71	666,02	407858,72	< LOD
253	134,5	105,62	502,46	12,43	696,1	26782,55	< LOD	10,49	< LOD	< LOD	< LOD	< LOD	< LOD	< LOD	< LOD	< LOD	< LOD	18567,54	36822,85	38333,3	51375,68	< LOD	361625,56	20421,35
254	134,6	36,77	150,37	41,37	503,28	27593,71	< LOD	< LOD	< LOD	< LOD	< LOD	< LOD	< LOD	< LOD	< LOD	< LOD	< LOD	24850,89	77754,83	26385,31	62364,59	553,47	293064,78	< LOD
255	134,8	34,01	161,73	10,69	623,09	26318,71	< LOD	8,5	< LOD	< LOD	< LOD	5,31	< LOD	< LOD	< LOD	< LOD	< LOD	27748,74	11632,77	36711,56	52547,43	561,59	389058,19	< LOD
256	135	37,78	213,54	27,67	645,43	36565,41	< LOD	4,88	< LOD	< LOD	< LOD	< LOD	< LOD	201,23	3,84	< LOD	< LOD	18825,26	24818,28	33992,71	69048,96	602,71	335322,88	< LOD
257	135,2	63,68	209,38	28,86	426,72	40168,51	< LOD	5,53	< LOD	< LOD	< LOD	6,55	< LOD	< LOD	< LOD	< LOD	< LOD	29200,56	31547,65	< LOD	50684,63	< LOD	386661,53	16324,64
258	135,4	41,28	261,08	25,4	605,97	44011,6	< LOD	3,4	< LOD	< LOD	< LOD	6,58	< LOD	< LOD	3,38	< LOD	< LOD	26017,47	41003,12	< LOD	66882,29	1264,75	352281,81	< LOD
259	135,6	32,3	14,14	< LOD	133,11	945,91	< LOD	< LOD	< LOD	< LOD	< LOD	< LOD	< LOD	< LOD	< LOD	< LOD	< LOD	15788,92	35414,1	< LOD	4337,48	575,71	444573,19	< LOD
260	135,8	< LOD	124,9	24,43	219,89	26841,22	< LOD	< LOD	< LOD	< LOD	< LOD	< LOD	< LOD	< LOD	< LOD	< LOD	< LOD	18287,49	56015,23	< LOD	39345,46	749,2	354209,28	< LOD
261	136	38,63	178,57	16,51	869,62	50045,79	< LOD	5,55	< LOD	< LOD	< LOD	7,69	48,86	< LOD	< LOD	< LOD	< LOD	24281,82	29657,13	41733,42	76375,95	< LOD	308360,63	16298,42
262	137,2	37,31	184,31	21,38	527,64	41049,83	< LOD	< LOD	< LOD	< LOD	< LOD	< LOD	< LOD	< LOD	< LOD	< LOD	< LOD	13359,56	128123,9	< LOD	55951,68	1061,56	280853,38	< LOD
263	137,4	18,61	86,49	16,99	533,9	24818,36	< LOD	< LOD	< LOD	< LOD	< LOD	< LOD	< LOD	< LOD	< LOD	< LOD	< LOD	10917	120970,7	< LOD	34229,72	625,96	341267,69	18619,42
264	137,6	< LOD	33,87	< LOD	184,54	8049,87	< LOD	< LOD	< LOD	< LOD	< LOD	< LOD	< LOD	< LOD	< LOD	< LOD	< LOD	19622,95	13163,79	< LOD	10364,45	< LOD	453277,31	< LOD
265	137,8	37,64	108,98	32,67	434,6	23235,57	< LOD	11,86	< LOD	< LOD	< LOD	< LOD	< LOD	< LOD	< LOD	< LOD	< LOD	13912,87	75148,84	< LOD	49405,31	1166,45	386880,56	12009,37
266	138,1	82,13	109,61	68,92	448,3	44500,98	< LOD	< LOD	< LOD	< LOD	< LOD	< LOD	< LOD	< LOD	< LOD	< LOD	< LOD	31050,14	159962,9	< LOD	91724,45	1965,16	224743,91	< LOD
267	138	45,32	58,59	6,18	718,37	18075,6	< LOD	6,9	< LOD	< LOD	< LOD	4,52	< LOD	< LOD	< LOD	< LOD	< LOD	29327,79	8103,52	23379,03	39088,75	< LOD	443597,03	15709,57
268	138,2	21,76	108,22	16,34	888,28	14985,11	< LOD	7,52	< LOD	< LOD	< LOD	< LOD	< LOD	< LOD	< LOD	< LOD	< LOD	23646,76	14610,73	24974,89	53060,04	< LOD	403195,31	< LOD
269	138,4	< LOD	97,73	13,15	626,3	16095,79	< LOD	< LOD	< LOD	< LOD	< LOD	< LOD	< LOD	< LOD	< LOD	< LOD	< LOD	32955,95	20955,68	24714,51	43409,61	< LOD	398008,63	< LOD
270	138,6	51,43	178,32	26,69	799,34	26099,25	< LOD	5,51	< LOD	< LOD	< LOD	< LOD	< LOD	< LOD	< LOD	< LOD	< LOD	37197,96	23519,52	27588,3	66283,21	< LOD	350832,09	19468,31
271	138,8	32,55	79,57	< LOD	707,95	19670,22	< LOD	12,14	< LOD	< LOD	< LOD	< LOD	< LOD	< LOD	< LOD	< LOD	< LOD	32089,87	8456,46	22774,42	39903,42	< LOD	428723,44	< LOD
272	139	20,51	169,85	37,81	356,66	20587,12	< LOD	< LOD	< LOD	< LOD	< LOD	< LOD	< LOD	< LOD	< LOD	< LOD	< LOD	13033,89	68790,17	< LOD	50783,76	2280,63	331479,59	13129,83
273	139,2	43,27	298,25	36,85	961,83	40909,1	< LOD	< LOD	< LOD	< LOD	< LOD	< LOD	< LOD	< LOD	< LOD	< LOD	2645,35	19051,46	154854,3	25086,75	49987,23	< LOD	220382,52	19203,03
274	139,3	18,66	86,34	19,86	603,45	14821,33	< LOD	< LOD	< LOD	< LOD	< LOD	< LOD	< LOD	< LOD	< LOD	< LOD	< LOD	9009,67	28162,43	< LOD	50886,13	< LOD	417399,75	< LOD

Simon Fredrik Gundersen

Structural controls on selected sulphide deposits in the Møfjellet Group

NTNU
Kunnskap for en bedre verden